Accelerator Physics

Second Edition

of low-emittance electron storage rings. Since this is a textbook on basic accelerator physics, topics such as nonlinear beam dynamics, collective beam instabilities, etc., are mentioned only briefly, in Chapters 2 and 3.

Attention is paid to deriving the action-angle variables of the phase space coordinates because the transformation is basic and the concept is important in understanding the phenomena of collective instability and nonlinear beam dynamics. In the design of synchrotrons, the dispersion function plays an important role in particle stability, beam performance, and beam transport. An extensive section on the dispersion function is provided in Chapter 2. This function is also important in the design of low-emittance electron storage ring lattices.

The SI units are used throughout this book. I have also chosen the engineer's convention of $j = -i$ for the imaginary number. The exercises in each section are designed to have the student apply a specific technique in solving an accelerator physics problem. By following the steps provided in the homework, each exercise can be easily solved.

The field of accelerator physics and technology is multi-disciplinary. Many related subjects are not extensively discussed in this book: linear accelerators, induction linacs, high brightness beams, collective instabilities, nonlinear dynamics, beam cooling physics and technology, linear collider physics, free-electron lasers, electron and ion sources, neutron spallation sources, muon colliders, high intensity beams, vacuum technology, superconductivity, magnet technology, instrumentation, etc. Nevertheless, the book should provide the understanding of basic accelerator physics that is indispensable in accelerator physics and technology research.

S.Y. Lee
Bloomington, Indiana, U.S.A.
January, 1998

Contents

Preface vii

Preface to the first edition ix

1 Introduction 1
- I Historical Developments 4
  - I.1 Natural Accelerators 5
  - I.2 Electrostatic Accelerators 6
  - I.3 Induction Accelerators 6
  - I.4 Radio-Frequency (RF) Accelerators 9
  - I.5 Colliders and Storage Rings 17
  - I.6 Synchrotron Radiation Storage Rings 18
- II Layout and Components of Accelerators 19
  - II.1 Acceleration Cavities 19
  - II.2 Accelerator Magnets 20
  - II.3 Other Important Components 22
- III Accelerator Applications 23
  - III.1 High Energy and Nuclear Physics 23
  - III.2 Solid-State and Condensed-Matter Physics 24
  - III.3 Other Applications 24
  - Exercise 24

2 Transverse Motion 35
- I Hamiltonian for Particle Motion in Accelerators 36
  - I.1 Hamiltonian in Frenet-Serret Coordinate System 37
  - I.2 Magnetic Field in Frenet-Serret Coordinate System 39
  - I.3 Equation of Betatron Motion 41
  - I.4 Particle Motion in Dipole and Quadrupole Magnets 41
  - Exercise 42
- II Linear Betatron Motion 47
  - II.1 Transfer Matrix and Stability of Betatron Motion 47
  - II.2 Courant–Snyder Parametrization 51
  - II.3 Floquet Transformation 52

II.4 Action-Angle Variable and Floquet Transformation 57
II.5 Courant–Snyder Invariant and Emittance 60
II.6 Stability of Betatron Motion: A FODO Cell Example 65
II.7 Symplectic Condition 66
II.8 Effect of Space-Charge Force on Betatron Motion 67
Exercise 73
III Effect of Linear Magnet Imperfections 85
III.1 Closed-Orbit Distortion due to Dipole Field Errors 85
III.2 Extended Matrix Method for the Closed Orbit 91
III.3 Application of Dipole Field Error 92
III.4 Quadrupole Field (Gradient) Errors 101
III.5 Basic Beam Observation of Transverse Motion 105
III.6 Application of quadrupole field error 108
III.7 Transverse Spectra 110
III.8 Beam Injection and Extraction 115
III.9 Mechanisms of emittance dilution and diffusion 117
Exercise 121
IV Off-Momentum Orbit 129
IV.1 Dispersion Function 129
IV.2 $\mathcal{H}$-Function, Action, and Integral Representation 133
IV.3 Momentum Compaction Factor 136
IV.4 Dispersion Suppression and Dispersion Matching 139
IV.5 Achromat Transport Systems 141
IV.6 Transport Notation 143
IV.7 Experimental Measurements of Dispersion Function 145
IV.8 Transition Energy Manipulation 146
A. γ_T jump schemes 146
B. Flexible momentum compaction (FMC) lattices 149
C. Other similar FMC modules 155
D. FMC in double-bend (DB) lattices 156
IV.9 Minimum $\langle\mathcal{H}\rangle$ Modules 157
Exercise 161
V Chromatic Aberration 172
V.1 Chromaticity Measurement and Correction 173
V.2 Nonlinear Effects of Chromatic Sextupoles 178
V.3 Chromatic Aberration and Correction 178
V.4 Lattice Design Strategy 183
Exercise 184
VI Linear Coupling 186
VI.1 The Linear Coupling Hamiltonian 186
VI.2 Effects of an isolated Linear Coupling Resonance 189
VI.3 Experimental Measurement of Linear Coupling 193
VI.4 Linear Coupling Correction with Skew Quadrupoles 196
VI.5 Linear Coupling Using Transfer Matrix Formalism 197
Exercise 197
VII Nonlinear Resonances 202
VII.1 Nonlinear Resonances Driven by Sextupoles 202
VII.2 Higher-Order Resonances 209
VII.3 Nonlinear Detuning from Sextupoles 211
VII.4 Betatron Tunes and Nonlinear Resonances 212
Exercise 213
VIII Collective Instabilities and Landau Damping 216
VIII.1 Impedance 216
VIII.2 Transverse Wave Modes 220
VIII.3 Effect of Wakefield on Transverse Wave 221
VIII.4 Frequency Spread and Landau Damping 225
Exercise 228
IX Synchro-Betatron Hamiltonian 232
Exercise 237

3 Synchrotron Motion **239**
I Longitudinal Equation of Motion 240
I.1 The Synchrotron Hamiltonian 244
I.2 The Synchrotron Mapping Equation 245
I.3 Evolution of Synchrotron Phase-Space Ellipse 246
I.4 Some Practical Examples 247
I.5 Summary of Synchrotron Equations of Motion 248
Exercise 249
II Adiabatic Synchrotron Motion 251
II.1 Fixed Points 252
II.2 Bucket Area 253
II.3 Small-Amplitude Oscillations and Bunch Area 255
II.4 Small-Amplitude Synchrotron Motion at the UFP 258
II.5 Synchrotron Motion for Large-Amplitude Particles 259
II.6 Experimental Tracking of Synchrotron Motion 261
Exercise 263
III RF Phase and Voltage Modulations 268
III.1 Normalized Phase-Space Coordinates 268
III.2 RF Phase Modulation and Parametric Resonances 271
III.3 Measurements of Synchrotron Phase Modulation 277
III.4 Effects of Dipole Field Modulation 280
III.5 RF Voltage Modulation 288
III.6 Measurement of RF Voltage Modulation 295
Exercise 297

IV Nonadiabatic and Nonlinear Synchrotron Motion . . . 301
IV.1 Linear Synchrotron Motion Near Transition Energy . . . 302
IV.2 Nonlinear Synchrotron Motion at $\gamma \approx \gamma_T$ . . . 305
IV.3 Beam Manipulation Near Transition Energy . . . 308
IV.4 Synchrotron Motion with Nonlinear Phase Slip Factor . . . 309
IV.5 The QI Dynamical Systems . . . 312
Exercise . . . 315
V Beam Manipulation in Synchrotron Phase Space . . . 317
V.1 RF Frequency Requirements . . . 318
V.2 Capture and Acceleration of Proton and Ion Beams . . . 320
V.3 Bunch Compression and Rotation . . . 322
V.4 Debunching . . . 326
V.5 Beam Stacking and Phase Displacement Acceleration . . . 326
V.6 Double rf Systems . . . 327
V.7 The Barrier RF Bucket . . . 334
Exercise . . . 340
VI Fundamentals of RF Systems . . . 343
VI.1 Pillbox Cavity . . . 343
VI.2 Low Frequency Coaxial Cavities . . . 345
VI.3 Beam Loading . . . 353
VI.4 Beam Loading Compensation and Robinson Instability . . . 356
Exercise . . . 359
VII Longitudinal Collective Instabilities . . . 362
VII.1 Longitudinal Spectra . . . 363
VII.2 Collective Microwave Instability in Coasting Beams . . . 367
VII.3 Longitudinal Impedance . . . 369
VII.4 Microwave Single Bunch Instability . . . 373
Exercise . . . 381
VIII Introduction to Linear Accelerators . . . 383
VIII.1 Historical Milestones . . . 383
VIII.2 Fundamental Properties of Accelerating Structures . . . 387
A. Transit time factor . . . 387
B. Shunt impedance . . . 388
C. The quality factor Q . . . 388
VIII.3 Particle Acceleration by EM Waves . . . 389
A. EM waves in a cylindrical wave guide . . . 390
B. Phase velocity and group velocity . . . 391
C. TM modes in a cylindrical pillbox cavity . . . 392
D. Alvarez structure . . . 395
E. Loaded wave guide chain and the space harmonics . . . 396
F. Standing wave, traveling wave, and coupled cavity linacs . . . 399
G. HOMs . . . 401
VIII.4 Longitudinal Particle Dynamics in a Linac . . . 402
VIII.5 Transverse Beam Dynamics in a Linac . . . 407
Exercise . . . 410

4 Physics of Electron Storage Rings **417**
I Fields of a Moving Charged Particle . . . 422
I.1 Non-relativistic Reduction . . . 424
I.2 Radiation Field for Particles at Relativistic Velocities . . . 424
I.3 Frequency and Angular Distribution . . . 427
I.4 Quantum Fluctuation . . . 433
Exercise . . . 435
II Radiation Damping and Excitation . . . 437
II.1 Damping of Synchrotron Motion . . . 438
II.2 Damping of Betatron Motion . . . 441
II.3 Damping Rate Adjustment . . . 445
II.4 Radiation Excitation and Equilibrium Energy Spread . . . 448
II.5 Radial Bunch Width and Distribution Function . . . 453
II.6 Vertical Beam Width . . . 455
II.7 Radiation Integrals . . . 456
II.8 Beam Lifetime . . . 456
Exercise . . . 462
III Emittance in Electron Storage Rings . . . 466
III.1 Emittance of Synchrotron Radiation Lattices . . . 467
A. FODO cell lattice . . . 467
B. Double-bend achromat (Chasman-Green lattice) . . . 469
C. Minimum $\langle\mathcal{H}\rangle$-function lattice . . . 473
D. Minimizing emittance in a combined function DBA . . . 475
E. Three-bend achromat . . . 476
III.2 Insertion Devices . . . 478
III.3 Beam Physics of High Brightness Storage Rings . . . 486
Exercise . . . 489

5 Special Topics in Beam Physics **497**
I Free Electron Laser (FEL) . . . 498
I.1 Small Signal Regime . . . 500
I.2 Interaction of the Radiation Field with the Beam . . . 506
I.3 Experiments on High Gain FEL Generation . . . 509
Exercise . . . 510
II Beam-Beam Interaction . . . 513
II.1 The beam-beam force . . . 517
II.2 The Coherent Beam-Beam Effects . . . 519
II.3 Nonlinear Beam-Beam Effects . . . 521

II.4 Experimental Observations and Numerical Simulations 522
II.5 Beam-Beam Interaction in Linear Colliders 525
Exercise 527

A Basics of Classical Mechanics **533**
I Hamiltonian Dynamics 533
I.1 Canonical Transformations 533
I.2 Fixed Points 534
I.3 Poisson Bracket 534
I.4 Liouville Theorem 535
I.5 Floquet Theorem 536
II Stochastic Beam Dynamics 537
II.1 Central Limit Theorem 537
II.2 Langevin Equation of Motion 538
II.3 Stochastic Integration Methods 539
II.4 Fokker-Planck Equation 541

B Numerical Methods and Physical Constants **543**
I Fourier Transform 543
I.1 Nyquist Sampling Theorem 544
I.2 Discrete Fourier Transform 544
I.3 Digital Filtering 545
I.4 Some Simple Fourier Transforms 546
II Model Independent Analysis 546
II.1 Model Independent Analysis 547
II.2 Independent Component Analysis 548
II.3 Accelerator Modeling 549
III Cauchy Theorem and the Dispersion Relation 549
III.1 Cauchy Integral Formula 549
III.2 Dispersion Relation 550
IV Useful Handy Formulas 551
IV.1 Generating functions for the Bessel functions 551
IV.2 The Hankel transform 551
IV.3 The complex error function 551
IV.4 A multipole expansion formula 552
IV.5 Cylindrical Coordinates 552
IV.6 Gauss' and Stokes' theorems 553
IV.7 Vector Operation 553
V Maxwell's equations 553
V.1 Lorentz Transformation of EM fields 554
V.2 Cylindrical waveguides 554
V.3 Voltage Standing Wave Ratio 556

VI Physical Properties and Constants 557

Bibliography **561**

Index **563**

Symbols and Notations **571**

Acknowledgments

I would like to thank students and colleagues, particularly D. Li, H. Huang, X. Kang, M. Ellison, K.M. Fung, M. Bai, A. Riabko, who helped me polish the lecture notes into a book form. I would like to thank S. Cousineau, C. Beltran, S. Breitzmann, W. Guo, X. Huang, V. Ranjbar, and Y. Zhang, who made many useful suggestions to this revised edition. I would like to thank Angela Bellavance for pointing out mis-prints during a USPAS program in 2001. During the course of this work, I have benefited greatly from the collaboration with Drs. David Caussyn, Y. Wang, D. Jeon, K.Y. Ng, Y. Yan and Prof. A. Chao. I owe special thanks to Margaret Dienes for editing the first edition of this book. I owe special thanks to Prof. Jau-Jiun Hsiao for making critical suggestions to the new chapter in this revised edition. The responsibility for all errors lies with me. Your comments and corrections will be highly appreciated.

Chapter 1

Introduction

The first accelerator dates back to prehistoric-historic times, when men built bows and arrows for hunting. The race to build modern particle accelerators began in 1911 when Rutherford discovered the nucleus by scattering α-particles off Aluminum foil. The physics and technology of accelerators and storage rings involves many branches of science. These include electromagnetism, solid-state properties of materials, atomic physics, superconductivity,[1] nonlinear mechanics, spin dynamics, plasma physics, and quantum physics. In recent years, accelerators have found many applications: they are used in nuclear and particle physics research, in industrial applications such as ion implantation and lithography, in biological and medical research with synchrotron light sources, in material science and medical research with spallation neutron sources, etc. Accelerators have also been used for radiotherapy, food sterilization, waste treatment, etc.

A major application of particle accelerators is experimental nuclear and particle physics research. Advances in technology have allowed remarkable increases in energy and luminosity[2] for fundamental physics research. High energy was measured in MeV's in the 1930's, and is measured in TeV's in the 1990's. The beam intensity was about 10^9 particles per pulse (ppp) in the 1950's, and is about 10^{14} ppp in the 1990's. Since 1970, high energy and high luminosity colliders have become basic tools in nuclear and particle physics research. As physicists probe deeper into the inner structure of matter, high energy provides new territory for potential discoveries, and indeed new energy frontiers usually lead to new physics discoveries. The evolution of

[1] Superconductivity was discovered by Heike Kamerlingh Onnes in 1911. The Meissner effect was discovered in 1933. Understanding of the microscopic basis of superconductivity was achieved by John Bardeen, Leon Cooper, and Robert Schrieffer in 1957. High temperature superconductor was discovered by K.A. Mueller and J.G. Bednorz in 1986. Fine meshed superconducting wires are usually used in high-field magnets. Superconducting thin films deposited on the cavity surface are used for superconducting cavities.

[2] The luminosity $\mathcal{L}$ is defined as the probability of particle encountering rate per unit area in a collision process (see Exercise 1.7). The commonly used dimension is $\text{cm}^{-2}\ \text{s}^{-1}$. The counting rate in a detector is given by $\mathcal{L}\sigma$, where σ is the cross-section of a reaction process.

accelerator development can be summarized by the Livingston chart shown in Fig. 1.1, where the equivalent fixed target proton energy, $KE = s/(2m_pc^2)$ (see Exercise 1.6), is plotted as a function of time.

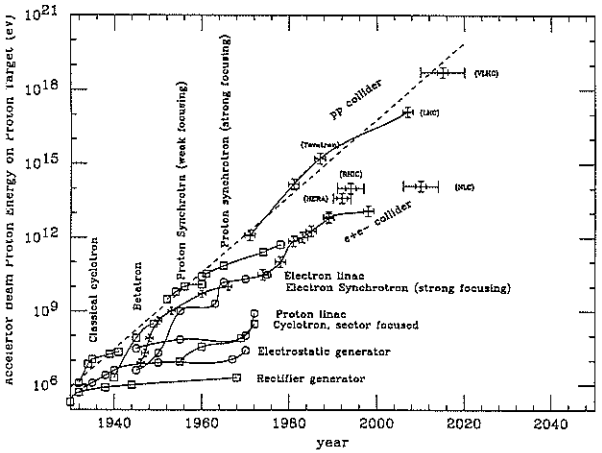

Figure 1.1: The Livingston Chart: The equivalent fixed target proton beam energy versus time in years. Note that innovative ideas provide substantial jump in beam energy. The dashed line is drawn to guide the trend, which is beam energy doubling in every two years.

In recent years, high-brilliance photon beams from high-brightness electron beams in storage rings[3] have been extensively used in biomedical and condensed-matter physics research. Figure 1.2 shows the peak photon brilliance (number of photons/(mm^2 mrad^2 s (0.1% $\Delta\omega/\omega$)) as a function of photon beam energy from storage rings and linacs.

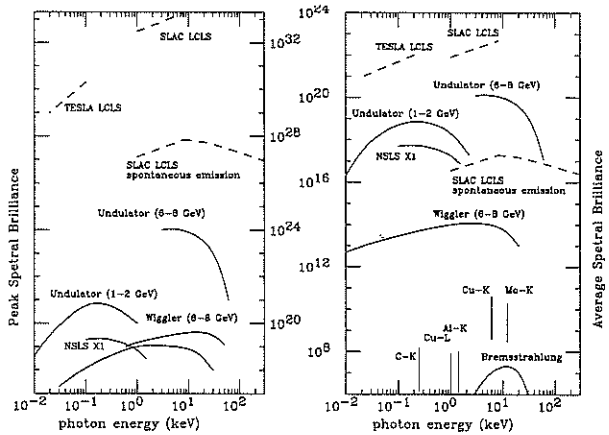

Figure 1.2: The peak and average Photon Brilliance defined as photons/(mm^{2}mrad^{2}s (0.1%$\Delta\omega/\omega$)) is plotted as a function photon beam energy generated by high quality electron beams in storage rings and in linacs.

Besides being used for fundamental material science research, high-intensity neutron sources driven by powerful proton beam sources may provide energy amplification for future global energy needs. High intensity heavy-ion beams have also been actively pursued for inertial fusion evaluation.

[3]The brightness of a beam is defined as the beam's intensity divided by its phase-space volume.

Frontiers in accelerator physics and technology research

Accelerator physics is a branch of applied science. Innovations in technology give rise to new frontiers in beam physics research. Since higher energy leads to new discoveries, and higher luminosity leads to higher precision in experimental results, the frontiers of accelerator physics research are classified into the frontiers of high energy and high brightness. Some of these topics in beam physics are as follows.

- High energy: For high energy hadron accelerators such as the Tevatron at Fermilab, the Large Hadron Collider (LHC) at CERN, and the contemplated Very Large Hadron Collider (VLHC), high-field superconducting magnets and the stability of high-brightness beams are important issues. For lepton colliders, high acceleration gradient structures, wakefields, and high power rf sources are important. Some proposed e^+e^- colliders are the Next Linear Collider (NLC), the Japan Linear Collider (JLC), the CERN Linear Collider (CLIC), and the TeV Superconducting Linear Accelerator (TESLA), which employs superconducting rf cavities. Current research topics include high rf power sources, high acceleration gradients, wakefield control, etc.
- High luminosity: To provide a detailed understanding of CP violation and other fundamental symmetry principles of interactions, dedicated meson factories such as the Φ-factory at Frascati National Laboratory in Italy and the B-factories at SLAC and Cornell in the U.S. and at KEK in Japan were built in the 1990's, and the Tau-Charm factory is being contemplated in Beijing, China. Since the neutron flux from spallation neutron sources is proportional to the proton beam power, physics and technology for high-intensity low-loss proton sources are important.[4] Furthermore, a high-intensity proton source can be used to drive secondary beams such as kaons, pions, and muons. With high-intensity μ beams, $\mu^+\mu^-$ collider studies are also of current interest.
- High-brightness beams: Beam-cooling techniques have been extensively used in attaining high-brightness hadron beams. Stochastic cooling has been successfully applied to accumulate anti-protons. This led to the discovery of W and Z bosons, and b and t quarks. Electron cooling and laser cooling have been applied to many low energy storage rings used in atomic and nuclear physics research. Ionization cooling is needed for muon beams in $\mu^+\mu^-$ colliders. Taking advantage of radiation cooling, synchrotron light sources with high-brightness electron beams are used in medical, biological, and condensed-matter physics

[4]See e.g., the *National Spallation Neutron Source Design Report* (Oak Ridge, 1997).

research. Sub-picosecond photon beams would be important to time-resolved experiments. A high power tunable free-electron laser would be useful for chemical and technical applications.

- Accelerator applications: The medical use of accelerators for radiation treatment,[5] isotope production, sterilization of medical tools, etc., requires safety, reliability, and ease in operation. Higher beam power density with minimum beam loss can optimize safety in industrial applications such as ion implantation, electron-beam welding, material testing, food sterilization, etc.

Recent research topics in accelerator physics include beam cooling, nonlinear beam dynamics, beam-beam interactions, collective beam instability, beam manipulation techniques, ion sources, space-charge effects, beam instrumentation development, novel acceleration techniques, etc. Accelerator technology research areas include superconducting materials, high power rf sources, high gradient accelerating structures, etc. This book deals only with the fundamental aspects of accelerator physics. It serves as an introduction to more advanced topics such as collective beam instabilities, nonlinear beam dynamics, beam-cooling physics and technologies, rf physics and technology, magnet technology, etc. First, the technical achievements in accelerator physics of past decades will be described.

I Historical Developments

A charged particle with charge q and velocity $\vec{v}$ in the electromagnetic fields $(\vec{E}, \vec{B})$ is exerted by the Lorentz's force $\vec{F}$:

$$\vec{F} = q(\vec{E} + \vec{v} \times \vec{B}). \tag{1.1}$$

The charge particle can only gain or lose its energy by its interaction with the electric field $\vec{E}$. Since the magnetic force is perpendicular to both $\vec{v}$ and $\vec{B}$, the charged particle will move on a circular arc. In particular, when the magnetic flux density is perpendicular to $\vec{v}$, the bending radius is

$$\rho = \frac{mv}{qB} = \frac{p}{qB}, \tag{1.2}$$

where m and $p = mv$ are the mass and momentum of the particle. The **momentum rigidity** of the charged particle is

$$B\rho\ [\mathrm{T-m}] = \frac{p}{q} = \frac{A}{Z} \times 3.33564 \times p\ [\mathrm{GeV/c/u}], \tag{1.3}$$

[5]See e.g., P.L. Petti and A.J. Lennox, ARNS **44**, 155 (1994).

where $B\rho$ is measured in Tesla-meter, and the momentum is measured in GeV/c per amu, and A and Ze are the atomic mass number and charge of the particle.

Accelerators are composed of ion sources, cavity and magnet components that can generate and maintain electromagnetic fields for beam acceleration and manipulation, devices to detect beam motion, high vacuum components for attaining excellent beam lifetime, undulators and wigglers to produce high brilliance photon beam, targets for producing secondary beams, etc. Accelerators can be classified as linear or circular, electrostatic or radio frequency, continuous (CW, DC or coasting beam) or bunched and pulsed. They are designed to accelerate electrons (leptons) or hadrons, stable or radioactive ions. Accelerators are classified as follows, in no specific chronological order.

I.1 Natural Accelerators

Radioactive accelerators

In 1911, Rutherford employed α particles escaping the Coulomb barrier of Ra and Th nuclei to investigate the inner structure of atoms.[6] He demonstrated, to the surprise of many physicists, the existence of a positively charged nucleus with a diameter less than 10^{-11} cm. This led to the introduction of Bohr's atomic model, and the revolution of quantum mechanics in the early 20th century. In 1919, Rutherford also used α particles to induce the first artificial nuclear reaction, $\alpha + {}_{14}\mathrm{N} \rightarrow {}_{17}\mathrm{O} + \mathrm{H}$. This discovery created an era of search for high-voltage sources for particle acceleration that can produce high-intensity high-energy particles for the study of nuclear transmutation.

Cosmic rays

Cosmic rays arise from galactic source accelerators. Nuclei range from n and H to Ni; heavy elements have been measured with energies up to 3×10^{20} eV.[7] Muons were discovered in cosmic-ray emulsion experiments in 1936 by C.D. Anderson, S.H. Neddermeyer, and others. Pions were discovered in 1947 in emulsion experiments. Interest in the relativistic heavy ion collider (RHIC) was amplified by the cosmic ray emulsion experiments.

[6]The kinetic energy of α particles that tunnel through the Coulomb barrier to escape the nuclear force is typically about 6 MeV.

[7]See J.A. Simpson, *Ann. Rev. Nucl. Sci.* **33**, 323 (1983) and R. Barnett *et al.*, *Phys. Rev.* (Particle Data Group) **D54**, 1 (1996). An event with energy 3×10^{20} eV had been recorded in 1991 by the Fly's Eye atmospheric-fluorescence detector in Utah (see *Physics Today*, p. 19, Feb. 1997; p. 31, Jan. 1998).

I.2 Electrostatic Accelerators

X-ray tubes

William David Coolidge in 1926 achieved 900-keV electron beam energy by using three X-ray tubes in series. The cascade type of X-ray tube is called the Coolidge tubes.

Cockcroft-Walton electrostatic accelerator

In 1930, John Douglas Cockcroft and Ernst Thomas Sinton Walton developed a high-voltage source by using high-voltage rectifier units. In 1932, they reached 400-kV terminal voltage to achieve the first man-made nuclear transmutation: $p + \mathrm{Li} \to 2\ \mathrm{He}$.[8] The maximum achievable voltage was limited to about 1 MV because of sparking in air. Since then, Cockcroft-Walton accelerators have been widely used in first-stage ion-beam acceleration. More recently, they are being replaced by more compact, economical, and reliable radio frequency quadrupole (RFQ) accelerators.

Van de Graaff and tandam accelerators

In 1931, R.J. Van de Graaff developed the electrostatic charging accelerator.[9] In the Van de Graaff accelerator, the rectifier units are replaced by an electrostatic charging belt, and the high-voltage terminal and the acceleration tube are placed in a common tank with compressed gas for insulation, which increases the peak acceleration voltage. Placement of the high-voltage terminal at the center of the tank and use of the charge-exchange process in the tandem accelerator can increase the beam energy for nuclei.[10] Today the voltage attained in tandem accelerators is about 25 MV. When the Van de Graaff accelerator is used for electron acceleration, it has the brand name Pelletron.

I.3 Induction Accelerators

According to Faraday's law of induction, when the magnetic flux changes, the induction electric field along a beam path is given by

$$\oint \mathcal{E} \cdot d\vec{s} = \dot{\Phi}, \qquad \Phi = \int_S \vec{B} \cdot d\vec{S}. \tag{1.4}$$

Here $\mathcal{E}$ is the induced electric field, Φ is the total magnetic flux, $d\vec{s}$ is the differential for the line integral that surrounds the surface area, $d\vec{S}$ is the differential for the surface integral, and $\vec{B}$ is the "magnetic field"[11] enclosed by the contour C. The induced electric field can be used for beam acceleration.

[8] J.D. Cockcroft and E.T.S. Walton, *Proc. Roy. Soc.* A**136**, 619 (1932); A**137**, 229 (1932); A**144**, 704 (1934). Cockcroft and Walton shared 1951 Nobel Prize in physics.

[9] R.J. Van de Graaff, J.G. Trump, and W.W. Buechner, *Rep. Prog. Phys.* **11**, 1 (1946).

[10] R.J. Van de Graaff, *Nucl. Inst. Methods* **8**, 195 (1960).

A: Induction linac

The induction linac was invented by N.C. Christofilos in the 50's for the acceleration of high-intensity beams.[12] A linear induction accelerator (LIA) employs a ferrite core arranged in a cylindrically symmetric configuration to produce an inductive load to a voltage gap. Each LIA module can be viewed as a low-Q 1:1 pulse transformer. When an external current source is discharged through the circuit, the electric field at the voltage gap along the beam axis is used to accelerate the beam. A properly pulsed stack of LIA modules can be used to accelerate high-intensity short-pulse beams with a gradient of about 1 MeV/m and a power efficiency of about 50%.[13] Table 1.1 lists the achievements of some LIA projects.

Table 1.1: Induction linac projects and achievements

Project	Laboratory	I (kA)	E (MeV)	Beam width (ns)	Repetition rate (Hz)
ETA II	LLNL	3	70	50	1
ETA III	LLNL	2	6	50	2000
ATA	LLNL	10	50	50	1000

B: Betatron

Let ρ be the mean radius of the beam pipe in a basic magnet configuration of a betatron. If the total magnetic flux enclosed by the beam circumference is ramped up by a time-dependent magnetic flux density, the induced electric field along the beam axis is given, according to Faraday's law of induction, by

$$\oint \mathcal{E} \cdot ds = 2\pi\rho\mathcal{E} = \pi\rho^2 \dot{B}_{\mathrm{av}}, \qquad \text{or} \qquad \mathcal{E} = \frac{1}{2}\dot{B}_{\mathrm{av}}\rho. \tag{1.5}$$

[11] We will use magnetic field as a synonym for magnetic flux density.

[12] See e.g., J.W. Beal, N.C. Christofilos and R.E. Hester, *IEEE Trans. Nucl. Sci.* NS **16**, 294 (1958) and references therein; Simon Yu, Review of new developments in the field of induction accelerators, in *Proc. LINAC96* (1996).

[13] See e.g., R.B. Miller, in *Proc. NATO ASI on High Brightness Transport in Linear Induction Accelerators*, A.K. Hyder, M.F. Rose, and A.H. Guenther, Eds. (Plenum Press, 1988); R.J. Briggs, *Phys. Rev. Lett.* **54**, 2588 (1985); D.S. Prono, *IEEE Trans. Nucl. Sci.* NS**32**, 3144 (1985); G.J. Caporaso, *et al.*, *Phys. Rev. Lett.* **57**, 1591 (1986); R.B. Miller, *IEEE Trans. Nucl. Sci.* NS**32**, 3149 (1985); G.J. Caporaso, W.A. Barletta, and V.K. Neil, *Part. Accel.* **11**, 71 (1980).

Here $\mathcal{E}$ is the induced electric field, and B_{av} is the average magnetic flux density inside the circumference of the beam radius. The final particle momentum can be obtained by integrating Newton's law, $\dot{p} = e\mathcal{E}$, i.e.

$$p = \frac{1}{2} e B_{av} \rho = e B_g \rho, \qquad \text{or} \qquad B_g = \frac{1}{2} B_{av}. \tag{1.6}$$

The betatron principle that *the guide field B_g is equal to 1/2 of the average field B_{av}*, was first stated by R. Wiederöe in 1928.[14] Figure 1.3 is a schematic drawing of a betatron, where particles circulate in the vacuum chamber with a guide field B_g, and the average flux density enclosed by the orbiting particle is B_{av}.

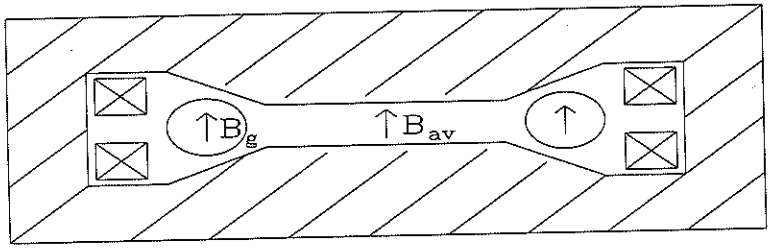

Figure 1.3: Schematic drawing of a betatron. The guide field for beam particles is B_g, and the average flux density enclosed by the orbiting path is B_{av}.

It took many years to understand the stability of transverse motion. This problem was solved in 1941 by D. Kerst and R. Serber.[15] When the magnetic field is shaped according to

$$B_z = B_0 \left(\frac{R}{r}\right)^n, \tag{1.7}$$

where R is the reference orbit radius, r is the beam radius, and n is the index of focusing given by (see Exercise 1.14)

$$n = -\frac{R}{B_0}\left(\frac{dB_z}{dr}\right)_{r=R}. \tag{1.8}$$

Let $x = r - R$ and z be small radial and vertical displacements from a reference orbit, then the equations of motion become

$$\frac{d^2 z}{dt^2} + \omega^2 n z = 0, \qquad \frac{d^2 x}{dt^2} + \omega^2 (1-n) x = 0. \tag{1.9}$$

[14] In 1922, Joseph Slepian patented the principle of applying induction electric field for electron beam acceleration in the U.S. patent 1645304.

[15] D. Kerst and R. Serber, *Phys. Rev.* **60**, 53 (1941). See also Exercise 1.14. Since then, the transverse particle motion in all types of accelerators has been called *betatron motion*.

Thus the motion is stable if $0 \le n \le 1$. The resulting frequencies of harmonic oscillations are $f_x = f_0\sqrt{1-n}$ and $f_z = f_0\sqrt{n}$, where $f_0 = \omega/2\pi$ is the revolution frequency.

In 1940 D. Kerst was the first to operate a betatron to achieve 2.3 MeV. In 1949 he constructed a 315-MeV betatron[16] at the University of Chicago with the parameters $\rho = 1.22$ m, $B_g = 9.2$ kG, $E_{inj} = 80 - 135$ keV, $I_{inj} = 13$ A. The magnet weighed about 275 tons and the repetition rate was about 6 Hz. The limitations of the betatron principle are (1) synchrotron radiation loss (see Chapter 4) and (2) the transverse beam size limit due to the intrinsic weak-focusing force.

I.4 Radio-Frequency (RF) Accelerators

Since the high-voltage source can induce arcs and corona discharges, it is difficult to attain very high voltage in a single acceleration gap. It would be more economical to make the charged particles pass through the acceleration gap many times. This concept leads to many different rf accelerators,[17] which can be classified as linear (RFQ, linac) and cyclic (cyclotron, microtron, and synchrotron). Accelerators using an rf field for particle acceleration are described in the following subsections.

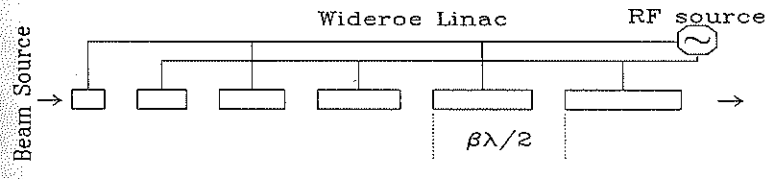

Figure 1.4: Schematic drawing of the Wiederöe rf LINAC structure. Wideröe used a 1-MHz, 25-kV oscillator to make 50-kV potassium ions.

A. LINAC

In 1925 G. Ising pointed out that particle acceleration can be achieved by using an alternating radio-frequency field. In 1928 R. Wiederöe reported the first working rf accelerator, using a 1-MHz, 25-kV oscillator to produce 50-kV potassium ions (see Fig. 1.4). In 1931 D.H. Sloan and E.O. Lawrence built a linear accelerator using a 10-MHz, 45 kV oscillator to produce 1.26 MV Hg^+ ion.[18] An important milestone

[16] D.W. Kerst *et. al.*, Phys. Rev. **78**, 297 (1950).

[17] The rf sources are classified into VHF, UHF, microwave, and millimeter waves bands. The microwave bands are classified as follows: L band, 1.12-1.7 GHz; S band, 2.6-3.95 GHz; C band, 3.95-5.85 GHz; X band, 8.2-12.4 GHz; K band, 18.0-26.5 GHz; millimeter wave band, 30-300 GHz. See also Exercise 1.2.

[18] D.H. Sloan and E.O. Lawrence, *Phys. Rev.* **38**, 2021 (1931).

in rf acceleration is the discovery of the phase-focusing principle by E. M. McMillan and V. Veksler in 1945 (see Ref. [17] and Chap. 2, Sec. IV.3).

Since the length of drift tubes is proportional to $\beta\lambda/2$, it would save space by employing higher frequency rf sources. However, the problem associated with a high frequency structure is that it radiates rf energy at a rate of

$$P = \omega_{\rm rf} C V_{\rm rf}^2, \tag{1.10}$$

where $\omega_{\rm rf}$ is the rf frequency, C is the gap capacitance, and $V_{\rm rf}$ is the rf voltage. The rf radiation power loss increases with the rf frequency. To eliminate rf power loss, the drift tube can be placed in a cavity so that the electromagnetic energy is stored in the form of a magnetic field (inductive load). At the same time, the resonant frequency of the cavity can be tuned to coincide with that of the accelerating field.

In 1948 Louis Alvarez and W.K.H. Panofsky constructed the first 32-MV drift-tube linac (DTL or Alvarez linac) for protons.[19] Operational drift-tube linacs for protons are the 200-MeV linacs at BNL and Fermilab, and the 50-MeV linacs at KEK and CERN. In the 1970's Los Alamos constructed the first side-coupled cavity linac (CCL), reaching 800 MeV. Fermilab upgraded part of its linac with the CCL to reach 400 MeV kinetic energy in 1995. The coupled cavity drift tube linac (CCDTL) that combines CCL and DTL has been shown to be efficient in accelerating high intensity low energy proton beams.

After World War II, rf technology had advanced far enough to make magnetron and klystron[20] amplifiers that could provide rf power of about 1 MW at 3 GHz (S band). Today, the highest energy linac has achieved 50-GeV electron energy operating at S band (around 2.856 GHz) at SLAC, and has achieved an acceleration gradient of about 20 MV/m, fed by klystrons with a peak power of 40 MW in a 1-μs pulse length. To achieve 100 MV/m, about 25 times the rf power would be needed.

The next linear collider (NLC), proposed by SLAC and KEK, at a center-of-mass energy of 500 GeV to 2 TeV beam energy, calls for X band with an acceleration gradient of 50 MV/m or more. The required klystron peak power is about 50 MW in a pulse duration is about 1.5 μs. The peak power is further enhanced by pulse compression schemes.

[19] L. Alvarez, *Phys. Rev.* **70**, 799 (1946).

[20] The klystron, invented by Varian brothers in 1937, is a narrow-band high-gain rf amplifier. The operation of a high power klystron is as follows. A beam of electrons is drawn by the induced voltage across the cathode and anode by a modulator. The electrons are accelerated to about 400 kV with a current of about 500 A. As the beam enters the input cavity, a small amount of rf power ($<$ 1 kW) is applied to modulate the beam. The subsequent gain cavities resonantly excite and induce micro-bunching of the electron beam. The subsequent drift region and penultimate cavity are designed to produce highly bunched electrons. The rf energy is then extracted at the output cavity, which is designed to decelerate the beam. The rf power is then transported by rf waveguides. The wasted electrons are collected at a water-cooled collector. If the efficiency were 50%, a klystron with the above parameters would produce 100 MW of rf power. See also E.L. Ginzton, "The $100 idea", *IEEE Spectrum*, **12**, 30 (1975).

Superconducting cavities have also become popular in recent years. At the Continuous Electron Beam Accelerator Facility (CEBAF) at the Thomas Jefferson National Accelerator Laboratory in Virginia, about 160 m of superconducting cavity was installed for attaining a beam energy up to 4 GeV in 5 paths using 338 five-kW CW klystrons. During the LEP-II upgrade more than 300 m of superconducting rf cavity was installed for attaining an almost 100-GeV beam energy. Many accelerator laboratories, such as Cornell and Fermilab in the U.S. and DESY in Germany, are collaborating in the effort to achieve a high-gradient superconducting cavity for a linear collider design called the TeV Superconducting Linear Accelerator (TESLA). Normally, a superconducting cavity operates at about 5–10 MV/m. After extensive cavity wall conditioning, single-cell cavities have reached beyond 25 MV/m.[21]

B: RFQ

In 1970, I.M. Kapchinskij and V.A. Teplyakov invented a low energy radio-frequency quadrupole (RFQ) accelerator – a new type of low energy accelerator. Applying an rf electric field to the four-vane quadrupole-like longitudinally modulated structure, a longitudinal rf electric field for particle acceleration and a transverse quadrupole field for focusing can be generated simultaneously. Thus the RFQs are especially useful for accelerating high-current low-energy beams. Since then many laboratories, particularly Los Alamos National Laboratory (LANL), Lawrence Berkeley National Laboratory (LBNL), and CERN, have perfected the design and construction of RFQ's, which are replacing Cockcroft-Walton accelerators as injectors to linac and cyclic accelerators.

C: Cyclotron

The *synchrotron frequency* for a non-relativistic particle in a constant magnetic field is nearly independent of the particle velocity, i.e.,

$$\omega_{\rm syn} = \frac{eB_0}{\gamma m} \approx \omega_{\rm cyc} = \frac{eB_0}{m}, \tag{1.11}$$

where $\gamma \approx 1$ for non-relativistic particles, B_0 is the magnetic field, and m is the particle mass. In 1929 E.O. Lawrence combined the idea of a constant revolution frequency and Ising's idea of the rf accelerator (see Sec. I.4A of Wiederöe linac), he invented the *cyclotron*.[22] Historical remarks in E.O. Lawrence's Nobel lecture are

[21] See e.g., J. Garber, *Proc. PAC95*, p. 1478 (IEEE, New York 1996). Single-cell cavities routinely reach 30 MV/m and beyond.

[22] E.O. Lawrence and N.E. Edlefsen, *Science*, **72**, 376 (1930). See e.g. E.M. McMillan, *Early Days in the Lawrence Laboratory (1931-1940)*, in *New directions in physics*, eds. N. Metropolis, D.M. Kerr, Gian-Carlo Rota, (Academic Press, Inc., New York, 1987). The *cyclotron* was coined by Malcolm Henderson, popularized by newspaper reporters; see M.S. Livingston, *Particle Accelerators: A Brief History*, (Harvard, 1969).

reproduced below:

> One evening early in 1929 as I was glancing over current periodicals in the University library, I came across an article in a German electrical engineering journal by Wideröe on the multiple acceleration of positive ions. ... This new idea immediately impressed me as the real answer which I had been looking for to the technical problem of accelerating positive ions, ... Again a little analysis of the problem showed that a uniform magnetic field had just the right properties – that the angular velocity of the ion circulating in the field would be independent of their energy so that they would circulate back and forth between suitable hollow electrodes in resonance with an oscillating electric field of a certain frequency which has come to be known as the *cyclotron frequency*.
>
> Now this occasion affords me a felicitous opportunity in some measure to correct an error and an injustice. For at that time I did not carefully read Wiederöe's article and note that he had gotten the idea of multiple acceleration of ions from one of your distinguished colleagues, Professor G. Ising, who in 1924 published this important principle. It was several years had passed that I became aware of Professor Ising's prime contribution. I should like to take this opportunity to pay tribute to his work for he surely is the father of the developments of the methods of multiple acceleration.

If two D plates (dees) in a constant magnetic field are connected to an rf electric voltage generator, particles can be accelerated by repeated passage through the rf gap, provided that the rf frequency is an integer multiple of the cyclotron frequency, $\omega_{\rm rf} = h\omega_0$. On January 2, 1931 M.S. Livingston demonstrated the cyclotron principle by accelerating protons to 80 keV in a 4.5-inch cyclotron, where the rf potential applied across the the accelerating gap was only 1000 V. In 1932 Lawrence's 11-inch cyclotron reached 1.25-MeV proton kinetic energy that was used to split atoms, just a few months after this was accomplished by the Cockcroft-Walton electrostatic accelerator. Since then, many cyclotrons were designed and built in Universities.[23] Figure 1.5 shows a schematic drawing of a classical cyclotron.

The momentum p and kinetic energy T of the extracted particle are $p = m\gamma\beta c$ and $T = mc^2(\gamma - 1) = p^2/[(\gamma+1)m]$. Using Eq. (1.3), we obtain the kinetic energy per amu as

$$\frac{T}{A} = \frac{e^2\gamma^2 B_0^2 R_0^2}{(\gamma+1)m_u}\left(\frac{Z}{A}\right)^2 \equiv K\left(\frac{Z}{A}\right)^2, \tag{1.12}$$

where $B_0R_0 = B\rho$ is the magnetic rigidity, Z and A are the charge and atomic mass numbers of the particle, m_u is the atomic mass unit, and K is called the *K-value* or *bending limit* of a cyclotron. In the non-relativistic limit, the K-value is equal to the proton kinetic energy T in MeV, e.g. K200 cyclotron can deliver protons with 200 MeV kinetic energy.

[23] M.S. Livingston, *J. Appl. Phys*, **15**, 2 (1944); **15**, 128 (1944); W.B. Mann, *The Cyclotron*, (Wiley, 1953); M.E. Rose, *Phys. Rev.*, **53**, 392 (1938); R.R. Wilson, *Phys. Rev.*, **53**, 408 (1938); *Am. J. Phys.*, **11**, 781 (1940); B.L. Cohen, *Rev. Sci. Instr.*, **25**, 562 (1954).

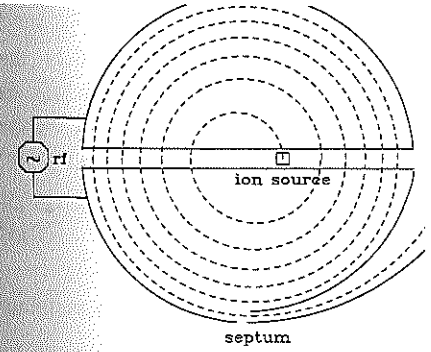

Figure 1.5: Schematic drawing of a classical cyclotron. Note that the radial distance between adjacent revolutions becomes smaller as the turn number increases [see Eq. (1.13)].

The iron saturates at a field of about 1.8 T (depending slightly on the quality of iron and magnet design). The total volume of iron-core is proportional to the cubic power of the beam rigidity $B\rho$. Thus the weight of iron-core increases rapidly with its K-value: Weight of iron $= W \sim K^{1.5} \sim (B\rho)^3$, where $B\rho$ is the beam rigidity. Typically, the magnet for a K-100 cyclotron weighs about 160 tons. The weight problem can be alleviated by using superconducting cyclotrons.[24]

The design of beam extraction systems in cyclotrons is challenging. Let V_0 be the energy gain per revolution. The kinetic energy at N revolutions is $K_N = eNV_0 = e^2B^2r^2/2m$, where e is the charge, m is the mass, B is the magnetic field, and r is the beam radius at the N-th revolution. The radius r of the beam at the N-th revolution becomes

$$r = \frac{1}{B}\left(\frac{2mV_0}{e}\right)^{1/2} N^{1/2}, \tag{1.13}$$

i.e. the orbiting radius increases with the square root of the revolution number N. The beam orbit separation in successive revolutions may becomes small, and thus the septum thickness becomes a challenging design problem.

Two key difficulties associated with classical cyclotrons are the orbit stability and the relativistic mass effect. The orbit stability problem was partially solved in 1945 by D. Kerst and R. Serber (see Exercise 1.14). The maximum kinetic energy was limited by the kinetic mass effect. Because the relativistic mass effect can destroy particle synchronism [see Eq. (1.11)], the upper limit of proton kinetic energy attainable in a cyclotron is about 12 MeV (See Exercise 1.4.).[25] Two ideas proposed to solve the dilemma are the isochronous cyclotron and the synchrocyclotron.

[24] See H. Blosser, in *Proc. 9th Int. Conf. on Cyclotrons and Applications*, p. 147 (1985).
[25] H. Bethe and M. Rose, *Phys. Rev.* **52**, 1254 (1937).

Isochronous cyclotron

In 1938 R.H. Thomas pointed out that, by using an azimuthal varying field, the orbit stability can be retained while maintaining the isochronism. The isochronous cyclotron is also called the azimuthal varying field (AVF) cyclotron. From the cyclotron principle, we observe that

$$\rho = \frac{p}{eB} = \frac{p}{\gamma m\omega} = \frac{c}{\omega}\left(1 - \frac{E_0^2}{E^2}\right)^{1/2}, \tag{1.14}$$

where $E_0 = mc^2$ and ω is the angular revolution frequency. Thus, to maintain isochronism with constant ω, the B field must be shaped according to

$$B_z = \frac{\gamma m\omega}{e} = \frac{\omega}{ec^2}E(\rho) = \frac{\omega E_0}{ec^2}\left[1 - \left(\frac{\omega\rho}{c}\right)^2\right]^{-1/2}. \tag{1.15}$$

When the magnetic flux density is shaped according to Eq. (1.15), the focusing index becomes $n < 0$, and the vertical orbit is unstable.

Orbit stability can be restored by shaping the magnetic pole-face. In 1938 L.H. Thomas introduced pole plates with hills and valleys in an isochronous cyclotron to achieve vertical orbit stability.[26] Such isochronous cyclotrons are also called AVF cyclotrons. The success of sector-focused cyclotron led by J.R. Richardson *et al.* led to the proliferation of the separate sector cyclotron, or ring cyclotron in the 1960's.[27] It gives stronger "edge" focusing for attaining vertical orbit stability. Ring cyclotrons are composed of three, four, or many sectors. Many universities and laboratories built ring cyclotrons in the 1960's.

Synchrocyclotron

Alternatively, synchronization between cyclotron frequency and rf frequency can be achieved by using rf frequency modulation (FM). FM cyclotrons can reach 1-GeV proton kinetic energy.[28] The synchrocyclotron uses the same magnet geometry as the weak-focusing cyclotrons. Synchronism between the particle and the rf accelerating voltage is achieved by ramping the rf frequency. Because the rf field is cycled, i.e. the rf frequency synchronizes with the revolution frequency as the energy is varied, synchrocyclotrons generate pulsed beam bunches. Thus the average intensity is low. The synchrocyclotron is limited by the rf frequency detuning range, the strength of the magnet flux density, etc. Currently two synchrocyclotrons are in operation, at CERN and at LBL.

[26] L.H. Thomas, *Phys. Rev.* **54**, 580 (1938).
[27] H.A. Willax, *Proc. Int. Cyclotron Conf.* 386 (1963).
[28] For a review, see R. Richardson, *Proc. 10th Int. Conf. on Cyclotrons and Their Applications*, IEEE CH-1996-3, p. 617 (1984).

D: Microtron

As accelerating rf cavities are expensive, it would be economical to use the rf structure repetitively: microtrons, originally proposed by V. Veksler in 1944, are designed to do this. Repetitive use requires synchronization between the orbiting and the rf periods. For example, if the energy gain per turn is exactly equal to the rest mass of the electron, the cyclotron frequency at the $n-1$ passage is given by

$$\omega_{n-1} = \frac{eB_0}{nm_0}, \tag{1.16}$$

i.e., the orbit period is an integral multiple of the fundamental cyclotron period. Thus, if the rf frequency $\omega_{\rm rf}$ is an integral multiple of the fundamental cyclotron frequency, the particle acceleration will be synchronized. Such a scheme or its variation was invented by V. Veksler in 1945.

The synchronization concept can be generalized to include many variations of magnet layout, e.g. the race track microtron (RTM), the bicyclotron, and the hexatron. The resonance condition for the RTM with electrons traveling at the speed of light is given by

$$n\lambda_{\rm rf} = 2\pi\frac{\Delta E}{ecB}, \tag{1.17}$$

where ΔE is the energy gain per passage through the rf cavity, B is the bending dipole field, $\lambda_{\rm rf}$ is the rf wavelength, and n is an integer. This resonance condition simply states that the increase in path length is an integral multiple of the rf wavelength.

Some operational microtrons are the three-stage MAMI microtron at Mainz, Germany,[29] and the 175-MeV microtron at Moscow State University. Several commercial models have been designed and built by Scanditron. The weight of the microtron also increases with the cubic power of beam energy.

E: Synchrotrons, weak and strong focusing

After E.M. McMillan and V. Veksler discovered the phase focusing principle of the rf acceleration field in 1945, a natural evolution of the cyclotron was to confine the particle orbit in a well-defined path while tuning the rf system and magnetic field to synchronize particle revolution frequency.[30] The first weak-focusing proton synchrotron, with focusing index $0 < n < 1$, was the 3-GeV Cosmotron in 1952 at BNL.

[29] see e.g., H. Herminghaus, in *Proc. 1992 EPAC*, p. 247 (Edition Frontieres, 1992).
[30] Frank Goward and D.E. Barnes converted a betatron at Telecommunication Research Laboratory into a synchrotron in August 1946. A few months earlier, J.R. Richardson, K. MacKenzie, B. Peters, F. Schmidt, and B. Wright had converted the fixed frequency 37-inch cyclotron at Berkeley to a synchro-cyclotron for a proof of synchrotron principle. A research team at General Electric Co. at Schenectady built a 70 MeV electron synchrotron to observe synchrotron radiation in October 1946. See also E.J.N. Wilson, *50 years of synchrotrons*, Proc. of the EPAC96 (1996).

A 6-GeV Bevatron constructed at LBNL in 1954, led to the discovery of [illegible] in 1955.

An important breakthrough in the design of synchrotron came in 1952 with the discovery of the strong-focusing or the alternating-gradient (AG) focusing principle by E.D. Courant, H.S. Snyder and M.S. Livingston.[31] Immediately, J. Blewett invented the electric quadrupole and applied the alternating-gradient-focusing concept to linac[32] solving difficult beam focusing problems in early day rf linacs. Here is *Some Recollection on the Early History of Strong Focusing* in the publication BNL 51377 (1980) by E.D. Courant:

> Came the summer of 1952. We have succeeded in building the Cosmotron, the world's first accelerator above one billion volts. We heard that a group of European countries were contemplating a new high-energy physics lab with a Cosmotron-like accelerator (only bigger) as its centerpiece, and that some physicists would come to visit us to learn more about the Cosmotron. ...
>
> Stan (Livingston) suggested one particular improvement: In the Cosmotron, the magnets all faced outward. This made it easy to get negative secondary beam from a target in the machine, but much harder to get positive ones. Why not have some magnets face inward so that positive secondaries could have a clear path to experimental apparatus inside the ring?
>
> ... I did the calculation and found to my surprise that the focusing would be strengthened simultaneously for both vertical and horizontal motion. ... Soon we tried to make the gradients stronger and saw that there was no theoretical limit – provided the alterations were made more frequent as the gradient went up. Thus it seemed that aperture could be made as small as one or two inches – against 8×24 inches in the Cosmotron, 12×48 in the Bevatron, and even bigger energy machines as we then imagined them. With these slimmer magnets, it seemed one could now afford to string them out over a much bigger circles, and thus go to 30 or even 100 billion volts.

The first strong-focusing 1.2 GeV electron accelerator was built by R. Wilson at Cornell University. Two strong-focusing or alternating-gradient (AG) proton synchrotrons, the 28-GeV CERN PS (CPS) and the 33-GeV BNL AGS, were completed in 1959 and 1960 respectively. The early strong-focusing accelerators used combined-function magnets, i.e., the pole-tips of dipoles were shaped to attain a strong quadrupole field. For example, the bending radius and quadrupole field gradients of AGS magnets are respectively $\rho = 85.4$ m, and $B_1 = (\partial B/\partial x) = \pm 4.75$ T/m at $B = 1.15$ T. This corresponds to a focusing index of $n = \pm 352$. The strengths of a string of alternating focusing and defocussing lenses were adjusted to produce net strong focusing effects in both planes.

The strong focusing idea was patented by a U.S. engineer, N.C. Christofilos,[33] living in Athens, Greece. Since then, the strong-focusing (AG) principle and a cascade of AG synchrotrons, proposed by M. Sands,[34] has become a standard design concept of high energy accelerators.

Since the saturation properties of quadrupole and dipole fields in a combined function magnet are different, there is advantage in machine tuning with separate quadrupole and dipole magnets. The Fermilab Main Ring was the first separate function accelerator.[35] Most present-day accelerators are separate-function machines. For conventional magnets, the maximum dipole field strength is about 1.5 T and the maximum field gradient is approximately $1/a$ [T/m] (see Exercise 1.12), where a is the aperture of the quadrupole in meters. For superconducting magnets, the maximum field and field gradient depends on superconducting coil geometry, superconducting coil material, and magnet aperture.

I.5 Colliders and Storage Rings

The total center-of-mass energy obtainable by having an energized particle smash onto a stationary particle is limited by the kinematic transformation (see Exercise 1.6). To boost the available center-of-mass energy, two beams are accelerated to high energy and made to collide at interaction points.[36] Since the lifetime of a particle beam depends on the vacuum pressure in the beam pipe, stability of the power supply, intrabeam Coulomb scattering, Touschek scattering, quantum fluctuations, collective instabilities, nonlinear resonances, etc., accelerator physics issues have to be evaluated in the design, construction, and operation of colliders. Beam manipulation techniques such as beam stacking, bunch rotation, stochastic beam cooling, invented by S. Van de Meer,[37] electron beam cooling, invented by Budker in 1966,[38] etc., are essential in making the collider a reality.

The first proton-proton collider was the intersecting storage rings (ISR) at CERN completed in 1969. ISR was the test bed for physics ideas such as stochastic beam cooling, high vacuum, collective instabilities, beam stacking, phase displacement acceleration, nonlinear beam-beam force, etc. It reached 57 A of single beam current at 30 GeV. It stopped operation in 1981.

The first electron storage ring (200 MeV) was built by B. Touschek *et al.* in 1960

[31] E.D. Courant, H.S. Snyder and M.S. Livingston, *Phys. Rev.* **88**, 1188 (1952).

[32] J. Blewett, *Phys. Rev.* **88**, 1197 (1952).

[33] N.C. Christofilos, *Focusing system for ions and electrons*, U.S. Patent No. 2736799 (issued 1956). Reprinted in *The Development of High Energy Accelerators*, M.S. Livingston, ed. (Dover, New York, 1966).

[34] M. Sands, *A proton synchrotron for 300 GeV*, MURA Report 465 (1959).

[35] The Fermi National Accelerator Laboratory was established in 1967. The design team adopted a cascade of accelerators including proton linac, rapid cycling booster synchrotron, and a separate function Main Ring.

[36] A.M. Sessler, *The Development of Colliders*, LBNL-40116, (1997). The collider concept was patented by R. Wiederöe in 1943. The first collider concept based on "storage rings" was proposed by G.K. O'Neill in Phys. Rev. Lett. **102**, 1418 (1956).

[37] S. Van de Meer, *Stochastic Damping of Betatron Oscillations in the ISR*, CERN internal report CERN/ISR-PO/72-31 (1972).

[38] See e.g., H. Poth, *Phys. Rep.* **196**, 135 (1990) and references therein.

in Rome. It had only one beam line and an internal target to produce positrons, and it was necessary to flip the entire ring by 180° to fill both beams. Since the Laboratoire de l'Accelerateur Lineaire (LAL) in Orsay had a linac, the storage ring was transported to Orsay in 1961 to become the first e^+e^- collider. The Stanford-Princeton electron-electron storage ring was proposed in 1956 but completed only in 1966. The e^-e^- collider moved from Moscow to Novosibirsk in 1962 began its beam collision in 1965. Since the 1960's, many e^+e^- colliders have been built. Experience in the operation of high energy colliders has led to an understanding of beam dynamics problems such as beam-beam interactions, nonlinear resonances, collective (coherent) beam instability, wakefield and impedance, intrabeam scattering, etc.

Some e^+e^- colliders now in operation are CESR at Cornell, SLC and PEP at SLAC, PETRA and DORIS at DESY, VEPP's at Novosibirsk, TRISTAN at KEK, and LEP at CERN. The drive to reach higher energy provided the incentive for the high power klystron. The power compression method SLED (SLAC Energy Development), originated by P. Wilson, D. Farkas, H. Hogg, *et al.*, paved the way to the SLAC Linear Collider (SLC). High energy lepton colliders such as NLC, JLC, and CLIC are expanding linear accelerator technology. On the luminosity frontier, the Φ-factory at Frascati and B-factories such as PEP-II at SLAC and TRISTAN-II at KEK aim to reach 10^{33-34} cm^{-2}·s^{-1}.

Proton-antiproton colliders include the Tevatron at Fermilab and Sp$\bar{p}$S at CERN. The discovery of type-II superconductors[39] led to the successful development of superconducting magnets, which have been successfully used in the Tevatron to attain 2-TeV c.m. energy, and in HERA to attain 820-GeV proton beam energy. At present, the CERN LHC (14-TeV c.m. energy) and the BNL RHIC (200-GeV/u heavy ion c.m. energy) are under construction. The (40-TeV) SSC proton collider in Texas was canceled in October 1993. Physicists are contemplating a very large hadron collider with about 60–100 TeV beam energy.

I.6 Synchrotron Radiation Storage Rings

Since the discovery of synchrotron light from a then high energy (80-MeV) electron synchrotron in 1947, the synchrotron light source has become an indispensable tool in basic atomic and molecular physics, condensed-matter physics, material science, biological, chemical, and medical research, and material processing. Worldwide, about 70 light sources are in operation or being designed or built.

Specially designed high-brightness synchrotron radiation storage rings are classified into generations. Those in the first generation operate in the parasitic mode from existing high energy e^+e^- colliders. The second generation comprises dedicated low-emittance light sources. Third-generation light sources produce high-brilliance photon beams from insertion devices using dedicated high-brightness electron beams. These include the advanced photon source (APS) at Argonne National Laboratory, the advanced light source (ALS) at Lawrence Berkeley National Laboratory, the European synchrotron radiation facility (ESRF), the Japan synchrotron radiation facility (JSRF), etc. There are research efforts toward fourth generation light sources based on free electron laser from a long undulator.

[39] Type II superconductors allow partial magnetic flux penetration into the superconducting material so that they have two critical fields $B_{c1}(T)$ and $B_{c2}(T)$ in the phase transition, where T is the temperature. The high critical field makes them useful for technical applications. Most type II superconductors are compounds or alloys of niobium; commonly used alloys are NbTi and Nb_3Sn.

II Layout and Components of Accelerators

A high energy accelerator complex is composed of ion sources, buncher/debuncher, chopper, pre-accelerators such as the high-voltage source or RFQ, drift-tube linac (DTL), booster synchrotrons, storage rings, and colliders. Figure 1.6 is a schematic drawing of a small accelerator complex at the Indiana University Cyclotron Facility. Particle beams are produced from ion sources, where charged ions are extracted by a high-voltage source to form a beam. Before injection into various types of accelerators, the beam pulse is usually prebunched and chopped into appropriate sizes. The beam can be accelerated by a DC accelerator or RFQ to attain the proper velocity needed for a drift-tube linac. The beams can be injected into a chain of synchrotrons to reach high energy. Some basic accelerator components are described in the following subsections.

II.1 Acceleration Cavities

The electric fields used for beam acceleration are of two types: the DC acceleration column and the rf cavity.[40] The DC acceleration column is usually used in low energy accelerators such as the Cockcroft-Walton, Van de Graaff, etc.

The rf acceleration cavity provides a longitudinal electric field at an rf frequency that ranges from a few hundred kHz to 10–30 GHz. For a particle with charge e, the energy gain/loss per passage through a cavity gap is

$$\Delta E = e\Delta V, \tag{1.18}$$

where $\Delta V = V_0 \sin(\omega_{\rm rf} t + \phi)$ is the effective gap voltage, $\omega_{\rm rf}$ is the rf frequency, V_0 is the effective peak accelerating voltage, and ϕ is the phase angle. Low frequency rf cavities are usually used to accelerate hadron beams, and high frequency rf cavities to accelerate electron beams.

[40] In recent years, new acceleration schemes such as inverse free-electron laser acceleration, laser plasma wakefield acceleration, etc., have been proposed for high-gradient accelerators. See e.g., *Advanced Accelerator Concepts*, AIP Conf. Proc. No. 398, S. Chattopadhyay, *et al.*, Eds. (1996) and reference therein.

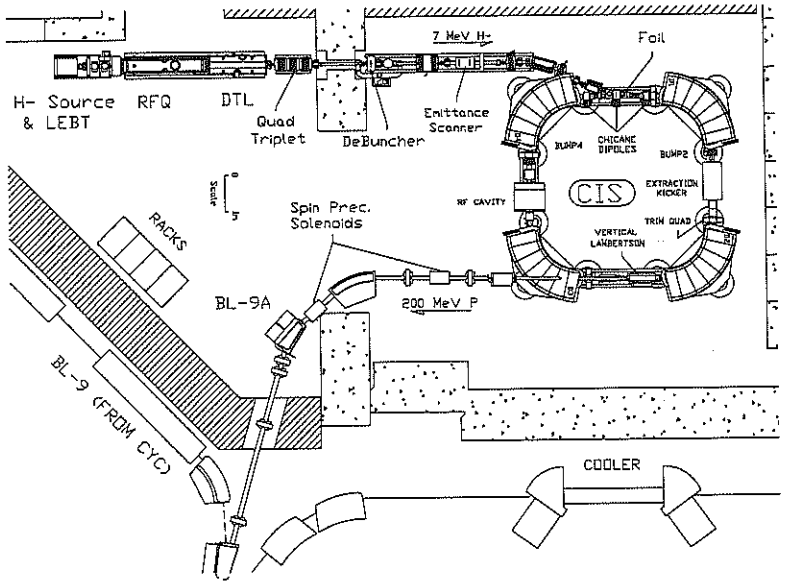

Figure 1.6: A small accelerator, the Cooler Injector Synchrotron (CIS) at the Indiana University Cyclotron Facility. The source, RFQ, DTL, debuncher, chopper, the CIS synchrotron with 4 dipoles, and a transfer line are shown to illustrate the basic structure of an accelerator system. The circumference is 17.36 m.

Acceleration of the bunch of charged particles to high energies requires synchronization and phase focusing. The synchronization is achieved by matching the rf frequency with particle velocity, and the phase focusing is achieved by choosing a proper phase angle between the rf wave and the beam bunch.

II.2 Accelerator Magnets

Accelerator magnets requires stringent field uniformity condition in order to minimize un-controllable beam orbit distortion and beam loss. Accelerator magnets are classified into field type of dipole magnets for beam orbit control, quadrupole magnets for beam size control, sextupole and higher-order multipole magnets for the control of chromatic and geometric aberrations.

Accelerator magnets are also classified into conventional iron magnets and superconducting magnets. The conventional magnets employ iron or silicon-steel with OFHC copper conductors. The superconducting magnets employ superconducting coils to produce high field magnets.

Dipoles

Dipole magnets are used to guide charged particle beams along a desired orbit. From the Lorentz force law, the bending angle θ is given by

$$\theta = \frac{e}{p_0}\int_{s_1}^{s_2} Bdl = \frac{1}{B\rho}\int_{s_1}^{s_2} Bdl, \tag{1.19}$$

where p_0 is the momentum of the beam, and $B\rho = p_0/e$ is the momentum rigidity of the beam. The total bending angle for a circular accelerator is 2π, and the total integrated dipole field is

$$\oint Bdl = 2\pi p_0/e = 2\pi B\rho. \tag{1.20}$$

The conventional dipole magnets are made of laminated silicon-steel plates for the return magnetic flux for minimizing eddy current loss and hysteresis loss. Solid block of high permeability soft-iron can also be used for magnets in the transport line or cyclotrons, that requires DC magnetic field. A gap between the iron yoke is used to shape dipole field. The iron plate can be C-shaped for a C-dipole (see Exercise 1.10 and the left plot of Fig. 1.7), or H-shaped for H-dipole. Since iron saturates at about 1.7 T magnet flux, the maximum attainable field for iron magnet is about 1.8 T. To attain a higher dipole field, superconducting coils can be used. These magnets are called superconducting magnets.

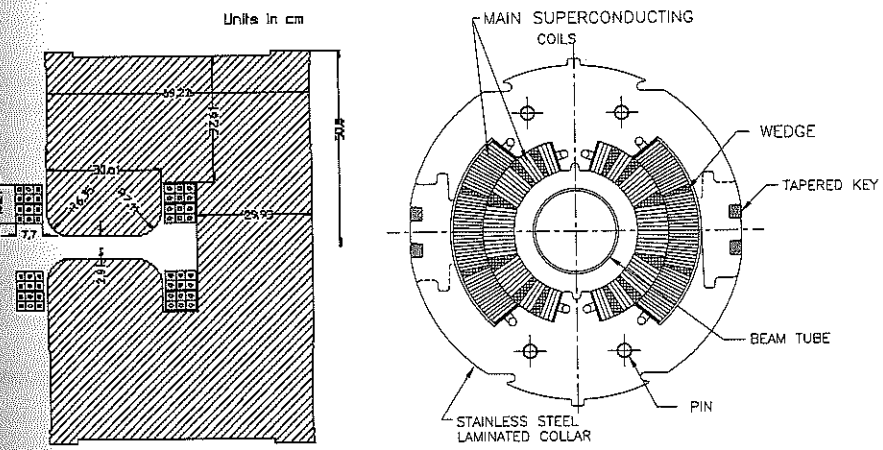

Figure 1.7: The cross-sections of a C-shaped conventional dipole magnet (left, courtesy of G. Berg at IUCF) and an SSC superconducting dipole magnet (right, courtesy of R. Gupta at LBNL). For conventional magnets, the pole shape is designed to attain uniform field in the gap. The rectangular blocks shown in the left plot are oxygen free high conductivity (OFHC) copper coils. For superconducting magnets, the superconducting coils are arranged to simulate the cosine-theta like distribution.

Superconducting magnets that use iron to enhance the attainable magnetic field is also called superferric magnets. For high field magnets, e.g. 5-12 T, blocks of superconducting coils are used to simulate the cosine-theta current distribution (see Exercise 1.9). The right plot of Fig. 1.7 shows the cross-section of the high field SSC dipole magnets.

Quadrupoles

A stack of laminated iron plates with a hyperbolical profile can be used to produce quadrupole magnet (see Exercise 1.12), where the magnetic field of an ideal quadrupole is given by

$$\vec{B} = B_1(z\hat{x} + x\hat{z}), \tag{1.21}$$

where $B_1 = \partial B_z/\partial x$ evaluated at the center of the quadrupole, and $\hat{x}, \hat{s}$, and $\hat{z}$ are the unit vectors in the horizontal, azimuthal, and vertical directions. For a charged particle passing through the center of a quadrupole, the magnetic field and the Lorentz force are zero. At a displacement (x, z) from the center, the Lorentz force for a particle with charge e and velocity v along the $\hat{s}$ direction is given by

$$\vec{F} = evB_1\hat{s} \times (z\hat{x} + x\hat{z}) = -evB_1 z\hat{z} + evB_1 x\hat{x}. \tag{1.22}$$

The equations of motion become

$$\frac{1}{v^2}\frac{d^2x}{dt^2} = \frac{eB_1}{\gamma mv}x, \qquad \frac{1}{v^2}\frac{d^2z}{dt^2} = -\frac{eB_1}{\gamma mv}z. \tag{1.23}$$

Thus a focusing quadrupole in the horizontal plane is also a defocussing quadrupole in the vertical plane and vice versa. Defining the focusing index as

$$n = R^2\frac{eB_1}{\gamma mv} = \frac{R^2}{B\rho}\frac{\partial B_z}{\partial x}, \tag{1.24}$$

we obtain

$$\frac{d^2x}{ds^2} = \frac{n}{R^2}x, \qquad \frac{d^2z}{ds^2} = -\frac{n}{R^2}z \tag{1.25}$$

in a quadrupole, where $s = vt$ is the longitudinal distance along the $\hat{s}$ direction.

II.3 Other Important Components

Other important components in accelerators are ion sources;[41] monitors for beam position, beam current and beam loss; beam dump; emittance meters; vacuum ports and pumps; beam orbit and stopband correctors; skew quadrupoles, sextupoles, octupoles, and other nonlinear magnets for nonlinear stopband correction; orbit bumps, kickers, and septum; power supplies, etc. For high energy experiments, sophisticated particle detectors are the essential sources of discovery. For synchrotron radiation applications in electron storage rings, wigglers and undulators are used to enhance the photon beam quality.

[41] B. Wolf, ed., *Handbook of Ion Sources* (CRC Press, New York, 1995); R. Geller, *Electron Cyclotron Resonance Ion Sources and ECR Plasma* (Inst. of Phys. Pub., Bristol, 1996).

The timing and operation of all accelerator components (including experimental devices) are controlled by computers. Computer control software retrieves beam signals, and sets proper operational conditions for accelerator components. The advance in computer hardware and software provides advanced beam manipulation schemes such as slow beam extraction, beam stacking accumulation, stochastic beam cooling, etc.

III Accelerator Applications

III.1 High Energy and Nuclear Physics

To probe into the inner structure of the fundamental constituents of particles, high energy accelerators are needed. Historical advancement in particle and nuclear physics has always been linked to advancement in accelerators. High energy accelerators have provided essential tools in the discovery of $\bar{p}$, Ω, J/Ψ, Z^0, $W^{\pm}\cdots$, etc. Observation of a parton-like structure inside a proton provided proof of the existence of elementary constituents known as quarks. The IUCF cyclotron has provided the opportunity to understand the giant M1 resonances in nuclei. The Tevatron at Fermilab facilitated the discovery of the top quark in 1995. Radioactive beams may provide nuclear reactions that will lead to understanding of the nucleo-synthesis of elements in the early universe.

High energy colliders such as HERA (30-GeV electrons and 820-GeV protons), Tevatron (1-TeV on 1-TeV proton-antiproton collider), SLC (50-GeV on 50-GeV e^+e^- collider), LEP (50-100-GeV on 50-100-GeV e^+e^- collider) led the way in high energy physics in the 1990's. High luminosity colliders, such as the B-factories at SLAC and KEK and the Φ-factory at DAΦNE, will provide dedicated experiments for understanding the symmetry of the fundamental interactions. The RHIC (100-GeV/u on 100-GeV/u heavy ion collider) will provide important information on the phase transitions of quark-gluon plasma. The CEBAF 4-6-GeV continuous electron beams allow high resolution (0.1 fm) studies of the electromagnetic properties of nuclei. The LHC (7-TeV on 7-TeV proton-proton collider) at CERN will lead high energy physics research at the beginning of the 21st century.

III.2 Solid-State and Condensed-Matter Physics

Ion implantation,[42] synchrotron radiation sources, and neutron back-scattering have provided important tools for solid-state and condensed-matter physics research. Neutron sources have been important sources for research aimed at understanding the properties of metals, semiconductors, and insulators. Free-electron lasers with short pulses and high brightness in a wide spectrum of frequency ranges have been used extensively in medical physics, solid-state physics, biology, and biochemistry.

III.3 Other Applications

Electron beams can be used to preserve and sterilize agricultural products. Beam lithography is used in industrial processing. Radiation has been used in the manufacture of polymers, radiation hardening for material processing, etc. Particle beams have been used to detect defects and metal fatigue of airplanes, ships, and strategic equipment.

Since the discovery of X-ray in 1895, radiation has been used in medical imaging, diagnosis, and radiation treatments. Radiation can be used to terminate unwanted tumor growth with electron, proton, or ion beams. In particular, proton and heavy-ion beams have become popular in cancer radiation therapy because these beam particles deposit most of their energy near the end of their path. By controlling the beam energy, most of the beam energy can be deposited in the cancerous tumor with little damage to surrounding healthy cells. Beams have been used in radiation sterilization, isotope production for radionuclide therapy,[43] etc.

Exercise 1: Basics

1. Show that the magnet rigidity $B\rho$ is related to the particle momentum p by

$$B\rho\ [\mathrm{Tm}] = \frac{p}{Ze} = \begin{cases} 3.3357\ p & [\mathrm{GeV/c}] \quad \text{for singly charged particles} \\ \frac{3.3357}{Z}\ p & [\mathrm{GeV/c}] \quad \text{for particles with charge } Ze \end{cases},$$

where B is the magnetic flux density, ρ is the bending radius, p is the beam momentum, and Ze is the charge of the particle.

(a) Estimate the magnetic rigidity of proton beams at the IUCF Cooler Ring (kinetic energy 500 MeV), RHIC (momentum 250 GeV/c), Tevatron (momentum 1 TeV/c) and SSC (momentum 20 TeV/c).

(b) If the maximum magnetic flux density for a conventional dipole is 1.7 Tesla, what is the total length of dipole needed for each of these accelerators?

[42] The ion implantation, invented by W. Shockley in 1954 (U.S. Patent 2787564), has become an indispensable tool in the semiconductor industry.

[43] see e.g. Bert M. Coursey and R. Nath, *Phys. Today*, p. 25, April 2000.

(c) If superconducting magnets are used with magnetic fields $B = 3.5$ T (RHIC), 5 T (Tevatron) and 6.6 T (SSC), what is the total length of dipoles needed in each accelerator?

2. The resonance frequency of a LC circuit is $f_r = 1/2\pi\sqrt{LC}$. Assuming that you can build a capacitor with a minimum capacitance of $C = 1$ pF, what value of inductance L is needed to attain 3 GHz resonance frequency? What is your conclusion from this exercise? Can you use a conventional LC circuit for microwave tuning?[44]

3. Consider a uniform cylindrical beam with N particles per unit length in a beam of radius a; show that a test charged particle traveling along at the same velocity as the beam, v, experiences a repulsive *space-charge* force,

$$\vec{F} = \begin{cases} \dfrac{e^2 N}{2\pi\epsilon_0 a^2\gamma^2}\vec{r} & r \le a \\ \dfrac{e^2 N}{2\pi\epsilon_0 r^2\gamma^2}\vec{r} & r > a \end{cases}$$

where $\gamma = 1/\sqrt{1-\beta^2}$ and e is the charge of the beam particle.

(a) Estimate the space-charge force for the SSC low energy booster at injection with kinetic energy 800 MeV and $N_B = 10^{10}$ particles per bunch, with rms bunch length $\sigma_s = 2$ m and beam diameter 4 mm. Here the number of particles per unit length is $N = N_B/(\sqrt{2\pi}\sigma_s)$.

(b) What happens if the test charged particle travels in the opposite direction in the head-on collision process? Estimate the space-charge force for the e^+e^- colliding beam at SLC, where the beam parameters are $E = 47$ GeV and $N_B = 2\times10^{10}$, the rms bunch length is $\sigma_s = 0.6$ mm, and the beam size is 3 μm. If this force is exerted by a quadrupole, what is the equivalent field gradient?

4. In a cyclotron, the *synchronous* frequency is $\omega = eB/\gamma m = \omega_0/\gamma$, where $\omega_0 = eB/m$ is the cyclotron frequency, and γ is the relativistic energy factor. Use the following steps, in the uniform acceleration approximation, to prove that, if a sinusoidal voltage $V_{rf} = V\cos\omega_0 t$ is applied to the dees, the maximum attainable kinetic energy is $\sqrt{2eVmc^2/\pi}$, where e and m are the charge and mass of the particle.

(a) Let ψ be the rf phase of the particle. Show that the equation of motion in a uniform acceleration approximation is $d\psi/dt = (\gamma^{-1}-1)\omega_0$, $\quad d\gamma^2/dt = a\cos\psi$, where $a = 2\omega_0 eV/\pi mc^2$.

(b) Defining a variable $q = a\cos\psi$, show that the equation of motion becomes $(q/\sqrt{a^2-q^2})dq = (2\gamma-2)\omega_0\ d\gamma$. Integrate this equation and show that the maximum kinetic energy attainable is $\sqrt{2eVmc^2/\pi}$.

5. The total power radiated by an accelerated charged particle is given by Larmor's formula:

$$P = \frac{1}{4\pi\epsilon_0}\frac{2e^2\dot{v}^2}{3c^3} = \frac{1}{4\pi\epsilon_0}\frac{2e^2}{3m^2c^3}\left(\frac{dp_\mu}{d\tau}\cdot\frac{dp_\mu}{d\tau}\right)$$

[44] See V.F.C. Veley, *Modern Microwave Technology* (Prentice Hall, Englewood Cliffs, NJ, 1987). For an order of magnitude estimation, a 5-cm-radius single loop with wire 0.5 mm thick will yield an inductance of about 3×10^{-7} H.

where $d\tau = dt/\gamma$ is the proper time and p_μ is the four-momentum.[45]

(a) In a linear accelerator, the motion is along a straight path. The power radiated is

$$P = \frac{1}{4\pi\epsilon_0}\frac{2e^2}{3m^2c^3}(\frac{dp}{dt})^2 = \frac{1}{4\pi\epsilon_0}\frac{2e^2}{3m^2c^3}(\frac{dE}{dx})^2,$$

where dE/dx is the rate of energy change per unit distance. The ratio of radiation power loss to power supply from an external accelerating source is

$$\frac{P}{dE/dt} = \frac{1}{4\pi\epsilon_0}\frac{2e^2}{3m^2c^3v}(\frac{dE}{dx}) \approx \frac{2}{3}\frac{r_e}{mc^2}(\frac{dE}{dx}),$$

where $r_e = 2.82 \times 10^{-15}$ m is the classical radius of the electron. Assuming that electrons gain energy from 1 GeV to 47 GeV in 3 km at SLC, what is the ratio of power loss to power supply? In the Next Linear Collider (NLC), the gradient of the accelerating cavities will increase by a factor of 10. What will be the ratio of radiation power loss to power supply? What is your conclusion from this exercise?

(b) In a circular accelerator, $\vec{p}$ changes direction while the change in energy per revolution is small, i.e.

$$\frac{d\vec{p}}{d\tau} = \gamma\omega|\vec{p}| \gg \frac{1}{c}\frac{dE}{d\tau},$$

where $\omega = \beta c/\rho$, and ρ is the bending radius. The radiated power becomes

$$P = \frac{2}{3}\frac{r_0}{mc}\gamma^2\omega^2|\vec{p}|^2 = \frac{\beta^4 c C_\gamma}{2\pi}\frac{E^4}{\rho^2},$$

where r_0 is the classical radius of the particle, m is the mass, and

$$C_\gamma = \frac{4\pi r_0}{3(mc^2)^3} = \begin{cases} 8.85 \times 10^{-5}[\mathrm{m/(GeV)^3}] & \text{for electrons,} \\ 7.78 \times 10^{-18}[\mathrm{m/(GeV)^3}] & \text{for protons.} \end{cases}$$

The radiative energy loss per revolution of an isomagnetic storage ring becomes

$$U_0 = \beta^3 C_\gamma E^4/\rho.$$

i. Calculate the energy dissipation per revolution for electrons at energy $E =$ 50 GeV and 100 GeV in LEP, where $\rho = 3096.175$ m and the circumference is 26658.853 m.

ii. Find the energy loss per turn for protons in SSC, where the magnetic field is 6.6 Tesla at 20 TeV, the circumference is 87120 m, and the bending radius is 10187 m.

iii. Show that the power radiated per unit length in dipoles for a beam is

$$P(\mathrm{W/m}) = 10^6 \cdot \frac{U_0[\mathrm{MeV}]}{2\pi\rho\ [\mathrm{m}]} I\ [\mathrm{A}],$$

where U_0 is the energy loss per revolution, I is the total beam current, and ρ is the radius of curvature in the dipole. Find the synchrotron radiation power loss per unit length in LEP and SSC, where the circulating beam currents are respectively 3 mA and 70 mA.

[45] See J.D. Jackson, *Classical Electrodynamics*, 2nd ed., p. 468 (1975).

6. Show that the total energy for a head-on collision of two beams at an energy of $\gamma_{\mathrm{cm}}mc^2$ each is equivalent to a fixed target collision at the laboratory energy of γmc^2 with $\gamma = 2\gamma_{\mathrm{cm}}^2 - 1$.

7. The luminosity, $\mathcal{L}$ [$\mathrm{cm}^{-2}\,\mathrm{s}^{-1}$], is a measure of the probability (rate) of particle encounters per unit area in a collision process. Thus the total counting rate of a physics event is $R = \sigma_{\mathrm{phys}}\mathcal{L}$, where σ_{phys} is the cross-section of a physics process.

(a) In fixed target experiments, the luminosity is given by $\mathcal{L} = (dN_{\mathrm{B}}/dt)n_{\mathrm{target}}$, where dN_{B}/dt is the number of beam particles per second on target, and n_{target} is the target thickness measuring the number of atoms per cm^2. The average luminosity is given by $\langle\mathcal{L}\rangle = \langle dN_{\mathrm{B}}/dt\rangle n_{\mathrm{target}}$, where $\langle dN_{\mathrm{B}}/dt\rangle = N_{\mathrm{B}}f$. Here N_{B} is the number of particles per pulse (bunch) and f is the pulse repetition rate. Consider a fixed target experiment, where the beam repetition rate is 0.4 Hz, beam particle per pulse is 10^{13}, the beam pulse length is 150 ns, and the target thickness is 4 $\mathrm{mg/cm}^2$ Au foil. Find the instantaneous and average luminosities of the fixed target experiment. What is the advantage of stretching the beam pulse length to 1 s in this experiment?

(b) When two beams collide head-on, the luminosity is

$$\mathcal{L} = 2\,f\,N_1\,N_2 \int \rho_1(x,z,s_1)\rho_2(x,z,s_2)dxdzdsd(\beta ct),$$

where $s_1 = s + \beta ct, s_2 = s - \beta ct$, f is the encountering frequency, N_1 and N_2 are the numbers of particles, and ρ_1 and ρ_2 are the normalized distribution functions for these two bunches. Using a Gaussian bunch distribution,

$$\rho(x,z,s) = \frac{1}{(2\pi)^{3/2}\sigma_x\sigma_z\sigma_s}\exp\left\{-\frac{x^2}{2\sigma_x^2} - \frac{z^2}{2\sigma_z^2} - \frac{s^2}{2\sigma_s^2}\right\},$$

where σ_x, σ_z, and σ_s are respectively the horizontal and vertical rms bunch widths and the rms bunch length, show that the luminosity for two bunches with identical distribution profiles is

$$\mathcal{L} = \frac{fN_1N_2}{4\pi\sigma_x\sigma_z}.$$

Show that when two beams are offset by a horizontal distance b, the luminosity is reduced by a factor $\exp\{-b^2/4\sigma_x^2\}$.

8. Show that the magnetic field on the axis of a circular cylindrical winding of uniform cross-section is

$$B_{\|}(s) = \frac{\mu_0 J}{2}\left\{(\ell - s)\ln\frac{b + (b^2 + [\ell - s]^2)^{1/2}}{a + (a^2 + [\ell - s]^2)^{1/2}} + s\ln\frac{b + (b^2 + s^2)^{1/2}}{a + (a^2 + s^2)^{1/2}}\right\}$$

where ℓ is the length of the solenoid, J is the current density, a, b are the inner and outer cylindrical radii respectively, and s is the distance from one end of the solenoid.

(a) For an ideal solenoid, show that the magnetic field becomes[46]

$$B_{\|} = \mu_0 n I,$$

where n is the number of turns per unit length, and I is the current in each turn.

(b) For an ideal solenoid, show that the inductance is

$$L = \mu_0 n^2 \ell S = \mu_0 n^2 \times \text{ volume of the solenoid},$$

where S is the cross-section area of the solenoid. Note that the total energy stored in the magnet is given by the magnetic energy.

9. From elementary physics, the field at a distance r from a long straight wire carrying current I is

$$B = \mu_0 I / 2\pi r$$

along a direction tangential to a circle with radius r around the wire.

(a) Show that the 2D magnetic field at location $y = x + jz$ for a long straight wire is

$$B_z(x,z) + jB_x(x,z) = \frac{\mu_0 I}{2\pi(y - y_0)},$$

where j is an imaginary number, the current I is positive if it points out of paper, and $y_0 = x_0 + jz_0$ is the position of the current filament.[47]

(b) If the current per unit area of an infinitely long circular current sheet is

$$\lambda(r, \phi) = (I_1/2a)\cos\phi\ \delta(r - a),$$

where I_1 is the total dipole current and (r, ϕ) are the cylindrical coordinates with $x = r\cos\phi$ and $z = r\sin\phi$, show that the magnetic field inside the current sheet is

$$B_z = -\mu_0 I_1 / 4a, \quad B_x = 0.$$

This is the cosine-theta current distribution for a dipole. High-field superconducting dipoles are normally made of current blocks that simulate the cosine-theta distribution.

(c) The Beth current sheet theorem states that the magnetic fields in the immediate neighborhood of a two-dimensional current sheet are

$$B(y_+) - B(y_-) = j\mu_0 (dI/dy),$$

where y_+ and y_- are the complex coordinates $y = x + jz$ at an infinitesimal distance from the current sheet, and dI/dy is the current per unit length. Apply this theorem to show that the cosine-theta current distribution on a circular cylinder gives rise to a pure dipole field inside the cylinder.

[46] Set $s = \ell/2, b \to a$.
[47] See R.A. Beth, *J. Appl. Phys.* **37**, 2568 (1966); **38**, 4689 (1967).

10. Show that the magnetic field at the coordinate $y = x + jz$, due to a thin current wire located at coordinates $y_0 = x_0 + jz_0$, between two sheets of parallel plates with infinite permeability is[48]

$$B_z + jB_x = \frac{\mu_0 I}{4g}\left[\tanh\frac{\pi(y - y_0^*)}{2g} + \coth\frac{\pi(y - y_0)}{2g}\right],$$

where g is the gap between two parallel plates. The current flows in the $\hat{x}\times\hat{z}$ direction.

11. Show that the dipole field of a window-frame dipole with two sheets of parallel plates having infinite permeability is given by

$$B = \mu_0 NI/g = \mu_0 nI,$$

where N is the number of turns, I is the current in each turn, g is the gap between two iron plates, and $n = N/g$ is the number of turns per unit gap length. Show that the inductance is

$$L = \mu_0 N^2 \ell w/g = \mu_0 n^2 \times \text{ volume of the dipole},$$

where ℓ and w are the length and width of the dipole. The total power dissipation is $P = (NI)^2 R$, where $R = \rho\ell/A$ is the resistance, A as the cross-sectional area of the conductor, and ρ is the resistivity of the coil.

12. Following Maxwell's equation, $\nabla \times \vec{B} = 0$ in the current-free region, and the magnetic field can be derived from a magnetic potential, Φ_m, with $\vec{B} = -\nabla\Phi_m$. For a quadrupole field with $B_z = Kx, B_x = Kz$, show that the magnetic potential is $\Phi_m = -Kxz$. The equipotential curve is $xz =$ constant. Thus the pole shapes of quadrupoles are hyperbolic curves with $xz = a^2/2$. The pole-tip field is $B_{\text{pole tip}} = Ka$. To avoid the magnetic field saturation in iron, the pole-tip field in a quadrupole is normally designed to be less than 0.9 Tesla. The achievable gradient is $B_1 = B_{\text{pole tip}}/a$. Show that the gradient field is

$$B_1 = 2\mu_0 NI/a^2,$$

where NI is the number of ampere-turns per pole, and a is the half-aperture of the quadrupole. The inductance in an ideal quadrupole is

$$L = \frac{8\mu_0 N^2 \ell}{a^2}\left(x_c^2 - \frac{a^4}{12x_c^2}\right) \approx \frac{8\mu_0 N^2 \ell}{a^2} x_c^2,$$

where x_c is the distance of the conductor from the center of the quadrupole. In reality, x_c^2 should be replaced by $x_c^2 + x_c w_c$, where w_c is the width of the pole.

[48] S.Y. Lee, *Nucl. Inst. Meth.* **A300**, 151 (1991). Use the following identities:

$$\tanh\frac{\pi y}{2} = \frac{4y}{\pi}\sum_{k=1}^{\infty}\frac{1}{(2k-1)^2 + y^2}, \quad \coth\frac{\pi y}{2} = \frac{2}{\pi y} + \frac{4y}{\pi}\sum_{k=1}^{\infty}\frac{1}{(2k)^2 + y^2}.$$

13. Consider a pair of conductors with cross-sections independent of the azimuthal coordinate s, and surrounded by isotropic and homogeneous medium with permittivity ϵ and permeability μ. Maxwell's equations are

$$\nabla \cdot (\epsilon \vec{E}) = 0, \qquad \nabla \times \vec{E} = -\frac{\partial \vec{B}}{\partial t},$$
$$\nabla \cdot \vec{B} = 0, \qquad \nabla \times \vec{H} = \frac{\partial \epsilon \vec{E}}{\partial t},$$

where the external charge and current are zero. Let $\hat{x}, \hat{z}$ and $\hat{s}$ form the basis of an orthonormal coordinate system. For a transverse guided field propagating in the $+\hat{s}$ direction, we assume

$$\vec{E}(\vec{r}, t) = \vec{E}_\perp(x, z) e^{-j(ks-\omega t)},$$
$$\vec{H}(\vec{r}, t) = \vec{H}_\perp(x, z) e^{-j(ks-\omega t)}, \qquad \vec{B}_\perp = \mu \vec{H}_\perp,$$

where fields are all transverse with phase velocity $v_p = \omega/k$.

(a) Show that the frequency ω and the wave number k of the electromagnetic wave satisfy the dispersion relation $\omega = k/\sqrt{\epsilon\mu}$. Show that the transverse electromagnetic fields satisfy the static electromagnetic field equation,

$$\left(\frac{\partial^2}{\partial x^2} + \frac{\partial^2}{\partial z^2}\right) \vec{E}_\perp(x, z) = 0, \qquad \left(\frac{\partial^2}{\partial x^2} + \frac{\partial^2}{\partial z^2}\right) \vec{H}_\perp(x, z) = 0,$$

and the transverse plane wave obeys the relation $\vec{H} = \frac{1}{Z}\, \hat{s} \times \vec{E}_\perp$, where $Z = \sqrt{\mu/\epsilon}$ is the intrinsic impedance of the medium.

(b) Show that, because of the transverse nature of the electromagnetic field, the electric field can be represented by

$$\vec{E}(x, z) = -\nabla_\perp \phi(x, z),$$

where ϕ is the electric potential, and $\nabla_\perp$ is the transverse gradient with respect to the transverse coordinates. By definition, the capacitance per unit length is $C = \lambda/V$, where $V = \phi_1 - \phi_2$ is the potential difference between two conductors, and λ is the charge per unit length on conductors. Using Ampere's law, show that

$$\oint \vec{H} \cdot d\vec{r} = \lambda/\epsilon Z = \lambda v_p,$$

where $I = \lambda v_p$ is the current per unit length, and $d\vec{r} = dx\hat{x} + dz\hat{z}$.

(c) Similarly, the inductance per unit length is

$$L = \frac{1}{I}\frac{d\Phi}{ds} = \frac{\mu}{I}\int_{c_1}^{c_2} \vec{H} \cdot (\hat{s} \times d\vec{r}),$$

where the integral is carried out between two conductors. Show that there is a general relation:

$$C\,L = \mu\epsilon = 1/v_p^2.$$

The characteristic impedance of the transmission line is given by $R_c = \sqrt{L/C} = V/I$, where C and L are the capacitance and the inductance per unit length.

(d) Show that the capacitance and the inductance per unit length of a coaxial cable with inner and outer radii r_1 and r_2 are

$$C = \frac{2\pi\epsilon}{\ln(r_2/r_1)}, \qquad L = \frac{\mu}{2\pi}\ln\frac{r_2}{r_1}.$$

Fill out the following table for some commonly used coaxial cables.

Type	Diameter [cm]	Capacitance [pF/m]	Inductance [μH/m]	R_c [Ω]	Delay time [ns/m]
RG58/U	0.307	93.5		50	
RG174/U	0.152	98.4		50	
RG218/U	1.73	96.8		50	

14. Derive the transverse equations of motion for electrons in a betatron[49] by the following procedures. In the cylindrical coordinate system, the equation of motion for electrons is

$$\frac{dp_r}{dt} - \gamma m r \dot{\theta}^2 = -e r \dot{\theta} B_z, \qquad \frac{dp_z}{dt} = e r \dot{\theta} B_r,$$

where $\hat{r}, \hat{z}$ are respectively the radially outward and vertically upward directions, B_r, B_z are the radial and vertical components of the magnetic flux density, θ is the azimuthal angle, and $\dot{\theta} = v/r$ is the angular velocity.

(a) Assume that the vertical component of the magnetic flux density is

$$B_z = B_0\left(\frac{r}{R}\right)^{-n} \approx B_0\left(1 - n\frac{r-R}{R} + \cdots\right),$$

where n is the field index. Show that the radial magnetic field with $B_r = 0$ at $z = 0$ is

$$B_r = z\left(\frac{\partial B_z}{\partial r}\right)_{r=R} = -\frac{nB_0}{R}z + \cdots.$$

(b) Using

$$\xi = (r - R)/R \quad \text{and} \quad \zeta = z/R,$$

show that the equations of motion become

$$\ddot{\xi} + \omega_0^2(1-n)\xi = 0, \qquad \ddot{\zeta} + \omega_0^2 n \zeta = 0,$$

where $\omega_0 = v/R = eB_0/\gamma m$ is the angular velocity of the orbiting particle. Show that the stability of betatron motion requires $0 \le n \le 1$.

15. Ion sources are indispensable to all applications in accelerators. For electron beams, there are thermionic sources, rf gun sources, laser-driven electron sources, etc. For charged ion beams, there are many different configurations for generating plasma

[49] See D. Kerst and R. Serber, *Phys. Rev.* **60**, 53 (1941). Because of this seminal work, the transverse oscillations of charged particles in linear or circular accelerators are generally called *betatron oscillations*.

sources for beam extraction.[50] Charged ion beams are usually drawn from a space-charge ion source at zero initial velocity. The flow of charged ions is assumed to be laminar. In the space-charge dominated limit, the electric field between the anode and the cathode is maximally shielded by the beam charge. The maximum beam current occurs when the electric field becomes zero at the emitter. Assume a simplified geometry of two infinite parallel plates so that the the motion of ions is one-dimensional. Let s be the distance coordinate between the parallel plates with $s = 0$ at the emitter, and $s = a$ at the anode. The Poisson equation becomes

$$\frac{d^2V}{ds^2} = -\frac{\rho}{\epsilon_0},$$

where V is the electric potential, ρ is the ion density in the parallel plate, and ϵ_0 is the permittivity.

(a) In the non-relativistic limit with laminar flow, show that the Poisson equation becomes

$$\frac{d^2V}{ds^2} = \frac{J}{\epsilon_0}\left(\frac{m}{2e}\right)^{1/2} V^{-1/2},$$

where $J = \rho v$ is the current density, e and m are the charge and mass of the ion, and v is the velocity of the ion.

(b) For a space-charge dominated beam, the condition of maximum space-charge shielding is equivalent to $V = 0$ and $dV/ds = 0$ at $s = 0$. Show that the maximum current is

$$J = \chi V_0^{3/2}/a^2,$$

where V_0 is the extraction voltage at the anode, and

$$\chi = \frac{4\epsilon_0}{9}\left(\frac{2e}{m}\right)^{1/2}$$

is the perveance of the ion source. The relation of the current to the extraction voltage is called Child's law.[51]

(c) Show that the space-charge perveance parameters for electron, proton, deuteron, He^+, N^+, and Ar^+ ion sources are given by the following table. Here the micro-perveance is defined as $1\ \mu\mathrm{P} = 1 \times 10^{-6}\ \mathrm{A/V^{3/2}}$.

	e	p	D^+	He^+	N^+	A^+
χ (μP)	2.334	0.0545	0.0385	0.0272	0.0146	0.00861

16. **The Paraxial Ray Equation**: In the free space, the electric potential obeys the Laplace equation $\nabla^2 V = 0$. Using the basis vectors $(\hat{r}, \hat{\phi}, \hat{s})$ for the cylindrical coordinates in paraxial geometry, where r is the radial distance from the axis of symmetry, ϕ is the azimuthal coordinate, and s is the longitudinal coordinate, we expand the

[50] See e.g. *Proc. Int. Symp. on Electron Beam Ion Sources, AIP Conf. Proc.* No. 188 (1988); *Production and Neutralization of Negative Ions and Beams, AIP Conf. Proc.* No. 210 (1990).

[51] C.D. Child, *Phys. Rev.* **32**, 492 (1911); I. Langmuir, *Phys. Rev.* **32**, 450 (1913). See also A.T. Forrester, *Large Ion Beams* (Wiley, New York, 1988).

position vector as $\vec{R} = r\hat{r} + s\hat{s}$. Let $V_0(s)$ be the electric potential on the axis of symmetry. Show that the electric potential $V(r,s)$ and the electric field $\vec{E} = E_r\hat{r} + E_s\hat{s}$ are

$$V(r,s) = V_0(s) - \frac{V_0^{(2)}}{4}r^2 - \frac{V_0^{(4)}}{64}r^4 + \cdots,$$
$$E_r = \frac{V_0^{(2)}}{2}r + \frac{V_0^{(4)}}{16}r^3 + \cdots,$$
$$E_s = -V_0^{(1)} + \frac{V_0^{(3)}}{4}r^2 + \frac{V_0^{(5)}}{64}r^4 + \cdots,$$

where $V_0^{(n)}$ correspond to nth-derivative of V_0 with respect to s. The equation of motion for a non-relativistic particle in the electric field is $m\ddot{\vec{R}} = e\vec{E}$, where the overdot represents the time derivative. Show that the equation of motion for the radial coordinate, known as *the paraxial ray equation*, becomes

$$Vr'' + \frac{1}{2}V'r' + \frac{1}{4}V''r = 0,$$

where V replaces V_0 for simplicity and the prime is the derivative with respective to s. The paraxial ray equation can be used to analyze the beam envelope in electrostatic accelerators.[52]

17. Consider a line charge inside an infinitely long circular conducting cylinder with radius b. The line-charge density per unit length is λ, and the coordinates of the line charge are $\vec{a} = (a\cos\phi, a\sin\phi)$, where a is the distance from the center of the cylinder, and ϕ is the phase angle with respect to the $\hat{x}$ axis. Show that the induced surface charge density on the cylinder is[53]

$$\begin{aligned}\sigma(b,\phi_w) &= -\frac{\lambda}{2\pi b}\frac{b^2 - a^2}{b^2 + a^2 - 2ba\cos(\phi_w - \phi)} \\ &= -\frac{\lambda}{2\pi b}\left[1 + 2\sum_{i=1}^{\infty}\left(\frac{a}{b}\right)^n \cos n(\phi_w - \phi)\right].\end{aligned}$$

where ϕ_w is the angular coordinate of the cylindrical wall surface. This result is the basis of beam position monitor design.

[52] V.K. Zworykin *et al.*, *Electron Optics and the Electron Microscope*, (Wiley, 1945); J.R. Pierce, *Theory and Design of Electron Beams*, (Van Nostrand, 1949); V.E. Cosslett, *Introduction to Electron Optics*, (Oxford, 1950); F. Terman, *Radio Engineers' Handbook*, (McGraw-Hill, 1943).

[53] Let the image charge be located at $\vec{c} = (c\cos\phi,\ c\sin\phi)$, then the electric potential for infinite line charges at $\vec{r}$ is

$$\Phi(r) = \frac{\lambda}{2\pi\epsilon_0}\ln|\vec{r} - \vec{a}| + \frac{\lambda_i}{2\pi\epsilon_0}\ln|\vec{r} - \vec{c}|.$$

The electric field is $E = -\nabla\Phi$. Using the condition $E_\phi = 0$ on the conducting wall surface in the cylindrical coordinate, we obtain $c = b^2/a$ and $\lambda_i = -\lambda$. The induced surface charge density is $\sigma = \epsilon_0 E_r$. The multipole expansion can be obtained by using the identity $\cos n\theta + j\sin n\theta = e^{jn\theta}$.

Chapter 2

Transverse Motion

In an accelerator, the transverse particle motion is divided into a closed orbit[1] and a small-amplitude betatron motion around the closed orbit. The terminology of betatron motion is derived from the seminal work of D. Kerst and R. Serber on the transverse particle motion in a betatron. It is now used for transverse motion in all types of accelerators.

In synchrotrons, bending magnets are needed to provide complete revolution of the particle beam. This defines a closed orbit. Betatron motion around the closed orbit is determined by an arrangement of quadrupoles, called the accelerator *lattice*. In actual accelerators, magnetic field errors are unavoidable; therefore the closed orbit and the betatron motion will be perturbed. Lattice design has to take these field errors into account. In particular, since the bending angle of a dipole depends on the particle momentum, the resulting closed orbits will also depend on the particle momentum. In the first-order approximation, the deviation of the closed orbit is proportional to the fractional off-momentum deviation $(p - p_0)/p_0$, where p_0 is the momentum of a reference particle. The dispersion function, defined as the derivative of the closed orbit with respect to the fractional off-momentum variable, and the chromatic aberration of the betatron motion play a major role in the accelerator's performance. Furthermore, high-intensity and high-brightness beams require measurement and correction of linear and nonlinear resonances, and measurement, control and feedback-correction of collective beam instabilities.

Various aspects of transverse particle motion in synchrotrons will be discussed in this chapter.[2] In Sec. I, we derive the particle Hamiltonian in the Frenet-Serret coordinate system. In Sec. II, we examine the properties of linear betatron motion. We discuss the Floquet transformation to action-angle variables, beam distribution,

[1] A closed orbit in a synchrotron is defined as a particle trajectory that closes on itself after a complete revolution. A closed orbit in a linac is the orbit with zero betatron oscillation amplitude. Particle motion with a small deviation from the closed orbit will oscillate around the closed orbit.

[2] In principle, the method discussed in this chapter can also be applied to a linac or a transport line, where the betatron motion is equivalent to an initial value problem.

beam emittance, and properties of the envelope function. In Sec. III, we study the effects of linear magnetic imperfections (dipole and quadrupole field errors) and their application in beam manipulation. Section IV deals with the off-momentum closed orbit and its implications for longitudinal synchrotron motion, and also with the lattice design strategies for variable γ_T and minimum dispersion action. Section V describes the chromatic aberration and its correction, and Section VI describes linear betatron coupling. In Sec. VII, we examine the effects of low-order nonlinear resonances. Section VIII introduces the basic concept of transverse collective instabilities and Landau damping. Section IX lays out a general framework for the synchrotron-betatron coupling Hamiltonian.

I Hamiltonian for Particle Motion in Accelerators

The motion of a charged particle in electromagnetic field $\vec{E}$ and $\vec{B}$ is governed by the Lorentz force,

$$\frac{d\vec{p}}{dt} = \vec{F} = e(\vec{E} + \vec{v} \times \vec{B}), \tag{2.1}$$

where $\vec{p} = \gamma m \vec{v}$ is the relativistic kinetic momentum, $\vec{v} = d\vec{r}/dt$ is the velocity, m is the mass, e is the charge, and $\gamma = 1/\sqrt{1 - v^2/c^2}$ is the relativistic Lorentz factor. The energy and momentum of the particle can be expressed as $E = \gamma mc^2 = mc^2 dt/d\tau$ and $\vec{p} = m\gamma\vec{v} = md\vec{r}/d\tau$, where τ is the proper time with $dt/d\tau = \gamma$. Thus Eq. (2.1) can be derived from Lagrange's equation

$$\frac{d}{dt}\left(\frac{\partial L}{\partial \vec{v}}\right) - \frac{\partial L}{\partial \vec{r}} = 0,$$

where the Lagrangian is $L = -mc^2\sqrt{1 - v^2/c^2} - e\Phi + e\vec{v}\cdot\vec{A}$. The electric and magnetic fields are related to the vector potential $\vec{A}$ and the scalar potential Φ by

$$\vec{E} = -\nabla\Phi - \partial\vec{A}/\partial t, \quad \vec{B} = \nabla \times \vec{A}. \tag{2.2}$$

The canonical momentum $\vec{P} = \partial L/\partial\vec{v} = \vec{p} + e\vec{A}$, and $\vec{p}$ is the mechanical momentum.

The Hamiltonian for particle motion is given by

$$H = \vec{P}\cdot\vec{v} - L = c[m^2c^2 + (\vec{P} - e\vec{A})^2]^{1/2} + e\Phi, \tag{2.3}$$

and Hamilton's equations of motion are

$$\dot{x} = \frac{\partial H}{\partial P_x}, \quad \dot{P}_x = -\frac{\partial H}{\partial x}, \quad \text{etc.}, \tag{2.4}$$

where the overdot is the derivative with respect to time t, and $(x, P_x), \cdots$ pairs are conjugate phase-space coordinates.

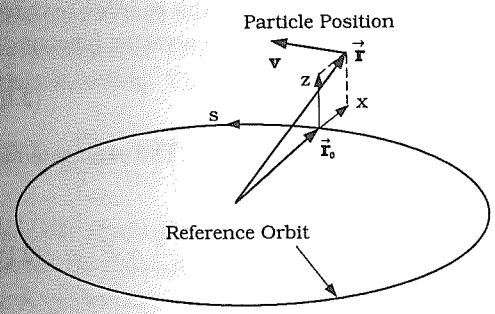

Figure 2.1: Curvilinear coordinate system for particle motion in synchrotrons. $\vec{r}_0(s)$ is the reference orbit, $\hat{x}, \hat{s}$ and $\hat{z}$ form the basis of the curvilinear coordinate system. Any point in the phase space can be expressed by $\vec{r} = \vec{r}_0 + x\hat{x} + z\hat{z}$. Here x and z are betatron coordinates.

I.1 Hamiltonian in Frenet-Serret Coordinate System

Let $\vec{r}_0(s)$ be the reference orbit (see Fig. 2.1), where s is the arc length measured along the closed orbit from a reference initial point. The tangent unit vector to the closed orbit is given by

$$\hat{s}(s) = \frac{d\vec{r}_0(s)}{ds}. \tag{2.5}$$

The unit vector perpendicular to the tangent vector and on the tangential plane is[3]

$$\hat{x}(s) = -\rho(s)\frac{d\hat{s}(s)}{ds}, \tag{2.6}$$

where $\rho(s)$ defines the radius of curvature. The unit vector orthogonal to the tangential plane is given by

$$\hat{z}(s) = \hat{x}(s) \times \hat{s}(s). \tag{2.7}$$

The vectors $\hat{x}, \hat{s}$ and $\hat{z}$ form the orthonormal basis for the right-handed Frenet-Serret curvilinear coordinate system with

$$\hat{x}'(s) = \frac{1}{\rho(s)}\hat{s}(s) + \tau(s)\hat{z}(s), \quad \hat{z}'(s) = -\tau(s)\hat{x}(s), \tag{2.8}$$

where the prime denotes differentiation with respect to s, and $\tau(s)$ is the torsion of the curve. For simplicity, we discuss only plane geometry, where $\tau(s) = 0$. The particle trajectory around the reference orbit can be expressed as

$$\vec{r}(s) = \vec{r}_0(s) + x\hat{x}(s) + z\hat{z}(s). \tag{2.9}$$

[3]Using Eq. (2.5), we find $a_{\text{centripetal}} = |d^2\vec{r}_0/dt^2| = (ds/dt)^2|(d/ds)(d\vec{r}_0/ds)| = v^2|(d\hat{s}/ds)|$, where $v = ds/dt$ is the tangential velocity. The magnitude of the bending radius is $\rho = v^2/a_{\text{centripetal}} = |ds/d\hat{s}|$.

To express the equation of motion in terms of the reference orbit coordinate system (x, s, z), we perform a canonical transformation by using the generating function

$$F_3(\vec{P}; x, s, z) = -\vec{P} \cdot [\vec{r}_0(s) + x\hat{x}(s) + z\hat{z}(s)] \,, \tag{2.10}$$

where $\vec{P}$ is the momentum in the Cartesian coordinate system. The conjugate momenta for the coordinates (x, s, z) are (see Appendix A)

$$p_s = -\frac{\partial F_3}{\partial s} = (1 + x/\rho)\, \vec{P} \cdot \hat{s}, \quad p_x = -\frac{\partial F_3}{\partial x} = \vec{P} \cdot \hat{x}, \quad p_z = -\frac{\partial F_3}{\partial z} = \vec{P} \cdot \hat{z}. \tag{2.11}$$

The new Hamiltonian becomes

$$H = e\phi + c\left\{m^2c^2 + \frac{(p_s - eA_s)^2}{(1 + x/\rho)^2} + (p_x - eA_x)^2 + (p_z - eA_z)^2\right\}^{1/2}, \tag{2.12}$$

where A_s, A_x and A_z are obtained by substituting the vector $\vec{A}$ in Eq. (2.11), i.e.

$$A_s = (1 + x/\rho)\, \vec{A} \cdot \hat{s}, \quad A_x = \vec{A} \cdot \hat{x}, \quad A_z = \vec{A} \cdot \hat{z} \,. \tag{2.13}$$

Note that A_s and p_s are not simply the projections of vectors $\vec{A}$ and $\vec{P}$ in the $\hat{s}$ direction. In the new coordinate system, Hamilton's equation becomes

$$\dot{s} = \frac{\partial H}{\partial p_s}, \dot{p}_s = -\frac{\partial H}{\partial s}; \quad \dot{x} = \frac{\partial H}{\partial p_x}, \dot{p}_x = -\frac{\partial H}{\partial x}; \quad \dot{z} = \frac{\partial H}{\partial p_z}, \dot{p}_z = -\frac{\partial H}{\partial z}. \tag{2.14}$$

The next step is to use s as the independent variable instead of time t [16]. Using the relation $dH = (\partial H/\partial p_x)dp_x + (\partial H/\partial p_s)dp_s = 0$ or

$$x' = \frac{dx}{ds} = \frac{\dot{x}}{\dot{s}} = \left(\frac{\partial H}{\partial p_x}\right)\left(\frac{\partial H}{\partial p_s}\right)^{-1} = \frac{\partial(-p_s)}{\partial p_x}, \quad \text{etc.}, \tag{2.15}$$

where the prime denotes differentiation with respect to s, we find

$$t' = \frac{\partial p_s}{\partial H}, H' = -\frac{\partial p_s}{\partial t}; \quad x' = -\frac{\partial p_s}{\partial p_x}, p'_x = \frac{\partial p_s}{\partial x}; \quad z' = -\frac{\partial p_s}{\partial p_z}, p'_z = \frac{\partial p_s}{\partial z}. \tag{2.16}$$

This is Hamilton's equations of motion with s as the independent variable, $-p_s$ as the new Hamiltonian, and the conjugate phase-space coordinates given by

$$x, p_x; \quad z, p_z; \quad t, -H. \tag{2.17}$$

When the scalar and vector potentials ϕ and $\vec{A}$ are independent of time, the new Hamiltonian $-p_s$ is also time independent. The transformation reduces the degrees of freedom from three to two. But the price to pay is that the new Hamiltonian depends on the new variable s. Because of the repetitive nature of the accelerator,

the dependence of the new Hamiltonian on s is periodic. The periodic nature of the new Hamiltonian can be fruitfully exploited in the analysis of linear and nonlinear betatron motion. The new Hamiltonian $\tilde{H} = -p_s$ is then given by

$$\tilde{H} = -\left(1 + \frac{x}{\rho}\right)\left[\frac{(H - e\phi)^2}{c^2} - m^2c^2 - (p_x - eA_x)^2 - (p_z - eA_z)^2\right]^{1/2} - eA_s, \tag{2.18}$$

where the phase-space coordinates are $(x, p_x, z, p_z, t, -H)$. The total energy and momentum of the particle are $E = H - e\phi$ and $p = \sqrt{E^2/c^2 - m^2c^2}$. Since the transverse momenta p_x and p_z are much smaller than the total momentum, we expand the Hamiltonian up to second order in p_x and p_z

$$\tilde{H} \approx -p\left(1 + \frac{x}{\rho}\right) + \frac{1 + x/\rho}{2p}\left[(p_x - eA_x)^2 + (p_z - eA_z)^2\right] - eA_s. \tag{2.19}$$

I.2 Magnetic Field in Frenet-Serret Coordinate System

In the Frenet-Serret coordinate system, $(\hat{x}, \hat{s}, \hat{z})$, the scale factor becomes

$$h_x = 1, \quad h_s = 1 + \frac{x}{\rho}, \quad h_z = 1. \tag{2.20}$$

We have

$$\begin{aligned}
\nabla\Phi &= \frac{\partial\Phi}{\partial x}\hat{x} + \frac{1}{h_s}\frac{\partial\Phi}{\partial s}\hat{s} + \frac{\partial\Phi}{\partial z}\hat{z}, \\
\nabla \cdot \vec{A} &= \frac{1}{h_s}\left[\frac{\partial(h_sA_1)}{\partial x} + \frac{\partial A_2}{\partial s} + \frac{\partial(h_sA_3)}{\partial z}\right], \\
\nabla \times \vec{A} &= \frac{1}{h_s}\left[\frac{\partial A_3}{\partial s} - \frac{\partial(h_sA_2)}{\partial z}\right]\hat{x} + \left[\frac{\partial A_1}{\partial z} - \frac{\partial A_3}{\partial x}\right]\hat{s} + \frac{1}{h_s}\left[\frac{\partial(h_sA_2)}{\partial x} - \frac{\partial A_1}{\partial s}\right]\hat{z}, \\
\nabla^2\Phi &= \frac{1}{h_s}\left[\frac{\partial}{\partial x}h_s\frac{\partial\Phi}{\partial x} + \frac{\partial}{\partial s}\frac{1}{h_s}\frac{\partial\Phi}{\partial s} + \frac{\partial}{\partial z}h_s\frac{\partial\Phi}{\partial z}\right],
\end{aligned}$$

where $A_1 = \vec{A} \cdot \hat{x}$, $A_2 = \vec{A} \cdot \hat{s}$, and $A_3 = \vec{A} \cdot \hat{z}$. In accelerator applications, we consider only the case with zero electric potential with $\Phi = 0$, furthermore, for an accelerator with transverse magnetic fields, we can assume $A_x = A_z = 0$. The two-dimensional magnetic field can be expressed as

$$\vec{B} = B_x(x, z)\hat{x} + B_z(x, z)\hat{z}, \tag{2.21}$$

where

$$B_x = -\frac{1}{h_s}\frac{\partial(h_sA_2)}{\partial z} = -\frac{1}{h_s}\frac{\partial A_s}{\partial z}, \quad B_z = \frac{1}{h_s}\frac{\partial(h_sA_2)}{\partial x} = \frac{1}{h_s}\frac{\partial A_s}{\partial x}, \tag{2.22}$$

with $A_s = h_s A_2$. Using Maxwell's equation $\nabla \times \vec{B} = 0$, we have

$$\frac{\partial}{\partial z}\frac{1}{h_s}\frac{\partial A_s}{\partial z} + \frac{\partial}{\partial x}\frac{1}{h_s}\frac{\partial A_s}{\partial x} = 0. \tag{2.23}$$

General solutions of B_x, B_z and A_s can be obtained through power series expansion (see Exercise 2.1.3).

For straight geometry with $h_s = 1$, we obtain $\nabla_\perp^2 A_s = 0$, and A_s can be expanded in power series as

$$A_s = B_0 \Re\left[\sum_{n=0}^{\infty} \frac{b_n + ja_n}{n+1}(x+jz)^{n+1}\right], \tag{2.24}$$

where j is the imaginary number, $\Re[...]$ represents the real part, and $B_z = \frac{\partial A_s}{\partial x}$ and $B_x = -\frac{\partial A_s}{\partial z}$. Normally the normalization constant B_0 is chosen as the main dipole field strength such that $b_0 = 1$. Thus we have $B_0 b_0 = -[B\rho]/\rho$, where $B\rho$ is the momentum rigidity of the beam, ρ is the bending radius, and $b_0 = 1$. The resulting magnetic flux density is given by[4]

$$B_z + jB_x = B_0 \sum_{n=0}^{\infty}(b_n + ja_n)(x+jz)^n \tag{2.25}$$

with

$$b_n = \frac{1}{B_0 n!}\frac{\partial^n B_z}{\partial x^n}\bigg|_{x=z=0}, \quad a_n = \frac{1}{B_0 n!}\frac{\partial^n B_x}{\partial x^n}\bigg|_{x=z=0}, \tag{2.26}$$

where b_n, a_n are called $2(n+1)$th multipole coefficients with dipole b_0, dipole roll a_0, quadrupole b_1, skew quadrupole a_1, sextupole b_2, skew sextupole a_2, etc.[5] The effective multipole field on the beams becomes

$$\frac{1}{B\rho}(B_z + jB_x) = \mp\frac{1}{\rho}\sum_{n=0}^{\infty}(b_n + ja_n)\,(x+jz)^n, \tag{2.27}$$

where, in our coordinate system, the $-$ and $+$ signs are used for particles with positive and negative charges respectively. The complex 2D magnetic field representation in $B_z + jB_x$ is called the Beth representation (see Exercise 1.10).

[4]The multipole expansion of the magnetic field is usually rescaled to obtain

$$B_z + jB_x = B_0 \sum_{n=0}^{\infty}(b_n + ja_n)(\frac{x+jz}{r_b})^n,$$

where r_b is a reference radius. For high energy accelerators such as the SSC and LHC, $r_b = 1$ cm, and for RHIC and Tevatron, $r_b = 2.54$ cm. The resulting b_n and a_n coefficients are dimensionless.

[5]Note that the multipole convention used in Europe differs from that in the U.S. In Europe, physicists use b_1, a_1 for dipole and dipole roll, b_2, a_2 for quadrupole and skew quadrupole, etc.

Since $\nabla \times \vec{B} = 0$ in the current free region, the magnetic field can also be derived from a scalar magnetic potential Φ_m, i.e. $\vec{B} = -\nabla\Phi_m$ (see Exercise 2.1.3). The scalar magnetic potential is

$$\Phi_m = -B_0 \Im\left[\sum_{n=0}^{\infty}\frac{b_n + ja_n}{n+1}(x+jz)^{n+1}\right], \tag{2.28}$$

where $\Im[...]$ represents the imaginary part of the expression.

I.3 Equation of Betatron Motion

Disregarding the effect of synchrotron motion (see Sec. IX), Hamilton's equations of betatron motion are given by

$$x' = \frac{\partial \tilde{H}}{\partial p_x}, \quad p_x' = -\frac{\partial \tilde{H}}{\partial x}, \qquad z' = \frac{\partial \tilde{H}}{\partial p_z}, \quad p_z' = -\frac{\partial \tilde{H}}{\partial z}.$$

With the transverse magnetic fields of Eq. (2.22), the betatron equations of motion become

$$\begin{cases} x'' - \dfrac{\rho + x}{\rho^2} = \pm\dfrac{B_z}{B\rho}\dfrac{p_0}{p}\left(1+\dfrac{x}{\rho}\right)^2, \\ z'' = \mp\dfrac{B_x}{B\rho}\dfrac{p_0}{p}\left(1+\dfrac{x}{\rho}\right)^2, \end{cases} \tag{2.29}$$

where we neglect higher-order terms, the upper and lower signs correspond to the positive and negative charged particle respectively, p is the momentum of the particle, p_0 is the momentum of a reference particle, $B\rho = p_0/e$ is the *magnetic rigidity*, and e is the charge of a particle. The sign convention is chosen such that $B\rho$ is positive. Alternatively, Eq. (2.29) can be derived through Newton's law of acceleration (see Exercise 2.1.2). The equations of motion are given by

$$\ddot{r} - r\dot{\theta}^2 = \frac{ev_s B_z}{\gamma m} = \pm\frac{v_s^2 B_z}{B\rho}, \qquad \ddot{z} = \mp\frac{v_s^2 B_x}{B\rho},$$

which can be transformed into Eq. (2.29) by changing the time variable to the coordinate of orbital distance s, i.e. $x'' = \ddot{r}/v_s^2$.

I.4 Particle Motion in Dipole and Quadrupole Magnets

We consider a on-momentum particle with $p = p_0$, expand the magnetic field up to first order in x and z, i.e.

$$B_z = -B_0 + \frac{\partial B_z}{\partial x}x = \mp B_0 + B_1 x, \qquad B_x = \frac{\partial B_z}{\partial x}z = B_1 z, \tag{2.30}$$

where $B_0/B\rho = 1/\rho$ signifies the dipole field in defining a closed orbit, and the quadrupole gradient function $B_1 = \partial B_z/\partial x$ is evaluated at the closed orbit. The betatron equation of motion, Eq. (2.29), becomes

$$x'' + K_x(s)x = 0, \qquad K_x = 1/\rho^2 \mp K_1(s), \tag{2.31}$$
$$z'' + K_z(s)z = 0, \qquad K_z = \pm K_1(s), \tag{2.32}$$

where $K_1(s) = B_1(s)/B\rho$ is the effective focusing function, and the upper and lower signs correspond respectively to the positive and negative charged particles. The focusing index is given by $n(s) = \rho^2 K_1(s)$. A weak focusing accelerator requires $0 \le n(s) \le 1$. For a strong-focusing accelerator, $|n| \gg 1$, e.g. $n(s) \approx \pm 350$ for the AGS. Some observations about the linear betatron equations (2.31) and (2.32) are given below.

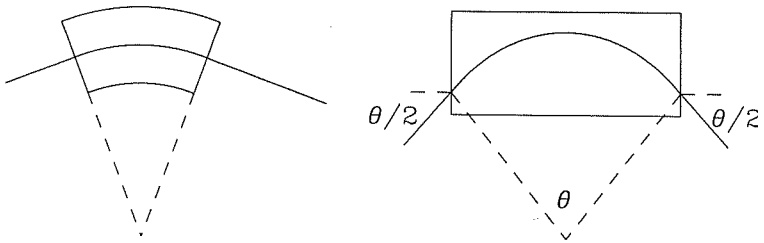

(a) sector dipole (b) rectangular dipole

Figure 2.2: Schematic drawing of the particle trajectory in a *sector dipole* and in a *rectangular dipole*. Note that the particle orbit is perpendicular to the pole-faces of the sector dipole magnet, and makes an angle $\theta/2$ with the pole-faces in the rectangular dipole.

- In a quadrupole, where $1/\rho = 0$, we have $K_x = -K_z$. This means that a horizontally focusing quadrupole is also a vertically defocussing quadrupole and vice versa.
- A horizontal bending dipole has a focusing function $K_x = 1/\rho^2$, and $K_z = 0$. Such a dipole is called a *sector dipole* with perpendicular entrance and exit angles to the edge of the dipole field (see Fig. 2.2a). For non-sector type dipoles, where the entrance and exit angles of particle trajectories are not perpendicular to the dipole edge, there is an edge focusing/defocussing effect (see Exercise 2.2.2).
- The focusing functions K_x, K_z are periodic functions of the longitudinal coordinate s. Thus Eqs. (2.31) and (2.32) are Hill's equations with periodic boundary conditions. The solution of Hill's equation satisfies the Floquet theorem, to be discussed in next section.

Exercise 2.1

1. In the Frenet-Serret coordinate system $(\hat{x}, \hat{s}, \hat{z})$, transverse magnetic fields are

$$B_x = -\frac{1}{1+x/\rho}\frac{\partial A_s}{\partial z}, \quad B_z = \frac{1}{1+x/\rho}\frac{\partial A_s}{\partial x}.$$

Derive Eq. (2.29) from the Hamiltonian of Eq. (2.19).

2. Derive Eq. (2.29) through the following geometric argument. Let $(\hat{x}, \hat{s}, \hat{z})$ be local polar coordinates inside a dipole. The particle coordinate is

$$\vec{r} = (\rho + x)\hat{x} + z\hat{z},$$

where ρ is the bending radius. The momentum of the particle is $\vec{p} = \gamma m\dot{\vec{r}}$, where γ is constant in the static magnetic field, and the overdot corresponds to the derivative with respect to time t. Similarly, $d\vec{p}/dt = \gamma m\ddot{\vec{r}}$.

(a) Using Eq.(2.8), show that

$$\dot{\vec{r}} = \dot{x}\hat{x} + (\rho + x)\dot{\theta}\hat{s} + \dot{z}\hat{z},$$
$$\ddot{\vec{r}} = [\ddot{x} - (\rho + x)\dot{\theta}^2]\hat{x} + [2\dot{x}\dot{\theta} + (\rho + x)\ddot{\theta}]\hat{s} + \ddot{z}\hat{z},$$

where $\theta = s/\rho$ is the angle associated with the reference orbit, i.e. $ds = \rho d\theta$.

(b) Using $d\vec{p}/dt = e\vec{v} \times \vec{B}$, with $\vec{B} = B_x\hat{x} + B_z\hat{z}$, show that

$$\ddot{x} - (\rho + x)\dot{\theta}^2 = \frac{v_s^2 B_z}{B\rho}, \quad \ddot{z} = -\frac{v_s^2 B_x}{B\rho},$$

where $B\rho = \gamma m v_s/e$ is the momentum rigidity and v_s is the longitudinal velocity.

(c) Transform the time coordinate to the longitudinal distance s with $ds = \rho d\theta$, where $d\theta = v_s dt/(\rho + x)$, and show that

$$x'' - \frac{\rho + x}{\rho^2} = \frac{B_z}{B\rho}(1 + \frac{x}{\rho})^2, \qquad z'' = -\frac{B_x}{B\rho}(1 + \frac{x}{\rho})^2,$$

where the prime is the derivative with respect to s.

3. Inside the vacuum chamber of an accelerator, we have $\nabla \times \vec{B} = 0$ and $\nabla \times \vec{E} = 0$. Thus the electric field and magnetic field can be expanded by scalar potentials with $\vec{B} = -\nabla\Phi_m, \vec{E} = -\nabla\Phi_e$, where both scalar potentials satisfy the Laplace equation with $\nabla^2\Phi$, where Φ stands for either Φ_m or $\Phi_e = 0$. In the curvilinear coordinates (x, s, z), we then have

$$\nabla^2\Phi = \frac{1}{1+hx}\frac{\partial}{\partial x}([1+hx]\frac{\partial\Phi}{\partial x}) + \frac{\partial^2\Phi}{\partial z^2} + \frac{1}{1+hx}\frac{\partial}{\partial s}(\frac{1}{1+hx}\frac{\partial\Phi}{\partial s}) = 0,$$

where $h = 1/\rho$, and ρ is the radius of curvature. Expressing the scalar potential in power series of particle coordinates,

$$\Phi = \sum_{i,j>0} A_{ij}\frac{x^i}{i!}\frac{z^j}{j!},$$

show that A_{ij} satisfies the following iteration relation:

$$\begin{aligned} A_{i,j+2} &= -A''_{i,j} - ihA''_{i-1,j} + ih'A'_{i-1,j} - A_{i+2,j} - (3i+1)hA_{i+1,j} \\ &\quad -3ihA_{i-1,j+2} - i(3i-1)h^2A_{i,j} - 3i(i-1)h^2A_{i-2,j+2} \\ &\quad -i(i-1)^2h^3A_{i-1,j} - i(i-1)(i-2)h^3A_{i-3,j+2}, \end{aligned}$$

where the prime is the derivative with respect to s. Assuming $A_{00} = 0, A_{10} = 0$, and $A_{01} = -B_{00}$ in a rectangular coordinate system with $h = h' = 0$, show that the magnetic potential, up to the fourth order with $i + j \leq 4$, is[6]

$$\begin{aligned} \Phi &= -B_{00}z + \frac{1}{2}A_{20}(x^2 - z^2) + A_{11}xz + \frac{1}{6}A_{30}(x^3 - 3xz^2) + \frac{1}{2}B''_{00}xz^2 \\ &\quad + \frac{1}{2}A_{21}x^2z + \frac{1}{6}(B''_{00} - A_{21})z^3 + \frac{1}{24}A_{40}(x^4 - 6x^2z^2 + z^4) \\ &\quad + \frac{1}{12}A''_{20}(-3x^2z^2 + z^4) + \frac{1}{6}A_{31}(x^3z - xz^3) - \frac{1}{6}A''_{11}xz^3. \end{aligned}$$

4. The field components in the current-free region of an axial symmetric solenoid are

$$B_x = x\sum_{k=0}^{\infty} b_{2k+1}(x^2+z^2)^k, \quad B_z = z\sum_{k=0}^{\infty} b_{2k+1}(x^2+z^2)^k, \quad B_s = \sum_{k=0}^{\infty} b_{2k}(x^2+z^2)^k.$$

(a) Show that the coefficients are

$$b_{2k+1} = \frac{-1}{2(k+1)}b'_{2k}, \quad b_{2k+2} = \frac{1}{2(k+1)}b'_{2k+1},$$

where the prime is the derivative with respect to s. Show that the vector potential is

$$A_x = z\sum_{k=0}^{\infty}\frac{b_{2k}}{2(k+1)}(x^2+z^2)^k, \quad A_z = -x\sum_{k=0}^{\infty}\frac{b_{2k}}{2(k+1)}(x^2+z^2)^k, \quad A_s = 0.$$

In a cylindrical coordinate system, where $\vec{r} = x\hat{x} + z\hat{z}$, $r = \sqrt{x^2+z^2}$, and $\hat{\phi} = (-z\hat{x} + x\hat{z})/r$, show that the vector potential can be expressed as

$$\vec{A} = -\left[\frac{1}{2}r\,b_0(s) - \frac{1}{16}r^3\,b''_0(s) + \cdots\right]\hat{\phi}.$$

(b) The Hamiltonian of Eq. (2.19) for the particle motion in the solenoid is

$$H = -p + \frac{1}{2p}[(p_x - eA_x)^2 + (p_z - eA_z)^2].$$

[6] A word of caution: the magnetic potential obtained here can not be used as the potential in the Hamiltonian of Eq. (2.18). In particular, the potential for a quadrupole is given by the A_{11} term and the skew quadrupole arises from the A_{20} term, etc. However, this serves as a general method for deriving the magnetic field map.

Show that the linearized equation of motion is (see also Exercise 2.6.2)

$$\begin{aligned} x'' + 2gz' + g'z &= 0, \\ z'' - 2gx' - g'x &= 0, \end{aligned}$$

where $g = eb_0/2p = eB_{\|}/2p$ is the strength of the solenoid. The linearized equation can be solved analytically. Letting $y = x + jz$, show that the coupled equation of motion becomes

$$y'' - j2gy' - jg'y = 0.$$

Transforming the coordinates into the rotating frame with

$$\bar{y} = ye^{-j\theta(s)}, \quad \text{where} \quad \theta = \int_0^s g\,ds,$$

show that the system is decoupled, and the decoupled equation of motion becomes

$$\bar{y}'' + g^2\bar{y} = 0.$$

Thus the solenoidal field, in the rotating frame, provides both horizontal and vertical focusing, independent of the direction of the solenoidal field. Note also that the effects of the ends of a solenoid, included in the g' terms, have been included to obtain this Hill's equation in the rotating frame.

(c) Up to third order, show that the equation of motion is

$$\begin{aligned} x'' + 2gz' + g'z &= \frac{g''}{2}z'(x^2+z^2) + \frac{g'''}{8}z(x^2+z^2), \\ z'' - 2gx' - g'x &= -\frac{g''}{2}x'(x^2+z^2) - \frac{g'''}{8}x(x^2+z^2). \end{aligned}$$

5. Consider the transverse magnetic field in the Frenet-Serret coordinate system.[7] For normal multipoles with mid-plane symmetry with

$$B_z(z) = B_z(-z), \quad B_x(z) = -B_x(-z), \quad B_s(z) = -B_s(-z),$$

the most general form of expansion is

$$B_z = \sum_{i,k=0}^{\infty} b_{i,k}x^iz^{2k}, \quad B_x = z\sum_{i,k=0}^{\infty} a_{i,k}x^iz^{2k}, \quad B_s = z\sum_{i,k=0}^{\infty} c_{i,k}x^iz^{2k},$$

where a, b, c can be determined from Maxwell's equations: $\nabla \times \vec{B} = 0$ and $\nabla \cdot \vec{B} = 0$. Show that Maxwell's equations give the following relations:

$$a_{i,k} = \frac{i+1}{2k+1}b_{i+1,k}, \qquad c_{i,k} + \frac{1}{\rho}c_{i-1,k} = \frac{1}{2k+1}b'_{i,k},$$

$$c'_{i,k} + \frac{(i+1)^2}{\rho(2k+1)}b_{i+1,k} + \frac{(i+1)(i+2)}{2k+1}b_{i+2,k} + \frac{2(k+1)}{\rho}b_{i-1,k+1} + 2(k+1)b_{i,k+1} = 0,$$

[7] See K. Steffen, CERN **85-19**, p. 25 (1985).

where the prime is the derivative with respect to s. Assuming that we can measure the B_z at the mid-plane as a function of x, s, i.e.

$$B_z(z=0) = B_{0,0} + B_{1,0}x + B_{2,0}x^2 + B_{3,0}x^3 + \cdots,$$

where $B_{i,0}$ are functions of s, show that the field map is

$$\begin{aligned}
B_z &= B_{0,0} + B_{1,0}x + B_{2,0}x^2 - (B_{2,0} + \frac{B''_{0,0}}{2} + \frac{B_{1,0}}{2\rho})z^2 + B_{3,0}x^3 \\
&\quad -\{3B_{3,0} + \frac{2B_{2,0}}{\rho} - \frac{1}{\rho}(B_{2,0} + \frac{B_{1,0}}{2\rho} + \frac{B''_{0,0}}{2}) + \frac{1}{2}[B''_{1,0} - (\frac{B'_{0,0}}{\rho})']\}xz^2 + \cdots, \\
B_x &= B_{1,0}z + 2B_{2,0}xz + 3B_{3,0}x^2z - \frac{1}{3}\{3B_{3,0} + \frac{2B_{2,0}}{\rho} \\
&\quad -\frac{1}{\rho}(B_{2,0} + \frac{B_{1,0}}{2\rho} + \frac{B''_{0,0}}{2}) + \frac{1}{2}[B''_{1,0} - (\frac{B'_{0,0}}{\rho})']\}z^3 + \cdots, \\
B_s &= B'_{0,0}z + (B'_{1,0} - \frac{B'_{0,0}}{\rho})xz + (B'_{2,0} - \frac{B'_{1,0}}{\rho} + \frac{B'_{0,0}}{\rho^2})x^2z \\
&\quad -\frac{1}{3}(B'_{2,0} + (\frac{B_{1,0}}{2\rho})' + \frac{B'''_{0,0}}{2})z^3 + \cdots.
\end{aligned}$$

Show that in a pure multipole magnet, where $\rho \to \infty$, the magnetic field can be expanded as

$$B_z + jB_x = \sum_{n=0} B_{n,0}(x+jz)^n - \frac{B''_{0,0}}{2}z^2 + \frac{B''_{1,0}}{2}(x+jz)z^2 + \cdots,$$

where j is the complex number. Thus for a finite length quadrupole with $B'_{1,0} \neq 0$, the end field has an octupole-like magnetic multipole field.

II Linear Betatron Motion

Particle motion around a closed orbit is called betatron motion. Since the amplitude of betatron motion is small, we study, in this section, the linearized betatron equation of motion governed by Hill's equation

$$x'' + K_x(s)x = 0, \quad z'' + K_z(s)z = 0, \tag{2.33}$$

where $K_x = 1/\rho^2 - B_1(s)/B\rho$, $K_z(s) = B_1(s)/B\rho$, and $B_1(s) = \partial B_z/\partial x$ evaluated at the closed orbit.[8] The focusing functions are periodic with $K_{x,z}(s+L) = K_{x,z}(s)$, and L is the length of a periodic structure in an accelerator. For example, Fig. 2.3 shows a schematic drawing of the Fermilab booster lattice, where four combined function magnets are arranged to form a basic focusing-defocussing periodic (FODO) cell. Exploiting the periodic nature, we can apply the Floquet theorem (see Appendix A, Sec. I.5) to facilitate the design of an accelerator lattice, In this section we study linear betatron motion, Floquet transformation, the Courant–Snyder invariant and emittance, betatron tune, and the envelope equation.

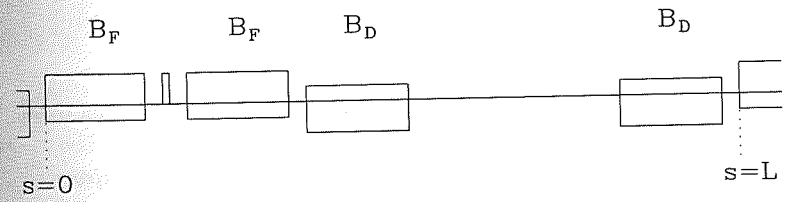

Figure 2.3: A schematic drawing of the Fermilab booster lattice. It consists of four combined-function magnets of length 2.889612 m and focusing function $K_F = 0.0244817$ m^{-2} and $K_D = -0.0208186$ m^{-2}. A small trim focusing quadrupole is used to change the betatron tune. The total length of a repetitive cell is 19.7588448 m. The accelerator is made of 24 such FODO cells, and thus the superperiod of the machine is 24. The nominal betatron tunes are $\nu_x = 6.7$ and $\nu_z = 6.8$.

II.1 Transfer Matrix and Stability of Betatron Motion

Because accelerator components usually have uniform or nearly uniform magnetic fields, the focusing functions $K_{x,z}(s)$ are piecewise constant. Let y, y' represent either horizontal or vertical phase-space coordinates, then Eq. (2.33) becomes

$$y'' + K_y(s)y = 0, \tag{2.34}$$

[8] The focusing functions are $K_x = 1/\rho^2 + B_1(s)/B\rho$ and $K_z(s) = -B_1(s)/B\rho$ for negative charged particles.

with the periodic condition $K_y(s+L) = K_y(s)$. The solutions of Hill's equation with constant K_y are[9]

$$y(s) = \begin{cases} a\ \cos(\sqrt{K}s + b), & K > 0, \\ as + b, & K = 0, \\ a\ \cosh(\sqrt{-K}s + b), & K < 0. \end{cases} \tag{2.35}$$

Since K is finite, y and y' must be continuous, and the integration constants a and b are determined by the initial values of y_0 and y_0'.

Letting

$$\mathbf{y}(s) = \begin{pmatrix} y(s) \\ y'(s) \end{pmatrix} \tag{2.36}$$

be the betatron state-vector, we can express the solution of Eq. (2.34) as

$$\mathbf{y}(s) = M(s|s_0)\mathbf{y}(s_0), \tag{2.37}$$

where $M(s|s_0)$ is the betatron transfer matrix. For any two linearly independent solutions y_1, y_2 of Hill's equation, the Wronskian is independent of time, i.e.

$$W(y_1, y_2, s) \equiv y_1 y_2' - y_1' y_2, \quad \frac{dW}{ds} = 0. \tag{2.38}$$

Since the Wronskian obeys $W(s) = [\det M]W(s_0)$, we obtain $\det M = 1$.

The transfer matrix for a constant focusing function K is

$$M(s|s_0) = \begin{cases} \begin{pmatrix} \cos\sqrt{K}\ell & \frac{1}{\sqrt{K}}\sin\sqrt{K}\ell \\ -\sqrt{K}\sin\sqrt{K}\ell & \cos\sqrt{K}\ell \end{pmatrix} & K > 0\text{: focusing quad.} \\ \begin{pmatrix} 1 & \ell \\ 0 & 1 \end{pmatrix} & K = 0\text{: drift space} \\ \begin{pmatrix} \cosh\sqrt{|K|}\ell & \frac{1}{\sqrt{|K|}}\sinh\sqrt{|K|}\ell \\ \sqrt{|K|}\sinh\sqrt{|K|}\ell & \cosh\sqrt{|K|}\ell \end{pmatrix} & K < 0\text{: defocussing quad.} \end{cases}$$

where $\ell = s - s_0$. In thin-lens approximation with $\ell \to 0$, the transfer matrix for a quadrupole reduces to

$$M_{\text{focusing}} = \begin{pmatrix} 1 & 0 \\ -1/f & 1 \end{pmatrix}, \quad M_{\text{defocussing}} = \begin{pmatrix} 1 & 0 \\ 1/f & 1 \end{pmatrix}, \tag{2.39}$$

where f is the focal length given by[10]

$$f = \lim_{\ell \to 0} \frac{1}{|K|\ell}.$$

[9] To simplify our notation, we neglect the subscript y hereafter.

[10] The convention for the transfer matrix of a thin-lens quadrupole is

$$M_{\text{quad}} = \begin{pmatrix} 1 & 0 \\ -1/f & 1 \end{pmatrix},$$

where $f > 0$ for a focusing quadrupole and $f < 0$ for a defocussing quadrupole. In this case, $f = \lim_{\ell \to 0} 1/(K\ell)$.

Similarly, the transfer matrix for a pure sector dipole with $K_x = 1/\rho^2$ is

$$M_x(s, s_0) = \begin{pmatrix} \cos\theta & \rho\sin\theta \\ -\frac{1}{\rho}\sin\theta & \cos\theta \end{pmatrix}, \tag{2.40}$$

where $\theta = \ell/\rho$ is the orbiting angle and ρ is the bending radius. In the small-angle approximation, the transfer matrix becomes

$$M_x(s, s_0) = \begin{pmatrix} 1 & \ell \\ 0 & 1 \end{pmatrix}, \tag{2.41}$$

where ℓ is the length of the dipole. This means that the effect of a dipole with a small bending angle is equivalent to that of a drift space.

The transfer matrix for any intervals made up of subintervals is just the product of the transfer matrices of the subintervals, e.g.

$$M(s_2|s_0) = M(s_2|s_1)M(s_1|s_0). \tag{2.42}$$

Using these matrices, particle motion can be tracked through accelerator elements. Combining all segments, the solution of a second-order differential equation can be expressed as

$$y(s) = C(s, s_0)y_0 + S(s, s_0)y_0', \quad y'(s) = C'(s, s_0)y_0 + S'(s, s_0)y_0', \tag{2.43}$$

where C' and S' are the derivatives of C and S with respect to s, and y_0 and y_0' are the initial phase-space coordinates at s_0. The solutions $C(s, s_0)$ and $S(s, s_0)$ are respectively called the cosine-like and sine-like solutions with boundary conditions

$$C(s_0, s_0) = 1, \ S(s_0, s_0) = 0, \quad C'(s_0, s_0) = 0, \ S'(s_0, s_0) = 1. \tag{2.44}$$

Thus the solution of Eq. (2.33) can be expressed in terms of the transfer matrix as[11]

$$\mathbf{y}(s) = M(s|s_0)\mathbf{y}(s_0), \quad M(s|s_0) = \begin{pmatrix} C(s, s_0) & S(s, s_0) \\ C'(s, s_0) & S'(s, s_0) \end{pmatrix}, \tag{2.45}$$

where (y_0, y_0') and (y, y') are the particle phase-space coordinates at the entrance and exit of accelerator elements, and, using the Wronskian of Eq. (2.44), we obtain $\det M(s|s_0) = W(C, S, s) = 1$. The 2×2 matrix M depends only on the function $K(s)$ between s and s_0.

[11] The transfer matrix for the uncoupled betatron motion can be expressed as

$$\begin{pmatrix} x \\ x' \\ z \\ z' \end{pmatrix}_2 = \begin{pmatrix} M_x(s_2|s_1) & 0 \\ 0 & M_z(s_2|s_1) \end{pmatrix} \begin{pmatrix} x \\ x' \\ z \\ z' \end{pmatrix}_1,$$

where the M's are the 2×2 transfer matrices.

An accelerator is usually constructed with repetitive modules. Let L be the length of a module with $K(s+L) = K(s)$. The number of identical modules that form a complete accelerator is called the *superperiod* P. For example, the Fermilab booster shown in Fig. 2.3 has 24 superperiods, the AGS at BNL has 12, and the LEP at CERN has 8. The transfer matrix M of one repetitive period composed of n elements is a periodic function of s with a period L, i.e.

$$\mathbf{M}(s) = M(s+L|s) = M_n \cdots M_2 M_1, \tag{2.46}$$

where the M_i's are the transfer matrices of the constituent elements.

Using the periodicity condition, we obtain

$$M(s_2+L|s_1) = \mathbf{M}(s_2)M(s_2|s_1) = M(s_2|s_1)\mathbf{M}(s_1). \tag{2.47}$$

Thus $\mathbf{M}(s_2)$ and $\mathbf{M}(s_1)$ are related by a similarity transformation:

$$\mathbf{M}(s_2) = M(s_2|s_1)\mathbf{M}(s_1)[M(s_2|s_1)]^{-1}. \tag{2.48}$$

This implies that the transfer matrix of a periodic section has identical eigenvalues. The transfer matrix for passing through P superperiods is $M(s+PL|s) = [\mathbf{M}(s)]^P$, and for passing through m revolutions becomes $[\mathbf{M}(s)]^{mP}$.

The necessary and sufficient condition for stable orbital motion is that all matrix elements of the matrix $[\mathbf{M}(s)]^{mP}$ remain bounded as m increases. Let λ_1, λ_2 be the eigenvalues and v_1, v_2 be the corresponding eigenvectors of the matrix $\mathbf{M}$. Since $\mathbf{M}$ has a unit determinant, the eigenvalues are the reciprocals of each other, i.e. $\lambda_1 = 1/\lambda_2$, and $\lambda_1 + \lambda_2 = \mathrm{Trace}(\mathbf{M})$. The eigenvalue satisfies the equation

$$\lambda^2 - \mathrm{Trace}(\mathbf{M})\lambda + 1 = 0.$$

Let $\mathrm{Trace}(\mathbf{M}) = 2\cos(\Phi)$. We find that Φ is real if $\mathrm{Trace}(\mathbf{M}) \le 2$, and Φ is complex if $\mathrm{Trace}(\mathbf{M}) > 2$. The eigenvalues are

$$\lambda_1 = e^{j\Phi}, \quad \lambda_2 = e^{-j\Phi}, \tag{2.49}$$

where Φ is the betatron phase advance of a periodic cell.

Expressing the initial condition of beam coordinates (y_0, y_0') as a linear superposition of the eigenvectors, i.e.

$$\begin{pmatrix} y_0 \\ y_0' \end{pmatrix} = a v_1 + b v_2, \tag{2.50}$$

where v_1 and v_2 are the eigenvectors associated with eigenvalues λ_1 and λ_2 respectively, we find that the particle coordinate after the mth revolution becomes

$$\begin{pmatrix} y_m \\ y_m' \end{pmatrix} = \mathbf{M}^m \begin{pmatrix} y_0 \\ y_0' \end{pmatrix} = a\lambda_1^m v_1 + b\lambda_2^m v_2. \tag{2.51}$$

The stability of particle motion requires that λ_1^m and λ_2^m not grow with m. Thus a necessary condition for orbit stability is to have a real betatron phase advance Φ, or

$$|\mathrm{Trace}(\mathbf{M})| \le 2. \tag{2.52}$$

II.2 Courant–Snyder Parametrization

The most general form for matrix $\mathbf{M}$ with *unit modulus* can be parametrized as

$$\mathbf{M} = \begin{pmatrix} \cos\Phi + \alpha\sin\Phi & \beta\sin\Phi \\ -\gamma\sin\Phi & \cos\Phi - \alpha\sin\Phi \end{pmatrix} = \mathbf{I}\cos\Phi + \mathbf{J}\sin\Phi, \tag{2.53}$$

where α, β and γ are Courant–Snyder parameters,[12] Φ is the phase advance, $\mathbf{I}$ is the unit matrix, and

$$\mathbf{J} = \begin{pmatrix} \alpha & \beta \\ -\gamma & -\alpha \end{pmatrix}, \quad \text{with} \quad \mathrm{Trace}(\mathbf{J}) = 0, \quad \mathbf{J}^2 = -\mathbf{I} \text{ or } \beta\gamma = 1 + \alpha^2. \tag{2.54}$$

The ambiguity in the sign of $\sin\Phi$ can be resolved by requiring β to be a positive definite number if $|\mathrm{Trace}(\mathbf{M})| \le 2$, and by requiring $\mathrm{Im}(\sin\Phi)>0$ if $|\mathrm{Trace}(\mathbf{M})| > 2$. The definition of the phase factor Φ is still ambiguous up to an integral multiple of 2π. This ambiguity will be resolved when the matrix is tracked along the accelerator elements. Using the property of matrix $\mathbf{J}$, we obtain the De Moivere's theorem:

$$\begin{aligned} \mathbf{M}^k &= (\mathbf{I}\cos\Phi + \mathbf{J}\sin\Phi)^k = \mathbf{I}\cos k\Phi + \mathbf{J}\sin k\Phi, \\ \mathbf{M}^{-1} &= \mathbf{I}\cos\Phi - \mathbf{J}\sin\Phi. \end{aligned} \tag{2.55}$$

Using the similarity transformation of Eq. (2.48), the values of the Courant–Snyder parameters $\alpha_2, \beta_2, \gamma_2$ at s_2 are related to $\alpha_1, \beta_1, \gamma_1$ at s_1 by

$$\begin{pmatrix} \beta \\ \alpha \\ \gamma \end{pmatrix}_2 = \begin{pmatrix} M_{11}^2 & -2M_{11}M_{12} & M_{12}^2 \\ -M_{11}M_{21} & M_{11}M_{22} + M_{12}M_{21} & -M_{12}M_{22} \\ M_{21}^2 & -2M_{21}M_{22} & M_{22}^2 \end{pmatrix} \begin{pmatrix} \beta \\ \alpha \\ \gamma \end{pmatrix}_1, \tag{2.56}$$

where M_{ij} are the matrix elements of $M(s_2|s_1)$. The evolution of betatron functions is shown in the following examples.

1. The evolution of the betatron amplitude function in a drift space is

$$\begin{aligned} \beta_2 &= \frac{1}{\gamma_1} + \gamma_1\left(s - \frac{\alpha_1}{\gamma_1}\right)^2 = \beta^* + \frac{(s-s^*)^2}{\beta^*}, \\ \alpha_2 &= \alpha_1 - \gamma_1 s = -(s-s^*)/\beta^*, \\ \gamma_2 &= \gamma_1 = 1/\beta^*. \end{aligned} \tag{2.57}$$

We note that γ is constant in a drift space, and $s^* = \alpha_1/\gamma_1$ is the location for an extremum of the betatron amplitude function with $\alpha(s^*) = 0$.

[12] The α, β, and γ parameters have nothing to do with the relativistic Lorentz factor.

2. Passing through a thin-lens quadrupole, the evolution of betatron function is given by

$$\begin{aligned} \beta_2 &= \beta_1, \\ \alpha_2 &= \alpha_1 + \beta_1/f, \\ \gamma_2 &= \gamma_1 + 2\alpha_1/f + \beta_1/f^2, \end{aligned} \tag{2.58}$$

where f is the focal length of the quadrupole. Thus a thin-lens quadrupole gives rise to an angular kick to the betatron amplitude function without changing its magnitude.

II.3 Floquet Transformation

Since the focusing function $K(s)$ is a periodic function, Eq. (2.34) can be solved by using the Floquet transformation:

$$y(s) = aw(s)e^{j\psi(s)}, \quad y^*(s) = aw(s)e^{-j\psi(s)}, \tag{2.59}$$

where a is a constant, and w and ψ are the amplitude and phase functions. Since $K(s)$ is real, the amplitude and phase functions satisfy

$$w'' + Kw - \frac{1}{w^3} = 0, \tag{2.60}$$

$$\psi' = \frac{1}{w^2}. \tag{2.61}$$

Here, Eq. (2.60) is called the *betatron envelope equation*, Eq. (2.61) is the betatron phase equation, and we have chosen a normalization for the amplitude and phase functions.

Any solution of Eq. (2.34) is a linear superposition of the linearly independent solutions y and y^*. Thus the mapping matrix $M(s_2|s_1)$ can be obtained easily as

$$M(s_2|s_1) = \begin{pmatrix} \frac{w_2}{w_1}\cos\psi - w_2 w_1' \sin\psi & w_1 w_2 \sin\psi \\ -\frac{(1+w_1 w_1' w_2 w_2')}{w_1 w_2}\sin\psi - (\frac{w_1'}{w_2} - \frac{w_2'}{w_1})\cos\psi & \frac{w_1}{w_2}\cos\psi + w_1 w_2' \sin\psi \end{pmatrix}, \tag{2.62}$$

where $w_1 = w(s_1), w_2 = w(s_2), \psi = \psi(s_2) - \psi(s_1)$, $w_1' = w'(s_1), w_2' = w'(s_2)$, and the prime is the derivative with respect to s.

Let $s_2 - s_1 = L$ be the length of a periodic beam line, where the focusing function $K(s)$ satisfies $K(s) = K(s+L)$. Using the Floquet theorem (see Appendix A, Sec I.5), we set the periodic boundary conditions to the amplitude and phase functions:

$$w_1 = w_2 = w, \quad w_1' = w_2' = w', \quad \psi(s_1 + L) - \psi(s_1) = \Phi.$$

Equating the matrix $\mathbf{M}$ of a complete period in Eq. (2.62) to Eq. (2.53), we obtain

$$w^2 = \beta, \tag{2.63}$$

$$\alpha = -ww' = -\beta'/2. \tag{2.64}$$

Thus the amplitude of the betatron motion is proportional to the square root of the Courant–Snyder parameter $\beta(s)$, which will be referred to as the *betatron amplitude function*. The Courant–Snyder parameter α is related to the slope of the betatron amplitude function. The betatron phase advance is

$$\Phi = \int_0^L \frac{ds}{\beta(s)}. \tag{2.65}$$

Here the amplitude function $\beta(s)$ is also the local wave number of betatron oscillations. In the smooth approximation, we have $\Phi = L/\langle\beta\rangle$, or $\langle\beta\rangle = L/\Phi$. The betatron wavelength is $\lambda_\beta = 2\pi\langle\beta\rangle$. Substituting $\beta = w^2$ back into Eq. (2.60), we obtain

$$\frac{1}{2}\beta'' + K\beta - \frac{1}{\beta}\left[1 + (\frac{\beta'}{2})^2\right] = 0, \quad \text{or} \quad \alpha' = K\beta - \frac{1}{\beta}(1+\alpha^2). \tag{2.66}$$

The transfer matrix from s_1 to s_2 in any beam transport line becomes

$$\begin{aligned} M(s_2|s_1) &= \begin{pmatrix} \sqrt{\frac{\beta_2}{\beta_1}}(\cos\psi + \alpha_1\sin\psi) & \sqrt{\beta_1\beta_2}\sin\psi \\ -\frac{1+\alpha_1\alpha_2}{\sqrt{\beta_1\beta_2}}\sin\psi + \frac{\alpha_1-\alpha_2}{\sqrt{\beta_1\beta_2}}\cos\psi & \sqrt{\frac{\beta_1}{\beta_2}}(\cos\psi - \alpha_2\sin\psi) \end{pmatrix} \\ &= \begin{pmatrix} \sqrt{\beta_2} & 0 \\ -\frac{\alpha_2}{\sqrt{\beta_2}} & \frac{1}{\sqrt{\beta_2}} \end{pmatrix} \begin{pmatrix} \cos\psi & \sin\psi \\ -\sin\psi & \cos\psi \end{pmatrix} \begin{pmatrix} \frac{1}{\sqrt{\beta_1}} & 0 \\ \frac{\alpha_1}{\sqrt{\beta_1}} & \sqrt{\beta_1} \end{pmatrix} \\ &\equiv \mathbf{B}(s_2) \begin{pmatrix} \cos\psi & \sin\psi \\ -\sin\psi & \cos\psi \end{pmatrix} \mathbf{B}^{-1}(s_1), \end{aligned} \tag{2.67}$$

where $\beta_1, \alpha_1, \gamma_1$, and $\beta_2, \alpha_2, \gamma_2$ are values of betatron amplitude functions at s_1 and s_2 respectively, $\psi = \psi(s_2) - \psi(s_1)$, and we have defined the betatron amplitude matrix $\mathbf{B}(s)$ and its inverse as

$$\mathbf{B}(s) = \begin{pmatrix} \sqrt{\beta(s)} & 0 \\ -\frac{\alpha(s)}{\sqrt{\beta(s)}} & \frac{1}{\sqrt{\beta(s)}} \end{pmatrix} \quad \text{and} \quad \mathbf{B}^{-1}(s) = \begin{pmatrix} \frac{1}{\sqrt{\beta(s)}} & 0 \\ \frac{\alpha(s)}{\sqrt{\beta(s)}} & \sqrt{\beta(s)} \end{pmatrix}. \tag{2.68}$$

We note, from Eq. (2.67), that the linear betatron motion becomes coordinate rotation after the normalization of the phase-space coordinates with the $\mathbf{B}^{-1}$ matrix. Applying Floquet theorem to a repetitive period, where $s_2 = s_1 + L$ with $K(s_2) = K(s_1)$, we obtain $\beta_1 = \beta_2$, $\alpha_1 = \alpha_2$, and the transfer matrix of Eq. (2.67) reduces to the Courant–Snyder parametrization of Eq. (2.53).

Betatron tune

We consider an accelerator of circumference $C = PL$ with P identical superperiods. The phase change per revolution is $P\Phi$. The betatron tune ν_y, or Q_y, defined as the number of betatron oscillations in one revolution, is

$$Q_y = \nu_y = \frac{P\Phi_y}{2\pi} = \frac{1}{2\pi}\int_s^{s+C} \frac{ds}{\beta_y(s)}. \tag{2.69}$$

The betatron oscillation frequency is $\nu_y f_0$, where f_0 is the revolution frequency. The general solution of Eq. (2.34) becomes

$$y(s) = a\sqrt{\beta_y(s)}\cos[\psi_y(s) + \xi_y] \quad \text{with} \quad \psi_y(s) = \int_0^s \frac{ds}{\beta_y(s)}, \tag{2.70}$$

where a, ξ_y are constants to be determined from initial conditions. This is a pseudo-harmonic oscillation with varying amplitude $\beta_y^{1/2}(s)$. The local betatron wavelength is $\lambda = 2\pi\beta_y(s)$.

We define new variables η and ϕ_y:[13]

$$\eta = \frac{y}{\sqrt{\beta_y}}, \quad \phi_y(s) = \frac{1}{\nu_y}\int^s \frac{ds}{\beta_y(s)}. \tag{2.71}$$

The phase function ϕ_y increases by 2π in one revolution, and its derivative is periodic. Hill's equation can be transformed to

$$\frac{d^2\eta}{d\phi^2} + \nu_y^2\eta = 0. \tag{2.72}$$

Thus the linear betatron motion is in fact a simple harmonic motion.

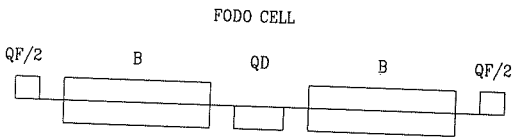

Figure 2.4: A schematic plot of a FODO cell, where the transfer matrix for the dipoles (B) can be approximated by drift spaces, and QF and QD indicate the focusing and defocussing quadrupoles.

Example 1: FODO cell in thin-lens approximation

A FODO cell (Fig. 2.4) is made of a pair of focusing and defocussing quadrupoles with or without dipoles in between, i.e.

$$\left\{\frac{1}{2}\text{QF} \quad \text{O} \quad \text{QD} \quad \text{O} \quad \frac{1}{2}\text{QF}\right\},$$

[13]This transformation, from $y(s)$ to the amplitude and phase functions $\beta_y(s)$ and $\phi_y(s)$, is called Floquet transformation.

where O represents either a dipole or a drift space. FODO cells are usually repetitively used for beam transport in arcs and transport lines.[14] The transfer matrix for the horizontal betatron motion, in the thin-lens approximation, is[15]

$$\begin{aligned}\mathbf{M} &= \begin{pmatrix} 1 & 0 \\ -\frac{1}{2f} & 1 \end{pmatrix}\begin{pmatrix} 1 & L_1 \\ 0 & 1 \end{pmatrix}\begin{pmatrix} 1 & 0 \\ \frac{1}{f} & 1 \end{pmatrix}\begin{pmatrix} 1 & L_1 \\ 0 & 1 \end{pmatrix}\begin{pmatrix} 1 & 0 \\ -\frac{1}{2f} & 1 \end{pmatrix} \\ &= \begin{pmatrix} 1 - \frac{L_1^2}{2f^2} & 2L_1(1 + \frac{L_1}{2f}) \\ -\frac{L_1}{2f^2}(1 - \frac{L_1}{2f}) & 1 - \frac{L_1^2}{2f^2} \end{pmatrix}\end{aligned}$$

where f is the magnitude of the focal lengths for the focusing and defocussing quadrupoles, and L_1 is the drift length between quadrupoles.

Because of the repetitive nature of FODO cells, the transfer matrix can be identified with the Courant–Snyder parametrization of Eq. (2.53) to obtain

$$\cos\Phi = \frac{1}{2}\text{Trace}(\mathbf{M}) = 1 - \frac{L_1^2}{2f^2} \quad \text{or} \quad \sin\frac{\Phi}{2} = \frac{L_1}{2f}, \tag{2.73}$$

$$\beta_{\text{F}} = \frac{2L_1\,(1 + \sin(\Phi/2))}{\sin\Phi}, \quad \alpha_{\text{F}} = 0. \tag{2.74}$$

The parameter Φ is the phase advance per cell, and β_{F} and α_{F} are values of the betatron amplitude functions at the center of the focusing quadrupole. The betatron tune for a machine with N FODO cells is $\nu = N\Phi/2\pi$. The above procedure can be performed at any position of the FODO cell, and the corresponding Courant–Snyder parameters are values of the betatron amplitude functions at that position. For example, we have

$$\beta_{\text{D}} = \frac{2L_1\,(1 - \sin(\Phi/2))}{\sin\Phi}, \quad \alpha_{\text{D}} = 0 \tag{2.75}$$

at the center of the defocussing quadrupole, and

$$\beta_{\text{mid. point}} = \frac{L_1}{\sin\Phi}\left(2 - \sin^2\frac{\Phi}{2}\right), \quad \alpha_{\text{mid. point}} = \pm\frac{1}{\cos(\Phi/2)} \tag{2.76}$$

at the midpoint between the QF and the QD. We can also use the transfer matrix of Eq. (2.67) to find the betatron amplitude functions at other locations (see Exercise 2.2.8).

[14]The accelerator lattice is usually divided into arcs and insertions. Arcs are curved sections that transport beams for a complete revolution. Insertions (or straight sections) are usually used for physics experiments, rf cavities, injection and extraction systems, etc.

[15]The transfer matrices of dipoles are represented by those of drift spaces, where we neglect the effect of $1/\rho^2$ focusing and edge focusing. The transfer matrix for vertical motion can be obtained by reversing focusing and defocussing elements.

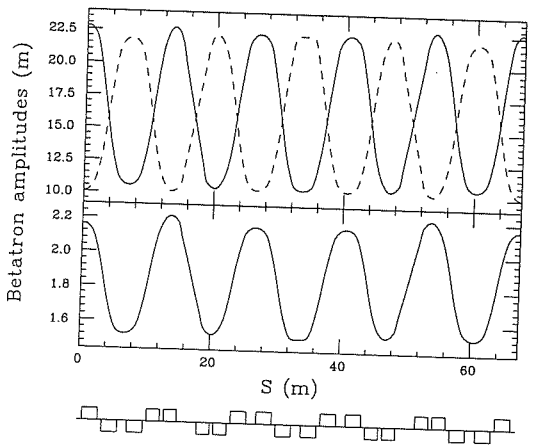

Figure 2.5: The betatron amplitude functions for one superperiod of the AGS lattice, which made of 20 combined-function magnets. The upper plot shows β_x (solid line) and β_z (dashed line). The middle plot shows the dispersion function D_x. The lower plot shows schematically the placement of combined-function magnets. Note that the superperiod can be well approximated by five regular FODO cells. The phase advance of each FODO cell is about 52.8°.

The solid and dashed lines in the upper plot of Fig. 2.5 show the betatron amplitude functions $\beta_x(s)$ and $\beta_z(s)$ for the AGS. The middle plot shows the dispersion function $D(s)$, to be discussed in Sec. IV. The AGS lattice has 12 superperiods, each composed of 20 combined-function dipoles, shown schematically in the bottom plot of Fig. 2.5. The AGS lattice can be well approximated by 60 FODO cells with a phase advance of 52.8° for a betatron tune of 8.8, and a half-cell length of $L_1 = 6.726$ m for a complete circumference of 807.12 m.

Example 2: Doublet cells

The values of the horizontal and vertical betatron functions in FODO cells alternate in magnitude, i.e.

$$\frac{\beta_x}{\beta_z} \approx \frac{1+\sin\Phi/2}{1-\sin\Phi/2}, \quad \text{and} \quad \frac{1-\sin\Phi/2}{1+\sin\Phi/2},$$

at the focusing and defocussing quadrupoles respectively. The beam size variation increases with the phase advance of the FODO cell. In some applications, a paraxial beam transport system provides a simpler geometrical beam matching solution. Some examples of paraxial beam transport beam lines are the doublet, the triplet, and the solenoidal transport systems. In the following example, we consider a doublet beam line, shown schematically in Fig. 2.6.

The phase advance of a doublet cell, in thin-lens approximation, is

$$\sin\frac{\Phi}{2} = \frac{\sqrt{L_1 L_2}}{2f}, \tag{2.77}$$

where we have assumed equal focusing strength for the focusing and the defocussing quadrupoles, f is the focal length of the quadrupoles, and L_1 and L_2 are the lengths

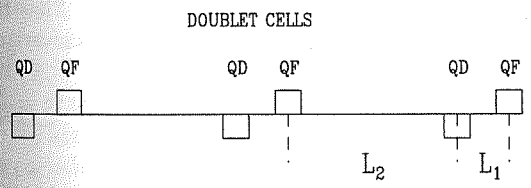

Figure 2.6: A schematic plot of a doublet transport line, where two quadrupoles are separated by a distance L_1, and the long drift space L_2 between two quadrupoles can be filled with dipoles.

of the drift spaces shown in Fig. 2.6. The maximum and minimum values of the betatron amplitude function are (see Exercise 2.2.13)

$$\beta_{\max} = \frac{L_1 + L_2 + L_1 L_2/f}{\sin\Phi}, \tag{2.78}$$

$$\beta_{\min} = \frac{f^2}{L_2}\sin\Phi. \tag{2.79}$$

If $L_1 \ll L_2$, the horizontal and vertical betatron amplitude functions are nearly identical along the transport line. Thus the doublet can be considered as an example of the paraxial transport system. Other paraxial transport systems are triplets and solenoidal focusing channels (see Exercise 2.2.12).

II.4 Action-Angle Variable and Floquet Transformation

The Hill equation, $y'' + K(s)y = 0$, can be derived from a pseudo-Hamiltonian

$$H = \frac{1}{2}y'^2 + \frac{1}{2}K(s)y^2, \tag{2.80}$$

where (y, y') are conjugate phase-space coordinates. We observe that Eq. (2.70) is a solution of Hill's equation, provided that β satisfies Eq. (2.66). Thus we obtain

$$y' = -\frac{y}{\beta}(\tan\psi - \frac{\beta'}{2}), \tag{2.81}$$

where ψ is the phase factor. This suggests a generating function

$$F_1(y,\psi) = \int_0^y y' dy = -\frac{y^2}{2\beta}(\tan\psi - \frac{\beta'}{2}), \tag{2.82}$$

where $y' = \partial F_1/\partial y$ is verified easily, and the conjugate action variable is

$$J = -\frac{\partial F_1}{\partial\psi} = \frac{y^2}{2\beta}\sec^2\psi = \frac{1}{2\beta}[y^2 + (\beta y' + \alpha y)^2]. \tag{2.83}$$

Applying the canonical transformation and using Eq. (2.66), we find the new Hamiltonian

$$\tilde{H} = H + \frac{\partial F_1}{\partial s} = \frac{J}{\beta}. \tag{2.84}$$

Hamilton's equation gives $\psi' = \partial\tilde{H}/\partial J = 1/\beta(s)$, which recovers Eq. (2.61). Since the new Hamiltonian is independent of the phase coordinate ψ, the action J is invariant, i.e.

$$\frac{dJ}{ds} = -\frac{\partial\tilde{H}}{\partial\psi} = 0. \tag{2.85}$$

Using Eq. (2.83), we obtain

$$y = \sqrt{2\beta J}\,\cos\psi, \qquad y' = -\sqrt{\frac{2J}{\beta}}\,[\sin\psi + \alpha\cos\psi], \tag{2.86}$$

where $\alpha = -\beta'/2$. Now it is easy to verify that the action J is[16]

$$J = \frac{1}{2\pi}\int_{\text{torus}} dy'dy = \frac{1}{2\pi}\oint y'dy. \tag{2.87}$$

The phase space area enclosed by the invariant torus is equal to $2\pi J$.

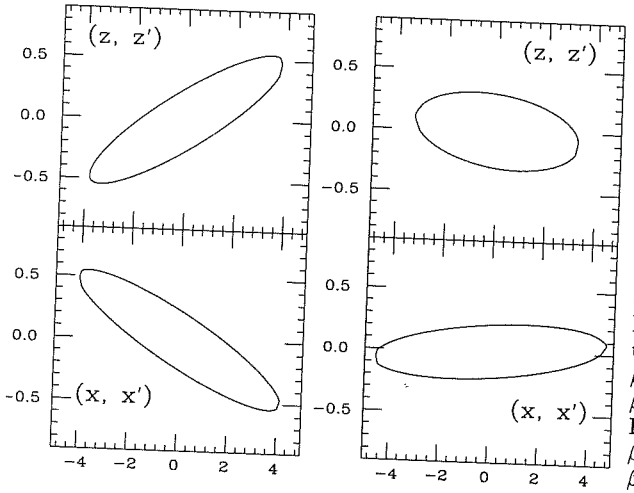

Figure 2.7: The horizontal and vertical betatron ellipses for a particle with actions $J_x = J_z = 0.5\pi$ mm-mrad at the end of the first dipole (left plots) and the end of the fourth dipole of the AGS lattice (see Fig. 2.5). The scale for the ordinate x or z is in mm, and that for the coordinate x' or z' is in mrad. For the left plots, the betatron amplitude functions are $\beta_x = 17.0$ m, $\alpha_x = 2.02$, $\beta_z = 14.7$ m, and $\alpha_z = -1.84$. For the right plots they are $\beta_x = 21.7$ m, $\alpha_x = -0.33$, $\beta_z = 10.9$ m, and $\alpha_z = 0.29$.

Figure 2.7 shows the phase-space ellipses (x, x') and (z, z') for a particle with actions $J_x = J_z = 0.5\pi$ mm-mrad at the ends of the first and the fourth dipoles of the AGS lattice (see Fig. 2.5). Such a phase-space ellipse is also called the Poincaré map, where the particle phase-space coordinates are plotted in each revolution. The consecutive phase-space points can be obtained by multiplying the transfer matrices, i.e.

$$\begin{pmatrix} x \\ x' \end{pmatrix}_{n+1} = \mathbf{M}_x \begin{pmatrix} x \\ x' \end{pmatrix}_n, \qquad \begin{pmatrix} z \\ z' \end{pmatrix}_{n+1} = \mathbf{M}_z \begin{pmatrix} z \\ z' \end{pmatrix}_n, \tag{2.88}$$

[16]The Jacobian of the transformation from (y, y') to (J, ψ) is equal to 1.

where $\mathbf{M}_x$ and $\mathbf{M}_z$ are the transfer matrices of one complete revolution. The Poincaré map of betatron motion at a fixed azimuth s is also called the Poincaré surface of section. If the betatron tune is not a rational number, the consecutive phase-space points of the particle trajectory will trace out the entire ellipse. The areas enclosed by the horizontal and vertical ellipses are equal to $2\pi J_x$ and $2\pi J_z$ respectively. As the particle travels in the accelerator, the shape of the phase-space ellipse may vary but the area enclosed by the ellipse is invariant.

A. Normalized phase space coordinates

We define the normalized conjugate phase-space coordinate $\mathcal{P}_y$ as

$$\mathcal{P}_y = \beta y' + \alpha y = -\sqrt{2\beta J}\sin\psi. \tag{2.89}$$

A particle trajectory in the normalized phase-space coordinates $(y, -\mathcal{P}_y)$ is a circle with radius $\sqrt{2\beta J}$. The shape of the normalized phase-space ellipse is independent of the location s. In terms of the betatron amplitude matrix of Eq. (2.68), the normalized phase space coordinates are expressed as

$$\begin{pmatrix} y \\ \mathcal{P}_y \end{pmatrix} = \sqrt{\beta}\,\mathbf{B}^{-1}\begin{pmatrix} y \\ y' \end{pmatrix} \quad \text{and} \quad \begin{pmatrix} y \\ y' \end{pmatrix} = \frac{1}{\sqrt{\beta}}\,\mathbf{B}\begin{pmatrix} y \\ \mathcal{P}_y \end{pmatrix}. \tag{2.90}$$

B. Using the orbital angle θ as the independent variable

The Hamiltonian $\tilde{H}$ of Eq. (2.84) depends on the independent variable s. Because $\beta(s)$ is not a constant, the phase advance is modulated along the accelerator orbital trajectory. Sometimes it is useful to obtain a global Fourier expansion of particle motion by using the generating function

$$F_2(\psi, \bar{J}) = \left(\psi - \int_0^s \frac{ds}{\beta} + \nu\theta\right)\bar{J} \tag{2.91}$$

to compensate the modulated phase-advance function. Here $\theta = s/R$ is the orbiting angle of the reference orbit. The new conjugate coordinates $(\bar{\psi}, \bar{J})$ are

$$\bar{\psi} = \psi - \int_0^s \frac{ds}{\beta} + \nu\theta, \quad \bar{J} = J, \tag{2.92}$$

and the new Hamiltonian becomes $\tilde{H} = \nu\bar{J}/R$. Changing the time coordinate from s to θ, the new Hamiltonian is re-scaled and becomes

$$\bar{H} = R\tilde{H} = \nu\bar{J}. \tag{2.93}$$

The transformation from betatron phase-space coordinates to action-angle variables is

$$y = \sqrt{2\beta\bar{J}}\cos(\bar{\psi} + \chi(s) - \nu\theta), \tag{2.94}$$

$$\mathcal{P}_y = \beta y' + \alpha y = -\sqrt{2\beta\bar{J}}\sin(\bar{\psi} + \chi(s) - \nu\theta), \tag{2.95}$$

where $\chi = \int_0^s ds/\beta$ and $(\bar{\psi}, \bar{J})$ are conjugate phase-space coordinates. The transformation is useful in expressing a general betatron Hamiltonian in action-angle variables for obtaining a global Fourier expansion in the nonlinear resonance analysis. Hereafter, the notation $(\bar{\psi}, \bar{J})$ will be simplified to (ψ, J).

II.5 Courant–Snyder Invariant and Emittance

Using the general solution $y(s)$ of Eq. (2.70), we obtain

$$\beta y' + \alpha y = -a\beta^{1/2}(s)\sin(\nu\phi(s) + \delta). \tag{2.96}$$

The Courant–Snyder invariant defined by

$$C(y, y') = \frac{1}{\beta}\left[y^2 + (\alpha y + \beta y')^2\right] = \gamma y^2 + 2\alpha y y' + \beta y'^2 \tag{2.97}$$

is equal to *twice the action*, which is independent of s. The trajectory of particle motion with initial condition (y_0, y_0') follows an ellipse described by $C(y, y') = \epsilon$. The phase space enclosed by (y, y') of Eq. (2.97) is equal to $\pi\epsilon$ (see Fig. 2.8).

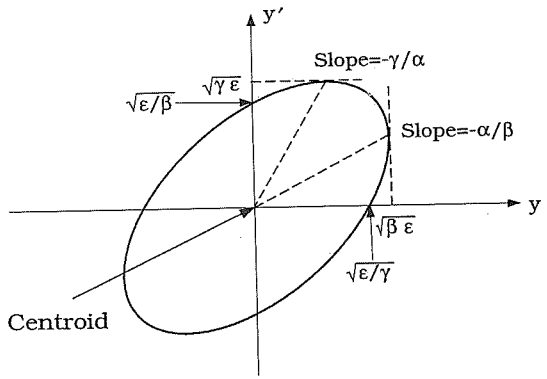

Figure 2.8: The Courant–Snyder invariant ellipse. The area enclosed by the ellipse is equal to $\pi\epsilon$, where ϵ is twice the betatron action; α, β and γ are betatron amplitude functions. The maximum amplitude of betatron motion is $\sqrt{\beta\epsilon}$, and the maximum divergence (angle) of the betatron motion is $\sqrt{\gamma\epsilon}$.

A. The emittance of a beam

A beam is usually composed of particles distributed in the phase space. Depending on the initial beam preparation, we approximate a realistic beam distribution function

by some simple analytic formula. Neglecting dissipation and diffusion processes, each particle in the distribution function has its invariant Courant–Snyder ellipse.

Given a normalized distribution function $\rho(y, y')$ with $\int \rho(y, y')dydy' = 1$, the moments of the beam distribution are

$$\langle y\rangle = \int y\rho(y, y')dydy', \quad \langle y'\rangle = \int y'\rho(y, y')dydy', \tag{2.98}$$

$$\sigma_y^2 = \int (y - \langle y\rangle)^2\rho(y, y')dydy', \quad \sigma_{y'}^2 = \int (y' - \langle y'\rangle)^2\rho(y, y')dydy', \tag{2.99}$$

$$\sigma_{yy'} = \int (y - \langle y\rangle)(y' - \langle y'\rangle)\rho(y, y')dydy' = r\sigma_y\sigma_{y'}, \tag{2.100}$$

where σ_y and $\sigma_{y'}$ are the rms beam widths, $\sigma_{yy'}$ is the correlation, and r is the correlation coefficient. The rms beam emittance is then defined as

$$\epsilon_{\rm rms} = \sqrt{\sigma_y^2\sigma_{y'}^2 - \sigma_{yy'}^2} = \sigma_y\sigma_{y'}\sqrt{1 - r^2}. \tag{2.101}$$

If the accelerator is composed of linear elements such as dipoles and quadrupoles, the emittance defined in Eq. (2.101) is invariant. The rms emittance is equal to the phase-space area enclosed by the Courant–Snyder ellipse of the rms particle (see Exercise 2.2.14).

Although incorrect, the term "emittance" is often loosely used as twice the action variable of betatron oscillations. The betatron oscillations of "a particle" with an "emittance" ϵ is

$$y(s) = \sqrt{\beta\epsilon}\,\cos[\nu\phi(s) + \delta]. \tag{2.102}$$

Figure 2.8 shows a Courant–Snyder invariant ellipse for a given emittance of a beam. For a beam with rms emittance $\pi\epsilon$,[17] the rms beam width is $\sqrt{\beta(s)\epsilon}$, and the beam rms divergence y' is $\sqrt{\gamma(s)\epsilon}$. Since $\gamma = (1 + \alpha^2)/\beta$, the transverse beam divergence is smaller at a location with a large $\beta(s)$ value, i.e. all particles travel in parallel paths. In accelerator design, a proper $\beta(s)$ value is therefore important for achieving many desirable properties.

B. The σ-matrix

The σ-matrix of a beam distribution is defined as

$$\sigma = \begin{pmatrix} \sigma_{11} & \sigma_{12} \\ \sigma_{12} & \sigma_{22} \end{pmatrix} = \begin{pmatrix} \sigma_y^2 & \sigma_{yy'} \\ \sigma_{yy'} & \sigma_{y'}^2 \end{pmatrix} = \langle(\mathbf{y} - \langle\mathbf{y}\rangle)(\mathbf{y} - \langle\mathbf{y}\rangle)^\dagger\rangle, \tag{2.103}$$

where $\mathbf{y}$ is the betatron state-vector of Eq. (2.36), $\mathbf{y}^\dagger = (y, y')$ is the transpose of $\mathbf{y}$, and $\langle\mathbf{y}\rangle$ is the first moment. The rms emittance defined by Eq. (2.101) is the

[17] The accelerator scientists commonly use π-mm-mrad for the unit of emittance. However, the factor π is often omitted. In beam width calculation, we get $\sigma_y = \sqrt{\pi\epsilon_y\beta_y/\pi}$. The synchrotron light source community also uses nano-meter (nm) as the unit for emittance. In fact, the factor π is implied and omitted in the literature.

determinant of the σ-matrix, i.e. $\epsilon_{\rm rms} = \sqrt{\det\sigma}$ (see also Exercise 2.2.14). Using the transfer matrix of Eq. (2.37), we obtain

$$\sigma(s_2) = M(s_2|s_1)\sigma(s_1)M(s_2|s_1)^\dagger. \tag{2.104}$$

It is easy to verify that $\mathbf{y}^\dagger\sigma^{-1}\mathbf{y}$ is invariant under linear betatron motion, thus the invariant beam distribution is

$$\rho(y, y') = \rho(\mathbf{y}^\dagger\sigma^{-1}\mathbf{y}). \tag{2.105}$$

C. Emittance measurement

The emittance can be obtained by measuring the σ-matrix. The beam profile of protons and ions is usually measured by using wire scanners or ionization profile monitors. Synchrotron light monitors are commonly used in electron storage rings. More recently, laser light has been used to measure electron beam size in the sub-micron range. Using the rms beam size and Courant–Snyder parameters, we can deduce the emittance of the beam. Two methods commonly used to measure the rms emittance are discussed below.

C1. Quadrupole tuning method

Using Eq. (2.104), we find the rms beam radius R_2 at a drift-distance L downstream of a quadrupole:[18]

$$\sigma_{11}(s_2) = R_2^2 = \sigma_{11}(s_1)\left(1 + \frac{\sigma_{12}(s_1)L}{\sigma_{11}(s_1)} - Lg\right)^2 + \frac{\epsilon_{\rm rms}^2}{\sigma_{11}(s_1)}L^2, \tag{2.106}$$

where $g = B_1\ell_{\rm q}/B\rho$ is the effective quadrupole field strength, L is the distance between the quadrupole and the beam profile monitor, and $\sigma_{ij}(s_1)$'s are elements of the σ matrix at the entrance of the quadrupole with $\epsilon_{\rm rms}^2 = \sigma_{11}\sigma_{22} - \sigma_{12}^2$, and $\sigma_{11}(s_2)$ is the 11-element of the σ-matrix at the profile monitor location s_2 (see Exercise 2.2.14(d) for an equation with thick quadrupole lens).

The R_2^2 data measured with varying quadrupole strength g can be used to fit a parabola. The rms emittance $\epsilon_{\rm rms}$ can be obtained from the fitted parameters. This method is commonly used at the end of a transport line, where a fluorescence screen or a wire detector (harp) is used to measure the rms beam size.

[18] If the transfer matrix between the tuning quadrupole at s_1 and the profile monitor at s_2 is m, we obtain $\tilde\sigma_{11} = \sigma_{11}\left[m_{11} + (\sigma_{12}m_{12}/\sigma_{11}) - m_{12}g\right]^2 + (m_{12}^2\epsilon_{\rm rms}^2)/\sigma_{11}$, where $\tilde\sigma_{11}$ is the 11-element of the σ-matrix at s_2, σ_{ij}'s are elements of the σ-matrix at s_1, m_{ij}'s are elements of the transfer matrix, and $g = B_1\ell_{\rm q}/B\rho$ is the effective focusing strength of the quadrupole.

C2. Moving screen method

Using a movable fluorescence screen, the beam size at three spots can be used to determine the emittance. Employing the transfer matrix of drift space, the rms beam radii at the second and third positions are

$$\begin{cases} R_2^2 = \sigma_{11} + 2L_1\sigma_{12} + L_1^2\sigma_{22}, \\ R_3^2 = \sigma_{11} + 2(L_1 + L_2)\sigma_{12} + (L_1 + L_2)^2\sigma_{22}, \end{cases} \tag{2.107}$$

where $\sigma_{11} = R_1^2$, σ_{12} and σ_{22} are elements of the σ matrix at the first screen location, and L_1 and L_2 are respectively drift distances between screens 1 and 2 and between screens 2 and 3. The solution σ_{12} and σ_{22} of Eq. (2.107) can be used to obtain the rms beam emittance: $\epsilon_{\rm rms} = \sqrt{\sigma_{11}\sigma_{22} - \sigma_{12}^2}$.

If screen 2 is located at the waist, i.e. $dR_2^2/dL_1 = 0$, then the emittance can be determined from rms beam size measurements of screens 1 and 2 alone. The resulting emittance is

$$\epsilon^2 = \left(R_1^2R_2^2 - R_2^4\right)/L_1^2. \tag{2.108}$$

This method is commonly used to measure the electron emittance in a transfer line.

D. The Gaussian distribution function

The equilibrium beam distribution in the linearized betatron phase space may be any function of the invariant action. However, the Gaussian distribution function

$$\rho(y, y') = \mathcal{N}\exp\left(\frac{-1}{2\det\sigma}(\sigma_{22}y^2 - 2\sigma_{12}yy' + \sigma_{11}y'^2)\right) \tag{2.109}$$

is commonly used to evaluate the beam properties. Expressing the normalized Gaussian distribution in the normalized phase space, we obtain

$$\rho(y, \mathcal{P}_y) = \frac{1}{2\pi\sigma_y^2}e^{-(y^2+\mathcal{P}_y^2)/2\sigma_y^2}, \tag{2.110}$$

where $\langle y^2\rangle = \langle p_y^2\rangle = \sigma_y^2 = \beta_y\epsilon_{\rm rms}$ with an rms emittance $\epsilon_{\rm rms}$. Transforming $(y, \mathcal{P}_y)$ into the action-angle variables (J, ψ) with

$$y = \sqrt{2\beta_yJ}\cos\psi, \quad \mathcal{P}_y = -\sqrt{2\beta_yJ}\sin\psi, \tag{2.111}$$

where the Jacobian of the transformation is

$$\frac{\partial(y, \mathcal{P}_y)}{\partial(\psi, J)} = \beta_y, \tag{2.112}$$

the distribution function becomes

$$\rho(J) = \frac{1}{\epsilon_{\rm rms}}e^{-J/\epsilon_{\rm rms}}, \quad \rho(\epsilon) = \frac{1}{2\epsilon_{\rm rms}}e^{-\epsilon/2\epsilon_{\rm rms}}, \tag{2.113}$$

Table 2.1: Percentage of particles in the confined phase-space volume

$\epsilon/\epsilon_{\rm rms}$	2	4	6	8
Percentage in 1D [%]	63	86	95	98
Percentage in 2D [%]	40	74	90	96

where $\epsilon = 2J$. The percentage of particles contained within $\epsilon = n\epsilon_{\rm rms}$ is $1 - e^{-n/2}$, shown in Table 2.1.

The maximum phase-space area that particles can survive in an accelerator is called the *admittance*, or the dynamical aperture. The admittance is determined by the vacuum chamber size, the kicker aperture, and nonlinear magnetic fields. To achieve good performance of an accelerator, the emittance should be kept much smaller than the admittance. Note that some publications assume 95% emittance, i.e. the phase-space area contains 95% of the beam particles, $\epsilon_{95\%} \approx 6\,\epsilon_{\rm rms}$ for a Gaussian distribution. For superconducting accelerators, a dynamical aperture of 6σ or more is normally assumed for magnet quench protection. For electron storage rings, quantum fluctuations due to synchrotron radiation are important; the machine acceptance usually requires about 10σ for good quantum lifetime.

Accelerator scientists in Europe use $\epsilon = 4\epsilon_{\rm rms}$ to define the beam emittance. This convention arises from the KV distribution, where the rms beam emittance is equal to 1/4 of the total emittance [see Eq. (2.131)].

E. Adiabatic damping and the normalized emittance

The Courant–Snyder invariant of Eq. (2.97), derived from the phase-space coordinate y, y', is not invariant when the energy is changed. To obtain the Liouville invariant phase-space area, we should use the conjugate phase-space coordinates (y, p_y) of the Hamiltonian in Eq. (2.18). Since $p_y = py' = mc\beta\gamma y'$, where m is the particle's mass, p is its momentum, and $\beta\gamma$ is the Lorentz relativistic factor, the *normalized emittance* defined by

$$\epsilon_{\rm n} = \beta\gamma\epsilon \tag{2.114}$$

is invariant. Thus the beam emittance decreases with increasing beam momentum, i.e. $\epsilon = \epsilon_{\rm n}/\beta\gamma$. This is called *adiabatic damping*. The adiabatic phase-space damping of the beam can be visualized as follows. Because the transverse velocity of a particle does not change during acceleration, the transverse angle $y' = p_y/p$ becomes smaller as the momentum of the particle increases, and the beam emittance $\epsilon = \epsilon_{\rm n}/\beta\gamma$ becomes smaller.

It is worth pointing out that the beam emittance in electron storage rings increases with energy as γ^2 because of the quantum fluctuation to be discussed in Chap. 4. The

corresponding normalized emittance is proportional to γ^3, where γ is the relativistic Lorentz factor. On the other hand, the beam emittance in electron linac will be adiabatically damped at high energies.

II.6 Stability of Betatron Motion: A FODO Cell Example

In this section, we illustrate the stability of betatron motion using a FODO cell example. We consider a FODO cell with quadrupole focal length f_1 and $-f_2$, where the $\pm$ signs designates the focusing and defocussing quadrupoles respectively. The transfer matrix of $\{\frac{1}{2}\mathrm{QF}_1\ \mathrm{O}\ \mathrm{QD}_2\ \mathrm{O}\ \frac{1}{2}\mathrm{QF}_1\}$ is

$$\begin{aligned}
\mathbf{M} &= \begin{pmatrix} 1 & 0 \\ -\frac{1}{2f_1} & 1 \end{pmatrix}\begin{pmatrix} 1 & L_1 \\ 0 & 1 \end{pmatrix}\begin{pmatrix} 1 & 0 \\ \frac{1}{f_2} & 1 \end{pmatrix}\begin{pmatrix} 1 & L_1 \\ 0 & 1 \end{pmatrix}\begin{pmatrix} 1 & 0 \\ -\frac{1}{2f_1} & 1 \end{pmatrix} \\
&= \begin{pmatrix} 1 + \frac{L_1}{f_2} - \frac{L_1}{f_1} - \frac{L_1^2}{2f_1f_2} & 2L_1(1 + \frac{L_1}{2f_2}) \\ \frac{1}{f_2} - \frac{1}{f_1} - \frac{L_1}{f_1f_2} + \frac{L_1}{2f_1^2} + \frac{L_1^2}{4f_1^2f_2}) & 1 + \frac{L_1}{f_2} - \frac{L_1}{f_1} - \frac{L_1^2}{2f^2} \end{pmatrix},
\end{aligned} \tag{2.115}$$

where L_1 is the drift length between quadrupoles. Identifying the transfer matrix with the Courant–Snyder parametrization, we obtain

$$\cos\Phi_x = 1 + \frac{L_1}{f_2} - \frac{L_1}{f_1} - \frac{L_1^2}{2f_1f_2}, \tag{2.116}$$

$$\cos\Phi_z = 1 - \frac{L_1}{f_2} + \frac{L_1}{f_1} - \frac{L_1^2}{2f_1f_2}. \tag{2.117}$$

The stability condition, Eq. (2.52), of the betatron motion is equivalent to the following conditions:

$$|1 + 2X_2 - 2X_1 - 2X_1X_2| \le 1 \quad \text{and} \quad |1 - 2X_2 + 2X_1 - 2X_1X_2| \le 1, \tag{2.118}$$

where $X_1 = L_1/2f_1$ and $X_2 = L_1/2f_2$. The solution of Eq. (2.118) is shown in Fig. 2.9, which is usually called the necktie diagram. The lower and the upper boundaries of the shaded area correspond to $\Phi_{x,z} = 0$ or π respectively. Since the stable region is limited by $X_{1,2} \le 1$, the focal length should be larger than one-fourth of the *full cell length*.

The stability condition of the above FODO cell example seems to suggest that the phase advances Φ_x and Φ_z of a repetitive module should be less than π.[19] However, this is not a necessary condition. The phase advances of a complex repetitive lattice-module can be larger than π. For example, the phase advance of a flexible momentum compaction (FMC) module is about $3\pi/2$ (see Sec. IV.8 and Exercise 2.4.17) and the phase advance of a minimum emittance double-bend achromat module is about 2.4π

[19] The phase advance Φ_x of a double-bend achromat is larger than π (see Sec. IV.5). Thus a simple FODO cell working as double-bend achromat is unstable.

(see Sec. III.1; Chap. 4). In general, the stability of betatron motion is described by $|\cos\Phi_x| \leq 1$ and $|\cos\Phi_z| \leq 1$ for any type of accelerator lattice or repetitive transport line.

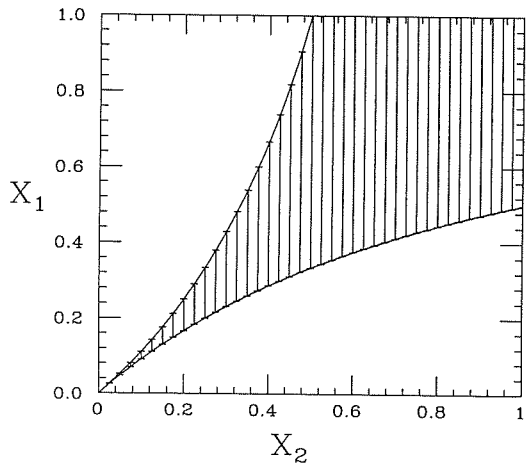

Figure 2.9: Stability diagram of a FODO cell lattice. The lower and upper boundaries correspond to $\Phi_{x,z} =$ 0 or 180° respectively.

II.7 Symplectic Condition

The 2×2 transfer matrix M with $\det M = 1$ satisfies $\tilde{M}JM = J$, where $\tilde{M}$ is the transpose of the matrix M, and $J = \begin{pmatrix} 0 & 1 \\ -1 & 0 \end{pmatrix}$. In general, the transfer matrix of a Hamiltonian flow of n degrees of freedom satisfies

$$\tilde{M}JM = J, \tag{2.119}$$

where $\tilde{M}$ is the transpose of the matrix M, and

$$J = \begin{pmatrix} 0 & I \\ -I & 0 \end{pmatrix}, \quad \text{with} \quad J^2 = -I, \quad \tilde{J} = -J, \quad J^{-1} = -J \tag{2.120}$$

with I as the $n \times n$ unit matrix. A $2n \times 2n$ matrix, M, is said to be symplectic if it satisfies Eq. (2.119). The matrices I and J are symplectic.

If the matrix M is symplectic, then M^{-1} is also symplectic and $\det M = 1$. If M and N are symplectic, then MN is also symplectic. Since the set of symplectic matrices satisfies the properties that (1) the unit matrix I is symplectic, (2) if M is symplectic then M^{-1} is symplectic, and (3) if M and N are symplectic, then MN is also symplectic, the set of symplectic matrices form a group denoted by $Sp(2n)$. The properties of real symplectic matrices are described below.

- The eigenvalues of symplectic matrix M must be real or must occur in complex conjugate pairs, i.e. λ and λ^*. The eigenvalues of a real matrix M or the roots of the characteristic polynomial $P(\lambda) = |M - \lambda I| = 0$ have real coefficients.

- Since $|M| = 1$, zero can not be an eigenvalue of a symplectic matrix.

- If λ is an eigenvalue of a real symplectic matrix M, then $1/\lambda$ must also be an eigenvalue. They should occur at the same multiplicity. Thus eigenvalues of a symplectic matrix are pairs of reciprocal numbers. For a symplectic matrix, we have

$$K^{-1}(\tilde{M} - \lambda I)K = M^{-1} - \lambda I = -\lambda M^{-1}(M - \lambda^{-1}I) \tag{2.121}$$

or

$$P(\lambda) = \lambda^{2n}P(\frac{1}{\lambda}) \tag{2.122}$$

If we define $Q(\lambda) = \lambda^{-n}P(\lambda)$, then

$$Q(\lambda) = Q(\frac{1}{\lambda}). \tag{2.123}$$

II.8 Effect of Space-Charge Force on Betatron Motion

The betatron amplitude function $w = \sqrt{\beta_y}$ of the Floquet transformation satisfies Eq. (2.60). Defining the envelope radius of a beam as

$$R_y = \sqrt{\beta_y \epsilon_y}, \tag{2.124}$$

where ϵ_y is the emittance, the envelope equation becomes

$$R_y'' + K_y R_y - \frac{\epsilon_y^2}{R_y^3} = 0, \tag{2.125}$$

where the prime corresponds to the derivative with respect to s. Based on the Floquet theorem, if K_y is a periodic function of s, i.e. $K_y(s) = K_y(s + L)$, where L is the length of a repetitive period, the solution of the envelope equation can be imposed with a periodic condition, $R_y(s) = R_y(s + L)$. The periodic envelope solution, aside from a multiplicative constant, is equal to the betatron amplitude function. The envelope function of an *emittance dominated beam* is equal to $\sqrt{\beta_y \epsilon_y}$. What happens to the beam envelope when the space-charge force dominates the beam dynamics? Here we discuss some effects of the space-charge force on betatron motion.

A. The Kapchinskij-Vladimirskij Distribution

It is known that the Coulomb mean-field from an arbitrary beam distribution is likely to be nonlinear. In 1959, Kapchinskij and Vladimirskij (KV) discovered an ellipsoid beam distribution that leads to a perfect linear space-charge force within the beam radius. This distribution function is called the KV distribution.[20]

Particles, in the KV distribution, are uniformly distributed on a constant total emittance surface of the 4-dimensional phase space, i.e.

$$\rho(x,\mathcal{P}_x,z,\mathcal{P}_z) = \frac{Ne}{\pi^2 a^2 b^2}\delta\left(\frac{1}{a^2}\left(x^2+\mathcal{P}_x^2\right)+\frac{1}{b^2}\left(z^2+\mathcal{P}_z^2\right)-1\right), \tag{2.126}$$

where N is the number of particles per unit length, e is the particle's charge, a and b are envelope radii of the beam, x and z are the transverse phase-space coordinates, and $\mathcal{P}_x = R_x'$, and $\mathcal{P}_z = R_z'$ are the corresponding normalized conjugate phase-space coordinates. Some properties of the KV distribution are as follows.

1. With the phase-space coordinates transformed into action-angle variables, the KV distribution function becomes

$$\rho(J_x,J_z) = \frac{4Ne}{\epsilon_x\epsilon_z}\delta\left(\frac{2J_x}{\epsilon_x}+\frac{2J_z}{\epsilon_z}-1\right) \tag{2.127}$$

Thus beam particles are uniformly distributed along an action line

$$\frac{J_x}{\epsilon_x}+\frac{J_z}{\epsilon_z}=\frac{1}{2} \tag{2.128}$$

where ϵ_x and ϵ_z are the horizontal and vertical emittances. The envelope radii are

$$a=\sqrt{\beta_x\epsilon_x}, \quad b=\sqrt{\beta_z\epsilon_z}. \tag{2.129}$$

2. Integrating the conjugate momenta, the distribution function becomes

$$\rho(x,z) = \frac{Ne}{\pi ab}\,\Theta\left(1-\frac{x^2}{a^2}-\frac{z^2}{b^2}\right) \tag{2.130}$$

where the $\Theta(\xi)$ function is equal to 1 if $\xi \geq 0$, and 0 if $\xi < 0$. In fact, the KV particles are uniformly distributed in any two-dimensional projection of the four-dimensional phase space.

3. The rms emittances of the KV beam are

$$\epsilon_{x,\text{rms}} = \frac{\langle x^2\rangle}{\beta_x} = \frac{\epsilon_x}{4}, \quad \epsilon_{z,\text{rms}} = \frac{\langle z^2\rangle}{\beta_z} = \frac{\epsilon_z}{4}. \tag{2.131}$$

Thus the rms envelope radii are equal to half of the beam radii in the KV beam.

[20] I.M. Kapchinskij and V.V. Vladimirskij, *Proc. Int. Conf. on High Energy Accelerators*, p. 274 (CERN, Geneva, 1959).

B. The Coulomb mean-field due to all beam particles

The next task is to calculate the effect of the average space-charge force. Neglecting the longitudinal variations, beam particles can be viewed as a charge distribution in an infinite long wire with a line-charge density given by Eq. (2.130). The electric field at the spatial point (x,z) is

$$\begin{aligned}\vec{E}(x,z) &= \frac{Ne}{2\pi\epsilon_0\,\pi ab}\int\int dx'dz'\;\Theta(1-\frac{x'^2}{a^2}-\frac{z'^2}{b^2})\frac{(x-x')\hat{x}+(z-z')\hat{z}}{(x-x')^2+(z-z')^2}\\ &= \frac{2Ne}{2\pi\epsilon_0}\left(\frac{x}{a(a+b)}\hat{x}+\frac{z}{b(a+b)}\hat{z}\right),\end{aligned} \tag{2.132}$$

where ϵ_0 is the vacuum permittivity. A noteworthy feature of the KV distribution function is that the resulting mean-field inside the beam envelope radii is linear! If the external focusing force is also linear, the KV distribution is a self-consistent distribution function. Including the mean-magnetic-field, the force on the particle at (x,z) is

$$\vec{F}(x,z) = \frac{2Ne^2}{2\pi\epsilon_0\gamma^2}\left(\frac{x}{a(a+b)}\hat{x}+\frac{z}{b(a+b)}\hat{z}\right), \tag{2.133}$$

where γ is the relativistic energy factor. Thus Hill's equations of motion become

$$x''+\left(K_x(s)-\frac{2K_{\text{sc}}}{a(a+b)}\right)x=0, \tag{2.134}$$

$$z''+\left(K_z(s)-\frac{2K_{\text{sc}}}{b(a+b)}\right)z=0, \tag{2.135}$$

where the prime is a derivative with respect to the longitudinal coordinate s, and K_{sc} is the "normalized" space-charge *perveance* parameter given by

$$K_{\text{sc}} = \frac{2Nr_0}{\beta^2\gamma^3}, \tag{2.136}$$

where $r_0 = e^2/4\pi\epsilon_0 mc^2$ is the classical radius of the particle, and N is the number of particles per unit length. Performing Floquet transformation of the linear KV-Hill equation

$$x = w_x e^{j\psi_x} \quad \text{and} \quad z = w_z e^{j\psi_z}, \tag{2.137}$$

we obtain

$$w_x''+\left(K_x-\frac{2K_{\text{sc}}}{a(a+b)}\right)w_x+\frac{1}{w_x^3}=0, \qquad \psi_x''=\frac{1}{w_x^2}, \tag{2.138}$$

$$w_z''+\left(K_z-\frac{2K_{\text{sc}}}{b(a+b)}\right)w_z+\frac{1}{w_z^3}=0, \qquad \psi_z''=\frac{1}{w_z^2}. \tag{2.139}$$

Multiplying Eq. (2.138) by $\sqrt{\epsilon_x}$ and Eq. (2.139) by $\sqrt{\epsilon_z}$, and identifying $a = w_x\sqrt{\epsilon_x}$ and $b = w_z\sqrt{\epsilon_z}$, we obtain the KV envelope equations, or simply the KV equations:

$$a'' + K_x a - \frac{2K_{\rm sc}}{a+b} - \frac{\epsilon_x^2}{a^3} = 0, \tag{2.140}$$

$$b'' + K_z b - \frac{2K_{\rm sc}}{a+b} - \frac{\epsilon_x^2}{b^3} = 0. \tag{2.141}$$

Solving the KV envelope equation is equivalent to finding the betatron amplitude function in the presence of the space-charge force. The usefulness of the KV equation has been further extended to arbitrary ellipsoid distribution functions provided that the envelope functions a and b are equal to twice the rms envelope radii, and the emittances ϵ_x and ϵ_z are equal to four times the rms emittances.[21]

If the external force is periodic, i.e. $K_x(s) = K_x(s+L)$, the KV equation can be solved by imposing the periodic boundary (closed orbit) condition (Floquet theorem)

$$a(s) = a(s+L), \quad b(s) = b(s+L). \tag{2.142}$$

A numerical integrator or differential equation solvers can be used to find the envelope function of the space-charge dominated beams. The matched beam envelope solution can be obtained by a proper closed orbit condition of Eq. (2.142).

For beams with an initial mismatched envelope, the envelope equation can be solved by using the initial value problem to find the behavior of the mismatched beams. For space-charge dominated beams, the envelope solution can vary widely depending on the external focusing function, the space-charge parameter, and the beam emittance. To understand the physics of the mismatched envelope, it is advantageous to extend the envelope equation to Hamiltonian dynamics as discussed below.

C. Hamiltonian formalism of the envelope equation

Introducing the pseudo-envelope momenta as

$$p_a = a', \quad p_b = b', \tag{2.143}$$

we can derive the KV equations (2.140) and (2.141) from the envelope Hamiltonian:

$$H_{\rm env} = \frac{1}{2}\left(p_a^2 + p_b^2 + K_x a^2 + K_z b^2\right) - 2K_{\rm sc}\ln(a+b) + \frac{\epsilon_x^2}{2a^2} + \frac{\epsilon_z^2}{2b^2}. \tag{2.144}$$

With the envelope potential defined as

$$V_{\rm env}(a,b) = \frac{1}{2}(K_x a^2 + K_z b^2) - 2K_{\rm sc}\ln(a+b) + \frac{\epsilon_x^2}{2a^2} + \frac{\epsilon_z^2}{2b^2}, \tag{2.145}$$

[21] P.M. Lapostolle, *IEEE Trans. Nucl. Sci.* **NS-18**, 1101 (1971); F.J. Sacherer, *ibid.* 1105 (1971); J.D. Lawson, P.M. Lapostolle, and R.L. Gluckstern, *Part. Accel.* **5**, 61 (1973); E.P. Lee and R.K. Cooper, *ibid.* **7**, 83 (1976).

the matched beam envelope can be easily understood as the equilibrium solution of the envelope Hamiltonian. For example, if we start from the condition with envelope momenta $p_a = p_b = 0$, the matched envelope radii are located at the minimum potential energy location, i.e.

$$\frac{\partial V_{\rm env}}{\partial a}(a_{\rm m}, b_{\rm m}) = \frac{\partial V_{\rm env}}{\partial b}(a_{\rm m}, b_{\rm m}) = 0, \tag{2.146}$$

where $a_{\rm m}$ and $b_{\rm m}$ are the matched envelope radii. The envelope oscillations of a mismatched beam can be determined by the perturbation around the matched solution

$$V_{\rm env} = \frac{1}{2}\frac{\partial^2 V_{\rm env}}{\partial a^2}(a-a_{\rm m})^2 + \frac{1}{2}\frac{\partial^2 V_{\rm env}}{\partial b^2}(b-b_{\rm m})^2 + \cdots. \tag{2.147}$$

Using the second-order derivatives, we can obtain the tune of the envelope oscillation.

D. An example of a uniform focusing paraxial system

First we consider a beam in a uniform paraxial focusing system, where the focusing function is

$$K_x = (2\pi/L)^2.$$

Here L is the betatron wavelength, and the betatron amplitude function is equal to $L/2\pi$. With $a = b$ in Eq. (2.140), the envelope Hamiltonian is

$$H_{\rm env} = \frac{1}{2}p_a^2 + \frac{1}{2}\left(\frac{2\pi}{L}\right)^2 a^2 - K_{\rm sc}\ln a + \frac{\epsilon_x^2}{2a^2} = \frac{1}{2}p_a^2 + V_{\rm env}(a). \tag{2.148}$$

When the space-charge force is negligible, the matched envelope solution is

$$a_{\rm m0} = \sqrt{\epsilon_x L/2\pi} = \sqrt{\epsilon_x \beta_x}.$$

The second-order derivative at the matched radius becomes

$$\left(\frac{d^2 V_{\rm env}}{da^2}\right)^{1/2} = 2\left(\frac{2\pi}{L}\right). \tag{2.149}$$

The tune of the mismatched envelope oscillation is twice the tune of betatron motion (see also Exercise 2.2.15) independent of the envelope-oscillation amplitude.

Now, we consider the effect of space charge on the envelope function. The matched envelope radius is obtained from the solution of $dV_{\rm env}/da = 0$, i.e.

$$a_{\rm m}^2 = \left(\frac{\epsilon_x L}{2\pi}\right)\left[\kappa + \sqrt{\kappa^2+1}\right], \tag{2.150}$$

where

$$\kappa = \frac{K_{\rm sc} L}{2\epsilon_x 2\pi} = \frac{K_{\rm sc} L_{\rm tot}}{2\epsilon_x \Phi_{\rm tot}} \tag{2.151}$$

is the effective space-charge parameter, and $L_{\rm tot}$ and $\Phi_{\rm tot}$ are the total length and total phase advance of a transport system.[22] Equation (2.150) indicates that the betatron amplitude function increases by a factor $\kappa + \sqrt{\kappa^2+1}$ due to the space-charge force.

Next we evaluate the second-order derivative of the potential at the matched radius, and obtain

$$\left(\frac{d^2V_{\rm env}}{da^2}\right)^{1/2} = 2\frac{2\pi}{L}\left(1 - \frac{\kappa}{(\kappa+\sqrt{\kappa^2+1})}\right)^{1/2}, \tag{2.152}$$

which is the phase advance per unit length of small amplitude envelope oscillation in the presence of the Coulomb potential. When the space-charge perveance parameter is zero, the phase advance of the envelope oscillation is twice of that of the betatron oscillation, and when the space-charge force is large, as $\kappa \to \infty$, the phase advance of the small-amplitude envelope oscillations can maximally be depressed to $2\sqrt{2}\,\pi/L$. There is a large envelope detuning from 2μ to $\sqrt{2}\mu$, where μ is the betatron phase advance. A nonlinear envelope resonance can be excited when perturbation exists and a resonance condition is satisfied.[23]

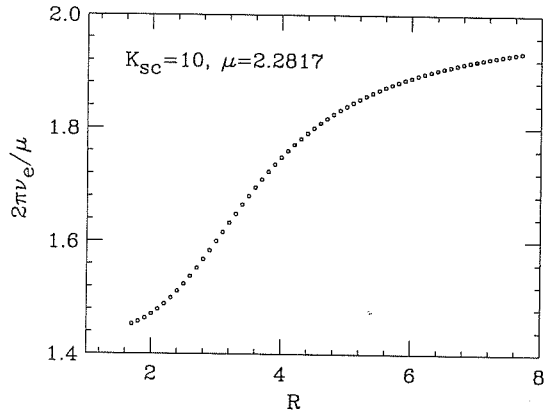

Figure 2.10: The phase advance of the envelope oscillations divided by the original betatron phase advance for a high space charge beam with $K_{\rm sc} = 10$, $\mu = 2.28175$. The ordinate R is the normalized maximum envelope radius of the beam. The matched radius is $R_0 = a_{\rm m}\sqrt{2\pi/(\mu\epsilon_x L)} = 1.4199$ in this example. See Eq. (2.150) for the matched envelope radius.

Figure 2.10 shows the envelope tune of a space charge dominated beam with $K_{\rm sc} = 10$ and a phase advance of $\mu = 2.2817$ radian (or $\nu = \mu/2\pi$ for the unperturbed betatron tune) as a function of the maximum amplitude of the envelope oscillation amplitude. At a large envelope amplitude, the envelope tune approaches

[22]The Laslett (linear) space-charge tune shift is related to the space-charge perveance parameter by $\xi_{\rm sc} \equiv \Delta\nu_{\rm sc} = K_{\rm sc}L_{\rm tot}/4\pi\epsilon_x = \kappa\nu$, where ν is the tune.

[23]S.Y. Lee and A. Riabko, *Phys. Rev.* E **51**, 1609 (1995); A. Riabko *et al.*, *Phys. Rev.* E **51**, 3529 (1995); C. Chen and R.C. Davidson, *Phys. Rev.* E**49**, 5679 (1994); *Phys. Rev. Lett.* **72**, 2195 (1994). See also Ref. [4] for an exploration of the space-charge dynamics.

twice the unperturbed betatron tune. Near the matched envelope radius (or small amplitude envelope oscillations), the envelope tune approaches $\sqrt{2}$ times the unperturbed betatron tune.

Effect of space charge force on particle motion

The single particle betatron phase advance per unit length is obtained by substituting Eq. (2.150) into Eq. (2.135), i.e.

$$\Phi_x = \frac{2\pi}{L}(\sqrt{\kappa^2+1} - \kappa). \tag{2.153}$$

When the space charge parameter κ is small, the incoherent space-charge (Laslett) tune shift is equal to $\Delta\nu_{\rm sc} = \xi_{\rm sc} = \kappa\nu$, where $\nu = \Phi_{\rm tot}/(2\pi)$ is the tune of the accelerator. When the space charge parameter κ is large, the betatron tune can be depressed to zero.

Exercise 2.2

1. The focusing function $K(s)$ for most accelerator magnets can be assumed to be piecewise constant. Show that

$$K(s) = 0, \qquad M(s_2|s_1) = \begin{pmatrix} 1 & s \\ 0 & 1 \end{pmatrix},$$

$$K(s) = K \geq 0, \quad M(s_2|s_1) = \begin{pmatrix} \cos\sqrt{K}s & \frac{1}{\sqrt{K}}\sin\sqrt{K}s \\ -\sqrt{K}\sin\sqrt{K}s & \cos\sqrt{K}s \end{pmatrix},$$

$$K(s) = K < 0, \quad M(s_2|s_1) = \begin{pmatrix} \cosh\sqrt{|K|}s & \frac{1}{\sqrt{|K|}}\sinh\sqrt{|K|}s \\ \sqrt{|K|}\sinh\sqrt{|K|}s & \cosh\sqrt{|K|}s \end{pmatrix},$$

with $s = s_2 - s_1$. Show that the mapping matrix M for a short quadrupole of length ℓ, in the thin-lens approximation, is

$$M = \begin{pmatrix} 1 & 0 \\ -\frac{1}{f} & 1 \end{pmatrix}$$

where $f = \lim_{\ell\to 0}(K\ell)^{-1}$, is the focal length of a quadrupole. For a focusing quad, $f > 0$; and for a defocussing quad, $f < 0$.

2. When a particle enters a dipole at an angle δ with respect to the normal edge of a dipole (see drawing below), there is a quadrupole effect. This phenomenon is usually referred to as edge focusing.[24] We use the convention that $\delta > 0$ if the particle trajectory is closer to the center of the bending radius. Show that the transfer matrices for the horizontal and vertical betatron motion due to the edge focusing are

[24]Using edge focusing, the zero-gradient synchrotron (ZGS) was designed and constructed in the 1960's at Argonne National Laboratory. The ZGS was made of 8 dipoles with a circumference of 172 m attaining the energy of 12.5 GeV. Its first proton beam was commissioned on Sept. 18, 1963. See L. Greenbaum, *A Special Interest* (Univ. of Michigan Press, Ann Arbor, 1971).

$$M_x = \begin{pmatrix} 1 & 0 \\ \frac{\tan\delta}{\rho} & 1 \end{pmatrix} \quad M_z = \begin{pmatrix} 1 & 0 \\ -\frac{\tan\delta}{\rho} & 1 \end{pmatrix}$$

where δ is the entrance or the exit angle of the particle with respect to the normal direction of the dipole edge. Thus the edge effect with $\delta > 0$ gives rise to horizontal defocussing and vertical focusing.

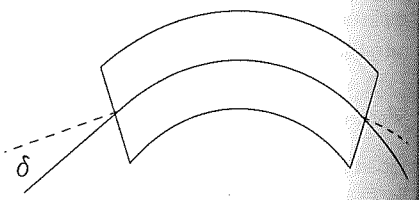

3. The particle orbit enters and exits a *sector dipole* magnet perpendicular to the dipole edges. Assuming that the gradient function of the dipole is zero, i.e. $\partial B_z/\partial x = 0$, show that the transfer matrix is

$$M_x = \begin{pmatrix} \cos\theta & \rho\sin\theta \\ -\frac{\sin\theta}{\rho} & \cos\theta \end{pmatrix}, \quad M_z = \begin{pmatrix} 1 & \ell \\ 0 & 1 \end{pmatrix}$$

where θ is the bending angle, ρ is the bending radius, and ℓ is the length of the dipole. Note that a sector magnet gives rise to horizontal focusing.

4. The entrance and exit edge angles of a rectangular dipole are $\delta_1 = \theta/2$ and $\delta_2 = \theta/2$, where θ is the bending angle. Find the horizontal and vertical transfer matrices for a rectangular dipole (Fig. 2.2b).

5. For a weak-focusing accelerator, $K_z(s) = n/\rho^2 =$ constant and $K_x = (1-n)/\rho^2$, where ρ is the radius of the accelerator. The focusing index n is

$$n(s) = \frac{\rho(s)}{B_z(s,0,0)} \frac{\partial B_z(s,x,0)}{\partial x}\bigg|_{x=0},$$

where we have chosen the coordinate system shown in Fig. 2.1. Solve the following problems by using the uniform focusing approximation with constant n.

(a) Show that the horizontal and vertical transfer matrices are

$$M_x = \begin{pmatrix} \cos(\sqrt{1-n}\, s/\rho) & (\rho/\sqrt{1-n})\sin(\sqrt{1-n}\, s/\rho) \\ -(\sqrt{1-n}/\rho)\sin(\sqrt{1-n}\, s/\rho) & \cos(\sqrt{1-n}\, s/\rho) \end{pmatrix},$$
$$M_z = \begin{pmatrix} \cos(\sqrt{n}\, s/\rho) & (\rho/\sqrt{n})\sin(\sqrt{n}\, s/\rho) \\ -(\sqrt{n}/\rho)\sin(\sqrt{1-n}\, s/\rho) & \cos(\sqrt{n}\, s/\rho) \end{pmatrix}.$$

(b) Show that the betatron tunes are $\nu_x = (1-n)^{1/2}$ and $\nu_z = n^{1/2}$, and the stability condition is $0 \le n \le 1$.

(c) If N equally spaced straight sections, with $K_x = K_z = 0$, are introduced into the accelerator lattice adjacent to each combined-function dipole, calculate the mapping matrix for the basic period and discuss the stability condition.

6. The path length for a particle orbit in an accelerator is

$$C = \oint \sqrt{[1+(x/\rho)]^2 + x'^2 + z'^2}\, ds.$$

Show that the average orbit length of the particle with a vertical betatron action J_z is longer by

$$\frac{\Delta C}{C} = \frac{1}{2}\langle\frac{1+\alpha_z^2}{\beta_z}\rangle J_z,$$

where α_z and β_z are betatron amplitude functions. In the smooth approximation, the betatron amplitude function is approximated by $\langle\beta_z\rangle = R/\nu_z$, and the betatron oscillations can be expressed as

$$z = \hat{z}\cos\left(\frac{s}{\langle\beta_z\rangle} + \chi_z\right),$$

where R, ν_z and $\hat{z}$ are the average radius, the vertical betatron tune, and the vertical betatron amplitude respectively, and χ_z is an arbitrary betatron phase angle of the particle. Show that the average orbit length of a particle executing betatron oscillations is longer by

$$\frac{\Delta C}{C} = \frac{\nu_z^2}{4R^2}\hat{z}^2.$$

Thus the orbit length depends quadratically on the betatron amplitude.

7. In a strong-focusing synchrotron, the art (or science) of magnet arrangement is called lattice design. The basic building blocks of a lattice are usually FODO cells. A FODO cell is composed of QF OO QD OO, where QF is a focusing quadrupole, OO represents either a drift space or bending dipoles of length L_1, and QD is a defocussing quadrupole. The length of a FODO cell is $L = 2L_1$. Using the thin-lens approximation,

(a) Find the mapping matrix and the phase advance of the FODO cell and discuss the stability condition.

(b) Find the parameters β, α at the quadrupoles and at the center of the drift space as a function of L_1 and Φ.

(c) Verify that $\beta' = -2\alpha$ numerically at the center of the drift space.[25]

(d) Find the phase advance Φ that minimizes the betatron amplitude function at the focusing quadrupole location.

8. Using Eq. (2.66), show that $\beta''' + 4\beta' K + 2\beta K' = 0$. Solve this equation for a drift space and a quadrupole respectively, and show that the solution of this equation must be one of the following forms:

$$\begin{cases} \beta = a + bs + cs^2, & \text{drift space} \\ \beta = a\cos 2\sqrt{K}s + b\sin 2\sqrt{K}s + c, & \text{focusing quadrupole} \\ \beta = a\cosh 2\sqrt{|K|}s + b\sinh 2\sqrt{|K|}s + c, & \text{defocussing quadrupole.} \end{cases}$$

(a) Express a, b, and c in terms of parameters α_0, β_0 and γ_0 at the beginning of the element.

(b) In a drift space, where there are no quadrupoles, show that the betatron amplitude function is

$$\beta(s) = \beta^* + \frac{(s-s^*)^2}{\beta^*},$$

[25] Find β's at $s_1 = s_0 - \Delta s$ and $s_2 = s_0 + \Delta s$, and calculate the derivative from these numbers.

where β^* is the betatron function at the symmetry point $s = s^*$ with $\beta' = 0$. Show also that $\gamma = (1+\alpha^2)/\beta$ is equal to $1/\beta^*$, i.e. γ is constant in a drift space.

(c) Using the similarity transformation Eq. (2.48), show that the Courant–Snyder parameters $\alpha_2, \beta_2, \gamma_2$ at s_2 are related to $\alpha_1, \beta_1, \gamma_1$ at s_1 by

$$\begin{pmatrix} \beta_2 \\ \alpha_2 \\ \gamma_2 \end{pmatrix} = \begin{pmatrix} M_{11}^2 & -2M_{11}M_{12} & M_{12}^2 \\ -M_{11}M_{21} & M_{11}M_{22}+M_{12}M_{21} & -M_{12}M_{22} \\ M_{21}^2 & -2M_{21}M_{22} & M_{22}^2 \end{pmatrix} \begin{pmatrix} \beta_1 \\ \alpha_1 \\ \gamma_1 \end{pmatrix},$$

where M_{ij} are the matrix elements of $M(s_2|s_1)$. Use these equations to verify your solution to part (a).

9. Use the transfer matrix $M(s_2|s_1)$ of Eq. (2.67) to show that, when a particle is kicked at s_1 by an angle θ, the displacement at a downstream location is

$$\Delta x_2 = \theta\sqrt{\beta_1\beta_2}\sin\psi,$$

where β_1 and β_2 are values of betatron functions at s_1 and s_2 respectively, and $\psi = \psi(s_2) - \psi(s_1)$ is the betatron phase advance between s_1 and s_2. The quantity $\sqrt{\beta_1\beta_2}\sin\psi$ is usually called the kicker arm. To minimize the kicker magnet strength θ, the injection or extraction kickers are located at a high β locations with a 90° phase advance.

10. Transforming the betatron phase-space coordinates onto the normalized coordinates with

$$Y = \frac{1}{\sqrt{\beta}}y, \quad \mathcal{P}_Y = \frac{1}{\sqrt{\beta}}(\alpha y + \beta y'),$$

or

$$\begin{pmatrix} Y \\ \mathcal{P}_Y \end{pmatrix} = \mathbf{B}^{-1}\begin{pmatrix} y \\ y' \end{pmatrix} \quad \text{with} \quad \mathbf{B}^{-1} = \begin{pmatrix} 1/\sqrt{\beta} & 0 \\ \alpha/\sqrt{\beta} & \sqrt{\beta} \end{pmatrix} \quad \text{and} \quad \mathbf{B} = \begin{pmatrix} \sqrt{\beta} & 0 \\ -\alpha/\sqrt{\beta} & \sqrt{\beta} \end{pmatrix},$$

show that the betatron transfer matrix in normalized coordinates becomes

$$\tilde{M}(s_2|s_1) = \begin{pmatrix} \cos\psi & \sin\psi \\ -\sin\psi & \cos\psi \end{pmatrix},$$

i.e. the betatron transfer matrix becomes coordinate rotation with rotation angle equal to the betatron phase advance. Show that the transfer matrix of Eq. (2.67) becomes $M(s_2|s_1) = \mathbf{B}_2\tilde{M}\mathbf{B}_1^{-1}$, where $\mathbf{B}_2$ and $\mathbf{B}_1$ are the betatron amplitude matrices at $s = s_2$ and s_1 respectively.

11. Show that the Floquet transformation of Eq. (2.94) transforms the Hamiltonian of Eq. (2.80) into Eq. (2.93).

12. Often a solenoidal field has been used to provide both the horizontal and the vertical beam focusing for the production of secondary beams from a target (see Exercise 2.1.4). The focusing channel can be considered as a focusing-focusing (FOFO) channel. We consider a FOFO focusing channel where the focusing elements are separated by a distance L. Use the thin-lens approximation to evaluate beam transport properties of a periodic FOFO channel.

(a) Show that the phase advance of a FOFO cell is

$$\sin\frac{\Phi}{2} = \frac{1}{2}\sqrt{\frac{L}{f}},$$

where f is the focal length given by $f^{-1} = g^2\ell = \Theta^2/\ell$, ℓ is the length of the solenoid, $g = B_{\|}/2B\rho$ is the effective solenoid strength, $B_{\|}$ is the solenoid field, and $\Theta = g\ell$ is the solenoid rotation angle.

(b) Show that the maximum and minimum values of the betatron amplitude function are

$$\beta_{\max} = L/\sin\Phi, \quad \beta_{\min} = f\sin\Phi.$$

13. The doublet configuration consists of a focusing and defocussing quadrupole pair separated by a small distance L_1 as a beam focusing unit. The doublet pairs are repeated at intervals $L_2 \gg L_1$ for beam transport (Fig. 2.6). These quadrupole doublets can be used to maintain round beam configuration during beam transport. Using the thin-lens approximation with equal focal length for the focusing and defocussing quadrupoles, describe the properties of betatron motion in a doublet transport line.

(a) Show that the betatron phase advance in a doublet cell is

$$\psi = \psi_{x,z} = \arcsin\left(\sqrt{L_1L_2}/2f\right),$$

where f is the focal length of the quadrupoles.

(b) Show that the maximum betatron amplitude function is approximately

$$\beta_{\max} = (L_1 + L_2 + L_1L_2/f)/\sin\psi.$$

(c) Show that the minimum betatron amplitude function is

$$\beta^* = \sqrt{L_1\left(4f^2 - L_1L_2\right)/4L_2}.$$

(d) Sketch the betatron amplitude functions and compare your results with that of the FODO cell transport line.

14. *Statistical definition of beam emittance:*[26] We consider a statistical distribution of N non-interacting particles in phase space (x, x'). Let $\rho(x, x')$ be the distribution function with

$$\int \rho(x,x')dxdx' = 1.$$

The first and second moments of beam distribution are

$$\langle x\rangle = \frac{1}{N}\sum x_i = \int x\rho(x,x')dxdx', \quad \langle x'\rangle = \frac{1}{N}\sum x_i' = \int x'\rho(x,x')dxdx',$$

$$\sigma_x^2 = \frac{1}{N}\sum(x_i - \langle x\rangle)^2, \quad \sigma_{x'}^2 = \frac{1}{N}\sum(x_i' - \langle x'\rangle)^2,$$

$$\sigma_{xx'} = \frac{1}{N}\sum(x_i - \langle x\rangle)(x_i' - \langle x'\rangle) = r\sigma_x\sigma_{x'}.$$

[26] See P. Lapostolle, *IEEE Trans. Nucl. Sci.* **NS-18**, 1101 (1971), and J. Buon, CERN **91-04**, 30 (1991). The statistical definition of beam emittance is applicable to all phase space coordinates.

Here σ_x and $\sigma_{x'}$ are rms beam widths, and r is the correlation coefficient. The rms emittance is defined as

$$\epsilon_{\rm rms} = \sigma_x \sigma_{x'} \sqrt{1-r^2}.$$

(a) Assuming that particles are uniformly distributed in an ellipse

$$x^2/a^2 + x'^2/b^2 = 1,$$

show that the total phase-space area is $\mathcal{A} = \pi ab = 4\pi\epsilon_{\rm rms}$. The factor 4 has often been used in the definition of the full emittance, i.e. $\epsilon = 4\epsilon_{\rm rms}$, to ensure that the phase-space area of such an ellipse is $\pi\epsilon$.

(b) Show that the rms emittance defined above is invariant under a coordinate rotation

$$X = x\cos\theta + x'\sin\theta, \quad X' = -x\sin\theta + x'\cos\theta,$$

and show that the correlation coefficient $R = \sigma_{XX'}/\sigma_X\sigma_{X'}$ is zero if we choose the rotation angle to be

$$\tan 2\theta = \frac{2\sigma_x\sigma_{x'}r}{\sigma_x^2 - \sigma_{x'}^2}.$$

Show that σ_X and $\sigma_{X'}$ reach extrema at this rotation angle.

(c) In accelerators, particles are distributed in the Courant-Snyder ellipse:

$$I(x,x') = \gamma x'^2 + 2\alpha x x' + \beta x^2,$$

where α, β, γ are betatron amplitude functions. Use the coordinate rotation to show that

$$\epsilon_{\rm rms} = \frac{\sigma_x^2}{\beta} = \frac{\sigma_{x'}^2}{\gamma}, \quad r = -\frac{\alpha}{\sqrt{\beta\gamma}},$$

or

$$\begin{pmatrix} \sigma_x^2 & \sigma_{xx'} \\ \sigma_{xx'} & \sigma_{x'}^2 \end{pmatrix} = \epsilon_{\rm rms} \begin{pmatrix} \beta & -\alpha \\ -\alpha & \gamma \end{pmatrix}.$$

Show that

$$\mathbf{x}^\dagger \sigma^{-1} \mathbf{x} = \frac{1}{\epsilon_{\rm rms}}(\gamma x^2 + 2\alpha x x' + \beta x'^2).$$

(d) Show that the σ matrix is transformed, in the linear betatron motion, according to

$$\begin{pmatrix} \sigma_x^2 & \sigma_{xx'} \\ \sigma_{xx'} & \sigma_{x'}^2 \end{pmatrix}_2 = M(s_2|s_1) \begin{pmatrix} \sigma_x^2 & \sigma_{xx'} \\ \sigma_{xx'} & \sigma_{x'}^2 \end{pmatrix}_1 M(s_2|s_1)^\dagger,$$

where $M^\dagger$ is the transpose of the matrix M. Use this result to show that $\mathbf{x}^\dagger\sigma^{-1}\mathbf{x}$ of Eq. (2.105) is invariant under betatron motion and thus an invariant beam distribution function is a function of $\mathbf{x}^\dagger\sigma^{-1}\mathbf{x}$. The transport equation for the σ-matrix can be used to measure the σ-matrix elements and derive the rms beam emittance. For a thick quadrupole lens, show that Eq. (2.106) becomes

$$\begin{aligned}\sigma_x^2(s_2) &= \sigma_x^2(s_1)\left\{\cos\sqrt{K}\ell_{\rm q} - L\sqrt{K}\sin\sqrt{K}\ell_{\rm q} + \frac{\sigma_{xx'}(s_1)}{\sigma_x^2(s_1)}\left(\frac{1}{\sqrt{K}}\sin\sqrt{K}\ell_{\rm q}\right.\right. \\ &\left.\left. + L\cos\sqrt{K}\ell_{\rm q}\right)\right\}^2 + \frac{\epsilon_{\rm rms}^2}{\sigma_x^2(s_1)}\left[\frac{1}{\sqrt{K}}\sin\sqrt{K}\ell_{\rm q} + L\cos\sqrt{K}\ell_{\rm q}\right]^2,\end{aligned}$$

where $K = B_1/B\rho$ and $\ell_{\rm q}$ and the focusing function and the length of the quadrupole, and L is the length of the drift space between the quadrupole and the profile monitor.

(e) Particle motion in synchrotrons obeys Hamiltonian dynamics with

$$x' = \frac{dx}{ds}, \quad \frac{dx'}{ds} = -\frac{\partial H}{\partial x}.$$

Show that

$$\frac{d\epsilon^2}{ds} = -2\sigma_x^2(\langle x'\frac{\partial H}{\partial x}\rangle - \langle x'\rangle\langle\frac{\partial H}{\partial x}\rangle) + 2\sigma_{xx'}(\langle x\frac{\partial H}{\partial x}\rangle - \langle x\rangle\langle\frac{\partial H}{\partial x}\rangle).$$

For a linear Hamiltonian, we have $\partial H/\partial x = Kx$, where $K(s)$ is the focusing function. Show that the rms emittance is conserved. What would your conclusion be if the Hamiltonian were nonlinear?

15. Consider a beam of noninteracting particles in an accelerator with focusing function $K_y(s)$, where the particle betatron coordinate obeys Hill's equation

$$y'' + K_y(s)y = 0.$$

Let Y be the envelope radius of the beam with emittance ϵ, i.e. $Y(s) = \sqrt{\beta(s)\epsilon}$.

(a) Show that the envelope equation of motion is

$$Y'' + K_y(s)Y - \frac{\epsilon^2}{Y^3} = 0.$$

(b) Show that the envelope equation can be derived from the envelope Hamiltonian[27]

$$H_{\rm env} = \frac{1}{2}P^2 + \frac{1}{2}K_y(s)Y^2 + \frac{\epsilon^2}{2Y^2},$$

where (P, Y) are conjugate envelope phase-space coordinates with $P = Y'$. The "potential energy" of the envelope Hamiltonian is

$$V_{\rm env} = \frac{1}{2}K_yY^2 + \frac{\epsilon^2}{2Y^3}.$$

In a smooth focusing approximation, $K_y(s) = (2\pi/L)^2$, where L is the wavelength of the betatron oscillations.[28] The equivalent betatron amplitude function is $\beta_y = L/2\pi$. The matched beam radius is given by $dV_{\rm env}/dY = 0$, i.e. $Y_{\rm m} = \sqrt{L\epsilon/2\pi}$. Show that the betatron motion is

$$y = \sqrt{\frac{L\epsilon}{2\pi}}\cos(\frac{2\pi s}{L} + \chi_\beta),$$

[27] See S.Y. Lee and A. Riabko, *Phys. Rev.* **E51**, 1609 (1995); A. Riabko *et al.*, *Phys. Rev.* **E51**, 3529 (1995).

[28] Using the smooth approximation, we have $\langle K_y\rangle = (2\pi Q_y/C)^2$ obtained from Floquet transformation to Hill's equation, where C is the circumference, and Q_y is the betatron tune. The corresponding average betatron wavelength is C/Q_y, and the average betatron amplitude function is $\langle\beta_y\rangle = R/Q_y$, where R is the average radius.

and the solution of the envelope equation is

$$Y^2 = \sqrt{A^2 + \left(\frac{L\epsilon}{2\pi}\right)^2} + A\cos(2\frac{2\pi s}{L} + \chi),$$

where the parameters A and χ are determined by the initial beam conditions. Thus the envelope of a mis-injected beam bunch will oscillate at twice the betatron oscillation frequency (the quadrupole mode).

(c) Let us make Floquet transformation to the envelope equation in part (a) with

$$R = \frac{Y}{\sqrt{\beta\epsilon}}, \qquad \phi = \frac{1}{\nu}\int_0^s \frac{ds}{\beta(s)},$$

where β is the betatron amplitude function, and ν is the betatron tune. Show that the normalized envelope R satisfies the equation:

$$\frac{d^2}{d\phi^2}R + \nu^2 R - \frac{\nu^2}{R^3} = 0.$$

Using $(R, P_R = dR/d\phi)$ as the conjugate phase space coordinates, we obtain the envelope Hamiltonian as $H = \frac{1}{2}P_R^2 + V_{\text{env}}(R)$, where the envelope potential is

$$V_{\text{env}} = \frac{1}{2}\nu^2 R^2 + \frac{\nu^2}{2R^2}.$$

Show that the exact solution of the envelope equation is

$$R^2 = \sqrt{1+a^2} + a\cos(2\nu\phi + \chi),$$

where a is the envelope mismatch amplitude. Note: if the *square* of the rms beam width is plotted as a function of revolution turns, the resulting oscillation will be sinusoidal. The envelope Hamiltonian is, in fact, linear.

16. The Courant–Snyder phase-space ellipse of a synchrotron is $\gamma y^2 + 2\alpha y y' + \beta y'^2 = \epsilon$, where α, β and γ are the Courant–Snyder parameters. If the injection optics is mis-matched with $\gamma_1 y^2 + 2\alpha_1 y y' + \beta_1 y'^2 = \epsilon$, find the emittance growth factor.[29]

(a) Transform the injection ellipse into the normalized coordinates of the ring lattice, and show that the injection ellipse becomes

$$\left(\frac{\beta}{\beta_1} + \frac{(\alpha_1\beta - \beta_1\alpha)^2}{\beta\beta_1}\right)Y^2 + 2\frac{\alpha_1\beta - \alpha\beta_1}{\beta}YP + \frac{\beta_1}{\beta}P^2 = \epsilon,$$

where

$$Y = \frac{1}{\sqrt{\beta}}y, \quad P = \frac{1}{\sqrt{\beta}}(\alpha y + \beta y').$$

[29]The easiest way to estimate the emittance growth is to transform the injection ellipse into the normalized coordinates of the ring optics. The deviation of the injection ellipse from a circle in the normalized phase space corresponds to the emittance growth.

(b) Transform the ellipse to the upright orientation, and show that the major and minor axes of the ellipse are

$$F_+ = \left(X_{\text{mm}} + \sqrt{X_{\text{mm}}^2 - 1}\right)^{1/2}, \quad F_- = \left(X_{\text{mm}} - \sqrt{X_{\text{mm}}^2 - 1}\right)^{1/2},$$

where the mismatch factor X_{mm} is (see Exercise 2.2.14)

$$X_{\text{mm}} = \frac{1}{2}(\gamma_1\beta + \beta_1\gamma - 2\alpha_1\alpha) = \frac{1}{2\epsilon_{\text{rms}}}(\beta\sigma_{x'}^2 + \gamma\sigma_x^2 + 2\alpha\sigma_{xx'}).$$

Note that the rms quantities $\sigma_x, \sigma_{x'}$ and $\sigma_{xx'}$ can be measured from the injected beam. What happens to the beam if the beam is injected into a perfect linear machine where there is no betatron tune spread? Show that the tune of the envelope oscillations is twice the betatron tune (see Exercise 2.2.15).

(c) In general, nonlinear betatron detuning arises from space-charge forces, nonlinear magnetic fields, chromaticities, etc. Because the betatron tune depends on the betatron amplitude, the phase-space area of the mis-injected beam will decohere and grow. Show that the emittance growth factor is

$$F_+^2 = \left(X_{\text{mm}} + \sqrt{X_{\text{mm}}^2 - 1}\right).$$

(d) Let the betatron amplitude function at the injection point be $\beta_x = 17.0$ m and $\alpha_x = 2.02$. The injection ellipse of a beam with emittance 5π mm-mrad is given by $x^2/a^2 + x'^2/b^2 = 1$, where $a = 5.00$ mm and $b = 1.00$ mrad. Find the final beam emittance after nonlinear decoherence.

17. At an interaction point (IP) of a collider, or at a symmetry point in a storage ring, the lattice betatron functions are usually designed to an appropriate $\beta_{x,z}^*$ value with symmetry condition: $\alpha_{x,z}^* = 0$. The resulting betatron amplitude functions in the straight section become $\beta_{x,z} = \beta_{x,z}^* + s^2/\beta_{x,z}^*$ (see Exercise 2.2.8). The luminosity, $\mathcal{L}$, measuring the probability of particle encounters in a head on collision of two beams, is

$$\mathcal{L} = 2fN_1N_2\int \rho_1(x,z,s_1)\rho_2(x,z,s_2)\,dx\,dz\,ds\,d(\beta ct),$$

where $s_1 = s + \beta ct$ and $s_2 = s - \beta ct$.

(a) Assuming Gaussian bunch distribution with

$$\rho(x,z,s) = \frac{1}{(2\pi)^{3/2}\sigma_x\sigma_z\sigma_s}\exp\left\{-\frac{x^2}{2\sigma_x^2} - \frac{z^2}{2\sigma_z^2} - \frac{s^2}{2\sigma_s^2}\right\},$$

where $\sigma_x = \sqrt{\beta_x\epsilon_x}$, $\sigma_z = \sqrt{\beta_z\epsilon_z}$, σ_s are respectively the rms beam sizes in x, z, s directions, show that the luminosity, in a short bunch condition with $\sigma_s \ll \beta_{x,z}^*$, is

$$\mathcal{L} = R(A)\frac{fN_1N_2}{4\pi\sigma_x^*\sigma_z^*},$$

where R is the reduction factor, and $\sigma_x^* = \sqrt{\beta_x^*\epsilon_x}$ and $\sigma_z^* = \sqrt{\beta_z^*\epsilon_z}$ are rms beam size at the IP.

(b) Because of finite bunch-length σ_s, show that the luminosity reduction factor for two identical Gaussian distributions is

$$R(A_x, A_z) = \frac{2}{\sqrt{\pi}} \int \frac{e^{-\zeta^2} d\zeta}{\sqrt{(1+(\zeta^2/A_x^2))(1+(\zeta^2/A_z^2))}}$$

where $A_{x,z} = \beta^*_{x,z}/\sigma_s$ is a measure of the betatron amplitude variation at the interaction point. In a short bunch approximation with $A_x \gg 1$ and $A_z \gg 1$, we obtain $R(A_x, A_z) \approx 1$. Most colliders operate at a condition $A_{x,z} \approx 1$. The luminosity reduction due to finite bunch-length is called the hour-glass effect.

(c) For a round beam with $A = A_x = A_z$, show that (see Section 7.1.3. in Ref. [25])

$$R(A) = \sqrt{\pi} A e^{A^2} \operatorname{erfc}(A) \approx \frac{\sqrt{\pi} A(1 + 0.2836A + 0.07703A^2)}{(1 + 0.47047A)^3},$$

where the latter approximate identity is valid up to about $A \leq 2.5$. Asymptotically, we have $R(A) \to 1$ for $A \to \infty$. Plot $R(A)$ as a function of A and show that the actual luminosity is

$$\mathcal{L} = R(A)\mathcal{L}_0 = \frac{f N_1 N_2}{4\pi\epsilon_\perp \sigma_s} \sqrt{\pi} e^{A^2} \operatorname{erfc}(A)$$

for a given σ_s, where $\epsilon_\perp = \epsilon_x = \epsilon_z$. Plot $\mathcal{L}$ as a function of A. Does the luminosity decrease at $A < 1$?

(d) For a flat beam with $\beta^*_x \gg \sigma_s$, i.e. $A_x \gg 1$, show that the reduction factor becomes

$$R = \frac{2A_z}{\sqrt{\pi}} \int \frac{e^{-A_z^2\zeta^2} d\zeta}{\sqrt{1+\zeta^2}} = \frac{A_z}{\sqrt{\pi}} e^{\frac{A_z^2}{2}} K_0\left(\frac{A_z^2}{2}\right),$$

where K_0 is the modified Bessel function. Calculate the reduction factor as a function of A_z and show that the luminosity is (use 3.364.3 of Ref. [26])

$$\mathcal{L} = R(A_z)\mathcal{L}_0 = \frac{f N_1 N_2}{4\pi\sqrt{\beta_x \epsilon_x \epsilon_z \beta_z}} \frac{1}{\sqrt{\pi}} \sqrt{A_z} e^{\frac{A_z^2}{2}} K_0\left(\frac{A_z^2}{2}\right).$$

18. **Focusing of atomic beams:**[30] There are now two types of polarized ion sources: the atomic-beam polarized ion source (ABS), and the optically pumped polarized ion source (OPPIS) producing mainly hydrogen and deuterium ions.[31] The principle of the ABS is to form atomic beams in a discharge tube called a *dissociator*. As the beam travels through the beam tube, the spin states of the atoms are selected in a *separation magnet*, which is a quadrupole or a sextupole.[32] The non-uniform magnetic field preferentially selects one spin state (Stern-Gerlach effect). This exercise illustrates

[30] See e.g., W. Haberli, *Ann. Rev. Nucl. Sci.*, **17**, 373 (1967).

[31] The ABS has produced polarized H^- ions with about 75% polarization at a peak current of 150 μA with 100 μs duration and 5 Hz repetition rate. Similarly, OPPIS has been able to produce a polarized H^- ion source up to 400 μA with 80% polarization at a normalized emittance near 1 π mm-mrad.

[32] H. Friedburg, and W. Paul, *Naturwiss.* **38**, 159 (1951); H.G. Bennewitz and W. Paul, *Z. Phys.* **139**, 489 (1954).

the focusing effect due to a sextupole field. Let $\vec{\mu} = \tilde{g}\mu_B \vec{J}$ be the magnetic moment of the atomic beam, where $\tilde{g}$ is the Landé g-factor, $\mu_B = 5.788 \times 10^{-5}$eV/T is the Bohr magneton, and $\vec{J}$ is the angular momentum of the atom. The magnetic energy of the atomic beam in the magnetic field $\vec{B}$ is

$$W = -\vec{\mu} \cdot \vec{B}.$$

Thus the force acting on the hydrogen atom is

$$\vec{F} = \nabla(\vec{\mu} \cdot \vec{B}) = \pm\mu_a \nabla|\vec{B}|$$

for two quantized spin 1/2 states of the hydrogen atom, i.e. the electron spin is quantized along the $\vec{B}$ direction, and $\mu_a \approx \mu_B$ for the hydrogen-like atom.

(a) Show that the sextupole field focuses the spin state of the atomic beam with lower magnetic dipole energy; in other words, it defocuses the spin state with higher magnetic dipole energy. The atoms not contained in the beam pipe will be pumped away. It is worth pointing out that there is no preferred direction of the spin projection inside the sextupole. The electron spin is quantized with respect to the magnetic field. The selected atoms, which have a preferential one-spin state, will pass through the *transition* region. Here the the magnetic field is slowly changed to align all atomic polarization into the uniform field *ionizer* region, where in the high-field regime the nuclear spin can be flipped by rf field, the polarized ions are formed by the bombardment of electron beams, and the polarized ions are drawn by the electric field to form a polarized ion beam.

(b) When a quadrupole is used to replace the sextupole magnet, show that the effective force on the atom is a dipole field.

(c) If the temperature of the dissociator is 60 K, what is the velocity spread of the atomic beam? Discuss the effect of velocity spread of the atomic beam.

19. **A paraxial focusing system (lithium lens):** A strong paraxial focusing system can greatly increase the yield of the secondary beams. To this end, the lithium lens or a strong solenoid has been used. The Li lens was first used at Novosibirsk for focusing the e^+e^- beams. It became the essential tool for anti-proton collection at Fermilab.[33] A cylindrical lithium rod carrying a uniform current pulse can create a large magnetic field. The magnetic flux density is

$$B_\theta(r) = \frac{\mu I r}{2\pi r_0^2},$$

where I is the current, r is the distance from the center of the rod, r_0 is the radius of the Li conductor, and $\mu \approx \mu_0 = 4\pi \times 10^{-7}$ Tm/A is the permeability.

(a) Find the focusing function for the 8-GeV kinetic energy antiprotons if $I = 500$ kA, $r_0 = 10$ mm, and the length is 15 cm. What is the focal length?

[33] B.F. Bayanov, *et al.*, *Nucl. Inst. Methods.* **190**, 9 (1981).

(b) The total nuclear reaction cross-section between the antiprotons and the Li nucleus is given by the geometric cross-section, i.e. $\sigma_{\mathrm{p,A}} = \pi(r_{\mathrm{p}}^2 + R_{\mathrm{A}}^2)$, where $r_p = 0.8$ fm, $R_{\mathrm{A}} = 1.3 \times A^{1/3}$ fm, and A is the atomic mass number. The atomic weight is 6.941 g, and the density is 0.5 g/cm^3, show that the nuclear reaction length is about 1 m. To minimize the beam loss, choose the length of the Li lens to be less than 10% of the nuclear reaction length.

(c) Find the magnetic pressure $P = B^2/2\mu_0$ that acts to compress the Li cylinder in units of atmospheric pressure (1 atm $= 1.013 \times 10^5$ N/m).

20. Low energy synchrotrons often rely on the bending radius $K_x = 1/\rho^2$ for horizontal focusing and edge angles in dipoles for vertical focusing. Find the lattice property of the low energy synchrotron described by the following input data file (MAD). What is the effects of changing the edge angle and dipole length? Discuss the stability limit of the lattice.

```
TITLE,"CIS BOOSTER (1/5 Cooler), (90degDIP)"
! CIS =1/5 of Cooler circumference =86.82m / 5 =17.364m
! It accelerates protons from 7 MeV to 200 MeV in 1-5 Hz.
LCELL:=4.341          ! cell length 17.364m/4
L1:= 2.0              ! dipole length
L2:=LCELL-L1          ! straight section length
RHO:=1.27324
EANG:=12.*TWOPI/360 ! use rad. for edge angle
ANG := TWOPI/4
OO : DRIFT,L=L2
BD : SBEND,L=L1, ANGLE=ANG, E1=EANG,E2=EANG, K2=0.
SUP: LINE=(BD,OO)    ! a superperiod
USE,SUP,SUPER=4
PRINT,#S/E
TWISS,DELTAP=0.0,TAPE
STOP
```


III Effect of Linear Magnet Imperfections

In the presence of magnetic field errors, Hill's equations are

$$x'' + K_x(s)x = \frac{\Delta B_z}{B\rho}, \qquad z'' + K_z(s)z = -\frac{\Delta B_x}{B\rho}, \tag{2.154}$$

where the perturbing fields ΔB_z and ΔB_x, similar to Eq. (2.25), can be represented by

$$\Delta B_z + j\Delta B_x = B_0 \sum_{n=0}^{\infty} (b_n + ja_n)\,(x + jz)^n.$$

Here j is an imaginary number, B_0 is the main dipole field, b_0 and b_1 are respectively the dipole and quadrupole field errors, b_2 is the sextupole field error, etc. The a's are skew magnetic field errors. This section addresses the linear betatron perturbations resulting from the dipole and quadrupole field errors, and illustrates possible beam manipulation by using the perturbing fields.

Based on our study of the betatron motion in Sec. II, we will show that linear magnet imperfections have two major effects: (1) closed-orbit distortion due to dipole field error, and (2) betatron amplitude function distortion due to quadrupole field error. The effect of linear betatron coupling due to the skew quadrupole term, a_1, and the solenoid will be discussed in Sec. VI.

III.1 Closed-Orbit Distortion due to Dipole Field Errors

Up to now, we have assumed perfect dipole magnets with an ideal reference closed orbit that passes through the center of all quadrupoles. In reality, dipole field errors may arise from errors in dipole length or power supply, dipole roll giving rise to a horizontal dipole field, a closed orbit not centered in the quadrupoles, and feed-down from higher-order multipoles.

A. The perturbed closed orbit and Green's function

First, we consider a single thin dipole field error at a location $s = s_0$ with a kick-angle $\theta = \Delta B dt/B\rho$ in an otherwise ideal accelerator, where $\Delta B dt$ is the integrated dipole field error and $B\rho = p_0/e$ is the momentum rigidity of the beam. Let

$$\mathbf{y}_- = \begin{pmatrix} y_0 \\ y_0' - \theta \end{pmatrix}, \quad \mathbf{y}_+ = \begin{pmatrix} y_0 \\ y_0' \end{pmatrix}$$

be the phase-space coordinates of the closed orbit just before and just after the kick element located at s_0. The closed-orbit condition becomes

$$\mathbf{M}\begin{pmatrix} y_0 \\ y_0' \end{pmatrix} = \begin{pmatrix} y_0 \\ y_0' - \theta \end{pmatrix}, \tag{2.155}$$

where $\mathbf{M}$ is the one-turn transfer matrix of Eq. (2.53) for an ideal accelerator. The resulting closed orbit at s_0 is

$$y_0 = \frac{\beta_0\theta}{2\sin\pi\nu}\cos\pi\nu, \qquad y_0' = \frac{\theta}{2\sin\pi\nu}(\sin\pi\nu - \alpha_0\cos\pi\nu), \tag{2.156}$$

where ν is the betatron tune and α_0, β_0 are the values of the betatron amplitude functions at kick dipole location s_0.

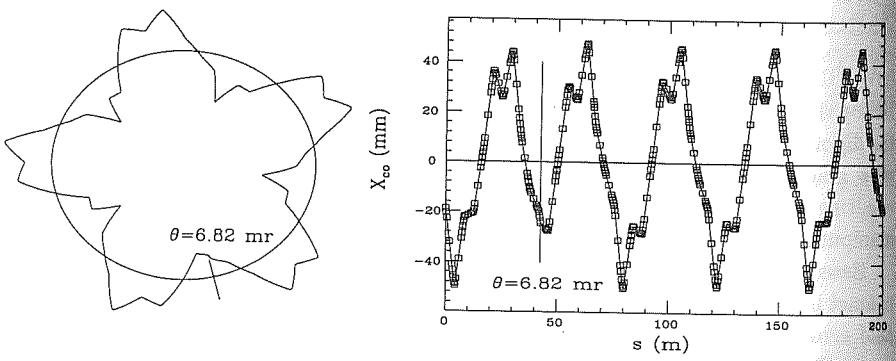

Figure 2.11: The left plot shows schematically the closed-orbit error of the AGS booster resulting from a horizontal kicker with kick-angle $\theta = 6.82$ mr at the location marked by a straight vertical line. Since the betatron tune of 4.82 is close to the integer 5, the closed orbit is dominated by the fifth error harmonic. The right plot shows the same closed orbit as a function of the longitudinal distance.

The closed orbit at other location s in the accelerator can be obtained from the propagation of betatron oscillations, i.e.

$$\begin{pmatrix} y(s) \\ y'(s) \end{pmatrix}_{co} = M(s|s_0)\begin{pmatrix} y_0 \\ y_0' \end{pmatrix}. \tag{2.157}$$

Using Eq. (2.67), we obtain

$$y_{co}(s) = G(s, s_0)\theta(s_0), \tag{2.158}$$

where

$$G(s, s_0) = \frac{\sqrt{\beta(s)\beta(s_0)}}{2\sin\pi\nu}\cos(\pi\nu - |\psi(s) - \psi(s_0)|) \tag{2.159}$$

is the Green function of Hill's equation. The orbit response arising from a dipole field error is given by the product of the Green function and the kick angle. The right plot of Fig. 2.11 shows the closed-orbit perturbation in the AGS booster due to a dipole field error of 6.82 mr. The left plot is a schematic drawing of the resulting closed orbit around an ideal orbit. Since the betatron tune of the AGS booster is 4.82, the

closed-orbit perturbation is dominated by the $n = 5$ harmonic, showing 5 complete oscillations in Fig. 2.11.

Equation (2.159) shows that the closed orbit becomes infinite when the condition $\sin\pi\nu = 0$ is encountered. The orbit kicks in every turn due to a dipole error coherently add up, making the closed orbit unstable. The left plot of Fig. 2.12 shows schematically the evolution of a phase-space trajectory (y, y') in the presence of a dipole error when the betatron tune is an integer. Since the angular kick $\Delta y' = \theta$, where θ is the kick angle of the error dipole, is in the same direction in each revolution, the closed orbit does not exist. This is why the betatron tunes are designed to avoid an integer value. In other words, if the betatron tune is near an integer, the closed orbit becomes very sensitive to dipole field error.

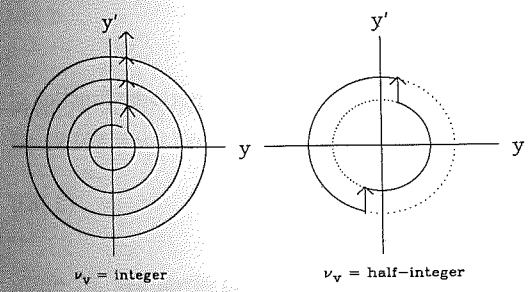

Figure 2.12: Left, a schematic plot of the closed-orbit perturbation due to an error dipole kick when the betatron tune is an integer. Here $\Delta y' = \theta$, where θ is the dipole kick angle. Right, a schematic plot of the particle trajectory resulting from a dipole kick when the betatron tune is a half-integer; here the angular kicks from two consecutive orbital revolutions cancel each other.

On the other hand, if the betatron tune is a half-integer, the angular kicks of two consecutive revolutions cancel each other (see right plot of Fig. 2.12). For the closed orbit, it is better to choose a betatron tune closer to a half-integer. However, we will show later that the quadrupole field error will produce betatron amplitude instability at a half integer tune. Thus the betatron tunes should also avoid half integers.

B. Distributed dipole field error

In reality, dipole field errors are distributed around the accelerator. Since Hill's equation with dipole field errors, $\Delta\theta(t) = (\Delta B(t)/B\rho)dt$, is linear, the closed orbit can be obtained by a linear superposition of dipole kicks, i.e.

$$\begin{aligned} y_{co}(s) &= \frac{\sqrt{\beta(s)}}{2\sin\pi\nu}\int_s^{s+C}\sqrt{\beta(t)}\frac{\Delta B(t)}{B\rho}\cos(\pi\nu + \psi(s) - \psi(t))dt \\ &= \frac{\nu\sqrt{\beta(s)}}{2\sin\pi\nu}\int_\phi^{\phi+2\pi}\left[\beta^{3/2}(\varphi)\frac{\Delta B(\varphi)}{B\rho}\right]\cos\nu(\pi + \phi - \varphi)d\varphi, \end{aligned} \tag{2.160}$$

where $\phi(s) = (1/\nu)\int_0^s dt/\beta(t)$, and $\psi(s) = \nu\phi(s)$. It is easy to verify that Eq. (2.160) is the closed-orbit solution of the inhomogeneous Hill equation

$$\frac{d^2y}{ds^2} + K(s)y = \frac{\Delta B}{B\rho}, \tag{2.161}$$

where $\Delta B = \Delta B_z$ for horizontal motion and $\Delta B = -\Delta B_x$ for vertical motion. The orbit response of the inhomogeneous Hill equation is

$$y_{\rm co}(s) = \int_s^{s+C} G(s,t)\,\frac{\Delta B(t)}{B\rho}\,dt, \tag{2.162}$$

where the Green function is given by Eq. (2.159).

C. The integer stopband integrals

Since square bracketed term in the integrand of Eq. (2.160) is a periodic function of 2π, we expand it in a Fourier series:

$$f(\phi) \equiv \beta^{3/2}(\phi)\frac{\Delta B(\phi)}{B\rho} = \sum_{k=-\infty}^{\infty} f_k\, e^{jk\phi}, \tag{2.163}$$

where the Fourier amplitude f_k is the integer stopband integral given by

$$f_k = \frac{1}{2\pi}\oint \beta^{3/2}\,\frac{\Delta B}{B\rho}\,e^{-jk\phi}\,d\phi = \frac{1}{2\pi\nu}\oint \sqrt{\beta}\,\frac{\Delta B}{B\rho}\,e^{-jk\phi}\,ds \tag{2.164}$$

with $f_{-k} = f_k^*$. In Fourier harmonics, the closed-orbit displacement $y_{\rm co}(s)$ becomes

$$y_{\rm co}(s) = \sqrt{\beta(s)}\sum_{k=-\infty}^{\infty}\frac{\nu^2 f_k}{\nu^2 - k^2}e^{jk\phi}, \tag{2.165}$$

which has simple poles at all integer harmonics. The presence of $\sin\pi\nu$ in the denominator of Eq. (2.160) shows that the closed orbit may not exist at all if the betatron tune is an integer. The simple pole structure in Eq. (2.165) indicates that the closed orbit is most sensitive to the error harmonics closest to the betatron tune. The resulting closed orbit is usually dominated by a few harmonics near $[\nu]$, which is an integer nearest to the betatron tune. In a single stopband approximation, the closed orbit can be approximated by

$$y_{\rm co}(s) \approx \frac{\sqrt{\beta(s)}\,\nu\,|f_{[\nu]}|\,\cos([\nu]\phi + \chi)}{2\,(\nu - [\nu])}.$$

D. Statistical estimation of closed-orbit errors

In practice, the perturbing field error $\Delta B/B\rho$, due mainly to random construction errors in the dipole magnets and misalignment errors in the quadrupoles, is not known a priori. During the design stage of an accelerator, a statistical argument is usually used to estimate the rms closed orbit,

$$y_{\rm co,rms} \approx \frac{\beta_{\rm av}}{2\sqrt{2}|\sin\pi\nu|}\sqrt{N}\theta_{\rm rms}, \tag{2.166}$$

where $\beta_{\rm av}$, N, and $\theta_{\rm rms}$ are respectively the average β-function, the number of dipoles with field errors, and the rms angular kick angle.

Now we consider the dipole field error generated by quadrupole misalignment. When quadrupole magnets are misaligned by a distance Δy, the effective angular kick is

$$\theta = \frac{B_1\ell}{B\rho}\Delta y = \frac{\Delta y}{f}, \tag{2.167}$$

where $B_1 = \partial B_z/\partial x$ is the quadrupole gradient, and f is the focal length. Substituting Eq. (2.167) into Eq. (2.166), we obtain

$$y_{\rm co,rms} \approx \left\{\frac{\beta_{\rm av}}{2\sqrt{2}f_{\rm av}|\sin\pi\nu|}\sqrt{N_{\rm q}}\right\}\Delta y_{\rm rms}, \tag{2.168}$$

where $N_{\rm q}$ is the number of quadrupoles and $f_{\rm av}$ is the average focal length. The coefficient in curly brackets is called a *sensitivity factor* for quadrupole misalignment. For example, if the sensitivity factor is 20, an rms quadrupole misalignment of 0.1 mm will result in a rms closed-orbit distortion of 2 mm. The sensitivity factor increases with the size of an accelerator.

E. Closed-orbit correction

Closed-orbit correction is an important task in accelerator commissioning. If the closed orbit is large, the beam lifetime and dynamical aperture can be severely reduced. First, any major known source of dipole error should be corrected. The remaining closed orbit can generally be corrected by the stopband correction scheme, the harmonic correction scheme, or the χ^2-minimization method.

With a few dipole correctors, the stopband near $k = [\nu]$ is

$$f_{[\nu]} = \frac{1}{2\pi\nu}\sum_i \sqrt{\beta_i}\,\theta_i\,e^{-j[\nu]\phi_i}, \tag{2.169}$$

where θ_i is the angular kick of the ith corrector. Placing these correctors at high-β locations with a phase advance between correctors of $[\nu]\phi_i \approx \pi/2$, one can adjust the real and imaginary parts independently.

The harmonic closed-orbit correction method uses distributed dipole correctors powered with a few harmonics nearest the betatron tune to minimize a set of stopband integrals f_k. For example, if N_c dipole correctors are powered with

$$\theta_i = \frac{1}{\sqrt{\beta_i}}(a_k \cos k\phi_i + b_k \sin k\phi_i), \quad (i = 1, \cdots, N_c),$$

where β_i and ϕ_i are the betatron amplitude function and the betatron phase at the ith kicker location, the kth stopband can be corrected by adjusting the a_k and b_k coefficients. A few harmonics can be superimposed to eliminate all dangerous stopbands.

Another orbit correction method is the χ^2-minimization procedure. Let N_m be the number of BPMs and N_c the number of correctors. Let $y_{i,co}$ and Δ_i be the closed-orbit deviation and BPM resolution of the ith BPM.[34] The aim is to minimize

$$\chi^2 = \sum_{i=1}^{N_m} \frac{|y_{i,co}|^2}{\Delta_i^2}$$

by varying $\theta_1, \theta_2, \ldots$ of N_c correctors.

These orbit correction schemes minimize only the errors in harmonics nearest the betatron tune. Because the closed orbit is not sensitive to errors in harmonics far from the betatron tune, these harmonics can hardly be changed by closed-orbit correction schemes.

In many beam manipulation applications such as injection, extraction, manipulation with an internal target, etc., local closed-orbit bumps are often used. Possible schemes of local orbit bumps are the "four-bump method" discussed in Sec. III.3 and the "three-bump method" (see Exercise 2.3.4).

F. Effects of dipole field error on orbit length

The path length of a circulating particle is

$$C = \oint \sqrt{(1 + x/\rho)^2 + x'^2 + z'^2}\, ds \approx C_0 + \oint \frac{x}{\rho} ds + \cdots, \tag{2.170}$$

where C_0 is the orbit length of the unperturbed orbit, and higher order terms associated with betatron motion are neglected. Since a dipole field error gives rise to a closed-orbit distortion, the circumference of the closed orbit may be changed as well.

[34]The BPM resolution depends on the stability of the machine and on the number of bits and the effective width of the pickup electrode (PUE). For example, the BPM resolution for the data acquisition system with a 12-bit ADC and a 40-mm effective width PUE is about 10 μm. If an 8-bit ADC is used, the resolution is reduced by a factor of 16. The BPM resolution for proton storage rings is about 10 to 100 μm.

We consider the closed-orbit change due to a single dipole kick at $s = s_0$ with kick angle θ_0. Using Eq. (2.162), we find the change in circumference as

$$\Delta C = C - C_0 = \theta_0 \oint \frac{G_x(s, s_0)}{\rho} ds = D(s_0)\,\theta_0, \tag{2.171}$$

where

$$\begin{aligned} D(s_0) &= \oint \frac{G_x(s, s_0)}{\rho} ds \\ &= \frac{\sqrt{\beta_x(s_0)}}{2 \sin \pi\nu_x} \oint \frac{\sqrt{\beta_x(s)}}{\rho} \cos\left(\pi\nu_x - |\psi_x(s) - \psi(s_0)|\right) ds \end{aligned} \tag{2.172}$$

is the value of the dispersion function at s_0 (see Sec. IV). Thus the change in orbit length due to a dipole field error is equal to the dispersion function times the orbital kick angle. When dipole field errors are distributed in a ring, the change in the total path length becomes

$$\Delta C = \oint D(s) \frac{\Delta B_z(s)}{B\rho} ds. \tag{2.173}$$

In many cases, the dipole field errors are generated by power supply ripple, ground vibration, traffic and mechanical vibration, tidal action, etc., and thus the circumference is modulated at some modulation frequencies. The modulation frequency from ground vibration is typically less than 10 Hz, the power supply ripple can produce modulation frequency at some harmonics of 50 or 60 Hz, and the frequency generated by mechanical vibrations is usually of the order of kHz. Normally, particle motion in an accelerator will not be affected by a small-amplitude modulation provided that the modulation frequencies do not induce betatron or synchrotron resonances. However, if the modulation frequency is equal to the betatron or synchrotron frequency, particle motion will be strongly perturbed. For example, an rf dipole field operating at a betatron sideband[35] can kick the beam out of the vacuum chamber; this is called *rf knock-out*. This method can be used to measure the betatron tune.

III.2 Extended Matrix Method for the Closed Orbit

The inhomogeneous differential equation (2.154) for the closed orbit of the betatron oscillation can be solved by the extended 3×3 transfer matrix method. For example, the equation of motion for a dipole field error in a constant-focusing quadrupole is

$$x'' + Kx = \frac{\Delta B_z}{B\rho}. \tag{2.174}$$

[35]The FFT spectra of a transverse phase-space coordinate display rotational harmonics at integer multiples of the revolution frequency and the betatron lines next to the rotation harmonics. These betatron frequency lines are called the betatron sidebands. See Sec. III.7 for details.

The betatron phase-space coordinates before and after the focusing quadrupole can be obtained from the extended transfer matrix by

$$\begin{pmatrix} x \\ x' \\ 1 \end{pmatrix}_2 = \begin{pmatrix} \cos\sqrt{K}\ell & \frac{1}{\sqrt{K}}\sin\sqrt{K}\ell & \frac{\Delta B_z}{B\rho K}(1-\cos\sqrt{K}\ell) \\ -\sqrt{K}\sin\sqrt{K}\ell & \cos\sqrt{K}\ell & \frac{\Delta B_z}{B\rho\sqrt{K}}\sin\sqrt{K}\ell \\ 0 & 0 & 1 \end{pmatrix} \begin{pmatrix} x \\ x' \\ 1 \end{pmatrix}_1, \tag{2.175}$$

where $\ell = s_2 - s_1$. In thin lens approximation, Eq. (2.175) becomes

$$M(s_2|s_1) = \begin{pmatrix} 1 & 0 & 0 \\ -1/f & 1 & \theta \\ 0 & 0 & 1 \end{pmatrix}, \tag{2.176}$$

where $\theta = \Delta B_z \ell / B\rho$ and $f = 1/K\ell$ are respectively the dipole kick angle and the focal length of the perturbing element. The dipole field error can also arise from quadrupole misalignments. Let Δy_q be the quadrupole misalignment. The resulting extended transfer matrix in the thin-lens approximation is

$$M_{\text{quad}} = \begin{pmatrix} 1 & 0 & 0 \\ -1/f & 1 & \Delta y_q/f \\ 0 & 0 & 1 \end{pmatrix}. \tag{2.177}$$

The 3×3 extended transfer matrix can be used to obtain the closed orbit of betatron motion. For example, the closed-orbit equation (2.155) is equivalent to

$$\begin{pmatrix} y_0 \\ y_0' \\ 1 \end{pmatrix} = \begin{pmatrix} 1 & 0 & 0 \\ 0 & 1 & \theta \\ 0 & 0 & 1 \end{pmatrix} \begin{pmatrix} M_{11} & M_{12} & 0 \\ M_{21} & M_{22} & 0 \\ 0 & 0 & 1 \end{pmatrix} \begin{pmatrix} y_0 \\ y_0' \\ 1 \end{pmatrix}, \tag{2.178}$$

where the M's are matrix elements of the 2×2 one-turn transfer matrix for an ideal machine, and θ is the dipole kick angle. Similarly, the 3×3 extended transfer matrix can be used to analyze the sensitivity of the closed orbit to quadrupole misalignment by multiplying the extended matrices along the transport line.[36]

III.3 Application of Dipole Field Error

Sometime, we create imperfections in an otherwise perfect accelerator for beam manipulation. Examples are the local-orbit bump, one-turn kicker for fast extraction, rf knock-out, etc.

[36] S.Y. Lee, S. Tepikian, *Proc. IEEE PAC Conf.*, p. 1639, (IEEE, Piscataway, N.J., 1991).

A. Orbit bumps

To facilitate injection, extraction, or special-purpose beam manipulation,[37] the orbit of the beam can be bumped to a desired transverse position at specified locations. In this example, we discuss the four-bump method facilitated by four thin dipoles with kick angles θ_i ($i = 1, 2, 3, 4$). Using Eq. (2.160), we obtain

$$y_{\text{co}}(s) = \frac{\sqrt{\beta(s)}}{2\sin\pi\nu} \sum_{i=1}^{4} \sqrt{\beta_i}\ \theta_i\ \cos(\pi\nu - |\psi - \psi_i|), \tag{2.179}$$

where $\theta_i = (\Delta B \Delta s)_i / B\rho$ and $(\Delta B \Delta s)_i$ are the kick-angle and the integrated dipole field strength of the i-th kicker. The conditions that the closed orbit is zero outside these four dipoles are $y_{\text{co}}(s_4) = 0$, $y'_{\text{co}}(s_4) = 0$, or

$$\sqrt{\beta_1}\theta_1 \cos[\pi\nu - \psi_{41}] + \sqrt{\beta_2}\theta_2 \cos[\pi\nu - \psi_{42}] + \sqrt{\beta_3}\theta_3 \cos[\pi\nu - \psi_{43}] + \sqrt{\beta_4}\theta_4 \cos\pi\nu = 0,$$
$$\sqrt{\beta_1}\theta_1 \sin[\pi\nu - \psi_{41}] + \sqrt{\beta_2}\theta_2 \sin[\pi\nu - \psi_{42}] + \sqrt{\beta_3}\theta_3 \sin[\pi\nu - \psi_{43}] + \sqrt{\beta_4}\theta_4 \sin\pi\nu = 0,$$

where $\psi_{ji} = \psi_j - \psi_i$ is the phase advance from s_i to s_j. Expressing θ_3 and θ_4 in terms of θ_1 and θ_2, we obtain

$$\begin{cases} \sqrt{\beta_3}\theta_3 = -(\sqrt{\beta_1}\theta_1 \sin\psi_{41} + \sqrt{\beta_2}\theta_2 \sin\psi_{42})/\sin\psi_{43}, \\ \sqrt{\beta_4}\theta_4 = (\sqrt{\beta_1}\theta_1 \sin\psi_{31} + \sqrt{\beta_2}\theta_2 \sin\psi_{32})/\sin\psi_{43}. \end{cases} \tag{2.180}$$

The orbit displacement inside the region of the orbit bump can be obtained by applying the transfer matrix to the initial coordinates. Using four bumps, we can adjust the orbit displacement and the orbit angle to facilitate ease of injection and extraction, to avoid unwanted collisions, and to avoid the limiting-aperture in the accelerator.

The three-bump method (see Exercise 2.3.4) has also been used for local orbit bumps. Although the slope of the bumped particle orbit can not be controlled in the three-bump method, this method is usually used for the local orbit correction because of its simplicity. Occasionally, the two-bump method has been used at favorable phase-advance locations in accelerators. Figure 2.13 shows an example of a local orbit bump using three dipoles. Since the two outer bumps happen to be nearly 180° apart in the betatron phase advance, the middle bump dipole has negligible field strength.

B. Fast kick for beam extraction

To extract a beam bunch from the accelerator, a fast kicker magnet is usually powered in about 20–100 ns rise and fall times in order to bump beam bunches into the ex-

[37] Other examples are orbit bump at the aperture restricted area, internal target area, avoiding unwanted collisions in colliders, etc. For example, the counter-circulating e^+ and e^- beams, or the $\bar{p}$ and p beams in a collider can be made to avoid crossing each other in a common vacuum chamber with electrostatic separators.

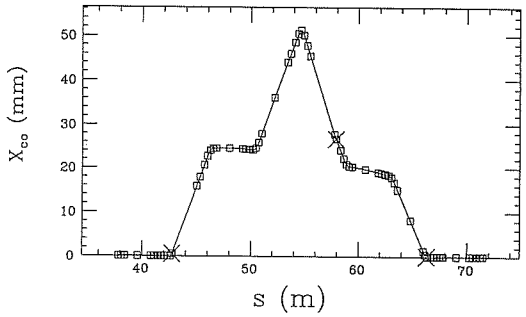

Figure 2.13: A simple orbit bump in the AGS booster lattice. The symbol X marks the three dipole kicker locations. Since the first and third kickers are nearly 180° apart in the betatron phase advance, the local orbit bump is essentially accomplished with these outer two kickers. In this example, there are 3 focusing and 2 defocussing quadrupoles between two outer bump dipoles.

traction channel, where a septum is located.[38] With the transfer matrix of Eq. (2.67), the transverse displacement of the beam is

$$\Delta x_{\rm co}(s) = \left\{\sqrt{\beta_x(s_{\rm k})\beta_x(s)}\sin(\Delta\phi_x(s))\right\}\theta_{\rm k}, \tag{2.181}$$

where $\theta_{\rm k} = \int B_{\rm k} ds/B\rho$ is the kicker strength (angle), $B_{\rm k}$ is the kicker dipole field, $\beta_x(s_{\rm k})$ is the betatron amplitude function evaluated at the kicker location, $\beta_x(s)$ is the amplitude function at location s, and $\Delta\phi_x(s)$ is the phase advance from $s_{\rm k}$ of the kicker to location s. The quantity in curly brackets in Eq. (2.181) is called the *kicker lever arm*.

To achieve a minimum kicker angle, the septum is located about 90° phase advance from the kicker, and the values of the betatron amplitude function at the septum and kicker locations are also optimized to obtain the largest kicker lever arm. Similar constraints apply to the kicker in the transverse feedback system, the kicker array for stochastic cooling, etc.

Figure 2.14 shows a schematic drawing of the cross-section of a Lambertson septum magnet. A beam is bumped from the center orbit $x_{\rm c}$ to a bumped orbit $x_{\rm b}$. At the time of fast extraction, a kicker kicks the beam from the bumped orbit to the the extraction channel at $x_{\rm k}$, where the uniform dipole field bends the beam into the extraction channel. The iron in the Lambertson magnet is shaped to minimize the field leakage into the field-free region and the septum thickness, that is of the order of 4-10 mm depending on the required magnetic field strength.

[38]The **kicker** is an electric or magnetic device that provides an angular deflection to the charged particle beam in fast rise and fall times so that it can selectively deflect beam bunches. The electric kicker applies the traveling wave to a stripline type waveguide. The magnetic kicker employs ferrite material to minimize eddy-current effects. The rise and fall times of the kickers range from 10 ns to 100's ns. The **septum** is a device with an aperture divided into a field-free region and a uniform-field region, where the former will not affect the circulating beams, and the latter can direct the beam into an extraction or injection channels. Depending on the application, one can choose among different types of septum, such as wire septum, current sheet septum, Lambertson septum, etc.

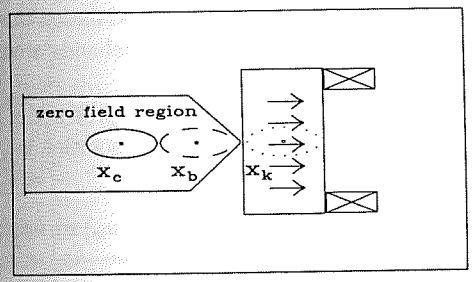

Figure 2.14: A schematic drawing of the central orbit $x_{\rm c}$, bumped orbit $x_{\rm b}$, and kicked orbit $x_{\rm k}$ in a Lambertson septum magnet. The blocks marked with X are conductor-coils, The ellipses marked beam ellipses with closed orbits x_c, x_b, and x_k. The arrows indicated a possible magnetic field direction for directing the kicked beams downward or upward.

C. Effects of rf dipole field, rf knock-out

In the presence of a localized rf dipole, Hill's equation is

$$\frac{d^2y}{ds^2} + K(s)y = \theta_a \sin\omega_{\rm m} t \sum_{n=-\infty}^{\infty} \delta(s - nC), \tag{2.182}$$

where $\theta_a = \Delta B\ell/B\rho$ and $\omega_{\rm m}$ are respectively the kick angle and the angular frequency of the rf dipole, C is the circumference, and $t = s/\beta c$ is the time coordinate. The periodic delta function reflects the fact that the beam particles encounter the kicker field only once per revolution.

Performing the Floquet transformation to Eq. (2.182) with

$$\eta = \frac{y}{\sqrt{\beta_0}}, \quad \phi = \frac{1}{\nu}\int_0^s \frac{ds}{\beta},$$

Hill's equation becomes

$$\frac{d^2\eta}{d\phi^2} + \nu^2\eta = \frac{\nu^2\beta_0^{3/2}\theta_a}{2\pi R}\sum_{n=-\infty}^{\infty}\sin(n+\nu_{\rm m})\phi, \tag{2.183}$$

where $\nu_{\rm m} = \omega_{\rm m}/\omega_0$ is the modulation tune, β_0 is the value of the betatron amplitude function at the rf dipole location, and ω_0 is the orbital angular frequency. The solution of the inhomogeneous Hill's equation is

$$\eta = A\cos\nu\phi + B\sin\nu\phi + \eta_{\rm co}, \tag{2.184}$$

where A and B are the amplitude of betatron motion determined by the initial conditions, and the particular solution $\eta_{\rm co}$ is the coherent time dependent closed orbit,

$$\eta_{\rm co} = \sum_{n=-\infty}^{\infty}\frac{\nu^2\beta_0^{3/2}\theta_a}{2\pi R\left[\nu^2 - (n+\nu_{\rm m})^2\right]}\sin(n+\nu_{\rm m})\phi. \tag{2.185}$$

Note that the discrete nature of the localized kicker generates error harmonics $n+\nu_{\rm m}$ for all $n \in (-\infty, \infty)$. For example, if the betatron tune is 8.8, large betatron

oscillations can be generated by an rf dipole at any of the following modulation tunes $\nu_m = 0.2, 0.8, 1.2, 1.8, \ldots$. The localized repetitive kicks generate sidebands around the revolution lines.

Now we examine the coherent betatron motion of the beam in the presence of an rf dipole at $\nu_m \approx \nu$ (modulo 1) with initial condition $y = y' = 0$. The solution is

$$\begin{aligned} y(s) &= \frac{\beta(s)\beta_0^{3/2}\theta_a}{2\pi R} \sum_{n=-\infty}^{\infty} \frac{1}{\nu^2 - (n+\nu_m)^2} \left[\nu^2 \sin(n+\nu_m)\phi - \nu(n+\nu_m)\sin\nu\phi\right] \\ &\approx -\left[\frac{\beta(s)\beta_0^{3/2}\theta_a\nu}{4\pi R}\frac{s}{R}\right] \cos\frac{\nu s}{R} + \ldots, \end{aligned} \tag{2.186}$$

where the last approximate identity is obtained by expanding the term in the sum with $n + \nu_m \approx \nu$, and retaining only the dominant term. Equation (2.186) indicates that the beam is driven coherently by the rf dipole, and the amplitude of betatron motion grows linearly with time.[39]

Figure 2.15 shows the measured betatron coordinate (lower curve) at a beam position monitor (BPM) after applying rf knock-out kicks to the beam in the IUCF Cooler Ring, and the fractional part of the betatron tune (upper curve), that, in this experiment, is equal to the knockout tune. The rf dipole was on from 1024 to 1536 revolutions starting from the triggering time. At revolution number 2048, the beam was imparted a transverse kick. Note the linear growth of the betatron amplitude during the rf dipole-on time. Had the rf dipole stayed on longer, the beam would have been driven out of the vacuum chamber. Thus the method is called the "rf knock out."

The fractional betatron tune, shown in the upper trace, is measured by averaging the phase advance from the Poincaré map (see Sec. III.5), where data from two BPMs are used. This two-kick method can be used to provide a more accurate measurement of the dependence of the betatron tune on the betatron amplitude.[40]

The rf dipole can be adiabatically turned on to induce coherent betatron oscillations for betatron tune measurement without causing serious emittance dilution.[41]

[39] It is worth pointing out that the coherent growth time of the betatron oscillation is inversely proportional to $|\nu_m - \nu|$ (mod 1). Beyond the coherent time, the beam motion is out of phase with the external force and leads to damping. This process is related to the Landau damping to be discussed in Sec. VIII.4.

[40] The power supply ripple at the IUCF cooler ring gives rise to a betatron tune modulation of the order of 2×10^{-3} at 60 Hz and its harmonics. On the other hand, the dependence of the betatron tune on the betatron action is typically 10^{-4} per 1π mm-mrad. To measure this small effect in the environment of the existing power supply ripple, the two-kick method was used to measure the instantaneous betatron tune change at the moment of the second kick. See M. Ellison *et al.*, *Phys. Rev. E* **50**, 4051 (1994).

[41] M. Bai *et al.*, *Phys. Rev.* E**56**, 6002 (1997); *Phys. Rev. Lett.* **80**, 4673 (1998); Ph.D. Thesis, Indiana University (1999).

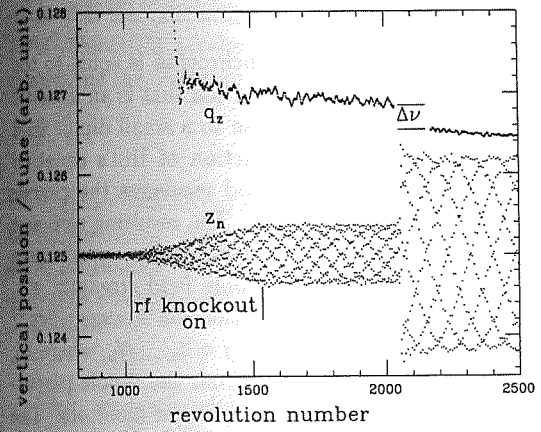

Figure 2.15: The lower curve shows the measured vertical betatron oscillations of the beam of one BPM at the IUCF cooler ring resulting from an rf dipole kicker at the betatron frequency. The rf dipole was turned on for 512 revolutions. After another 512 revolutions, the beam was imparted by a one-turn kicker. Note the linear growth of the betatron amplitude during the rf knockout-on time. The upper curve shows the fractional part of the betatron tune obtained by counting the phase advance in the phase-space map, where data from two BPMs are used.

Figure 2.16 shows the vertical beam profile measured at the AGS during the adiabatic turn-on/off of an rf dipole. When the rf dipole was on, the beam profile became larger because the beam was executing coherent betatron oscillations, and the profile was obtained from the integration of many coherent betatron oscillations. As the rf dipole is adiabatically turned off, the beam profile restored to its original shape.

The induced coherent betatron motion can be used to overcome the intrinsic spin resonances during polarized beam acceleration. Furthermore, the measurement of the coherent betatron tune shift as a function of the beam current can be used to measure the real and imaginary parts of the transverse impedance (see Sec. VIII). This method is usually referred to as the beam transfer function (BTF).

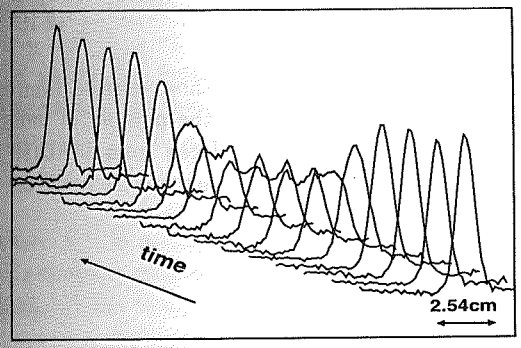

Figure 2.16: The beam profile measured from an ionization profile monitor (IPM) at the AGS during the adiabatic turn-on/off of an rf dipole. The beam profile appeared to be much larger during the time that the rf dipole was on because the profile was an integration of many coherent synchrotron oscillations. After the rf dipole was adiabatically turned off, the beam profile restored back to its original shape.

D. Orbit response matrix for accelerator modeling

Equation (2.162) shows that the beam closed orbit in a synchrotron is equal to the propagation of the dipole field error through the Green's function that is an intrinsic property of the betatron motion. If the closed-orbit response to a small dipole field perturbation can be accurately measured, the Green's function of Hill's equation can be modeled. The orbit response matrix (ORM) method measures the closed-orbit response induced by a known dipole field perturbation. The resulting response functions can be used to calibrate quadrupole strengths, BPM gains, quadrupole misalignments, quadrupole roll, dipole field integral, sextupole field strength, etc. The ORM method has been successfully used to model many electron storage rings.[42]

We consider a set of small dipole perturbation given by θ_j, $j = 1, ..., N_\mathrm{b}$, where N_b is the number of dipole kickers. The measured closed orbit from the dipole perturbation is y_i, $i = 1, ..., N_\mathrm{m}$, where N_m is the number of beam position monitors. The response matrix $\mathbf{R}$, defined as

$$y_i = \mathbf{R}_{ij}\theta_j, \quad j = 1, ..., N_\mathrm{b} \quad i = 1, ..., N_\mathrm{m}, \tag{2.187}$$

is equal to Green's function $\mathbf{R}_{ij} = G_y(s_i, s_j)$ of the actual machine, where y stands for either x or z. It is worth mentioning that N_b is not necessarily equal to N_m. Experimentally, we measure $\mathbf{R}_{ij}$ $(i = 1, \cdots, N_\mathrm{m})$ vs the dipole kick at θ_j $(j = 1, \cdots, N_\mathrm{b})$. The full set of the measured response matrix $\mathbf{R}$ can be employed to model the dipole and quadrupole field errors, the calibration of the BPM gain factor, sextupole misalignment, etc. The outcome of response matrix modeling depends on the BPM resolution, the number of BPMs and kickers, and the machine stability during the experimental measurement.

The ORM method minimizes the difference between the measured and model matrices $\mathbf{R}_\mathrm{exp}$ and $\mathbf{R}_\mathrm{model}$. Let

$$\mathbf{W}_k = \frac{|\mathbf{R}_{\mathrm{model},ij} - \mathbf{R}_{\mathrm{exp},ij}|}{\sigma_i} \tag{2.188}$$

be the difference between the closed-orbit data measured and those derived from a model, where σ_i is the rms error of ith measurements. Here the number of index k is $N_\mathrm{b} \times N_\mathrm{m}$, and the model response matrix can be calculated from MAD[19], SYNCH[20], or COMFORT[21] programs. The measured response matrix needs calibration in the kicker angle and BPM gain, i.e.

$$\mathbf{R}_{\mathrm{exp},ij} = \frac{\mathbf{R}_{\mathrm{data},ij}}{f_j g_i},$$

[42]See J. Safranek and M.J. Lee, *Proc. Orbit Correction and Analysis in Circular Accelerators*, AIP Conf. Proc. No. **315**, 128 (1994); J. Safranek and M.J. Lee, *Proc. 1994 European Part. Accel. Conf.* 1027 (1997). J. Safranek, *Proc. 1995 IEEE Part. Accel. Conf.*, 2817 (1995).

where f_j is the calibration factor of the jth kicker, and g_i is the gain factor of the ith BPM. The ORM accelerator modeling is to minimize the error of the vector $\mathbf{W}$ by minimizing the χ-square (χ^2) defined as

$$\chi^2 = \frac{1}{N_b \cdot N_m} \sum_k \mathbf{W}_k^2. \tag{2.189}$$

We consider sets of parameters w_m's that are relevant to accelerator model and orbit measurement. Some of these parameters are kicker angle calibration factor, the BPM gain factor, the dipole angle and dipole roll, the quadrupole strength and roll, sextupole strength, etc. The ORM modeling is to find a new set of w_m-parameters such that

$$||\mathbf{W}(w_m)|| = 0. \tag{2.190}$$

First, we begin with parameters w_m and evaluate $\mathbf{W}(w_m)$. The idea is to find a new set of parameters $w_m + \Delta w_m$ that satisfies Eq. (2.190), i.e.

$$\mathbf{W}_k(w_m + \Delta w_m) \approx \mathbf{W}_k(w_m) + \frac{d\mathbf{W}_k}{dw_m}\Delta w_m = 0. \tag{2.191}$$

To evaluate Δw_m, we invert matrix $\mathcal{W} \equiv \frac{d\mathbf{W}_k}{dw_m}$, which has the dimension of is $(N_b \cdot N_m) \times N_p$. Here, N_p is the number of parameters. In our application to accelerator physics, $(N_b \cdot N_m) \gg N_p$.

The singular value decomposition (SVD) algorithm decomposes the matrix $\mathcal{W}$ into

$$\mathcal{W} = \frac{\mathbf{dW_k}}{\mathbf{dw_m}} = \mathbf{U\Lambda V}^\mathrm{T}, \tag{2.192}$$

where $\mathbf{V}^\mathrm{T}$ is a real orthonormal $N_p \times N_p$ matrix with $\mathbf{VV}^\mathrm{T} = \mathbf{V}^\mathrm{T}\mathbf{V} = 1$, $\mathbf{\Lambda}$ is a diagonal $N_p \times N_p$ matrix with elements $\mathbf{\Lambda}_{11} = \sqrt{\lambda_1} \geq \mathbf{\Lambda}_{22} = \sqrt{\lambda_2} \cdots \geq 0$, and $\mathbf{U} = \mathbf{AV\Lambda^{-1}}$ is a $(N_m \cdot N_b) \times N_p$ matrix with $\mathbf{U}^\mathrm{T}\mathbf{U} = \mathbf{1}$.[43] Here $\lambda_1, \lambda_2, \cdots$ are eigenvalues of the matrix $\mathcal{W}^\mathrm{T}\mathcal{W}$, and $\mathbf{V}$ is composed of orthonormal eigenvectors of $\mathcal{W}^\mathrm{T}\mathcal{W}$, i.e. $\mathcal{W}^\mathrm{T}\mathcal{W} = \mathbf{V\Lambda^2V}^\mathrm{T}$. The SVD-method sets all eigenvalues $\lambda_i \leq \lambda_c$, $(i > r)$ to $\lambda_i = 0$, $(i > r)$, where λ_c is called the tolerance level and r is called the *rank* of the matrix $\mathcal{W}$. Setting all $\lambda_i = 0$ $(i > r)$ is equivalent setting $\Delta w_i = 0$ for $i > r$. This means that these dynamical parameters have no relevance to the measured data. Once the SVD of matrix $\mathcal{W}$ is obtained, one finds Δw_m as

$$\Delta w_m = -\left(\mathbf{V\Lambda^{-1}U}^\mathrm{T}\right)\mathbf{W}(w_m), \tag{2.193}$$

where $\mathbf{\Lambda}^{-1}$ is a diagonal matrix with $\mathbf{\Lambda}_{11}^{-1} = 1/\sqrt{\lambda_1}, \cdots, \mathbf{\Lambda}_{rr}^{-1} = 1/\sqrt{\lambda_r}$ and 0 for all remaining diagonal elements with $i > r$. The iterative procedure continues until $|\Delta w_m|$ or the change of χ^2 are small.

[43]The SVD decomposition of a $m \times n$ matrix $\mathcal{W}$ in Eq. (2.192) can also be carried out in such a way that $\mathbf{U}$ and $\mathbf{V}$ are respectively orthonormal real $m \times m$ and $n \times n$ matrices with $\mathbf{U}^\mathrm{T}\mathbf{U} = \mathbf{UU}^\mathrm{T} = \mathbf{1}$ and $\mathbf{V}^\mathrm{T}\mathbf{V} = \mathbf{VV}^\mathrm{T} = \mathbf{1}$, and $\mathbf{\Lambda}$ is a $m \times n$ diagonal matrix.

The response matrix modeling has been successfully implemented in many electron storage rings, where the BPM resolution is about 1~10 μm. The method has been used to calibrate kicker angle, BPM gain, quadrupole strength and roll, sextupole misalignment, dipole and quadrupole power supplies, etc. The method is also applicable to proton synchrotrons, where the BPM resolution is usually of the order of 100 μm.[44]

In accelerator modeling, the dimension of the matrix $\mathcal{W}$, $(N_m \cdot N_b) \times N_p$, can be large. The inversion of a very large matrix may become time consuming. It is advantageous to model accelerator parameters in sequences, e.g., (1) kicker angle calibration f_j, (2) BPM gain g_i, (3) quadrupole strength ΔK_i, (4) dipole angle calibration, (5) dipole roll, etc. These steps are sometimes essential in attaining a reliable set of model parameters.

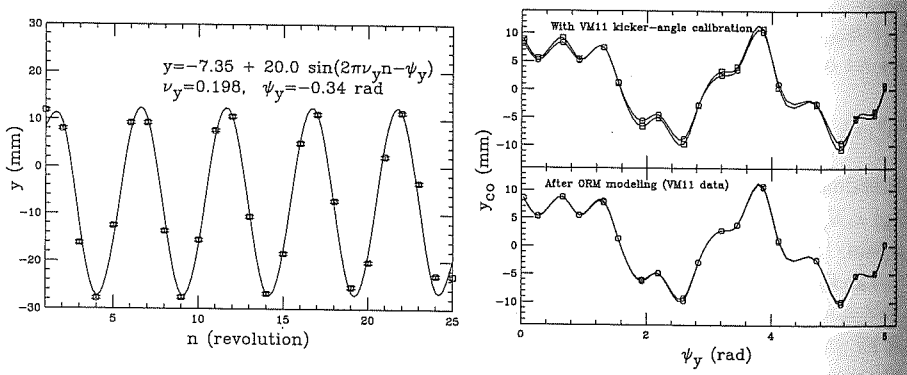

Figure 2.17: Left, digitized betatron oscillation data of one BPM are used to derive betatron amplitude, phase and tune, and closed orbit offset. Right, top plot shows the closed orbit data compared with Green's function of Eq. (eq23green) at a calibrated vertical steerer angle. The bottom right plot shows a similar comparison after ORM modeling.

For high-power synchrotrons, beam particles are injected, accelerated and extracted in a short time duration. For example, the proton storage ring (PSR) at Los Alamos National Laboratory accumulates protons for 3000 turns and the beam bunch is extracted after accumulation for high-intensity short-pulse neutron production. The closed orbit data can be obtained by averaging betatron oscillations in a single turn injection. The betatron oscillations of each BPM can be used to obtain the betatron amplitude, phase and tune, and the closed orbit (see the left plot of Fig. 2.17). These information can be used in the ORM analysis for accelerator modeling.[45] The right plots of Fig. 2.17 shows an example of typical fit in ORM modeling.

[44] C.M. Chu, *et al.*, "First Test of Orbit Response Matrix in Proton Storage Ring", Proceedings of PAC 1997, p. 1481 (1997).

[45] X. Huang *et al.*, *Analysis of the Orbit Response Matrix Measurement for PSR*, Technote: PSR-03-001 (2003).

The success of accelerator modeling depends critically on the orbit and tune stability, the number of BPMs and orbit steerers, proper set of experimental data for attaining relevant parameters.

E. Model Independent Analysis

Using turn-by-turn BPM data excited by resonant pinger discussed in Sec. III.3C, one can also carry out response matrix analysis for accelerator modeling, called Model Independent Analysis (MIA). This method has been successfully applied to SLC linac, PEP-II and Advanced Photon Source.[46] For the application of MIA in a storage ring, one uses an rf dipole pinger to excite coherent betatron oscillation and measures the response function with turn-by-turn BPM digitizing system (See Sec. II, in Appendix B).

III.4 Quadrupole Field (Gradient) Errors

The betatron amplitude function discussed in Sec. II depends on the distribution of quadrupole strengths. What happens to the betatron motion if some quadrupole strengths deviate from their ideal design values? We found in Sec. III.1 that the effect of dipole field error on the closed orbit would be minimized if the betatron tune was a half-integer. Why don't we choose a half-integer betatron tune?

This section addresses the effect of quadrupole field errors that can arise from variation in the lengths of quadrupoles, from errors in the quadrupole power supply, from the horizontal closed-orbit deviation in sextupoles,[47] etc. These errors correspond to the b_1 term in Eq. (2.25).

A. Betatron tune shift

Including the gradient error, Hill's equation for the perturbed betatron motion about a closed orbit is

$$\frac{d^2y}{ds^2} + [K_0(s) + k(s)]\, y = 0, \tag{2.194}$$

where $K_0(s)$ is the focusing function of the ideal machine discussed in Sec. II, and $k(s)$ is a small perturbation. The perturbed focusing function $K(s) = K_0(s)+k(s)$ satisfies

[46] J. Irwin, C.X. Wang, and Y.T. Yan, Phys. Rev. Lett. **82**, 1684 (1999); C.X. Wang, Ph.D. Thesis, Stanford University (1999); J. Irwin and Y.T. Yan, Proceedings of EPAC 2000, p. 151 (2000); C.X. Wang, Vadim Sajaev, and C.Y. Yao, Phys. Rev. ST Accel. Beams **6**, 104001 (2003).

[47] Substituting $x = x_{\rm co} + x_\beta$ and $z = z_\beta$ into the sextupole field of Eq. (2.25), we obtain

$$\Delta B_z = \frac{1}{2}B_2(x_{\rm co}^2 + 2x_{\rm co}x_\beta + x_\beta^2 - z_\beta^2), \qquad \Delta B_x = B_2(x_{\rm co}z_\beta + x_\beta z_\beta),$$

where $B_2 = \partial^2 B_z/\partial x^2$. Thus an off-center horizontal orbit in a sextupole generates a dipole field $\frac{1}{2}B_2x_{\rm co}^2$, and a quadrupole field gradient $B_2x_{\rm co}$. This process is called *feed-down*.

a weaker superperiod condition $K(s+C) = K(s)$, where C is the circumference. Let $\mathbf{M}_0$ be the one-turn transfer matrix of the ideal machine, i.e.

$$\mathbf{M}_0(s) = I\cos\Phi_0 + J\sin\Phi_0,$$

where $\Phi_0 = 2\pi\nu_0$ is the unperturbed betatron phase advance in one complete revolution, ν_0 is the unperturbed betatron tune, I is the 2×2 unit matrix, and

$$J(s) = \begin{pmatrix} \alpha(s) & \beta(s) \\ -\gamma(s) & -\alpha(s) \end{pmatrix}.$$

Here $\alpha(s)$, $\beta(s)$, and $\gamma(s)$ are betatron amplitude functions of the unperturbed machine. We consider now the gradient perturbation with an infinitesimal length ds_1 at s_1. The transfer matrix of this infinitesimal localized perturbing quadrupole error is

$$m(s_1) = \begin{pmatrix} 1 & 0 \\ -k(s_1)ds_1 & 1 \end{pmatrix}. \tag{2.195}$$

The one-turn transfer matrix $\mathbf{M}(s_1) = \mathbf{M}_0(s_1)m(s_1)$ becomes

$$\mathbf{M}(s_1) = \begin{pmatrix} \cos\Phi_0 + \alpha_1\sin\Phi_0 - \beta_1 k(s_1)ds_1\sin\Phi_0 & \beta_1\sin\Phi_0 \\ -\gamma_1\sin\Phi_0 - [\cos\Phi_0 + \alpha_1\sin\Phi_0]k(s_1)ds_1 & \cos\Phi_0 - \alpha_1\sin\Phi_0 \end{pmatrix},$$

where $\alpha_1 = \alpha(s_1)$, $\beta_1 = \beta(s_1)$, and $\gamma_1 = \gamma(s_1)$. The phase advance of the perturbed machine can be obtained from the trace of $\mathbf{M}$, i.e.

$$\cos\Phi - \cos\Phi_0 = -\frac{1}{2}\beta(s_1)k(s_1)ds_1\sin\Phi_0, \quad \text{or} \quad \Delta\Phi \approx \frac{1}{2}\beta(s_1)k(s_1)ds_1,$$

where $\Delta\Phi \equiv \Phi - \Phi_0$, and the betatron tune shift is $\Delta\nu = \frac{1}{4\pi}\beta(s_1)k(s_1)ds_1$. Here the betatron tune shift depends on the product of the gradient error and the betatron amplitude function at the error quadrupole; it is positive for a focusing quadrupole, and negative for a defocussing quadrupole.

For a distributed gradient error, the tune shift is

$$\Delta\nu = \frac{1}{4\pi}\oint \beta(s_1)k(s_1)ds_1. \tag{2.196}$$

The betatron tunes are particularly sensitive to gradient errors at high-β locations. Thus the power supply for high-β quadrupoles should be properly regulated in high energy colliders, and high-brightness storage rings.

B. Betatron amplitude function modulation (beta-beat)

To evaluate the effect of the gradient error on the betatron amplitude function, we again consider an infinitesimal quadrupole kick at s_1 of Eq. (2.195). The one-turn transfer matrix at s_2 is

$$\mathbf{M}(s_2) = M(s_2 + C|s_1)\; m(s_1)\; M(s_1|s_2).$$

Using Eq. (2.67), we find the change of the off-diagonal matrix element as

$$\Delta[\mathbf{M}(s_2)]_{12} = -k_1 ds_1\beta_1\beta_2\,\sin[\nu_0(\phi_1 - \phi_2)]\,\sin[\nu_0(2\pi + \phi_2 - \phi_1)],$$

where $\beta_1 = \beta(s_1)$, $\beta_2 = \beta(s_2)$ $\phi_1 = \psi(s_1)/\nu_0$, and $\phi_2 = \psi(s_2)/\nu_0$ are the values of the unperturbed betatron functions. Since $\mathbf{M}_{12} = \tilde{\beta}_2\sin\Phi$, where $\tilde{\beta}_2 = \tilde{\beta}(s_2)$ is the value of the perturbed betatron function and Φ is the perturbed betatron phase advance, we obtain

$$\begin{aligned}(\Delta\beta_2)\sin\Phi_0 &= \Delta\mathbf{M}_{12} - \beta_2\cos\Phi_0\Delta\Phi \\ &= -\frac{1}{2}k_1 ds_1\beta_1\beta_2\cos[2\nu_0(\pi - \phi_1 + \phi_2)],\end{aligned} \tag{2.197}$$

where $\Delta\beta_2 = \tilde{\beta}_2 - \beta_2$ and $\Delta\Phi = \Phi - \Phi_0$.

Removing the subscript 2 in Eq. (2.197) and integrating over the distributed gradient errors, we obtain

$$\begin{aligned}\frac{\Delta\beta(s)}{\beta(s)} &= -\frac{1}{2\sin\Phi_0}\int_s^{s+C} k(s_1)\beta(s_1)\cos[2\nu_0(\pi + \phi - \phi_1)]\,ds_1 \\ &= -\frac{\nu_0}{2\sin\Phi_0}\int_\phi^{\phi+2\pi} k(\phi_1)\beta^2(\phi_1)\cos[2\nu_0(\pi + \phi - \phi_1)]\,d\phi_1,\end{aligned} \tag{2.198}$$

where $\phi = (1/\nu_0)\int_0^s ds/\beta$. It is easy to verify that $\Delta\beta/\beta$ satisfies (see Exercise 2.3.10)

$$\frac{d^2}{d\phi^2}\left[\frac{\Delta\beta(s)}{\beta(s)}\right] + 4\nu_0^2\left[\frac{\Delta\beta(s)}{\beta(s)}\right] = -2\nu_0^2\beta^2 k(s). \tag{2.199}$$

C. The half-integer stopband integrals

In a manner similar to the closed-orbit analysis, the gradient error function $\nu_0\beta^2 k(s)$, which is a periodic function of s, can be expanded in a Fourier series

$$\nu_0\beta^2 k(s) = \sum_{p=-\infty}^{\infty} J_p\, e^{jp\phi}, \tag{2.200}$$

where

$$J_p = \frac{1}{2\pi}\oint \beta\; k(s)\; e^{-jp\phi}\; ds \tag{2.201}$$

is the pth harmonic half-integer stopband integral. We note that the tune shift of Eq. (2.196) is equal to the zero harmonic of the stopband integral, i.e. $\Delta\nu = J_0/2$. The solution of Eq. (2.199) becomes

$$\frac{\Delta\beta(s)}{\beta(s)} = -\frac{\nu_0}{2}\sum_{p=-\infty}^{\infty}\frac{J_p e^{jp\phi}}{\nu_0^2 - (p/2)^2}. \tag{2.202}$$

This indicates that the betatron amplitude function is most sensitive to those error harmonics of $\beta^2 k(s)$ nearest $2\nu_0$. The amplitude function becomes infinite when $2\nu_0$ approaches an integer; this is called a half-integer resonance. When the betatron tune is a half-integer, a quadrupole error can generate coherent additive phase-space kicks every revolution. The "closed orbit" of the betatron amplitude function will cease to exist, as shown in the left plot of Fig. 2.18. Therefore the betatron tune should not be a half-integer.

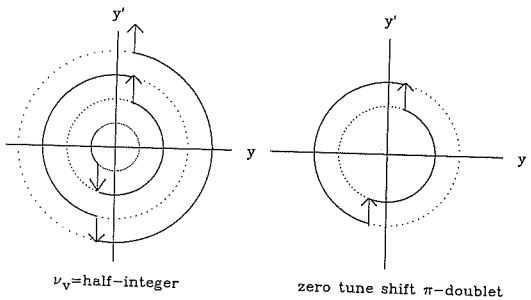

Figure 2.18: Left, schematic plot of a particle trajectory at a half-integer betatron tune resulting from a defocussing error quadrupole kick $\Delta y' = -y/f$. Since the quadrupole kick is proportional to the displacement y, which changes sign in each consecutive revolution at a half-integer betatron tune, the coherent addition of the kick angle in each revolution gives rise to the unstable particle motion. The right plot shows the effect of zero tune shift π-doublets, that produce a local perturbation to betatron motion.

The evolution of phase-space coordinates resulting from a quadrupole kick is [using Eq. (2.195)] $\Delta y = 0$ and $\Delta y' = -k(s_1)y\,ds_1 = -y/f$, where $f = 1/(k_1 ds_1)$ is the focal length of the error quadrupole, and y is the displacement from the center of the closed orbit. The change of the slope y' is proportional to the displacement y. The left plot of Fig. 2.18 shows the behavior of a quadrupole kick at a half-integer tune, where the quadrupole kicks are coherently additive. This will lead to an ever increasing betatron amplitude. Thus the half-integer stopband gives rise to unstable betatron motion. When the betatron tune is an integer, quadrupole kicks will resemble the left plot in Fig. 2.12. Thus an integer betatron tune is also a half-integer resonance. The right plot shows the effect of zero tune shift π-doublets, which give rise only to local betatron perturbation.

The leading term of Eq. (2.199) is

$$\frac{\Delta\beta(s)}{\beta(s)} \approx -\frac{J_p \cos(p\phi + \chi)}{(2\nu_0 - p)}, \tag{2.203}$$

where χ is a phase angle, and p is the integer nearest $2\nu_0$. The stopband width is defined by $\delta\nu_p \equiv |J_p|$ such that $|\Delta\beta(s)/\beta(s)|_{\max} \approx 1$ at $\nu_0 \approx \frac{p}{2} \pm \frac{1}{2}\delta\nu_p$. This means that the betatron tune should differ from a half-integer by at least the stopband width. When the betatron tunes are inside the stopband, the beam size will increase by at least a factor of $\sqrt{2}$, and beam loss may occur.

D. Statistical estimation of stopband integrals

Again, in the design stage of an accelerator, if we do not know a priori the gradient error, the stopband integral can be estimated by statistical argument as

$$J_p \approx \frac{1}{4\pi f_{\rm av}} \beta_{\rm av} \sqrt{N_{\rm q}} \left(\frac{\Delta K}{K}\right)_{\rm rms}, \tag{2.204}$$

where $\beta_{\rm av}$, $f_{\rm av}$, $N_{\rm q}$, and $(\Delta K/K)_{\rm rms}$ are respectively the average β value, the average focal length, the number of quadrupoles, and the rms relative gradient error.

E. Effect of a zero tune shift π-doublet quadrupole pair

A zero tune shift π-doublet (or the zero tune shift half-wave doublet) is composed of two quadrupoles separated by 180° in betatron phase advance with zero tune shift. Using the zero tune shift condition, we obtain

$$\beta_1 \Delta K_1 \Delta L_1 + \beta_2 \Delta K_2 \Delta L_2 = 0, \tag{2.205}$$

where $\beta_{1,2}$ are betatron amplitude functions at quadrupole pair locations, and $\Delta K_i \Delta L_i$ is the integrated field strength of the ith quadrupole. The zero tune shift condition of Eq. (2.205) also produces a zero stopband integral at $p = [2\nu]$, i.e.

$$J_{[2\nu]} = 0.$$

Since the stopband integral $J_{[2\nu]}$ of a zero tune shift π-doublet is zero, the doublet has little effect on the global betatron perturbation shown in the right plot of Fig. 2.18, where the betatron perturbation due to the first quadrupole is canceled by the second quadrupole. Zero tune shift π-doublets can be used to change the dispersion function and the transition energy (to be discussed in Sec. IV.8).

F. Zero tune shift half-integer stopband correctors

We find that the zero tune shift π-doublet produces a zero stopband width. On the other hand, a zero tune shift *quarter-wave* quadrupole pair produces a maximum contribution to the half-integer stopband. Employing such modules, we can correct half-integer betatron stopbands.

III.5 Basic Beam Observation of Transverse Motion

Measurements of beam properties are important in improving the performance of a synchrotron. In this section we discuss some basic beam diagnosis tools. Further detailed discussions can be found in the literature.[48]

[48] R. Littauer, AIP Conf. Proc. **105**, 869 (1983); R. Shafer, *IEEE Trans. Nucl. Sci.* NS**32**, 1933 (1985); J.L. Pellegrin, SLAC PUB-2522 (1980), and *Proc. 11th Int. Conf. on High Energy Accelerators*, p. 459 (1980); H. Koziol, CERN **89-05**, p. 63 (1989); M. Serio, CERN **91-04**, p. 136 (1991); P. Strehl, CERN **87-10**, p. 99 (1987); J. Boer, R. Jung, CERN **84-15**, p. 385 (1984).

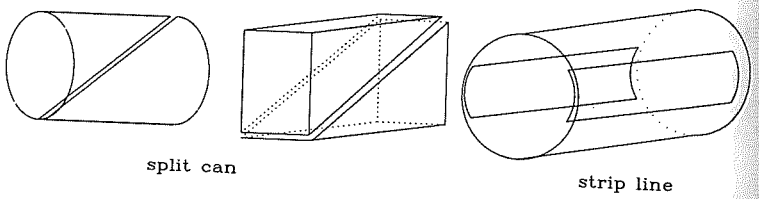

Figure 2.19: A schematic drawing of electric beam position monitors. The split-can type BPM has the advantage of linear response; the strip-line type has a larger transfer function.

A. Beam position monitor (BPM)

Transverse beam position monitors (BPMs) or pickup electrodes (PUEs) are usually composed of two or four conductor plates or various button-like geometries. Figure 2.19 shows a sketch of some simple electric BPM geometries used mainly in proton synchrotrons. The button BPMs are used mainly in electron storage rings, where the bunch length is small. As the beam passes by, the induced image electric charges on the plates can be transmitted into a low impedance circuit, or the induced voltage can be measured on a high impedance port such as the capacitance between the electrode and the surrounding vacuum chamber.

The BPM can have an electrostatic, e.g. split electrodes and buttons, or a magneto-static, e.g. small secondary loop winding, configurations. An electrostatic monitor is equivalent to a current generator, where the image charge is detected by the shunt capacitance of the electrode to ground. Similarly, a magnetic loop monitor is equivalent to a voltage generator with a series inductor, which is the self-inductance of the loop. The voltage is proportional to the rate of variation of the magnetic flux associated with the beam current linked to the loop.

In general, the beam position is

$$y \approx \frac{w}{2}\,\frac{U_+ - U_-}{U_+ + U_-} = \frac{w}{2}\,\frac{\Delta}{\Sigma}, \tag{2.206}$$

where U_+ and U_- are either the current or the voltage signals from the right (up) and left (down) plates, $\Delta = U_+ - U_-$ is called the difference signal or the Δ-signal, $\Sigma = U_+ + U_-$ is the sum signal, and $w/2$ is the effective width of the PUE. Depending on the geometry of the PUE, the relation Eq. (2.206) may require nonlinear calibration. Measurements of the normalized difference signal with proper calibration provide information about the beam transverse coordinates. If we digitize beam centroid positions turn by turn, we can measure the betatron motion. On the other hand, sampling the position data at a slower rate, we can obtain the closed-orbit information from the DC component.

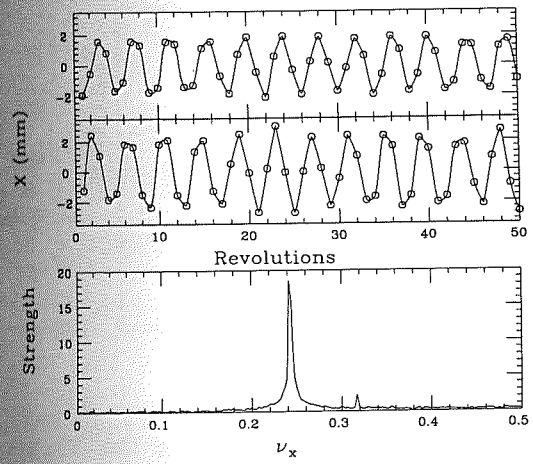

Figure 2.20: The measured betatron coordinates at two horizontal BPMs, after the beam is imparted a magnetic kick, vs the revolution number. The solid line is drawn to guide the eye. The FFT spectrum of the BPM data (middle plot) shows the fractional part of the horizontal betatron tune. Here a total of 385 data points are used in the FFT calculation. The fractional part of the horizontal betatron tune is $\nu_x = 0.242 \pm 0.002$. The observed vertical betatron tune at $\nu_z = 0.317$ may result from linear coupling or from a tilted horizontal kicker.

B. Measurements of betatron tune and phase-space ellipse

If the betatron oscillations from the BPM systems can be digitized turn by turn, the betatron tune can be determined from the FFT of the transverse oscillations (see Appendix B). Figure 2.20 shows the data for the horizontal betatron oscillation of a beam after a transverse kick at the IUCF cooler ring. The top plot shows the digitized data at two BPM positions (x_1 and x_2). The lower plot shows the FFT spectrum of the x_1 data. From the FFT spectrum, we find that the horizontal and vertical tunes of this experiment were $\nu_x = 3.758$ and $\nu_z = 4.683$ respectively.

The phase-space trajectory can be optimally derived from the measured betatron coordinates at two locations with a phase advance of an odd multiple of 90°. Using Eq. (2.62), we obtain

$$x_1' = \frac{\csc\psi_{21}}{\sqrt{\beta_1\beta_2}}\,x_2 - \frac{(\cot\psi_{21} + \alpha_1)}{\beta_1}\,x_1, \tag{2.207}$$

where $\psi_{21} = \psi_2 - \psi_1$ is the betatron phase advance between two BPMs, β_1 and β_2 are the values of betatron amplitude function at two BPMs, and $\alpha_1 = -\beta_1'/2$ at the first BPM. The invariant phase-space ellipse becomes

$$x_1^2 + \left(\sqrt{\frac{\beta_1}{\beta_2}}\csc\psi_{21}\;x_2 - \cot\psi_{21}\;x_1\right)^2 = 2\beta_1 J, \tag{2.208}$$

where the area enclosed by the (x_2, x_1) ellipse is $2\pi\sqrt{\beta_1\beta_2}\;|\sin\psi_{21}|J$, and J is the betatron action. Dots in the left plot of Fig. 2.21 shows the measured (x_2, x_1) ellipse, where the solid line is obtained from Eq. (2.208) by fitting $\sqrt{\beta_1/\beta_2}$ and ψ_{21} parameters

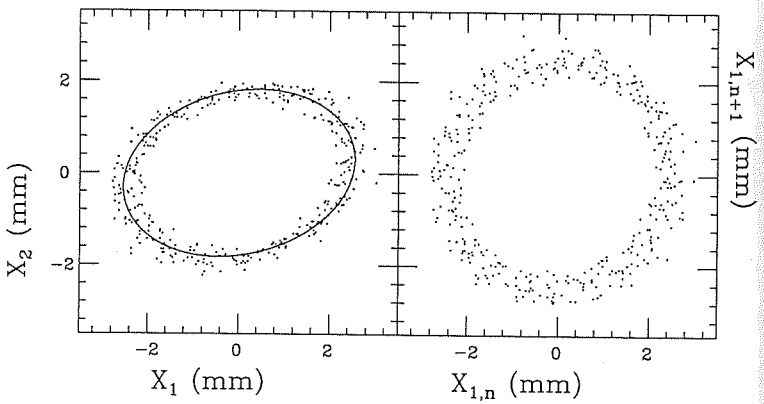

Figure 2.21: The left plot shows the phase-space ellipse (x_2, x_1) of Fig. 2.20. The area enclosed by the ellipse is $2\pi\sqrt{\beta_1\beta_2}\,|\sin\psi_{21}|\,J$. The solid line shows the ellipse of Eq. (2.208) with $\sqrt{\beta_2/\beta_1} = 1.4$, $\psi_{21} = 80°$, and $2\beta_1 J = 8 \times 10^{-6}$ m^2. If β_1 is independently measured, the action of the betatron orbit can be obtained. The right plot shows a poor man's phase-space ellipse, obtained by plotting betatron coordinates of successive revolutions of single digitized BPM data. Because the betatron tune is nearly 3.75 (see Fig. 2.20), the phase space is an upright circle. The area enclosed by this nearly circular ellipse is $2\pi\beta_1|\sin 2\pi\nu_x|J$.

for the orientation, and $\beta_1 J_1$ for the size of the ellipse. If the betatron amplitude function β_1 is independently measured, the action of the ellipse can be determined.

Two BPMs separated by about 90° in phase advance are useful for obtaining a nearly upright transverse phase-space ellipse. The turn by turn digitized data require a high bandwidth digitizer and a large memory transient recorder. However, if available hardware is limited, the phase-space ellipse can be obtained by using digitized data of successive turns of a single BPM. The right plot of Fig. 2.21 shows $x_{1,n+1}$ vs $x_{1,n}$. Because the horizontal tune in this example is 3.758, the phase-space ellipse of $(x_{1,n}, x_{1,n+1})$ is nearly a circle. The area enclosed is $2\pi\beta_1|\sin 2\pi\nu_x|J$.

III.6 Application of quadrupole field error

By using the quadrupole field error, the optical properties of the lattice can be altered, measured, or manipulated. Examples of β-function measurement and the betatron tune jump are described below. Other applications, such as π-doublets for dispersion function manipulation, will be discussed in Sec. IV.8.

A. β-Function measurement

Using Eq. (2.196), we can derive the betatron amplitude function by measuring the betatron tune as a function of the quadrupole strength. The average betatron amplitude function $\langle\beta_{x,z}\rangle$ at a quadrupole becomes

$$\langle\beta_{x,z}\rangle = 4\pi\frac{\Delta\nu_{x,z}}{\Delta K\ell},$$

where $\Delta K\ell$ is the change in the integrated quadrupole strength. Figure 2.22 shows an example of the measured fractional part of the betatron tune vs the strength of a quadrupole at the IUCF cooler ring. The "average" betatron amplitude function at the quadrupole can be derived from the slopes of the betatron tunes. In this example, the slope of the horizontal betatron tune is larger than that of the vertical, and thus the horizontal betatron function is larger than the vertical one. Since the fractional part of the horizontal tune increases with the defocussing quadrupole strength, the actual horizontal tune is below an integer. For the IUCF cooler ring, we have $\nu_x = 4 - q_x$ and $\nu_z = 5 - q_z$, where q_x and q_z are the fractional parts of the betatron tunes.

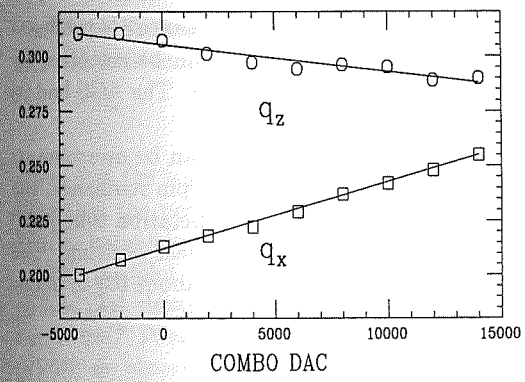

Figure 2.22: An example of betatron amplitude function measurements, where the horizontal and vertical tunes are determined from the FFT spectrum of the betatron oscillations. The slope of the betatron tune vs the quadrupole field variation is used to determine the betatron amplitude functions. Because the fractional parts of betatron tunes are $q_x = 4 - \nu_x$ and $q_z = 5 - \nu_z$, the fractional horizontal tune is seen to increase with the strength of the horizontal defocussing quadrupole.

B. Tune jump

The vector polarization of a polarized beam is defined as the percent of particles whose spins lie along a quantization axis, e.g. the polarization of a proton beam is $P = (N_+ - N_-)/(N_+ + N_-)$, where $N_\pm$ are the numbers of particles with their spin projection lying along and against the quantization axis. For polarized beams in a planar accelerator, the quantization axis can be conveniently chosen to lie along the vertical direction that coincides with the vertical guide field.

According to the Thomas-BMT equation, the polarization vector precesses about the vertical axis at $G\gamma$ turns per revolution, where $G = (g-2)/2$ is the anomalous g-factor and γ is the Lorentz relativistic factor.[49] Thus $G\gamma$ is called the spin tune. Since the spin tune increases with the beam energy, acceleration of a polarized beam may encounter spin depolarization resonances [22], where the "imperfection resonance"

[49] $G = 1.79284739$ for protons, and 0.0011596522 for electrons.

arises from the vertical closed-orbit error, and the "intrinsic resonance" is produced by the vertical betatron motion. The imperfection resonance can be corrected by vertical orbit correctors to achieve proper spin harmonic matching. The AGS had 96 closed-orbit correctors for imperfection resonance harmonics.[50]

The intrinsic resonance in low/medium energy synchrotrons can be overcome by the tune jump method. When the $G\gamma$ value reaches an intrinsic spin resonance, the betatron tune is suddenly changed to avoid the resonance. This betatron tune jump can be achieved by using a set of ferrite quadrupoles with a very fast rise time. The AGS had 10 fast ferrite quadrupoles to produce a tune jump of about 0.3 in about 2.5 μs.

The amount of tune change is

$$\Delta\nu_z = \frac{1}{4\pi}\oint \beta_z \frac{\Delta B_1}{B\rho} ds, \tag{2.209}$$

where ΔB_1 is the quadrupole gradient of tune jump quadrupoles. Because of the integer and half-integer stopbands, the magnitude of tune jump is limited to about $\Delta\nu_z \approx 0.3$. With a large tune jump, beam dynamics issues such as non-adiabatic betatron amplitude function mismatch, linear betatron coupling, nonlinear resonances, non-adiabatic closed-orbit distortion, etc., should be carefully evaluated. Since the betatron tune of AGS is about 8.8, the important half-integer stopbands are located at $p = 17$ and 18. Placement of tune jump quadrupoles to minimize the stopband integral can reduce non-adiabatic perturbation to the betatron motion. Similarly, the non-adiabatic closed-orbit perturbation due to the misalignment of tune jump quadrupoles can also be analyzed.[51]

III.7 Transverse Spectra

A. Transverse spectra of a particle

A circulating particle passes through the pickup electrode (PUE) at fixed time intervals T_0, where $T_0 = 2\pi R/\beta c$ is the revolution period, R is the average radius, and βc is the speed. The current of the orbiting charged particle observed at the PUE[52] is

$$I(t) = e\sum_{-\infty}^{\infty} \delta(t - nT_0), \tag{2.210}$$

[50] At AGS, a 5% partial snake has recently been used to overcome all imperfection resonances. See, e.g., H. Huang *et al.*, *Phys. Rev. Lett.* **73**, 2982 (1994).

[51] An rf dipole has recently been used to overcome these intrinsic spin resonances. See, e.g., M. Bai *et al.*, *Phys. Rev. Lett.* **80**, 4673 (1998). A 20 G-m rf dipole was used to replace 10 ferrite quadrupoles with an integrated field strength of $\int B_1 ds = 15$ T.

[52] We assume that the bandwidth of PUEs is much larger than the revolution frequency. In fact, the bandwidth of PUEs is normally from 100's MHz to a few GHz.

where e is the charge of the particle, and $\delta(t)$ is the Dirac δ-function. Expressing the periodic delta function in Fourier series, we obtain

$$I(t) = \frac{e}{T_0}\sum_{n=-\infty}^{\infty} e^{jn\omega_0 t} = \frac{e}{T_0} + 2\frac{e}{T_0}\sum_{n=1}^{\infty}\cos n\omega_0 t, \tag{2.211}$$

where j is the complex number, and $\omega_0 = \beta c/R = 2\pi f_0$ is the angular frequency. Note that the periodic occurrence of current pulses is equivalent to equally spaced Fourier harmonics.

The top plot of Fig. 2.23 shows the periodic time domain current pulses. The middle plot shows the frequency spectra of the particles occurring at all "rotation harmonics." Passing the signal into a spectrum analyzer for fast Fourier transform (FFT), we observe a series of power spectra at integral multiples of the revolution frequency nf_0, shown in the bottom plot. The DC current is e/T_0, and the rf current is $2e/T_0$. Because the negative frequency components are added to their corresponding positive frequency components, the rf current is twice the DC current.

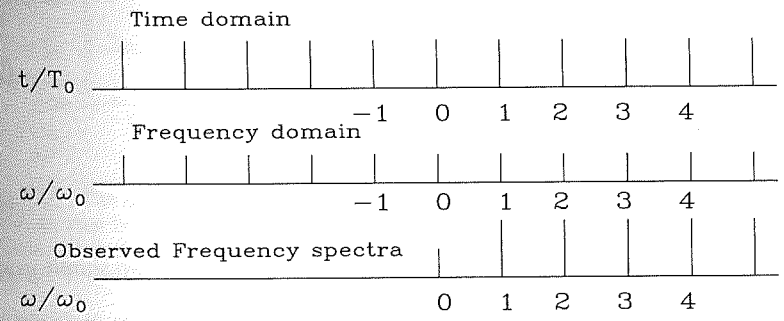

Figure 2.23: A schematic drawing of current pulses in the time domain (upper plot), in the frequency domain (middle plot), and observed in a spectrum analyzer (bottom plot). The rf current is twice the DC current because negative frequency components are added to their corresponding positive frequency components.

If we apply a transverse impulse (kick) to the beam bunch, the beam will begin betatron oscillations about the closed orbit. The BPM measures the transverse coordinates of the centroid of the beam charge distribution (dipole moment), given by

$$d(t) = I(t)y(t) = I(t)\left[y_0 + \hat{y}\cos\omega_\beta t\right], \tag{2.212}$$

where y_0 is the offset due to the closed-orbit error or the BPM misalignment, $\hat{y}$ is the amplitude of the betatron oscillation, and $\omega_\beta = Q_y\omega_0$ is the betatron angular frequency with betatron tune Q_y.

The DC component of the dipole moment can be obtained by applying a low-pass filter to the measured BPM signal, i.e.

$$\langle d(t)\rangle = \langle I(t)\rangle y_0, \tag{2.213}$$

where the betatron oscillation can effectively be removed. On the other hand, by employing a band-pass filter, the betatron oscillation can be measured. Expanding the dipole moment in Fourier harmonics, we obtain

$$d_\beta = \frac{e}{2T_0}\hat{y}\sum_{n=-\infty}^{\infty}\left(e^{j(n+Q_y)\omega_0 t} + e^{j(n-Q_y)\omega_0 t}\right). \tag{2.214}$$

In the frequency domain, the betatron oscillations obtained from the BPM signals contain sidebands around the revolution frequency lines, i.e. $f = (n \pm Q_y)f_0$ with integer n. Naturally, the betatron tune can be measured by measuring the frequency of betatron sidebands.[53]

B. Fourier spectra of a single beam with finite time span

We note that a periodic δ-function current pulse in time gives rise to equally spaced Fourier spectra at all revolution harmonics. We ask what happens if the beam distribution has a finite time span with

$$I(t) = N_B e \sum_{n=-\infty}^{\infty} \rho(t - nT_0), \tag{2.215}$$

where the density distribution is normalized according to

$$\int_{-T_0/2}^{T_0/2} \rho(t - nT_0)dt = 1. \tag{2.216}$$

There are many possible forms of beam distribution. We discuss two simple examples as follows.

1. If the beam is confined by a sinusoidal rf cavity to form a bunch, the distribution can be a cosine-like function. If the beam is confined by a barrier rf wave or a double rf system, the beam distribution can be approximated by the rectangular distribution:

$$\rho(t - nT_0) = \begin{cases} 1/2\Delta & \text{if } -\Delta < t - nT_0 < \Delta, \\ 0 & \text{otherwise,} \end{cases} \tag{2.217}$$

where Δ is the bunch width in time. The Fourier transform of the rectangular current pulse becomes

$$\begin{aligned} I(\omega) &= \frac{1}{2\pi}\int_{-\infty}^{\infty} I(t)e^{-j\omega t}dt \\ &= \left[\frac{N_B e\omega_0}{2\pi}\frac{\sin\omega\Delta}{\omega\Delta}\right]\sum_{n=-\infty}^{\infty}\delta(\omega - n\omega_0). \end{aligned} \tag{2.218}$$

[53] The sidebands are classified into fast wave, backward wave, and slow wave. This topic is important to collective instabilities, to be discussed briefly in Sec. VIII.

2. The beam distribution for electrons in storage rings is usually described by a Gaussian distribution due to the quantum fluctuation

$$\rho(t - nT_0) = \frac{1}{\sqrt{2\pi}\sigma_t}e^{-(t-nT_0)^2/2\sigma_t^2}. \tag{2.219}$$

The Fourier transform of the current pulse can be carried out easily to obtain

$$I(\omega) = \left[\frac{N_B e\omega_0}{2\pi}e^{-\omega^2\sigma_t^2/2}\right]\sum_{n=-\infty}^{\infty}\delta(\omega - n\omega_0). \tag{2.220}$$

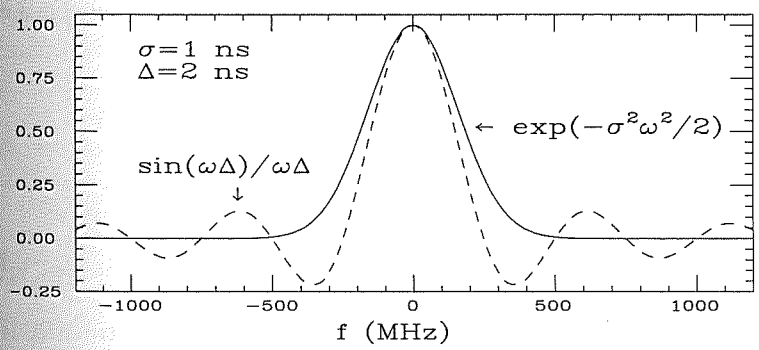

Figure 2.24: The form factors for the Fourier spectra of a Gaussian bunch and a rectangular bunch with rms bunch length $\sigma_t = 1$ ns. The form factor serves as the envelope of the revolution comb shown in Fig. 2.23. Note that the coherent signal of a rectangular bunch can extend beyond the Gaussian cut-off frequency.

Figure 2.24 shows the envelope factor for Gaussian and rectangular beam distributions with an rms bunch length of 1 ns. In the frequency domain, the spectrum of the beam pulse is truncated by a form factor that depends on the time domain distribution function. In general, if the beam has a time width σ_t, the Fourier spectra can extend to about $1/\sigma_t$. The frequency spectra of a long bunch, e.g. 1 m bunch length (3.3 ns), will have coherent spectra limited by a few hundred MHz. Since all particles in the bunch are assumed to have an identical revolution frequency, the Fourier spectra of Eqs. (2.218) and (2.220) are δ-function pulses bounded by the envelope factors. If there is a revolution frequency spread, the δ-function pulses are replaced by pulses with finite frequency width.

C. Fourier spectra of many particles and Schottky noise

We consider N charged particles evenly distributed in the ring. The beam current observed at a PUE is

$$I(t) = e\sum_{n=-\infty}^{\infty}\delta(t - n\frac{T_0}{N}) = \frac{Ne}{T_0}\sum_{n=-\infty}^{\infty}e^{jn(N\omega_0)t}. \tag{2.221}$$

Note that the first Fourier harmonic is located at $N\omega_0$, and the spacing of Fourier harmonics is also $N\omega_0$.[54] If the number of particles is large, e.g. $N > 10^8$, the frequency spectrum is practically outside the bandwidth of PUEs, and the spectrum is simply invisible. This means that the beam appears to have no rf signal. The beam that fills the accelerator is called a "DC beam," or a "coasting beam."

Similarly, the frequency spectra of the transverse dipole moment of N equally spaced particles give rise to a betatron sideband around the coherent orbital harmonics $N\omega_0 \pm \omega_\beta$. When N is a very large number, e.g. $N > 10^8$, the coherent betatron frequency becomes too high to be visible to PUEs.

It is important to realize that particles are not uniformly distributed in a circular accelerator. The longitudinal signal of N particles in a PUE is

$$\begin{aligned} I(t) &= e\sum_{i=1}^{N}\sum_{n=-\infty}^{\infty}\delta(t-t_i-nT_i) \\ &= 2\pi e\sum_{n=-\infty}^{\infty}\sum_{i=1}^{N}\omega_i e^{jn\omega_i(t-t_i)} \\ &\approx Nef_0 + 2ef_0\sum_{n=1}^{\infty}\sum_{i=1}^{N}\cos(n\omega_0 t+\Delta\phi_i(t)). \end{aligned} \tag{2.222}$$

The beam signal arising from random phase in charged particle distribution is called the Schottky noise. The power spectrum at each revolution harmonic from a low noise PUE is proportional to the number of particles.

Similarly, the dipole moment of the ith particle is

$$\begin{aligned} d_i(t) &= e\hat{y}_i\cos(\omega_{\beta i}t+\chi_i)\sum_{n=-\infty}^{\infty}\delta(t-nT_i-t_{0i}) \\ &= \frac{e\hat{y}_i}{T_i}\cos(\omega_{\beta i}t+\chi_i)\sum_{n=-\infty}^{\infty}e^{jn\omega_i(t-t_{0i})}. \end{aligned} \tag{2.223}$$

The dipole moment of the beam becomes

$$d(t) = \sum_{i=1}^{N}\frac{e\hat{y}_i}{T_i}\cos(\omega_{\beta i}t+\chi_i)\sum_{n=-\infty}^{\infty}e^{jn\omega_i(t-t_{0i})}. \tag{2.224}$$

Normally, the coherent betatron sidebands of a nearly uniform distribution are beyond the bandwidth of PUEs. However, the average power of the dipole moment can be measured. This is called the Schottky noise signal. If the particles are randomly distributed, the average power of the dipole moment is

$$P_{\text{av}} = \frac{1}{2T}\int_{-T}^{T}|d^2(t)|dt, \tag{2.225}$$

[54]The analysis of equally spaced short bunches in the ring has identical Fourier spectra, i.e. if there are B bunches in the ring, the first coherent Fourier harmonic is $B\omega_0$.

where $2T$ is the sampling time. For practical consideration, T is of the order of minutes, this means that dipole moments of particles with frequencies within $T^{-1} \approx 10^{-2}$ Hz may interfere with one another. The resulting Schottky power can be contaminated by particle-to-particle correlation. Measurements with varying sampling times can be used to minimize the effect of particle correlation.

Since the phases $\omega_i t_{0i}$ and χ_i are random and uncorrelated, the Schottky power is proportional to the number of particles, i.e.

$$P_{\text{av}} = \sum_{i=1}^{N}\frac{e^2\hat{y}_i^2}{4T_i^2} \quad \text{at} \quad \omega = n\langle\omega_0\rangle \pm \langle\omega_\beta\rangle. \tag{2.226}$$

The power spectrum resembles the single-particle frequency spectra located at $n\omega_0 \pm \omega_\beta$, i.e. betatron sidebands around all rotation harmonics. The Schottky signal can be used to monitor betatron and synchrotron tunes, frequency and phase space distributions, etc. It is the essential tool used for stochastic beam cooling.

III.8 Beam Injection and Extraction

A. Beam injection and extraction

Electrons generated from a thermionic gun or photocathode are accelerated by a high voltage gap to form a beam. The beam is captured in a linac or a microtron and accelerated to a higher energy for injection into other machines. Similarly, ions are produced from a source, e.g. a duoplasmatron, and extracted by a voltage gap to form a beam. The beam is accelerated by a DC accelerator or an RFQ for injection into a linac (DTL). The medium energy beam is then injected into various stage of synchrotrons.

A1. The strip or charge-exchange injection scheme

There are many schemes for beam injection into a synchrotron. The charge exchange injection involves H^- or H_2^+ ions, where a stripping foil with a thickness of a few $\mu g/cm^2$ to a few mg/cm^2 is used to strip electrons. The injection procedure is as follows. The closed orbit of the circulating beam is bumped onto the injection orbit of the H^- or H_2^+ beam by a closed-orbit bump and a set of *chicane magnets*, as shown in Fig. 2.25a.[55] Since the injection orbit coincides with the closed orbit of the circulating protons without violating Liouville's theorem, the resulting phase-space area will be minimized. The injected beam can be painted in phase space by changing the closed orbit during the injection. The injection efficiency for this injection scheme is high, except that we must take into account the effect of emittance blow-up through multiple Coulomb scattering due to the stripping foil (see Exercise 2.3.12).

[55]The chicane magnet may sometimes be replaced by punching a hole through the iron of a main dipole magnet provided that the saturation effect at high field is properly compensated.

Although the intensity of the H^- source is an order of magnitude lower than that of the H^+ source, a higher capture efficiency and a simpler injection scenario more than compensate the loss in source intensity. Most modern booster synchrotrons and some cyclotrons employ a H^- source. However, since the last electron in H^- has only about 0.7 eV binding energy, it can easily be stripped by a strong magnetic field at high energy.

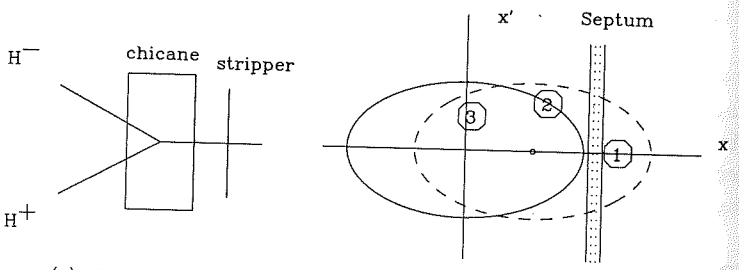

(a) strip injection (b) Betatron phase space painting

Figure 2.25: (a) A schematic drawing of a chicane magnet that merges the H^- and H^+ orbits onto the stripper. (b) The process of betatron phase-space accumulation. During the injection, the closed orbit is bumped near the septum (dashed ellipse) so that the injected beam marked (1) is captured within the dynamical aperture. Because of the betatron motion, the injected beam can avoid the septum in the succeeding revolutions marked (2) and (3), etc. As the bumped orbit is moved during the injection time, the phase space is painted and the injected beam is accumulated.

A2. Betatron phase-space painting, cooling, radiation damping

The injection of protons or heavy ions into a synchrotron needs careful phase-space manipulation. The procedure is to bump the closed orbit of the circulating beam near the injection septum. The stable phase-space ellipse is shown as the dashed line in Fig. 2.25b. If the betatron tune and the orbit bump amplitude are properly adjusted, the particle distribution in betatron phase space can be optimized. This procedure is called phase-space painting. The injection efficiency is usually lower. The efficiency may be enhanced by employing betatron resonances.

Injection of the electron beam is similar to that of proton or ion beams except that the injected electrons damp to the center of the phase space because of the synchrotron radiation damping (see Chap. 4). At the time of injection pulse, the closed-orbit of circulating beams is bumped (kicked) close to a septum magnet so that the injection beam bunch is within the dynamical aperture of the synchrotron. At the completion of the injection procedure, the bump is removed, and the injected beamlet will damp and merge with the circulating beam bunch. The combination of phase-space painting

and damping accumulation can be used to provide high-brightness electron beams in storage rings.

A3. Other injection methods

A method that has been successfully applied at the ISR is momentum phase-space stacking. This requires an understanding of the momentum closed orbit or the dispersion function, and of rf phase displacement acceleration. The method will be discussed in Chap. 3. This method is also commonly used in low energy cooler rings for cooling, and stacking accumulation of proton or polarized proton beams.

B. Beam extraction

B1. Fast single turn extraction and box-car injection

When a beam bunch is ready for extraction, orbit bump is usually excited. A fast kicker is fired to take the beam into the extraction channel of a septum magnet (see Sec. III.3). The extracted beam can be delivered to experimental areas, or be transferred into a another synchrotrons, called the box-car injection scheme.

B2. Slow extraction

Slow (beam) extraction by peeling-off high intensity beams can provide a higher duty factor[56] for many applications such as high reaction rate nuclear and particle physics experiments, medical treatment, etc. Slow extraction employs nonlinear magnets to drive a small fraction of the beam particles onto a betatron resonance.

The slow extraction using the third order resonance will be discussed in Sec. VII.1. Similarly, beam particles can be slowly extracted by employing the half integer resonance (see Exercise 3.3.3). Large-amplitude particles moving along the separatrix are intercepted by a thin (wire) septum that takes the particles to another septum on the extraction channel. The efficiency depends on the thin-septum thickness, the value of the betatron amplitude function at the septum location, betatron phase advance between the nonlinear magnet and the septum location, etc. More recently, efforts have been made to improve the uniformity of the extracted beam by stochastic excitation of the beam with noise; this is called stochastic slow extraction.

III.9 Mechanisms of emittance dilution and diffusion

A. Emittance diffusion resulting from random scattering processes

In actual accelerators, noise may arise from various sources such as power supply ripple, ground vibration, intrabeam scattering, residual gas scattering, etc. This

[56]The duty factor is defined as the ratio of beam usage time to cycle time.

can induce emittance dilution and beam lifetime degradation. Our understanding of betatron motion provides us with a tool to evaluate the effect of noise on emittance dilution.

If the betatron angle y' is instantaneously changed by an angular kick θ, the resulting change in the betatron action is

$$\Delta I = I(y, y' + \theta) - I(y, y') = \theta(\alpha y + \beta y') + \frac{1}{2}\beta\theta^2. \tag{2.227}$$

If the angular kicks are uncorrelated, and the beam is composed of particles with many different betatron phases, the increase in emittance due to the random scattering processes is obtained by averaging betatron oscillations and kick angles, i.e.

$$\Delta\epsilon_{\rm rms} = 2\langle\Delta I\rangle = \langle\beta\theta^2\rangle \approx \langle\beta_\perp\rangle\langle\theta^2\rangle. \tag{2.228}$$

Random angular kicks to the beam particles arise from dipole field errors, non-resonant and non-adiabatic ground vibration, injection and extraction kicker noises, intrabeam Coulomb scattering, and multiple Coulomb scattering from gas molecules. Multiple scattering from gas molecules inside the vacuum chamber can cause beam emittance dilution, particularly at high $\beta_\perp$-function locations. This effect can also be important in the strip-injection of the H^- and H_2^+ ion sources from the stripping foil. The emittance growth rate can be obtained from the well-known multiple Coulomb scattering. Exercise 2.3.12 gives an example of estimating the emittance growth rate.

Other effects are due to the angular kicks from synchrotron radiation, quantum fluctuation resulting from energy loss, diffusion processes caused by rf noise, etc.; these will be addressed in Chaps. 3 and 4.

A1. Beam Lifetime

The single beam lifetime is determined by nuclear scattering on residual gas in the beam pipe, multiple scattering on the residual gas, ion or electron trapping due to residual gas scattering, photo desorption, intrabeam Coulomb scattering, Touschek effect (to be discussed in Chap.4 II.8), lifetime effect due to nonlinear resonances (see Sec. VII), etc. In a collider, beam lifetime is further reduced by beam-beam effects, particle loss due to beam-beam collisions, beam aperture limitation, etc.

B. Space charge effects

The repulsive Coulomb mean-field field of a beam can generate defocussing force to reduce the effective external focusing. The space-charge effect is characterized by an incoherent Laslett tune shift parameter $\xi_{\rm sc} = \Delta\nu_{\rm sc}$ (see Exercise 2.3.2). The tune shift parameter for low energy linacs at the ion source can be large, i.e. the betatron tune can be detuned to a value nearly 0 (see Sec. II.8). The incoherent space-charge

tune shift for low energy synchrotron has a typical value of 0.2 – 0.6, which is about 10% or less of the betatron tunes. Yet, almost all low energy synchrotrons suffer space-charge induced emittance growth. We try to illustrate possible mechanisms.

B1. The coherent envelope oscillations due to space-charge force

We consider a simple KV model of 1D paraxial system (see Sec. II.8, where Hill's and the envelope equations are

$$\begin{cases} y'' + \left(k(s) - \dfrac{K_{\rm sc}}{R_{\rm b}^2(s)}\right) y = 0, & |y| \le R_{\rm b}(s) \\ y'' + k(s)y - \dfrac{K_{\rm sc}}{y} = 0, & |y| > R_{\rm b}(s) \end{cases} \tag{2.229}$$

$$R_{\rm b} + k(s)R_{\rm b} - \frac{\epsilon^2}{R_{\rm b}^3} - \frac{K_{\rm sc}}{R_{\rm b}} = 0. \tag{2.230}$$

Here y stands for either the particle's horizontal or vertical betatron coordinate, $k(s)$ is the focusing function, $K_{\rm sc}$ is the space-charge perveance parameter, defined in Eq. (2.136), $\epsilon = 4\epsilon_{\rm rms}$ is the KV beam emittance, $R_{\rm b} = \sqrt{\beta(s)\epsilon}$ is the KV beam envelope radius, and $\beta(s)$ is the betatron amplitude function. For a KV beam, all particles are within the envelope radius. Making Floquet transformation with

$$R = \frac{R_{\rm b}}{\sqrt{\beta(s)\epsilon}}, \quad \eta = \frac{y}{\sqrt{\beta(s)}}, \quad \phi = \frac{1}{\nu}\int_0^s \frac{ds}{\beta(s)}, \tag{2.231}$$

we transform Hill's and envelope equations into

$$\ddot{\eta} + \nu^2\eta - \frac{\nu^2\beta(s)K_{\rm sc}}{\epsilon R^2}\eta = 0 \qquad (y \le R_{\rm b}), \tag{2.232}$$

$$\ddot{R} + \nu^2 R - \frac{\nu^2}{R^3} - \frac{\nu^2\beta(s)K_{\rm sc}}{\epsilon R} = 0, \tag{2.233}$$

where ν is the betatron tune, and the over-dots are derivative with respect to the independent variable (time-coordinate) ϕ.

For synchrotrons, the space-charge terms in Hill's and envelope equations can be considered as a small perturbation unless a resonance condition is encountered. We expand the envelope radius around the unperturbed closed orbit with $R = 1 + r + \Delta$, where Δ is a ϕ-independent constant shift in the equilibrium radius and r is the ϕ-dependent term depending on the dynamics of the machine. We expand the space-charge factor:

$$\frac{\nu\beta(s)K_{\rm sc}}{2\epsilon} = \xi_{\rm sc}\left(1 + \sum_{n=1}^{\infty} q_n \cos(n\phi + \chi_n)\right) \tag{2.234}$$

in Fourier series, where

$$\xi_{sc} = \frac{1}{2\pi}\oint \frac{\nu\beta(s)K_{sc}}{2\epsilon}d\phi = \frac{1}{4\pi}\oint \frac{\beta(s)K_{sc}}{[R_b(s)]^2}ds, \tag{2.235}$$

$$\xi_{sc}q_n = \frac{1}{\pi}\oint \frac{\nu\beta(s)K_{sc}}{2\epsilon}\cos(n\phi+\chi_n)d\phi. \tag{2.236}$$

The parameter ξ_{sc} is the Laslett (incoherent) linear space-charge tune shift parameter and $\xi_{sc}q_n$ and χ_n are the Fourier amplitude and phase of the n-th harmonic. Substituting Eq. (2.234) into Eq. (2.233), we obtain $\Delta = \xi_{sc}/2\nu$ and

$$\ddot{r} + (4\nu^2 - 4\nu\xi_{sc})r \approx 2\nu\xi_{sc}\sum_{n=1}^{\infty} q_n\cos(n\phi+\chi_n). \tag{2.237}$$

The space-charge force plays two roles in the envelope equation. It decreases the envelope tune from $\nu_{env} = 2\nu$ to $\nu_{env} = 2\nu - \xi_{sc}$, and it generates a perturbation term, where the Fourier harmonic in the intrinsic betatron amplitude function serves as a harmonic perturbation to the envelope equation. The envelope radius, or the *perturbed betatron amplitude function*, is resonantly excited by the harmonic $n \approx \nu_{env}$ with

$$r \approx \frac{2\nu\xi_{sc}q_n}{-n^2 + (4\nu^2 - 4\nu\xi_{sc})}\cos(n\phi+\chi_n). \tag{2.238}$$

Figure 2.26 shows the space-charge perturbed vertical betatron amplitude function (solid line), the original betatron amplitude function (dashed line), and the normalized envelope radius R (dotted line), obtained from a PIC simulation calculation for the Proton Storage Ring (PSR) at Los Alamos National Laboratory.[57] The PSR is a fixed energy synchrotron with 90.26 m circumference, $\nu_x = 3.19$ and $\nu_z = 2.19$. It serves as a compressor to compress 1.16 ms (3214 turns in PSR) of proton pulse from the 800 MeV Linac into a high intensity proton pulse of about 180 ns. Since the vertical betatron tune of the PSR is about 2.19, the dominant perturbing harmonic in the envelope equation is 4. The reduced envelope radius R shown in Fig. 2.26 clearly shows 4 oscillations in one circumference.

Substituting Eq. (2.234) into Hill's equation (2.232), we obtain

$$\ddot{\eta} + \nu^2\eta - \frac{2\nu\xi_{sc}}{R^2}\left(1 + \sum_{n=1}^{\infty} q_n\cos(n\phi+\chi_n)\right)\eta = 0. \tag{2.239}$$

The particle tune is $\nu_p \approx \nu - \xi_{sc}$. Rightfully, ξ_{sc} is called the linear space-charge tune shift parameter. One speculates that a large envelope oscillation shown in Eq. (2.238) may cause a large particle oscillation at $n = 2(\nu - \xi_{sc})$ for the Mathieu instability. However, after a closer inspection by substituting $R = 1 + \Delta + r$ into Eq. (2.239),

[57] S. Cousineau, Ph.D. thesis, Indiana University, 2002.

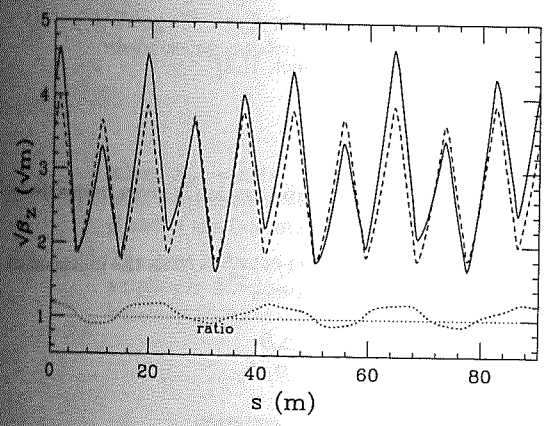

Figure 2.26: The square root of the perturbed vertical betatron amplitude function (solid line), for a beam with high intensity (4.37×10^{13} particles) in the PSR at LANL, is compared with the square root of the intrinsic betatron amplitude function (dashed line). The ratio of these two betatron amplitude function, shown as dotted line, is the reduced envelope radius R defined in Eq. (2.231). Note that the average of R is slightly larger than 1.

we find that the resonance strength is actually zero, i.e. *the envelope oscillation of a beam can not affect particle motion inside the envelope.*

If particle motion inside the beam core is not affected by the envelope oscillation, what is the mechanism for emittance dilution? In the following, we illustrate a possible emittance dilution mechanism. We consider a stable beam orbiting in a synchrotron with space-charge tune shift parameter ξ_{sc} at an equilibrium beam radius $R_b(s)$. When new particles are injected into the beam core, the space-charge parameter ξ_{sc} increases, the envelope tune is pushed toward an integer stopband $\nu_{env} \to n$. If the stopband width $\xi_{sc}q_n$ is not zero, the envelope radius will be resonantly excited as shown in Eq. (2.238). This causes a mismatch in the betatron phase-space ellipses for all particles inside and near the beam envelope radius and results in emittance dilution due to phase space mismatch.

We note that the envelope stopband can arise from the harmonic content of the intrinsic betatron amplitude function. No artificial quadrupole error is needed in generating the envelope stopband. In reality, the harmonic content of the betatron amplitude function arises from the distribution of the focusing function. For example, if an accelerator has a 12-superperiod symmetry in its focusing function, its stopbands will only occur at the betatron tune values of 0, 6, 12, 18, $\cdots$. The Fourier components of its betatron amplitude functions will be zero except harmonics 0, 6, 12, 18, $\cdots$. Likewise, the envelope equation of Eq. (2.238) will not be resonantly excited if the envelope tune is chosen to be far away from these stopbands. We speculate that the emittance dilution for space charge dominated beams can be minimized by correcting some half-integer harmonics of betatron amplitude functions. However, this difficult experiment has not been successfully demonstrated. Detailed theoretical and numerical nalyses of 2D Hill's and envelope equations (including the effect of off-momentum particles) would be very valuable.

Exercise 2.3

1. Particle motion in the presence of dipole errors is (Sect. II.2)

$$y'' + K(s)y = \frac{\Delta B}{B\rho},$$

where the error field ΔB for vertical and radial betatron motion is given, respectively, by $\Delta B = -\Delta B_x$ and $\Delta B = \Delta B_z$.

(a) Defining a new coordinate $\eta = y/\sqrt{\beta}$ with $\phi = (1/\nu)\int_0^s ds/\beta$ as the independent variable, show that the equation of motion becomes

$$\frac{d^2\eta}{d\phi^2} + \nu^2\eta = \nu^2\beta^{3/2}\frac{\Delta B}{B\rho}.$$

Show that Eq. (2.160) is a solution of the above equation.

(b) Show that the Green function $G(\phi, \phi_1)$ in

$$\left(\frac{d^2}{d\phi^2} + \nu^2\right) G(\phi, \phi_1) = \delta(\phi - \phi_1)$$

is $G(\phi, \phi_1) = [\cos\nu(\pi - |\phi - \phi_1|)]/2\nu\sin\pi\nu$. Use the Green function to verify the solution given by Eq. (2.160).

(c) Expanding $\beta^{3/2}\Delta B/B\rho$ in Fourier series

$$\beta^{3/2}\frac{\Delta B}{B\rho} = \sum_{k=-\infty}^{\infty} f_k e^{jk\phi} \quad \text{with} \quad f_k = \frac{1}{2\pi\nu}\oint \sqrt{\beta}\frac{\Delta B}{B\rho}e^{-jk\phi}ds,$$

where f_k are integer stopband integrals, show that the closed orbit arising from the dipole error is

$$y_{\rm co}(s) = \sqrt{\beta(s)}\sum_{k=-\infty}^{\infty}\frac{\nu^2 f_k}{\nu^2 - k^2}e^{jk\phi}.$$

(d) Using a single stopband approximation. and limiting the closed-orbit deviation to less than 20% of the rms beam size, show that the integer stopband width $\Gamma_{[\nu]}$ is given by $\Gamma_{[\nu]} \approx 5\nu|f_{[\nu]}|/\sqrt{\epsilon_{\rm rms}}$, where $[\nu]$ is the integer nearest the betatron tune.

2. From Exercise 1.3, we find that a particle at a distance r from a uniformly distributed paraxial beam bunch experiences a space-charge defocussing force

$$\vec{F} = \frac{2mc^2 N r_0}{a^2\gamma^2}\vec{r},$$

where γ is the relativistic Lorentz factor, a is the radius of the beam bunch, r_0 is the classical radius of the particle, N is the number of particles per unit length, and $\vec{r} = x\hat{x} + z\hat{z}$. In a Gaussian bunch, we should replace N by $N = N_{\rm B}/\sqrt{2\pi}\sigma_s$, where $N_{\rm B}$ is the number of particles per bunch and σ_s is the bunch length.

(a) Using the result of Sec. I.3, show that the space-charge force is equivalent to a defocussing quadrupole with strength

$$K(s) = \frac{2Nr_0}{a^2\beta^2\gamma^3} = \frac{K_{\rm sc}}{a^2},$$

where $K_{\rm sc} = 2Nr_0/(\beta^2\gamma^3)$ is the normalized space-charge perveance parameter used frequently in the transport of space-charge-dominated beams in linacs, and β and γ are Lorentz's relativistic factors.

(b) The rms beam radius is $a^2 = \langle\beta_y\rangle\epsilon_{\rm N}/\beta\gamma$, where $\langle\beta_y\rangle$ is the average betatron amplitude function and $\epsilon_{\rm N}$ is the rms normalized emittance. Show that the betatron (Laslett) tune shift induced by the space-charge force is given by[58]

$$\Delta\nu_{\rm sc} = \frac{F_{\rm B}N_{\rm B}r_0}{2\pi\epsilon_{\rm N}\beta\gamma^2} = \frac{2\pi R K_{\rm sc}}{4\pi\epsilon},$$

where $F_{\rm B} = \frac{2\pi R}{\sqrt{2\pi}\sigma_\ell}$ is the bunching factor and $\epsilon = \epsilon_{\rm N}/\beta\gamma$ is the emittance of the beam.

(c) The Fermilab booster synchrotron is operating at 15 Hz with a circumference of 474.2 m. The rms bunch length at injection is about 1 m. Find the space-charge tune shift by using the data shown in the figure below. Draw a line in the figure for emittance vs the number of particles per bunch for a space-charge tune shift of 0.4.

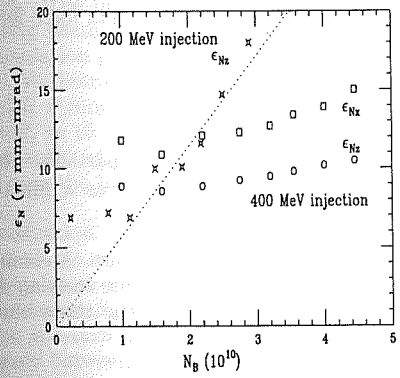

In estimating the space-charge tune shift for an actual accelerators, the formula for the space-charge tune shift should be adjusted by a beam distribution form factor $F_{\rm dist}$, i.e.

$$\Delta\nu_{\rm sc} = \frac{F_{\rm dist}F_{\rm B}N_{\rm B}r_0}{2\pi\epsilon_{\rm N}\beta\gamma^2}.$$

For a round Gaussian distribution, we have $F_{\rm Gauss.} = (1 - e^{-1}) \approx 0.632$, i.e. the fraction of particles within 1σ of a round Gaussian beam is $1 - e^{-1}$.

3. Using $\eta = y/\sqrt{\beta_y}$ and $p_\eta = d\eta/d\phi$ with $\phi = (1/\nu_y)\int_0^s ds/\beta_y$ as conjugate phase-space coordinates, and ϕ as time variable, show that Eq. (2.161) can be derived from the

[58] This formula is derived on the basis of uniform beam distribution. When you are applying this formula to an actual accelerator, where the beam distribution is not uniform, a factor that depends on the distribution function should be used to estimate the space-charge tune shift [see part (c) of this Exercise]. This is called the Laslett space-charge tune shift. It is in fact a tune spread. The Laslett tune shift is the betatron tune shift for particles with small betatron amplitudes. Particles with large betatron amplitudes have a small space-charge tune shift. Thus the Laslett space-charge tune shift is also called the incoherent space-charge tune shift. The beam intensity in low energy synchrotrons is usually limited by the space-charge tune shift.

Hamiltonian

$$H = \frac{1}{2}(p_\eta^2 + \nu^2\eta^2) + \Delta H(\eta),$$
$$\Delta H = -\nu^2 \int_0^\eta \beta^{3/2} g(\eta')d\eta', \quad g(\eta) = \frac{\Delta B}{B\rho}.$$

(a) Letting $\eta = \sqrt{2J/\nu}\cos\psi$ and $d\psi/d\phi = \nu$, show that the Hamiltonian becomes

$$H = \nu J + \langle \Delta H(J,\psi)\rangle_\psi + [\Delta H - \langle \Delta H(J,\psi)\rangle_\psi],$$

where

$$\langle \Delta H(J,\psi)\rangle_\psi = -\frac{\nu^2}{2\pi}\int_0^{2\pi}\left[\int_0^\eta \beta^{3/2} g(\eta')d\eta'\right] d\psi.$$

Show that the betatron tune is shifted by the perturbation $\Delta\nu = \partial\langle\Delta H\rangle_\psi/\partial J$.

(b) We consider a cylindrical Gaussian bunch distribution

$$\rho(x,s,z) = N_B\rho(r)\rho(s),$$

where N_B is the number of particles in a bunch, and

$$\rho(r) = \frac{1}{2\pi\sigma_r^2}e^{-(x^2+z^2)/2\sigma_r^2}, \qquad \rho(s) = \frac{1}{\sqrt{2\pi}\sigma_s}e^{-s^2/2\sigma_s^2},$$

are respectively the transverse and longitudinal Gaussian distributions with rms width σ_r and σ_s. Assuming $\sigma_s \gg \sigma_r$, show that the Lorentz force for a particle at distance r from the center of the bunch is

$$g(r,s) = \frac{2N_B r_0}{\beta^2\gamma^3 r}\left(1 - e^{-r^2/2\sigma_r^2}\right)\rho(s),$$

where $r_0 = e^2/4\pi\epsilon_0 mc^2$ is the classical radius of the particle. Replacing r by $\sqrt{2\beta J/\nu}\cos\psi$, evaluate the space-charge tune shift as a function of the amplitude r.

4. The closed orbit can be locally corrected by using steering dipoles. A commonly used algorithm is based on the "three-bumps" method, where three steering dipoles are used to adjust local-orbit distortion. Let θ_1, θ_2, and θ_3 be the three bump angles. Show that these angles must be related by

$$\theta_2 = -\theta_1\sqrt{\frac{\beta_1}{\beta_2}}\frac{\sin\psi_{31}}{\sin\psi_{32}}, \qquad \theta_3 = \theta_1\sqrt{\frac{\beta_1}{\beta_3}}\frac{\sin\psi_{21}}{\sin\psi_{32}},$$

where β_i is the β-function at the ith steering magnet, $\psi_{ji} = \psi_j - \psi_i$ is the phase advance from the ith to the jth steering dipoles, and the orbit distortion is localized between the first and third steering magnets. Obviously, a local orbit bump can be attained by two steering dipoles θ_1 and θ_3 if and only if $\psi_{31} = n\pi$, where the phase advance is an integer multiple of π.

5. The AGS is composed of 12 superperiods with 5 nearly identical FODO cells per superperiod, i.e. it can be considered as a lattice made of 60 FODO cells with betatron tunes $\nu_z = 8.8$ and $\nu_x = 8.6$. The circumference is 807.12 m.

(a) Estimate the closed orbit sensitivity factor of Eq. (2.168).

(b) Estimate the the rms half-integer stopband width of Eq. (2.202) for the AGS.

(c) During the polarized beam acceleration at AGS, a set of 10 ferrite quadrupoles located at high-β_z locations are powered to change the vertical tune by $\Delta\nu_z = -0.25$ in about 2.5 μs. This means that each quadrupole changes the betatron tune by -0.025.

i. What is the effect of these tune jump quadrupoles on the horizontal tune?

ii. What are the stopband integrals due to these tune jump quadrupoles?

iii. What are the favorable configurations for these quadrupoles from the beam dynamics point of view?

iv. Are there advantages to installing 12 quadrupoles? What are they?

6. In the H^- or H_2^+ strip injection process, the closed orbit is bumped onto the stripper location during the injection pulse. The injection beam and the circulating beam merge at the same phase-space point. We assume that the values of the betatron amplitude functions are $\beta_x = \beta_z = 10$ m, the emittances are $\epsilon_x = \epsilon_z = 2.5\pi$ mm-mrad for the injection beam, and $\epsilon_x = \epsilon_z = 40\pi$ mm-mrad for the circulating beam. Where should the stripper be located with respect to the center of the circulating beam? What is the minimum width of the stripper? Sketch a possible injection system scenario including local orbit bumps.

7. Multi-turn injection of heavy ion beams requires intricate phase-space painting techniques. The injection beam arrives through the center of a septum while the circulating beam closed orbit is bumped near the septum position. During the beam accumulation process, the orbit bump is reduced to avoid beam loss through the septum. We assume that the 95% emittances are 50 π mm-mrad for the stored beam and 2.5 π mm-mrad for the injection beam, the betatron amplitude functions are $\beta_x = \beta_z = 10$ m, and the thickness of the wire septum is 1 mm. How far from the closed orbit of the circulating beam should the septum be located? What effect, if any, does the betatron tune have on the beam-accumulation efficiency?

8. At extraction, the 95% emittance of the beam is adiabatically damped to 5 π mm-mrad at $B\rho = 10$ Tm. The extraction septum is located 40 mm from the center of the closed orbit of the circulating beam. At the septum location, the betatron functions are $\beta_x = 10$ m, $\beta_z = 8$ m. The septum (current sheet) thickness is 7 mm. A ferrite one-turn kicker is located upstream with $\beta_x = 10$ m and $\beta_z = 8$ m. The phase advance between the septum and the kicker is 60°. Discuss a scenario for efficient single-bunch extraction. What is the kicker angle required for single-turn extraction? Assuming that the maximum magnetic flux density for a kicker is 0.1 T, what is the minimum length of the kicker? What advantage, if any, does an orbit bump provide?

9. Particle motion in the presence of closed-orbit error is

$$x = x_{co} + x_\beta,$$

where x_{co} is the closed orbit and x_β is the betatron displacement.

(a) Show that an off-center horizontal closed orbit in quadrupoles gives rise to vertical dipole field error, and a vertical one to horizontal dipole field error.

(b) The magnetic field of a nonlinear sextupole is

$$\Delta B_z + j\Delta B_x = \frac{B_2}{2}(x^2 - z^2 + 2jxz),$$

where $B_2 = \partial^2 B_z/\partial x^2|_{x=0,z=0}$. Show that a horizontal closed-orbit error in a normal sextupole produces quadrupole field error. Show that the effective quadrupole gradient is $\partial B_z/\partial x|_{\text{eff}} = x_{\text{co}} B_2$.

10. In the presence of gradient error, the betatron amplitude functions and the betatron tunes are modified. This exercise provides an alternative derivation of Eq. (2.199).[59] We define the betatron amplitude deviation functions A and B as

$$A = \frac{\alpha_1\beta_0 - \alpha_0\beta_1}{\sqrt{\beta_0\beta_1}}, \quad B = \frac{\beta_1 - \beta_0}{\sqrt{\beta_0\beta_1}},$$

where β_0 and β_1 are respectively the unperturbed and the perturbed betatron amplitude functions associated with the gradient functions K_0 and K_1, and α_0 and α_1 are related to the derivatives of the betatron amplitude functions. Thus β_0 and β_1 satisfy the Floquet equation:

$$\begin{aligned} \beta_0' &= -2\alpha_0, \quad \alpha_0' = K_0\beta_0 - \gamma_0, \quad d\psi_0/ds = 1/\beta_0, \\ \beta_1' &= -2\alpha_1, \quad \alpha_1' = K_1\beta_1 - \gamma_1, \quad d\psi_1/ds = 1/\beta_1, \end{aligned}$$

where ψ_0 and ψ_1 are the unperturbed and the perturbed betatron phase functions.

(a) Show that

$$\frac{dB}{ds} = -A\left(\frac{1}{\beta_0} + \frac{1}{\beta_1}\right), \quad \frac{dA}{ds} = +B\left(\frac{1}{\beta_0} + \frac{1}{\beta_1}\right) + \sqrt{\beta_0\beta_1}\,\Delta K,$$

where $\Delta K = K_1 - K_0$.

(b) In a region with no gradient error, show that $A^2 + B^2 =$ constant, i.e. the phase-space trajectory of A vs B is a circle.

(c) In thin-lens approximation, show that the change of A at a quadrupole with gradient error is

$$\Delta A = \int \sqrt{\beta_0\beta_1}\,\Delta K\, ds \approx \langle\beta_0\rangle g,$$

where $g = +\int \Delta K\, ds$ is the integrated gradient strength of the error quadrupole, and $\langle\beta_0\rangle$ is the averaged value of betatron function in the quadrupole.

(d) In thin-lens approximation, show that the change of A in a sextupole is

$$\Delta A \approx \beta_0 g_{\text{eff}},$$

where $g_{\text{eff}} = (B_2\Delta s/B\rho)x_{\text{co}}$ is the effective quadrupole strength, $(B_2\Delta s/B\rho)$ is the integrated sextupole strength, and x_{co} is the closed-orbit deviation from the center of the sextupole.

[59] See also H. Zgngier, LAL report 77-35, 1977; B.W. Montague, CERN **87-03**, 75-90 (1987).

(e) If we define the average betatron phase function as

$$\bar{\phi} = \frac{1}{2\bar{\nu}}\int_{s_0}^{s}\left(\frac{1}{\beta_0} + \frac{1}{\beta_1}\right) ds,$$

where

$$\bar{\nu} = \frac{1}{4\pi}\int_{s_0}^{s_0+C}\left(\frac{1}{\beta_0} + \frac{1}{\beta_1}\right) ds,$$

show that the function B satisfies

$$\frac{d^2B}{d\bar{\phi}^2} + 4\bar{\nu}^2 B = -4\bar{\nu}^2\frac{(\beta_0\beta_1)^{3/2}}{\beta_0 + \beta_1}\Delta K.$$

Show that this equation reduces to Eq. (2.199) in the limit of small gradient error.

11. Show that the half-integer stopband integral J_p is *approximately* zero at $p = [2\nu]$ for two quadrupole kickers separated by 180° in betatron phase advance with zero betatron tune shift. Such a *zero tune shift π-doublet* can be used to change γ_{T} with minimum effects on betatron motion (see Sec. IV.8.A.3).

12. Multiple scattering from gas molecules inside the vacuum chamber can cause beam emittance dilution, particularly at high-β locations. This effect can also be important in the strip-injection process. This exercise estimates the emittance dilution rate based on the multiple scattering formula (see the particle properties data) for the rms scattering angle

$$\theta^2 = 2\theta_0^2 \approx 2\left(\frac{13.6[\text{MeV}]z_{\text{p}}}{\beta cp}\right)^2 \frac{x}{X_0},$$

where p, βc and z_{p} are momentum, velocity, and charge number of the beam particles, X_0 is the radiation length, and x is the target thickness. The radiation length is

$$X_0 = \frac{716.4A}{Z(Z+1)\ln(287/\sqrt{Z})}\ [\text{g/cm}^2]$$

where Z and A are the atomic charge and the mass number of the medium.

(a) Using the ideal gas law, $PV = nRT$, where P is the pressure, V is the volume, n is the number of moles, T is the temperature, and $R = 8.314$ [J (°K mol)$^{-1}$], show that the equivalent target thickness in [g/cm^2/s] at room temperature is

$$x = 1.641 \times 10^{-6}\beta P_{\text{g}}[\text{ntorr}]A_{\text{g}} \quad [\text{g/cm}^2/\text{s}],$$

where βc is the velocity of the beam, P_{g} is the equivalent partial pressure of a gas at room temperature $T = 293$ °K, and A_{g} is the gram molecular weight of a gas. Show that the emittance growth rate is

$$\frac{1}{\tau_\epsilon} = \frac{1}{\epsilon}\frac{d\epsilon}{dt} = 2.345\frac{\gamma\langle\beta_\perp\rangle\ [\text{m}]}{\beta\epsilon_{\text{N}}\ [\pi\ \text{mm mrad}]}\left(\frac{z_{\text{p}}}{pc\ [\text{GeV}]}\right)^2\frac{P_{\text{g}}\ [\text{nTorr}]A_{\text{g}}}{X_{0g}\ [\text{g/cm}^2]} \quad [\text{h}^{-1}],$$

where $\langle\beta_\perp\rangle$ is the average transverse betatron amplitude function in the accelerator, X_{0g} is the radiation length of the gas, γ is the Lorentz relativistic factor, z_{p} is the charge of the projectile, and p is the momentum of the beam. Because the emittance growth is proportional to the betatron function, better vacuum at high-$\beta_\perp$ location is useful in minimizing the multiple scattering effects.

(b) During the H^- strip-injection process, the H^- passes through a thin foil of thickness t_{foil} [μg/cm^2]. Show that the emittance growth per passage is

$$\Delta\epsilon = 117.8\,\frac{\beta_{\perp,\text{foil}}}{\beta^2(pc[\text{MeV}])^2}\,\frac{t_{\text{foil}}[\mu\text{g/cm}^2]}{X_0[\text{g/cm}^2]}\quad [\pi\,\text{mm mrad}],$$

where $\beta_{\perp,\text{foil}}$ is the betatron amplitude function at the stripper location, p is the momentum of the injected beam, βc is the velocity of the beam, and X_0 is the radiation length. Estimate the emittance growth rate per passage through carbon foil with H^- beams at an injection energy of 7 MeV if $\beta_{\perp,\text{foil}} = 2$ m and $t_{\text{foil}} = 4$ [μg/cm^2].[60]

[60] If the stripping foil is too thin, the efficiency of charge exchange is small, and the proton yield is little. If the foil is too thick, the beam emittance will increase because of multiple Coulomb scattering. A compromise between various processes is needed in the design of accelerator components.

IV Off-Momentum Orbit

In Sec. III, we discussed the closed orbit for a reference particle with momentum p_0, including dipole field errors and quadrupole misalignment. By using closed-orbit correctors, we can achieve an optimized closed orbit that essentially passes through the center of all accelerator components. This closed orbit is called the "golden orbit," and a particle with momentum p_0 is called a *synchronous* particle.[61]

However, a beam is made of particles with momenta distributed around the synchronous momentum p_0. What happens to particles with momenta different from p_0? Here we study the effect of off-momentum on the closed orbit. Its effect on betatron motion will be addressed in Sec V.

For a particle with momentum p, the momentum deviation is $\Delta p = p - p_0$ and the fractional momentum deviation is $\delta = \Delta p/p_0$. The fractional momentum deviation $\delta = \Delta p/p$ is typically small, e.g. $|\delta| \le 10^{-4}$ for SSC, $\le 5\cdot 10^{-3}$ for RHIC, $\le 3\cdot 10^{-2}$ for anti-proton accumulators, $\le 10^{-4}$ for the IUCF Cooler Ring, and $\le 2\cdot 10^{-2}$ for typical electron storage rings. Since δ is small, we can study the motion of off-momentum particles perturbatively. In Sec. IV.1, we will find that the off-momentum closed orbit is proportional to δ in the first-order approximation, and the dispersion function is defined as the derivative of the off-momentum closed orbit with respect to δ. We will discuss the properties of the dispersion function; in particular, the integral representation, the dispersion action, and the $\mathcal{H}$-function will be introduced in Sec. IV.2. The momentum compaction factor and transition energy are discussed in Sec. IV.3, where we introduce the phase focusing principle of synchrotron motion. In Sec. IV.4, we examine the method of dispersion suppression in a beam line. In Sec. IV.5 we discuss the achromat transport system, and in Sec. IV.6 we introduce the standard transport notation. In Sec. IV.7 we describe methods of dispersion measurements and correction, and in Sec. IV.8 methods of transition energy manipulation. Minimum ($\mathcal{H}$) lattices are discussed in Sec. IV.9.

IV.1 Dispersion Function

Expanding Eq. (2.29) to first order in x/ρ, we obtain

$$x'' + \left(\frac{1-\delta}{\rho^2(1+\delta)} - \frac{K(s)}{(1+\delta)}\right)x = \frac{\delta}{\rho(1+\delta)}, \tag{2.240}$$

where $K(s) = B_1/B\rho$ is the quadrupole gradient function with $B_1 = \partial B_z/\partial x$ evaluated at the closed orbit. Solutions of Eq. (2.240) for $\delta = 0$ were discussed in Sec. II.

[61] The revolution frequency of a synchronous particle is defined as the revolution frequency of the beam. The frequency of the radio-frequency (rf) cavities has to be an integer multiple of the revolution frequency of the beam, i.e. a synchronous particle synchronizes with the rf electric field applied to the beam. The name "synchrotron" for circular accelerators is derived from the synchronism between the orbiting particles and the rf field.

For an off-momentum particle with $\delta \neq 0$, the solution of the linearized inhomogeneous equation (2.240) can be expressed as a linear superposition of the particular solution and the solution of the homogeneous equation:[62]

$$x = x_\beta(s) + D(s)\delta, \tag{2.241}$$

where $x_\beta(s)$ and $D(s)$ satisfy the equations

$$x_\beta'' + (K_x(s) + \Delta K_x)x_\beta = 0, \tag{2.242}$$

$$D'' + (K_x(s) + \Delta K_x)D = \frac{1}{\rho} + O(\delta), \tag{2.243}$$

with

$$K_x = \frac{1}{\rho^2} - K(s), \qquad \Delta K_x = [-\frac{2}{\rho^2} + K(s)]\delta + O(\delta^2).$$

In this section, we will neglect the chromatic perturbation term $\Delta K_x(s)$. The solution of the inhomogeneous equation is called the dispersion function, where $D(s)\delta$ is the *off-momentum closed orbit.* Aside from the chromatic perturbation ΔK_x, the solution of the homogeneous equation x_β is the betatron motion around the off-momentum closed orbit.

To the lowest order in δ, the dispersion function obeys the inhomogeneous equation

$$D'' + K_x(s)D = 1/\rho. \tag{2.244}$$

Since $K_x(s)$ and $\rho(s)$ are periodic functions of s, the closed-orbit condition is imposed on the dispersion function[63]

$$D(s+L) = D(s), \quad D'(s+L) = D'(s), \tag{2.245}$$

where L is the length of a repetitive period. Since $K_x(s)$ and $\rho(s)$ are usually piecewise constant for accelerator components, the inhomogeneous equation can easily be solved by the matrix method. The solution of a linear inhomogeneous dispersion equation is a sum of the particular solution and the solution of the homogeneous equation:

$$\begin{pmatrix} D(s_2) \\ D'(s_2) \end{pmatrix} = M(s_2|s_1)\begin{pmatrix} D(s_1) \\ D'(s_1) \end{pmatrix} + \begin{pmatrix} d \\ d' \end{pmatrix}, \tag{2.246}$$

[62]Including the dipole field error, the displacement x is $x = x_{co}(s) + x_\beta(s) + D(s)\delta$, where x_{co} is the closed-orbit error discussed in Sec. III.

[63]The closed-orbit condition for the dispersion function is strictly required only for one complete revolution $D(s) = D(s+C)$ and $D'(s) = D'(s+C)$, where C is the circumference. The local closed-orbit condition of Eq. (2.245) for repetitive cells is not a necessary condition. However, this local periodic closed-orbit condition facilitates accelerator lattice design.

where the 2×2 matrix $M(s_2|s_1)$ is the transfer matrix for the homogeneous equation, and d and d' are the particular solution. Let $\bar{d}$ be shorthand notation for the *two-component dispersion vector* with $\bar{d}^\dagger = (d, d')$. The transfer matrix in Eq. (2.246) can be expressed by the 3×3 matrix

$$\begin{pmatrix} D(s_2) \\ D'(s_2) \\ 1 \end{pmatrix} = \begin{pmatrix} M(s_2|s_1) & \bar{d} \\ 0 & 1 \end{pmatrix}\begin{pmatrix} D(s_1) \\ D'(s_1) \\ 1 \end{pmatrix}. \tag{2.247}$$

For a magnet with constant dipole field and field gradient, we obtain

$$\bar{d} = \begin{cases} \begin{pmatrix} \frac{1}{\rho K_x}(1-\cos\sqrt{K_x}s) \\ \frac{1}{\rho\sqrt{K_x}}\sin\sqrt{K_x}s \end{pmatrix} & \text{if } K_x > 0, \\ \begin{pmatrix} \frac{1}{\rho|K_x|}(-1+\cosh\sqrt{|K_x|}s) \\ \frac{1}{\rho\sqrt{|K_x|}}\sinh\sqrt{|K_x|}s \end{pmatrix} & \text{if } K_x < 0. \end{cases} \tag{2.248}$$

The transfer matrix for a pure sector dipole, where $K_x = 1/\rho^2$, is

$$M = \begin{pmatrix} \cos\theta & \rho\sin\theta & \rho(1-\cos\theta) \\ -(1/\rho)\sin\theta & \cos\theta & \sin\theta \\ 0 & 0 & 1 \end{pmatrix}, \tag{2.249}$$

where ρ is the bending radius, and θ is the bending angle. In the small angle approximation, the transfer matrix of a sector dipole becomes

$$M = \begin{pmatrix} 1 & \ell & \frac{1}{2}\ell\theta \\ 0 & 1 & \theta \\ 0 & 0 & 1 \end{pmatrix},$$

where $\ell = \rho\theta$ is the length of the dipole.

Example 1: Dispersion function of a FODO cell in thin-lens approximation

A FODO cell with dipole, as shown in Fig. 2.4, is represented by

$$\mathrm{C} = \{\frac{1}{2}\mathrm{QF} \quad \mathrm{B} \quad \mathrm{QD} \quad \mathrm{B} \quad \frac{1}{2}\mathrm{QF}\},$$

where QF and QD are focusing and defocussing quadrupoles, and B represents bending dipole(s). Using thin-lens approximation, we obtain

$$\mathrm{M} = \begin{pmatrix} 1 & 0 & 0 \\ -\frac{1}{2f} & 1 & 0 \\ 0 & 0 & 1 \end{pmatrix}\begin{pmatrix} 1 & L & \frac{1}{2}L\theta \\ 0 & 1 & \theta \\ 0 & 0 & 1 \end{pmatrix}\begin{pmatrix} 1 & 0 & 0 \\ \frac{1}{f} & 1 & 0 \\ 0 & 0 & 1 \end{pmatrix}\begin{pmatrix} 1 & L & \frac{1}{2}L\theta \\ 0 & 1 & \theta \\ 0 & 0 & 1 \end{pmatrix}\begin{pmatrix} 1 & 0 & 0 \\ -\frac{1}{2f} & 1 & 0 \\ 0 & 0 & 1 \end{pmatrix},$$

where L is the half cell length, θ is the bending angle of a half cell, and f is the focal length of the quadrupoles.

The closed-orbit condition of Eq. (2.245) becomes

$$\begin{pmatrix} D \\ D' \\ 1 \end{pmatrix} = \begin{pmatrix} 1-\frac{L^2}{2f^2} & 2L(1+\frac{L}{2f}) & 2L\theta(1+\frac{L}{4f}) \\ -\frac{L}{2f^2}+\frac{L^2}{4f^3} & 1-\frac{L^2}{2f^2} & 2\theta(1-\frac{L}{4f}-\frac{L^2}{8f^2}) \\ 0 & 0 & 1 \end{pmatrix} \begin{pmatrix} D \\ D' \\ 1 \end{pmatrix}. \tag{2.250}$$

Note that D and D' in Eq. (2.250) are values of the dispersion function and its derivative at the focusing quadrupole location. Using the Courant-Snyder parameterization for the 2×2 matrix, we obtain

$$\sin\frac{\Phi}{2} = \frac{L}{2f}, \quad \beta_{\text{F}} = \frac{2L(1+\sin(\Phi/2))}{\sin\Phi}, \quad \alpha_{\text{F}} = 0, \tag{2.251}$$

where Φ is the phase advance per cell. The dispersion function at the focusing quadrupole location becomes

$$D_{\text{F}} = \frac{L\theta(1+\frac{1}{2}\sin(\Phi/2))}{\sin^2(\Phi/2)}, \quad D'_{\text{F}} = 0. \tag{2.252}$$

The dispersion function at other locations in the accelerator can be obtained by the matrix propagation method, Eq. (2.247). The dispersion function at the defocussing quadrupole location is

$$D_{\text{D}} = \frac{L\theta(1-\frac{1}{2}\sin(\Phi/2))}{\sin^2(\Phi/2)}, \quad D'_{\text{D}} = 0. \tag{2.253}$$

The middle plot of Fig. 2.5 shows the dispersion function of the AGS lattice, which can be approximated by a lattice made of 60 FODO cells. We list here some characteristic properties of the dispersion function of FODO cells.

- The dispersion function at the focusing quadrupole is larger than that at the defocussing quadrupole by a factor $(2+\sin(\Phi/2))/(2-\sin(\Phi/2))$, which is about 2 at $\Phi = 90°$.
- The dispersion function is proportional to $L\theta$, the product of the cell length and the bending angle of a FODO cell, and it is smaller with shorter cell length and smaller bending angle.
- When the phase advance is small, the dispersion function is proportional to the inverse quadratic power of the phase advance.

Example 2: Dispersion function in terms of transfer matrix

In general, the transfer matrix of a periodic cell can be expressed as

$$\text{M} = \begin{pmatrix} M_{11} & M_{12} & M_{13} \\ M_{21} & M_{22} & M_{23} \\ 0 & 0 & 1 \end{pmatrix}, \tag{2.254}$$

where M_{11}, M_{12}, M_{21} and M_{22} are given by Eq. (2.53). Using the closed-orbit condition of Eq. (2.245), we obtain

$$D = \frac{M_{13}(1-M_{22})+M_{12}M_{23}}{2-M_{11}-M_{22}} = \frac{M_{13}(1-\cos\Phi+\alpha\sin\Phi)+M_{23}\beta\sin\Phi}{2(1-\cos\Phi)}, \tag{2.255}$$

$$D' = \frac{M_{13}M_{21}+(1-M_{11})M_{23}}{2-M_{11}-M_{22}} = \frac{-M_{13}\gamma\sin\Phi+M_{23}(1-\cos\Phi-\alpha\sin\Phi)}{2(1-\cos\Phi)}, \tag{2.256}$$

where Φ is the horizontal betatron phase advance of the periodic cell, α, β and $\gamma = (1+\alpha^2)/\beta$ are the Courant–Snyder parameters for the horizontal betatron motion at a periodic-cell location s, and D and D' are the value of the dispersion function and its derivative at the same location.

Solving M_{13} and M_{23} as functions of D and D', the 3×3 transfer matrix is

$$\text{M} = \begin{pmatrix} \cos\Phi+\alpha\sin\Phi & \beta\sin\Phi & (1-\cos\Phi-\alpha\sin\Phi)\ D-\beta\sin\Phi\ D' \\ -\gamma\sin\Phi & \cos\Phi-\alpha\sin\Phi & \gamma\sin\Phi\ D+(1-\cos\Phi+\alpha\sin\Phi)\ D' \\ 0 & 0 & 1 \end{pmatrix}. \tag{2.257}$$

This representation of the transfer matrix is sometimes useful in studying the general properties of repetitive accelerator sections.

IV.2 $\mathcal{H}$-Function, Action, and Integral Representation

The dispersion $\mathcal{H}$-function is defined as

$$\mathcal{H}(D,D') = \gamma_x D^2 + 2\alpha_x DD' + \beta_x D'^2 = \frac{1}{\beta_x}[D^2 + (\beta_x D' + \alpha_x D)^2]. \tag{2.258}$$

Since the dispersion function satisfies the homogeneous betatron equation of motion in regions with no dipole ($1/\rho = 0$), the $\mathcal{H}$-function is invariant, but in regions with dipoles, it is not invariant. For a FODO cell, the dispersion $\mathcal{H}$-function at the defocussing quadrupole is larger than that at the focusing quadrupole, i.e. $\mathcal{H}_{\text{F}} \le \mathcal{H}_{\text{D}}$, where

$$\mathcal{H}_{\text{F}} = \frac{L\theta^2\sin\Phi(1+\frac{1}{2}\sin\frac{\Phi}{2})^2}{2(1+\sin\frac{\Phi}{2})\sin^4\frac{\Phi}{2}}, \quad \mathcal{H}_{\text{D}} = \frac{L\theta^2\sin\Phi(1-\frac{1}{2}\sin\frac{\Phi}{2})^2}{2(1-\sin\frac{\Phi}{2})\sin^4\frac{\Phi}{2}}, \tag{2.259}$$

and the dispersion $\mathcal{H}$-function is proportional to the inverse cubic power of the phase advance.

Now we define the *normalized* dispersion phase-space coordinates as

$$\begin{cases} X_{\rm d} = \dfrac{1}{\sqrt{\beta_x}} D = \sqrt{2J_{\rm d}}\cos\Phi_{\rm d}, \\ P_{\rm d} = \sqrt{\beta_x} D' + \dfrac{\alpha_x}{\sqrt{\beta_x}} D = -\sqrt{2J_{\rm d}}\sin\Phi_{\rm d}, \end{cases} \tag{2.260}$$

where the dispersion action is given by

$$J_{\rm d} = \frac{1}{2}\mathcal{H}(D, D'). \tag{2.261}$$

In a straight section, $J_{\rm d}$ is invariant and $\Phi_{\rm d}$, aside from a constant, is identical to the betatron phase advance. In a region with dipoles, $J_{\rm d}$ is not constant. The change of the dispersion function across a *thin* dipole is $\Delta D = 0$ and $\Delta D' = \theta$, i.e.

$$\Delta X_{\rm d} = 0, \quad \Delta P_{\rm d} = \sqrt{\beta_x}\,\Delta D' = \sqrt{\beta_x}\,\theta \tag{2.262}$$

where θ is the bending angle of the dipole, and the change in dispersion action is $\Delta J_{\rm d} = (\beta_x D' + \alpha_x D)\theta$.

For FODO-cell lattice shown in Sec. IV.1 Example 1, the normalized dispersion coordinate $X_{\rm d}$ is nearly constant, i.e. $D \sim \sqrt{\beta_x}$, and $P_{\rm d}$ is small. Figure 2.27 shows the normalized dispersion phase-space coordinates in one superperiod of AGS lattice (see Fig. 2.5) that is approximately made of 5 FODO cells. Note that $X_{\rm d}$ is indeed nearly constant, and $(P_{\rm d}, X_{\rm d})$ propagate in a very small region of the dispersion phase-space (see also Fig. 2.34).

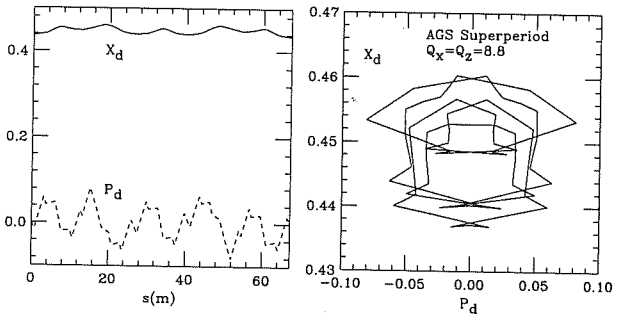

Figure 2.27: Left: Normalized dispersion phase-space coordinates $X_{\rm d}$ and $P_{\rm d}$ are plotted in a superperiod of the AGS lattice. Right: the coordinates are shown in $X_{\rm d}$ vs $P_{\rm d}$. The scales for both $X_{\rm d}$ and $P_{\rm d}$ are $\rm m^{1/2}$.

In contrast, the normalized dispersion phase-space coordinates for the double-bend achromat (DBA) lattice (see Sec. IV.5.A) shows different behavior. Figure 2.28 shows the normalized dispersion coordinates for the IUCF Cooler Ring, which is composed of 3 achromat straight-sections for electron cooling, rf cavities, etc., and 3 dispersive-sections for injection, momentum stacking, etc. The machine is made of six 60°-bends

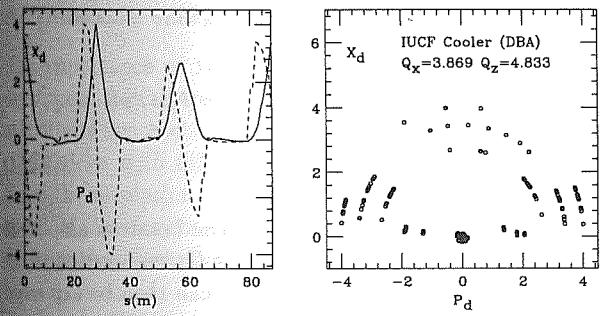

Figure 2.28: Left: Normalized dispersion phase-space coordinates $X_{\rm d}$ and $P_{\rm d}$ of the IUCF Cooler lattice are plotted. Right: The coordinates are shown in $X_{\rm d}$ vs $P_{\rm d}$ at the end of each lattice elements. The scales for both $X_{\rm d}$ and $P_{\rm d}$ are $\rm m^{1/2}$.

forming a 3 similar double-bend achromat modules, where the dispersion function is shown in Fig. 2.31.

Note that the achromat sections are described by a single point at origin with $X_{\rm d} = P_{\rm d} = 0$. Inside dipoles, the normalized dispersion coordinates increase in magnitude. In dispersion matching sections, the normalized dispersion coordinates are located on invariant circles, that are nearly half-circles as shown in Fig. 2.28. Thus the dispersion phase $\Phi_{\rm d}$ advances nearly π in the dispersion matching section. Since the dispersion phase-advance is equal to the horizontal betatron phase-advance in a straight section, the horizontal betatron phase-advance is also nearly π.

It is worth pointing out that the lattice function and the dispersion phase-space coordinates of the IUCF Cooler Ring differ substantially from the low emittance DBA lattice to be shown in Figs. 2.38 and 2.39. For an ion storage ring, the minimization of $\langle\mathcal{H}\rangle$ plays no important role in beam dynamics. Instead, a minimum β_z inside dipole will provide a criterion for the magnet gap g. Since the power required in the operation of a storage ring is proportional to g^2, it is preferable to design a machine with a minimum β_z inside dipoles. Thus the corresponding β_x will be large in dipole. The resulting dispersion phase-space coordinates are much larger than those of minimum emittance DBA lattices shown in Fig. 2.38.

Integral representation of the dispersion function

The dispersion function can also be derived from the dipole field error resulting from the momentum deviation. The angular kick due to the off-momentum deviation is given by

$$\theta = \frac{\Delta p}{p_0}\frac{ds}{\rho}, \tag{2.263}$$

where ρ is the bending radius, and ds is the infinitesimal length of the dipole. With the substitutions

$$\frac{\Delta B}{B\rho} \to \frac{\Delta p}{p_0}\frac{1}{\rho}, \qquad y_{\rm co} \to D(s)\frac{\Delta p}{p_0}$$

in Eq. (2.160), the dispersion function becomes

$$\begin{aligned} D(s) &= \frac{\sqrt{\beta_x(s)}}{2\sin\pi\nu_x}\int_s^{s+C}\frac{\sqrt{\beta_x(t)}}{\rho}\cos(\pi\nu_x - |\psi_x(t)-\psi_x(s)|)dt \\ &= \int_s^{s+C}\frac{G_x(s,t)}{\rho(t)}dt, \end{aligned} \tag{2.264}$$

where C is the circumference, ν_x is the betatron tune, β_x is the betatron amplitude function, ψ_x is the betatron phase function, and $G_x(s,t)$ is the Green function of the horizontal Hill equation. The normalized dispersion functions can then be expressed as

$$\begin{cases} X_{\rm d}(s) = \dfrac{1}{2\sin\pi\nu_x}\displaystyle\int_s^{s+C}\frac{\sqrt{\beta_x(t)}}{\rho}\cos(\psi_x(t)-\psi_x(s)-\pi\nu_x)dt \\ P_{\rm d}(s) = \dfrac{1}{2\sin\pi\nu_x}\displaystyle\int_s^{s+C}\frac{\sqrt{\beta_x(t)}}{\rho}\sin(\psi_x(t)-\psi_x(s)-\pi\nu_x)dt. \end{cases} \tag{2.265}$$

IV.3 Momentum Compaction Factor

Since the synchronization of particle motion in a synchrotron depends critically on the total path length, it is important to evaluate the effect of the off-momentum closed orbit on path length. Since the change in path length due to betatron motion is proportional to the square of the betatron amplitude [see Eq. (2.170)], the effect is small. On the other hand, the deviation of the total path length for an off-momentum particle from that of the on-momentum closed orbit is given by

$$\Delta C = \oint\frac{x}{\rho}ds = \left[\oint\frac{D(s)}{\rho}ds\right]\delta, \tag{2.266}$$

which depends linearly on the dispersion function $D(s)$. Since $D(s)$ is normally positive, the total path length for a higher momentum particle is longer.

The momentum compaction factor is then defined by

$$\alpha_{\rm c} \equiv \frac{1}{C}\frac{d\Delta C}{d\delta} = \frac{1}{C}\oint\frac{D(s)ds}{\rho} \approx \frac{1}{C}\sum_i\langle D\rangle_i\theta_i, \tag{2.267}$$

where $\langle D\rangle_i$ and θ_i are the average dispersion function and the bending angle of the ith dipole, and the last approximate identity uses thin-lens approximation. For example, the momentum compaction factor for a FODO lattice is given by

$$\alpha_{\rm c} \approx \frac{(D_{\rm F}+D_{\rm D})\theta}{2L} \approx \frac{\theta^2}{\sin^2(\Phi/2)} \approx \frac{1}{\nu_x^2},$$

where L and θ are the length and the bending angle of one half-cell, Φ is the phase advance of a FODO cell, and ν_x is the betatron tune (see Exercise 2.4.2).

A. Transition energy and the phase-slip factor

The importance of the momentum compaction factor will be fully realized when we discuss synchrotron motion in Chap. 3. In the meantime, we discuss the phase stability of synchrotron motion discovered by McMillan and Veksler [17].

Particles with different momenta travel along different paths in an accelerator. Since the revolution period is $T = C/v$, where C is the circumference, and v is the speed of the circulating particle, the fractional difference of the revolution periods between the off-momentum and on-momentum particles is

$$\frac{\Delta T}{T_0} = \frac{\Delta C}{C} - \frac{\Delta v}{v} = (\alpha_{\rm c} - \frac{1}{\gamma^2})\frac{\Delta p}{p_0} = \eta\delta, \tag{2.268}$$

or equivalently, $\Delta f/f_0 = -\eta\delta$, where f is the revolution frequency, $T_0 = 1/f_0$ is the revolution period of a synchronous particle, and $\delta = \Delta p/p_0$ is the fractional momentum deviation. The *phase-slip factor* η is

$$\eta = \alpha_{\rm c} - \frac{1}{\gamma^2} = \frac{1}{\gamma_{\rm T}^2} - \frac{1}{\gamma^2}. \tag{2.269}$$

Here $\gamma_{\rm T} \equiv \sqrt{1/\alpha_{\rm c}}$ is called the transition-γ, and $\gamma_{\rm T}mc^2$ or simply $\gamma_{\rm T}$ is the transition energy. For FODO cell lattices, $\gamma_{\rm T} \approx \nu_x$.

Below the transition energy, with $\gamma < \gamma_{\rm T}$ and $\eta < 0$, a higher momentum particle will have a revolution period shorter than that of the synchronous particle. Because a high energy particle travels faster, its speed compensates its longer path length in the accelerator, so that a higher energy particle will arrive at a fixed location earlier than a synchronous particle. Above the transition energy, with $\gamma > \gamma_{\rm T}$, the converse is true. Without a longitudinal electric field, the time slippage between a higher or lower energy particle and a synchronous particle is $T_0\eta\delta$ per revolution.

At $\gamma = \gamma_{\rm T}$ the revolution period is independent of the particle momentum. All particles at different momenta travel rigidly around the accelerator with equal revolution frequencies. This is the isochronous condition, which is the operating principle of AVF isochronous cyclotrons.

B. Phase stability of the bunched beam acceleration

Let $V(t) = V_0\sin(h\omega_0 t + \phi)$ be the gap voltage of the rf cavity (see Fig. 2.29), where V_0 is the amplitude, ϕ is an arbitrary phase angle, h is an integer called the harmonic number, $\omega_0 = 2\pi f_0$ is the angular revolution frequency, and f_0 is the revolution frequency of a synchronous particle. A *synchronous* particle is defined as an ideal particle that arrives at the rf cavity at a constant phase angle $\phi = \phi_{\rm s}$, where $\phi_{\rm s}$ is the synchronous phase angle. The acceleration voltage at the rf gap and the acceleration rate for a synchronous particle are respectively given by

$$V_{\rm s} = V_0\sin\phi_{\rm s}, \quad \dot{E}_0 = f_0 eV_0\sin\phi_{\rm s}, \tag{2.270}$$

where e is the charge, E_0 is the energy of the synchronous particle, and the overdot indicates the derivative with respect to time t.

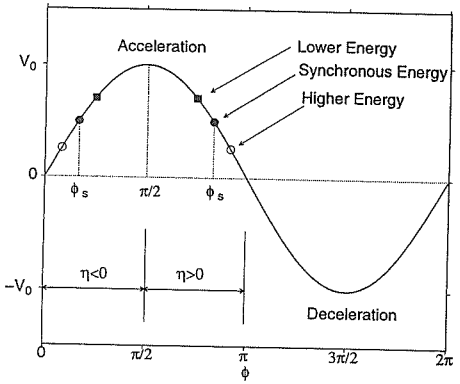

Figure 2.29: Schematic drawing of an rf wave, and the rf phase angles of a synchronous particle, and the higher and lower energy particles. For a stable synchrotron motion, the phase focusing principle requires $0 < \phi_s \leq \pi/2$ for $\eta < 0$, and $\pi/2 < \phi_s \leq \pi$ for $\eta > 0$. (Courtesy of D. Li, LBNL).

A non-synchronous particle will arrive at the rf cavity at a phase angle ϕ with respect to the rf field, where ϕ can vary with time. At phase angle ϕ, the acceleration rate is $\dot{E} = feV_0 \sin\phi$, where f is the revolution frequency. The rate of change of the energy deviation is (see Chap. 3, Sec. I)

$$\frac{d}{dt}\left(\frac{\Delta E}{\omega_0}\right) = \frac{1}{2\pi} eV_0(\sin\phi - \sin\phi_s), \tag{2.271}$$

where $\Delta E = E - E_0$ is the energy difference between the non-synchronous and the synchronous particles. Similarly, the equation of motion for the rf phase angle $\phi = -h\theta$, where θ is the actual angular position of the particle in a synchrotron, is

$$\frac{d}{dt}(\phi - \phi_s) = -h\Delta\omega = h\omega_0 \frac{\Delta T}{T_0} = h\eta\omega_0 \frac{\Delta p}{p_0} = \frac{\eta h \omega_0^2}{\beta^2 E_0}\frac{\Delta E}{\omega_0}. \tag{2.272}$$

Equations (2.271) and (2.272) form the basic synchrotron equation of motion for conjugate phase-space coordinates ϕ and $\Delta E/\omega_0$. This is the equation of motion for a biased physical pendulum system. It is usually called synchrotron motion. The differential equation for the small amplitude phase oscillation is

$$\frac{d^2(\phi - \phi_s)}{dt^2} = \frac{\eta h \omega_0^2 eV_0}{2\pi\beta^2 E_0}(\sin\phi - \sin\phi_s) \approx \frac{\eta\cos\phi_s h\omega_0^2 eV_0}{2\pi\beta^2 E_0}(\phi - \phi_s). \tag{2.273}$$

Thus the phase stability condition is given by $\eta\cos\phi_s < 0$, i.e.

$$\begin{cases} 0 \leq \phi_s \leq \pi/2 & \text{if } \gamma < \gamma_T \text{ or } \eta < 0, \\ \pi/2 \leq \phi_s \leq \pi & \text{if } \gamma > \gamma_T \text{ or } \eta > 0. \end{cases}$$

Below the transition energy, with $0 \leq \phi_s < \pi/2$, a higher energy particle arrives at the rf gap earlier and receives less energy from the rf cavity (see Fig. 2.29). Thus the energy of the particle will becomes smaller than that of the synchronous particle. On the other hand, a lower energy particle arrives later and gains more energy from the cavity. This process gives rise to the phase stability of synchrotron motion. Similarly, the synchronous phase angle should be $\pi/2 < \phi_s \leq \pi$ at $\gamma > \gamma_T$. The synchrotron frequency of small-amplitude phase oscillations is given by

$$\omega_{syn} = \omega_0\sqrt{\frac{heV_0|\eta\cos\phi_s|}{2\pi\beta^2 E_0}}. \tag{2.274}$$

Particles are accelerated through the transition energy in many medium energy synchrotrons such as the AGS, the Fermilab booster and main injector, the CERN PS, and the KEK PS. The synchronous angle has to be shifted from ϕ_s to $\pi - \phi_s$ across the transition energy within 10 to 100 μs. Fortunately, synchrotron motion around the transition energy region is very slow, i.e. $\omega_{syn} \to 0$ as $\gamma \to \gamma_T$. A sudden change in the synchronous phase angle of the rf wave will not cause much beam dilution.

However, when the beam is accelerated through the transition energy, beam loss and serious beam phase-space dilution can result from space-charge-induced mismatch, nonlinear synchrotron motion, microwave instability due to wakefields, etc. An accelerator lattice with a negative momentum compaction factor, where the transition γ_T is an imaginary number, offers an attractive solution to these problems. Such a lattice is called an imaginary γ_T lattice. Particle motion in an imaginary γ_T lattice is always below transition energy, thus the transition energy problems can be eliminated. Attaining an imaginary γ_T lattice requires a negative horizontal dispersion in most dipoles, i.e. $\sum_i \langle D\rangle_i \theta_i < 0$. Methods of achieving a negative compaction lattice will be addressed in Sec. IV.8.

IV.4 Dispersion Suppression and Dispersion Matching

Since bending dipoles are needed for beam transport in arc sections, the dispersion function can not be zero there. If the arc is composed of modular cells, such as FODO cells, etc., the dispersion function is usually constrained by the periodicity condition, Eq. (2.245), which simplifies lattice design. In many applications, the dispersion function should be properly matched in straight sections for optimal operation.[64] We discuss here the general strategy for dispersion suppression.

[64]The curved transport line is usually called the arc, and the straight section that connects arcs is usually called the insertion, needed for injection, extraction, rf cavities, internal targets, insertion devices, and interaction regions for colliders. If the betatron and synchrotron motions are independent of each other, the rms horizontal beam size is given by $\sigma_x^2(s) = \beta_x(s)\epsilon_{x,\text{rms}} + D^2(s)\langle(\Delta p/p_0)^2\rangle$, where $\epsilon_{x,\text{rms}}$ is the rms emittance. Thus the beam size of a collider at the interaction point can be minimized by designing a zero dispersion straight section. A zero dispersion function in the rf cavity region can also be important to minimize the effect of synchro-betatron coupling resonances.

First-order achromat theorem

The first-order achromat theorem states that a lattice of n repetitive cells is achromatic to first order if and only if $M^n = I$ or each cell is achromatic.[65] Here M is the 2×2 transfer matrix of each cell, and I is a 2×2 unit matrix. The proof of this theorem is given as follows.

Let the 3×3 transfer matrix of a basic cell be

$$R = \begin{pmatrix} M & \bar{d} \\ 0 & 1 \end{pmatrix}, \quad \bar{d} = \begin{pmatrix} d \\ d' \end{pmatrix}, \tag{2.275}$$

where M is the 2×2 transfer matrix for betatron motion, and $\bar{d}$ is the dispersion vector. The transfer matrix of n cells is

$$R^n = \begin{pmatrix} M^n & (M^{n-1} + M^{n-2} + \cdot + 1)\bar{d} \\ 0 & 1 \end{pmatrix} = \begin{pmatrix} M^n & \bar{w} \\ 0 & 1 \end{pmatrix}, \tag{2.276}$$

where $\bar{w} = (M^n - I)(M - I)^{-1}\bar{d}$. Thus the achromat condition $\bar{w} = 0$ can be attained if and only if $M^n = I$ or $\bar{d} = 0$. An achromat section matches any zero dispersion function modules. A unit matrix achromat works like a transparent transport section for any dispersion functions.

Dispersion suppression

Applying the first-order achromat theorem, a strategy for dispersion function suppression can be derived. We consider a curved (dipole) achromatic section such that $M^n = I$. We note that one half of this achromatic section can generally be expressed as

$$R = \begin{pmatrix} -I & \bar{d} \\ 0 & 1 \end{pmatrix}, \quad \bar{d} = \begin{pmatrix} d \\ d' \end{pmatrix}. \tag{2.277}$$

Using the closed-orbit condition, Eq. (2.245), the dispersion function of the repetitive half achromat is

$$D = d/2, \quad D' = d'/2.$$

If the dipole bending strength of the adjoining $-I$ section is halved, the transfer matrix becomes

$$R_{1/2} = \begin{pmatrix} -I & \frac{1}{2}\bar{d} \\ 0 & 1 \end{pmatrix},$$

and the dispersion function will be matched to zero value in the straight section, i.e.

$$\begin{pmatrix} d/2 \\ d'/2 \\ 1 \end{pmatrix} = \begin{pmatrix} -I & \frac{1}{2}\bar{d} \\ 0 & 1 \end{pmatrix} \begin{pmatrix} 0 \\ 0 \\ 1 \end{pmatrix}.$$

[65] See K. Brown and R Servranckx, p. 121 in Ref. [12].

Thus we reach the conclusion that the matched dispersion function is equal to the dispersion function of the matched arc. When edge focusing is included, a small modification in the quadrupole strengths is needed for dispersion suppression. This is usually called the missing dipole dispersion suppressor (see Exercise 2.4.3c). The reduced bending strength scheme for dispersion suppression is usually expensive because of the wasted space in the cells. A possible variant uses $-I$ sections with full bending angles for dispersion suppression by varying the quadrupole strengths in the $-I$ sections. With use of computer programs such as MAD and SYNCH, the fitting procedure is straightforward.

Is the dispersion function unique?

A trivial corollary of the first-order achromat theorem is that a dispersion function of arbitrary value can be transported through a unit achromat transfer matrix, i.e. a 3×3 unit matrix.

Now we consider the case of an accelerator or transport line with many repetitive modules, which however do not form a unit transfer matrix. Is the dispersion function obtained unique? This question is easily answered by the closed-orbit condition Eq. (2.245) for the entire ring. The transport matrix of n identical modules is

$$R^n = \begin{pmatrix} M^n & (M^n - I)(M - I)^{-1}\bar{d} \\ 0 & 1 \end{pmatrix}, \tag{2.278}$$

where M is the transfer matrix of the basic module with dispersion vector $\bar{d}$. Using the closed-orbit condition, Eq. (2.245), we easily find that the dispersion function of the transport channel is uniquely determined by the basic module unless the transport matrix is a unit matrix, i.e. $M^n = I$. In the case of unit transport, any arbitrary value of dispersion function can be matched in the unit achromat. Since the machine tune can not be an integer because of the integer stopbands, the dispersion function of an accelerator lattice is uniquely determined.

IV.5 Achromat Transport Systems

If the dispersion function is not zero in a transport line, the beam closed orbit depends on particle momentum. However, it is possible to design a transport system such that the beam positions do not depend on beam momentum at both ends of the transport line. Such a beam transport system is called an achromat. The achromat theorem of Sec. IV.4 offers an example of an achromat.

A. The double-bend achromat

A double-bend achromat (DBA) or Chasman-Green lattice is a basic lattice cell frequently used in the design of low emittance synchrotron radiation storage rings. A

DBA cell consists of two dipoles and a dispersion-matching section such that the dispersion function outside the DBA cell is zero. It is represented schematically by

$$[\mathrm{OO}] \quad \mathrm{B} \quad \{\mathrm{O} \quad \mathrm{QF} \quad \mathrm{O}\} \quad \mathrm{B} \quad [\mathrm{OO}],$$

where [OO] is the zero dispersion straight section and {O QF O} is the dispersion matching section. The top plot of Fig. 2.30 shows a basic DBA cell.

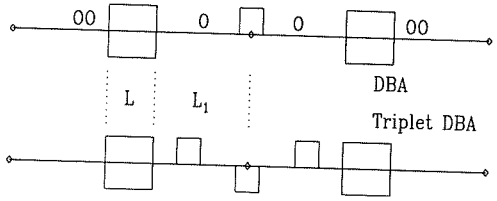

Figure 2.30: Schematic plots of DBA cells. Upper plot: standard DBA cell, where O and OO can contain doublets or triplets for optical match. Lower plot: triplet DBA, where the quadrupole triplet is arranged to attain betatron and dispersion function match of the entire module.

We consider a simple DBA cell with a single quadrupole in the middle. In thin-lens approximation, the dispersion matching condition is (see Exercise 2.4.13)

$$\begin{pmatrix} D_c \\ 0 \\ 1 \end{pmatrix} = \begin{pmatrix} 1 & 0 & 0 \\ -1/(2f) & 1 & 0 \\ 0 & 0 & 1 \end{pmatrix} \begin{pmatrix} 1 & L_1 & 0 \\ 0 & 1 & 0 \\ 0 & 0 & 1 \end{pmatrix} \begin{pmatrix} 1 & L & L\theta/2 \\ 0 & 1 & \theta \\ 0 & 0 & 1 \end{pmatrix} \begin{pmatrix} 0 \\ 0 \\ 1 \end{pmatrix}, \tag{2.279}$$

where f is the focal length of the quadrupole, θ and L are the bending angle and length of the dipole, and L_1 is the distance from the end of the dipole to the center of the quadrupole. The zero dispersion value at the entrance to the dipole is matched to a *symmetric* condition $D_c' = 0$ at the center of the focusing quadrupole. The required focal length and the resulting dispersion function become

$$f = \frac{1}{2}\left(L_1 + \frac{1}{2}L\right), \quad D_c = \left(L_1 + \frac{1}{2}L\right)\theta. \tag{2.280}$$

Note that the focal length needed in the dispersion function matching condition is independent of the dipole bending angle in thin-lens approximation, and it can easily be obtained from the geometric argument. The dispersion function at the symmetry point is proportional to the product of the effective length of the DBA cell and the bending angle.

Although this simple example shows that a single focusing quadrupole can attain dispersion matching, the betatron function depends on the magnet arrangement in the [OO] section, and possible other quadrupoles in the dispersion matching section. The dispersion matching condition of Eq. (2.280) renders a horizontal betatron phase advance Φ_x larger than π in the dispersion matching section (from the beginning of the dipole to the other end of the other dipole). The stability condition of betatron motion (see Sec. II.6) indicates that betatron function matching section [OO] can not

be made of a simple defocussing quadrupole. A quadrupole doublet, or a triplet, is usually used in the [OO] section. Such DBA lattice modules have been widely applied in the design of electron storage rings.

A simple DBA cell is the triplet DBA (lower plot of Fig. 2.30), where a quadrupole triplet is located symmetrically inside two dipoles. This compact lattice was used for the SOR ring in Tokyo. Some properties of the triplet DBA storage ring can be found in Exercise 4.3.6.

B. Other achromat modules

The beam transport system in a synchrotron or a storage ring requires proper dispersion function matching. The design strategy is to use achromatic subsystems. An example of achromatic subsystem is the unit matrix module (see Sec. IV.4 on the first order achromat theorem). A unit matrix module can be made of FODO or other basic cells such that the total phase advance of the entire module is equal to an integer multiple of 2π. Achromatic modules can be optically matched with straight sections to form an accelerator lattice.

The achromatic transport modules are also important in the transport beamlines (see Exercises 2.4.13 to 2.4.16). The achromatic transport system find applications in high energy and nuclear physics experiments, medical radiation treatment, and other beam delivering systems.

IV.6 Transport Notation

In many applications, the particle coordinates in an accelerator can be characterized by a state vector

$$\vec{W} = \begin{pmatrix} W_1 \\ W_2 \\ W_3 \\ W_4 \\ W_5 \\ W_6 \end{pmatrix} = \begin{pmatrix} x \\ x' \\ z \\ z' \\ \beta c \Delta t \\ \delta \end{pmatrix}, \tag{2.281}$$

where βc is the speed of the particle, $\beta c \Delta t$ is the path length difference with respect to the reference orbit, and $\delta = \Delta p/p_0$ is the fractional momentum deviation of a particle.

The transport of the state vector in linear approximation is given by

$$W_i(s_2) = \sum_{j=1}^{6} R_{ij}(s_2|s_1)\, W_j(s_1), \quad (i, j = 1, \cdots, 6). \tag{2.282}$$

Note that the 2×2 diagonal matrices for the indices 1,2, and 3,4 are respectively the horizontal and vertical M matrices. The $R_{13}, R_{23}\ R_{14}, R_{24}$ elements describe the linear

betatron coupling. The R_{16}, R_{26} elements are the dispersion vector $\vec{d}$ of Eq. (2.275). Without synchrotron motion, we have $R_{55} = R_{66} = 1$. All other elements of the R matrix are zero.

In general, the nonlinear dependence of the state vector can be expanded as

$$\begin{aligned} W_i(s_2) &= \sum_{j=1}^{6} R_{ij} W_j(s_1) + \sum_{j=1}^{6}\sum_{k=1}^{6} T_{ijk} W_j(s_1) W_k(s_1) \\ &\quad + \sum_{j=1}^{6}\sum_{k=1}^{6}\sum_{l=1}^{6} U_{ijkl} W_j(s_1) W_k(s_1) W_l(s_1) + \cdots . \end{aligned} \tag{2.283}$$

For example, particle transport through a thin quadrupole is given by

$$\Delta x' = -\frac{x}{f(1+\delta)} = -\frac{x}{f} + \frac{x\delta}{f} - \frac{x\delta^2}{f} + \cdots,$$
$$\Delta z' = \frac{z}{f(1+\delta)} = \frac{z}{f} - \frac{z\delta}{f} + \frac{z\delta^2}{f} + \cdots,$$

and we obtain

$$R_{21} = -\frac{1}{f}, \quad T_{216} = +\frac{1}{f}, \quad U_{2166} = -\frac{1}{f},$$
$$R_{43} = +\frac{1}{f}, \quad T_{436} = -\frac{1}{f}, \quad U_{4366} = +\frac{1}{f}.$$

Similarly, particle transport through a thin sextupole is given by

$$\Delta x' = -\frac{S}{2(1+\delta)}(x^2 - z^2),$$
$$\Delta z' = \frac{S}{1+\delta} xz,$$

where $S = -B_2\ell/B\rho$ is the integrated sextupole strength. Here we used the convention that $S > 0$ corresponds to a focusing sextupole. The corresponding transport matrix elements are

$$T_{211} = -\frac{S}{2}, \quad T_{233} = \frac{S}{2}, \quad T_{413} = S, \quad \cdots .$$

Tracing the transport in one complete revolution, we get the momentum compaction factor as $\alpha_c = R_{56}$. The program TRANSPORT[66] has often been used to calculate the transport coefficients in transport lines.

[66]K.L. Brown, D.C. Carey, Ch. Iselin and F. Rothacker, CERN 80-04 (1980); D.C. Carey, FNAL Report TM-1046 (1981); D.C. Carey *et al.*, SLAC-R-530, Fermilab-Pub-98-310 (1998).

IV.7 Experimental Measurements of Dispersion Function

Digitized BPM turn by turn data can be used to measure the betatron motion. On the other hand, if the BPM signals are sampled at a longer time scale, the fast betatron oscillations are averaged to zero. The DC output provides the closed orbit of the beam. The dispersion function can be measured from the derivative of the closed orbit with respect to the off-momentum of the beam, i.e.

$$D = \frac{dx_{co}}{d(\Delta p/p_0)} = -\eta\, f_0 \frac{dx_{co}}{df_0}, \tag{2.284}$$

where x_{co} is the closed orbit, f_0 is the revolution frequency, η is the phase-slip factor, and the momentum of the beam is varied by changing the rf frequency.

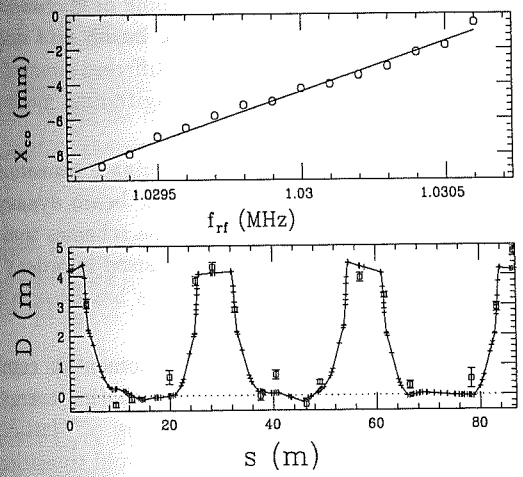

Figure 2.31: The upper plot shows the closed orbit at a BPM vs the rf frequency for the IUCF Cooler Ring. The slope of this measurement is used to obtain the "measured" dispersion function. The lower plot compares the measured dispersion function (rectangles) with that obtained from the MAD program (solid line).

The upper plot of Fig. 2.31 shows the closed orbit at a BPM location vs the rf frequency at the IUCF Cooler Ring. Using Eq. (2.284), we can deduce the dispersion function at the BPM location. In the lower plot of Fig. 2.31 the "measured" dispersion functions of the IUCF Cooler Ring is compared with that obtained from the MAD program [19].[67] The accuracy of the dispersion function measurement depends on the precision of the BPM system, and also on the effects of power supply ripple. To improve the accuracy of the dispersion function measurement, we can induce frequency modulation to the rf frequency shift. The resulting closed orbit will have the characteristic modulation frequency. Fitting the resulting closed orbit with the known modulation frequency, we can determine the dispersion function more accurately.

[67]Note here that the IUCF Cooler Ring lattice belongs generally to the class of double-bend achromats (see Exercise 2.4.13). A high dispersion straight section is used for momentum-stacking injection and zero dispersion straight sections are used for rf and electron cooling.

IV.8 Transition Energy Manipulation

Medium energy accelerators often encounter problems during transition energy crossing, such as longitudinal microwave instability and nonlinear synchrotron motion. These problems can be avoided by an accelerator having a negative momentum compaction factor. The revolution period deviation ΔT for an off-momentum particle $\Delta p = p - p_0$ is given by Eq. (2.268). The accelerator becomes isochronous at the transition energy ($\gamma = \gamma_T$).

There are many unfavorable effects on the particle motion near the transition energy. For example, the momentum spread of a bunch around transition can become so large that it exceeds the available momentum aperture, causing beam loss (see Chap. 3, Sec. IV). Since the frequency spread of the beam $\Delta\omega = -\eta\omega(\Delta p/p_0)$ vanishes at the transition energy, there is little or no Landau damping of microwave instability near transition (see Chap. 3, Sec. VII). As a result, the bunch area may grow because of collective instabilities. Furthermore, particles with different momenta may cross transition at different times, which leads to unstable longitudinal motion resulting in serious beam loss.

To avoid all the above unfavorable effects, it is appealing to eliminate transition crossing. The γ_T jump schemes have been used successfully to ease beam dynamics problems associated with the transition energy crossing; in these schemes some quadrupoles are pulsed so that the transition energy is lowered or raised in order to enhance the acceleration rate at the transition energy crossing. This has become a routine operation at the CERN Proton Synchrotron (PS).

Alternatively, one can design an accelerator lattice such that the momentum compaction factor α_c is negative, and thus the beam never encounters transition energy. This is called the "negative momentum compaction" or the "imaginary γ_T" lattice. All modern medium energy synchrotrons can be designed this way to avoid transition energy. We discuss below the methods of α_c manipulation, the transition energy jump scheme, and the design principle of the imaginary γ_T lattices.

A. γ_T jump schemes

In many existing low to medium energy synchrotrons, particle acceleration through the transition energy is unavoidable. Finding a suitable γ_T jump scheme can provide beam acceleration through transition energy without much emittance dilution and beam loss. Here we examine the strategy of γ_T jump schemes pioneered by the CERN PS group.[68]

[68] W. Hardt, *Proc. 9th Int. Conf. on High Energy Accelerators* (USAEC, Washington, DC, 1974). See also T. Risselada, *Proc. CERN Accelerator School*, CERN-91-04, p. 161, 1991.

In the presence of dipole field error, the closed orbit is

$$\Delta x_{co}(s) = \int_s^{s+C} G_x(s, s_0)\frac{\Delta B}{B\rho}ds_0 \approx \sum_i G_x(s, s_i)\theta_{k,i}, \tag{2.285}$$

where $\theta_{k,i}$ is the dipole angular kick in thin-lens approximation, and $G_x(s, s_0)$ is the Green's function of Eq. (2.159). Similarly, the dispersion function is given by

$$D(s_0) = \int_0^C \frac{G_x(s, s_0)}{\rho(s)}ds \approx \sum_i G_x(s_i, s_0)\theta_i, \tag{2.264}$$

where θ_i is the dipole angle. Note here that the kick angle θ_i from quadrupoles at nonzero-dispersion function locations can be used to perturb the dispersion function and change the orbit length for off-momentum particles.

A.1 The effect of quadrupole field errors on the closed orbit

Consider N quadrupoles for the γ_T jump. We would like to evaluate the change of orbit length for off-momentum particles due to the γ_T jump quadrupoles. From Hill's equation, the angular kick resulting from the ith γ_T jump quadrupole is given by

$$\theta_i = -K_i\ [x_{co}(s_i) + D_i^*\delta], \tag{2.286}$$

where $K_i = -B_1\ell/B\rho$ is the strength of the ith γ_T jump quadrupole, assumed positive for a focusing quadrupole, and D_i^* is the perturbed dispersion function at $s = s_i$. Thus the change of the orbit length for the off-momentum particle is given by

$$\Delta C \approx \sum_i D_i\theta_i \approx -\left(\sum_i K_i D_i^* D_i\right)\delta, \tag{2.287}$$

where D_i is the unperturbed dispersion function, and we neglect higher-order terms in δ. Equation (2.287) indicates that quadrupoles at nonzero dispersion locations can be used to adjust the momentum compaction factor.

If N γ_T-jump quadrupoles are used to change the momentum compaction factor, we obtain

$$C_0\Delta\alpha_c = -\sum_{i=1}^N K_i D_i^* D_i. \tag{2.288}$$

Note that the change in momentum compaction (called γ_T jump) depends on the unperturbed and perturbed dispersion functions at kick-quadrupole locations. An important constraint is that the betatron tunes should be maintained constant during the γ_T jump in order to avoid nonlinear betatron resonances, i.e.

$$\Delta Q_x = \frac{1}{4\pi}\sum_{i=1}^N \beta_{x,i}K_i = 0, \quad \Delta Q_z = -\frac{1}{4\pi}\sum_{i=1}^N \beta_{z,i}K_i = 0. \tag{2.289}$$

Thus we usually employ zero tune shift quadrupole pairs for the γ_T jump.

A.2 The perturbed dispersion function

The change in the closed orbit resulting from the quadrupole kicks can be obtained by substituting Eq. (2.286) into Eq. (2.285):

$$[D^*(s) - D(s)]\,\delta = -\sum_i G_x(s, s_i) K_i D_i^*\,\delta. \tag{2.290}$$

Thus the closed orbit solution is

$$D_j^* = D_j + \sum_i F_{ji} D_i^*, \tag{2.291}$$

where $F_{ji} = -G_x(s_j, s_i)K_i$. The perturbed dispersion function at these quadrupole locations can be solved to obtain

$$\vec{D}^* = (1 - F)^{-1}\vec{D} = (1 + F + F^2 + F^3 + \ldots)\vec{D}. \tag{2.292}$$

The resulting change in momentum compaction becomes

$$C_0 \Delta\alpha_c = -\sum_{ij}^{N} K_i (1 + F + F^2 + \ldots)_{ij} D_j D_i. \tag{2.293}$$

A.3 γ_T jump using zero tune shift π-doublets

When zero tune shift pairs of quadrupoles separated by π in the betatron phase advance are used to produce a γ_T jump, the matrix F satisfies

$$F^n = 0 \quad \text{for} \quad n \geq 2. \tag{2.294}$$

This result can be easily proved by using the zero tune shift condition: $\beta_{x,k}K_k + \beta_{x,k+1}K_{k+1} = 0$ and the π phase advance condition:

$$\cos(\pi\nu_x - |\psi_k - \psi_j|) = -\cos(\pi\nu_x - |\psi_{k+1} - \psi_j|),$$
$$\cos(\pi\nu_x - |\psi_i - \psi_k|) = -\cos(\pi\nu_x - |\psi_i - \psi_{k+1}|).$$

Using the π-doublets, the perturbed dispersion function becomes

$$D_i^* = (1 + F)_{ij} D_j, \tag{2.295}$$

and the change in the momentum compaction factor is given by

$$C_0 \Delta\alpha_c = -\sum_i K_i D_i^2 + \sum_{ij} K_i K_j G_x(s_i, s_j) D_i D_j. \tag{2.296}$$

Here three points are worth mentioning:

1. The change in the dispersion function is linear in K, i.e.

$$\Delta D_i = D_i^* - D_i = -G_x(s_i, s_j) K_j D_j.$$

2. The change in the momentum compaction factor contains a linear and a quadratic term in K. If the γ_T jump quadrupole pairs are located in the arc, where the unperturbed dispersion function is dominated by the zeroth harmonic in the Fourier decomposition, the term linear in K_i vanishes because of the zero tune shift condition.[69] The resulting change in the momentum compaction factor is a quadratic function of K_i.
3. Since the stopband integral of Eq. (2.201) at $p = [2\nu_x]$ due to the tune jump quadrupole pair is zero because of the zero tune shift condition, the π-doublet does not produce a large perturbation in the betatron amplitude function.

Thus if all quadrupoles used for γ_T jump are located in FODO cells, the amount of tune jump is second order in the quadrupole strength. On the other hand, γ_T jump using quadrupoles in straight sections can be made linear in quadrupole strength.

B. Flexible momentum compaction (FMC) lattices

Alternatively, a lattice having a *very small* or even *negative* momentum compaction factor can also be designed. Vladimirskij and Tarasov[70] introduced reverse bends in an accelerator lattice and succeeded in getting a negative orbit-length increase with momentum, thus making a negative momentum compaction factor. Another method of designing an FMC lattice is called the *harmonic approach.*[71] In this method a systematic closed-orbit stopband is created near the betatron tune to induce dispersion-wave oscillations resulting in a high γ_T or an imaginary γ_T. However, the resulting lattice is less tunable and the dispersion functions can be large. Thus the dynamical aperture may be reduced accordingly.

In 1972, Teng proposed an innovative scheme using negative dispersion at dipole locations, where the dispersion function can be matched by a straight section with a phase advance of π to yield little or no contribution to positive orbit-length increment.[72] This concept is the basis for *flexible momentum compaction* (FMC) lattices, which require parts of the lattice to have negative dispersion functions.

---

[69] This statement can be expressed mathematically as follows. If the zeroth harmonic term dominates, we have $D_i^2 \propto \beta_i$, and thus $\sum_i K_i D_i^2 \propto \sum_i K_i \beta_i = 0$ because of the zero tune shift condition.

[70] V.V. Vladimirski and E.K. Tarasov, *Theoretical Problems of the Ring Accelerators* (USSR Academy of Sciences, Moscow, 1955).

[71] R. Gupta and J.I.M. Botman, *IEEE Trans. Nucl. Sci.* **NS-32**, 2308 (1985); T. Collins, *Beta Theory*, Technical Memo, Fermilab (1988); G. Guignard, *Proc. 1989 IEEE PAC*, p. 915 (1989); E.D. Courant, A.A. Garren, and U. Wienands, *Proc. 1991 IEEE PAC*, p. 2829 (1991).

[72] L.C. Teng, *Part. Accel.* **4**, 81 (1972).

Recently, Trbojevic *et al.*[73] re-introduced a *modular approach* for the FMC lattice with a prescribed dispersion function. The dispersion phase-space maps are carefully matched to attain a lattice with a pre-assigned γ_T value. The module forms the basic building blocks for a ring with a negative momentum compaction factor or an imaginary γ_T. The module can be made very compact without much unwanted empty space and, at the same time, the maximum value of the dispersion function can be optimized to less than that of the FODO lattice.

For attaining proper dispersion function matching, the normalized dispersion coordinates X_d and P_d of Eq. (2.260) are handy, i.e.

$$X = \frac{1}{\sqrt{\beta_x}} D = \sqrt{2J_d}\cos\psi_d, \qquad P = \sqrt{\beta_x} D' + \frac{\alpha_x}{\sqrt{\beta_x}} D = -\sqrt{2J_d}\sin\psi_d.$$

In the thin-element approximation, Eq. (2.244) indicates that $\Delta D = 0$ and $\Delta D' = \theta$ in passing through a thin dipole with bending angle θ. Therefore, in normalized P_d-X_d space, the normalized dispersion vector changes by $\Delta P = \sqrt{\beta_x}\theta$ and $\Delta X = 0$. Outside the dipole ($\rho = \infty$), the dispersion function satisfies the homogeneous equation, and the dispersion action J_d is invariant, i.e. P_d and X_d lie on a circle $P^2 + X^2 = 2J_d$. The phase angle ψ_d of the normalized coordinates is equal to the betatron phase advance. This dispersion phase-space plot can be helpful in the design of lattices and beam-transfer lines. It has also been used to lower the dispersion excursion during a fast γ_T jump at RHIC.[74]

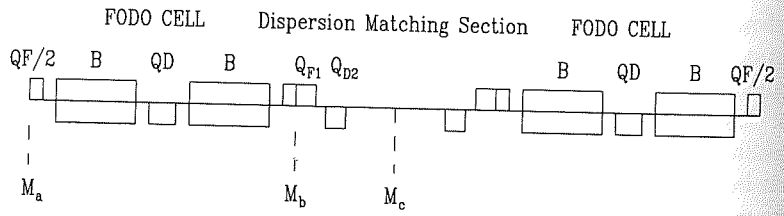

Figure 2.32: A schematic drawing of a basic module made of two FODO cells and an optical matching section.

B.1 The basic module and design strategy

A basic FMC module has two parts: (1) the FODO or DOFO cell, where the negative dispersion function in dipoles provides a negative momentum compaction factor, and

[73]D. Trbojevic, D. Finley, R. Gerig, and S. Holmes, *Proc. 1990 EPAC*, p. 1536 (1990); K.Y. Ng, D. Trbojevic, and S.Y. Lee, *Proc. 1991 PAC*, p. 159 (1991); S.Y. Lee, K.Y. Ng, and D. Trbojevic, Fermilab Internal Report FN-595 (1992); S.Y. Lee, K.Y. Ng, and D. Trbojevic, *Phys. Rev.* E48, 3040 (1993).

[74]D. Trbojevic, S. Peggs, and S. Tepikian, *Proc. 1993 IEEE Part. Accel. Conf.* p. 168 (1993).

(2) a matching section that matches the optical functions. We also assume reflection symmetry for all Courant-Snyder functions at symmetric points of the module. Although not strictly necessary, reflection symmetry considerably simplifies the analysis and optical matching procedure. For example, we consider a basic module composed of two FODO cells and a dispersion matching section shown schematically in Fig. 2.32:

$$\mathrm{M_a}\left\{\frac{1}{2}\mathrm{QF}\,B\,\mathrm{QD}\,B\,\frac{1}{2}\mathrm{QF}\right\}\mathrm{M_b}\ \{\mathrm{Q_{F_1}}\ \mathrm{O_1}\ \mathrm{Q_{D_2}}\ \mathrm{O_2}\}\ \mathrm{M_c}\ +\ \text{reflection symmetry}\ ,$$

where $\mathrm{M_{a,b,c}}$ are marker locations, Q's are quadrupoles, O's are drift spaces, and B's stand for dipoles. The horizontal betatron transfer matrix of the FODO cell from the marker $\mathrm{M_a}$ to the marker $\mathrm{M_b}$ is given by [see Eq. (2.257) and Exercise 2.4.3]

$$M_{\mathrm{FODO}} = \begin{pmatrix} \cos\Phi & \beta_{\mathrm{F}}\sin\Phi & D_{\mathrm{F}}(1-\cos\Phi) \\ -\frac{1}{\beta_{\mathrm{F}}}\sin\Phi & \cos\Phi & \frac{D_{\mathrm{F}}}{\beta_{\mathrm{F}}}\sin\Phi \\ 0 & 0 & 1 \end{pmatrix}, \tag{2.297}$$

where, for simplicity, we have chosen $\Phi_x = \Phi_z = \Phi$ for the betatron phase advance of the FODO cell, β_{F} and D_{F} are respectively the betatron amplitude and dispersion functions at the center of the focusing quadrupole for the regular FODO cell, and a symmetry condition $\beta'_{\mathrm{F}} = 0$ and $D'_{\mathrm{F}} = 0$ is assumed to simplify our transfer matrix in Eq. (2.297).

The procedure of betatron amplitude function matching is given as follows. First, the desired value D_a of the dispersion function at the marker M_a is chosen; the dispersion function is propagated through FODO cell to obtained a dispersion vector at the marker M_b. Then, the dispersion function is matched in the matching section. Figure 2.33 shows the betatron amplitude functions for a matched FMC basic module with an added dipole in dispersion matching section in order to increase the packing factor.[75] Because the dispersion function inside dipoles in FODO cells is mostly negative, the resulting momentum compaction factor can become negative. Adjusting the initial dispersion function value D_a, the momentum compaction factor of the accelerator can be varied.

Figure 2.34 shows an example of dispersion function matching for an FMC module by plotting the normalized dispersion phase-space coordinates X_d vs P_d. A negative-momentum-compaction module requires $X_d < 0$ in dipoles as demonstrated in the left plot of Fig. 2.34. The right plot shows a similar plot in thin-lens approximation. Although they look slightly different, the thin-element approximation can provide essential insight in the preliminary design where dispersion matching is required. Since there is no dipole in this example shown in Fig. 2.32, the dispersion phase-space coordinates are located on a circle as shown in Fig. 2.34. If the lattice has a reflection symmetry at the marker M_c, the matched dispersion phase-space coordinate is $P_d = 0$. Detailed matching process is given in following subsections.

[75]The packing factor is defined as the fraction of the circumference of an accelerator that is occupied by magnets.

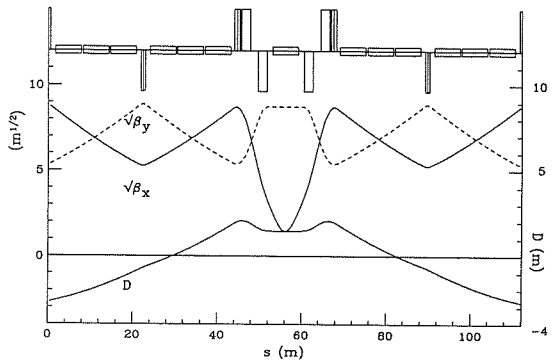

Figure 2.33: The lattice function of an FMC basic module. In this example, a dipole is added in the middle of dispersion matching section in order to increase the machine packing factor. Although the dipole in the matching section will contribute a positive value to the momentum compaction. The overall compaction factor can still be adjusted by a properly chosen D_a.

B.2 Dispersion matching

The dispersion function at the beginning of the FODO cell is *prescribed* to have a negative value of D_a with $D'_a = 0$. As we shall see, the choice of D_a essentially determines the dispersion excursion and the γ_T value of the module. Using the transfer matrix in Eq. (2.297), we find the dispersion function at marker M_b to be

$$D_b = D_F - (D_F - D_a)\cos\Phi, \quad D'_b = \frac{D_F - D_a}{\beta_b}\sin\Phi\,, \tag{2.298}$$

where β_b is the betatron amplitude function at marker M_b with $\beta_b = \beta_F$. Now we assume that there is no dipole in the matching section, and the dispersion action is invariant in this region, i.e.

$$J_{d,c} = J_{d,b} = \frac{1}{2}\left[\frac{D_b^2}{\beta_b} + \beta_b D_b'^2\right] = J_{d,F}[1 - 2(1-\zeta)\cos\Phi + (1-\zeta)^2]\,, \tag{2.299}$$

where $\zeta = D_a/D_F$ is the ratio of the desired dispersion at marker M_a to the dispersion function of the regular FODO cell, $J_{d,b}, J_{d,c}$ are dispersion actions at markers M_b and M_c, and $J_{d,F}$ is the dispersion action of the regular FODO cell at the focusing quadrupole location, given in thin-lens approximation by

$$J_{d,F} = \frac{1}{2}\left[L\theta^2\,\frac{\cos\frac{\Phi}{2}(1+\frac{1}{2}\sin\frac{\Phi}{2})^2}{\sin^3\frac{\Phi}{2}(1+\sin\frac{\Phi}{2})}\right]. \tag{2.300}$$

Figure 2.35 shows $\sqrt{J_{d,b}/J_{d,F}}$ as a function of ζ for various values of phase advance per cell. The ratio of the dispersion action has a minimum at $\zeta = 1 - \cos\Phi$, and it increases when the initial dispersion D_a at marker M_a is chosen to be more negative. It is preferable to have a smaller dispersion action in the matching section in order to minimize the dispersion function of the module.

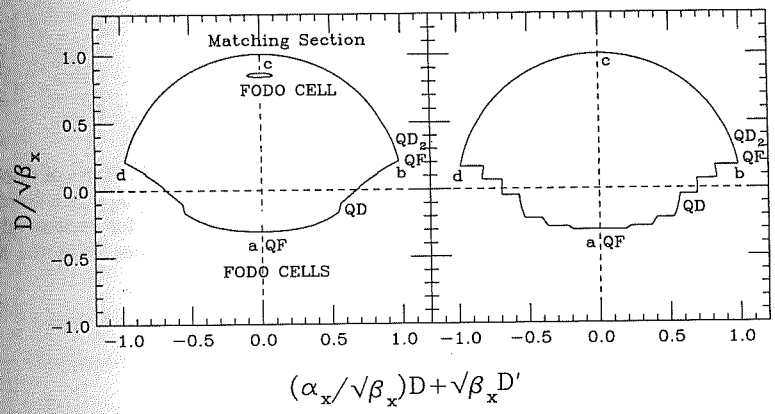

Figure 2.34: Left: an example of dispersion matching for a basic FMC module, where the normalized dispersion phase-space coordinates $X_d = D/\sqrt{\beta_x}$ vs $P_d = (\alpha_x/\sqrt{\beta_x})D + \sqrt{\beta_x}D'$ are shown. The normalized dispersion phase-space coordinates for periodic FODO cells are marked "FODO CELLS." The corresponding thin-lens approximation for the FMC is shown in the right plot, where horizontal steps are associated with a dipole that is divided into three segments. There is no dipole in the matching section and thus the normalized phase-space contour is a perfect circle in the matching section.

One might conclude from Fig. 2.35 that a smaller phase advance in the FODO cell would be preferred. This can be true if we compare the dispersion of the basic module with that of the regular FODO lattice with the same phase advance. However, the dispersion amplitude $\sqrt{2J_{d,F}}$ in Eq. (2.300) is inversely proportional to $(\sin(\Phi/2))^{3/2}$, and thus we should choose a larger phase advance for the FODO cell in order to obtain a smaller overall $\sqrt{2J_{d,c}}$. A compromise choice for the phase advance of the FODO cell is between 60° and 75°.

The dispersion functions and other Courant-Snyder parameters are then matched at the symmetry point at marker M_c with a doublet (or triplet). The betatron transfer matrix for the matching section is

$$M_{b\to c} = \begin{pmatrix} \sqrt{\frac{\beta_c}{\beta_b}}\cos\psi & \sqrt{\beta_b\beta_c}\sin\psi & 0 \\ -\frac{1}{\sqrt{\beta_b\beta_c}}\sin\psi & \sqrt{\frac{\beta_b}{\beta_c}}\cos\psi & 0 \\ 0 & 0 & 1 \end{pmatrix}, \tag{2.301}$$

where β_b and β_c are values of the betatron amplitude function at markers M_b and M_c, ψ is the betatron phase advance between M_b and M_c, and we have assumed the symmetry conditions $\beta'_b = 0$ and $\beta'_c = 0$ for the Courant-Snyder parameters.

The dispersion matching condition at marker M_c is $D'_c = 0$. Using Eq. (2.298), we obtain

$$\tan\psi = \frac{(1-\zeta)\sin\Phi}{1-(1-\zeta)\cos\Phi}\,. \tag{2.302}$$

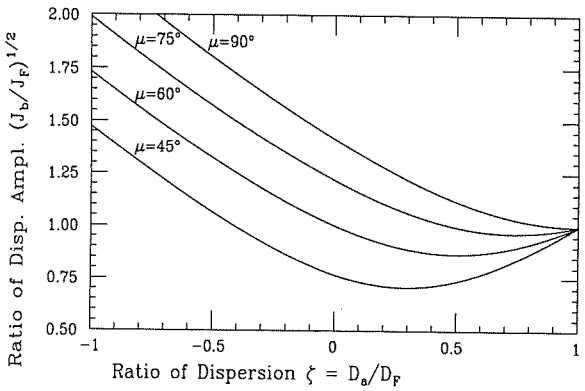

Figure 2.35: Ratio of dispersion actions $J_{d,b}/J_{d,F}$ as a function of $\zeta = D_a/D_F$ for various values of phase advance Φ in the FODO cell.

This means that the phase advance of the matching section is not a free parameter, but is determined completely by the initial dispersion value D_a at marker M_a and the phase advance of the FODO cell. This condition is independent of whether we use a FODO-type insertion, or a low-beta insertion with doublets or triplets for the matching section. Furthermore, the phase advance ψ and the quadrupole strengths in the dispersion matching section are constrained by the stability condition of betatron motion (see Sec. II.6 and Exercise 2.4.17). Figure 2.36 shows the required betatron phase advance 2ψ (in unit of 2π) in the matching section as a function of phase advance Φ of the FODO cell for various values of $\zeta = D_a/D_F$.

The total phase advance of the whole basic module is then given by $2(\Phi + \psi)$, which is a function only of the desired dispersion function at marker M_a and the phase advance Φ in the FODO cell. Figure 2.36 shows the total phase advance of the whole module as a function of the phase advance of the FODO cell for $\zeta = -0.3$ to -0.6. Quadrupoles Q_{F_1} and Q_{D_2} in the matching section can be adjusted to attain the required phase advance ψ given by Eq. (2.302) and to produce low betatron amplitude functions at marker M_c. To achieve a $\frac{3}{2}\pi$ phase advance for a quarter-wave module, $\zeta \approx -0.3 \sim -0.4$ and a phase advance per FODO cell of $\Phi = 60°$ to $75°$ can be used.

B.3 Evaluation of momentum compaction factor

In small-angle approximation, the values of the dispersion function at the midpoints of dipoles in the FODO cell are given by

$$\begin{cases} D_{B_1} = D_a(1 - \frac{1}{2}\sin(\Phi/2)) + D_F \dfrac{\sin^2(\Phi/2)}{8 + 4\sin(\Phi/2)}, \\ D_{B_2} = D_a(1 - \frac{1}{2}\sin(\Phi/2) - \sin^2(\Phi/2)) + D_F \dfrac{(9 + 4\sin(\Phi/2))\sin^2(\Phi/2)}{8 + 4\sin(\Phi/2)}. \end{cases} \tag{2.303}$$

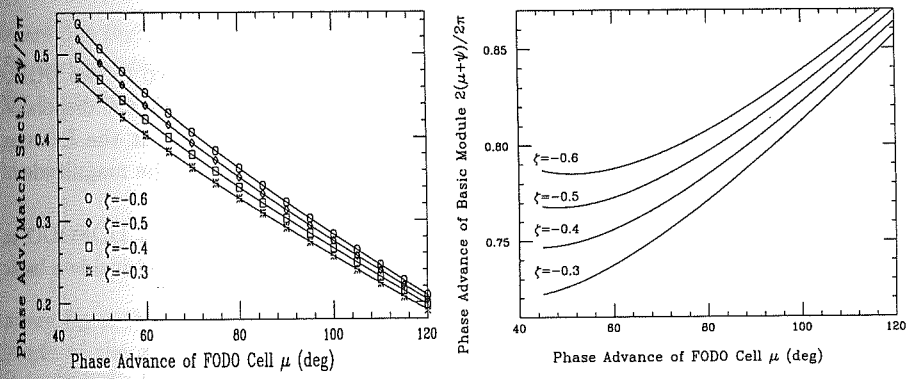

Figure 2.36: Left: Phase advance in the matching section as a function of phase advance Φ in the FODO cell for various values of $\zeta = D_a/D_F$. Right: The total phase advance of a FMC module as a function of the phase Advance Φ in the FODO cell for various values of $\zeta = D_a/D_F$.

The momentum compaction becomes

$$\alpha_c = \frac{(D_{B_1} + D_{B_2})}{L_m}\theta = \frac{D_F\theta}{L_m}\left[(1 - \sin\frac{\Phi}{2} - \sin^2\frac{\Phi}{2})\zeta + \frac{(5 + 2\sin\frac{\Phi}{2})\sin^2\frac{\Phi}{2}}{4 + 2\sin\frac{\Phi}{2}}\right], \tag{2.304}$$

where θ is the bending angle of each dipole and L_m is the length of the half-module. In comparison with the momentum compaction factor of a lattice made of conventional FODO cells, we obtain

$$\frac{\alpha_c}{\alpha_{c,\mathrm{FODO}}} = \frac{2L}{L_m}\left[\frac{4 - 2S - 6S^2 - 2S^3}{4 - 2S - S^2}\zeta + \frac{S^2(5 + 2S)}{4 - 2S - S^2}\right], \tag{2.305}$$

where $S = \sin(\Phi/2)$. Note that the momentum compaction factor of the module is determined entirely by the choice of D_a, the phase advance of the FODO cell, and the ratio of the lengths of the FODO cell and the module. When the length of the module is constant, the momentum compaction factor depends linearly on the initial dispersion function D_a. If the horizontal phase advance Φ_x of the FODO cell differs from its vertical phase advance Φ_z, Eqs. (2.303) should be modified as follows:

$$\begin{cases} D_{B_1} = D_a\left[1 - \frac{1}{8}(\sqrt{S_-^2 + 8S_+} + S_-)\right] + \frac{1}{8}L\theta, \\ D_{B_2} = D_a\left[1 - \frac{3}{8}(\sqrt{S_-^2 + 8S_+} + S_-) + \frac{1}{4}(\sqrt{S_-^2 + 8S_+} - S_-) - \frac{1}{2}S_+\right] \\ \quad + L\theta\left[\frac{9}{8} + \frac{1}{8}(\sqrt{S_-^2 + 8S_+} - S_-)\right], \end{cases} \tag{2.306}$$

where $S_\pm = \sin^2\frac{1}{2}\Phi_x \pm \sin^2\frac{1}{2}\Phi_z$. The momentum compaction factor should be modified accordingly.

C. Other similar FMC modules

The above analysis can be applied to a basic FMC module composed of two DOFO cells and a dispersion matching section (see Exercise 2.4.17). Because the dispersion value at the defocussing quadrupole location is smaller than that at the focusing quadrupole location, a slightly smaller $|\zeta|$ can be used to minimize the magnitude of the dispersion function in the module.

To design a lattice with a higher packing factor,[76] one may use a DOFODO in place of the FODO cell, i.e. three FODO cells instead of two are placed inside a basic module. The betatron transfer matrix in the DOFODO cell becomes

$$M_{a\to b} = \begin{pmatrix} \sqrt{\frac{\beta_F}{\beta_D}}\cos\frac{3}{2}\Phi & \sqrt{\beta_F\beta_D}\sin\frac{3}{2}\Phi & D_F - D_D\sqrt{\frac{\beta_F}{\beta_D}}\cos\frac{3}{2}\Phi \\ -\frac{1}{\sqrt{\beta_F\beta_D}}\sin\frac{3}{2}\Phi & \sqrt{\frac{\beta_D}{\beta_F}}\cos\frac{3}{2}\Phi & \frac{D_D}{\sqrt{\beta_F\beta_D}}\sin\frac{3}{2}\Phi \\ 0 & 0 & 1 \end{pmatrix}, \tag{2.307}$$

where Φ is the phase advance of a FODO cell, and β_F, β_D, D_F, D_D are the betatron amplitudes and dispersion values at the focusing and defocussing quadrupoles of the FODO cell. A similar analysis with a different number of FODO cells can be easily done. In general, the result will be a larger total dispersion value.

D. FMC in double-bend (DB) lattices

A double-bend module (Fig. 2.30) is made of two dipoles located symmetrically with respect to the center of the basic module given by

$$\mathrm{M_a}\begin{pmatrix}\text{Triplet}\\ \text{or}\\ \text{Doublet}\end{pmatrix}\mathrm{B}\ \{\text{dispersion matching section}\}\ \mathrm{M_c} + \{\text{reflection symmetry}\}.$$

A triplet or doublet matching section on the left side of the dipole B is the betatron amplitude matching section. If the achromat condition is imposed, the module is called a double-bend achromat (DBA). The zero dispersion region is usually used for insertion devices such as the undulator, the wiggler, and rf cavities. The dispersion matching section on the right side of the dipole can be made of a single quadrupole, a doublet, or a triplet.

The dispersion function inside a sector dipole is given by

$$D(s) = \rho(1-\cos\phi) + D_0\cos\phi + \rho D_0'\sin\phi, \tag{2.308}$$

$$D'(s) = \sin\phi - \frac{D_0}{\rho}\sin\phi + D_0'\cos\phi, \tag{2.309}$$

[76] The packing factor of a lattice is defined as the ratio of the total dipole length to the circumference.

where ρ is the bending radius of the dipole, $\phi = s/\rho$ is the bend angle, and D_0 and D_0' are respectively the values of the dispersion function and its derivative at $s = 0$. For a matched double-bend module, the momentum compaction is given by

$$\begin{aligned}\alpha_c &= \frac{\rho}{L_m}\left[\theta - \sin\theta + \frac{D_0}{\rho}\sin\theta + D_0'(1-\cos\theta)\right] \\ &= \frac{\rho\theta^3}{L_m}\left(\frac{1}{6} + \frac{D_0}{L\theta} + \frac{D_0'}{2\theta}\right) + \cdots,\end{aligned} \tag{2.310}$$

where L_m is the length of one half of the double-bend module, $\theta = L/\rho$, and L is the length of the dipole. Note here that the momentum compaction factor depends on the initial dispersion function at the entrance of the dipole.

In small-angle approximation, the condition for negative momentum compaction is given by

$$6d_0 + 3d_0' \le -1, \tag{2.311}$$

where $d_0 = D_0/L\theta$, and $d_0' = D_0'/\theta$. The dispersion function in the rest of the module can be matched by quadrupole settings.

Since the DBA module has $D_0 = 0$ and $D_0' = 0$, the momentum compaction in small dipole angle approximation becomes

$$\alpha_{c,\mathrm{DBA}} \approx \frac{\rho\theta^2}{6R} \tag{2.312}$$

where R is the average radius of the storage ring. The momentum compaction factor of a DBA lattice is independent of the betatron tune.

Finally, a reverse-bend dipole placed at the high dispersion straight section can also be used to adjust the momentum compaction factor of a DBA lattice. Such a lattice can provide a small-emittance negative momentum compaction lattice for synchrotron radiation sources.

IV.9 Minimum $\langle\mathcal{H}\rangle$ Modules

In electron storage rings, the natural (horizontal) emittance of the beam is determined by the average of the $\mathcal{H}$-function in the dipoles (see Chap. 4). In this section, the strategy of minimizing $\langle\mathcal{H}\rangle$ inside dipoles will be discussed. To simplify our discussion, we will consider a single dipole lattice unit where the dispersion and betatron amplitude functions can be independently controlled.

The evolution of the $\mathcal{H}$-function in a sector dipole is given by (see Exercise 2.4.11)

$$\begin{aligned}\mathcal{H} &= \mathcal{H}_0 + 2(\alpha_0 D_0 + \beta_0 D_0')\sin\phi - 2(\gamma_0 D_0 + \alpha_0 D_0')\rho(1-\cos\phi) \\ &\quad + \beta_0\sin^2\phi + \gamma_0\rho^2(1-\cos\phi)^2 - 2\alpha_0\rho\sin\phi(1-\cos\phi),\end{aligned} \tag{2.313}$$

where $\mathcal{H}_0 = \gamma_0 D_0^2 + 2\alpha_0 D_0 D_0' + \beta_0 D_0'^2$; $\alpha_0, \beta_0, \gamma_0, D_0$ and D_0' are the Courant-Snyder parameters and dispersion functions at $s = 0$; and $\phi = s/\rho$ is the coordinate of the bending angle inside the dipole. The average $\mathcal{H}$-function in the dipole becomes[77]

$$\begin{aligned}\langle\mathcal{H}\rangle &= \mathcal{H}_0 + (\alpha_0 D_0 + \beta_0 D_0')\theta^2 E(\theta) - \frac{1}{3}(\gamma_0 D_0 + \alpha_0 D_0')\rho\theta^2 F(\theta) \\ &\quad + \frac{\beta_0}{3}\theta^2 A(\theta) - \frac{\alpha_0}{4}\rho\theta^3 B(\theta) + \frac{\gamma_0}{20}\rho^2\theta^4 C(\theta),\end{aligned} \tag{2.314}$$

where θ is the bend angle of the dipole, and

$$E(\theta) = \frac{2(1-\cos\theta)}{\theta^2}, \quad F(\theta) = \frac{6(\theta - \sin\theta)}{\theta^3}, \quad A(\theta) = \frac{6\theta - 3\sin 2\theta}{4\theta^3},$$
$$B(\theta) = \frac{6 - 8\cos\theta + 2\cos 2\theta}{\theta^4}, \quad C(\theta) = \frac{30\theta - 40\sin\theta + 5\sin 2\theta}{\theta^5}.$$

In the small-angle limit, $A \to 1, B \to 1, C \to 1, E \to 1$, and $F \to 1$.

With the normalized scaling parameters

$$d_0 = \frac{D_0}{L\theta}, \quad d_0' = \frac{D_0'}{\theta}, \quad \tilde{\beta}_0 = \frac{\beta_0}{L}, \quad \tilde{\gamma}_0 = \gamma_0 L, \quad \tilde{\alpha}_0 = \alpha_0, \tag{2.315}$$

where $L = \rho\theta$ is the length of the dipole, the average $\mathcal{H}$-function becomes

$$\begin{aligned}\langle\mathcal{H}\rangle &= \rho\theta^3\Big\{\tilde{\gamma}_0 d_0^2 + 2\tilde{\alpha}_0 d_0 d_0' + \tilde{\beta}_0 d_0'^2 + (\tilde{\alpha}_0 E - \frac{\tilde{\gamma}_0}{3}F)d_0 \\ &\quad + (\tilde{\beta}_0 E - \frac{\tilde{\alpha}_0}{3}F)d_0' + \frac{\tilde{\beta}_0}{3}A - \frac{\tilde{\alpha}_0}{4}B + \frac{\tilde{\gamma}_0}{20}C\Big\}.\end{aligned} \tag{2.316}$$

Note that $\langle\mathcal{H}\rangle$ obeys a scaling law, i.e. $\langle\mathcal{H}\rangle \sim \rho\theta^3$.

A. Minimum $\langle\mathcal{H}\rangle$-function with achromat condition

In the special case with the achromat condition $d_0 = 0$ and $d_0' = 0$, the average $\mathcal{H}$-function is

$$\langle\mathcal{H}\rangle = \rho\theta^3\left\{\frac{\tilde{\beta}_0}{3}A - \frac{\tilde{\alpha}_0}{4}B + \frac{\tilde{\gamma}_0}{20}C\right\}. \tag{2.317}$$

Using the condition $\tilde{\beta}_0\tilde{\gamma}_0 = (1 + \tilde{\alpha}_0^2)$, we obtain

$$\langle\mathcal{H}\rangle_{\text{min,A}} = \frac{G}{4\sqrt{15}}\rho\theta^3, \tag{2.318}$$

[77] The average of the $\mathcal{H}$ function is given by

$$\langle\mathcal{H}\rangle = \frac{1}{L}\int_0^L \mathcal{H}(\phi)ds = \frac{1}{\theta}\int_0^\theta \mathcal{H}(\phi)d\phi.$$

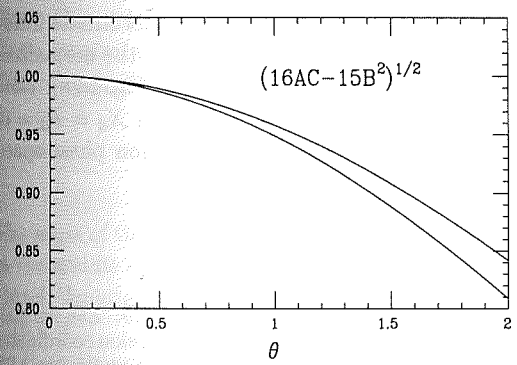

Figure 2.37: The minimum $\langle\mathcal{H}\rangle$ factors $G = \sqrt{16AC - 15B^2}$ for the DBA (lower curve) and $\tilde{G} = \sqrt{16\tilde{A}\tilde{C} - 15\tilde{B}^2}$ for the ME (upper curve) lattices are plotted as a function of the bending angle θ. The ME lattice data are for minimum $\langle\mathcal{H}\rangle$ without the achromat constraint. Note that $\langle\mathcal{H}\rangle$ is slightly smaller in a long dipole because of the $1/\rho^2$ focusing effect of the sector dipole.

where $G = \sqrt{16AC - 15B^2}$, $\tilde{\beta}_0 = \sqrt{12}\,C,/\sqrt{5}\,G$ and $\tilde{\alpha}_0 = \frac{\sqrt{15}}{}B/G$. The factor $G = \sqrt{16AC - 15B^2}$ (see Fig. 2.37) decreases slowly with increasing dipole bending angle θ because of the horizontal focusing of the bending radius. The evolution of the betatron amplitude function in the dipole can be obtained from Eq. (2.56). In the small-angle approximation, the minimum betatron amplitude and its location are given by

$$\beta^*_{\text{min,A}} = \frac{3}{4\sqrt{60}}L, \quad s^*_{\text{min,A}} = \frac{3}{8}L.$$

Figure 2.38 shows the betatron amplitude functions of a low-emittance DBA-lattice at the advanced photon source (APS) in Argonne National Laboratory. Here, β_x is minimum inside a dipole in order to attain a minimum $\langle\mathcal{H}\rangle$. In the APS lattice, the dispersion matching quadrupole at the center is also split into two in order to leave space for a sextupole.

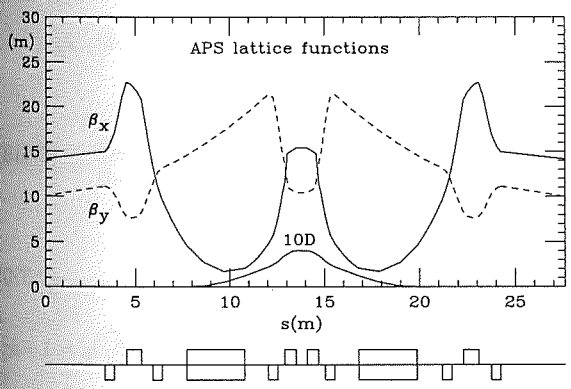

Figure 2.38: The low emittance lattice functions for a superperiod of APS. The APS lattice has 40 superperiods so that the circumference is 1104 m. The tunes of this lattice are $Q_x = 35.219$, $Q_z = 14.298$. The momentum compaction factor is $\alpha_c = 2.28 \times 10^{-4}$ in agreement with that of Eq. (2.312).

To study the behavior of the lattice dispersion function, we show the normalized dispersion coordinates (P_d, X_d) in Fig. 2.39, where the dipole has been split into 10

slices in order to show the propagation of the normalized dispersion coordinates inside a dipole. Since the lattice is designed to minimize $\langle\mathcal{H}\rangle$ inside dipole, the normalized dispersion coordinates are small (to be compared with that shown in Fig. 2.28). Note that the achromat section of the DBA lattice is located at the origin $X_d = P_d = 0$. In the dispersion matching straight section, the normalized dispersion phase-space coordinates are located on a circle with the center at the origin.

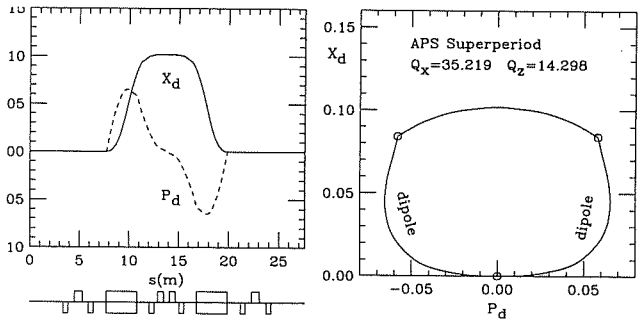

Figure 2.39: The normalized dispersion coordinates for the low emittance APS lattice is shown in one superperiod. See Fig. 2.38 for the corresponding lattice functions.

Many third generation high-brilliance light sources such as the ESRF, JSRF, APS, ELETTRA, etc. employ low emittance DBA-lattice for their storage ring. Since we emphasize the dispersion function in this section, the details of emittance minimization procedure will be addressed in Chapter 4, Sec. III.

B. Minimum $\langle\mathcal{H}\rangle$ without achromat constraint

Without the achromat constraint, minimization of the $\mathcal{H}$-function can be achieved through the following steps. First, $\langle\mathcal{H}\rangle$ can be minimized by finding the optimal dispersion functions with

$$\frac{\partial\langle\mathcal{H}\rangle}{\partial d_0} = 0, \quad \frac{\partial\langle\mathcal{H}\rangle}{\partial d_0'} = 0$$

to obtain

$$d_{0,\min} = \frac{1}{6}F, \quad d_{0,\min}' = -\frac{1}{2}E. \tag{2.319}$$

The resulting $\langle\mathcal{H}\rangle$ becomes

$$\langle\mathcal{H}\rangle = \frac{1}{12}\rho\theta^3\left(\tilde{\beta}_0\tilde{A} - \tilde{\alpha}_0\tilde{B} + \frac{4\tilde{\gamma}_0}{15}\tilde{C}\right), \tag{2.320}$$

where $\tilde{A} = 4A - 3E^2$, $\tilde{B} = 3B - 2EF$, $\tilde{C} = \frac{9}{4}C - \frac{5}{4}F^2$. Using the relation $\tilde{\beta}_0\tilde{\gamma}_0 = 1 + \tilde{\alpha}_0^2$, we obtain the minimum $\langle\mathcal{H}\rangle$ as

$$\langle\mathcal{H}\rangle_{\min} = \frac{\tilde{G}}{12\sqrt{15}}\rho\theta^3, \tag{2.321}$$

where $\tilde{G} = \sqrt{16\tilde{A}\tilde{C} - 15\tilde{B}^2}$ (see Fig. 2.37). Thus the minimum $\langle\mathcal{H}\rangle$ without achromatic constraint is a factor of 3 smaller than that with the achromat condition. The betatron amplitude function at the minimum $\langle\mathcal{H}\rangle$ is

$$\tilde{\beta}_0 = \frac{8}{\sqrt{15}\,\tilde{G}}\tilde{C}, \quad \tilde{\alpha}_0 = \frac{\sqrt{15}}{\tilde{G}}\tilde{B}, \quad \tilde{\gamma}_0 = \frac{2\sqrt{15}}{\tilde{G}}\tilde{A}. \tag{2.322}$$

The waist of the optimal betatron amplitude function for the minimum $\langle\mathcal{H}\rangle$ is located at the middle of the dipole, i.e. $s^* = L/2$. The corresponding minimum betatron amplitude function at the waist location is $\beta^*_{\min} = L/\sqrt{60}$ in small-angle approximation with $\theta \ll 1$.

Even though the minimum $\langle\mathcal{H}\rangle$ is one third of that with the achromat condition, the required minimum betatron amplitude function is less stringent, i.e.

$$\beta^*_{\min} = \frac{4}{3}\beta^*_{\min,A}.$$

The corresponding maximum betatron amplitude function will be reduced accordingly. We have discussed the minimum $\langle\mathcal{H}\rangle$ only in sector dipoles. In actual machine design, combined-function magnets with defocussing field may be used (see Exercise 2.4.18), where we will find that $\langle\mathcal{H}\rangle_{\min}$ is actually larger than for a separate function lattice. Computer codes such as MAD [19] and SYNCH [20] can be used to optimize $\langle\mathcal{H}\rangle$.

Exercise 2.4

1. The dispersion function in a combined-function dipole satisfies the equation $D'' + K_x D = 1/\rho$.

   (a) Show that the solution for constant $K_x = K > 0$ is

   $$D = a\cos\sqrt{K}s + b\sin\sqrt{K}s + 1/\rho K.$$

   Let D_0 and D_0' be the dispersion function and its derivative at $s = 0$. Show that the solution can be expressed as

   $$\begin{pmatrix} D(s) \\ D'(s) \\ 1 \end{pmatrix} = M \begin{pmatrix} D_0 \\ D_0' \\ 1 \end{pmatrix},$$

   where the transfer matrix is

   $$M = \begin{pmatrix} \cos\sqrt{K}s & \frac{1}{\sqrt{K}}\sin\sqrt{K}s & \frac{1}{\rho K}(1-\cos\sqrt{K}s) \\ -\sqrt{K}\sin\sqrt{K}s & \cos\sqrt{K}s & \frac{1}{\rho\sqrt{K}}\sin\sqrt{K}s \\ 0 & 0 & 1 \end{pmatrix}.$$

(b) Show that the transfer matrix for constant $K_x = K < 0$ is

$$M = \begin{pmatrix} \cosh\sqrt{|K|}s & \frac{1}{\sqrt{|K|}}\sinh\sqrt{|K|}s & \frac{1}{\rho|K|}(-1+\cosh\sqrt{|K|}s) \\ \sqrt{|K|}\sinh\sqrt{|K|}s & \cosh\sqrt{|K|}s & \frac{1}{\rho\sqrt{|K|}}\sinh\sqrt{|K|}s \\ 0 & 0 & 1 \end{pmatrix}.$$

(c) Show that the transfer matrix of a sector magnet is given by Eq. (2.249).

(d) For a rectangular magnet, show that the horizontal transfer matrix is (see Exercise 2.2.3)

$$M_{\text{rectangular dipole}} = \begin{pmatrix} 1 & \rho\sin\theta & \rho(1-\cos\theta) \\ 0 & 1 & 2\tan(\theta/2) \\ 0 & 0 & 1 \end{pmatrix},$$

where ρ and θ are the bending radius and the bending angle.

(e) In thin-lens (small-angle) approximation, show that the transfer matrices M for quadrupoles and dipoles become

$$M_{\text{quad}} = \begin{pmatrix} 1 & 0 & 0 \\ -1/f & 1 & 0 \\ 0 & 0 & 1 \end{pmatrix}, \quad M_{\text{dipole}} = \begin{pmatrix} 1 & \ell & \ell\theta/2 \\ 0 & 1 & \theta \\ 0 & 0 & 1 \end{pmatrix},$$

where f is the focal length, and ℓ and θ are the length and bending angle of the dipole.

2. The bending arc of an accelerator lattice is usually composed of FODO cells. Each FODO cell is given by [$\frac{1}{2}$QF B QD B $\frac{1}{2}$QF], where QF and QD are the focusing and defocussing quadrupoles with focal length f_1 and $-f_2$ respectively, and B is a dipole with bending angle θ. Let L be the half cell length.

(a) Using thin-lens approximation, show that the dispersion function and the betatron amplitude functions are given by

$$D_{\text{F}} = \frac{L\theta}{\sin^2(\Phi_x/2)}(1+\frac{1}{4}T_-), \quad D_{\text{D}} = \frac{L\theta}{\sin^2(\Phi_x/2)}(1-\frac{1}{4}T_+),$$

$$\beta_{x,\text{F}} = \frac{L}{\sin(\Phi_x/2)}\sqrt{\frac{1+T_-}{1-T_+}}, \quad \beta_{x,\text{D}} = \frac{L}{\sin(\Phi_x/2)}\sqrt{\frac{1-T_+}{1+T_-}},$$

where

$$S_\pm = \sin^2\frac{\Phi_x}{2} \pm \sin^2\frac{\Phi_z}{2}, \quad T_\pm = \frac{1}{4}\left(\sqrt{S_-^2+8S_+} \pm S_-\right),$$

and Φ_x and Φ_z are the horizontal and vertical betatron phase advance per cell.

(b) Simplify your result in part (a) with $\Phi_x = \Phi_z = \Phi$ and calculate the dispersion actions $J_{\text{d}}(\text{QF}), J_{\text{d}}(\text{QD})$ as a function of the phase advance per cell Φ. Plot $J_{\text{d}}(\text{QF})/J_{\text{d}}(\text{QD})$ as a function of Φ.

(c) Part of the SYNCH program input deck for the TEVATRON (1988) is given below. Use the thin-lens approximation to find the phase advance per cell and the betatron and dispersion functions at the focusing quadrupole.


```
TEV   RUN          DOUBLER LATTICE
C  DOUBLER lattice using two shell normal quads and special
C  length matching quads. all quads run at same excitation as the
C  35 turn, 21 foot dipoles.
C  All quantities in units of m, kG, kG/m, kG-m.
BRHO  =            33387.702
BZ    =            44.27664
GF    =            760.32056
GD    =            -760.32056
BL    =            6.1214
QL    =            1.67894
O     DRF          0.2794
OO    DRF          2.14028
OOO   DRF          0.60038
C magnet declare:  length     gradient  brho      dipole    type
B     MAG          BL         0.        BRHO      BZ        $
QF    MAG          QL         GF        BRHO
QD    MAG          QL         GD        BRHO
C     beam line declaration for a CELL
HC    BML          OO   B     O    B    O    B    O    B    OOO
CELL  BML          QD   HC    QF   HC
```

(d) Use the data in the table below to estimate the dispersion function of AGS, RHIC and SSC lattices in thin-lens approximation. Estimate the momentum beam size vs the betatron beam size in the arc.

	AGS	RHIC	Tevatron	SSC	LHC
L_{cell} (m)	13.45	29.6		180	97.96
Φ (deg)	52.5	90		90	90
Energy (GeV)	25	250	1000	20000	8000
ϵ_N ($\pi\mu$m)	30	30	30	10	15
$(\Delta p/p_0)_{\text{rms}}$	.005	0.003	0.001	0.0001	0.0001

(e) A collider lattice is usually made of arcs and insertions. The arc section is composed of regular FODO cells with bends, and the straight insertion section is composed of quadrupoles without dipoles. The dispersion suppressor matches the dispersion function in the arc to a zero dispersion value in the straight section. Show that the momentum compaction factor of such a lattice is given by

$$\alpha_{\text{c}} \approx \frac{1}{\nu_{\text{arc}}^2(1+L_{\text{s}}/L_{\text{a}})},$$

where $2\pi\nu_{\text{arc}}$ is the total accumulated phase advance in the arcs, and L_{s} and L_{a} are the length of the straight section and the arc.

3. Show that the 3×3 transfer matrix of a repetitive cell is generally given by Eq. (2.257). Show that the transfer matrix of repetitive FODO cell is

$$M = \begin{pmatrix} \cos\Phi & \beta_{\text{F}}\sin\Phi & 2D_{\text{F}}\sin^2(\Phi/2) \\ -\gamma_{\text{F}}\sin\Phi & \cos\Phi & \gamma_{\text{F}}D_{\text{F}}\sin\Phi \\ 0 & 0 & 1 \end{pmatrix},$$

where the symmetry conditions $\alpha_F = 0$ and $D'_F = 0$ are used, Φ is the phase advance per cell, β_F and γ_F are the Courant–Snyder parameters, and D_F is the dispersion function at the center of the quadrupole.

(a) Show that

$$M^2_{\Phi=90^\circ} = \begin{pmatrix} -1 & 0 & 2D_F \\ 0 & -1 & 0 \\ 0 & 0 & 1 \end{pmatrix}, \quad M^4_{\Phi=90^\circ} = \begin{pmatrix} 1 & 0 & 0 \\ 0 & 1 & 0 \\ 0 & 0 & 1 \end{pmatrix}.$$

(b) Show that two FODO cells, each with 90° phase advance, match a zero dispersion region to a final dispersion of $D = 2D_F$ and $D' = 0$.

(c) To match the dispersion function from a regular FODO cell in the arc to a zero value at the straight section, we need a dispersion suppressor. Adjoining the regular arc, the dispersion suppressor is composed of two reduced bending FODO cells, with bending angle θ_2 and θ_1 for each dipole.[78] Show that the conditions for zero dispersion after the dispersion suppressor are

$$\frac{\theta_1}{\theta} = \frac{1}{2(1-\cos\Phi)}, \quad \text{and} \quad \theta_1 + \theta_2 = \theta,$$

where θ is the bending angle of each dipole in the regular cell, and Φ is the phase advance of the FODO cell. At $\Phi = \pi/2$, these two FODO cells form the $-I$ unit. The theorem of dispersion suppression of Section IV.4 is thus verified.

(d) This exercise shows the effect of dispersion mismatch. Assuming that the accelerator lattice is made of n FODO cells, where $(n-1)$ FODO cells are [$\frac{1}{2}$QF B QD B $\frac{1}{2}$QF] with dipoles, and the bending magnets in the last FODO cell are replaced by drift spaces, show that the dispersion function at the entrance of the first FODO cell with a dipole is

$$D_1 = \frac{1 - \cos n\Phi + \cos\Phi - \cos(n-1)\Phi}{2(1-\cos n\Phi)} D_F,$$
$$D'_1 = -\frac{\sin\Phi - \sin n\Phi + \sin(n-1)\Phi}{2(1-\cos n\Phi)} \gamma D_F,$$

where D_F is the dispersion function of the regular FODO cell at the center of the focusing quadrupole and Φ is the phase advance per cell. The resulting mismatched dispersion function can be very large at $n\Phi \approx 0 \pmod{2\pi}$, which is related to the integer stopband.

4. Using thin-lens approximation, show that the momentum compaction factor α_c of an accelerator made of N FODO cells is given by

$$\alpha_c = \frac{1}{2\pi R}\oint \frac{D_x}{\rho} ds = \left(\frac{2\pi}{2N\sin\frac{\Phi}{2}}\right)^2 \approx \frac{1}{\nu_x^2},$$

[78] A reduced bending cell can be represented by the following matrix with $\xi_1 = \theta_1/\theta$:

$$\begin{pmatrix} \cos\Phi & \beta_F \sin\Phi & \xi_1 D_F(1-\cos\Phi) \\ -\gamma_F \sin\Phi & \cos\Phi & \xi_1 \gamma_F D_F \sin\Phi \\ 0 & 0 & 1 \end{pmatrix}.$$

where R is the average radius of the accelerator, Φ is the phase advance per cell, and ν_x is the horizontal betatron tune.

5. Consider a weak-focusing synchrotron (Exercise 2.2.5) with a constant focusing index $0 < n < 1$. Show that the lattice and dispersion functions are $\beta_x = \rho/\sqrt{1-n}$, $\beta_z = \rho/\sqrt{n}$, $D = \rho/(1-n)$, and the transition energy is $\gamma_T = \sqrt{1-n}$.

6. Using the Floquet transformation, show that Eq. (2.244) can be transformed to

$$\frac{d^2\tilde{X}}{d\phi^2} + \nu^2\tilde{X} = \frac{\nu^2\beta^{3/2}}{\rho},$$

where $\tilde{X} = D/\sqrt{\beta}$, and $\phi = \int_0^s ds/\nu\beta$.

(a) Using the Fourier expansion,

$$\frac{\beta^{3/2}}{\rho} = \sum_{k=-\infty}^{\infty} a_k e^{ik\phi},$$

show that

$$D(s) = \nu^2\sqrt{\beta(s)} \sum_{k=-\infty}^{\infty} \frac{a_k e^{ik\phi(s)}}{\nu^2 - k^2}, \quad a_k = \frac{1}{2\pi}\int_0^{2\pi} \frac{\beta^{3/2}}{\rho} e^{-ik\phi} d\phi.$$

Note here that $D(s)$ can be approximated by $a_0\sqrt{\beta(s)}$ in a regular FODO lattice, where the zeroth harmonic a_0 dominates.

(b) Using Eq. (2.266), show that

$$\alpha_c = \frac{\nu^3}{R} \sum_{k=-\infty}^{\infty} \frac{|a_k|^2}{\nu^2 - k^2},$$

where $R = C/2\pi$ is the mean radius. In most accelerator design, the a_0 harmonic dominates. Assuming $\rho \approx$ constant for all magnets, show that

$$a_0 = \frac{1}{2\pi\nu}\oint \frac{\beta^{1/2}}{\rho} ds \approx \frac{\langle\sqrt{\beta}\rangle}{\nu}.$$

Since $\nu = \oint ds/2\pi\beta \approx R/\langle\beta\rangle$, show that $\alpha_c \approx 1/\nu^2$.

7. Show that the integral representation of the dispersion function in Eq. (2.264) satisfies Eq. (2.243). Substituting the betatron coordinate into Eq. (2.266), show that the path-length change due to the betatron motion is[79]

$$\begin{aligned} \Delta L &= \int_s^{s+C} \frac{x}{\rho} ds \\ &= [\sin 2\pi\nu_x X_d - (1-\cos 2\pi\nu_x)P_d]X_\beta + [(1-\cos 2\pi\nu_x)X_d + \sin 2\pi\nu_x P_d]P_\beta \end{aligned}$$

where $X_\beta = x/\sqrt{\beta_x}$ and $P_\beta = (\alpha_x x + \beta_x x')/\sqrt{\beta_x}$ are normalized betatron coordinates, and X_d, P_d are the normalized dispersion function phase-space coordinates of Eq. (2.265). Since the time average of the betatron motion is zero, $\langle X_\beta\rangle = \langle P_\beta\rangle = 0$, the path length depends on the betatron amplitude quadratically.

[79] Use the integral representation of Eq. (2.265).

8. The closed orbit of a horizontal dipole field kicker at location s_0 in a synchrotron is given by (see Sec. III)

$$x_{\rm co}(s) = \frac{\sqrt{\beta_x(s)\beta_x(s_0)}}{2\sin\pi\nu_x}\,\theta_0\,\cos\left(\pi\nu_x - |\psi_x(s) - \psi_x(s_0)|\right),$$

where θ_0 is the kick angle, and ψ_x is the phase advance function. Show that the effect of the dipole kicker on the orbit length is

$$\Delta C = \oint \frac{x_{\rm co}}{\rho} ds = D(s_0)\theta_0.$$

The change of orbit length due to a dipole error is the product of the dipole kick angle and the dispersion function at the kicker location.

9. In the presence of a skew quadrupole field with $\Delta B_x = (\partial B_x/\partial x)x$, Hill's equation for the vertical closed orbit is[80]

$$z'' + K_z(s)z = \frac{1}{B\rho}\frac{\partial B_x}{\partial x} D_x\,\delta,$$

where $B\rho = p_0/e$ is the momentum rigidity, and D_x is the horizontal dispersion function at the skew quadrupole location. Show that the vertical dispersion function is

$$D_z(s) = \nu_z^2\sqrt{\beta_z(s)}\sum_{k=-\infty}^{\infty}\frac{f_k e^{ik\phi(s)}}{\nu_z^2 - k^2},$$

where

$$f_k = \frac{1}{2\pi B\rho}\int_0^{2\pi}\sqrt{\beta_z}D_x\frac{\partial B_x}{\partial x}e^{-ik\phi}ds.$$

The vertical dispersion function can sometimes be approximated by a simple pole

$$D_z \approx \nu_z\sqrt{\beta_z(s)}\frac{|f_k|\cos(k\phi(s)+\xi)}{\nu_z - k},$$

where $k = [\nu_z]$ is the integer nearest the vertical betatron tune and ξ is the phase of f_k.

10. In a straight section of an accelerator, $M_{13} = 0$ and $M_{23} = 0$. The values of the dispersion function at two locations in the beam line are related by

$$D_2 = M_{11}D_1 + M_{12}D_1', \quad D_2' = M_{21}D_1 + M_{22}D_1'.$$

Show that $\mathcal{H} = \gamma D^2 + 2\alpha DD' + \beta D'^2$ is invariant in the straight section.

11. In general, the dispersion function transfer matrix is given by Eq. (2.254). Show that the evolution of the $\mathcal{H}$-function is

$$\begin{aligned}\mathcal{H} \;=\; & \mathcal{H}_0 + 2(\alpha_0 D_0 + \beta_0 D_0')[M_{23}M_{11} - M_{13}M_{21}] \\ & +2(\gamma_0 D_0 + \alpha_0 D_0')[M_{13}M_{22} - M_{23}M_{12}] + \beta_0[M_{13}M_{21} - M_{23}M_{11}]^2 \\ & +\gamma_0[M_{13}M_{22} - M_{23}M_{12}]^2 - 2\alpha_0[M_{13}M_{21} - M_{23}M_{11}][M_{13}M_{22} - M_{23}M_{12}]\end{aligned}$$

[80]This exercise demonstrates that residual vertical dispersion can be generated by skew quadrupoles. Vertical dispersion can also be induced by vertical closed-orbit error in quadrupoles, dipole rolls, feed-down from magnetic multipoles, etc.

where $\mathcal{H}_0 = \gamma_0 D_0^2 + 2\alpha_0 D_0 D_0' + \beta_0 D_0'^2$; M_{ij} is a matrix element of the transfer matrix; and α_0, β_0, and γ_0 are Courant-Snyder parameters at the initial location.

(a) Using the M_{ij} of Eq. (2.249), show that $\mathcal{H}$ in a sector dipole is given by Eq. (2.313).

(b) Find $\mathcal{H}$ in a rectangular dipole (use the result of Exercise 2.4.1).

12. Using the beam position data (in mm) in the table below at three different revolution frequencies (in MHz) at the IUCF cooler ring, calculate the horizontal and vertical dispersion function at two horizontal and two vertical BPM locations. The parameters for this experiment were (1) proton kinetic energy = 45 MeV, (2) circumference = 86.82 m, (3) reference orbit frequency = 1.03168 MHz, and (4) transition energy γ_T=4.6.

Table: Some Beam Positions $x_{\rm co}$ or $z_{\rm co}$ (mm) vs f_0 (MHz) of the IUCF Cooler.

f_0 (MHz)	1.03268	1.03168	1.03068		1.03268	1.03168	1.03068
H.BPM	$x_{\rm co}$	$x_{\rm co}$	$x_{\rm co}$	V.BPM	$z_{\rm co}$	$z_{\rm co}$	$z_{\rm co}$
PHI	0.5	−5.4	−12.3				
PH12	−0.7	−5.3	−10.3	PV12	0.6	0.9	1.2
PH14	2.2	2.1	0.6	PV14	−2.4	−4.0	−4.6
PHT	1.3	4.1	5.5	PVT	−1.0	−2.8	−3.7
				PV26	3.9	6.7	8.0
PH24	−0.4	0.0	0.8	PV24	0.9	1.4	1.6

13. **Double-Bend Achromat:** Consider an achromatic bending system with two sector magnets and a focusing quadrupole midway between two dipoles, i.e.

$$\mathrm{B}[\rho,\theta]\quad \mathrm{O}[l]\quad \mathrm{Q_F}[K,l_{\rm q}]\quad \mathrm{O}[l]\quad \mathrm{B}[\rho,\theta].$$

Here K and $l_{\rm q}$ represent the focusing strength function and the length of the quadrupole. Show that the dispersion matching condition is given by

$$\rho\tan\frac{\theta}{2} + l = \frac{1}{\sqrt{K}}\cot\frac{\sqrt{K}l_{\rm q}}{2},$$

and that, in thin-lens approximation, the matching condition reduces to Eq. (2.280). This basic achromat is also called a Chasman-Green lattice cell. The double-bend achromat (DBA) is commonly used in the design of low emittance storage rings, where quadrupole configurations are arranged to minimize $\langle\mathcal{H}\rangle$ in the dipole. Other achromat modules are

(a) the triple-bend achromat (TBA)

$$\mathrm{B}[\rho,\theta_{\rm o}]\ \mathrm{O}[l_1]\ \mathrm{Q_F}[K,l_{\rm q}]\ \mathrm{O}[l_2]\ \mathrm{B}[\rho,\theta_{\rm c}]\ \mathrm{O}[l_2]\ \mathrm{Q_F}[K,l_{\rm q}]\ \mathrm{O}[l]\ \mathrm{B}[\rho,\theta_{\rm o}]$$

which has been used in many synchrotron radiation light sources such as the ALS (Berkeley), TLS (Taiwan), KLS (Korea), and BESSY (Berlin), and

(b) the reverse-bend DBA

$$\mathrm{B}[\rho,\theta]\ \mathrm{O}[l_1]\ \mathrm{Q_F}[K,l_{\rm q}]\ \mathrm{O}[l_2]\ \mathrm{B}[-\rho,-\theta_{\rm r}]\ \mathrm{O}[l_2]\ \mathrm{Q_F}[K,l_{\rm q}]\ \mathrm{O}[l]\ \mathrm{B}[\rho,\theta]$$

where the reverse bend angle $\theta_{\rm r} \ll \theta$ can be used to adjust the desired momentum compaction factor.

14. **Achromatic translating system:** Show that the transport line with two sector dipoles given by B[ρ,θ] O[l_1] Q$_F$[K,l_q] O[l_c] Q$_F$[K,l_q] O[l_1] B[$-\rho,-\theta$] is achromatic if the following condition is satisfied:[81]

$$\rho\sin\frac{\theta}{2}+l_1=\frac{l_c\cos\sqrt{K}l_q+\frac{2}{\sqrt{K}}\sin\sqrt{K}l_q}{l_c\sqrt{K}\sin\sqrt{K}l_q-2\cos\sqrt{K}l_q}.$$

Show that, in thin-lens approximation,

$$f_q=\frac{\ell_c(\ell_1+\ell_B)}{\ell_c+2\ell_1+\ell_B},$$

where f_q is the focal length of the quadrupole and ℓ_B is the length of the dipole.

15. Show the three sector dipole system B[ρ,θ] O[l] B[ρ,θ] O[l] B[ρ,θ] is achromatic if the following condition is satisfied:

$$\frac{l}{\rho}=\frac{2\cos\theta+1}{\sin\theta}.$$

16. A set of four rectangular dipoles with zero net bending angle

B[ρ,θ] O[l_1] B[$-\rho,-\theta$] O[l_2] B[$-\rho,-\theta$] O[l_1] B[ρ,θ]

has many applications. It can be used as a beam translation (chicane) unit to facilitate injection, extraction, internal target operation, etc. It can also be used as one unit of the wiggler magnet for modifying electron beam characteristics or for producing synchrotron radiation.

(a) Show that the rectangular magnet beam translation unit is achromatic to all orders, and show that the R_{56} element of the transport matrix, in small angle approximation, is

$$R_{56}=2\theta^2(\ell_1+\frac{2}{3}\rho\theta).$$

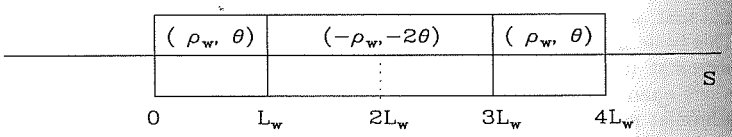

(b) A simplified compact geometry with $l_1=l_2=0$ (shown in the figure above) is often used as a unit of the wiggler magnet in electron storage rings. Assuming that $D_0=D_0'=0$, show that the dispersion function created by the wiggler magnet is[82]

$$\frac{D(s)}{\rho_w}=\begin{cases}-(1-\cos\phi), & 0<s<L_w\\ (1-\cos\bar{\phi})-(1-\cos\theta)\cos\bar{\phi} & \\ \quad -[\sin\theta+2\tan\theta(1-\cos\theta)]\sin\bar{\phi}, & L_w<s<2L_w\end{cases}$$

[81] At the symmetry point of the antisymmetric bending section $D=0$.
[82] Be sure to take the edge focusing into account.

where $\phi=s/\rho_w$ and $\bar{\phi}=(s-L_w)/\rho_w$, and

$$D'(s)=\begin{cases}-\sin\phi, & 0<s<L\\ -\sin\theta-2\tan\theta(1-\cos\theta), & s=L_{w+}\\ \sin\bar{\phi}+(1-\cos\theta)\sin\bar{\phi} & \\ \quad -[\sin\theta+2\tan\theta(1-\cos\theta)]\cos\bar{\phi}, & L_w<s<2L_w.\end{cases}$$

Show that

$$D(s=2L_w)=2\rho_w\frac{1-\cos\theta}{\cos\theta},\quad D'(s=2L_w)=0.$$

Since $D'=0$ at the symmetry point, the wiggler is an achromat. In small bending-angle approximation, show that the dispersion function becomes

$$D(s)=\begin{cases}-s^2/2\rho_w, & 0<s<L_w\\ -(2L_w^2-(2L_w-s)^2)/2\rho_w, & L_w<s<2L_w,\end{cases}$$
$$D'(s)=\begin{cases}-s/\rho_w, & 0<s<L_w\\ -(2L_w-s)/\rho_w, & L_w<s<2L_w.\end{cases}$$

17. An FMC basic module can also be made of two DOFO cells with a dispersion matching section (shown schematically below).

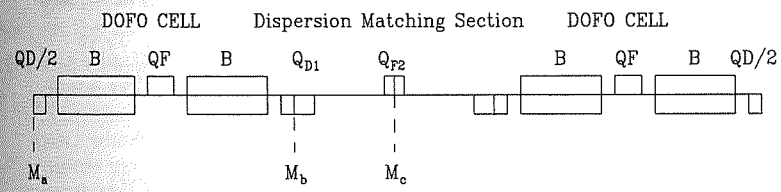

Use the following notations
Φ: phase advance of the FODO cell,
β_D, $\gamma_D=1/\beta_D$: values of betatron functions at the center of QD.
$2L$: length of the DOFO cell,
θ: bending angle of a half DOFO cell,
D_D dispersion function at the defocussing quadrupole,
D_a: prescribed dispersion function at marker M$_a$ with $\zeta=D_a/D_D$.
L_c: half length of the matching section from M$_b$ to M$_c$.
L_m: length of half a complete module,
f_1: focal length of Q$_{D1}$,
f_2: focal length of Q$_{F2}$,
ψ_x,ψ_z: betatron phase advances of one half of the dispersion matching section.

(a) Show that the phase advance of the dispersion matching section is determined completely by the prescribed dispersion function D_a and the phase advance of the DOFO cell,

$$\tan\psi_x=\frac{(1-\zeta)\sin\Phi}{1-\cos\Phi+\zeta\cos\Phi}.$$

(b) In thin-lens approximation, show that

$$\cos^2\psi_x=\left(1+\frac{L_c}{f_1}\right)\left(1-\frac{L_c}{2f_2}\right),\quad \cos^2\psi_z=\left(1-\frac{L_c}{f_1}\right)\left(1+\frac{L_c}{2f_2}\right).$$

Show that the stability of the betatron motion is a necktie region bounded by four lines:

$$\frac{L_c}{2f_2} \le 1, \quad \frac{L_c}{f_1} \le 1, \quad \frac{L_c}{2f_2} \le \frac{L_c/f_1}{1 - L_c/f_1}, \quad \frac{L_c}{2f_2} \ge \frac{L_c/f_1}{1 + L_c/f_1}.$$

Plot the necktie diagram of L_c/f_2 vs L_c/f_1. Since ψ_x is determined by parameters Φ and ζ, the parameter L_c/f_2 is a function of L_c/f_1, i.e.

$$\frac{L_c}{f_2} = 2 - \frac{2\cos^2\psi_x}{1 + L_c/f_1}.$$

Draw the line L_c/f_2 vs L_c/f_1 for constant ψ_x, e.g. $\psi_x = \pi/4$. This means that the dispersion matching section is a one-parameter lattice. Once L_c/f_1 is chosen, L_c/f_2 and ψ_z are determined. Furthermore, show that the length of the matching section is

$$L_c = \frac{\beta_{x,D} \sin\psi_x \cos\psi_x}{1 - L_c/2f_2},$$

where $\beta_{x,D}$ is the horizontal betatron amplitude function at the center of QD.

(c) Show that the values of the betatron amplitude functions at M_c are

$$\beta_{x,c} = \beta_{x,a}\frac{(1 + L_c/f_1)^2}{\cos^2\psi_x}, \quad \beta_{z,c} = \beta_{z,a}\frac{(1 - L_c/f_1)^2}{\cos^2\psi_z}.$$

(d) Show that the dispersion action in the matching section is

$$J_b = J_c = J_D\left(1 - 2(1-\zeta)\cos\Psi + (1-\zeta)^2\right).$$

(e) Show that the dispersion function at the middle of the dipole is

$$D_{B1} = \left(1 + \frac{1}{2}\sin\frac{\Phi}{2}\right)D_a + \frac{L\theta}{8},$$
$$D_{B2} = \left(1 + \frac{1}{2}\sin\frac{\Phi}{2} - \sin^2\frac{\Phi}{2}\right)D_a + L\theta\left(1 + \frac{1}{8} - \frac{1}{2}\sin\frac{\Phi}{2}\right).$$

Show that the momentum compaction is

$$\alpha_c = \frac{D_D\theta}{L_m}\left[\left(2 + \sin\frac{\Phi}{2} - \sin^2\frac{\Phi}{2}\right)\zeta + \frac{\sin^2\frac{\Phi}{2}}{1 - \frac{1}{2}\sin\frac{\Phi}{2}}\left(\frac{5}{4} - \frac{1}{2}\sin\frac{\Phi}{2}\right)\right].$$

18. To simplify the design of a DBA in a synchrotron storage ring, combined-function dipole magnets have often been used, e.g. in ELETTRA in Trieste and in the UVU and X-ray rings in the National Synchrotron Light Source (NSLS) at BNL. The dispersion function in the combined-function dipole satisfies $D'' + K_x D = 1/\rho$, where $K_x = 1/\rho^2 + (1/B\rho)(\partial B_z/\partial x)$ is the effective defocussing strength function and ρ is the bending radius of the dipole.[83]

[83] Because the electron has a negative charge, the gradient term in K_x has a sign opposite that in Eq. (2.31).

(a) Show that

$$\langle\mathcal{H}\rangle = \rho\theta^3\left[\frac{\tilde\beta_0}{3}A(q) - \frac{\tilde\alpha_0}{4}B(q) + \frac{\tilde\gamma_0}{20}C(q)\right],$$

where

$$A(q) = \frac{3(\sinh 2q - 2q)}{4q^3}, \quad B(q) = \frac{6 - 8\cosh q + 2\cosh 2q}{q^4},$$
$$C(q) = \frac{30q - 40\sinh q + 5\sinh 2q}{q^5},$$

with $q = \sqrt{|K_x|}L$, $\tilde\beta_0 = \beta_0/L$, $\tilde\alpha_0 = \alpha_0$, and $\tilde\gamma_0 = \gamma_0 L$.

(b) Show that the minimum of $\langle\mathcal{H}\rangle$ is

$$\langle\mathcal{H}\rangle_{\min} = \frac{G}{4\sqrt{15}}\rho\theta^3,$$

where $G = \sqrt{16AC - 15B^2}$. Plot $G = \sqrt{16AC - 15B^2}$ vs the quadrupole strength and show that $\sqrt{16AC - 15B^2} \ge 1$, i.e. the combined-function DBA gives rise to a larger $\langle\mathcal{H}\rangle$. In Chapter 4 the effect of damping partition number on the natural emittance of electron beams will be discussed.

(c) Use thin-lens approximation to verify the strength of matching quadrupole Q4 of the NSLS lattice input data (MAD) file (shown below) for the achromat condition. Note that the dipole is declared as RBEND for a rectangular magnet, where in principle, we should take into account the edge focusing of the dipole magnet. Neglecting the edge focusing, however, discuss the effect of the combined-function dipole on $\langle\mathcal{H}\rangle$.

```
TITLE, "NSLS X-ray RING"
Q1      :QUADRUPOLE,L=.45,K1=-1.50186576
Q2      :QUADRUPOLE,L=.8,K1=1.33731236
Q3      :QUADRUPOLE,L=.4132,K1=-1.4018946
Q4      :QUADRUPOLE,L=.225,K1=1.29943942
B       :RBEND,L=2.7,K1=-.026848954,ANGLE=.39269908
SF      :SEXTUPOLE,L=0.,K2=0.
SD      :SEXTUPOLE,L=0.,K2=0.
D1      :DRIFT,L=2.25
D2      :DRIFT,L=.685
D3      :DRIFT,L=.3484
D4      :DRIFT,L=.70825
D5      :DRIFT,L=.9
D6      :DRIFT,L=.25
HSUP    :LINE=(D1,Q1,D2,Q2,D3,Q3,D4,B,D5,SD,D5,SF,D6,Q4)
USE,HSUP,SYMM,SUPER=8
PRINT,#S/E
TWISS
STOP
```

V Chromatic Aberration

A particle with momentum p executes betatron oscillations around an off-momentum closed orbit $x_{co}(s)+D(s)\delta$, where x_{co} is the closed orbit for the on-momentum particle, D is the dispersion function, and $\delta = (p-p_0)/p_0$ is the fractional momentum deviation from the on-momentum p_0. Equation (2.242) is Hill's equation of the horizontal betatron motion. A higher energy particle with $\delta > 0$ has a larger momentum rigidity and thus a weaker effective focusing strength; a lower energy particle with $\delta < 0$ has a smaller momentum rigidity and a stronger effective focusing strength. This is reflected in the gradient error ΔK_x in Eq. (2.242). Similar gradient error exists in the vertical betatron motion. The resulting gradient errors ΔK_x and ΔK_z are given by[84]

$$\begin{cases} \Delta K_x = \left[-\dfrac{2}{\rho^2} + K(s)\right]\delta + O(\delta^2) \approx -K_x\delta, \\ \Delta K_z = -K(s)\delta + O(\delta^2) \approx -K_z\delta, \end{cases} \tag{2.323}$$

where $K = B_1/B\rho$ and $B_1 = \partial B_z/\partial x$.

Note, in particular, that the chromatic gradient error is essentially equal to the product of the momentum deviation δ and the main focusing functions $-K_x$ and $-K_z$. The dependence of the focusing strength on the momentum of a circulating particle is called "chromatic aberration." Furthermore, the gradient error arising from the chromatic aberration is proportional to the designed focusing functions K_x and K_z, and thus the chromatic gradient error is a "systematic" error that can cause major perturbation in the designed betatron amplitude functions and reduce the dynamical aperture for off-momentum particles. The effects of chromatic aberration include the chromaticity, the "beta-beat" associated with the half-integer stopbands, etc.

In this section we study the effects of systematic chromatic aberration and its correction. In Sec. V.1 we define chromaticity and discuss its measurement and correction; in Sec. V.2 we examine the nonlinear perturbation due to chromatic sextupoles; in Sec. V.3 we study systematic half-integer stopbands and their effects on higher-order chromaticity; and in Sec. V.4 we outline basic machine design strategy.

[84] Including the effect of off-momentum orbits, the chromatic gradient error should include the effects of dispersion functions, fringe fields, etc. Some of these terms are includes below:

$$\Delta K_x = \left[-\frac{2}{\rho^2} + K + 2\frac{D}{\rho}\left(\frac{1}{\rho^2} - K\right) - \left(\frac{1}{\rho}\right)' D' + \frac{\gamma_x}{\beta_x\rho}D\right](\delta - \delta^2 + \cdots) + \cdots,$$

$$\Delta K_z = \left[-K + \frac{K}{\rho}D + \left(\frac{1}{\rho}\right)' D' + \frac{\gamma_x}{\beta_x\rho}D\right](\delta - \delta^2 + \cdots) + \cdots,$$

where $K = B_1/B\rho$ is the gradient function of quadrupoles. Note that the higher-order gradient error depends on the betatron amplitude and dispersion functions. We will neglect all chromatic effects arising from the dispersion function and fringe fields of magnets. For details see, e.g., K. Steffen, *High Energy Beam Optics* (Wiley, New York, 1965); S. Guiducci, *Proc. CERN Accelerator School*, CERN **91-04**, p. 53, 1991.

V.1 Chromaticity Measurement and Correction

In Sec. III.4, we find that the gradient error can induce betatron tune shift and betatron amplitude function perturbation. Since the chromatic effect of Eq. (2.323) gives rise to a systematic gradient error, the resulting betatron tune shift, given by Eq. (2.196), is

$$\begin{cases} \Delta\nu_x = \dfrac{1}{4\pi}\oint \beta_x \Delta K_x ds \approx \left(\dfrac{-1}{4\pi}\oint \beta_x K_x ds\right)\delta, \\ \Delta\nu_z = \dfrac{1}{4\pi}\oint \beta_z \Delta K_z ds \approx \left(\dfrac{-1}{4\pi}\oint \beta_z K_z ds\right)\delta. \end{cases} \tag{2.324}$$

The *chromaticity*, C_x or C_z, defined as the derivative of the betatron tunes vs fractional momentum deviation, is

$$C_y \equiv \frac{d(\Delta\nu_y)}{d\delta}, \tag{2.325}$$

where the subscript y stands for either x or z. The chromaticity arising solely from quadrupoles is called the "natural chromaticity,"

$$C_{y,\text{nat}} \approx \frac{-1}{4\pi}\oint \beta_y K_y ds. \tag{2.326}$$

Because the focusing function is weaker for higher energy particles, the betatron tune decreases with particle momentum, and the natural chromaticity is negative.[85]

The magnitude of the *natural chromaticity* $C_{y,\text{nat}}$ depends on the lattice design. The natural chromaticity of a FODO lattice is given by (see Exercise 2.5.3)

$$C_{y,\text{nat}}^{\text{FODO}} \approx -\frac{1}{4\pi}N\left(\frac{\beta_{\max}}{f} - \frac{\beta_{\min}}{f}\right) = -\frac{\tan(\Phi_y/2)}{\Phi_y/2}\nu_y \approx -\nu_y, \tag{2.327}$$

where N is the number of cells, f is the focal length, Φ_y is the phase advance per cell, and $\nu_y = N\Phi_y/2\pi$ is the betatron tune of the machine. The "specific chromaticity," defined as $\xi_y = C_y/\nu_y$, is nearly equal to -1 for a FODO lattice. On the other hand, for a collider lattice or a low-emittance lattice, the specific natural chromaticity can be as large as -3.

A beam is composed of particles with different momenta. The momentum spread of the beam is typically of the order of $\sigma_\delta \sim 10^{-5} - 10^{-2}$ depending on the application and the type of accelerator. Because of the chromaticity, the momentum spread gives

[85] In mathematical language, since the betatron amplitude function is always larger at a focusing location where $K_y > 0$, the integral $\oint \beta_y K_y ds > 0$, and $C_y < 0$.

rise to tune spread in the beam. If the chromaticity and the momentum spread of the beam become large enough that the betatron tunes overlap a low-order nonlinear resonance, particle loss may imminently occur. Furthermore, the growth of transverse head-tail instabilities depends on the sign of the chromaticity (see Sec. VIII and Ref. [3]).

A. Chromaticity measurement

Machine chromaticities can be derived from measurements of betatron tunes vs beam momentum. Since beam momentum is related to rf frequency, the chromaticity can be obtained from measurements of betatron tune vs rf frequency, i.e.

$$C_y = \frac{d\nu_y}{d\delta} = -\eta\omega_{\rm rf}\frac{d\nu_y}{d\omega_{\rm rf}}, \tag{2.328}$$

where η is the phase-slip factor, and $\omega_{\rm rf}$ is the angular frequency of the rf system (see Exercise 2.5.8).

Figure 2.40 shows the "measured specific" chromaticities of the AGS.[86] Note that the vertical chromaticity becomes positive above about 22 GeV, but the horizontal chromaticity becomes more negative. The dashed line shows the value of $-\frac{2}{\Phi}\tan\frac{\Phi}{2}$ of Eq. (2.327), where $\Phi \approx 53.8°$ is the phase advance of an AGS FODO cell. From the experimental data, we find that

$$\frac{1}{2}(C_{x,\rm data} + C_{z,\rm data}) \approx -\frac{2}{\Phi}\tan\frac{\Phi}{2}.$$

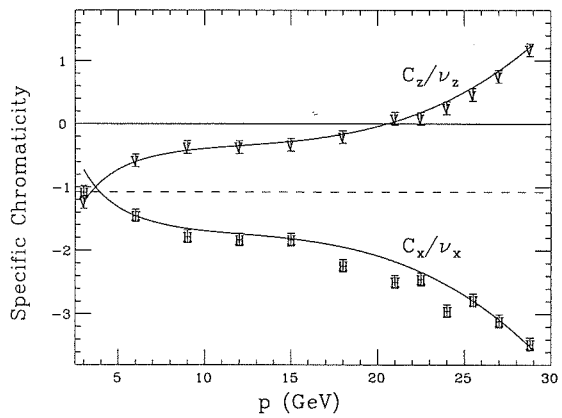

Figure 2.40: The measured chromaticities divided by the betatron tunes of the AGS vs the beam momentum. The dashed straight line shows the theoretical expected value. The solid curved line is obtained by modeling the sextupole field in the dipoles, as discussed in subsection C.

[86] E. Bleser, AGS Tech Note No. 288 (1987); E. Auerbach, E. Bleser, R. Thern, AGS Tech Note No. 276 (1987).

B. Chromatic correction

The natural chromaticity of a high-luminosity collider with low-β^* insertions is usually large. For example, the natural chromaticity for the Superconducting Super Collider (SSC) was expected to be about $C_{y,\rm nat} \approx -250$, which can lead to a natural tune spread of about $\Delta\nu \approx 0.1$ for a beam with an rms spread of $\delta = \pm 2\times 10^{-4}$. Similarly, the natural chromaticity for the RHIC injection lattice is about $C_{y,\rm nat} \approx -50$, and the resulting tune spread will be $\Delta\nu \approx 0.5$ with a beam momentum spread of $\delta = \pm 5\times 10^{-3}$. Since a circulating beam with such a large tune spread does not have a long storage lifetime, chromatic correction is needed to ensure good performance of a storage ring. This requires a magnet whose focusing function increases linearly with momentum in order to compensate the loss of focusing in quadrupoles.

First we examine the possibility of using sextupole magnets for chromaticity correction. The magnetic flux density of a sextupole magnet is

$$\frac{\Delta B_z}{B\rho} = \frac{B_2}{2B\rho}(x^2 - z^2), \quad \frac{\Delta B_x}{B\rho} = \frac{B_2}{B\rho}xz, \tag{2.329}$$

where $B_2 = \partial^2 B_z/\partial x^2|_{x=z=0}$. Substituting the transverse displacement of an off-momentum particle,

$$x = x_\beta(s) + D(s)\delta, \tag{2.330}$$

where x_β is the betatron displacement and $D(s)\delta$ is the off-momentum closed orbit, into Eq. (2.329), we obtain

$$\begin{cases} \dfrac{\Delta B_z}{B\rho} = -[S(s)D(s)\delta]x_\beta - \dfrac{S(s)}{2}(x_\beta^2 - z_\beta^2) - \dfrac{S(s)}{2}D^2(s)\delta^2, \\ \dfrac{\Delta B_x}{B\rho} = -[S(s)D(s)\delta]z_\beta - S(s)x_\beta z_\beta, \end{cases} \tag{2.331}$$

where $S(s) = -B_2/B\rho$ is the effective sextupole strength. Note that the first term of Eq. (2.331) depends linearly on the transverse betatron displacement. Since the effective quadrupole focusing functions

$$\Delta K_x = S(s)D(s)\delta, \quad \Delta K_z = -S(s)D(s)\delta \tag{2.332}$$

depend linearly on the off-momentum deviation, sextupoles can be used for chromaticity correction.[87]

Including the contribution of sextupoles, the chromaticity becomes

$$C_x = \frac{-1}{4\pi}\oint \beta_x[K_x(s) - S(s)D(s)]ds, \tag{2.333}$$

$$C_z = \frac{-1}{4\pi}\oint \beta_z[K_z(s) + S(s)D(s)]ds. \tag{2.334}$$

[87] It is also worth pointing out that the second term of Eq. (2.331) can produce nonlinear perturbation in betatron motion, called geometric aberration, to be discussed in Sec. VII, where we will find that the placement of sextupoles is important in minimizing nonlinear resonance strengths.

This shows that sextupoles located at nonzero dispersion function locations can be used to correct chromaticity; they are called chromatic sextupoles. Generally, two families of sextupoles are needed to correct horizontal and vertical chromaticities. Rules for their placement are as follows.

- In order to minimize their strength, the chromatic sextupoles should be located near quadrupoles, where $\beta_x D_x$ and $\beta_z D_x$ are maximum.
- A large ratio of β_x/β_z for the focusing sextupole and a large ratio of β_z/β_x for the defocussing sextupole are needed for optimal independent chromaticity control.
- The families of sextupoles should be arranged to minimize the the systematic half-integer stopbands and the third-order betatron resonance strengths.

For example, we consider a lattice of N repetitive FODO cells, where sextupoles are located near the focusing and defocussing quadrupoles. Let $S_{\rm F} = -B_2({\rm F})\ell_{\rm sf}/B\rho$ and $S_{\rm D} = -B_2({\rm D})\ell_{\rm sd}/B\rho$ be the integrated sextupole strengths at QF and QD respectively, where $\ell_{\rm sf}$, $\ell_{\rm sd}$, and $B_2({\rm F})$, $B_2({\rm D})$ are the length and the sextupole field strength at QF and QD. The sextupole strength needed to obtain zero chromaticity is (see Exercise 2.5.3)

$$S_{\rm F} = \frac{1}{2f^2\theta}\frac{\sin\frac{\Phi}{2}}{(1+\frac{1}{2}\sin\frac{\Phi}{2})}, \quad S_{\rm D} = -\frac{1}{2f^2\theta}\frac{\sin\frac{\Phi}{2}}{(1-\frac{1}{2}\sin\frac{\Phi}{2})}, \tag{2.335}$$

where f is the focal length, Φ the phase advance per cell, and θ the bending angle per half-cell.

For colliders or low-emittance storage rings, chromatic sextupoles are also arranged in families, located in the arcs, which consist mainly of FODO cells or DBA/TBA type cells. Since the low-β^* values in these lattices give rise to a large chromaticity, strong sextupoles are needed to correct it. If the intrinsic systematic half-integer stopband widths are large, the simple chromatic correction scheme using two families of sextupoles may not be sufficient to correct the higher-order chromatic effects.

Figure 2.41 shows an example of chromatic correction with two families of sextupoles in RHIC. Note that the second-order chromaticity $\Delta\nu_{x,z} \sim C^{(2)}_{x,z}\,\delta^2$ can cause substantial tune spread in a beam with a large momentum spread. In Sec. V.3, we will show that the chromatic gradient error can also create a large betatron amplitude function modulation (betabeat), which in turn induces a large second-order chromaticity. The second-order chromaticity and the betabeat can be simultaneously corrected by a proper chromatic stopband correction.

C. Nonlinear modeling from chromaticity measurement

The measurements of chromaticities can be used to model nonlinear sextupole fields in an accelerator. For example, we discuss the nonlinear sextupole modeling of the

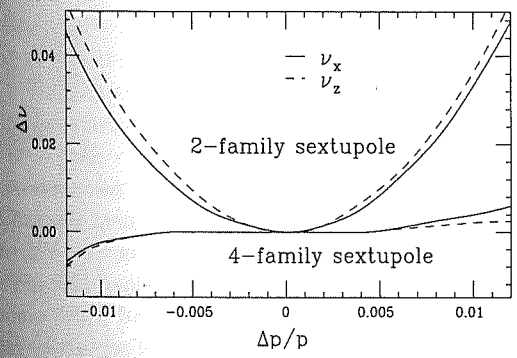

Figure 2.41: Variation of the betatron tune vs $\Delta p/p$ after chromatic correction with two and four families of sextupoles in RHIC.

AGS based on the measured chromaticities shown in Fig. 2.40. Since $C_{x,\rm data} < C_{x,\rm fodo}$, $C_{z,\rm data} > C_{z,\rm fodo}$, and $C_{x,\rm data} + C_{z,\rm data} = C_{x,\rm fodo} + C_{z,\rm fodo}$, the horizontally defocussing sextupoles must be located in dipoles, where $\beta_x \approx \beta_z$. To model the AGS, we assume that the sextupole fields arise from systematic error at the ends of each dipole, the eddy current sextupole due to the vacuum chamber wall, and the iron saturation sextupole at high field. The systematic error is independent of the beam momentum; the eddy current sextupole field depends inversely on the beam momentum; and the saturation sextupole field depends on a higher power of the beam momentum. The solid lines in Fig. 2.40 represent theoretical calculations with the integrated sextupole strengths

$$\begin{aligned} S_{\rm b} &= -5.2\times10^{-4} + 5.8\times10^{-2}/p \\ &\quad -(3.6\times10^{-4}p - 7.0\times10^{-5}p^2 + 2.8\times10^{-6}p^3)\ ({\rm m}^{-2}), \\ S_{\rm e} &= -0.017\ ({\rm m}^{-2}), \end{aligned}$$

for the body and the ends of the short AGS bending magnets (2.0066 m) respectively. Here p is the beam momentum in unit of (GeV/c), $S_{\rm b}$ is the integrated sextupole field in each dipole distributed in the whole dipole, and $S_{\rm e}$ is the integrated sextupole field distributed only at the end of each dipole. $S_{\rm e}$ and the first term in $S_{\rm b}$ may be considered as the systematic error in dipoles, and they are momentum independent. The second term in $S_{\rm b}$ is due to the eddy current on the vacuum chamber wall, which is inversely proportional to the beam momentum, and proportional to $\dot{B}$, where $\dot{B} = 2$ T/s in this experiment. The saturation term is nonlinear with respect to the momentum p. For the long magnets (2.3876 m) in the AGS, the integrated sextupole strength of the $S_{\rm b}$ term is assumed to be proportional to their length.

A chromaticity of about $-3\nu_x$ does not appear to cause difficulties in the AGS operation, which has recently attained an intensity of 6×10^{13} protons per pulse. Many low energy synchrotrons do not use chromatic correction sextupoles. However, chromaticity correction is absolutely essential in high energy synchrotrons and storage rings.

V.2 Nonlinear Effects of Chromatic Sextupoles

The Hamiltonian including sextupole nonlinearity is

$$H = \frac{1}{2}\left(x_\beta'^2 + K_x x_\beta^2 + z_\beta'^2 + K_z z_\beta^2\right) + \frac{S(s)}{6}(x_\beta^3 - 3x_\beta z_\beta^2). \tag{2.336}$$

This Hamiltonian can drive third-order and higher-order nonlinear resonances at $3\nu_x = \ell, \nu_x \pm 2\nu_z = \ell, \ldots$, where ℓ is an integer. However, the nonlinear resonance strength can be minimized by properly arranged sextupole families. In Sec. VII, we will show that if chromatic sextupoles are separated by an odd multiple of 180° in the betatron phase advance, their contributions to the third-order stopband width cancel each other in the first-order perturbation theory. Thus, four families of sextupoles can be arranged in a lattice with 90° phase advance per cell, and six families of sextupoles can be used in a lattice with 60° phase advance per cell. Such arrangements can also be used to correct the systematic half-integer stopband discussed in the next section.

V.3 Chromatic Aberration and Correction

The systematic chromatic gradient error can produce a large perturbation in the betatron amplitude functions for all off-momentum particles. Defining the betatron amplitude difference functions A and B as (see Exercise 2.3.10)

$$A = \frac{\alpha_1\beta_0 - \alpha_0\beta_1}{\sqrt{\beta_0\beta_1}}, \quad B = \frac{\beta_1 - \beta_0}{\sqrt{\beta_0\beta_1}},$$

we obtain

$$\frac{dB}{ds} = -A\left(\frac{1}{\beta_0} + \frac{1}{\beta_1}\right), \quad \frac{dA}{ds} = +B\left(\frac{1}{\beta_0} + \frac{1}{\beta_1}\right) + \sqrt{\beta_0\beta_1}\,\Delta K, \tag{2.337}$$

where $\Delta K = K_1 - K_0$ is the gradient error; the betatron amplitude functions β_0 and β_1 satisfy the Floquet equation

$$\begin{aligned} \beta_0' &= -2\alpha_0, \quad \alpha_0' = K_0\beta_0 - \gamma_0, \quad d\psi_0/ds = 1/\beta_0, \\ \beta_1' &= -2\alpha_1, \quad \alpha_1' = K_1\beta_1 - \gamma_1, \quad d\psi_1/ds = 1/\beta_1, \end{aligned}$$

and ψ_0 and ψ_1 are the unperturbed and perturbed betatron phase functions.

From Eq. (2.337), we find that $A^2 + B^2 =$ constant in regions where $\Delta K = 0$. In thin-lens approximation, the change of A across a quadrupole is given by

$$\Delta A = \int \sqrt{\beta_0\beta_1}\,\Delta K\, ds \approx -\frac{\beta_0}{f}\frac{\Delta p}{p_0},$$

where f is the focal length of the quadrupole. Similarly, the change of A across a sextupole is given by

$$\Delta A \approx -\beta_0\, g_{\text{eff}}\, \frac{\Delta p}{p_0},$$

where $g_{\text{eff}} = (B_2\Delta s/B\rho)D$ is the effective gradient error, $(B_2\Delta s/B\rho)$ is the integrated sextupole strength, and D is the dispersion function. Since the phase of A or B propagates at twice the betatron phase advance (see Exercise 2.3.10), two identical quadrupoles (sextupoles) separated by odd multiples of 90° in betatron phase advance cancel each other. Similarly, two identical quadrupoles (sextupoles) separated by an integer multiple of 180° in betatron phase advance will produce additive coherent kicks. By using sextupole families, the global chromatic perturbation function of the lattice can be minimized. The treatment is identical to the stopband integral to be discussed next.

A. Systematic chromatic half-integer stopband width

We have found that the perturbation of betatron function is most sensitive to stopband integrals near $p \approx [2\nu]$ harmonics (see Sec. III.4). Here we investigate the effect of systematic chromatic stopband integrals. We will show that systematic stopbands can generate a sizable second-order chromaticity.

The effect of systematic chromatic gradient error on betatron amplitude modulation can be analyzed by using the chromatic stopband integrals of Eq. (2.201):

$$\begin{cases} J_{p,x} = \dfrac{1}{2\pi}\displaystyle\oint \beta_x \Delta K_x e^{-jp\phi_x} ds, \\ J_{p,z} = \dfrac{1}{2\pi}\displaystyle\oint \beta_z \Delta K_z e^{-jp\phi_z} ds. \end{cases} \tag{2.338}$$

We consider a lattice made of P superperiods, where L is the length of a superperiod with $K(s+L) = K(s)$, $\beta(s+L) = \beta(s)$. Let $C = PL$ be the circumference of the accelerator. The integral of Eq. (2.338) becomes

$$\begin{aligned} J_{p,y} &= -\left\{\frac{\delta}{2\pi}\int_0^L \beta_y K_y e^{-jp\phi} ds\right\}\left[1 + e^{-jp\frac{2\pi}{P}} + e^{-j2p\frac{2\pi}{P}} + e^{-j3p\frac{2\pi}{P}} + \cdots\right] \\ &= -\left\{\frac{\delta}{2\pi}\int_0^L \beta_y K_y e^{-jp\phi} ds\right\} \zeta_P\left(\frac{p}{P}\right) e^{-j\pi p\frac{P-1}{P}}, \end{aligned} \tag{2.339}$$

where y stands for either x or z, and the diffracting function $\zeta_P(u)$ is given by

$$\zeta_P(u) = \frac{\sin(Pu\pi)}{\sin(u\pi)}. \tag{2.340}$$

Note that the diffracting structure function $\zeta_P \to P$ as $u \to$ integer. Note that

$$J_{p,y} = 0, \quad \text{unless} \quad p = 0 \ (\text{Mod } P).$$

At $p = 0$ (Mod P), the half-integer stopband integral increases by a factor of P, i.e. each superperiod contributes additively to the chromatic stopband integral.

Since the perturbation of betatron functions is most sensitive to the chromatic stopbands near $p \approx [2\nu_x]$ and $[2\nu_z]$, a basic design principle of strong-focusing synchrotrons is to avoid important systematic chromatic stopbands. This can be achieved by choosing the betatron tunes such that $[2\nu_x]$ and $[2\nu_z]$ are not divisible by the superperiod P. For example, the AGS lattice has $P = 12$, and the betatron tune should avoid a value of 6, 12, 18, etc. The actual betatron tunes at $\nu_{x/z} = 8.8$ are indeed far from systematic half-integer stopbands at $p = 6$ and 12, and the resulting chromatic perturbation is small. In fact, the AGS lattice can be approximated by a lattice made of 60 FODO cells. The important stopbands are located at $p = 30, 60, 90 \cdots$, which are far from the betatron tunes. Similarly, the TEVATRON has a super-periodicity of $P = 6$, and the betatron tune should avoid 18, 24, 30, etc.[88]

Generally, it is beneficial to design an accelerator with high super-periodicity so that the betatron tunes can be located far from the important chromatic stopbands. Some examples of high superperiod machines are $P = 12$ for the ALS, $P = 40$ for the APS, $P = 16$ for the ESRF, and $P = 22$ for the SPRING-8 at JSRF. However, a high energy accelerator or storage ring with large super-periodicity is costly. Thus the goal is to design an accelerator such that the chromatic stopband integral of each module is zero, or the stopband integrals of two modules cancel each other.

B. Chromatic stopband integrals of FODO cells

Now we examine the chromatic stopband integral of the arc, which is composed of N FODO cells. The chromatic stopband integral in thin-lens approximation is given by

$$\begin{aligned} J_p &= -\frac{\delta}{2\pi}\left(\frac{\beta_{\max}}{f} - \frac{\beta_{\min}}{f}e^{-jp\frac{\Phi}{2\nu}}\right)\left[1 + e^{-jp\frac{\Phi}{\nu}} + e^{-j2p\frac{\Phi}{\nu}} + e^{-j3p\frac{\Phi}{\nu}} + \cdots\right] \\ &= -\frac{2\delta}{\pi\cos\frac{\Phi}{2}}\left(\sin\frac{\Phi}{2}\cos\frac{p\Phi}{4\nu} + j\sin\frac{p\Phi}{4\nu}\right)\zeta_N\left(\frac{p\Phi}{2\pi\nu}\right)e^{-j\frac{(2N-1)p\pi}{2N}}, \end{aligned} \tag{2.341}$$

where Φ is the phase advance per cell, $\beta_{\max}$ and $\beta_{\min}$ are values of the betatron amplitude function at the focusing and defocussing quadrupoles respectively, f is the focal length of each quadrupole, and the diffracting function $\zeta_N(u)$ is given by Eq. (2.340). If $p\Phi/2\pi\nu = 0$ (Mod N), the diffracting function is equal to N. This means that each FODO cell contributes additively to the stopband integral. Fortunately, since $\Phi/2\pi$ is normally about 1/4 (90^0 phase advance) so that $p\Phi/2\pi\nu \approx p/4\nu \approx 1/2$, the chromatic stopband integral at $p \approx 2\nu$ due to N FODO cells is small. In particular, if $N\Phi = \text{integer} \times \pi$, the chromatic stopband of the arc adds up to zero at harmonics $p \approx 2\nu$, i.e. the stopband integrals at $p \approx [2\nu]$ resulting from N FODO cells in the arcs is small if the total phase advance of these FODO cells is $N\Phi = \text{integer} \times \pi$,

[88] The stopbands in a collider can also be minimized by local cancellation of various beam line modules, to be discussed in the next subsection.

where the transfer matrix of the arc becomes a unit matrix I or a half-unit matrix $-I$.

C. The chromatic stopband integral of insertions

Because of its small β^* value, the insertion may contribute a substantial amount to the chromatic stopband integral. Since it is difficult to design an insertion with zero chromatic half-integer stopband width,[89] cancellation of the chromatic stopband integrals between two adjacent insertions would be desirable.

Let Φ^{ins} and J_p^{ins} be respectively the phase advance and the chromatic stopband integral of an insertion. The total contribution of two adjacent insertions becomes

$$J_p = J_p^{\text{ins}}\left[1 + \exp\left(j\frac{p\Phi^{\text{ins}}}{\nu}\right)\right]. \tag{2.342}$$

At the harmonic $p \approx [2\nu]$, we obtain $J_p = 0$ if $\Phi^{\text{ins}} = (2n+1)\pi/2$. Thus, if the insertion is a quarter-wave module, the chromatic stopband integrals of two adjacent insertions cancel each other. This cancellation principle remains valid when two insertions are separated by a unit transfer matrix. Such a procedure was extensively used in the design of the RHIC lattice[90] and the SSC lattice.[91]

D. Effect of the chromatic stopbands on chromaticity

The chromatic stopband integrals for large colliders, such as the SSC and RHIC, remain important even after careful manipulation of piecewise cancellation, particularly when the beam momentum spread is large. They give rise to a large betatron amplitude modulation, called betabeat, and second-order chromaticity for off-momentum particles. The following example illustrates the effect of betatron amplitude function modulation on chromaticity.

We consider a lattice dominated by a single p harmonic half-integer chromatic stopband. The betatron modulation of the lattice is given by

$$\frac{\Delta\beta}{\beta} \approx -\frac{|J_p|\cos(p\phi + \chi)}{2(\nu - p/2)}, \tag{2.343}$$

where the chromatic stopband integral J_p is given by Eq. (2.338), and is proportional to δ. Substituting $\beta = \beta_0(1 + \Delta\beta/\beta_0)$ into Eq. (2.324), we obtain

$$\Delta\nu_y = C_y^{(1)}\delta + C_y^{(2)}\delta^2 + \cdots, \tag{2.344}$$

[89] In fact, high-β triplets or doublets on both sides of the IP contribute additively to the systematic half-integer stopband near $p \approx 2\nu_{x/z}$.

[90] S.Y. Lee, J. Claus, E.D. Courant, H. Hahn, G. Parzen, *IEEE Trans. Nucl. Sci.* **NS-32**, 1626 (1985).

[91] A. Garren, private communications. See also the SSC report.

where y stands for either x or z, and $C_y^{(1)}$ and $C_y^{(2)}$ are the first- and second-order chromaticities

$$C_y^{(1)} = -\frac{1}{4\pi}\oint \beta_y(K_y - S_y D)ds, \tag{2.345}$$

$$C_y^{(2)} = -C_y^{(1)} - \frac{|J_{p,y}|^2/\delta^2}{4(\nu_y - p/2)}. \tag{2.346}$$

If the first-order chromaticity is corrected, then $C_y^{(1)} = 0$. The remaining second-order tune shift $C_y^{(2)}\delta^2$ can arise from the chromatic stopband integral. Figure 2.41 shows an example of the second-order chromatic tune shift with δ.[92] The stopband correction that minimizes the β-modulation also minimizes the second-order chromaticity. We next discuss the half-integer chromatic stopband correction using sextupole families.

E. Effect of sextupoles on the chromatic stopband integrals

The chromatic sextupoles also contribute to the systematic chromatic stopbands. Here we present an example of chromatic correction for a collider lattice.

First we evaluate the stopband integral due to the chromatic sextupoles. Let S_F and S_D be the integrated sextupole strength at QF and QD of FODO cells in the arc. The p-th harmonic stopband integral from these chromatic sextupoles is

$$J_{p,\text{sext}} = \frac{\delta}{2\pi}\zeta_N\left(\frac{p\Phi}{2\pi\nu}\right)\left[\beta_F S_F D_F + \beta_D S_D D_D e^{-jp\Phi/2\nu}\right] e^{-j(N-1)p\Phi/2\nu}, \tag{2.347}$$

where N is the number of cells, and the diffraction function ζ_N is given by Eq. (2.340). As in Eq. (2.339), the stopband integral is zero or small if $N\Phi/\pi$ = integer, i.e. the chromatic sextupole does not contribute significantly to the chromatic stopband integral if the transfer matrix of the arc is I or $-I$.

To obtain a nonzero chromatic stopband integral, sextupoles are organized in families. We consider an example of a four-family scheme with

$$\{S_{F1} = S_F + \Delta_F,\ S_{D1} = S_D + \Delta_D,\ S_{F2} = S_F - \Delta_F,\ D_{D2} = S_D - \Delta_D\},$$

that is commonly used in FODO cells with 90° phase advance. Here the parameters S_F and S_D are determined from the first-order chromaticity correction, Since $\beta(s)$ and $D(s)$ are periodic functions of s in the repetitive FODO cells, the parameters Δ_F, Δ_D will not affect the first-order chromaticity, which is proportional to the zeroth harmonic of the stopband integral. However, the chromatic stopband integrals due to the parameters Δ_F and Δ_D are given by

$$\Delta J_{p,\text{sext}} = \frac{\delta}{2\pi}\zeta_N\left(\frac{p\Phi}{2\nu\pi} - \frac{1}{2}\right)\left[\beta_F\Delta_F D_F + \beta_D\Delta_D D_D e^{-jp\Phi/4\nu}\right] e^{-j(N-1)[(p\Phi/2\nu\pi)-(1/2)]\pi}. \tag{2.348}$$

[92] S.Y. Lee, G.F. Dell, H. Hahn, G. Parzen, *Proc 1987 Part. Accel. Conf.*, p. 1328, (1987).

At $p \approx [2\nu]$ and $\Phi/2\pi \approx 1/4$ (90° phase advance), we have $\zeta_N \to N$, i.e. every FODO cell contributes additively to the chromatic stopband. The resulting stopband width is proportional to Δ_F and Δ_D parameters. By adjusting Δ_F and Δ_D parameters, the betabeat and the second-order chromaticity can be minimized. The scheme works best for a nearly 90° phase advance per cell with $N\Phi$ = integer $\times\,\pi$, where the third-order resonance-driving term vanishes also for the four-family sextupole scheme. Fig. 2.41 shows an example of chromatic correction with four families of sextupoles in RHIC, where the second-order chromaticity and the betatron amplitude modulation can be simultaneously corrected.

Similarly, the six-family sextupole scheme works for 60° phase advance FODO cells, where the six-family scheme

$$\{S_{F1}, S_{D1}, S_{F2}, D_{D2}, S_{F3}, S_{D3}\} \tag{2.349}$$

has two additional parameters.

V.4 Lattice Design Strategy

Based on our study of linear betatron motion, the lattice design of accelerator can be summarized as follows. The lattice is generally classified into three categories: low energy booster, collider lattice, and low-emittance lattice storage rings.

- The betatron tunes should be chosen to avoid systematic integer and half-integer stopbands and systematic low-order nonlinear resonances; otherwise, the stopband width should be corrected.
- The chromatic sextupoles should be located at high dispersion function locations. The focusing and defocussing sextupole families should be located in regions where $\beta_x \gg \beta_z$, and $\beta_x \ll \beta_z$ respectively in order to gain independent control of the chromaticities.
- The betatron amplitude function and the betatron phase advance between the kicker and the septum should be optimized to minimize the kicker angle and maximize the injection or extraction efficiency. Local orbit bumps can be used to alleviate the demand for a large kicker angle. Furthermore, the injection line and the synchrotron optics should be properly "matched" or "mismatched" to optimize the emittance control. To improve the slow extraction efficiency, the β value at the (wire) septum location should be optimized. The β_x and β_z values at the injection area, particularly in the strip injection scheme, should be adjusted to minimize emittance blow-up due to multiple Coulomb scattering. The local vacuum pressure at the high-β value locations should be minimized to minimize the effect of beam gas scattering.

- It is advisable to avoid the transition energy for low to medium energy synchrotrons in order to minimize the beam dynamics problems during acceleration.
- Experience with low energy synchrotrons indicates that the Laslett space-charge tune shift should be limited to about 0.3 (see Exercise 2.3.2). This criterion usually determines beam emittance and intensity.

Besides these design issues, problems regarding the dynamical aperture, nonlinear betatron detuning, collective beam instabilities, rf system, vacuum requirement, beam lifetime, etc., should be addressed. Some of these issues will be addressed in this introductory textbook. The design of minimum emittance electron storage rings will be discussed in Chap. 4, Sec. III.

Exercise 2.5

1. Show that the chromaticity of an accelerator consisting of N FODO cells in thin-lens approximation is
$$C_{\rm nat}^{\rm FODO} = -\frac{\tan(\Phi/2)}{\Phi/2}\nu,$$
where Φ is the phase advance per cell and $\nu = N\Phi/2\pi$ is the betatron tune.

2. A set of three quadrupoles ($\{Q_{F1}\ Q_{D2}\ Q_{F3}\}$ or $\{Q_{D1}\ Q_{F2}\ Q_{D3}\}$), called a low-$\beta$ triplet, is commonly used in insertion regions to provide horizontal and vertical low-β squeeze.

   (a) Show that the low-beta triplets contribute about
$$-\frac{2\Delta s}{4\pi\beta^*} \approx -\frac{1}{2\pi}\sqrt{\frac{\beta_{\rm max}}{\beta^*}}$$
units of natural chromaticity, where Δs is the effective distance between the triplet and the interaction point (IP), β^* is the value of the betatron amplitude function at IP, and $\beta_{\rm max}$ is the maximum betatron amplitude function at the triplet.

   (b) If $\beta_{\rm max} \gg \beta^*$, show that the betatron phase advance between the triplet and IP is $\pi/2$.

   (c) Show that the triplets on both sides of IP contribute additively to the stopband integral at $p \approx 2\nu$, where ν is the betatron tune.

3. Show that the strengths of two sextupole families used to correct the chromaticities of FODO cells are
$$S_{\rm F} = \frac{1}{2f^2\theta}\frac{\sin(\Phi/2)}{(1+\frac{1}{2}\sin(\Phi/2))};\quad S_{\rm D} = -\frac{1}{2f^2\theta}\frac{\sin(\Phi/2)}{(1-\frac{1}{2}\sin(\Phi/2))},$$
where f is the focal length of the quadrupole in the FODO cell, θ is the dipole bending angle of a half FODO cell, and Φ is the phase advance of the FODO cell. Note that the required sextupole strength is larger at the defocussing quadrupole.

4. Show that the chromatic stopband integrals for a lattice made of N FODO cells in thin-lens approximation are
$$J_{p,x} = -\frac{\delta}{2\pi}\left(\frac{\beta_x({\rm F})}{f_{\rm F}} - \frac{\beta_x({\rm D})}{f_{\rm D}}e^{-jp\Phi_x/2\nu_x}\right)\zeta_N(\frac{p}{N})e^{-jp\pi(N-1)/N},$$
$$J_{p,z} = -\frac{\delta}{2\pi}\left(-\frac{\beta_z({\rm F})}{f_{\rm F}} + \frac{\beta_z({\rm D})}{f_{\rm D}}e^{-jp\Phi_z/2\nu_z}\right)\zeta_N(\frac{p}{N})e^{-jp\pi(N-1)/N},$$
where Φ_x, Φ_z, and ν_x, ν_z are the phase advances per cell and the betatron tunes, β_x, β_z are betatron amplitude functions, $f_{\rm F}$ and $f_{\rm D}$ are focal lengths for focusing and defocussing quadrupoles, and the diffraction function $\zeta_N(u)$ is given by Eq. (2.340). Assuming $f_{\rm F} = f_{\rm D}$ with $\Phi_x = \Phi_z = \Phi = 2\pi\nu/N$, show that the chromatic stopband integral is
$$J_{p,x} = -\frac{2\delta}{\pi\cos\frac{\Phi}{2}}\left[\sin\frac{\Phi}{2}\cos\frac{p\pi}{2N} + j\sin\frac{p\pi}{2N}\right]\zeta_N(p/N)e^{-jp\pi(2N-1)/2N}.$$

5. Verify Eq. (2.347) and Eq. (2.348).

6. The AGS is composed of 12 superperiods with 5 nearly identical FODO cells per superperiod. The betatron tunes are $\nu_z = 8.8$ and $\nu_x = 8.7$. Calculate the systematic stopband widths for harmonics 17 and 18 respectively. What region of betatron tunes should be avoided to minimize the effect of systematic stopbands?

7. The Fermilab booster is a combined function synchrotron. The lattice is made of 24 cells, as shown below.

   FNALBSTCELL : LINE = (BF S120 BF S050 BD S600 BD S050)
   BF : SBEND L = 2.889612 K1 = 0.0542203 ANGLE = 0.070742407
   BD : SBEND L = 2.889612 K1 = −0.0577073 ANGLE = 0.060157561
   Sabc : DRIFT L = a.bc

   Find the systematic stopband width and discuss the choice of the betatron tunes.

8. Use the experimental data below to calculate the chromaticity of the IUCF cooler ring, where $\gamma_{\rm T} = 4.6$ and $C = 86.82$ m, at 45 MeV proton kinetic energy.

Betatron tunes vs revolution frequencies of the cooler

Frequency [MHz]	1.032680	1.031680	1.030680
Q_x	3.7156	3.7243	3.7364
Q_z	4.6790	4.6913	4.7080

VI Linear Coupling

We have discussed uncoupled linear betatron motion, but in reality betatron motions are coupled through solenoidal and skew-quadrupole fields. The solenoidal field exists in electron cooling storage rings, and in high-energy detectors at the interaction point (IP). The skew-quadrupole field arises from quadrupole rolls, vertical closed-orbit error in sextupoles or horizontal closed-orbit error in skew sextupoles, fringe field of a Lambertson septum, and feed-downs from higher-order multipoles.

Linear betatron coupling is both a nuisance and a benefit in the operation of synchrotrons: the available dynamical aperture for particle motion may be reduced, but the vertical emittance of electron beams in storage rings can be adjusted, and the Touschek lifetime limitation can be alleviated by linear coupling.

Here we discuss the beam dynamics associated with linear betatron coupling arising from skew quadrupoles and solenoids. The effective linear coupling Hamiltonian and resonance strength will be derived based on perturbation approximation. Here we find that the linear coupling can induce amplitude exchange between horizontal and vertical betatron motions.[93] Measurement and correction of linear coupling will also be discussed.

VI.1 The Linear Coupling Hamiltonian

The vector potentials for skew quadrupoles and solenoids are given by

$$\begin{cases} A_x = A_z = 0, \quad A_s = \frac{1}{2}(\frac{\partial B_z}{\partial z} - \frac{\partial B_x}{\partial x})xz, & \text{for skew quadrupoles,} \\ A_x = \frac{1}{2}B_{\|}(s)z, \quad A_z = -\frac{1}{2}B_{\|}(s)x, \quad A_s = 0, & \text{for solenoids,} \end{cases} \tag{2.350}$$

where $\frac{1}{2}(\frac{\partial B_z}{\partial z} - \frac{\partial B_x}{\partial x})$ and $B_{\|}(s)$ are skew-quadrupole gradient[94] and solenoid field strength. Substituting the components of the vector potential in Eq. (2.350) into the Hamiltonian in Eq. (2.19), we obtain the linearized Hamiltonian for particle motion in accelerators as (see Exercise 2.6.3):

$$\begin{aligned} x'' + K_x(s)x + 2gz' - (q - g')z = 0, \\ z'' + K_z(s)z + 2gx' - (q + g')x = 0, \end{aligned} \tag{2.351}$$

[93] In Sec. IV, we show that a skew quadrupole at a high horizontal dispersion location can produce vertical dispersion, which can generate vertical emittance for electron beams and result in lower luminosity for colliders (see Exercise 2.4.10).

[94] The skew quadrupole can also arise from "feed-down" of an off-centered vertical closed orbit in sextupoles. Let z_{co} be the closed orbit at a sextupole with sextupole strength $B_2 = \partial^2 B_z/\partial x^2$. The effective skew quadrupole strength becomes $q = B_2 z_{co}/B\rho$.

where the primes are derivatives with respect to the independent variable s, K_x and K_z are quadrupole-like focusing functions, and

$$g(s) = \frac{B_{\|}(s)}{2B\rho}, \quad q(s) = \frac{1}{2B\rho}\left[\frac{\partial B_z}{\partial z} - \frac{\partial B_x}{\partial x}\right] = \frac{a_1}{\rho} \tag{2.352}$$

are effective solenoid and skew quadrupole strengths.

Let $(x, p_x/p; z, p_z/p)$ be the conjugate phase space coordinates. The betatron motion of Eq. (2.351) can be derived from the following linearized Hamiltonian:

$$\begin{aligned} \tilde{H} &= \frac{1}{2}\left[\left(\frac{p_x}{p}\right)^2 + \left(K_x(s) + g^2(s)\right)x^2 + \left(\frac{p_z}{p}\right)^2 + \left(K_z(s) + g^2(s)\right)z^2\right] \\ &\quad -q(s)xz - g(s)\left[\frac{p_x}{p}z - \frac{p_z}{p}x\right]. \end{aligned} \tag{2.353}$$

Here the linear coupling potential is

$$V_{\rm lc} = -qxz - g\left[\frac{p_x}{p}z - \frac{p_z}{p}x\right]. \tag{2.354}$$

Using Floquet transformation of Eq. (2.94) for the uncoupled Hamiltonian, we obtain the coupling-potential:

$$\begin{aligned} V_{\rm lc} &= (\beta_x\beta_z J_x J_z)^{1/2}\left\{\left[-q + g\left(\frac{\alpha_x}{\beta_x} - \frac{\alpha_z}{\beta_z}\right)\right][\cos(\Phi_x + \Phi_z) + \cos(\Phi_x - \Phi_z)]\right. \\ &\quad \left. + g\left(\frac{1}{\beta_x} - \frac{1}{\beta_z}\right)\sin(\Phi_x + \Phi_z) + g\left(\frac{1}{\beta_x} + \frac{1}{\beta_z}\right)\sin(\Phi_x - \Phi_z)\right\}, \end{aligned} \tag{2.355}$$

where

$$\Phi_x = \phi_x + \chi_x(s) - \nu_x\theta, \quad \chi_x = \int_0^s \frac{ds}{\beta_x},$$
$$\Phi_z = \phi_z + \chi_z(s) - \nu_z\theta, \quad \chi_z = \int_0^s \frac{ds}{\beta_z},$$

and (J_x, ϕ_x) and (J_z, ϕ_z) are pairs of conjugate phase-space coordinates. Since $V_{\rm lc}(s)$ is a periodic function of s, it can be expanded in Fourier harmonics as

$$V_{\rm lc}(\theta) = \frac{\sqrt{J_x J_z}}{2R}\sum_\ell \left\{\left(G_{1,-1,\ell}e^{j(\phi_x - \phi_z - \ell\theta + \chi_-)} + c.c\right) + \left(G_{1,1,\ell}e^{j(\phi_x + \phi_z - \ell\theta + \chi_+)} + c.c\right)\right\}, \tag{2.356}$$

where R is the average radius of the accelerator, ℓ is an integer. The Fourier coefficients of the difference and sum resonances, $G_{1,-1,\ell}e^{j\chi_-}$ and $G_{1,1,\ell}e^{j\chi_+}$, are given by

$$G_{1,\mp1,\ell}\, e^{j\chi_\mp} = \frac{1}{2\pi}\oint \sqrt{\beta_x\beta_z}\, A_{{\rm lc}\mp}(s)\, e^{j[\chi_x \mp \chi_z - (\nu_x \mp \nu_z - \ell)\theta]}ds. \tag{2.357}$$

Here ν_x, ν_z are betatron tunes, $\chi_x = \int_0^s ds/\beta_x, \chi_z = \int_0^s ds/\beta_z$ are betatron phases, and the linear coupling kernel $A_{\mathrm{lc}\mp}(s)$ are

$$A_{\mathrm{lc}\mp}(s) = -\frac{a_1}{\rho} + g(s)(\frac{\alpha_x}{\beta_x} - \frac{\alpha_z}{\beta_z}) + jg(s)(\frac{1}{\beta_x} \pm \frac{1}{\beta_z}), \tag{2.358}$$

obtained from the linear coupling potential of Eq. (2.355). Both skew quadrupoles and solenoids can drive the sum and difference linear coupling resonances. Table VI.1 lists the corresponding driving terms.

Table 2.2: Linear coupling resonances and their driving terms

Resonance	Driving phase	Amplitude-dependent factor	Classification
$\nu_x + \nu_z = \ell$	$(\Phi_x + \Phi_z)$	$J_x^{1/2} J_z^{1/2}$	sum resonance
$\nu_x - \nu_z = \ell$	$(\Phi_x - \Phi_z)$	$J_x^{1/2} J_z^{1/2}$	difference resonance

The linear coupling potential has been decomposed into terms of the difference and sum resonances located respectively at $\nu_x - \nu_z = \ell$ and $\nu_x + \nu_z = \ell'$, where ℓ and ℓ' are integers. In general, the coupling betatron sum-resonances are dangerous to the stable betatron motion,[95] the optics of the betatron motion is normally designed to avoid sum resonances.

If the linear coupling kernel $A_{\mathrm{lc}\mp}$ satisfies a periodic condition similar to that in a synchrotron with P superperiods, the resonance coupling coefficient $G_{1,\mp 1,\ell}$ will be zero unless ℓ is an integer multiple of P. If ℓ is an integer multiple of P, each superperiod contributes additively to the linear coupling resonance strength. This is called the systematic linear coupling resonance. For example, since the superperiodicity of the LEP lattice is 8, the difference between the integer part of the horizontal and vertical betatron tunes should *not* be 0, 8, 16, $\cdots$, to minimize the effect of the systematic linear coupling resonance. The strength of the linear coupling resonance due to random errors such as quadrupole roll and vertical closed orbit in sextupoles is smaller. It occurs at all integer ℓ.

Near a difference linear coupling resonance, the horizontal and vertical betatron motions are coupled. The coupling resonance can cause beam size increase and decrease the beam lifetime. Thus the linear-coupling resonance-strength should be minimized, and the resonance strength is usually small. Thus the effective Hamiltonian for betatron tunes near an isolated coupling resonance will be discussed in the following sections.

[95] We will show, in Sec. VII, that the horizontal and vertical betatron amplitudes can grow without bound near a betatron sum resonance.

VI.2 Effects of an isolated Linear Coupling Resonance

Since the betatron tunes are normally near the linear coupling line, this section studies the effects of an isolated coupling resonance on betatron motion.

A. Effective Hamiltonian for a Single Linear Coupling Resonance

Near an isolated coupling resonance $\nu_x - \nu_z = \ell$, the Hamiltonian Eq. (2.353), in action-angle phase space coordinates, can be approximated by

$$H \approx \nu_x J_x + \nu_z J_z + G_{1,-1,\ell}\sqrt{J_x J_z}\cos(\phi_x - \phi_z - \ell\theta + \chi), \tag{2.359}$$

where the Fourier amplitude $G_{1,-1,\ell}$ and the phase factor χ_- are given by Eq. (2.357).

The Hamiltonian Eq. (2.359) corresponds to two coupled linear oscillators, which can be expanded in terms of two normal modes with tunes (see Exercise 2.6.5)

$$\nu_{1,\pm} = \frac{1}{2}(\nu_x + \nu_z + \ell) \pm \frac{1}{2}\lambda, \quad \nu_{2,\pm} = \frac{1}{2}(\nu_x + \nu_z - \ell) \pm \frac{1}{2}\lambda \tag{2.360}$$

where

$$\lambda = \sqrt{(\nu_x - \nu_z - \ell)^2 + |G_{1,-1,\ell}|^2}. \tag{2.361}$$

This means that the betatron tunes are separated by λ, and the minimum separation between the normal mode tunes is $|G_{1,-1,\ell}|$. Figure 2.42 shows an example of measured betatron tunes vs quadrupole strength at the IUCF cooler ring. As the strength of a quadrupole is varied across the linear coupling resonance $\nu_x - \nu_z + 1 \approx 0$ ($\ell = -1$ for the IUCF Cooler), the betatron tunes of normal modes approach each other, reaching a minimum value of tune separation, $|G_{1,-1,\ell}|$ as demonstrated in Fig. 2.42. This method has been commonly applied to measure the linear coupling strength, and provide linear coupling correction.

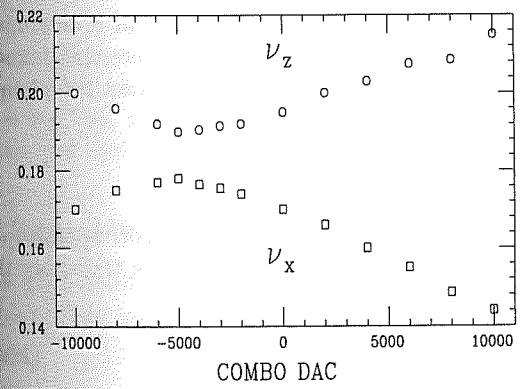

Figure 2.42: The measured betatron normal mode tunes vs the strength of an IUCF cooler quadrupole, showing that the horizontal and vertical motion are coupled. The minimum distance between two normal modes is equal to the coupling coefficient $|G_{1,-1,\ell}|$. The vertical axis is the fractional part of the betatron tunes, and the horizontal axis is the digital to analog conversion (DAC) unit of a COMBO power supply for a set of horizontally focusing quadrupoles.

B. Resonance precessing frame and Poincaré surface of section

We transform the Hamiltonian Eq. (2.359) into the "resonant precessing frame" by using the generating function

$$F_2(\phi_x, \phi_z, J_1, J_2) = (\phi_x - \phi_z - \ell\theta + \chi)J_1 + \phi_z J_2,$$

where the new action-angle variables are

$$\phi_1 = \phi_x - \phi_z - \ell\theta + \chi, \quad \phi_2 = \phi_z, \quad J_1 = J_x, \quad J_2 = J_x + J_z.$$

The new Hamiltonian is

$$\begin{aligned} H &= H_1(J_1, \phi_1, J_2) + H_2(J_2), \\ H_1 &= \delta_1 J_1 + G_{1,-1,\ell}\sqrt{J_1(J_2 - J_1)}\cos\phi_1, \\ H_2(J_2) &= \nu_z J_2, \end{aligned} \tag{2.362}$$

where $\delta_1 = \nu_x - \nu_z - \ell$ is the resonance proximity parameter. The system is integrable with two invariants J_2 and $H_1 = E_1$. Since J_2 is invariant, we obtain

$$J_x + J_z = J_2 = \text{constant}. \tag{2.363}$$

The horizontal and vertical betatron motions exchange their actions while the sum of actions is conserved.

Hamilton's equations of motion are

$$\dot{J}_1 = G_{1,-1,\ell}\sqrt{J_1(J_2 - J_1)}\sin\phi_1, \tag{2.364}$$

$$\dot{\phi}_1 = \delta_1 + G_{1,-1,\ell}\frac{J_2 - 2J_1}{2\sqrt{J_1(J_2 - J_1)}}\cos\phi_1. \tag{2.365}$$

For a given J_2, all tori can be described by a single parameter E_1 that is determined from the initial condition. The particle motion in the resonant precessing frame is determined completely by the condition of a constant J_2 and a constant Hamiltonian value $H_1(J_1, \phi_1, J_2) = E_1$.

C. Initial horizontal orbit

We first consider the simple orbit with "energy" $E_1 = \delta_1 J_2$, which corresponds to an initial horizontal betatron oscillation with $J_{1,\max} = J_2$. The particle trajectory that satisfies $H_1 = \delta_1 J_2$ is

$$P^2 + Q^2 = 2J_2, \tag{2.366}$$

$$Q^2 + \frac{\delta_1^2}{\lambda^2}P^2 = 2\frac{\delta_1^2}{\lambda^2}J_2, \tag{2.367}$$

where $\lambda = \sqrt{\delta_1^2 + |G_{1,-1,\ell}|^2}$, and the normalized coordinates Q, P are

$$Q = \sqrt{2J_1}\cos\phi_1, \quad P = -\sqrt{2J_1}\sin\phi_1. \tag{2.368}$$

Figure 2.43 shows a schematic plot of the Courant-Snyder circle and the coupling ellipse of Eqs (2.366) and (2.367). The phase coordinate ϕ_1 of Eq. (2.365) changes rapidly on the Courant-Snyder circle, where $J_1 = J_2$.

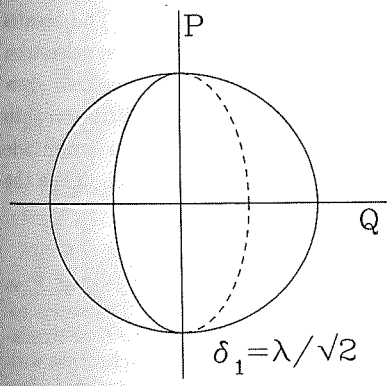

Figure 2.43: Schematic drawing of the Courant-Snyder circle of Eq. (2.366) and the coupling ellipse of (2.367) with $\delta_1 = \lambda/\sqrt{2}$. The size of the ellipses depends on the initial condition. If there is no other noise source, particle motion will follow the path of solid (or dashed) lines. Based on the equations of motion (2.364) and (2.365), the phase ϕ_1 rapidly varies on the Courant-Snyder circle (see the top right plot of Fig. 2.47).

When the particle trajectory moves along the Courant-Snyder circle shown in Eq. (2.366), the phase ϕ_1 varies very rapidly. As the betatron oscillation reaches $Q = 0, P = \sqrt{2J_2}$, the particle follows the coupling ellipse, Eq. (2.367), which is inside the Courant-Snyder circle. The minimum horizontal amplitude is

$$Q_{\min} = \frac{\delta_1}{\lambda}\sqrt{2J_2}. \tag{2.369}$$

If $\delta_1 \gg |G_{1,-1,\ell}|$, then $Q_{\min} \approx \sqrt{2J_2}$ and the betatron coupling is negligible. If $\delta_1 = 0$, the coupling ellipse becomes a straight line cutting through the origin $Q = 0$ and $P = 0$. This means that the horizontal action can be fully converted to vertical action and vice versa.

D. General linear coupling solution

The fixed points of the Hamiltonian are determined by the conditions $\dot{J}_1 = 0$ and $\dot{\phi}_1 = 0$. They are located at $\phi_1 = 0$ or π with

$$\delta_1 \pm G_{1,-1,\ell}\frac{J_2 - 2J_1}{2\sqrt{J_1(J_2 - J_1)}} = 0. \tag{2.370}$$

The stable fixed points (SFPs) of the Hamiltonian are

$$J_{1,\text{sfp}} = \begin{cases} \begin{cases} (\frac{1}{2} + \delta_1/2\lambda)J_2, & (\phi_1 = 0) \\ (\frac{1}{2} - \delta_1/2\lambda)J_2, & (\phi_1 = \pi) \end{cases} & \text{if } G_{1,-1,\ell} > 0 \\ \begin{cases} (\frac{1}{2} - \delta_1/2\lambda)J_2, & (\phi_1 = 0) \\ (\frac{1}{2} + \delta_1/2\lambda)J_2, & (\phi_1 = \pi) \end{cases} & \text{if } G_{1,-1,\ell} < 0. \end{cases} \tag{2.371}$$

At SFPs, the horizontal and vertical betatron motions are correlated in phase without exchange in betatron amplitudes. Figure 2.44 shows 6 Poincaré surfaces of section in the resonance rotating frame with a given value of $J_2 = J_x + J_z$. The results are obtained from simple tracking calculations of particle motion in a synchrotron with perfect linear decoupled betatron motion everywhere except a localized skew quadrupole kick, where the betatron tunes are $\nu_x = 4.820$, $\nu_z = 4.825$ and the strength of the skew quadrupole is $a_1/\rho = 0.00628$ m^{-1}. The values of betatron amplitude functions are $\beta_x = 10$ m and $\beta_z = 10$ m at the skew quadrupole location. Thus the effective resonance strength is about $G_{1,-1,0} = 0.01$.

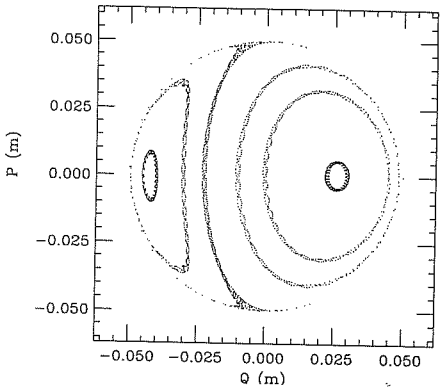

Figure 2.44: Phase space ellipses of P vs Q given by Eq. (2.368) in the resonance rotating frame obtained from numerical simulations of particle motion in a synchrotron with linear betatron motion and a localized skew quadrupole kick. The values of the betatron amplitude functions at the skew quadrupole location is $\beta_x = 10$ m, and $\beta_z = 10$ m; the betatron tunes of the machine are $\nu_x = 4.82$ and $\nu_z = 4.825$; the skew quadrupole strength is $a_1/\rho = 0.00628$ m^{-1}. These ellipses correspond to various initial J_1 and ϕ_1 values with $J_2 = 90\pi$ mm-mrad. Note that the structure of the phase space ellipses remains the same if J_2 is varied.

With the coupling ellipse Eq. (2.367) rewritten as $G_{1,-1,\ell}\sqrt{J_1}\cos\phi_1 = \delta_1\sqrt{J_2 - J_1}$, the Courant-Snyder ellipse Eq. (2.366) is divided into two halves (see Figs. 2.43 and 2.44). Using Hamilton's equations [Eqs. (2.364) and (2.365)], we obtain

$$\ddot{J}_1 + \lambda^2 J_1 = \lambda^2 \bar{J}, \tag{2.372}$$

where

$$\bar{J} = (2\delta_1 E + G_{1,-1,\ell}^2 J_2)/2\lambda^2$$

with a Hamiltonian value $E = \delta_1 J_1 + G_{1,-1,\ell}\sqrt{J_1(J_2 - J_1)}\cos\phi_1$. Thus the evolution of the action coordinate at a linear coupling resonance is given by

$$J_1 = \sqrt{\bar{J}^2 - (E/\lambda)^2}\cos[\lambda\theta + \varphi] + \bar{J}, \tag{2.373}$$

where $|E| \le \lambda\bar{J}$, and φ is an initial phase factor. The SFPs of Eq. (2.371) correspond to the orbit with $E = \pm\lambda\bar{J} = \pm\lambda J_{1,\text{sfp}}^{\pm}$. Note that the tune of the linear coupling motion is independent of betatron amplitude.[96]

If particles in a given bunch distribution have identical betatron tunes, linear coupling can cause bunch shape oscillations; the bunch will resume its original shape after λ^{-1} revolutions. But, if particles have different betatron tunes, they will orbit around different fixed points at different island tunes, and the motion will decohere after some oscillation periods.

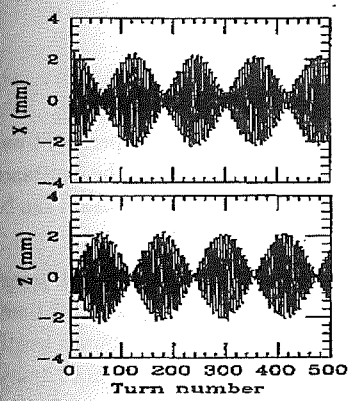

Figure 2.45: The measured coherent betatron oscillations excited by a horizontal kicker. The linear coupling gives rise to beating between the horizontal and vertical betatron oscillations. The tune of beating is equal to $\lambda = \sqrt{(\nu_x - \nu_z)^2 + |G_{1,-1,\ell}|^2}$. The beat period were measured to be about 120 revolutions, which corresponds to $\lambda \approx 0.0083$.

VI.3 Experimental Measurement of Linear Coupling

To measure the effect of linear coupling, the horizontal and vertical betatron tunes are tuned to the linear coupling resonance line at $\nu_x - \nu_z = \ell$. In the following, we discuss an experimental study of linear coupling at the IUCF cooler ring. The cooler is a proton storage ring with electron cooling. The circumference is about 86.82 m, and the betatron tunes for this experiment were chosen to be $\nu_x = 3.826, \nu_z = 4.817$ with $\nu_x - \nu_z \approx -1$.

The experiment started with a single bunch of about 5×10^8 protons with kinetic energy of 45 MeV at the Indiana University Cyclotron Facility cooler ring. The cycle time was 10 s, and the injected beam was electron-cooled for about 3 s before the measurement, producing a full-width at half-maximum bunch length of about 9 m

[96]The motion about SFPs of a nonlinear Hamiltonian resembles islands in the phase space and is thus called island motion. Stable islands are separated by the separatrix orbit that passes through unstable fixed points (UFPs). However, there is no UFP for the linear coupling Hamiltonian Eq. (2.362). The number of complete island motions in one revolution is called the "island tune." Here we find that the island tune of coupling motion around SFPs is equal to λ, which is independent of the betatron amplitude.

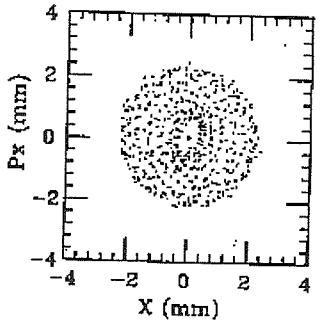

Figure 2.46: The betatron oscillations of Fig. 2.45 are transformed to the Poincaré map in the normalized coordinates $(x, \mathcal{P}_x)$. The amplitude modulation of betatron motion is translated into breathing motion in the Poincaré map. The vertical map $(z, \mathcal{P}_z)$ is out of phase with that of the horizontal map.

(or 100 ns) depending on the rf voltage. The rf system used in the experiment was operating at harmonic number $h = 1$ with frequency 1.0309 MHz. Since the emittance of the beam in the cooler is small (0.05 π-mm-mrad), the motion of the beam can be visualized as a macro-particle.

The coherent betatron oscillation of the beam was excited by a single-turn transverse dipole kicker. For the IUCF cooler ring, we used a kicker with rise and fall times at 100 ns and a 600 ns flat top. This is sufficient for a single bunch with a bunch length less than 100 ns at 1.0309 MHz revolution frequency. The subsequent bunch transverse oscillations from a BPM are detected and recorded. Figure 2.45 shows a typical example of the beating oscillations due to the linear betatron coupling following a horizontal kick.

The beat period were measured to be about 120 revolutions, which corresponds to $\lambda \approx 0.0083$. The linear coupling in the IUCF cooler ring arose mainly from the solenoid at the electron cooling section, and possibly also from quadrupole roll and vertical closed-orbit deviations in sextupoles. The Lambertson septum magnet at the injection area also contributed a certain amount of skew quadrupole field, which was locally corrected.

Note that the betatron beating between the x and z betatron motion gives rise to energy (action) exchange between the horizontal and vertical betatron oscillations. In the presence of linear coupling, the measured betatron tunes correspond to normal modes of the betatron oscillations. The tune separation between these two normal modes is equal to λ of Eq. (2.360). Figure 2.42 shows the normal-mode tune vs quadrupole combo.[97] The minimum tune splitting of these two normal modes is equal to the magnitude of the linear coupling constant, $|G_{1,-1,\ell}|$.

[97] A tune combo is a combination of power supply to a set of quadrupoles for achieving independent horizontal or vertical tune change.

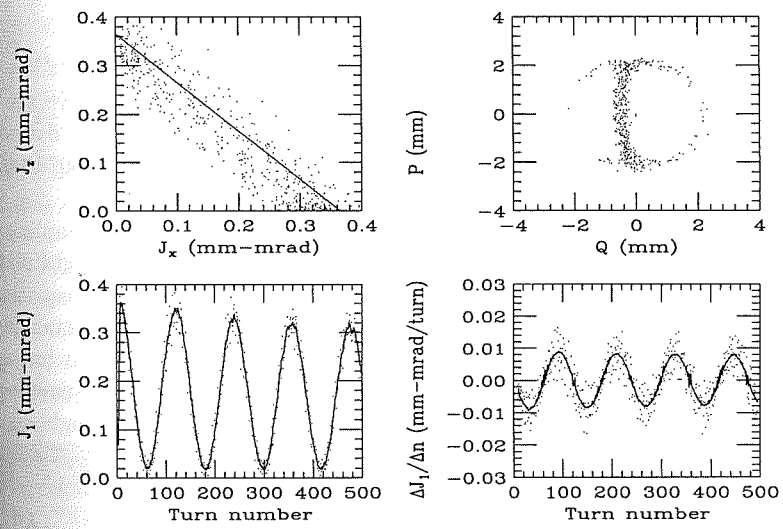

Figure 2.47: The top left shows the actions J_z vs J_x near a linear betatron resonance. The Poincaré surface of section in the resonant precessing frame derived from (x, x') and (z, z') is shown in the top right plot, where $Q = \sqrt{2J_1\beta_x}\cos\phi_1$, $P = -\sqrt{2J_1\beta_x}\sin\phi_1$, and $\beta_x = 7.55$ m. The resonance phase was fitted to obtain an upright torus. The bottom plots show the action J_1 (left) in [π-mm-mrad] and its time derivative, dJ_1/dN (right) in [π-mm-mrad/turn]. The solid line in the bottom left plot shows a five-point running average. The solid line in the bottom right plot shows a fit by using Eq. (2.364) to obtain the coupling strength $G_{1,-1,\ell} = 0.0078$ and the coupling phase $\chi = 1.59$ rad.

Measurement of linear coupling phase

To measure the linear coupling phase χ, we can transform the horizontal and the vertical Poincaré maps into the resonant precessing frame discussed in Sec. II. Figure 2.46 shows the normalized phase space $x, \mathcal{P}_x$ (a similar plot can be obtained for $z, \mathcal{P}_z$) of the data shown in Fig. 2.45. Because of linear coupling, the horizontal and vertical phase-space maps were completely smeared. Transforming the phase space into the resonant precessing frame, the torus of the 2D Hamiltonian is shown in the upper right plot in Fig. 2.47, where the particle motion follows the solid line of the Courant-Snyder invariant circle and the coupling ellipse shown in Fig. 2.43. The orientation of the resonant line was used to determine the coupling phase $\chi = 1.59$ rad, where the relative betatron phase advances at the locations of the horizontal and vertical BPMs were included.

Measurement of coupling strength $G_{1,-1,\ell}$

The measured action J_1 as a function of time and its time derivative $dJ_1/dN = 2\pi\dot{J}_1$ are plotted in the bottom plots of Fig. 2.47, where a five-point moving average of $\dot{J}_1$ is used to obtain a better behaved time derivative of the action J_1. The data of the time derivative dJ_1/dN are fitted with Eq. (2.364) to obtain $G_{1,-1,\ell} = 0.0078 \pm 0.0006$ and $\chi = 1.59$ rad, shown as a solid line in the lower graph of Fig. 2.47.[98]

The Poincaré map derived from experimental data at a 2D linear coupling resonance shows invariant tori of the Hamiltonian flow (see Fig. 2.47, top right plot and the solid line in Fig. 2.43). Using these invariant tori and Hamilton's equations of motion, we can determine the magnitude and the phase of the linear betatron coupling. The magnitude of the linear coupling obtained from the invariant tori agrees well with that obtained by the traditional method of finding the minimum separation of the betatron tunes with combos of quadrupole strengths. In a single digitized measurement, we can obtain the magnitude and phase of the linear coupling. Such a correction method can be used for on-line diagnosis to make the choice of skew quadrupole correction families more efficient.

Knowing the dynamics of the linear coupling of a single-particle motion may also help unravel questions concerning the dynamical evolution of the bunch distribution when the betatron tunes ramp through a coupling resonance. Such a problem is important for polarized proton acceleration in a low to medium energy synchrotron, where the vertical betatron tune jump method is used to overcome intrinsic depolarizing resonances. When the betatron tunes cross each other adiabatically after the tune jump, the increase in vertical emittance due to linear coupling may cause difficulty in later stages of polarized proton acceleration.

VI.4 Linear Coupling Correction with Skew Quadrupoles

The linear coupling resonance is usually corrected by maximizing the beat period of the transverse betatron oscillations using a pair, or at least two families, of skew quadrupoles. Figure 2.48 shows the output from a spectrum analyzer using the Δ-signal of a horizontal beam position monitor (BPM) as the input.[99] The spectrum analyzer was tuned to a horizontal betatron sideband and was triggered 1.5 ms before the beam was coherently excited by a horizontal kicker. The beat period shown in Fig. 2.45 corresponds to the time interval between the dips of Fig. 2.48. The procedure for linear coupling correction is as follows

[98] Note that the coupling line shown in the Poincaré surface section (upper left) plot of Fig. 2.47 has a small curvature. This implies a smaller nonlinear betatron detuning for the IUCF cooler ring.

[99] The difference signal or a Δ-signal from BPMs carries the information of betatron oscillations around the closed orbit. A spectrum analyzer operating at zero span mode is a tuned receiver that measures the power of betatron motion.

1. Maximize the peak to valley ratio in the spectrum by using quadrupole combos. This is equivalent to setting $\delta_1 = 0$ for attaining 100% coupling.
2. Maximize the time interval between dips (or peaks) of the spectrum by using families of skew quadrupoles. This reduces the coupling strength $G_{1,-1,\ell}$.

Repeated iteration of the above steps can efficiently correct the linear coupling provided that the skew quadrupole families have proper phase relations. This procedure is however hindered by the betatron decoherence and by the 60 Hz power supply ripple, which is evident in Fig. 2.48. Other possible complications are closed-orbit changes due to off-center orbits in the quadrupoles and skew quadrupoles. However, the most important issue is that there is no guarantee *a priori* that the set of skew quadrupoles can properly correct the magnitude and phase of the linear coupling. Thus measurement of the coupling phase is also important.

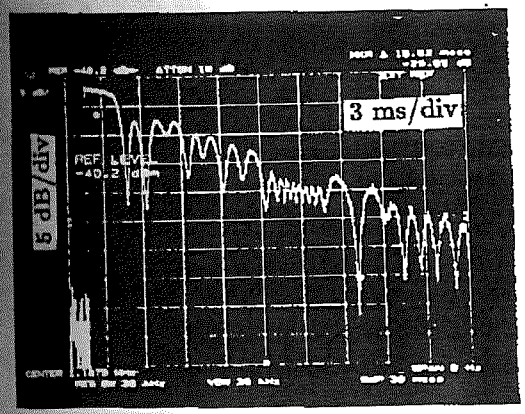

Figure 2.48: The spectrum of the Δ-signal from a horizontal BPM from a spectrum analyzer tuned to a betatron sideband frequency with resolution bandwidth 30 kHz and video bandwidth 30 kHz triggered 1.5 ms before a coherent horizontal kick. Note that (1) the time interval between these dips corresponded to the beat period of Fig. 2.45, (2) the decay of the power spectrum corresponded to betatron decoherence, and (3) the characteristic change in features at a 17 ms interval corresponded to a strong 60 Hz ripple, which altered betatron tunes.

VI.5 Linear Coupling Using Transfer Matrix Formalism

So far, our analysis of linear coupling has been based on single-resonance approximation in perturbation approach. The transfer matrix method of Sec. II can be expanded into 4×4 matrix by using transfer matrices for skew quadrupoles (Exercise 2.6.1) and solenoids (Exercise 2.6.2).

The 4×4 transfer matrix in one complete revolution can be diagonalized to obtain normal-mode betatron amplitude functions, and the coupling angle at each position in the ring.[100] This procedure has been implemented in MAD [19] and SYNCH [20] programs (see Exercise 2.6.6).

[100] D.A. Edwards and L.C. Teng, *IEEE Trans. Nucl. Sci.* **NS20**, 855 (1973); F. Willeke and G. Ripken, p. 758 in Ref. [11] (1988); J.P. Gourber *et al.*, *Proc. 1990 EPAC*, p. 1429 (1990); G. Guignard, *et al.*, *ibid.* p. 1432 (1990).

Exercise 2.6

1. This exercise derives the linear transfer matrix for a skew quadrupole, where the magnetic field is

$$B_z = -B_0 a_1 z, \quad B_x = B_0 a_1 x, \quad B_s = 0; \quad \text{with} \quad B_0 a_1 = \frac{1}{2}\left(\frac{\partial B_x}{\partial x} - \frac{\partial B_z}{\partial z}\right)_{x=z=0},$$

where B_0 is the main dipole field strength, and a_1 is the skew quadrupole coefficient in multipole expansion of Eq. (2.25). Apparently, the skew quadrupole field satisfies Maxwell's equation $\partial B_z/\partial z + \partial B_x/\partial x = 0$. The vector potential is

$$A_s = -B_0 a_1 xz, \quad A_x = 0, \quad A_z = 0.$$

(a) Show that the equation of motion in a skew quadrupole is

$$x'' + qz = 0, \quad z'' + qx = 0, \quad \text{where} \quad q = -\frac{1}{B\rho}\frac{\partial B_z}{\partial z} = \frac{a_1}{\rho}.$$

(b) Show that the transfer matrix of a skew quadrupole is

$$M = \begin{pmatrix} C_+ & S_+/\sqrt{q} & C_- & S_-/\sqrt{q} \\ -\sqrt{q}S_- & C_+ & -\sqrt{q}S_+ & C_- \\ C_- & S_-/\sqrt{q} & C_+ & S_+/\sqrt{q} \\ -\sqrt{q}S_+ & C_- & -\sqrt{q}S_- & C_+ \end{pmatrix}$$

where

$$C_+ = \frac{\cos\theta + \cosh\theta}{2}, \quad C_- = \frac{\cos\theta - \cosh\theta}{2},$$
$$S_+ = \frac{\sin\theta + \sinh\theta}{2}, \quad S_- = \frac{\sin\theta - \sinh\theta}{2},$$

$\theta = \sqrt{q}L$, and L is the length of the skew quadrupole.

(c) The coordinate rotation from (x, z) to $(\tilde{x}, \tilde{z})$ by an angle ϕ is

$$\begin{pmatrix} \tilde{x} \\ \tilde{x}' \\ \tilde{z} \\ \tilde{z}' \end{pmatrix} = R(\phi)\begin{pmatrix} x \\ x' \\ z \\ z' \end{pmatrix}, \quad R(\phi) = \begin{pmatrix} \cos\phi & 0 & \sin\phi & 0 \\ 0 & \cos\phi & 0 & \sin\phi \\ -\sin\phi & 0 & \cos\phi & 0 \\ 0 & -\sin\phi & 0 & \cos\phi \end{pmatrix}.$$

Show that the transfer matrix of a skew quadrupole is

$$M_{\text{skew quad}} = R(-45°)M_{\text{quad}}R(45°),$$

where M_{quad} is the transfer matrix of a quadrupole. This means that a skew quadrupole is equivalent to a quadrupole rotated by 45°.

(d) In the thin-lens limit, i.e. $L \to 0$ and $qL \to 1/f$, where f is the focal length, show that the 4×4 coupling transfer matrix reduces to

$$M = \mathbf{1} + \frac{-1}{f}\mathbf{U}, \quad \mathbf{U} = \begin{pmatrix} 0 & U \\ U & 0 \end{pmatrix}, \quad U = \begin{pmatrix} 0 & 0 \\ 1 & 0 \end{pmatrix}.$$

2. *Linear transfer Matrix of a Solenoid:* The particle equation of motion in an ideal solenoidal field is

$$x'' + 2gz' + g'z = 0, \qquad z'' - 2gx' - g'x = 0,$$

where the solenoidal field strength is $g = \frac{eB_{\|}(s)}{2p}$.

(a) Show that the coupled equation of motion becomes

$$y'' - j2gy' - jg'y = 0,$$

where $y = x + jz$, and j is the complex imaginary number.

(b) Transforming coordinates into rotating frame with

$$\bar{y} = ye^{-j\theta(s)}, \quad \text{where} \quad \theta = \int_0^s g ds,$$

show that the system is decoupled, and the equation of motion becomes

$$\bar{y}'' + g^2\bar{y} = 0.$$

Thus both horizontal and vertical planes are focused by the solenoid.

(c) Show that the transfer matrix in the rotating frame is

$$\tilde{M} = \begin{pmatrix} \cos\theta & \frac{1}{g}\sin\theta & 0 & 0 \\ -g\sin\theta & \cos\theta & 0 & 0 \\ 0 & 0 & \cos\theta & \frac{1}{g}\sin\theta \\ 0 & 0 & -g\sin\theta & \cos\theta \end{pmatrix},$$

where $\theta = gs$.[101]

(d) Transforming the coordinate system back to the original frame, i.e. $y = e^{j\theta}\bar{y}$, show that the transfer matrix for the solenoid becomes

$$M = \begin{pmatrix} \cos^2\theta & \frac{1}{g}\sin\theta\cos\theta & -\sin\theta\cos\theta & -\frac{1}{g}\sin^2\theta \\ -g\sin\theta\cos\theta & \cos^2\theta & g\sin\theta^2 & -\sin\theta\cos\theta \\ \sin\theta\cos\theta & \frac{1}{g}\sin^2\theta & \cos^2\theta & \frac{1}{g}\sin\theta\cos\theta \\ -g\sin^2\theta & \sin\theta\cos\theta & -g\sin\theta\cos\theta & \cos^2\theta \end{pmatrix}$$

3. Show that Hamilton's equations of motion for the Hamiltonian (2.353) in the presence of skew quadrupoles and solenoids are

$$x'' + K_x(s)x + 2gz' - (q - g')z = 0,$$
$$z'' + K_z(s)z + 2gx' - (q + g')x = 0.$$

where $g = B_{\|}(s)/2B\rho$ and $q = -(\partial B_z/\partial z)/B\rho = a_1/\rho$.

[101] Note here that the solenoid, in the rotating frame, acts as a quadrupole in both planes. The focusing function is equal to g^2. In small rotating angle approximation, the corresponding focal length is $f^{-1} = g^2L = \Theta^2/L$, where L is the length of the solenoid, and $\Theta = gL$ is the rotating angle of the solenoid.

(a) Show that the perturbation potential due to skew quadrupoles and solenoids is

$$V_{\rm lc} = -\frac{a_1}{\rho}xz + g(s)\left(\frac{p_z}{p}x - \frac{p_x}{p}z\right).$$

(b) Expand the perturbation potential in Fourier series and show that the coupling coefficient $G_{1,-1,\ell}$ for the ℓ-th harmonic is given by Eq. (2.357).

(c) If the accelerator lattice has P superperiods, show that $G_{1,-1,\ell} = 0$ unless $\ell = 0$ (Mod P).

4. Using the generating function

$$F_2(\phi_x, \phi_z, I_1, I_2) = (\phi_x - \phi_z - \ell\theta + \chi)I_1 + \phi_z I_2,$$

show that the linear coupling equation of motion for the Hamiltonian (2.359) can be transformed into the Hamiltonian (2.362) in *resonance rotating frame*.

(a) Show that the new conjugate phase-space variables are

$$I_1 = J_x, \quad I_2 = J_x + J_z, \quad \phi_1 = \phi_x - \phi_z - \ell\theta + \chi, \quad \phi_2 = \phi_z.$$

(b) Find the invariants of the Hamiltonian (2.359).

(c) Show that the equation of motion for I_1 is

$$\ddot{I}_1 + \lambda^2 I_1 = E_1\delta_1 + I_2 G_{1,-1,\ell}^2/2,$$

where the overdot corresponds to the derivative with respect to orbiting angle θ, $\delta_1 = \nu_x - \nu_z - \ell$ is the resonance proximity parameter, $\lambda = \sqrt{\delta_1^2 + G_{1,-1,\ell}^2}$, and $E_1 = \delta_1 I_1 + G_{1,-1,\ell}\sqrt{I_1(I_2 - I_1)}\cos\phi_1$ is a constant of motion.

(d) Discuss the solution in the resonance rotating frame.[102]

5. The Hamiltonian

$$H = \nu_x J_x + \nu_z J_z + G_{1,-1,\ell}\sqrt{J_x J_z}\cos(\phi_x - \phi_z + \chi)$$

for a single linear coupling resonance can be transformed to the normalized phase-space coordinates by

$$\begin{cases} X = \sqrt{2J_x}\cos(\phi_x + \chi_x), & P_x = -\sqrt{2J_x}\sin(\phi_x + \chi_x), \\ Z = \sqrt{2J_z}\cos(\phi_z + \chi_z), & P_z = -\sqrt{2J_z}\sin(\phi_z + \chi_z), \end{cases}$$

where $\chi_x - \chi_z = \chi$ is a constant linear coupling phase (Mod 2π) that depends on the location in the ring.

(a) Show that the Hamiltonian in the new phase-space coordinates is

$$H = \frac{1}{2}\nu_x(X^2 + P_x^2) + \frac{1}{2}\nu_z(Z^2 + P_z^2) + \frac{1}{2}G_{1,-1,\ell}(XZ + P_x P_z).$$

[102] For a general discussion on linear coupling with nonlinear detuning, see J.Y. Liu *et al.*, *Phys. Rev.* **E 49**, 2347 (1994).

(b) Show that the eigen-frequency of the Hamiltonian is

$$\nu_\pm = \frac{1}{2}(\nu_x + \nu_z) \pm \frac{1}{2}\lambda, \quad \lambda = \sqrt{(\nu_x - \nu_z)^2 + |G_{1,-1,\ell}|^2}.$$

(c) Solve X and Z in terms of the normal modes, and show that

$$\begin{cases} X = A_+\cos(\nu_+\varphi + \xi_+) - \dfrac{G_{1,-1,\ell}}{\lambda + |\delta|}A_-\cos(\nu_-\varphi + \xi_-), \\ Z = \dfrac{G_{1,-1,\ell}}{\lambda + |\delta|}A_+\cos(\nu_+\varphi + \xi_+) + A_-\cos(\nu_-\varphi + \xi_-), \end{cases}$$

where $A_\pm, \xi_\pm$ are obtained from the initial conditions. Particularly, we note that the "horizontal" and "vertical" betatron oscillations carry both normal-mode frequencies.

6. Analyze the linear stability of the simple tracking model shown in Fig. 2.44, i.e. the particle motion in a synchrotron with linear betatron motion and a localized skew quadrupole kick. Show that the condition of linear stability for betatron motion is

$$\frac{\sqrt{\beta_x\beta_z}}{f} \le \text{Min}\left\{ 2\sqrt{\frac{(1+\cos\Phi_x)(1+\cos\Phi_z)}{|\sin\Phi_x\sin\Phi_z|}},\ 2\sqrt{\frac{(1-\cos\Phi_x)(1-\cos\Phi_z)}{|\sin\Phi_x\sin\Phi_z|}} \right\},$$

where f is the focal length of the skew quadrupole, β_x and β_z are values of betatron amplitude functions at the skew quadrupole location, and Φ_x and Φ_z are betatron phase advances of the machine without the skew quadrupole. Based on your study of this problem, can you find the stability limit of a linearly coupled machine with superperiod P?

VII Nonlinear Resonances

Our discussion in Sec. V shows that chromaticity correction in particle accelerators is essential for attaining particle beam stability. Since sextupole and higher order multipole magnets are needed in chromaticity correction, they are an integral part of accelerator lattice design, and thus the nonlinear geometric aberration due to sextupoles and higher order multipoles needs to be addressed.

More generally, modern high energy storage rings usually use high field (superconducting) magnets that inherently possess systematic and random multipole fields. Although the nonlinearity is normally of the order of $10^{-3} - 10^{-4}$ relative to that of the linear component, the nonlinear magnetic field can give rise to geometric aberration in the beam ellipse if a resonance condition is encountered. Careful analysis of the nonlinear beam dynamics is instrumental in determining the dynamical aperture. This section provides an introduction to this important subject, but is limited to first-order perturbation treatment.

VII.1 Nonlinear Resonances Driven by Sextupoles

The vector potential for a sextupole magnet is

$$A_x = A_z = 0, \quad A_s = \frac{B_2}{6}(x^3 - 3xz^2), \tag{2.374}$$

where $B_2 = \partial^2 B_z/\partial x^2|_{x=z=0}$. Including the sextupole field, the betatron Hamiltonian is

$$H = \frac{1}{2}\left[x'^2 + K_x x^2 + z'^2 + K_z z^2\right] + V_3(x, z, s), \tag{2.375}$$

where $V_3(x, z, s) = \frac{1}{6}S(s)(x^3 - 3xz^2)$ is the nonlinear perturbation potential with $S(s) = -B_2/B\rho$. For off-momentum particles, the sextupole strength $S(s)$ should be replaced by $B_2/[(1+\delta)B\rho]$, where $\delta = \Delta p/p_0$.

A. Tracking methods

In the presence of sextupole magnetic field, Hill's equation of motion becomes

$$x'' + K_x(s)x = -\frac{1}{2}S(s)(x^2 - z^2), \qquad z'' + K_z(s)z = +S(s)xz. \tag{2.376}$$

The evolution of phase space coordinates of orbiting particles can be obtained by tracking the equation of motion. Since the sextupole magnets used in accelerator are usually short, thin lens approximation has often be used in particle tracking. Let $\bar{S} = \int S(s)ds$ be the integrated sextupole strength. The changes of phase space

coordinates at the sextupole magnet are[103]

$$\Delta x' = -\frac{1}{2}\bar{S}(x^2 - z^2), \qquad \Delta z' = \bar{S}xz. \tag{2.377}$$

The propagation of phase space coordinates outside the sextupole magnet is given by the mapping equation (2.45). Figure 2.49 shows the Poincaré maps with one sextupole in an otherwise perfectly linear accelerator near a third order resonance. The topology of the phase space maps rotates 120° when the tune moves across the third integer resonance. The region of stability decreases as the tune approaches the third order resonance.

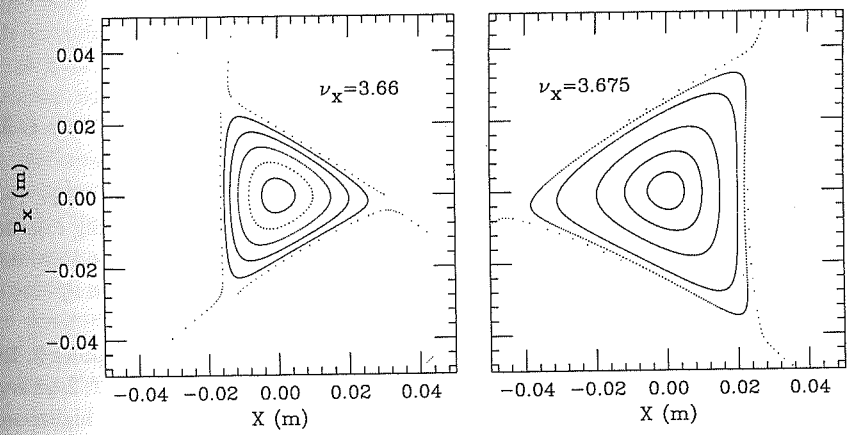

Figure 2.49: The Poincaré maps for the betatron motion perturbed by a single sextupole magnet at a tune below (left) and above (right) a third order resonance. The integrated sextupole strength is $S = 0.5\ \mathrm{m}^{-2}$.

B. The leading order resonances driven by sextupoles

In order to analyze the third order resonance analytically, we perform Floquet transformation to the Hamiltonian (2.375). With Eq. (2.94) for coordinate transformation, the nonlinear perturbing potential $V_3(x, z, s)$ becomes

$$\begin{aligned} V_3 &= -\frac{\sqrt{2}}{4}J_x^{1/2}J_z\beta_x^{1/2}\beta_z S(s)[2\cos\Phi_x + \cos(\Phi_x + 2\Phi_z) + \cos(\Phi_x - 2\Phi_z)] \\ &\quad + \frac{\sqrt{2}}{12}J_x^{3/2}\beta_x^{3/2}S(s)[\cos 3\Phi_x + 3\cos\Phi_x], \end{aligned} \tag{2.378}$$

[103] In this mapping equation for betatron motion, we disregard the effect of sextupoles on orbit length. Using Eq. (2.170), we find $\Delta C = (x\Delta x' + z\Delta z')$.

where

$$\Phi_x = \phi_x + \chi_x(s) - \nu_x\theta, \quad \chi_x = \int_0^s \frac{ds}{\beta_x},$$
$$\Phi_z = \phi_z + \chi_z(s) - \nu_z\theta, \quad \chi_z = \int_0^s \frac{ds}{\beta_z}.$$

Here (J_x, ϕ_x) and (J_z, ϕ_z) are pairs of conjugate phase-space coordinates. Since V_3 is a periodic function of s, it can be expanded in Fourier harmonics.[104] The Hamiltonian (2.375) expressed in action-angle variables becomes

$$\begin{aligned} H &= \nu_x J_x + \nu_z J_z + \sum_\ell G_{3,0,\ell} J_x^{3/2} \cos(3\phi_x - \ell\theta + \xi_{3,0,\ell}) \\ &\quad + \sum_\ell G_{1,2,\ell} H_{1,2,\ell} J_x^{1/2} J_z \cos(\phi_x + 2\phi_z - \ell\theta + \xi_{1,2,\ell}) \\ &\quad + \sum_\ell G_{1,-2,\ell} H_{1,-2,\ell} J_x^{1/2} J_z \cos(\phi_x - 2\phi_z - \ell\theta + \xi_{1,-2,\ell}) + \cdots, \end{aligned} \tag{2.379}$$

where ℓ is an integer, $G_{3,0,\ell}$, $G_{1,2,\ell}$, $G_{1,-2,\ell}$ are Fourier amplitudes, $\xi_{3,0,\ell}$, $\xi_{1,2,\ell}$, $\xi_{1,-2,\ell}$ are the phase of the Fourier components, and $\cdots$ describes the remaining resonance driving terms at $\nu_x =$ integers. The Fourier amplitude $G_{3,0,\ell}$ drives the third order resonance at $3\nu_x = \ell$, and similarly, $G_{1,2,\ell}$ and $G_{1,-2,\ell}$ drive $\nu_x + 2\nu_z = \ell$ and $\nu_x - 2\nu_z = \ell$ resonances.

Table VII.1 lists nonlinear resonances that can be excited by sextupoles in first-order perturbation theory. Other higher-order resonances, such as $4\nu_x = \ell$, $2\nu_x \pm 2\nu_z = \ell$, etc., can also be excited by strong sextupole fields through second- or higher-order perturbation expansion. We discuss below a 1D third-order resonance at $3\nu_x = \ell$.

Table 2.3: Resonances due to sextupoles and their driving terms

Resonance	Driving term	Lattice	Amplitude	Classification
$\nu_x + 2\nu_z = \ell$	$\cos(\Phi_x + 2\Phi_z)$	$\beta_x^{1/2}\beta_z$	$J_x^{1/2} J_z$	sum resonance
$\nu_x - 2\nu_z = \ell$	$\cos(\Phi_x - 2\Phi_z)$	$\beta_x^{1/2}\beta_z$	$J_x^{1/2} J_z$	difference resonance
$\nu_x = \ell$	$\cos\Phi_x$	$\beta_x^{1/2}\beta_z$; $\beta_x^{3/2}$	$J_x^{1/2} J_z$, $J_x^{3/2}$	parametric resonance
$3\nu_x = \ell$	$\cos 3\Phi_x$	$\beta_x^{3/2}$	$J_x^{3/2}$	parametric resonance

C. Third order resonance at $3\nu_x = \ell$

Near a third-order resonance at $3\nu_x = \ell$, the Hamiltonian (2.379) can be approximated by

$$H \approx \nu_x J_x + G_{3,0,\ell} J_x^{3/2} \cos(3\phi_x - \ell\theta + \xi), \tag{2.380}$$

[104] G. Guignard, p. 822 in Ref. [10] (1988); G. Guignard, CERN 76-06, (1976).

where J_x, ϕ_x are conjugate phase-space coordinates, θ is the orbiting angle serving the time coordinate, ν_x is the horizontal betatron tune, and the Fourier amplitude $G_{3,0,\ell}$ and the phase $\xi = \xi_{3,0,\ell}$ are

$$G_{3,0,\ell}\, e^{j\xi} = \frac{\sqrt{2}}{24\pi} \oint \beta_x^{3/2} S(s)\, e^{j[3\chi_x(s) - (3\nu_x - \ell)\theta]} ds. \tag{2.381}$$

The betatron phase space of the Hamiltonian (2.380) is distorted by the nonlinear resonance, i.e. the sextupole can cause "geometric aberration" to the betatron motion. The magnitude of the geometric aberration is proportional to the resonance strength $G_{3,0,\ell}$.

We note that if the accelerator has a superperiod P and the sextupole field satisfies a similar periodic condition, the resonance strength $G_{3,0,\ell}$ is zero unless ℓ is an integer multiple of P (see Exercise 2.7.1). For example, the systematic third-order resonance strength for the AGS will be zero except for $\ell = 12, 24$, etc. Thus the nonlinear resonances are classified into systematic and random resonances. Systematic nonlinear resonances are located at $\ell = P\times$ integer. At a systematic resonance, the contribution of each superperiod is coherently additive to the resonance strength. Since the chromatic sextupoles are usually arranged according to the superperiod of the machine, one should pay great attention to the systematic sextupolar nonlinear resonances. Random sextupole fields induce nonlinear resonances at all integer ℓ, and their resonance strengths are usually weak. Nevertheless, the betatron tunes should avoid low-order nonlinear resonances.

Using the generating function

$$F_2 = (\phi_x - \frac{\ell}{3}\theta + \frac{\xi}{3})J, \tag{2.382}$$

where the new phase-space coordinates are

$$\phi = \phi_x - \frac{\ell}{3}\theta + \frac{\xi}{3}, \quad J = J_x,$$

the Hamiltonian Eq. (2.380) becomes

$$H = \delta J + G_{3,0,\ell} J^{3/2} \cos 3\phi. \tag{2.383}$$

Here $\delta = \nu_x - \ell/3$ is the resonance proximity parameter. Since the Hamiltonian (2.383) is autonomous, the "Hamiltonian" is invariant. Particle motion in the phase space follows the contour of a constant Hamiltonian. Using Hamilton's equations of motion

$$\dot{\phi} = \delta + \frac{3}{2} G_{3,0,\ell} J^{1/2} \cos 3\phi, \quad \dot{J} = 3G_{3,0,\ell} J^{3/2} \sin 3\phi, \tag{2.384}$$

we obtain

$$\ddot{J} + 9\delta^2 J - \frac{27}{2} G_{3,0,\ell}^2 J^2 = 9\delta E, \tag{2.385}$$

where E is the Hamiltonian value, and the overdot indicates the derivative with respect to the orbiting angle θ. When the amplitude is small, the tune, in the resonance rotating frame, of the third-order resonance is 3δ because the betatron amplitude repeats three times in every revolution.

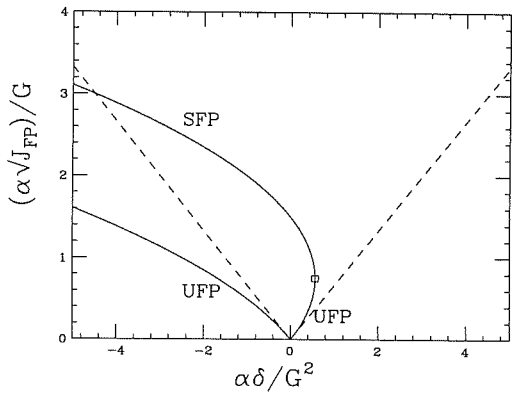

Figure 2.50: The dashed line shows the UFP, $J_{\rm UFP}^{1/2}/G_{3,0,\ell}$ vs $\delta/G_{3,0,\ell}^2$, of the third-order betatron resonance in the zero detuning limit. The solid line shows $\alpha J_{\rm FP}^{1/2}/G_{3,0,\ell}$ vs $\alpha\delta/G_{3,0,\ell}^2$ for the case $\alpha = \alpha_{xx} > 0$ and $G_{3,0,\ell} > 0$, where FP stands for both stable and unstable fixed points. The SFP section and the UFP section are marked. Bifurcation of the third-order resonance occurs at $\alpha\delta/G_{3,0,\ell}^2 = 9/16$ marked by the rectangular symbol.

Stable and unstable fixed points

The Hamiltonian Eq. (2.383) has three unstable fixed points (UFPs)[105] with

$$\frac{dJ}{d\theta} = 0, \quad \frac{d\phi}{d\theta} = 0.$$

These UFPs are located at

$$J_{\rm UFP}^{1/2} = \left|\frac{2\delta}{3G_{3,0,\ell}}\right| \quad \text{with} \quad \begin{cases} \phi_{\rm FP} = 0,\ \pm 2\pi/3, & \text{if } \delta/G_{3,0,\ell} < 0, \\ \phi_{\rm FP} = \pm\pi/3,\ \pi, & \text{if } \delta/G_{3,0,\ell} > 0. \end{cases} \tag{2.386}$$

At the fixed point, the Hamiltonian assumes the value

$$E_{\rm UFP} = \frac{\delta}{3}\left(\frac{2\delta}{3G_{3,0,\ell}}\right)^2. \tag{2.387}$$

These unstable fixed points can be easily verified as follows. Let $K = J - J_{\rm UFP}$ and $E = E_{\rm UFP}$. The equation of motion becomes

$$\ddot{K} - 3\delta^2 K - 6\frac{\delta^2}{J_{\rm UFP}}K^2 = 0. \tag{2.388}$$

[105] Fixed points of a Hamiltonian are phase-space loci with zero velocity field. Thus a particle can stay indefinitely at a fixed point. The fixed points are characterized as stable or elliptical fixed points (SFPs) and unstable or hyperbolic fixed points (UFPs). Small-amplitude motion around a SFP is a bounded ellipse; around an UFP it is hyperbolic.

Thus the motion near the fixed point is hyperbolic. Because of the nonlinear term in Eq. (2.388), the amplitude is seen to grow faster than an exponential.

Without a nonlinear detuning term, the third-order resonance appears at all values of δ. The stable motion is bounded by the curve of $J_{\rm UFP}^{1/2}(\delta)$ shown in Fig. 2.50. For a given aperture $\hat{J}$, the width of the third-order betatron resonance is then

$$|\delta|_{\rm width} = 3G_{3,0,\ell}\hat{J}^{1/2}/2. \tag{2.389}$$

Separatrix

The separatrix is the Hamiltonian torus that passes through the UFP. For the third-order resonance in the zero detuning limit, the separatrix can be obtained from Eq. (2.383) with the condition $H = E_{\rm UFP}$. With X and P defined as

$$X = \sqrt{\frac{J}{J_{\rm UFP}}}\cos\phi, \quad P = -\sqrt{\frac{J}{J_{\rm UFP}}}\sin\phi, \tag{2.390}$$

the equation for the separatrix orbit becomes

$$[2X-1]\left[P - \frac{1}{\sqrt{3}}(X+1)\right]\left[P + \frac{1}{\sqrt{3}}(X+1)\right] = 0 \tag{2.391}$$

for the case of $\delta/G_{3,0,\ell} > 0$. Thus the separatrix is given by three intersecting straight lines, and $(X,P)_{\rm UFP}$ is given by the intersection of these three lines:

$$(X,P)_{\rm UFP} = (-1,0), \quad (\frac{1}{2},\frac{\sqrt{3}}{2}), \quad (\frac{1}{2},-\frac{\sqrt{3}}{2}).$$

Three straight lines $X = 1/2$, $P = \frac{1}{\sqrt{3}}(X+1)$, and $P = -\frac{1}{\sqrt{3}}(X+1)$ divide the phase space into stable region and unstable regions. The dynamical aperture is defined as the maximum phase-space area for stable betatron motion. Near a third-order resonance, the stable phase-space area in (x, x') is equal to $\sqrt{3}\delta/2|G_{3,0,\ell}|$. Beam loss may occur when particles wander beyond the separatrix.

The third-order resonance can be applied to extract beam particles slowly from a synchrotron. Note that the stable phase-space area is proportional to the resonance proximity parameter δ^2 (see Eq. (2.386)). If the betatron tune ν_x ramps slowly through a third-order resonance, beam particles can be slowly squeezed out of the stable area and extracted to achieve high duty cycle for nuclear and high energy physics experiments.

Effect of nonlinear detuning

In fact, nonlinear magnetic multipoles also generate nonlinear betatron detuning, i.e. the betatron tunes depend on the betatron actions. Including the effect of nonlinear

betatron detuning, the Hamiltonian for the third-order resonance is

$$H = \delta J + \frac{1}{2}\alpha J^2 + G_{3,0,\ell} J^{3/2} \cos 3\phi, \tag{2.392}$$

where $\alpha = \alpha_{xx}$ is the nonlinear detuning parameter. With nonlinear detuning, stable fixed points appear. The fixed points of the Hamiltonian for $\alpha > 0$ and $G_{3,0,\ell} > 0$ are

$$\frac{\alpha J_{\rm FP}^{1/2}}{G_{3,0,\ell}} = \begin{cases} -3/4 + (3/4)\sqrt{1-(16\alpha\delta/9G_{3,0,\ell}^2)}, & \phi = 0, \pm 2\pi/3 \quad \delta < 0 \\ +3/4 + (3/4)\sqrt{1-(16\alpha\delta/9G_{3,0,\ell}^2)}, & \phi = \pi, \pm\pi/3 \quad \delta \le 9G_{3,0,\ell}^2/16\alpha \\ +3/4 - (3/4)\sqrt{1-(16\alpha\delta/9G_{3,0,\ell}^2)}, & \phi = \pi, \pm\pi/3 \quad 0 \le \delta \le 9G_{3,0,\ell}^2/16\alpha \end{cases} \tag{2.393}$$

The bifurcation of third-order resonance islands occurs at $16\alpha\delta \le 9G_{3,0,\ell}^2$. Figure 2.50 shows $\alpha J_{\rm UFP}^{1/2}/|G_{3,0,\ell}|$ vs $\alpha\delta/G_{3,0,\ell}^2$ for the bifurcation of third-order resonance. A similar analysis can be carried out for $\alpha < 0$ or $G_{3,0,\ell} < 0$.

D. Experimental measurement of a $3\nu_x = \ell$ resonance

Because beam particles may be unstable at a nonlinear resonance, experimental measurements are generally difficult. It is easy to observe degradation of beam intensity and lifetime near a resonance. Measurements of Poincaré maps near a third-order resonance have been successful at SPEAR, TEVATRON, Aladdin, and the IUCF cooler ring. Figure 2.51 shows a Poincaré map obtained from a nonlinear beam dynamics experiment at the IUCF cooler ring. Converting into action-angle variables, we can fit these data by the Hamiltonian (2.392) to obtain parameters $G_{3,0,\ell}$ and ξ, and obtain the parameter δ by measuring the betatron tune at a small betatron amplitude. Using these measured nonlinear resonance parameters, we can model sextupole strengths of the storage ring.[106]

E. Other 3rd-order resonances driven by sextupoles

Besides the third-order integer resonance, sextupoles contribute importantly to the nonlinear coupling resonances at $\nu_x \pm 2\nu_z = \ell$ with integer ℓ.[107] The third-order resonance strength can generally be obtained by taking the Fourier transform of Eq. (2.378). The difference resonance at $\nu_x - 2\nu_z = \ell$ induce betatron coupling, while the sum resonance can cause beam emittance blow-up in both horizontal and vertical planes and leads to beam loss. Experimental measurements of nonlinear resonances are usually difficult because of short lifetime at the resonance condition.

[106] D.D. Caussyn, *et al.*, *Phys. Rev.* A **46**, 7942 (1992).

[107] See M. Ellison *et al.*, *Phys. Rev.* E **50**, 4051 (1994) for the $\nu_x - 2\nu_z = \ell$ resonance, and J. Budnick *et al.*, *Nucl. Inst. Methods* **A368**, 572 (1996) for the $\nu_x + 2\nu_z = \ell$ resonance at the IUCF cooler ring.

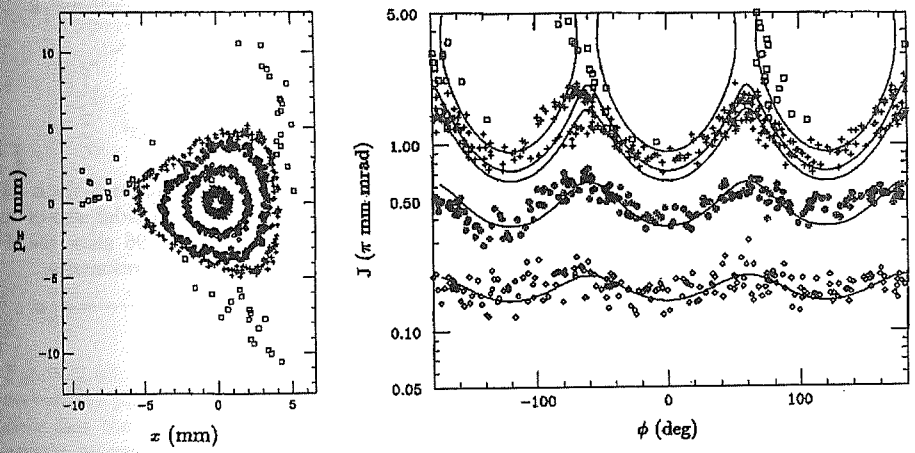

Figure 2.51: Left: The measured Poincaré map of the normalized phase-space coordinates (x, p_x) of betatron motion near a third-order resonance $3\nu_x = 11$ at the IUCF cooler ring. Note that particles outside the separatrix survive only about 100 turns. Tori for particles inside the separatrix are distorted by the third order resonance. The orientation of the Poincaré map, determined by sextupoles, rotates at a rate of betatron phase advance along the ring. The right plot shows the Poincaré map in action-angle variables (J, ϕ). The solid lines are Hamiltonian tori of Eq. (2.392).

VII.2 Higher-Order Resonances

It appears from Eq. (2.378) that sextupoles will not produce resonances higher than the third order ones listed in Table VII.1. However, strong sextupoles are usually needed to correct chromatic aberration. The concatenation of strong sextupoles can generate high-order resonances such as $4\nu_x, 2\nu_x \pm 2\nu_z, 4\nu_z, 5\nu_x, \ldots$, etc. Figure 2.52 shows the Poincaré maps of the single sextupole model of Fig. 2.49 at $\nu_x = 3.7496$. Note that a single sextupole can also drive the fourth and higher order resonances.

Employing strong sextupoles, nonlinear beam dynamics experiments at Fermilab Tevatron were used to study the concept of smear, nonlinear detuning, decoherence, and dynamical aperture.[108] Similarly, nonlinear beam dynamics studies at the IUCF cooler ring show the importance of nonlinear resonances. Nonlinear beam dynamics is beyond the scope of this book. Here we give an example of the fourth-order parametric resonance at $4\nu_x = 15$.[109]

[108] A. Chao, *et al.*, *Phys. Rev. Lett.* **61**, 2752 (1988); N. Merminga, *et al.*, *Proc. EPAC* p. 791 (1988); T. Satogata, *et al.*, *Phys. Rev. Lett.* **68**, 1838 (1992); T. Chen *et al.*, *Phys. Rev. Lett.* **68**, 33 (1992).

[109] S.Y. Lee, et al., *Phys. Rev. Lett.* **67**, 3768 (1991); M. Ellison *et al.*, *AIP Conf. Proc.* No. 292, p. 170 (1992); Y. Wang, *et al.*, *Phys. Rev.* E **49**, 5697 (1994).

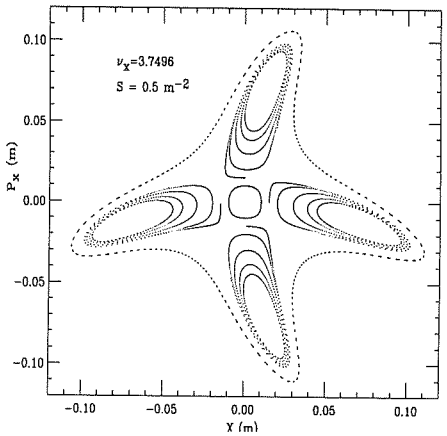

Figure 2.52: The Poincaré maps for the same sextupole model shown in Fig. 2.49 at $\nu_x = 3.7496$ show the effect of the fourth order resonance.

Near a fourth-order 1D resonance, the Hamiltonian can be approximated by

$$H = \nu_x J_x + \frac{1}{2}\alpha_{xx} J_x^2 + G_{4,0,\ell} J_x^2 \cos(4\psi_x - \ell\theta + \chi), \tag{2.394}$$

where the resonance strength $G_{4,0,\ell}$ can be obtained from the Fourier transformation of the effective particle Hamiltonian in the synchrotron. The Poincaré map near a fourth-order resonance $4\nu_x = 15$ measured at the IUCF cooler ring is shown in Fig. 2.53, where the left plot shows the Poincaré map in the normalized (x, P_x) phase space and the right plot shows the Poincaré map in action-angle variables. The solid lines shows the Hamiltonian tori of Eq. (2.394). Note that when the betatron tune is exactly 15/4, the betatron motion will be located at fixed points of the fourth-order resonance island. Small deviations from the fixed points will execute motion around the stable fixed points (SFP) shown in Fig. 2.53. The tune of motion around SFP of an island is called *island tune*. In this example, the fourth-order resonance islands are enclosed by stable invariant tori.

Systematic experimental measurements of nonlinear resonances can be used to derive the resonance parameters, and thus the Hamiltonian for particle motion in the accelerator can be modeled. Accelerator operators are keen to avoid low order strong resonances because of visibly short beam lifetime. Accelerator physicists are eager to apply their skill to correct or compensate the resonances for minimizing their effects on the beams.

In order to overcome nonlinear resonances, a few nonlinear magnets (usually up to octupole) are powered to eliminate the Fourier components of the nonlinear resonance near the machine operation condition. The chromatic sextupoles located in the ring can also be powered to eliminate the un-wanted nonlinear resonance Fourier components. The topic is beyond this introductory text.

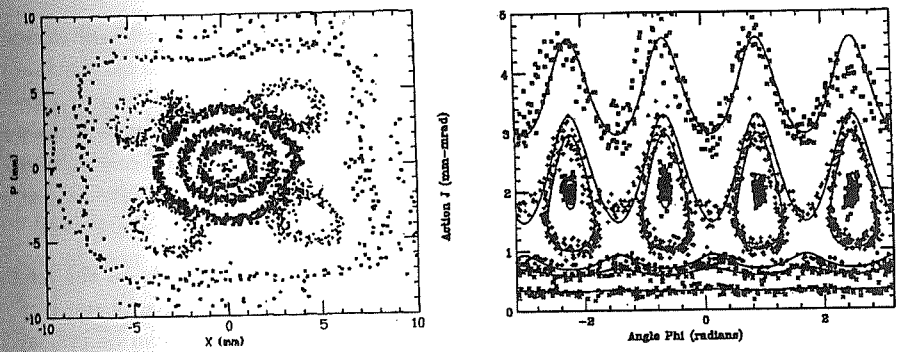

Figure 2.53: Left: The measured betatron Poincaré map (surface of section) (x, P_x) of normalized phase space near a fourth-order resonance $4\nu_x = 15$ at the IUCF cooler ring. Note that the phase-space ellipse is distorted into four island when the betatron tune sits exactly on resonance. The right plot shows the Poincaré map in action-angle variables $(J = J_x, \phi = \psi_x)$. The solid lines are the Hamiltonian tori of Eq. (2.394).

VII.3 Nonlinear Detuning from Sextupoles

Because the potential resulting from sextupole fields is an odd function of the betatron coordinates, the sextupoles will not, in linear approximation, contribute to the betatron amplitude detuning. Because sextupole strengths are large in high energy collider and storage rings, concatenation of sextupole perturbation to the betatron motion can induce substantial nonlinear betatron detuning. The dependence of the betatron tunes on the betatron amplitude can be approximated by

$$Q_x = \nu_x + \alpha_{xx} J_x + \alpha_{xz} J_z, \tag{2.395}$$

$$Q_z = \nu_z + \alpha_{xz} J_x + \alpha_{zz} J_z. \tag{2.396}$$

The detuning coefficients α_{xx}, α_{xz}, and α_{zz} can be obtained from the phase average of the concatenated one-turn Hamiltonian in a storage ring. These coefficients are

$$\begin{aligned}
\alpha_{xx} &= \frac{1}{64\pi}\sum_{i,j} S_i S_j \beta_{x,i}^{3/2}\beta_{x,j}^{3/2}\left[\frac{\cos 3(\pi\nu_x - |\psi_{x,ij}|)}{\sin 3\pi\nu_x} + 3\frac{\cos(\pi\nu_x - |\psi_{x,ij}|)}{\sin \pi\nu_x}\right], \\
\alpha_{xz} &= \frac{1}{32\pi}\left\{\sum_{i,j} S_i S_j \beta_{x,i}^{1/2}\beta_{x,j}^{1/2}\beta_{z,i}\beta_{z,j}\left[\frac{\cos[2(\pi\nu_z - |\psi_{z,ij}|) + \pi\nu_x - |\psi_{x,ij}|]}{\sin \pi(2\nu_z + \nu_x)}\right.\right. \\
&\quad \left. + \frac{\cos[2(\pi\nu_z - |\psi_{z,ij}|) - (\pi\nu_x - |\psi_{x,ij}|)]}{\sin \pi(2\nu_z - \nu_x)}\right] \\
&\quad \left. -2\sum_{i,j} S_i S_j \beta_{x,i}^{3/2}\beta_{x,j}^{1/2}\beta_{z,j}\frac{\cos(\pi\nu_x - |\psi_{x,ij}|)}{\sin \pi\nu_x}\right\},
\end{aligned}$$

$$\alpha_{zz} = \frac{1}{64\pi}\sum_{i,j} S_i S_j \beta_{x,i}^{1/2}\beta_{x,j}^{1/2}\beta_{z,i}\beta_{z,j}\left[\frac{\cos[2(\pi\nu_z - |\psi_{z,ij}|) + \pi\nu_x - |\psi_{x,ij}|]}{\sin\pi(2\nu_z+\nu_x)}\right.$$
$$\left. + \frac{\cos[2(\pi\nu_z - |\psi_{z,ij}|) - (\pi\nu_x - |\psi_{x,ij}|)]}{\sin\pi(2\nu_z-\nu_x)} + 3\frac{\cos(\pi\nu_x - |\psi_{x,i} - \psi_{x,j}|)}{\sin\pi\nu_x}\right],$$

where

$$\psi_{x,ij} = \psi_{x,i} - \psi_{x,j}, \quad \psi_{z,ij} = \psi_{z,i} - \psi_{z,j}$$

are betatron phase advances from s_j to s_i. Since the tune depends on the zeroth harmonic of a perturbed quadrupole field, the nonlinear detuning parameter is proportional to the superperiod of the accelerator. These coefficients can be evaluated from sextupole strengths distributed in one superperiod.

VII.4 Betatron Tunes and Nonlinear Resonances

The betatron tunes should avoid the linear betatron resonances at $\nu_x = m$ or $\nu_z = n$, where m, n are integers, and half-integer integer betatron resonances at $2\nu_x = m$ or $2\nu_z = n$ due to the linear imperfections discussed in Sec. III. Similarly, the betatron tunes should avoid linear coupling resonances at $\nu_x \pm \nu_z = \ell$ due to skew quadrupoles and solenoids. The left plot of Fig. 2.54 shows linear betatron resonances for the fractional parts of betatron tunes.

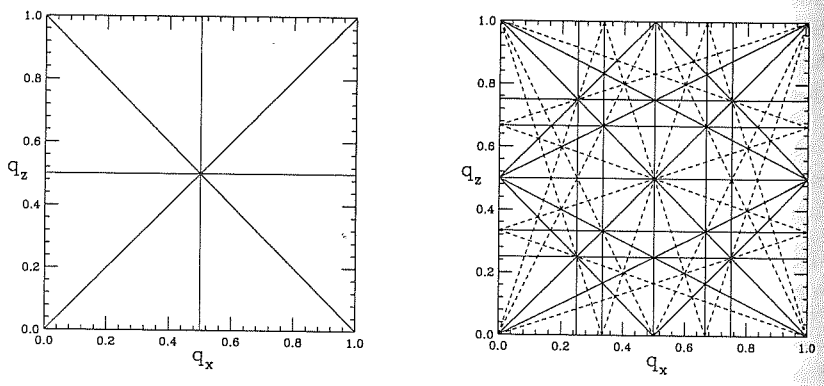

Figure 2.54: Left: the linear resonance lines, where $m_x\nu_x + m_z\nu_z = \ell$ with $|m_x| \le 1$ and $|m_z| \le 1$ and ℓ is an integer. Right: the resonance lines up to the fourth order coupling resonances, i.e $m_x\nu_x + m_z\nu_z = \ell$, where $|m_x| + |m_z| \le 4$. The solid lines corresponds to resonance lines associated with normal multipoles, and the dashed lines are those associated with skew multipoles. The symbol q_x and q_z are the fractional parts of betatron tunes ν_x and ν_z.

We have shown that sextupoles and higher multipoles are important to beam stability in Sec. V. Unfortunately, higher order multipoles can drive higher order

resonances discussed in this section. The right plot of Fig. 2.54 shows the betatron resonances up to the 4th order, where the solid lines correspond to resonances due to normal multipoles, while the dashed lines arise from skew multipoles. Note that the available resonance free tune space becomes small. When the betatron tune spread of the beam becomes large,[110] resonance (stopband) correction becomes important for attaining beam stability.

The lifetime of beams in many storage rings and colliders may suffer if the betatron tunes sit near a higher order betatron resonance. Lifetime degradation has been observed near the 7th order resonance at the SP$\bar{\text{P}}$S driven by beam-beam interaction with linear beam-beam tune shift parameter of $\xi_{\text{bb}} = 3.3 \times 10^{-3}$ per crossing (see Eq. (4.10) in Chap. 4).[111] Figure 2.55 shows betatron resonances up to the 8th order. The tune space that is free from high order resonances becomes very small. Betatron tune stability has becomes an important issue for successful operation of storage rings.

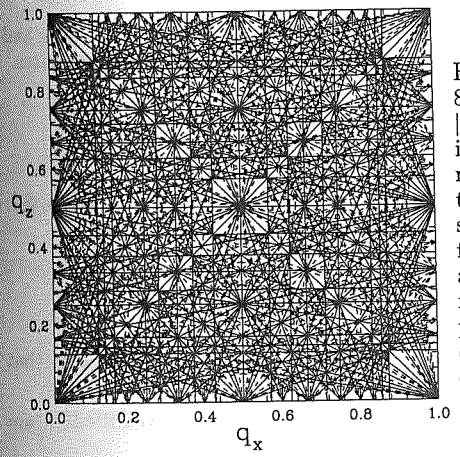

Figure 2.55: Resonance lines up to the 8th order, where $m_x\nu_x + m_z\nu_z = \ell$ with $|m_x| + |m_z| \le 8$ and integer ℓ, are shown in this figure. The solid lines corresponds to resonance lines associated with normal multipoles, and the dashed lines are those associated with skew multipoles. Resonance-free tune space becomes very small in storage rings, where higher order betatron resonances can decrease the beam lifetime. In particular, the beam-beam interaction can cause higher order resonance observed very early on at the SP$\bar{\text{P}}$S, and many e^+e^- colliders.

Exercise 2.7

1. Show that the $3\nu_x = \ell$ resonance strength is given by Eq. (2.381) in the first-order perturbation approximation.

   (a) Show that, for systematic resonances, $G_{3,0,\ell} = 0$ if $\ell \neq 0$ (Mod P), where P is the superperiodicity of the machine.

[110] The betatron tune spread of a beam may arise from the incoherent space charge (Laslett) tune shift, chromaticity, beam-beam interaction, betatron amplitude detuning, etc.

[111] See e.g. L.R. Evans, in the Proceedings of the CERN Accelerator School on *Antiprotons For Colliding Beam Facility*, p. 319, CERN 84-15 (1985); see also the Proceedings of the third ICFA Beam Dynamics Workshop on *Beam-Beam Effects in Circular Colliders*, edited by I. Koop and G. Tumaikin (Novosibirsk, 1989).

(b) Show that the resonance strength of the third-order resonance at $3\nu_x = \ell$ due to two sextupoles at s_1 and s_2 is proportional to

$$[\beta_x(s_1)]^{3/2}\,[S(s_1)\Delta s] + [\beta_x(s_2)]^{3/2}\,[S(s_2)\Delta s]\,e^{j[3\psi_{21}-(3\nu_x-\ell)\Delta\theta]},$$

where $\psi_{21} = \int_{s_1}^{s_2} ds/\beta_x$ is the betatron phase advance, $\Delta\theta = (s_2 - s_1)/R_0$, and R_0 is the average radius of the accelerator. Show that, at the $3\nu_x = \ell$ resonance, the "geometric aberrations" of these two sextupoles cancel each other if $\psi_{21} = \pi$ and $[\beta_x(s_1)]^{3/2}\,[S(s_1)\Delta s] = [\beta_x(s_2)]^{3/2}\,[S(s_2)\Delta s]$.

(c) Based on the above result, show that the geometric aberration of two chromatic sextupoles located in the arc of FODO cells separated by 180° in phase advance cancel each other.

2. Near a third-order coupling *difference* resonance at $\nu_x - 2\nu_z = \ell$, where ℓ is an integer, the Hamiltonian can be approximated by

$$H = \nu_x J_x + \nu_z J_z + g J_x^{1/2} J_z \cos(\phi_x - 2\phi_z - \ell\theta + \xi),$$

where ν_x, ν_z are the betatron tunes, $g = G_{1,-2,\ell}$ is the effective resonance strength, and $(J_x, \phi_x, J_z, \phi_z)$ are the horizontal and vertical action-angle phase-space coordinates.

(a) Using the generating function

$$F_2(\phi_x, \phi_z, J_1, J_2) = (\phi_x - 2\phi_z - \ell\theta + \xi)J_1 + \phi_z J_2,$$

transform the phase-space coordinates from $(J_x, \phi_x, J_z, \phi_z)$ to $(J_1, \phi_1, J_2, \phi_2)$, and show that the new Hamiltonian is $\tilde{H} = H_1 + H_2$, where

$$\begin{aligned} H_1(J_1, \phi_1) &= \delta_1 J_1 + g J_1^{1/2}(J_2 - 2J_1)\cos\phi_1, \\ H_2(J_2, \phi_2) &= \nu_z J_2, \end{aligned}$$

and $\delta_1 = \nu_x - 2\nu_z - \ell$ is the resonance proximity parameter. Show also that $2J_x + J_z$ is invariant.

(b) For a given J_2, show that the unstable fixed points of the Hamiltonian are located at

$$J_{1,\text{ufp}} = \frac{J_2}{2}, \quad \text{and} \quad \phi_1 = \pm\arccos\left(\frac{\delta_1}{g\sqrt{2J_2}}\right),$$

and the stable fixed points are located at

$$J_{1,\text{sfp}} = \pm\frac{\delta_1}{6g} + \sqrt{\left(\frac{\delta_1}{6g}\right)^2 + \frac{J_2}{6}}$$

for $\phi_1 = 0$ or π respectively.

3. Near a *sum* resonance at $\nu_x + 2\nu_z = \ell$, the Hamiltonian can be approximated by

$$H = \nu_x J_x + \nu_z J_z + g J_x^{1/2} J_z \cos(\phi_x + 2\phi_z - \ell\theta + \xi),$$

where ν_x, ν_z are betatron tunes, $g = G_{1,+2,\ell}$ is the effective resonance strength, and $(J_x, \phi_x, J_z, \phi_z)$ are horizontal and vertical action-angle phase-space coordinates. Discuss the difference between the sum and the difference resonances.

4. In general, betatron motion in storage rings can encounter many nonlinear resonances. Normally only low-order resonances are important. If the betatron tune of the machine is chosen such that $m\nu_x + n\nu_z \approx \ell$, where $m > 0, n$, and ℓ are integers, the Hamiltonian can be approximated by

$$H = H_0(J_x, J_z) + g J_x^{|m|/2} J_z^{|n|/2} \cos(m\phi_x + n\phi_z - \ell\theta + \xi) + \Delta H.$$

This is called a sum resonance if $mn > 0$, and a difference resonance if $mn < 0$. Neglecting the perturbing term ΔH that includes contributions from other resonances, derive the invariants of the approximated Hamiltonian.

(a) Transform the phase-space coordinates from

$$(J_x, \phi_x, J_z, \phi_z) \quad \text{to} \quad (J_1, \phi_1, J_2, \phi_2)$$

by using the generating function

$$F_2(\phi_x, \phi_z, J_1, J_2) = (m\phi_x + n\phi_z - \ell\theta + \xi)J_1 + \phi_z J_2,$$

and find the new Hamiltonian.

(b) Show that the new Hamiltonian is invariant.

(c) Show that the action J_2 is invariant, i.e.

$$nJ_x - mJ_z = \text{constant}.$$

Discuss the difference between the sum and the difference resonances.

VIII Collective Instabilities and Landau Damping

So far we have discussed only single-particle motion in synchrotrons, where each particle can be described by a simple harmonic oscillator. In reality, a circulating charged particle beam resembles an electric circuit, where the impedance plays an important role in determining the circulating current. Likewise, the *impedance* of an accelerator is related to the voltage drop with respect to the motion of the charged particle beams. The impedance is more generally defined as the Fourier transform of the *wakefield*, which is the electromagnetic waves induced by a passing charged particle beam. The induced electromagnetic field can, in turn, impart a force on the motion of each individual particle. Thus, single-particle motion is governed by the external focusing force and the wakefield generated by the beams, and the beam distribution is determined by the motion of each particle. A self-consistent distribution function may be obtained by solving the Poisson-Vlasov equation.

Since particle motion in an accelerator is classified as transverse betatron motion or longitudinal synchrotron motion, wakefields are classified as having transverse or longitudinal modes. Likewise, the impedances are classified as longitudinal or transverse. The effect of longitudinal impedances will be discussed in Chap. 3, Sec. VII. Here, we discuss some basic aspects of transverse collective beam instabilities and Landau damping. For a complete treatment of the subject, see Ref. [3]. In Sec. VIII.1, some properties of impedance are listed. In Section VIII.2 we discuss transverse wave modes, where the waves are classified as fast, backward, or slow waves. In Sec. VIII.3, we will show that a slow wave can become unstable in a simple impedance model. Landau damping and dispersion relation will be discussed in Sec. VIII.4.

VIII.1 Impedance

The impedance that a charged-particle beam experiences inside a vacuum chamber resembles the impedance in a transmission wire. For beams, there are transverse and longitudinal impedances. The longitudinal impedance has the dimension ohm, and by definition is equal to the energy loss per revolution in a unit beam current. The transverse impedance is related to the transverse force on betatron motion, and has the dimension ohm/meter.

The transverse impedance arises from accelerator components such as the resistive wall of vacuum chamber, space charge, image charge on the vacuum chamber, broad-band impedance due to bellows, vacuum ports, and BPMs, and narrow-band impedance due to high-Q resonance modes in rf cavities, septum and kicker tanks, etc. Without deriving them, we list these impedances as follows.

A. Resistive wall impedance

The resistive wall impedance is given by[112]

$$Z_{\perp,\mathrm{rw}}(\omega) = (1+j)\frac{RZ_0}{b^3}\delta_{\mathrm{skin}}, \tag{2.397}$$

where R is the mean radius of the accelerator, b is the vacuum chamber radius, $Z_0 = \mu_0 c = 377$ ohm is the vacuum impedance, $\delta_{\mathrm{skin}} = \sqrt{2/\sigma_c\mu_c\omega}$ is the skin depth of the electromagnetic wave in metal, σ_c is the conductivity, μ_c is the permittivity in metal, and ω is the wave frequency. For resistive wall impedance, the transverse impedance is related to the longitudinal impedance by

$$Z_{\perp,\mathrm{rw}} = \frac{2c}{b^2}\frac{Z_{\|,\mathrm{rw}}}{\omega}, \tag{2.398}$$

where c is the speed of light.

B. Space-charge impedance

Let a be the radius of a uniformly distributed beam in a circular cylinder. Let x_0 be an infinitesimal displacement from the center of the cylindrical vacuum chamber. The resulting beam current density is

$$i(r,\phi) = \frac{I_0}{\pi a^2}\Theta(a-r) + \frac{I_0 x_0\cos\phi}{\pi a^2}\delta(r-a), \tag{2.399}$$

where $\Theta(x) = 1$ if $x \geq 0$ and 0 otherwise, and $\delta(x)$ is the Dirac δ-function. Here, the first term corresponds to the unperturbed beam current, and the second term arises from an infinitesimal horizontal beam displacement. The perturbing current is a circular current sheet with cosine-theta current distribution. Using the result of Exercise 1.9, we find the induced dipole field inside the beam cross section to be $\Delta B_{z,\mathrm{b}} = \mu_0 I_0 x_0/2\pi a^2$. Similarly the induced image current is (see Exercise 1.16) $I_{\mathrm{w}} = -(I_0 x_0\cos\phi_{\mathrm{w}}/\pi b^2)\delta(r-b)$, and the induced dipole field due to the image wall current is $\Delta B_{z,\mathrm{w}} = -\mu_0 I_0 x_0/2\pi b^2$. The total induced vertical dipole field due to the beam displacement becomes

$$\Delta B_z = \frac{\mu_0 I_0 x_0}{2\pi}\left(\frac{1}{a^2} - \frac{1}{b^2}\right).$$

By definition, the impedance per unit length becomes

$$Z_{\perp,\mathrm{mag}} = j\frac{\beta c\Delta B_z}{\beta I_0 x_0} = j\frac{Z_0}{2\pi}\left(\frac{1}{a^2} - \frac{1}{b^2}\right),$$

[112] The imaginary number $j = -i$ of engineering convention is used throughout this textbook. Here, the resistive wall impedance consists of a resistive and an inductive component.

where βc is the velocity of the beam, and $Z_0 = \mu_0 c$ is the vacuum impedance. Similarly, the impedance due to the electric field is

$$Z_{\perp,\text{elec}} = -j\frac{Z_0}{2\pi\beta^2}\left(\frac{1}{a^2} - \frac{1}{b^2}\right).$$

Thus the transverse impedance due to space charge in one complete revolution is[113]

$$Z_{\perp,\text{sc}} = -j\frac{RZ_0}{\beta^2\gamma^2}\left(\frac{1}{a^2} - \frac{1}{b^2}\right), \tag{2.400}$$

where a is the beam transverse radius, b is the beam-pipe radius, R is the average radius of the accelerator, and γ is the Lorentz relativistic factor. Because of the $\beta^2\gamma^2$ factor in the denominator, the space-charge impedance is important for low energy beams.

Note that the space charge is capacitive because the beam radius a is less than the vacuum chamber radius b. However, when the oscillatory amplitude x_0 is large, the perturbation current of Eq. (2.399) is invalid, and the self space-charge force term may disappear. The remaining space charge impedance is the image current term, which is inductive.

C. Broad-band impedance

All vacuum chamber gaps and breaks, BPMs, bellows, etc., can be lumped into a term called the broad-band impedance, which is usually assumed to take the form of a RLC circuit:

$$Z_{\perp,\text{bb}} = \frac{2c}{b^2}\frac{Z_{\|,\text{bb}}}{\omega} = \frac{2c}{b^2\omega}\frac{R_s}{1 + jQ\left(\omega/\omega_r - \omega_r/\omega\right)}, \tag{2.401}$$

where $Q \approx 1$ is the quality factor, R_s is the shunt resistance, $\omega_r \approx (R/b)\omega_0$ is the cut-off frequency of the vacuum chamber, R is the average radius of the accelerator, and b is the beam pipe radius. The space-charge impedance can be considered as a broad-band impedance because it is independent of wave frequency.

D. Narrow-band impedance

Narrow-band impedances are usually represented by a sum of Eq. (2.401), where the corresponding Q-factor is usually large. Narrow-band impedances may arise from parasitic rf cavity modes, septum and kicker tanks, vacuum ports, etc.

[113]Note here that the derivation of the space charge impedance assumes a uniform circular beam distribution for the direct term and a circular vacuum chamber geometry for the induced charge term. The formula that takes into account the shape of the vacuum chamber can be found in Ref. [3].

E. Properties of the transverse impedance

When the beam centroid is displaced from the closed orbit, the motion can be expressed as a dipole current. The dipole current will set up a wakefield that acts on the beam. The transverse impedance of the ring is defined by

$$Z_\perp(\omega) = \frac{j}{e\beta I\langle y\rangle}\oint F_\perp ds = \frac{j}{I_1\beta}\oint(\vec{E} + \vec{v}\times\vec{B})_\perp ds = \frac{jC}{\beta}\int W_\perp(\tau)\, e^{-j\omega\tau}\, d\tau, \tag{2.402}$$

where $I_1 = I_0\langle y\rangle$ is the dipole current, $\langle y\rangle$ is the centroid of the beam in the betatron motion, and C is the circumference of the accelerator. The imaginary number j included in the definition of the impedance is needed to conform a real loss for a real positive resistance. This occurs because the driving force is leading the dipole current by a phase of $\pi/2$. The factor β in the denominator is included by convention. The wake function is then related to the impedance by

$$W_\perp(t) = -\frac{j\beta}{2\pi}\int_{-\infty}^{\infty} Z_\perp(\omega)e^{j\omega t}d\omega \tag{2.403}$$

with the causality condition

$$W_\perp(t) = 0 \quad (t < 0).$$

Thus, the impedance can not have singularities in the lower half of the complex ω plane; however, it may have poles in the upper half plane. For example, the impedance of RLC resonator circuit in Eq. (2.401) has two poles located at

$$\omega = \omega_r\left[\pm\sqrt{1 - (1/2Q)^2} + j(1/2Q)\right].$$

The analytic properties of impedances provide us with the Kramer-Kronig relation, i.e. the real and imaginary parts are related by a Hilbert transform

$$\text{Re}\, Z_\perp(\omega) = -\frac{1}{\pi}\int_{\text{P.V.}} d\omega'\frac{\text{Im}\, Z_\perp(\omega')}{\omega' - \omega}, \tag{2.404}$$

$$\text{Im}\, Z_\perp(\omega) = \frac{1}{\pi}\int_{\text{P.V.}} d\omega'\frac{\text{Re}\, Z_\perp(\omega')}{\omega' - \omega}, \tag{2.405}$$

where P.V. means taking the principal value integral. Since the wake function is real, the impedance at a negative frequency is related to that at a positive frequency by

$$Z_\perp(-\omega) = -Z_\perp^*(\omega), \tag{2.406}$$

or

$$\text{Re}Z_\perp(-\omega) = -\text{Re}Z_\perp(\omega), \quad \text{Im}Z_\perp(-\omega) = +\text{Im}Z_\perp(\omega). \tag{2.407}$$

Thus the real part of the transverse impedance is negative at negative frequency.

To summarize, various components of the transverse impedance $Z_\perp(\omega)$ are schematically shown in Fig. 2.56, where the real part of the impedance is an odd function of ω, and the imaginary part is an even function.

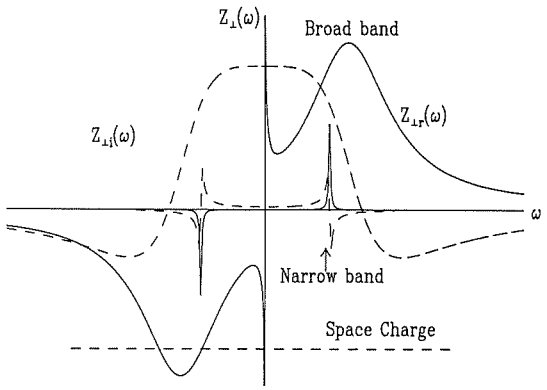

Figure 2.56: A schematic drawing of the transverse broad-band and narrow-band impedances. The real parts are shown as solid lines and the imaginary parts as dashed lines. A broad-band and a narrow-band impedance are represented by peaks in the real parts. The resistive wall impedance is important in the low-frequency region, and the space-charge impedance is independent of frequency.

VIII.2 Transverse Wave Modes

For a coasting (DC) beam, where particles continuously fill the accelerator, the transverse coordinate at any instant of time is given by[114]

$$y(t_0, \theta) = \sum_{n=-\infty}^{\infty} y_n e^{-jn\theta}, \tag{2.408}$$

where θ is the orbiting angle, and n is the mode number. At a fixed azimuth angle θ_0, the betatron oscillation of the transverse motion is

$$y(t, \theta_0) = \sum_{n=-\infty}^{\infty} y_n e^{j(Q\omega_0 t - n\theta_0)}, \tag{2.409}$$

where Q is the betatron tune, and ω_0 is the angular revolution frequency. Since $\theta = \theta_0 + \omega_0 t$, the nth mode of transverse motion is

$$y(t, \theta) = y_n e^{j[(n+Q)\omega_0 t - n\theta]}, \tag{2.410}$$

where the angular phase velocity is

$$\dot{\theta}_{n,\mathrm{w}} = \left(1 + \frac{Q}{n}\right)\omega_0. \tag{2.411}$$

There are three possible transverse wave modes: the fast wave, the backward wave, and the slow wave. The corresponding angular phase velocity is

$$\dot{\theta}_{n,\mathrm{w}} = \begin{cases} \left(1 + \dfrac{Q}{n}\right)\omega_0, & \text{if } n > 0: \quad \text{fast wave} \\ -\left(\dfrac{Q}{|n|} - 1\right)\omega_0, & \text{if } n < 0 \text{ and } |n| < Q: \quad \text{backward wave} \\ \left(1 - \dfrac{Q}{|n|}\right)\omega_0, & \text{if } n < 0 \text{ and } |n| > Q: \quad \text{slow wave.} \end{cases} \tag{2.412}$$

[114] Another extreme case is a beam with a delta-function pulse. Its Fourier harmonic contains all modes with equal amplitude (see Sec. III.7), i.e. y_n = constant.

The phase velocity of a fast wave is higher than the particle velocity, that of a slow wave is slower than the particle velocity, and a backward wave travels in the backward direction. The signal picked up in a transverse beam position monitor (BPM) will have a single frequency located at $|n+Q|\omega_0$, which is a sideband at rotation harmonic $n\omega_0$. We will show later that the characteristic responses of these waves to wakefields are different.

VIII.3 Effect of Wakefield on Transverse Wave

Let y_k be the horizontal or vertical transverse betatron displacement of the kth particle, and let $Q_k\omega_0$ be the corresponding angular frequency of betatron motion. The equation of motion in the presence of a wakefield can be expressed as a force oscillator equation[115]

$$\ddot{y}_k + (Q_k\omega_0)^2 y_k = \frac{F_\perp(t)}{\gamma m}, \tag{2.413}$$

where the overdot corresponds to the derivative with respect to time t, m is the mass, γ is the Lorentz relativistic factor, and $F_\perp$ is the time-dependent transverse force resulting from the wakefield. The EM force on a charged particle [see Eq. (2.402)] resulting from a broad-band impedance is

$$F_\perp(t) = -j\frac{e\beta I Z_\perp}{2\pi R}\langle y\rangle, \tag{2.414}$$

where R is the mean radius of the accelerator.

If beam particles encounter collective instability of mode n, they execute collective motion with a coherent frequency ω:

$$y_k = Y_k\, e^{j(\omega t - n\theta)}, \tag{2.415}$$

where n is the mode number, and Y_k is the amplitude of collective motion for the kth particle. Using the relation

$$\dot{y}_k = \frac{\partial y_k}{\partial t} + \dot{\theta}\frac{\partial y_k}{\partial \theta} = j(\omega - n\omega_0)y_k, \tag{2.416}$$

we obtain

$$\ddot{y}_k = -(\omega - n\omega_0)^2 y_k. \tag{2.417}$$

Substituting into Eq. (2.413), we obtain

$$\left[(Q\omega_0)^2 - (\omega - n\omega_0)^2\right] y_k = -j\frac{e\beta I Z_\perp}{2\pi R\gamma m}\langle y\rangle.$$

[115] In a global sense, the betatron motion is well approximated by simple harmonic motion.

or

$$(\omega - \omega_{n,\mathrm{w}})\, y_k = j\frac{e\beta I Z_\perp}{4\pi R\gamma m Q\omega_0}\langle y\rangle, \tag{2.418}$$

where

$$\langle y\rangle = \int \rho(\xi)\, y_k\, d\xi$$

is the centroid of the beam, $\rho(\xi)$ is the normalized beam distribution function with $\int \rho(\xi)d\xi = 1$, ξ represents a set of parameters that describe the dependence of the betatron tune on its amplitude, $\omega_{n,\mathrm{w}}$ is the wave frequency given by

$$\omega_{n,\mathrm{w}} = (n+Q)\omega_0, \quad \text{with} \quad \begin{cases} n > 0 & & \text{fast wave,} \\ n < 0, & |n| < Q & \text{backward wave,} \\ n < 0, & |n| > Q & \text{slow wave,} \end{cases} \tag{2.419}$$

and we have used the relation

$$\omega - n\omega_0 + Q\omega_0 \approx \omega_{n,\mathrm{w}} - n\omega_0 + Q\omega_0 = 2Q\omega_0.$$

Note that the real part of the slow wave frequency $\omega_{n,\mathrm{w}}$ is *negative.*[116] Averaging over the beam distribution, we obtain a *dispersion relation* for the collective frequency ω

$$1 = j\frac{e\beta I Z_\perp}{4\pi R\gamma m Q\omega_0}\int \frac{\rho(\xi)}{\omega - \omega_{n,\mathrm{w}}(\xi)}\, d\xi. \tag{2.420}$$

The set of parameters ξ represents any variables that $\omega_{n,\mathrm{w}}$ and the beam distribution function depend on. Since betatron tunes depend on betatron amplitudes due to space-charge force, sextupoles, and other higher-order magnetic multipoles, the betatron amplitude can serve as a ξ parameter. Since Q and ω_0 depend on the off-momentum parameter $\delta = \Delta p/p$, δ can also be chosen as a possible ξ parameter.

Now we discuss coherent frequency spread vs off-momentum variable δ. Using $\Delta\omega_0/\omega_0 = -\eta\delta$, and $\Delta Q = C_y\delta$, where ω_0 is the angular revolution frequency of the beam, η is the phase-slip factor, Q is betatron tune, and C_y is chromaticity, we obtain the collective wave frequency as

$$\omega_{n,\mathrm{w}} = \omega_{n,\mathrm{w}0} + [C_y - n\eta]\,\omega_0\,\delta, \tag{2.421}$$

where $\delta = \Delta p/p_0$ is the fractional off-momentum coordinate, Here, we have assigned the fractional off-momentum coordinate as a ξ parameter.

It is worth noting that, from Eq. (2.421), the wave frequency spread vanishes at mode number

$$n_0 = \frac{C_y}{\eta}. \tag{2.422}$$

Thus if $C_y/\eta < 0$, the mode number n_0 of Eq. (2.422) is a slow wave. The beam may become unstable against transverse collective instability, discussed as follows.

[116] When the transverse coordinate of collective motion is represented by Eq. (2.415), the slow wave frequency is negative. One can also use a positive frequency approach to express the slow wave, then the resulting dispersion relation changes sign.

A. Beam with zero frequency spread

For a beam with zero frequency spread, i.e. $\rho(\xi) = \delta(\xi - \xi_0)$, we obtain

$$\omega = \omega_{n,\mathrm{w}0} + j\frac{e\beta I Z_\perp}{4\pi R\gamma m Q\omega_0}. \tag{2.423}$$

Thus, the imaginary part of the impedance gives rise to a frequency shift, and the resistive part generates an imaginary coherent frequency ω. If the imaginary part of the coherent frequency is negative, the betatron amplitude grows exponentially with time, and the beam encounters collective instability.

For fast and backward waves, $\omega_{n,\mathrm{w}0}$ is positive. The real part of the impedance $Z_\perp(\omega)$ is positive (see Fig. 2.56), thus the imaginary part of the coherent frequency is positive, and there is no growth of collective instability.

On the other hand, the collective frequency $\omega_{n,\mathrm{w}0}$ of a slow wave is negative, where the real part of the transverse impedance is negative. *Since the imaginary part of the collective frequency is negative, a beam with zero frequency spread can suffer slow wave collective instability.*

Defining U and V parameters as

$$V + jU = \frac{e\beta I Z_\perp}{4\pi R\gamma m Q\omega_0}, \tag{2.424}$$

where V is related to growth rate, and U is related to collective frequency shift, we obtain

$$\mathrm{Re}\,[\omega_{\mathrm{coll}}] = \omega_{n,\mathrm{w}0} - U, \quad \mathrm{Im}\,[\omega_{\mathrm{coll}}] = V.$$

B. Beam with finite frequency spread

With parameters U and V, the dispersion relation for coherent dipole mode frequency ω becomes

$$(-U + jV)^{-1} = \int \frac{\rho(\xi)}{\omega - \omega_{n,\mathrm{w}}(\xi)}\, d\xi. \tag{2.425}$$

The solution of the dispersion relation corresponds to a coherent eigenmode of collective motion. If the imaginary part of the coherent frequency is negative, the amplitude of the coherent motion grows with time. On the other hand, if the imaginary part of each eigenmodes is positive, coherent oscillation is damped. The threshold of collective instability can be obtained by finding the solution with $\omega = \omega - j|0^+|$, where 0^+ is an infinitesimal positive number. The remarkable thing is that there are solutions of real ω even when $-U + jV$ is complex.

In general, the growth rate can be solved from the dispersion integral with known impedance and distribution function. Similarly, for a given growth rate, the dispersion relation provides a relation between $U(\omega)$ vs $V(\omega)$. If the distribution function

is symmetric in betatron frequency, the U vs V contour plot will have reflection symmetry with respect to the V axis. For any beam distribution $\rho(\xi)$ that does not have infinite tails, the threshold curve contains two straight vertical lines lying on the U axis. This means that if the coherent frequency shift is beyond the distribution tails, the beam can be, but may not necessarily be, unstable against collective instability, and the growth rate is proportional to the real part of the impedance.

C. A model of collective motion

We consider a macro-particle model of a beam with $\langle Y\rangle = \sum \rho_k Y_k$, where ρ_k is the distribution function with $\sum \rho_k = 1$. In matrix form, Eq. (2.418) becomes

$$[\omega - \omega_{n,\mathrm{w}}(k)]\, Y_k = W \sum_i \rho_i Y_i, \tag{2.426}$$

where $W = -U + jV$ for a broad-band impedance. If $\omega_{n,\mathrm{w}}(k) = \omega_{n,\mathrm{w0}}$ is independent of k, i.e. no frequency spread, the collective frequency is trivially given by[117]

$$\omega_{\mathrm{coll}} = \omega_{n,\mathrm{w0}} + W, \tag{2.427}$$

which is identical to the solution of Eq. (2.423). The corresponding eigenvector for collective mode is $Y_{k,\mathrm{coll}} = \rho_k Y_k$. Thus any amount of a negative real part of the impedance can produce a negative imaginary collective frequency and lead to collective instability. All other incoherent solutions have random phase with eigenvalue $\omega_{n,\mathrm{w0}}$. In fact, the coupling between external force and beam particles is completely absorbed by the collective mode.

Now, if there is a frequency spread between different particles, we have to diagonalize the matrix of Eq. (2.426). This is equivalent to solve the collective mode frequency from the dispersion relation of Eq. (2.425). In general, if the frequency spread $\Delta\omega_{n,\mathrm{w}}$ among beam particles is larger than the coherent frequency shift parameter W, the collective mode disappears, and there is no coherent motion. The disappearance of the collective mode due to tune spread is called *Landau damping*.

The requirement of a large frequency spread for Landau damping is a necessary condition but not a sufficient one. We consider the frequency spread model

$$\omega_{n,\mathrm{w}}(k) Y_k = \omega_{n,\mathrm{w0}} Y_k + \Delta\Omega(Y_k - \langle Y\rangle),$$

where $\Delta\Omega$ is a constant that determines the frequency spread of the beam. In this model, the frequency shift of a particle is proportional to the local density of the

[117] The collective mode occurs frequently in almost all many-body systems. In nuclear physics, the giant dipole resonance where protons oscillate coherently against neutrons presents a similar physical picture.

beam. This model of tune spread resembles space-charge tune shift. The resulting collective mode frequency is

$$\omega_{\mathrm{colla}} = \omega_{n,\mathrm{w0}} + W. \tag{2.428}$$

This means that the frequency spread that is proportional to the distribution function can not damp the collective motion. This is equivalent to the argument that the space-charge tune shift can not damp the transverse collective instability. Since the space-charge tune shift is a tune shift relative to the center of a bunch, and the coherent motion is relative to the closed orbit of the machine, the space-charge tune shift alone can not provide Landau damping against transverse collective instability.

VIII.4 Frequency Spread and Landau Damping

From Eq. (2.423), we see that a slow wave can suffer transverse collective instability for a beam with zero frequency spread. What is the effect of frequency spread on collective instabilities? The key is the Landau damping mechanism discussed below. The examples illustrate the essential physics of Landau damping.

A. Landau damping

The equation of collective motion (2.413) can be represented by a forced oscillator:

$$\ddot{y} + \omega_\beta^2 y = \hat{F}\sin\omega t, \tag{2.429}$$

where ω is the collective frequency, and $\omega_\beta = Q\omega_0$ is the betatron frequency. The solution is

$$y(t) = +\frac{\hat{F}}{\omega_\beta^2 - \omega^2}\left(\sin\omega t - \frac{\omega}{\omega_\beta}\sin\omega_\beta t\right) + y_0\cos\omega_\beta t + \frac{\dot{y}_0}{\omega_\beta}\sin\omega_\beta t, \tag{2.430}$$

where $y_0, \dot{y}_0$ are initial values at $t = 0$. We are interested in the response of the particle under external force. Since the second and third terms, which describe unperturbed particle motion, are of little interest here, we set $y_0 = 0$ and $\dot{y}_0 = 0$. The lower plot of Fig. 2.57 shows $y(t)$ for three particles with $\omega_\beta = 0.85$ (dash-dots), $\omega_\beta = 0.8$ (dashes), and $\omega_\beta = 0.76$ (line) under the action of an external force $\omega = 0.75, \hat{F} = 0.01$. Note particularly that if ω_β differs substantially from the driving frequency ω, the external force can not deliver energy to the system forever. The particle motion will be out of phase with the external force sooner or later, and the energy will be transferred back to the external force. A smaller $\omega - \omega_\beta$ results in a longer in-phase time, as shown in the lower plot of Fig. 2.57. As time goes on, the number of particles (oscillators) that remain in phase with the external force becomes smaller and smaller. This is the essence of Landau damping.

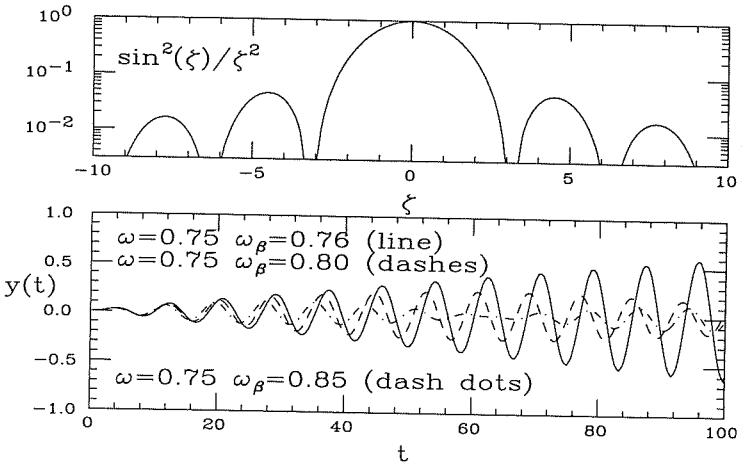

Figure 2.57: The upper plot shows the coherent function $(\sin^2\zeta)/\zeta^2$. Note that the function becomes smaller as the ζ variable increases. This means that the external force can not coherently act on a particle if $(\omega_\beta - \omega)T$ becomes large. The lower plot shows the response of three particles vs time t to an external sinusoidal driving force $F(t) = \hat{F}\sin\omega t$. Here the units of ω and t are related: if ω is in rad/s, t is in s, and if ω is in 10^6 rad/s, then t is in μs. The frequency difference of these three particles is $\Delta\omega = 0.01, 0.05$, and 0.1 shown respectively as solid line, dashes, and dots. Note that the particle with a large frequency difference will fall out of coherence with the external force.

In fact, we are interested in the average power that the external force exerts on the particle:[118]

$$\langle P(T)\rangle = \frac{1}{T}\int_0^T \dot{y}\,\hat{F}\sin\omega t dt = \left[\frac{\hat{F}^2\omega}{4(\omega+\omega_\beta)}\frac{\sin^2\zeta}{\zeta^2}\right]T + \cdots, \tag{2.431}$$

where $\zeta = \frac{1}{2}(\omega - \omega_\beta)T$. Here we retain only the leading term that is proportional to time T.

The upper plot of Fig. 2.57 shows the coherent functions $(\sin^2\zeta)/\zeta^2$. As time T increases, the coherent frequency window decreases, i.e.

$$|\omega - \omega_\beta| \sim 1/T, \tag{2.432}$$

or equivalently, fewer and fewer oscillators will be affected by the external force. When the external force can not pump power into a beam with a finite frequency spread, collective instability essentially disappears, i.e. the system is Landau damped.

[118]In general, when an external force $F(t)$ is applied to a Hamiltonian system with $\ddot{y}+dV/dy = F(t)$, where V is the potential energy, the total energy the external force delivered to the system after time T is $\Delta H = \int_0^T \dot{y}F(t)dt$, where H is the Hamiltonian of the system. Thus the average power is given by Eq. (2.431).

It is worth noting that the power dissipation to the oscillator in Eq. (2.431) comes entirely from the second term in parentheses in Eq. (2.430). That is to say, the term $y(t)$ that is in phase with the force is actually a reactive term, which does not dissipate energy. The term that will absorb power from the external force is the second term in parentheses in Eq. (2.430). This corresponds to a resistive term, which will absorb energy from the external force and lead to collective instability.

B. Solutions of dispersion integral with Gaussian distribution

We consider a beam with Gaussian distribution given by

$$\rho(\delta) = \frac{1}{\sqrt{2\pi}\sigma_\delta}e^{-\delta^2/2\sigma_\delta^2}, \tag{2.433}$$

where $\delta = \Delta p/p_0$ is the fractional off-momentum coordinate, and σ_δ is the rms momentum width of the beam. Using Eq. (2.421), the dispersion relation of Eq. (2.425) becomes

$$-u + jv = j\left[w\left(\frac{\omega - \omega_{n,w0}}{\sigma_\omega}\right)\right]^{-1}, \tag{2.434}$$

where

$$\sigma_\omega = \sqrt{2}\,|C_y - n\eta|\,\omega_0\sigma_\delta \tag{2.435}$$

is the rms frequency spread of the beam for mode n, $w(z)$ is the complex error function,[119] and

$$u = \frac{\sqrt{\pi}\,U}{\sigma_\omega}, \quad v = \frac{\sqrt{\pi}\,V}{\sigma_\omega}.$$

The curves u vs v for Gaussian distribution for $\mathrm{Im}(\omega/\sigma_\omega) = 0$ and -0.5 are shown in Fig. 2.58, where the rectangular symbols in each curve represent coherent frequency shifts at $\mathrm{Re}(\omega - \omega_{n,w0}) = \pm\sigma_\omega$ (inner ones) and $\pm 2\sigma_\omega$ (outer ones).

From Fig. 2.58, we observe that if the frequency of the coherent mode is within the width of the spectrum, then induction of collective beam instability requires a finite resistive impedance. This is because the coherent mode excites only a small fraction of the particles in the beam, and most of the beam particles are off resonance. Thus the collective beam motion is damped. Landau damping differs in essence from phase-space damping due to beam cooling, or phase space decoherence due to tune spread (see Exercise 2.8.5).

[119]The complex error function is

$$w(z) = e^{-z^2}\mathrm{erfc}(-jz) = \frac{j}{\pi}\int_{-\infty}^{\infty}\frac{e^{-t^2}}{z-t}dt.$$

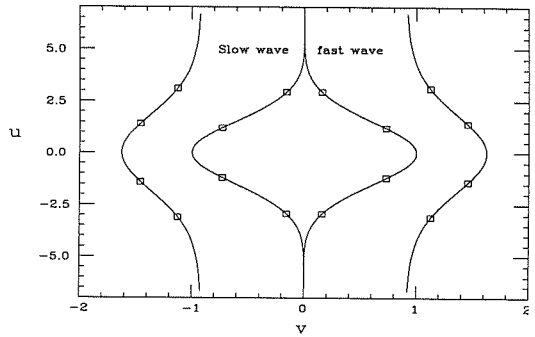

Figure 2.58: The normalized u vs v for Gaussian distribution is plotted with two different growth rates with $\mathrm{Im}(\omega) = 0$ and $-0.5\sigma_\omega$. The rectangular symbols represents the coherent frequency shifts at $\mathrm{Re}(\omega - \omega_{n,w0}) = \pm\sigma_\omega$ and $\pm 2\sigma_\omega$.

We note particularly that the frequency spread can vanish for mode number n_0 of Eq. (2.422). Because such modes have vanishing frequency spread, collective instabilities will not be Landau damped. However, if chromaticity C_y is negative below transition energy or if C_y is positive above transition energy, then mode n_0 with vanishing frequency spread is a fast wave. Since the real part of a fast wave is positive, the imaginary part of collective frequency is positive, and thus there is no collective instability. This has been commonly employed to overcome transverse collective instabilities.[120]

Exercise 2.8

1. Verify the wave angular velocity of Eq. (2.411), and show that fast, slow, and backward waves travel faster, slower, and backward relative to particle angular velocity, respectively.

2. Show that the solution given by Eq.(2.423) for the dispersion relation at zero frequency spread is identical to the collective frequency solution by matrix diagonalization of Eq. (2.426), and show that the eigenvector of collective motion is $Y_{k,\mathrm{coll}} = \rho_k Y_k$.

3. Using the Gaussian distribution of Eq. (2.433) to show that the dispersion relation becomes an algebraic equation, Eq. (2.434).

4. The solution of Eq. (2.429) with initial condition $y_0 = \dot{y}_0 = 0$ is

$$y = \frac{\hat{F}}{\omega_\beta^2 - \omega^2}\left(\sin\omega t - \frac{\omega}{\omega_\beta}\sin\omega_\beta t\right).$$

   (a) Plot $y(t)$ as a function of t for $\omega = 1$, $\hat{F} = 0.01$ with three particles at $\omega_\beta = 0.8$, 0.9, and 0.99.

[120] For *bunched beams*, the head-tail instability has been observed in SPS and Fermilab Main Ring above transition energy if the chromaticity is negative (see J. Gareyte, p. 134 in Ref. [14]). Treatment of head-tail instability is beyond the scope of this book.

   (b) Let $\omega_\beta = \omega + \epsilon$, where $|\epsilon|$ is a small frequency deviation. Show that

$$y(t) \approx \frac{\hat{F}}{2\omega}\left[\frac{1-\cos(\epsilon t)}{\epsilon}\sin\omega t - \frac{\sin(\epsilon t)}{\epsilon}\cos\omega t\right].$$

   Show that the first term in square brackets does not absorb energy from the external force but the second term can. The first term corresponds to a reactive coupling and the second term is related to a resistive coupling.

   (c) If a beam has a distribution function given by $\rho(\xi)$ with $\int \rho(\xi)d\xi = 1$, discuss the centroid of beam motion, i.e. $\langle y(t)\rangle = \int y(t)\rho(\xi)d\xi$. For example, we choose $\xi = \epsilon$ and $\rho(\epsilon) = 1/2\Delta$, if $|\epsilon| \le \Delta$; and 0, otherwise.

5. Consider a beam with uniform momentum distribution

$$\rho(\delta) = \begin{cases} 1/(2\Delta) & \text{if } |\delta| \le \Delta, \\ 0 & \text{otherwise.} \end{cases}$$

   (a) Show that the dispersion relation Eq. (2.425) becomes

$$(-u + jv)^{-1} = \ln\frac{\omega - \omega_{n,\mathrm{w0}} + \sigma_w}{\omega - \omega_{n,\mathrm{w0}} - \sigma_w},$$

   where $u = U/2\sigma_w$, $v = V/2\sigma_w$, and $\sigma_w = |C_y - n\eta|\omega_0\Delta$.

   (b) Show that the imaginary part of the coherent frequency is

$$\mathrm{Im}\,(\omega) = \sigma_w \frac{e^{-u}\sin[v/(u^2+v^2)]}{1 + e^{-2u/(u^2+v^2)} - 2e^{-u/(u^2+v^2)}\cos[v/(u^2+v^20]}.$$

   Show that the condition that $\mathrm{Im}\omega = 0^-$ is

$$u^2 + (v + \frac{1}{2\pi})^2 = \frac{1}{4\pi^2}.$$

   Plot u vs v, and compare your result with that shown in Fig. 2.58.

6. A beam is usually composed of particles with different frequencies.[121] Let $\rho(\omega_\beta)$ be the frequency distribution of the beam with $\int \rho(\omega_\beta)d\omega_\beta = 1$. If initially all particles are located at $y = \dot{y} = 0$, and at time $t = 0$ all particles are kicked to an amplitude A, i.e.

$$y(t) = A\cos\omega_\beta t,$$

   and begin coherent betatron motion, find the centroid of beam motion as a function of time with the following frequency distribution functions.

   (a) If the frequency distribution of the beam is

$$\rho(\omega_\beta) = \frac{1}{\sqrt{2\pi}\sigma}e^{-(\omega_\beta-\omega_0)^2/2\sigma^2},$$

   where σ is the rms frequency spread, show that $\langle y\rangle = Ae^{-\sigma^2t^2/2}\cos\omega_0 t$.

[121] This exercise illustrates the difference between Landau damping and beam decoherence (or filamentation). Note that coherent beam motion will decohere within a time range $\Delta t \sim 1/\sigma$, where σ is the rms frequency spread of the beam. As the coherent motion is damped, particles are not damped to the center of phase space. See also Fig. 2.15 for coherent betatron oscillation induced by an rf dipole kicker.

(b) If the frequency distribution is a one-sided exponential

$$\rho(\omega_\beta) = \begin{cases} (1/\sigma)e^{-(\omega_\beta-\omega_0)/\sigma}, & \text{if } \omega_\beta > \omega_0, \\ 0 & \text{otherwise,} \end{cases}$$

where σ is the rms frequency spread, and $\langle\omega_\beta\rangle = \omega_0 + \sigma$, show that

$$\langle y\rangle = \frac{A}{1+\sigma^2t^2}\left[\cos\omega t - \sigma t\sin\omega t\right].$$

(c) If the frequency distribution is a Lorentzian

$$\rho(\omega_\beta) = \frac{\Gamma}{\pi[(\omega_\beta-\omega_0)^2+\Gamma^2]},$$

where Γ is the width, show that $\langle y\rangle = Ae^{-\Gamma t}\cos\omega t$.

(d) If the frequency distribution is uniform with

$$\rho(\omega_\beta) = \begin{cases} 1/(2\Gamma), & \text{if } \omega_0-\Gamma < \omega_\beta < \omega_0+\Gamma, \\ 0, & \text{otherwise,} \end{cases}$$

where $\Gamma = \sqrt{3}\sigma$ and σ is the rms width, show that

$$\langle y\rangle = A\frac{\sin\Gamma t}{\Gamma t}\cos\omega_0 t.$$

(e) If the frequency distribution is parabolic with

$$\rho(\omega_\beta) = \begin{cases} (3/(4\Gamma))\left[1-((\omega_\beta-\omega_0)/\Gamma)^2\right], & \text{if } \omega_0-\Gamma < \omega_\beta < \omega_0+\Gamma, \\ 0, & \text{otherwise,} \end{cases}$$

where $\Gamma = \sqrt{5}\sigma$ and σ is the rms width, show that

$$\langle y\rangle = 3A\left(\frac{\sin\Gamma t}{(\Gamma t)^3} - \frac{\cos\Gamma t}{(\Gamma t)^2}\right)\cos\omega_0 t.$$

(f) If the frequency distribution is quadratic with

$$\rho(\omega_\beta) = \begin{cases} (2/\pi\Gamma)\sqrt{1-((\omega_\beta-\omega_0)/\Gamma)^2}, & \text{if } \omega_0-\Gamma < \omega_\beta < \omega_0+\Gamma, \\ 0, & \text{otherwise,} \end{cases}$$

where $\Gamma = 2\sigma$ and σ is the rms width, show that

$$\langle y\rangle = A\left[J_0(\Gamma t) + J_2(\Gamma t)\right]\cos\omega_0 t,$$

where J_0 and J_2 are Bessel functions.

(g) Plot $\langle y(t)\rangle$ vs t for the parabolic and Lorentzian distribution functions with $\omega_0 = 1$, $\sigma = 0.1$, and $A = 1$. Compare your result with the Gaussian, one-sided exponential, and uniform distribution results shown in the plot below.

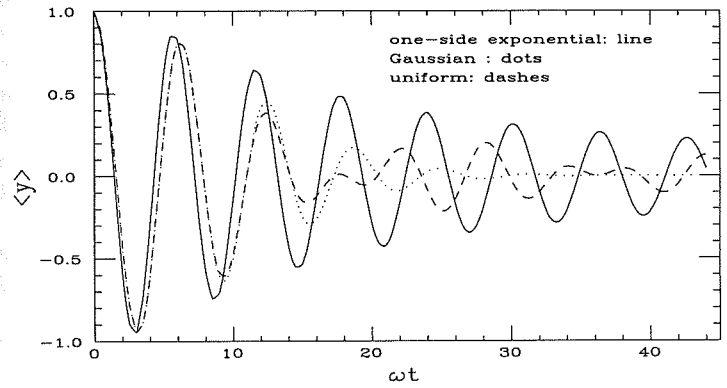

IX Synchro-Betatron Hamiltonian

So far, we have discussed particle motion only in (x, p_x, z, p_z) phase-space coordinates. The remaining phase-space coordinates $(t, -H)$ or $(t, -E)$ have not been mentioned. Here we will study the "synchrotron" equation of motion for phase-space coordinates $(t, -E)$. The terminology of synchrotron motion is derived from the synchronization of particle motion with rf electric field. The name "synchrotron" has been broadly used for all circular accelerators that employ rf electric field for beam acceleration.

This unified description has the advantage of treating synchrotron motion and betatron motion on an equal footing. It is particularly useful in the study of synchro-betatron coupling resonances.[122]

To simplify algebra, we disregard vertical betatron coordinates (z, p_z) and consider only a planar synchrotron. Neglecting vertical betatron phase-space coordinates, the Hamiltonian is [see Eq. (2.18)]

$$\begin{aligned} H_0 &= -(1+\frac{x}{\rho})\left[\left(\frac{E-e\Phi}{c}\right)^2 - m^2c^2 - p_x^2 - p_z^2\right]^{1/2} - eA_s \\ &\approx -(1+\frac{x}{\rho})\left(p - \frac{e\Phi}{\beta c}\right) + (1+\frac{x}{\rho})\left(\frac{p_x^2+p_z^2}{2p}\right) - eA_s, \end{aligned} \tag{2.436}$$

where the orbital length s is used as an independent variable, $p = \sqrt{(E/c)^2 - (mc)^2}$ is the momentum of a particle, ρ is the bending radius of the Frenet-Serret coordinate system, Φ is the scaler potential, A_s is the longitudinal vector potential, and $(x, p_x, z, p_z, t, -E)$ are canonical phase-space coordinates.

The static transverse magnetic field is

$$B_z = \frac{1}{1+(x/\rho)}\frac{\partial A_s}{\partial x}, \quad B_x = -\frac{1}{1+(x/\rho)}\frac{\partial A_s}{\partial z},$$

and the longitudinal varying electric field can be obtained from

$$E_s = -\frac{\partial A_s}{\partial t} = \sum_k V_k \delta_{\rm p}(s-s_k)\sin(\omega_{\rm rf}t + \phi_{0k}), \tag{2.437}$$

where $\delta_{\rm p}(s-s_k) = \sum_n \delta(s - s_k - 2\pi nR)$ is a periodic delta function with period $2\pi R$, V_k is the rf voltage, $\omega_{\rm rf}$ is the angular frequency of the rf field, and ϕ_{0k} is the initial phase of the kth cavity. Thus the rf accelerating field can be represented by

$$A_{s,\rm rf} = \frac{1}{\omega_{\rm rf}}\sum_k V_k \delta_{\rm p}(s-s_k)\cos(\omega_{\rm rf}t + \phi_{0k}). \tag{2.438}$$

[122]See T. Suzuki, *Part. Accel.* **18**, 115 (1985); see also S.Y. Lee and H. Okamoto, *Phys. Rev. Lett.* **80**, 5133 (1998) for the effects of space charge dominated beams.

The Hamiltonian is an implicit function of energy E. Let $E = E_0 + \Delta E$ and $p = p_0 + \Delta p$, where E_0 and p_0 are the energy and momentum of the reference particle. We obtain then

$$\frac{\Delta p}{p_0} \approx \frac{\Delta E}{\beta^2 E_0} - \frac{1}{2\gamma^2}(\frac{\Delta E}{\beta^2 E_0})^2, \qquad \frac{\Delta E}{\beta^2 E_0} \approx \frac{\Delta p}{p_0} + \frac{1}{2\gamma^2}(\frac{\Delta p}{p_0})^2. \tag{2.439}$$

Expanding the dipole field B_z in power series with $B_z = B_0 + B_1 x + \cdots$, where $B_1 = \partial B_z/\partial x$, we obtain

$$A_s = B_0 x + \frac{B_0}{2\rho}x^2 + \frac{1}{2}B_1(x^2 - z^2) + \cdots + A_{s,\rm rf} + A_{s,\rm sc}, \tag{2.440}$$

where $A_{s,\rm rf}$ given by Eq. (2.438) stands for the vector potential of rf cavities. The space charge force of the beam particles gives rise to a mean field, that can be represented by a scaler and vector potentials $\Phi = V_{\rm sc}$ and $A_{s,\rm sc}$ with $A_{s,\rm sc} = \beta^2 V_{\rm sc}/\beta c$. Substituting the scaler and vector potentials into the Hamiltonian, we obtain

$$\begin{aligned} H_0 &= -p_0 - p_0\frac{\Delta E}{\beta^2 E_0} + p_0\frac{1}{2\gamma^2}(\frac{\Delta E}{\beta^2 E_0})^2 - p_0\frac{\Delta E}{\beta^2 E_0}\frac{x}{\rho} \\ &\quad + \frac{p_x^2+p_z^2}{2p_0} + \frac{p_0}{2}(K_x x^2 + K_z z^2) - eA_{s,\rm rf} \end{aligned} \tag{2.441}$$

up to second order in phase-space coordinates, where $K_x = 1/\rho^2 - B_1/B\rho$ is the focusing function for the horizontal plane, and we used the identity condition $B_0 = -p_0/e\rho$, which signifies the expansion of x around the closed orbit at the reference energy.

The next step is to transform the coordinate system onto the closed orbit for a particle with off-energy ΔE. This procedure cancels the cross-term proportional to $(\Delta E/\beta^2 E_0)\cdot x$ in the Hamiltonian. Using the generating function

$$\begin{aligned} F_2(x, \bar{p}_x, t, -\bar{\Delta E}) &= (x - D\frac{\bar{\Delta E}}{\beta^2 E_0})\bar{p}_x - (E + \bar{\Delta E})t \\ &\quad + x\frac{D'}{\beta c}\bar{\Delta E} - \frac{1}{2}DD'p_0(\frac{\Delta E}{\beta^2 E_0})^2, \end{aligned}$$

where the new phase-space coordinates are

$$\bar{p}_x = p_x - D'\frac{\bar{\Delta E}}{\beta c}, \qquad \bar{x} = x - D\frac{\bar{\Delta E}}{\beta^2 E_0}$$

$$\bar{\Delta E} = E - E_0, \qquad \bar{t} = t + (\frac{D}{\beta^2 E_0}\bar{p}_x - \frac{D'}{\beta c}\bar{x}),$$

and the dispersion function D satisfies

$$D'' + K_x D = \frac{1}{\rho}, \tag{2.442}$$

we obtain a new Hamiltonian,

$$\begin{aligned} H_1 &= -p_0\frac{\Delta\bar{E}}{\beta^2E_0} - \frac{1}{2}p_0\left(\frac{D}{\rho}-\frac{1}{\gamma^2}\right)\left(\frac{\Delta\bar{E}}{\beta^2E_0}\right)^2 + \frac{\bar{p_x}^2}{2p_0} + \frac{p_0}{2}K_x\bar{x}^2 \\ &\quad -\frac{dE_0}{ds}\left(\bar{t}-\frac{D}{\beta^2E_0}\bar{p_x}+\frac{D'}{\beta c}\bar{x}\right) - eA_{s,\mathrm{rf}}. \end{aligned} \tag{2.443}$$

Note that $\bar{x}$ is the betatron phase-space coordinate around the off-momentum closed orbit, and the rf vector potential is

$$eA_{s,\mathrm{rf}} = \frac{1}{\omega_{\mathrm{rf}}}\sum_k eV_k\ \delta_{\mathrm{p}}(s-s_k)\ \cos\left[\omega_{\mathrm{rf}}\left(\bar{t}-\frac{D}{\beta^2E_0}\bar{p_x}+\frac{D'}{\beta c}\bar{x}\right)+\phi_{0k}\right]. \tag{2.444}$$

Now we expand the standing wave of the rf field into a traveling wave, i.e.

$$\delta_{\mathrm{p}}(s-s_k)\cos(\omega_{\mathrm{rf}}\bar{t}+\phi_{0k}) = \frac{1}{4\pi R}\sum_{n=-\infty}^{\infty}[e^{j(n\theta+\omega_{\mathrm{rf}}\bar{t}+\phi_{0k}-n\theta_k)}+e^{j(n\theta-\omega_{\mathrm{rf}}\bar{t}-\phi_{0k}-n\theta_k)}], \tag{2.445}$$

Keeping only terms that synchronize the beam arrival time with $n=\pm h$, we obtain

$$\delta_{\mathrm{p}}(s-s_k)\cos(\omega_{\mathrm{rf}}\bar{t}+\phi_{0k}) = \frac{1}{2\pi R}\cos(\omega_{\mathrm{rf}}\bar{t}-\frac{hs}{R}+\phi_{0k}+h\theta_k), \tag{2.446}$$

where $\phi_{0k}+h\theta_k$ should be an integer multiple of 2π. Using the corresponding function

$$F_2 = x\bar{p_x} + (\omega_{\mathrm{rf}}\bar{t}-\frac{hs}{R})W, \tag{2.447}$$

where

$$p_x=\bar{p_x},\quad x=\bar{x},\quad W=-\frac{\Delta\bar{E}}{\omega_{\mathrm{rf}}},\quad \phi=\omega_{\mathrm{rf}}\bar{t}-\frac{hs}{R}, \tag{2.448}$$

we obtain the Hamiltonian

$$\begin{aligned} H_2 &= -\frac{\omega_{\mathrm{rf}}^2}{2\beta^3cE_0}(\frac{D}{\rho}-\frac{1}{\gamma^2})W^2+\frac{p_x^2}{2p_0}+\frac{p_0}{2}K_xx^2 \\ &\quad -\frac{1}{2\pi R\omega_{\mathrm{rf}}}\sum_k eV_k\ \cos(\phi-D\frac{\omega_{\mathrm{rf}}p_x}{\beta cp_0}+D'\frac{\omega_{\mathrm{rf}}x}{\beta c}) \\ &\quad -\frac{\sin\phi_s}{2\pi R\omega_{\mathrm{rf}}}\sum_k eV_k\ (\phi-D\frac{\omega_{\mathrm{rf}}p_x}{\beta cp_0}+D'\frac{\omega_{\mathrm{rf}}x}{\beta c}). \end{aligned}$$

Making a scale change to canonical phase-space coordinates with

$$(x,p_x,\ \phi,W)\quad\rightarrow\quad(x,x'=\frac{p_x}{p_0},\ \phi,\frac{W}{p_0}),$$

we obtain the Hamiltonian

$$\begin{aligned} H_3=\frac{H_2}{p_0} &= \frac{1}{2}(x'^2+K_xx^2)-\frac{1}{2}\left(\frac{D}{\rho}-\frac{1}{\gamma^2}\right)\left(\frac{\omega_{\mathrm{rf}}W}{\beta^2E_0}\right)^2 \\ &\quad -\frac{1}{2\pi h\beta^2E_0}\sum_k eV_k\ \cos\left(\phi-\frac{h}{R}Dx'+\frac{h}{R}D'x\right) \\ &\quad -\frac{\sin\phi_s}{2\pi h\beta^2E_0}\sum_k eV_k\ \left(\phi-\frac{h}{R}Dx'+\frac{h}{R}D'x\right). \end{aligned}$$

Since ϕ and (x,x') are coupled through dispersion function (D,D') in rf cavities, synchrotron and betatron motions are coupled. This is called synchro-betatron coupling (SBC). If a resonance condition is encountered, it is called synchro-betatron resonance (SBR).

In general, the SBC potential must satisfy the Panofsky-Wenzel theorem, which relates the transverse kicks to the longitudinal energy gain. Consider a particle of charge e and velocity $\vec{v}=d\vec{s}/dt$ experiencing a kick from a component in an accelerator. The total transverse momentum change is

$$\Delta\vec{p}_\perp = e\int_{t_a}^{t_b}(\vec{E}+\vec{v}\times\vec{B})_\perp dt,$$

where $\vec{E}$ and $\vec{B}$ are electromagnetic fields, and t_b-t_a is the transit time of the kicker component. The total energy change will be

$$\Delta E = e\int_{s_a}^{s_b}\vec{E}\cdot d\vec{s},$$

where s_a, s_b are the entrance and exit azimuthal coordinates of the kicker. Then the Panofsky-Wenzel theorem yields a relation between the transverse kick and the energy gain[123]

$$\frac{h}{R}\frac{\partial}{\partial\phi}\left(\frac{\Delta p_\perp}{p_0}\right) = \nabla_\perp\left(-\frac{\Delta E}{\beta^2E_0}\right), \tag{2.449}$$

where $\Delta p_\perp/p_0$ is the transverse kick, $R\phi/h$ is the longitudinal phase-space coordinate of the particle, and $\nabla_\perp$ is the transverse gradient. Thus if the transverse kick depends on the longitudinal coordinates, then the energy gain depends on the transverse coordinates.

This synchro-betatron coupling potential, which satisfies the Panofsky-Wenzel theorem Eq. (2.449), can generally be expressed as a function of 6D phase-space coordinates. The synchrotron phase-space coordinates are chosen naturally to be $(R\phi/h, -\Delta p/p_0)$, and the Hamiltonian in 6D phase-space coordinates becomes

$$H_4 = \frac{1}{2}(x'^2+K_xx^2)+\frac{1}{2}(z'^2+K_zz^2)-\frac{1}{2}(\frac{D}{\rho}-\frac{1}{\gamma^2})(\frac{\Delta p}{p_0})^2$$

[123] D.A. Goldberg and G.L. Lambertson, *AIP Conf. Proc.* No. 249, p. 537 (1992).

$$-\frac{1}{2\pi h\beta^2 E_0}\sum_k eV_k\cos(\phi-\frac{h}{R}Dx'+\frac{h}{R}D'x)$$
$$-\frac{\sin\phi_s}{2\pi\beta^2 E_0}\sum_k eV_k(\phi-\frac{h}{R}Dx'+\frac{h}{R}D'x). \tag{2.450}$$

It is worth noting that if RF cavities are located in a straight section, the phase factor $-Dx'+D'x$ will be the same for all cavities (see Exercise 2.9.1). The driving terms for the synchro-betatron coupling in Eq. (2.450) coherently add up in all cavities arranged in one straight section. Thus it is beneficial to put rf cavities in dispersion free regions.

Neglecting synchro-betatron coupling, the Hamiltonian for canonical phase-space variables $(x, x', z, z', R\phi/h, -\Delta p/p_0)$ is

$$H = H_\perp(x,x',z,z') + H_s(\frac{R}{h}\phi, \frac{\Delta p}{p_0}) \tag{2.451}$$

with

$$H_\perp = \frac{1}{2}(x'^2+K_x x^2+z'^2+K_z z^2)+\cdots \tag{2.452}$$
$$H_s = \frac{1}{2}(\frac{1}{\gamma^2}-\frac{D}{\rho})(\frac{\Delta p}{p_0})^2-\sum_k\frac{eV_k}{h\beta^2 E}[\cos\phi+(\phi-\phi_s)\sin\phi_s]\delta(\theta-\theta_k), \tag{2.453}$$

where rf cavities are assumed to be at dispersion free locations.

Averaging over one revolution around the ring, the Hamiltonian for synchrotron motion becomes

$$\langle H_s\rangle = -\frac{1}{2}\eta(\frac{\Delta p}{p_0})^2-\frac{eV}{2\pi h\beta^2 E_0}[\cos\phi-\cos\phi_s+(\phi-\phi_s)\sin\phi_s]$$
$$= -\frac{1}{2}\eta(\frac{\Delta p}{p_0})^2-\frac{\nu_s^2}{h^2|\eta|}[\cos\phi-\cos\phi_s+(\phi-\phi_s)\sin\phi_s], \tag{2.454}$$

where η is the phase slip factor, and

$$\nu_s = \sqrt{\frac{h|\eta|eV}{2\pi\beta^2 E_0}}$$

is the synchrotron tune of the stationary bucket with $\phi_s = 0$.

The action of the synchrotron oscillations and the linearized betatron oscillations can be defined on an equal footing as

$$I_s = \frac{R}{2\pi h}\oint\frac{\Delta p}{p_0}d\phi, \quad I_x = \frac{1}{2\pi}\oint x'dx, \quad I_z = \frac{1}{2\pi}\oint z'dz. \tag{2.455}$$

Table 2.4 lists some properties of electron storage rings, where the transverse emittances and the longitudinal phase-space area are determined by the equilibrium between the quantum fluctuation of photon emission and the phase-space damping due to beam acceleration to compensate energy loss in the longitudinal direction.

The synchrotron action I_s (π-mm-mrad) is related to the commonly used phase area A (eV-s) of the phase-space coordinates $(\phi, \Delta E/h\omega_0)$ by

$$I_s = \frac{R\omega_0}{\beta^2 E_0}A = 3.2\times 10^5\frac{A[\text{eVs}]}{\beta\gamma}\quad[\pi\mu\text{m}]. \tag{2.456}$$

Since the typical longitudinal phase-space area is about 0.1 – 1.0 eV-s, the corresponding longitudinal action is 100–1000 times as large as the transverse action. This result has important implications for the synchro-betatron coupling resonances.

Table 2.4: Parameters of some electron storage rings.

	BEPC	CESR	LER	HER	LEP	APS	ALS
E [GeV]	2.2	6	3.1	9	55	7	1.5
ν_x	5.8	9.38	32.28	25.28	76.2	35.22	14.28
ν_z	6.8	9.36	35.18	24.18	70.2	14.3	8.18
ϵ_x [nm]	450	240	96	48	51	8	4.8
ϵ_z [nm]	35	8	3.86	1.93	0.51	0.08	0.48
ρ [m]	10.35	60	30.6	165.0	3096.2	38.96	4.01
α [$\times 10^{-4}$]	400	152	14.9	24.4	3.866	2.374	14.3
C [m]	240.4	768.4	2199.3	2199.3	26658.9	1104	196.8
h	160	1281	3492	3492	31320	1296	328
f_{rf} [MHz]	199.5	499.8	476	476	352.2	352.96	499.65
ν_s	0.016	0.064	0.0498	0.0522	0.085	0.0061	0.0082
$(\Delta E/E_0)$ [$\times 10^{-4}$]	4.0	6.3	9.5	6.1	8.4	9.6	7.1
$\mathcal{A}$ [$\times 10^{-4}$ eV-s]	3.5	7.2	3.1	5.7	78.	4.1	0.43
I_s [10^3 nm]	7.7	5.7	4.7	3.0	6.8	2.8	1.4
$\frac{I_x}{I_s}$	34	48	98	127	267	699	574
α_{ss} [m^{-1}]	-3.3	-25.5	-6.5	-10.6	-11.2	-0.27	-0.61

Exercise 2.9

1. Show that the function $-Dx'+D'x$ in the Hamiltonian H_4 is invariant in a straight section, where D is the dispersion function, x is the horizontal betatron function, and the primes are derivative with respect to the longitudinal coordinate s. Show that rf cavities located in a straight section contribute coherently to SBC if the dispersion function is not zero.

2. Show that if the SBC potential is an analytic function of 6D phase space coordinates $(x, x', z, z', R\phi/h, -\Delta p/p_0)$, it satisfies the Panofsky-Wenzel theorem.

Chapter 3

Synchrotron Motion

In general, particles gain energy from the electric field in the longitudinal direction.[1] Since the electric field strength of an electrostatic accelerator is limited by field breakdown and by the length of the acceleration column, electrostatic accelerators have been used mainly for low energy acceleration. Alternatively, a radio-frequency (rf) cavity operating in a resonance condition can be used to provide accelerating voltage with $V\sin(\phi_s + \omega_{rf}t)$, where V is the amplitude of the rf voltage, ϕ_s is a phase factor, and ω_{rf} is the angular frequency synchronized with the arrival time of beam particles. In this chapter we study particle dynamics in the presence of rf accelerating voltage waves.

Although we can derive a 6D Hamiltonian for both synchrotron and betatron oscillations (see Chap. 2, Sec. IX), here, for simplicity, we will derive the synchrotron Hamiltonian based only on the revolution frequency and energy gain relations. This formalism lacks the essential connection between synchrotron and betatron motions, but it simplifies the choice of synchrotron phase-space coordinates.

A particle synchronized with rf phase $\phi = \phi_s$ at revolution period T_0 and momentum p_0 is called a *synchronous particle.* A synchronous particle will gain or lose energy, $eV\sin\phi_s$, per passage through the rf cavity. Normally the magnetic field is ideally arranged in such a way that the synchronous particle moves on a closed orbit that passes through the center of all magnets. Particles with different betatron amplitudes execute betatron motion around this ideal closed orbit.

A beam bunch consists of particles with slightly different momenta. A particle with momentum p has its own off-momentum closed orbit, $D\delta$, where D is the dispersion function and $\delta = (p - p_0)/p_0$ is the fractional momentum deviation. Since the energy gain depends sensitively on the synchronization of rf field and particle arrival time, what happens to a particle with a slightly different momentum when the synchronous particle is accelerated?

[1]This statement also applies to beam acceleration in the betatron and the induction linac, in which the induced electromotive force is given by the time derivative of the magnetic flux.

The key answer is the discovery of the phase stability of synchrotron motion by McMillan and Veksler [17]. If the revolution frequency f is higher for a higher momentum particle, i.e. $df/d\delta > 0$, the higher energy particle will arrive at the rf gap earlier, i.e. $\phi < \phi_s$. Therefore if the rf wave synchronous phase is chosen such that $0 < \phi_s < \pi/2$, higher energy particles will receive less energy gain from the rf gap. Similarly, lower energy particles will arrive at the same rf gap later and gain more energy than the synchronous particle. This process provides the phase stability of synchrotron motion. In the case of $df/d\delta < 0$, phase stability requires $\pi/2 < \phi_s < \pi$.

The discovery of phase stability paved the way for all modern high energy accelerators, called "synchrotrons," and after half a century of research and development, it remains the cornerstone of modern accelerators. Particle acceleration without phase stability is limited to low energy accelerators, e.g. Cockcroft-Walton, Van de Graaff, betatron, etc. Furthermore, bunched beams can be shortened, elongated, combined, or stacked to achieve many advanced applications by using rf manipulation schemes. Phase-space gymnastics have become essential tools in the operation of high energy storage rings.

In this chapter we study the dynamics of synchrotron motion. In Sec. I, we derive the synchrotron equation of motion in various phase-space coordinates. Section II deals with adiabatic synchrotron motion, where an invariant *torus* corresponds to a constant Hamiltonian value. In Sec. III, we study the perturbation of synchrotron motion resulting from rf phase and amplitude modulation, synchro-betatron coupling through dipole field error, ground vibration, etc. In Sec. IV, we treat non-adiabatic synchrotron motion near transition energy, where the Hamiltonian is not invariant. In Sec. V, we study beam injection, extraction, stacking, bunch rotation, phase displacement acceleration, beam manipulations with double rf systems and barrier rf systems, etc. Section VI treats fundamental aspects of rf cavity design. In Sec. VII, we introduce collective longitudinal instabilities. In Sec. VIII, we provide an introduction to the linac.

I Longitudinal Equation of Motion

We assume that the longitudinal electric field at an rf gap is

$$\mathcal{E} = \mathcal{E}_0 \sin(\phi_{\rm rf}(t) + \phi_s), \quad \phi_{\rm rf} = h\omega_0 t, \tag{3.1}$$

where $\omega_0 = \beta_0 c/R_0$ is the angular revolution frequency of the reference (synchronous) particle, $\mathcal{E}_0$ is the amplitude of the electric field, $\beta_0 c$ and R_0 are respectively the speed and the average radius of the reference orbiting particle, h is an integer called the harmonic number, and ϕ_s is the phase angle for a synchronous particle with respect to the rf wave. We assume that the reference particle passes through the cavity gap in time $t \in nT_0 + (-g/2\beta c, g/2\beta c)$ (n = integer), where g is the rf cavity gap width.

The energy gain for the reference particle per passage is

$$\Delta E = e\mathcal{E}_0 \beta c \int_{-g/2\beta_0 c}^{g/2\beta_0 c} \sin(h\omega_0 t + \phi_s) dt = e\mathcal{E}_0 g T \sin\phi_s, \tag{3.2}$$

where e is the charge of the circulating particles, and T is the transit time factor:

$$T = \frac{\sin(hg/2R_0)}{(hg/2R_0)}. \tag{3.3}$$

The effective voltage seen by the orbiting particle is $V = \mathcal{E}_0 g T$. The transit time factor arises from the fact that a particle passes through the rf gap within a finite time interval so that the energy gain is the time average of the electric field in the gap during the transit time (see also Exercise 3.1). If the gap length is small, the transit time factor is approximately equal to 1. However, a high electric field associated with a small gap may cause sparking and electric field breakdown.

Since a synchronous particle synchronizes with the rf wave with a frequency of $\omega_{\rm rf} = h\omega_0$, where $\omega_0 = \beta_0 c/R_0$ is the revolution frequency and h is an integer, it encounters the rf voltage at the same phase angle ϕ_s every revolution. The acceleration rate for this synchronous particle is

$$\dot{E}_0 = \frac{\omega_0}{2\pi} eV \sin\phi_s, \tag{3.4}$$

where the dot indicates the derivative with respect to time t.

Now we consider a non-synchronous particle with small deviations of rf parameters from the synchronous particle, i.e.

$$\begin{cases} \omega = \omega_0 + \Delta\omega, & \phi = \phi_s + \Delta\phi, \quad \theta = \theta_s + \Delta\theta, \\ p = p_0 + \Delta p, & E = E_0 + \Delta E. \end{cases}$$

Here $\phi_s, \theta_s, \omega_0, p_0, E_0$ are respectively the synchronous phase angle, the azimuthal orbital angle, the angular revolution frequency, the momentum, and the energy of the synchronous particle, and $\phi, \theta, \omega, p, E$ are the corresponding parameters for an off-momentum particle.

The phase coordinate is related to the orbital angle by $\Delta\phi = \phi - \phi_s = -h\Delta\theta$, or

$$\Delta\omega = \frac{d}{dt}\Delta\theta = -\frac{1}{h}\frac{d}{dt}\Delta\phi = -\frac{1}{h}\frac{d\phi}{dt}. \tag{3.5}$$

The energy gain per revolution for this non-synchronous particle is $eV\sin\phi$, where ϕ is the rf phase angle. Thus the acceleration rate of a non-synchronous particle is

$$\dot{E} = \frac{\omega}{2\pi} eV \sin\phi, \tag{3.6}$$

and the equation of motion for the energy difference is[2]

$$\frac{d}{dt}\left(\frac{\Delta E}{\omega_0}\right) = \frac{1}{2\pi} eV(\sin\phi - \sin\phi_s). \tag{3.7}$$

Using the fractional off-momentum variable

$$\delta = \frac{\Delta p}{p_0} = \frac{\omega_0}{\beta^2 E}\frac{\Delta E}{\omega_0}, \tag{3.8}$$

we obtain

$$\dot{\delta} = \frac{\omega_0}{2\pi\beta^2 E} eV(\sin\phi - \sin\phi_s). \tag{3.9}$$

The next task is to find the time evolution of the phase angle variable ϕ, where, using Eq. (3.5), we have

$$\dot{\phi} = -h(\omega - \omega_0) = -h\Delta\omega. \tag{3.10}$$

Using the relation $\omega R/\omega_0 R_0 = \beta/\beta_0$, we obtain

$$\frac{\Delta\omega}{\omega_0} = \frac{\beta R_0}{\beta_0 R} - 1. \tag{3.11}$$

Following the result in Chap. 2, Sec. IV, the mean radius of a circular accelerator is

$$R = R_0(1 + \alpha_0\delta + \alpha_1\delta^2 + \alpha_2\delta^3 + \cdots), \tag{3.12}$$

where the momentum compaction factor is[3]

$$\alpha_c = \frac{1}{R_0}\frac{dR}{d\delta} = \alpha_0 + 2\alpha_1\delta + 3\alpha_2\delta^2 + \cdots \equiv \frac{1}{\gamma_T^2}, \tag{3.13}$$

and $\gamma_T mc^2$, or simply γ_T, is called the transition energy. Most accelerator lattices have $\alpha_0 > 0$ and the closed-orbit length for a higher energy particle is longer than the reference orbit. Some specially designed synchrotrons can achieve the condition $\alpha_0 = 0$, where the circumference, up to first order, is independent of particle momentum. Recently, medium energy proton synchrotrons have been designed to have an imaginary γ_T or a negative momentum compaction (see Chap. 2, Sec. IV.8). The orbit length in a negative compaction lattice is shorter for a higher energy particle.

[2]We use the relation

$$\frac{1}{\omega}\dot{E} - \frac{1}{\omega_0}\dot{E}_0 = \frac{1}{\omega_0}\Delta\dot{E} - \dot{E}\frac{\Delta\omega}{\omega_0^2} \approx \frac{1}{\omega_0}\Delta\dot{E} + \left[\dot{E}\frac{\Delta(1/\omega_0)}{\Delta E}\right]\Delta E + \cdots = \frac{d}{dt}\left(\frac{\Delta E}{\omega_0}\right).$$

[3]Typically, we have $\alpha_1\gamma_T^2 \approx \frac{1}{\nu_x}\frac{d\nu_x}{d\delta} \approx 1$ for accelerators without chromatic corrections. The α_1 term depends on the sextupole field in the accelerator.

Let $p = mc\beta\gamma = p_0 + \Delta p$ be the momentum of a non-synchronous particle. The fractional off-momentum coordinate δ is

$$\delta = \frac{\Delta p}{p_0} = \frac{\beta\gamma}{\beta_0\gamma_0} - 1. \tag{3.14}$$

Expressing β and γ in terms of the off-momentum coordinate δ, we obtain

$$\frac{\gamma}{\gamma_0} = \sqrt{1 + 2\beta_0^2\delta + \beta_0^2\delta^2}, \tag{3.15}$$

and

$$\frac{\beta}{\beta_0} = \frac{1+\delta}{\sqrt{1 + 2\beta_0^2\delta + \beta_0^2\delta^2}} = 1 + \frac{1}{\gamma_0^2}\delta - \frac{3\beta_0^2}{2\gamma_0^2}\delta^2 + \frac{\beta_0^2(5\beta_0^2 - 1)}{2\gamma_0^2}\delta^3 + \cdots. \tag{3.16}$$

Combining Eqs. (3.11) and (3.12), we obtain

$$\frac{\Delta\omega}{\omega_0} = -\eta(\delta)\delta = -(\eta_0 + \eta_1\delta + \eta_2\delta^2 + \cdots)\delta, \tag{3.17}$$

where

$$\eta_0 = (\alpha_0 - \frac{1}{\gamma_0^2}), \quad \eta_1 = \frac{3\beta_0^2}{2\gamma_0^2} + \alpha_1 - \alpha_0\eta_0, \tag{3.18}$$

$$\eta_2 = -\frac{\beta_0^2(5\beta_0^2 - 1)}{2\gamma_0^2} + \alpha_2 - 2\alpha_0\alpha_1 + \frac{\alpha_1}{\gamma_0^2} + \alpha_0^2\eta_0 - \frac{3\beta_0^2\alpha_0}{2\gamma_0^2}. \tag{3.19}$$

In the linear approximation, we have

$$\Delta\omega = -\eta_0\omega_0\delta = (\frac{1}{\gamma^2} - \frac{1}{\gamma_T^2})\omega_0\delta. \tag{3.20}$$

Below the transition energy, with $\gamma < \gamma_T$, a higher energy particle with $\delta > 0$ has a higher revolution frequency. The speed of the higher energy particle compensates more than the difference in path length. At the transition energy, the revolution frequency is independent of particle momentum. The AVF cyclotron operates in this isochronous condition. The nonlinear term in Eq. (3.17) becomes important near transition energy, to be addressed in Sec. IV. Above the transition energy, with $\gamma > \gamma_T$, a higher energy particle with $\delta > 0$ has a smaller revolution frequency, i.e. the particle appears to have a "negative mass."

With Eqs. (3.10) and (3.17), the phase equation becomes

$$\dot{\phi} = h\omega_0\eta\delta = \frac{h\omega_0^2\eta}{\beta^2 E}\left(\frac{\Delta E}{\omega_0}\right), \tag{3.21}$$

where $(\phi, \Delta E/\omega_0)$ or equivalently (ϕ, δ) are pairs of conjugate phase-space coordinates. Equations (3.7) and (3.21) form the "synchrotron equation of motion."

I.1 The Synchrotron Hamiltonian

The synchrotron equations of motion (3.7) and (3.21) can be derived from a "Hamiltonian"

$$H = \frac{1}{2}\frac{h\eta\omega_0^2}{\beta^2 E}\left(\frac{\Delta E}{\omega_0}\right)^2 + \frac{eV}{2\pi}[\cos\phi - \cos\phi_s + (\phi - \phi_s)\sin\phi_s] \tag{3.22}$$

for phase-space coordinates $(\phi, \Delta E/\omega_0)$ or

$$H = \frac{1}{2}h\omega_0\eta_0\delta^2 + \frac{\omega_0 eV}{2\pi\beta^2 E}[\cos\phi - \cos\phi_s + (\phi - \phi_s)\sin\phi_s] \tag{3.23}$$

for phase-space coordinates (ϕ, δ) with time t as an independent variable.

This Hamiltonian, although legitimate, is inconsistent with the Hamiltonian for transverse betatron oscillations, where s is the independent coordinate. To simplify our discussion, we will disregard the inconsistency and study only the synchrotron motion. A fully consistent treatment is needed in the study of synchro-betatron coupling resonances.[4]

With this simplified Hamiltonian, we now discuss the stability condition for small amplitude oscillations, where the linearized equation of motion is

$$\frac{d^2}{dt^2}(\phi - \phi_s) = \frac{h\omega_0^2 eV\eta_0\cos\phi_s}{2\pi\beta^2 E}(\phi - \phi_s). \tag{3.24}$$

The stability condition for synchrotron oscillation is

$$\eta_0\cos\phi_s < 0 \tag{3.25}$$

discovered by McMillan and Veksler [17]. Below the transition energy, with $\gamma < \gamma_T$ or $\eta_0 < 0$, the synchronous phase angle should be $0 < \phi_s < \pi/2$. Similarly the synchronous phase angle should be shifted to $\pi - \phi_s$ above the transition energy.[5] The *angular synchrotron frequency* is

$$\omega_s = \omega_0\sqrt{\frac{heV|\eta_0\cos\phi_s|}{2\pi\beta^2 E}} = \frac{c}{R}\sqrt{\frac{heV|\eta\cos\phi_s|}{2\pi E}}, \tag{3.26}$$

where c is the speed of light and R is the average radius of the synchrotron. The *synchrotron tune*, defined as the number of synchrotron oscillations per revolution, is

$$Q_s = \frac{\omega_s}{\omega_0} = \sqrt{\frac{heV|\eta_0\cos\phi_s|}{2\pi\beta^2 E}}. \tag{3.27}$$

Typically the synchrotron tune is of the order of $\leq 10^{-3}$ for proton synchrotrons and 10^{-1} for electron storage rings.

[4] S.Y. Lee, *Phys. Rev.* **E49**, 5706 (1994).

[5] This can be accomplished by a phase shift of $\pi - 2\phi_s$ to the rf wave.

The stability of particle motion in the rf force potential can be understood from the left plot of Fig. 3.1, where the rf potentials for $\phi_s = 0$ and $\phi_s = \pi/6$ are shown. The potential well near the synchronous phase angle provides restoring force for quasi-harmonic oscillations. The horizontal dashed line shows the maximum Hamiltonian value for a stable synchrotron orbit. The corresponding stable phase-space (bucket) area is shown in the right plots.

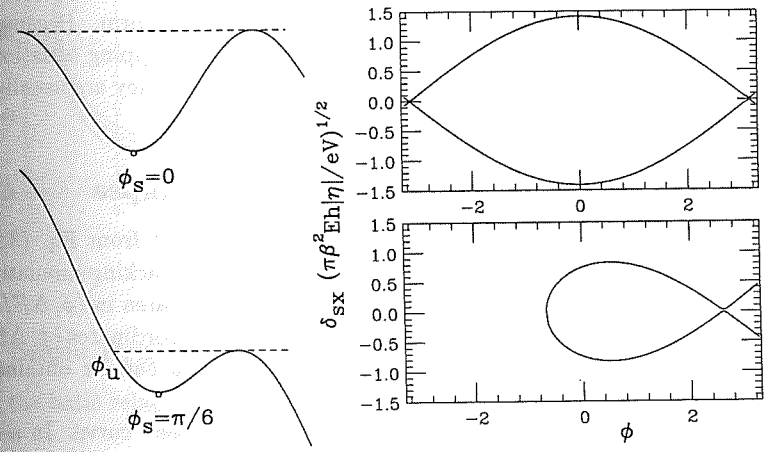

Figure 3.1: The left plot shows schematically the rf potential for $\phi_s = 0$ and $\pi/6$. The dashed line shows the maximum "energy" for stable synchrotron motion. The right plot shows the corresponding separatrix orbits in $(\pi h|\eta|/eV\beta^2 E)^{1/2}\Delta E_{sx}$ vs ϕ. The phase ϕ_u is the turning point of the separatrix orbit.

I.2 The Synchrotron Mapping Equation

In Hamiltonian formalism, the rf electric field is considered to be uniformly distributed in an accelerator. In reality, rf cavities are localized in a short section of a synchrotron, and therefore synchrotron motion is more realistically described by the symplectic mapping equation

$$\begin{cases} \delta_{n+1} = \delta_n + \dfrac{eV}{\beta^2 E}(\sin\phi_n - \sin\phi_s), \\ \phi_{n+1} = \phi_n + 2\pi h\eta(\delta_{n+1})\delta_{n+1}. \end{cases} \tag{3.28}$$

The physics of the mapping equation can be visualized as follows. First, the particle gains or loses energy at its nth passage through the rf cavity, then the rf phase ϕ_{n+1} depends on the new off-momentum coordinate δ_{n+1}. It is no surprise that Eq. (3.28)

satisfies the symplectic condition:

$$\text{Jacobian} = \frac{\partial(\delta_{n+1}, \phi_{n+1})}{\partial(\delta_n, \phi_n)} = 1. \tag{3.29}$$

Thus the mapping from (ϕ_n, δ_n) to $(\phi_{n+1}, \delta_{n+1})$ preserves phase-space area.

It is worth pointing out that Eq. (3.28) treats the rf cavity as a single lumped element in an accelerator. In reality, the rf cavities may be distributed non-uniformly. The rf phase change between different cavities may not be uniform. Because synchrotron motion is usually slow, Hamiltonian formalism and mapping equations are equivalent. Because of the simplicity of the mapping equations, they are usually used in particle tracking calculations.

I.3 Evolution of Synchrotron Phase-Space Ellipse

The phase-space area enclosed by a trajectory (ϕ, δ) obtained from Eq. (3.28) is independent of energy. Therefore, Eq. (3.28) can not be used in tracking simulations of beam acceleration. During beam acceleration, the phase-space area in $(\phi, \Delta E/\omega_0)$ is invariant. The phase-space mapping equation for phase-space coordinates $(\phi, \Delta E/\omega_0)$ should be used. The adiabatic damping of phase-space area can be obtained by transforming phase-space coordinates $(\phi, \Delta E/\omega_0)$ to (ϕ, δ).

The separatrix for the rf bucket shown in Fig. 3.1 is a closed curve. In a rapid cycling synchrotron or electron linac where the acceleration gradient is high, the separatrix is not a closed curve. The mapping equations for synchrotron phase-space coordinates $(\phi, \Delta E)$ are

$$\Delta E_{n+1} = \Delta E_n + eV(\sin\phi_n - \sin\phi_s), \tag{3.30}$$

$$\phi_{n+1} = \phi_n + \frac{2\pi h\eta}{\beta^2 E}\Delta E_{n+1}, \tag{3.31}$$

where the quantity $\eta/\beta^2 E$ in Eq. (3.30) depends on the acceleration rate according to $E = E_{0,n+1} = E_{0,n} + eV\sin\phi_s$, $\gamma = E/mc^2$, $\beta = \sqrt{1 - 1/\gamma^2}$, and $\eta = \alpha_c - 1/\gamma^2$. If the acceleration rate is low, the factor $h\eta/\beta^2 E$ is nearly constant, and the separatrix orbit shown in Fig. 3.1 can be considered as a closed curve.

When the acceleration rate is high, tori of the synchrotron mapping equations are not closed curves. Figure 3.2 shows two tori in phase-space coordinates $(\phi, \Delta E/\beta^2 E)$ with parameters $V = 100$ kV, $h = 1$, $\alpha_c = 0.04340$, $\phi_s = 30°$ at 45 MeV proton kinetic energy.[6] Note that the separatrix is not a closed curve when the acceleration rate is high. The phase-space tori change from a fish-like to a golf-club-like shape. This is equivalent to the adiabatic damping of phase-space area discussed earlier. Since the acceleration rate for proton (ion) beams is normally low, the separatrix torus shown

[6]The actual rf voltage V is about 200 V in a low energy proton synchrotron.

in Fig. 3.1 is a good approximation. When the acceleration rate is high, e.g. in many electron accelerators, the tori near the separatrix may resemble those in Fig. 3.2.

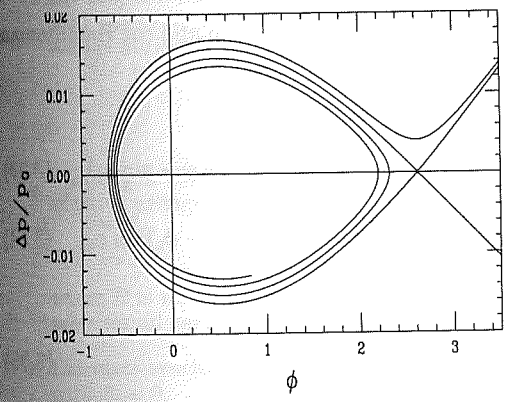

Figure 3.2: Two tori in phase-space coordinates $(\phi, \Delta E/\beta^2 E)$ obtained from mapping equations (3.30) and (3.31) with parameters $V = 100$ kV, $h = 1$, $\alpha_c = 0.04340$, and $\phi_s = 30°$ at 45 MeV proton kinetic energy.

I.4 Some Practical Examples

Using the basic relations

$$B\rho = \frac{p}{e}, \quad \dot{p} = \frac{1}{\beta c}\dot{E}, \quad f = \frac{\beta c}{2\pi R},$$

we find a basic rf cavity requirement:

$$V\sin\phi_s = 2\pi R\rho\dot{B}. \tag{3.32}$$

For example, proton acceleration in the IUCF cooler ring from 45 MeV to 500 MeV in one second requires

$$\dot{B} = \frac{\Delta[B\rho]}{\rho\Delta t} \approx 1.1 \text{ Tesla/sec},$$

where $\rho \approx 2.4$ m. Using $R \approx 14$ m, we obtain

$$V\sin\phi_s \approx 240 \text{ Volts},$$

which is independent of the harmonic number used.

Similarly, acceleration of protons from 9 GeV to 120 GeV in 1 s at the Fermilab Main Injector would require $\dot{B} \approx 1.6$ Tesla/s. The circumference is 3319.4 m with $\rho = 235$ m. The voltage requirement becomes

$$V\sin\phi_s = 1.2 \text{ MV}.$$

I.5 Summary of Synchrotron Equations of Motion

A. Using t as independent variable

Using time t as an independent variable, the equations of motion and the Hamiltonian are listed as follows.

- Using $(\phi, \Delta E/\omega_0)$ as phase-space coordinates:

$$\frac{d\phi}{dt} = \frac{h\omega_0^2\eta}{\beta^2 E}\left(\frac{\Delta E}{\omega_0}\right), \quad \frac{d(\Delta E/\omega_0)}{dt} = \frac{1}{2\pi}eV(\sin\phi - \sin\phi_s), \tag{3.33}$$

$$H = \frac{1}{2}\frac{h\eta\omega_0^2}{\beta^2 E}\left(\frac{\Delta E}{\omega_0}\right)^2 + \frac{eV}{2\pi}[\cos\phi - \cos\phi_s + (\phi - \phi_s)\sin\phi_s]. \tag{3.34}$$

- Using (ϕ, δ) as phase-space coordinates:

$$\frac{d\phi}{dt} = h\omega_0\eta\delta, \quad \frac{d\delta}{dt} = \frac{\omega_0 eV}{2\pi\beta^2 E}(\sin\phi - \sin\phi_s), \tag{3.35}$$

$$H = \frac{1}{2}h\omega_0\eta\delta^2 + \frac{\omega_0 eV}{2\pi\beta^2 E}[\cos\phi - \cos\phi_s + (\phi - \phi_s)\sin\phi_s]. \tag{3.36}$$

- Using $(\phi, \mathcal{P} = -(h|\eta|/\nu_s)\delta)$ as the normalized phase-space coordinates:

$$\frac{d\phi}{dt} = \omega_0\nu_s\mathcal{P}, \quad \frac{d\mathcal{P}}{dt} = \frac{\eta}{|\eta|}\omega_0\nu_s(\sin\phi - \sin\phi_s), \tag{3.37}$$

$$H = \frac{1}{2}\omega_0\nu_s\mathcal{P}^2 + \frac{\eta}{|\eta|}\omega_0\nu_s[\cos\phi - \cos\phi_s + (\phi - \phi_s)\sin\phi_s]. \tag{3.38}$$

- Using $(\tau = (\phi - \phi_s)/h\omega_0, \dot{\tau})$ as phase-space coordinates:

$$\frac{d\tau}{dt} = \dot{\tau}, \quad \frac{d\dot{\tau}}{dt} = -\frac{\eta\omega_0 eV}{2\pi\beta^2 E}[\sin(\phi_s - h\omega_0\tau) - \sin\phi_s], \tag{3.39}$$

$$H = \frac{1}{2}\dot{\tau}^2 + \frac{\eta eV}{2\pi h\beta^2 E}[\cos(\phi_s - h\omega_0\tau) - \cos\phi_s - h\omega_0\tau\sin\phi_s]. \tag{3.40}$$

The corresponding normalized phase space is $(\tau, \dot{\tau}/\omega_s)$.

B. Using longitudinal distance s as independent variable

- Using $(R\phi/h, -\Delta p/p_0)$ as phase-space coordinates, the Hamiltonian is

$$H = -\frac{1}{2}\eta\left(\frac{\Delta p}{p_0}\right)^2 - \frac{\nu_s^2}{h^2|\eta|}[\cos\phi - \cos\phi_s + (\phi - \phi_s)\sin\phi_s], \tag{3.41}$$

where $\nu_s = \sqrt{h|\eta|eV/2\pi\beta^2 E_0}$ is the synchrotron tune at $\phi_s = 0$. This synchrotron Hamiltonian is on an equal footing with the transverse betatron motion. In particular, the negative sign in the first term corresponds to negative mass above the transition energy, where $\eta > 0$.

Exercise 3.1

1. An rf cavity consists of an insulating gap g across which the rf voltage is applied. The gap length is finite and the rf field changes with time during transit time Δt. The total energy gain of a particle passing through the gap is the time average of the rf voltage during the transit time, i.e.

$$\Delta E = \frac{e}{\Delta t}\int_{-\Delta t/2}^{\Delta t/2} V(t)dt, \quad V(t) = V_g\sin(\phi + h\omega_0 t)$$

where V_g is the peak gap voltage, and ϕ the rf phase of the particle. Show that the effective voltage is

$$V = V_g T, \quad T = \frac{\sin(hg/2R)}{(hg/2R)},$$

where R is the mean radius of the accelerator. Thus the transit time factor T is the same for all particles.

2. Calculate synchrotron tunes for the proton synchrotrons listed in the following table with $\phi_s = 0$.

RF parameters of some synchrotrons

P-synchrotron	AGS	RHIC	FNAL-MI	FNAL-BST	SSC	Cooler
K.E. [GeV/u]	0.2	28	8	0.2	2000	0.045
V_{rf} [MV]	0.3	0.3	2	0.95	10	0.0001
h	12	342	588	84	17424	1
γ_T	8.5	24.5	21.8	5.446	140	4.6
C [m]	807.12	3833.84	3319.4	474.2	87120	86.8
ν_s						

3. Show that the relation between the rf frequency of an accelerator and the magnetic flux density $B(t)$ during particle acceleration at a constant radius is given by

$$\omega_{rf} = \frac{hc}{R_0}\left[\frac{B^2(t)}{B^2(t) + (mc^2/ec\rho)^2}\right]^{1/2},$$

where h is the harmonic number, ρ is the bending radius of the dipoles, R_0 is the mean radius of the accelerator, e and m are the charge and mass of the particle, and c is the speed of light.

4. Redefine $y \equiv h|\eta|\delta$, and $x = \phi/2\pi$.

   (a) Show that Eq. (3.28) of the symplectic mapping equation for a stationary bucket synchrotron motion can be transformed into the standard map:

$$y_{n+1} = y_n - 2\pi\nu_s^2\sin 2\pi x_n,$$
$$x_{n+1} = x_n + y_{n+1} \quad (\text{Mod } 1),$$

   where ν_s is the synchrotron tune.

(b) Write a program to track the phase-space points (x, y) such that $x \in [-1, 1]$, $y \in [-1, 1]$.

(c) Explore the phase-space evolution at $\nu_s > \nu_{s,c}$, where the critical synchrotron tune is $\nu_{s,c} = 0.39324366$ $[2\pi\nu_{s,c}^2 = 0.971635406]$.

5. Write a computer program to track synchrotron motion near the separatrix, explore the dependence of the separatrix on the acceleration rate, and verify the golf-club-like tori in Fig. 3.2.

6. Electrons in storage rings emit synchrotron radiation. The energy loss per turn is given by

$$U_0 = C_\gamma \beta^3 E_0^4/\rho,$$

where E_0 is the beam energy, βc is the beam velocity, ρ is the bending radius of dipoles, and

$$C_\gamma = 8.85 \times 10^{-5}\ \mathrm{m/(GeV)^3}.$$

The energy loss due to synchrotron radiation is compensated by the rf accelerating field, i.e. $U_0 = eV_{rf} \sin\phi_s$. Calculate synchrotron tunes for the electron storage rings listed in the following table.

	LEP	ALS	APS	NLC DR	BEPC	TRISTAN
C [m]	26658.9	196.8	1060	223	240.4	3018
Energy [GeV]	50	1.2	7.0	1.98	2.2	30.
ρ [m]	3096.2	4.01	38.96	4.35	10.35	246.5
V_{rf} [MV]	400	1.5	10	1.0	0.8	400
h	31320	328	1248	531	160	5120
γ_T	50.86	26.44	64.91	46.1	5.0	25.5
ν_x	76.2	14.28	35.22	23.81	6.18	36.8
ν_z	70.2	8.18	14.3	8.62	7.12	38.7
ϕ_s [deg]						
Q_s						

II Adiabatic Synchrotron Motion

With time t as an independent variable, the synchrotron Hamiltonian for phase-space coordinates (ϕ, δ) is

$$H = \frac{1}{2} h\omega_0\eta\delta^2 + \frac{\omega_0 eV}{2\pi\beta^2 E}[\cos\phi - \cos\phi_s + (\phi - \phi_s)\sin\phi_s], \tag{3.23}$$

where the first term can be considered as "kinetic energy" and the second as "potential energy." For simplicity in notation, hereafter, the subscript of the energy E_0 of the beam has been neglected. Figure 3.1 illustrates schematically the potential energy as a function of ϕ for $\phi_s = 0$ and $\phi_s = \pi/6$.

Hamilton's equations of motion are

$$\dot{\phi} = h\eta\omega_0\delta, \qquad \dot{\delta} = \frac{\omega_0 eV}{2\pi\beta^2 E}(\sin\phi - \sin\phi_s), \tag{3.42}$$

where the over-dots indicate derivatives with respect to time t. If $|\eta| \neq 0$, the small amplitude synchrotron tune is

$$Q_s = \sqrt{\frac{heV|\eta\cos\phi_s|}{2\pi\beta^2 E}} = \nu_s\sqrt{|\cos\phi_s|}, \tag{3.27}$$

where

$$\nu_s = \sqrt{\frac{h|\eta|eV}{2\pi\beta^2 E}}$$

is the synchrotron tune at $|\cos\phi_s| = 1$. The synchrotron period is $T_s = T_0/Q_s$, where T_0 is the revolution period.

The typical synchrotron tune in proton synchrotrons is of the order of 10^{-3}, i.e. it takes about 1000 revolutions to complete one synchrotron oscillation. The typical synchrotron tune in electron storage rings is of the order of 10^{-1}. If the rf parameters V and ϕ_s vary only slowly with time so that the gain in beam energy in each revolution is small, and η differs substantially from 0, the Hamiltonian is time independent or nearly time independent.

During beam acceleration, the Hamiltonian (3.23) generally depends on time. However, if the acceleration rate is low, the Hamiltonian can be considered as quasi-static. This corresponds to adiabatic synchrotron motion, where parameters in the synchrotron Hamiltonian change slowly so that the particle orbit is a torus of constant Hamiltonian value. The condition for adiabatic synchrotron motion is

$$\alpha_{ad} = \left|\frac{1}{\omega_s^2}\frac{d\omega_s}{dt}\right| = \frac{1}{2\pi}\left|\frac{dT_s}{dt}\right| \ll 1, \tag{3.43}$$

where ω_s is the angular synchrotron frequency and α_{ad} is called the adiabaticity coefficient. Typically, when $\alpha_{ad} \leq 0.05$, the time variation of synchrotron period is small and the trajectories of particle motion can be approximately described by tori of constant Hamiltonian values.

II.1 Fixed Points

The Hamiltonian for adiabatic synchrotron motion has two fixed points $(\phi_s, 0)$ and $(\pi - \phi_s, 0)$, where $\dot{\phi} = 0$ and $\dot{\delta} = 0$. The phase-space point $(\phi_s, 0)$ is the stable fixed point (SFP). Small amplitude phase-space trajectories around the stable fixed point are ellipses. Therefore the SFP is also called an elliptical fixed point.

On the other hand, the phase-space trajectories near the unstable fixed point (UFP) $(\pi - \phi_s, 0)$ are hyperbola. Thus the UFP is also called a hyperbolic fixed point. The torus that passes through the UFP is called the *separatrix*; it separates phase space into regions of bound and unbound oscillations. Figure 3.3 shows the separatrix orbit for $\eta < 0$ with $\phi_s = 0, \pi/6, \pi/3$ and for $\eta > 0$ with $\phi_s = 2\pi/3, 5\pi/6, \pi$. The synchrotron phase space is divided into stable and unstable regions, and only particles in the stable region can be accelerated to high energy. Thus particles in synchrotrons are naturally bunched. A beam in which particles are grouped together forming bunches is called a *bunched beam*.

For a slowly time-varying Hamiltonian, particle motion adiabatically follows a phase-space ellipse, which is also a contour (a torus) of constant Hamiltonian value. Particles outside the rf bucket drift along the longitudinal direction, and particles inside the rf bucket execute quasi-harmonic motion within the bucket. The phase-space area enclosed by a Hamiltonian torus is

$$\tilde{\mathcal{A}} = \oint \delta(\phi) d\phi.$$

The phase-space area enclosed by the separatrix orbit is called the *bucket area*. The maximum momentum deviation of the separatrix orbit is called the *bucket height*.

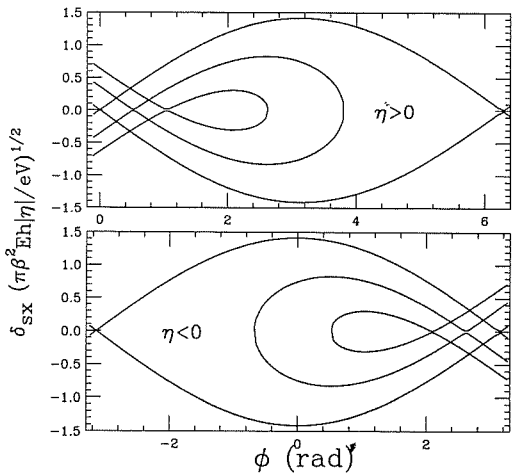

Figure 3.3: The separatrix orbits for $\eta > 0$ with $\phi_s = 2\pi/3, 5\pi/6, \pi$, and for $\eta < 0$ with $\phi_s = 0, \pi/6, \pi/3$. The phase space area enclosed by the separatrix is called the bucket area. The stationary buckets that have largest phase space areas correspond to $\phi_s = 0$ and π respectively.

II.2 Bucket Area

The separatrix passes through the unstable fixed point $(\pi - \phi_s, 0)$. Therefore the Hamiltonian value of the separatrix is

$$H_{sx} = \frac{\omega_0 eV}{2\pi\beta^2 E}\left[-2\cos\phi_s + (\pi - 2\phi_s)\sin\phi_s\right]. \tag{3.44}$$

The phase-space trajectory of the separatrix is $H = H_{sx}$, or

$$\delta_{sx}^2 + \frac{eV}{\pi\beta^2 Eh\eta}\left[\cos\phi + \cos\phi_s - (\pi - \phi - \phi_s)\sin\phi_s\right] = 0. \tag{3.45}$$

The separatrix has two turning points, ϕ_u and $\pi - \phi_s$, where ϕ_u is

$$\cos\phi_u + \phi_u \sin\phi_s = -\cos\phi_s + (\pi - \phi_s)\sin\phi_s. \tag{3.46}$$

For $\phi_s = 0$, the turning points are $-\pi$ and π.

The phase-space area enclosed by the separatrix is called the bucket area, i.e.

$$\tilde{\mathcal{A}}_B = \oint \delta_{sx}(\phi) d\phi = 16\sqrt{\frac{eV}{2\pi\beta^2 Eh|\eta|}}\,\alpha_b(\phi_s) = \frac{16 Q_s}{h|\eta|\sqrt{|\cos\phi_s|}}\,\alpha_b(\phi_s), \tag{3.47}$$

where the factor $\alpha_b(\phi_s)$ is the ratio of the bucket area between a running bucket $(\phi_s \neq 0)$ and a stationary bucket $(\phi_s = 0)$, i.e.

$$\alpha_b(\phi_s) = \frac{1}{4\sqrt{2}}\int_{\phi_u}^{\pi-\phi_s}\left[-\frac{|\eta|}{\eta}\left[\cos\phi + \cos\phi_s - (\pi - \phi - \phi_s)\sin\phi_s\right]\right]^{1/2} d\phi. \tag{3.48}$$

Table 3.1 lists $\alpha_b(\phi_s)$ as a function of the synchronous phase angle ϕ_s. Naturally $\alpha_b(0) = 1$, and $\alpha_b(\pi/2) = 0$, i.e. the bucket area vanishes at 90° synchronous phase angle. Note that $\alpha_b(\phi_s)$ can be approximated by a simple function

$$\alpha_b(\phi_s) \approx \frac{1 - \sin\phi_s}{1 + \sin\phi_s}. \tag{3.49}$$

The corresponding invariant bucket area in $(\phi, \Delta E/\omega_0)$ phase-space variables,

$$\mathcal{A}_B = \frac{\beta^2 E}{\omega_0}\tilde{\mathcal{A}}_B \approx h\Delta t \Delta E, \tag{3.50}$$

is the phase-space area of h buckets in the entire accelerator, where Δt is the bucket width in time (s), ΔE is the bucket energy height (eV), and the resulting bucket phase-space area is in eV-s. Table 3.2 lists some relevant formulas for rf bucket properties.

Table 3.1: Bucket length, bucket height and bucket area factors.

$\sin\phi_s$	ϕ_u	$\pi-\phi_s$	$Y(\phi_s)$	$\alpha_b(\phi_s)$	$\frac{1-\sin\phi_s}{1+\sin\phi_s}$
0.00	−180.00	180.00	1.0000	1.0000	1.0000
0.05	−136.47	177.13	0.9606	0.8888	0.9048
0.10	−118.90	174.26	0.9208	0.8041	0.8182
0.15	−105.32	171.37	0.8807	0.7294	0.7391
0.20	−93.71	168.46	0.8402	0.6611	0.6667
0.25	−83.26	165.52	0.7992	0.5980	0.6000
0.30	−73.59	162.54	0.7577	0.5388	0.5385
0.35	−64.45	159.51	0.7156	0.4832	0.4815
0.40	−55.66	156.42	0.6729	0.4305	0.4286
0.45	−47.11	153.26	0.6295	0.3806	0.3793
0.50	−38.69	150.00	0.5852	0.3333	0.3333
0.55	−30.31	146.63	0.5399	0.2885	0.2903
0.60	−21.88	143.13	0.4936	0.2460	0.2500
0.65	−13.31	139.46	0.4459	0.2058	0.2121
0.70	−4.48	135.57	0.3967	0.1679	0.1765
0.75	4.75	131.41	0.3455	0.1323	0.1429
0.80	14.59	126.87	0.2919	0.0991	0.1111
0.85	25.38	121.79	0.2349	0.0685	0.0811
0.90	37.77	115.84	0.1731	0.0408	0.0526
0.95	53.42	108.19	0.1028	0.0170	0.0256
1.00	90.00	90.00	0.	0.	0.

Table 3.2: Formula for bucket area in conjugate phase space variables.

	$(\phi, \frac{\Delta E}{\omega_0})$	(ϕ, δ)	$(\phi, \frac{h\lvert\eta\rvert}{\nu_s}\delta)$
Bucket Area	$16\left(\frac{\beta^2 EeV}{2\pi\omega_0^2 h\lvert\eta\rvert}\right)^{1/2}\alpha_b(\phi_s)$	$16\left(\frac{eV}{2\pi\beta^2 Eh\lvert\eta\rvert}\right)^{1/2}\alpha_b(\phi_s)$	$16\,\alpha_b(\phi_s)$
Bucket Height	$2\left(\frac{\beta^2 EeV}{2\pi\omega_0^2 h\lvert\eta\rvert}\right)^{1/2}Y(\phi_s)$	$2\left(\frac{eV}{2\pi\beta^2 Eh\lvert\eta\rvert}\right)^{1/2}Y(\phi_s)$	$2\,Y(\phi_s)$

The bucket length is $|(\pi-\phi_s)-\phi_u|$, and the bucket height or the maximum momentum width is

$$\delta_B = \left(\frac{2eV}{\pi\beta^2 Eh|\eta|}\right)^{1/2} Y(\phi_s) = \frac{2Q_s}{h|\eta|}\,\tilde{Y}(\phi_s). \tag{3.51}$$

Here the bucket height factor $Y(\phi_s)$ and $\tilde{Y}(\phi_s)$ are the ratios of the maximum momentum height to the height of the stationary bucket, i.e.

$$Y(\phi_s) = \left|\cos\phi_s - \frac{\pi-2\phi_s}{2}\sin\phi_s\right|^{1/2}, \quad \tilde{Y}(\phi_s) = \left|1 - \frac{\pi-2\phi_s}{2}\tan\phi_s\right|^{1/2}. \tag{3.52}$$

Table 3.1 lists the turning points, and the bucket height factor, $Y(\phi_s)$, of an rf bucket.

II.3 Small-Amplitude Oscillations and Bunch Area

The linearized synchrotron Hamiltonian around the SFP is

$$H = \frac{1}{2}h\omega_0\eta\delta^2 - \frac{\omega_0 eV\cos\phi_s}{4\pi\beta^2 E}\varphi^2, \tag{3.53}$$

where $\varphi = \phi - \phi_s$. The synchrotron frequency is given by Eq. (3.27), and

$$\varphi = \hat{\phi}\cos(\omega_s t + \chi), \quad \delta = -\frac{Q_s}{h|\eta|}\hat{\phi}\sin(\omega_s t + \chi), \tag{3.54}$$

where $\omega_s = Q_s\omega_0$ is the angular synchrotron tune. The phase-space ellipse of a particle becomes

$$\left(\frac{\delta}{\hat{\delta}}\right)^2 + \left(\frac{\varphi}{\hat{\phi}}\right)^2 = 1, \qquad \frac{\hat{\delta}}{\hat{\phi}} = \left(\frac{eV|\cos\phi_s|}{2\pi\beta^2 Eh|\eta|}\right)^{1/2} = \frac{Q_s}{h|\eta|}, \tag{3.55}$$

where $\hat{\delta}$ and $\hat{\phi}$ are maximum amplitudes of the phase-space ellipse. The phase-space area of the ellipse is $\pi\hat{\delta}\hat{\phi}$.

A. Gaussian beam distribution

The equilibrium beam distribution is a function of the invariant ellipse of Eq. (3.55). In many beam applications, we use the normalized Gaussian distribution given by

$$\rho(\delta,\phi) = \frac{1}{2\pi\sigma_\delta\sigma_\phi}\exp\left\{-\frac{1}{2}\left[\frac{\phi^2}{\sigma_\phi{}^2} + \frac{\delta^2}{\sigma_\delta{}^2}\right]\right\}, \tag{3.56}$$

where σ_δ and σ_ϕ are rms momentum spread and bunch length respectively. The corresponding rms phase-space area is $\tilde{\mathcal{A}}_{\rm rms} = \pi\sigma_\delta\sigma_\phi$. The phase-space area that contains 95% of the particles in a Gaussian beam distribution is

$$\tilde{\mathcal{A}}_{95\%} = 6\tilde{\mathcal{A}}_{\rm rms},$$

where the factor 6 depends on the distribution function.

Since the synchrotron phase-space area $\mathcal{A}$, usually measured in eV-s, is defined as the area in the phase space $(\phi/h, \Delta E/\omega_0)$ for *one* bunch,[7] it is related to $\tilde{\mathcal{A}}$ by

$$\tilde{\mathcal{A}} = \pi\hat{\delta}\hat{\phi} = h\mathcal{A}\left(\frac{\omega_0}{\beta^2 E}\right). \tag{3.57}$$

Using Eq. (3.55), the maximum momentum width and the bunch length are

$$\hat{\delta} = \mathcal{A}^{1/2}\left(\frac{\omega_0}{\pi\beta^2 E}\right)^{1/2}\left(\frac{heV|\cos\phi_s|}{2\pi\beta^2 E|\eta|}\right)^{1/4},$$

$$\hat{\theta} = \frac{1}{h}\hat{\phi} = \mathcal{A}^{1/2}\left(\frac{\omega_0}{\pi\beta^2 E}\right)^{1/2}\left(\frac{2\pi\beta^2 E|\eta|}{heV|\cos\phi_s|}\right)^{1/4}, \tag{3.58}$$

$$\frac{\hat{\delta}}{\hat{\theta}} = \left(\frac{heV|\cos\phi_s|}{2\pi\beta^2 E|\eta|}\right)^{1/2} = \frac{Q_s}{|\eta|}. \tag{3.59}$$

Note that here the phase-space area $\mathcal{A}$ is the invariant phase-space area for one bunch in eV-s. The scaling properties of the bunch length and bunch height of Eq. (3.58) become

$$\hat{\delta} \sim \mathcal{A}^{1/2}V^{1/4}h^{1/4}|\eta|^{-1/4}\gamma^{-3/4}, \qquad \hat{\theta} \sim \mathcal{A}^{1/2}V^{-1/4}h^{-1/4}|\eta|^{1/4}\gamma^{-1/4}, \tag{3.60}$$

where the adiabatic damping is also shown. As the energy approaches the transition energy with $\eta \to 0$, we expect that $\hat{\delta} \to \infty$, and $\hat{\theta} \to 0$. This is not true because the synchrotron motion around the transition energy is non-adiabatic. It will be discussed in Sec. IV.

Similarly, the invariant phase-space ellipse in (θ, δ) phase space is

$$\left(\frac{\delta^2}{\hat{\delta}}\right)^2 + \left(\frac{\theta}{\hat{\theta}}\right)^2 = 1, \qquad \frac{\hat{\delta}}{\hat{\theta}} = \frac{\nu_s}{|\eta|}, \tag{3.61}$$

where $\hat{\delta}$ and $\hat{\theta}$ are maximum amplitudes of the phase-space ellipse. The normalized Gaussian distribution in (θ, δ) space becomes

$$\rho(\delta, \theta) = \frac{1}{2\pi\sigma_\delta\sigma_\theta}\exp\left\{-\frac{1}{2}\left[\frac{\theta^2}{\sigma_\theta{}^2} + \frac{\delta^2}{\sigma_\delta{}^2}\right]\right\}. \tag{3.62}$$

[7]Since the energy of a heavy ion beam is usually expressed as [MeV/u] or [GeV/u], the E in the denominator of Eq. (3.57) can be expressed as $A \times (E/A)$, where A is the atomic mass number or the number of nucleons in a nucleus, $E/A = \gamma u c^2$, and $u = 0.931494$ GeV/c^2 is the atomic mass unit. Thus the phase-space area is commonly defined as phase-space area per amu expressed as [eV-s/u] for heavy ion beams. The factor eV/E in this chapter should be modified by a charge-to-mass ratio of Z/A for heavy ion beams, i.e. $e \to Ze$, and $E \to A \times (E/A)$, where $Z$is the charge number of the ion beam.

Here σ_θ and σ_δ are respectively the rms bunch angular width and the rms fractional momentum spread. The bunch length is $\sigma_s = R\sigma_\theta$ in meters, where R is the average radius of the accelerator, or $\sigma_t = \sigma_\theta/\omega_0$ in s.

Now we consider N_B particles distributed in a bunch, where N_B may vary from 10^8 to 10^{13} particles. The line distribution is

$$\rho(\phi) = \frac{N_B}{\sqrt{2\pi}\sigma_\phi}e^{-\phi^2/2\sigma_\phi^2} \quad \text{or} \quad \rho(\theta) = \frac{N_B}{\sqrt{2\pi}\sigma_\theta}e^{-\theta^2/2\sigma_\theta^2}. \tag{3.63}$$

The peak current (in Amperes) of the bunch is

$$\hat{I} = \frac{N_B e}{\sqrt{2\pi}\sigma_t} = \frac{N_B e\omega_0}{\sqrt{2\pi}\sigma_\theta} = \left(\frac{2\pi}{\sqrt{2\pi}\sigma_\theta}\right)\frac{N_B e}{T_0}. \tag{3.64}$$

B. Synchrotron motion in reference time coordinates

In the discussion of collective beam instabilities, it is sometimes useful to use the particle arrival time τ and its time derivative $\dot{\tau}$ for the synchrotron phase-space coordinates, i.e.

$$\tau = -\frac{\theta - \theta_0}{\omega_0}, \quad \text{and} \quad \dot{\tau} = \frac{\Delta\omega}{\omega_0} = +\eta\delta. \tag{3.65}$$

The linearized synchrotron Hamiltonian becomes

$$H = \frac{h\omega_0\omega_s^2}{2\eta}\left[\frac{\dot{\tau}^2}{\omega_s^2} + \tau^2\right], \tag{3.66}$$

where ω_s is the angular synchrotron frequency shown in Eq. (3.26). The phase-space ellipse that corresponds to a constant Hamiltonian is

$$\tau^2 + \frac{\dot{\tau}^2}{\omega_s^2} = \hat{\tau}^2. \tag{3.67}$$

The equation of motion is $\ddot{\tau} + \omega_s^2\tau = 0$, and the solution can be expressed as

$$\tau = \hat{\tau}\cos\psi, \quad -\frac{\dot{\tau}}{\omega_s} = \hat{\tau}\sin\psi, \quad \psi = \psi_0 + \omega_s t \tag{3.68}$$

where $\hat{\tau}$ and ψ are respectively the synchrotron amplitude and phase. See Eq. (3.333) for its application.

C. Approximate action-angle variables

Expanding the phase coordinate around the SFP with $\phi = \phi_s + \varphi$, the synchrotron Hamiltonian becomes (see Exercise 3.2.11)

$$H = \frac{1}{2}h\omega_0\eta\delta^2 + \frac{1}{2h\eta}\omega_0 Q_s^2\left[\varphi^2 - \frac{1}{3}\tan\phi_s\,\varphi^3 - \frac{1}{12}\varphi^4 + \cdots\right], \tag{3.69}$$

where $Q_s = \sqrt{heV|\eta\cos\phi_s|/2\pi\beta^2 E} = \nu_s\sqrt{|\cos\phi_s|}$ is the small amplitude synchrotron tune. For simplicity, we assume $\eta > 0$ in this section.

Using the generating function for linearized synchrotron motion

$$F_1(\phi,\psi) = -\frac{Q_s}{2h|\eta|}\varphi^2\tan\psi, \tag{3.70}$$

the synchrotron phase-space coordinates are transformed according to

$$\varphi = \sqrt{\frac{2h\eta J}{Q_s}}\cos\psi, \quad \delta = -\sqrt{\frac{2Q_s J}{h\eta}}\sin\psi, \tag{3.71}$$

where the conjugate variables (J,ψ) are approximate action-angle variables of the Hamiltonian in (ϕ,δ) phase space. If we use the approximate action-angle variables, the Hamiltonian for synchrotron motion becomes

$$H = \omega_0 Q_s J + \omega_0\frac{\sqrt{2h\eta Q_s}}{12}\tan\phi_s\, J^{3/2}\,[\cos 3\psi + 3\cos\psi] - \omega_0\frac{h\eta}{6}J^2\cos^4\psi. \tag{3.72}$$

If we apply the canonical perturbation method (see Exercise 3.2.11), the averaged synchrotron Hamiltonian becomes

$$H = \omega_0 Q_s J - \frac{\omega_0 h\eta}{16}\left(1+\frac{5}{3}\tan^2\phi_s\right)J^2 + \cdots. \tag{3.73}$$

Thus the synchrotron tune becomes

$$\tilde{Q}_s(J) \approx Q_s\left[1 - \frac{h\eta}{8Q_s}\left(1+\frac{5}{3}\tan^2\phi_s\right)J\right]. \tag{3.74}$$

II.4 Small-Amplitude Synchrotron Motion at the UFP

Small amplitude synchrotron motion around the unstable fixed point (UFP) is also of interest in accelerator physics. Expanding the Hamiltonian around the UFP, i.e. $\varphi = \phi - (\pi - \phi_s)$, we obtain

$$\dot{\delta} = -\frac{\omega_0 eV\cos\phi_s}{2\pi\beta^2 E}\varphi, \qquad \dot{\varphi} = h\eta\omega_0\delta \tag{3.75}$$

or

$$\ddot{\delta} = \omega_s^2\delta, \qquad \ddot{\varphi} = \omega_s^2\varphi. \tag{3.76}$$

Thus the particle motion is hyperbolic around the UFP.

Now, we study the evolution of an elliptical torus of Eq. (3.55) at the UFP. We would like to find the evolution of bunch shape when the center of the beam bunch is instantaneously kicked[8] onto the UFP at time $t = 0$. With normalized coordinates

$$\tilde{\varphi} = \frac{\varphi}{\hat{\phi}}, \quad \tilde{\delta} = \frac{\delta}{\hat{\delta}},$$

[8]In reality, the beam does not move in the phase space; instead, the phase of the rf wave is being shifted so that the UFP is located at the center of the bunch.

the solutions of Eq. (3.76) are

$$\tilde{\varphi} = ae^{\omega_s t} + be^{-\omega_s t}, \quad \tilde{\delta} = ae^{\omega_s t} - be^{-\omega_s t}, \tag{3.77}$$

where a and b are determined from the initial condition. With the constants a and b eliminated, the evolution of the bunch shape ellipse is

$$\tilde{\varphi}^2 - 2\left(\frac{\eta}{|\eta|}\tanh 2\omega_s t\right)\tilde{\varphi}\tilde{\delta} + \tilde{\delta}^2 = (\cosh 2\omega_s t)^{-1}. \tag{3.78}$$

Thus the upright phase-space ellipse will become a tilted phase-space ellipse encompassing the same phase-space area. The width and height of the phase-space ellipse increase or decrease at a rate $e^{\pm\omega_s t}$, where t is the length of time the bunch stays at the UFP (see Exercise 3.2.5). This scheme of bunch deformation can be used for bunch rotation or bunch compression. At $\omega_s t \gg 1$, the ellipse becomes a line $\tilde{\varphi} \pm \tilde{\delta} = 0$. However, the nonlinear part of the synchrotron Hamiltonian will distort the ellipse.

II.5 Synchrotron Motion for Large-Amplitude Particles

The phase space trajectory of adiabatic synchrotron motion follows a Hamiltonian torus $H(\phi,\delta) = H_0$, where $H(\phi,\delta)$ is the synchrotron Hamiltonian in Eq. (3.23) and the constant Hamiltonian value H_0 is

$$H_0 = \frac{1}{2}h\omega_0\eta\hat{\delta}^2 = \frac{\omega_0 eV}{2\pi\beta^2 E}[\cos\hat{\phi} - \cos\phi_s + (\hat{\phi} - \phi_s)\sin\phi_s].$$

Here $\hat{\phi}$ and $\hat{\delta}$ are respectively the maximum phase coordinate and fractional momentum deviation of synchrotron motion. Using Hamilton's equation $\dot{\phi} = h\omega_0\eta\delta$, we find the synchrotron oscillation period as

$$T = \oint\left(2h\omega_0\eta\left[H_0 - \frac{\omega_0 eV}{2\pi\beta^2 E}[\cos\phi - \cos\phi_s + (\phi - \phi_s)\sin\phi_s]\right]\right)^{-1/2}d\phi, \tag{3.79}$$

where H_0 is the Hamiltonian value of a torus. The angular synchrotron frequency is $2\pi/T$. The action of the torus is

$$J = \frac{1}{2\pi}\oint\left(\frac{2}{h\omega_0\eta}[H_0 - \frac{\omega_0 eV}{2\pi\beta^2 E}(\cos\phi - \cos\phi_s + (\phi - \phi_s)\sin\phi_s)]\right)^{1/2}d\phi. \tag{3.80}$$

The synchrotron period of Eq. (3.79) can also be derived by differentiating Eq. (3.80) with respect to J, and using $dH_0/dJ = \omega(J)$ to find the synchrotron frequency.

A. Stationary synchrotron motion

For simplicity, we consider the stationary synchrotron motion above the transition energy with $\eta > 0$, or $\phi_s = \pi$. The Hamiltonian value for a torus with a maximum phase coordinate $\hat{\phi}$ (or maximum off-momentum coordinate $\hat{\delta}$) is

$$H_0 = \frac{1}{2} h\omega_0 \eta \hat{\delta}^2 = \frac{\omega_0}{h\eta} \nu_s^2 (1 - \cos\hat{\phi}).$$

Note that the maximum off-momentum coordinate $\hat{\delta}$ is related to the maximum phase coordinate $\hat{\phi}$ a Hamiltonian torus by

$$\hat{\delta} = \frac{2\nu_s}{h\eta} \sin\frac{\hat{\phi}}{2}. \tag{3.81}$$

The Hamiltonian torus is the phase space trajectory given by $(\phi, \pm\delta(\phi))$, where

$$\delta(\phi) = \frac{\nu_s}{h\eta}\sqrt{2(\cos\phi - \cos\hat{\phi})}. \tag{3.82}$$

The phase space area $\mathcal{A}$, or the action J enclosed by the Hamiltonian torus is

$$\mathcal{A} = 2\pi J = 2\int_{-\hat{\phi}}^{\hat{\phi}} \delta(\phi) d\phi = 16\frac{\nu_s}{h\eta}\left[E(k) - (1-k^2)\,K(k)\right], \tag{3.83}$$

where the modulus of these integrals $k = \sin(\hat{\phi}/2)$ and

$$K(k) = \int_0^{\pi/2} \frac{dw}{\sqrt{1 - k^2 \sin^2 w}}, \qquad E(k) = \int_0^{\pi/2} \sqrt{1 - k^2 \sin^2 w}\; dw, \tag{3.84}$$

are the complete elliptic integrals of the first and second kind.

B. Synchrotron tune

The synchrotron tune of the Hamiltonian torus with maximum phase amplitude $\hat{\phi}$ becomes (see Exercise 3.2.8)

$$\tilde{Q}_s(\hat{\phi}) = \pi\nu_s / 2K(\sin(\hat{\phi}/2)) \tag{3.85}$$

Figure 3.4 compares the theoretical curve of Eq. (3.85) with a measured synchrotron tune at the IUCF Cooler. When the value of the Hamiltonian H_0 approaches that of the separatrix H_{sx} of Eq. (3.44), the synchrotron tune becomes zero and the synchrotron period becomes infinite. In the small angle approximation, we find $\tilde{Q}_s(\hat{\phi}) \approx (1 - \frac{1}{16}\hat{\phi}^2)\nu_s$, which is identical to Eq. (3.74) at $\phi_s = 0$.

Since the synchrotron tune is nonlinear, particles having different synchrotron amplitudes in a beam bunch can have different synchrotron tunes. If the bunch area is

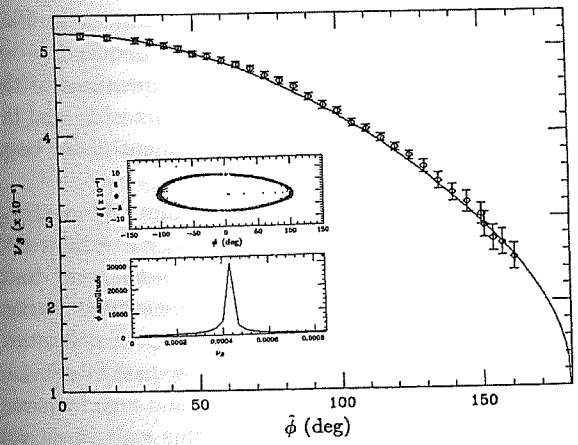

Figure 3.4: The measured synchrotron tune obtained by taking the FFT of the synchrotron phase coordinate is plotted as a function of the maximum phase amplitude of the synchrotron oscillations. The solid line shows the theoretical prediction of Eq. (3.85). The inset shows an example of the synchrotron phase-space map measured at the IUCF Cooler, and the corresponding FFT spectrum. The zero amplitude synchrotron tune was $\nu_s = 5.2 \times 10^{-4}$.

a substantial fraction of the bucket area, the synchrotron tune spread may be large. For a mismatched beam bunch, synchrotron tune spread can cause beam *decoherence*, a *filamentation* process, where beam particles spread out in the synchrotron phase space. Beam filamentation causes a mismatched beam bunch to evolve into spirals bounded by a Hamiltonian torus. The final bunch area is determined by the initial beam distribution and parameters of the rf system (see Fig. 3.19 in Sec. V). Filamentation can dilute the phase-space density of the beam. When the beam encounters longitudinal collective beam instability, or mis-injection in the rf bucket, or rf voltage and phase modulations, etc., the mismatched phase-space distribution will decohere and result in beam dilution. This process is important to rf capture in low energy synchrotrons during injection. On the other hand, synchrotron tune spread is useful in providing Landau damping for collective beam instabilities.

II.6 Experimental Tracking of Synchrotron Motion

Experimental measurements of synchrotron phase-space coordinates are important in improving the performance of synchrotrons. For example, a phase detector is needed in implementing a phase feedback loop to damp dipole or higher-order synchrotron modes. In this section we discuss the methods of measuring the off-momentum and rf phase coordinates of a beam.

The fractional off-momentum coordinate of a beam can be derived by measuring the closed orbit of transverse displacement Δx_{co} at a high dispersion function location. The off-momentum coordinate is

$$\frac{\Delta p}{p} = \frac{\Delta x_{co}}{D}, \tag{3.86}$$

where D is the horizontal dispersion function. Since synchrotron oscillation is rela-

tively slow in proton synchrotrons, the signal-to-noise ratio can be enhanced by using a low-pass filter at a frequency slightly higher than the synchrotron frequency.

The inset in Fig. 3.4 shows a synchrotron phase space ellipse measured at the IUCF Cooler Ring. The phase coordinate is obtained by a phase detector, and the fractional off-momentum coordinate is obtained from the displacement of the beam centroid measured with a beam position monitor (BPM).

The BPM system had an rms position resolution of about 0.1 mm. By averaging the position measurements the stability of the horizontal closed orbit was measured to be within 0.02 mm. The momentum deviation is related to the off-momentum closed orbit, $\Delta x_{\rm co}$, by $\Delta x_{\rm co} = D\delta$, where $\delta = \Delta p/p_0$ is the fractional momentum deviation, and the horizontal dispersion function D is about 4.0 m at a high-dispersion location. The position signals from the BPM were passed through a 3 kHz low-pass filter before digitization to remove effects due to coherent betatron oscillations and high frequency noise. Since the synchrotron frequency at the IUCF Cooler in this experiment was less than 1 kHz for an rf system with $h = 1$, a 3 kHz low-pass filter could be used to average out betatron oscillations of a few hundred kHz.

The synchrotron phase coordinate can be measured by comparing the bunch arrival time with the rf cavity wave. First, we examine the characteristics of beam current signal from a beam position monitor. We assume that the bunch length is much shorter than the circumference of an accelerator. With the beam bunch approximated by an ideal δ-function pulse, the signal from a beam position monitor (BPM) or a wall gap monitor (WGM)[9] is

$$I(t,\tau) = N_{\rm B} e \sum_{\ell=-\infty}^{\infty} \delta(t+\tau-\ell T_0) = N_{\rm B} e \sum_{n=-\infty}^{\infty} e^{in\omega_0(t+\tau)}, \tag{3.87}$$

where $N_{\rm B}$ is the number of particles in a bunch, T_0 is the revolution period, $\omega_0 = 2\pi/T_0$ is the angular revolution frequency, and $\tau = (\theta - \theta_{\rm s})/\omega_0$ is the arrival time relative to the synchronous particle. Equation (3.87) shows that the periodic delta-function pulse, in time domain, is equivalent to sinusoidal waves at all integer harmonics of the revolution frequency.

To measure the phase coordinate or equivalently the relative arrival time τ, we first select a sinusoidal wave by using the band-pass filter, or we select the fundamental harmonic with a low-pass filter including only the fundamental harmonic. The sinusoidal signal is compared with the rf wave; and the phase between the beam and the reference rf wave can be obtained by using phase detectors.[10] Normally, the

[9] A wall gap monitor consists of a break in the vacuum chamber. The wall current that flows through a resistor, typically about 50 Ohms with a stray capacitance of about 30 pF, can then be measured. The bandwidth is about 100 MHz.

[10] See Roland E. Best, *Phase Locked Loops, Theory, Design, and Applications*, pp. 7-9 (McGraw-Hill, New York, 1984). The type II phase detector utilizes XOR logic, and has a range of ±90°; the type III utilizes the edge triggered JK-master-slave flip-flop circuit, and has a range of ±180°. The

BPM sum signal or the WGM signal can be used to measure the relative phase of the beam.[11] Since the rf frequency was 1.03 MHz for the 45 MeV protons in this measurement at the IUCF Cooler, the BPM signal was passed through a 1.4 MHz low-pass filter to eliminate high harmonics noise before it was compared with an rf signal in a phase detector.

The phase-space map of synchrotron oscillations can be obtained by plotting $\Delta p/p_0$ vs ϕ in each revolution. Since the synchrotron tune of a proton synchrotron is small, the synchrotron motion can be tracked at N revolution intervals, where $N \ll 1/\nu_{\rm s}$. The top inset in Fig. 3.4 shows the Poincaré map of the longitudinal phase space at 10 turn intervals; the bottom inset shows the FFT of the phase data. The resulting synchrotron tune as a function of peak phase amplitude is compared with the theoretical prediction in Fig. 3.4.

Exercise 3.2

1. Write a simple program to calculate $\alpha_{\rm b}(\phi_0)$.

2. This exercise concerns the acceleration of protons in the AGS booster. The injection kinetic energy is 200 MeV from the linac. The circumference of the booster ring is 201.78 m, the transition energy is $\gamma_T = 4.5$, the extraction energy is 1.5 GeV kinetic energy, the acceleration time is 160 ms, and the harmonic number is $h = 3$.

   (a) Find the rf voltage needed for acceleration of a proton bunch in the booster.

   (b) The bunch area is determined by several factors, such as line charge density, microwave instabilities, transition crossing in the AGS, etc. If we need a bunch area of about 1 eV-s per bunch in $(\Delta E/\omega_0, \phi/h)$ phase space, and the bucket area is about 1.2 times as large as the bunch area, what is the minimum rf voltage needed?

   (c) What is the rf frequency swing needed to accelerate protons from 200 MeV to 1.5 GeV?

   (d) How does the rf bucket area change during the acceleration process?

3. For a constant rf voltage and synchronous phase angle, show that the rf bucket area in the $(\Delta E/\omega_0, \phi/h)$ phase space has a minimum at $\gamma = \sqrt{3}\gamma_T$.

4. Particle acceleration at a constant bucket is a possible "rf program" in synchrotrons. Find the relation between rf voltage and beam energy.

5. Verify Eq. (3.76). Rotate the phase-space ellipse of Eq. (3.78) into the upright position, show that the width and height of the bunch change by a factor $e^{\pm\omega_{\rm s}t}$, where t is the time the bunch stays at the UFP, and estimate the time needed to double the bunch height.

type III has a phase error of about ±10° near 0°, but can adequately measure the synchrotron tune. For more accurate measurement of phase amplitude response, the type II can be used. To extend the range of beam phase detection, a type IV phase detector with a range of ±360° can be used.

[11] M. Ellison *et al.*, *Phys. Rev.* **E 50**, 4051 (1994).

6. The anti-protons produced from the Main Injector (Main Ring) pulses have the following characteristics: $p_0 = 8.9$ GeV/c, $\sigma_t = 0.15$ ns, $\sigma_E = 180$ MeV, or $\Delta p/p_0 = \pm 2\%$. The antiprotons are captured in the Debuncher into the 53.1 MHz ($h = 90$) rf bucket with $V = 5$ MV, $\gamma_T = 7.7$, and $R = 83$ m.[12]

   (a) Find the bucket height, synchrotron tune, and synchrotron period of the Debuncher ring for the rf system.

   (b) At 1/4 of the synchrotron period after antiproton injection, the rf voltage is lowered suddenly to match the bunch shape. Show that the final rf voltage V_2 is related to the initial voltage V_1 by

$$\frac{V_2}{V_1} = \left(\frac{\nu_{s1}}{|\eta|}(\omega_0\sigma_{t1})\right)^2 \left(\frac{\sigma_{E1}}{\beta^2 E}\right)^{-2}.$$

   Find the final matched rf voltage for the Debuncher.

   (c) Show that the final energy spread in this debunching process is

$$\sigma_{E2} = \left[\frac{\nu_{s1}}{|\eta|}(\omega_0\sigma_{t1})\right]\beta^2 E.$$

   Find the final energy spread of the antiproton beams.

7. Assuming stationary bucket, fill out the beam properties of the proton synchrotrons in the table below.

P-synchrotron	AGS	RHIC	FNAL-MI	FNAL-BST	Cooler
K.E. [GeV]	25	250	120	8	0.045
V_{rf} [MV]	0.3	0.3	2	0.95	0.0001
h	12	342	588	84	1
γ_T	8.5	24.5	21.8	5.446	4.6
C [m]	807.12	3833.84	3319.4	474.2	86.8
$\mathcal{A}$ [eV-s]	1.5	0.5	0.15	0.15	0.0001
σ_E [MeV]					
σ_t [ns]					

8. Show that the synchrotron tune of a particle with phase amplitude $\hat{\phi}$ in a stationary bucket is

$$Q_s(\hat{\phi}) = \pi\nu_s/2K(\sin\frac{\hat{\phi}}{2}),$$

   where $K(x)$ is the complete elliptical integral of the first kind given in Eq. (3.84).

9. Define $p_\phi = h\omega\eta\delta$, and show that the synchrotron equations of motion become

$$\dot{\phi} = p_\phi, \quad \dot{p}_\phi = \frac{\eta}{|\eta|}\omega_s^2(\sin\phi - \sin\phi_s),$$

[12] See A.V. Tollestrup and G. Dugan, p. 954 in Ref. [13] (1983). Note that 5 MV is the maximum voltage that the Debuncher rf system can deliver.

where $\omega_s = \omega_0\sqrt{h|\eta|eV/2\pi\beta^2 E}$, and the overdot indicates the derivative with respect to time t. The Hamiltonian for a stationary rf system with ϕ_s becomes

$$H = \frac{1}{2}p_\phi^2 + \frac{\eta}{|\eta|}\omega_s^2(\cos\phi - 1).$$

   (a) Using the generating function

$$F_1 = -\frac{\omega_s}{2}\phi^2\tan\psi$$

   show that phase-space coordinates are

$$\phi = \sqrt{2J/\omega_s}\cos\psi, \quad p_\phi = -\sqrt{2J\omega_s}\sin\psi,$$

   where J and ψ are action-angle coordinates. Show that the Hamiltonian below the transition energy becomes

$$H = \omega_s J + \omega_s^2\left[1 - \frac{J}{\omega_s}\cos^2\psi - \cos\left(\sqrt{\frac{2J}{\omega_s}}\cos\psi\right)\right].$$

   (b) Using the phase averaging method, show that the synchrotron tune is approximately given by

$$Q_s(J) = \nu_s\left[\frac{1}{2} + \frac{J_1(w)}{w}\right], \quad w = \sqrt{\frac{2J}{\omega_s}},$$

   where $J_1(w)$ is the Bessel function.

   (c) Compare the accuracy of the above approximated synchrotron tune to that of the exact formula given by Exercise 3.2.8.

10. Let $\hat{\phi}$ be the maximum synchrotron phase amplitude. Show that the maximum off-momentum deviation is

$$\hat{\delta} = \frac{\sqrt{2}Q_s}{h|\eta|}\left[-1 + \frac{\cos\hat{\phi}}{\cos\phi_s} + (\hat{\phi} - \phi_s)\tan\phi_s\right].$$

11. Expanding the phase coordinate around the SFP with $\phi = \phi_s + \varphi$, the synchrotron Hamiltonian becomes

$$H = \frac{1}{2}h\omega_0\eta\delta^2 + \frac{1}{2h\eta}\omega_0 Q_s^2\left[\varphi^2 - \frac{1}{3}\tan\phi_s\,\varphi^3 - \frac{1}{12}\varphi^4 + \cdots\right],$$

   where

$$Q_s = \sqrt{\frac{heV|\eta\cos\phi_s|}{2\pi\beta^2 E}} = \nu_s\sqrt{|\cos\phi_s|}.$$

   For simplicity, we assume $\eta > 0$ in this exercise.

(a) Using the generating function

$$F_1(\phi,\psi) = -\frac{Q_s}{2h\eta}\varphi^2 \tan\psi,$$

show that the phase-space coordinates are related to action angle (J,ψ) by

$$\varphi = \sqrt{2h\eta J/Q_s}\cos\psi, \quad \delta = -\sqrt{2Q_s J/h\eta}\sin\psi,$$

and the Hamiltonian in action-angle coordinates is

$$H = \omega_0 Q_s J - \frac{\omega_0\sqrt{2h\eta Q_s}}{12}\tan\phi_s\, J^{3/2}\left[\cos 3\psi + 3\cos\psi\right] - \frac{\omega_0 h\eta}{6}J^2\cos^4\psi.$$

(b) Using the generating function

$$F_2(\psi, I) = \psi I + G_3(I)\sin 3\psi + G_1(I)\sin\psi,$$

show that terms proportional to $J^{3/2}$ in the Hamiltonian can be canceled if G_3 and G_1 are chosen to be

$$G_3 = \frac{\sqrt{2h\eta}}{36\sqrt{Q_s}}\tan\phi_s\, I^{3/2}, \quad G_1 = \frac{\sqrt{2h\eta}}{4\sqrt{Q_s}}\tan\phi_s\, I^{3/2}.$$

Finding new canonical variables to cancel low-order perturbation terms is called the *canonical perturbation technique.*

(c) Show that the new Hamiltonian is

$$\begin{aligned} H &= \omega_0 Q_s I - \frac{\omega_0 h\eta}{6} I^2\cos^4\psi \\ &\quad - \frac{\omega_0\sqrt{2h\eta Q_s}}{8}\tan\phi_s I^{1/2}[\cos 3\psi + 3\cos\psi][3G_3\cos 3\psi + G_1\cos\psi]. \end{aligned}$$

Now the perturbation in the new action variable is proportional to I^2.

(d) Show that the average Hamiltonian is

$$\langle H\rangle = \omega_0 Q_s I - \frac{\omega_0 h\eta}{16}\left(1 + \frac{5}{3}\tan^2\phi_s\right) I^2 + \cdots.$$

Show that the synchrotron tune for a particle with a synchrotron amplitude $\hat{\varphi}$ is

$$\tilde{Q}(\hat{\varphi}) = Q_s\left[1 - \frac{1}{16}\left(1 + \frac{5}{3}\tan^2\phi_s\right)\hat{\varphi}^2\right],$$

where $\hat{\varphi}$ is the maximum synchrotron amplitude in the quasi-harmonic approximation. Compare your result with that of Eq. (3.85) for $\phi_s = 0$.

12. The natural rms fractional momentum spread of electron beams in a storage ring is $\sigma_E/E = \sqrt{C_q\gamma^2/\mathcal{J}_E\rho}$, where $C_q = 3.83\times 10^{-13}$ m, ρ is the bending radius, and $\mathcal{J}_E \approx 2$ is the damping partition. In the NLC damping ring (DR) parameter list shown in Exercise 3.1.3, the rms fractional momentum spread of the electron beam is $\sigma_\delta = 0.000813$. Find the bunch length and rms phase-space area in eV-s.

13. The equilibrium distribution in linearized synchrotron phase space is a function of the invariant ellipse given by Eq. (3.61), where $\hat{\theta} = |\eta|\hat{\delta}/\nu_s$. When a mismatched Gaussian beam

$$\rho(\delta,\theta) = \frac{N_B e}{2\pi\sigma_\delta\sigma_\theta}\exp\left\{-\frac{1}{2}\left[\frac{\theta^2}{\sigma_\theta{}^2} + \frac{\delta^2}{\sigma_\delta{}^2}\right]\right\}$$

is injected into the synchrotron at time $t = 0$, what is the time evolution of the beam? Here σ_θ and σ_δ are respectively the initial rms bunch angular width and fractional momentum spread, and the mismatch condition for the linearized synchrotron motion is given by $\sigma_\theta \neq |\eta|\sigma_\delta/\nu_s$.

(a) Show that the projection of the beam distribution function onto the θ axis is[13]

$$\rho(\theta,t) = \frac{N_B e}{\sqrt{2\pi}\tilde{\sigma}}e^{-\theta^2/2\tilde{\sigma}^2} \qquad \tilde{\sigma}^2 = \sigma_\theta^2\cos^2\omega_s t + (|\eta|\sigma_\delta/\nu_s)^2\sin^2\omega_s t.$$

Show that the peak current is $\hat{I}(t) = N_B e\omega_0/\sqrt{2\pi}\tilde{\sigma}$.

(b) For a weakly mismatched beam, show that

$$\sigma_\theta^2 \approx \sigma_0^2(1 - \Delta V/2V), \quad (\eta\sigma_\delta/\nu_s)^2 \approx \sigma_0^2(1 + \Delta V/2V),$$

where $\sigma_0 = \sqrt{\sigma_\theta^2 + (\eta\sigma_\delta/\nu_s)^2}$ is the matched rms beam width, ΔV is the mismatched voltage, and V is the voltage for the matched beam profile. Show that the peak current for the weakly mismatched beam is

$$\hat{I}(t) \approx \frac{N_B e\omega_0}{\sqrt{2\pi\sigma_0^2}}\left(1 - \frac{\Delta V}{4V}\cos 2\omega_s t\right).$$

Discuss your result. Because the bunch tumbles at twice the synchrotron frequency, the resulting coherent beam motion is called the quadrupole synchrotron mode. The nonlinear synchrotron tune will cause the mismatched injection to filament and the resulting phase-space area will be larger.

[13] Transform the (θ,δ) coordinate system into the normalized coordinate system ($x = \theta$ and $p = |\eta|\delta/\nu_s$), where the matched beam profile is a circle. Make coordinate transformation into the synchrotron rotating frame. The beam profile in the x plane is equal to $\rho(x) = \int\rho(x,p)dp$.

III RF Phase and Voltage Modulations

Particle motion in accelerators experiences perturbations from rf phase and amplitude noise, power supply ripple, wakefields, etc. These perturbation sources cause rf phase or voltage modulations. In general, the frequency spectrum of rf noise may contain high frequency arising from random thermal (white) noise, low frequency from power supply ripple and ground motion, and medium frequency from mechanical vibration etc. In this section, we study the effects of a single frequency sinusoidal rf phase and voltage modulation on particle motion and beam distribution. The understanding of the beam response to a single frequency modulation can be applied to the analysis of more complicated situations.

III.1 Normalized Phase-Space Coordinates

Using normalized momentum deviation coordinate $\mathcal{P} = -(h|\eta|/\nu_s)(\Delta p/p)$, the Hamiltonian for a stationary synchrotron motion is

$$H_0 = \frac{1}{2}\nu_s \mathcal{P}^2 + 2\nu_s \sin^2\frac{\phi}{2}, \tag{3.88}$$

where $\nu_s = \sqrt{h|\eta|eV/2\pi\beta^2 E}$ is the synchrotron tune at $|\cos\phi_s| = 1$, the orbital angle θ is the independent variable, and $(\phi, \mathcal{P})$ are normalized conjugate phase-space coordinates. The Hamiltonian has fixed points at

$$(\phi, \mathcal{P})_{\text{SFP}} = (0, 0) \quad \text{and} \quad (\phi, \mathcal{P})_{\text{UFP}} = (\pi, 0).$$

The synchrotron Hamiltonian is autonomous (time independent), and thus the Hamiltonian value is a constant of motion.

Expressing the synchrotron coordinates in parameters k and w as

$$\sin\frac{\phi}{2} = k\sin w, \quad \frac{\mathcal{P}}{2} = k\cos w, \tag{3.89}$$

we obtain $H_0 = 2\nu_s k^2$, where $k = 0$ corresponds to the SFP and $k = 1$ corresponds to the separatrix orbit that passes through the UFP. The action is

$$J = \frac{1}{2\pi}\oint \mathcal{P} d\phi = \frac{8}{\pi}\left[E(k) - (1-k^2)K(k)\right], \tag{3.90}$$

where the complete elliptical function integrals are [25]

$$E(k) = \int_0^{\pi/2} \sqrt{1 - k^2\sin^2 w}\, dw, \quad K(k) = \int_0^{\pi/2} \frac{1}{\sqrt{1-k^2\sin^2 w}}\, dw.$$

In the normalized phase-space coordinates, the maximum action ($k = 1$) is $J_{\max} = 8/\pi$, and the maximum bucket area is $\mathcal{A} = 2\pi J_{\max} = 16$ (see Table 3.2).

For synchrotron motion with a small action, the power series expansions of elliptical integrals are

$$\begin{aligned} K(k) &= \frac{\pi}{2}\left[1 + (\tfrac{1}{2})^2 k^2 + (\tfrac{1\cdot 3}{2\cdot 4})^2 k^4 + (\tfrac{1\cdot 3\cdot 5}{2\cdot 4\cdot 6})^2 k^6 + \cdots\right], \\ E(k) &= \frac{\pi}{2}\left[1 - (\tfrac{1}{2})^2 \frac{k^2}{1} - (\tfrac{1\cdot 3}{2\cdot 4})^2 \frac{k^4}{3} - (\tfrac{1\cdot 3\cdot 5}{2\cdot 4\cdot 6})^2 \frac{k^6}{5} - \cdots\right]. \end{aligned}$$

Thus the action is related to the parameter k by

$$J = 2k^2\left(1 + \frac{1}{8}k^2 + \frac{3}{64}k^4 + \cdots\right), \tag{3.91}$$

$$2k^2 = J\left(1 - \frac{1}{16}J - \frac{1}{256}J^2 - \cdots\right). \tag{3.92}$$

In terms of the action, the Hamiltonian is $H_0(J)$. The *synchrotron tune* becomes

$$\tilde{Q}_s(J) = \frac{\partial H_0}{\partial J} = \frac{\pi\nu_s}{2K(k)} = \nu_s\left(1 - \frac{J}{8} - \frac{3J^2}{256} - \cdots\right), \tag{3.93}$$

where we have used the identities

$$2k^2\frac{dE(k)}{dk^2} = E(k) - K(k), \quad 2k^2\frac{dK(k)}{dk^2} = \frac{1}{1-k^2}E(k) - K(k).$$

Using the generating function

$$F_2(\phi, J) = \int_0^{\phi} \mathcal{P}(\tilde{\phi})\, d\tilde{\phi}, \tag{3.94}$$

we obtain the angle coordinate

$$\psi = \frac{\partial F_2}{\partial J} = \frac{\tilde{Q}_s(J)}{\nu_s}\int_0^{\phi} \frac{d\tilde{\phi}}{\mathcal{P}(\tilde{\phi})}. \tag{3.95}$$

The angle variable ψ, which is conjugate to the action J, can be obtained simply by integrating Eq. (3.93), i.e.

$$\psi = \frac{\pi\nu_s}{2K}\theta + \psi_0. \tag{3.96}$$

The next task is to express the normalized off-momentum coordinate $\mathcal{P}$, and the synchrotron phase coordinate ϕ, in Fourier harmonics of the conjugate angle parameter ψ. First, using Hamilton's equation $\dot{\phi} = \nu_s\mathcal{P}$, we can relate the orbital angle θ to the w parameter of Eq. (3.89) as

$$\nu_s(\theta - \theta_0) = \int_{\phi_0}^{\phi} \frac{d\phi}{\mathcal{P}} = u - u_0,$$

where

$$u = \int_0^w \frac{1}{\sqrt{1-k^2\sin^2 w}}\,dw, \quad u_0 = \int_0^{w_0} \frac{1}{\sqrt{1-k^2\sin^2 w}}\,dw.$$

The Jacobian elliptical functions, cn and sn, are then defined as

$$\sin w = \mathrm{sn}(u|k), \quad \cos w = \mathrm{cn}(u|k), \tag{3.97}$$

and the synchrotron phase-space coordinates are related to the Jacobian elliptical function by

$$\mathcal{P} = 2k\ \mathrm{cn}(u|k), \quad \sin\frac{\phi}{2} = k\ \mathrm{sn}(u|k). \tag{3.98}$$

Thus the expansion of $\mathcal{P}$ and $\sin(\phi/2)$ in Fourier harmonics of ψ is equivalent to the expansion of $\mathrm{cn}(u|k)$ and $\mathrm{sn}(u|k)$ in $\psi = \pi u/2K$. This can be achieved by using Eq. (16.23.2) in Ref. [25], i.e.

$$\begin{aligned}\mathcal{P} &= 2k\mathrm{cn}(u|k) = \frac{4\pi\sqrt{k}}{K(k)}\sum_0^\infty \frac{q^{n+1/2}}{1+q^{2n+1}}\cos(2n+1)\psi \\ &\approx (2J)^{1/2}\cos\psi + \frac{(2J)^{3/2}}{64}\cos 3\psi + \frac{(2J)^{5/2}}{4096}\cos 5\psi + \cdots,\end{aligned} \tag{3.99}$$

where ψ is the synchrotron phase with the q parameter given by

$$q = e^{-\pi K'/K} = \frac{k^2}{16} + 8(\frac{k^2}{16})^2 + 84(\frac{k^2}{16})^3 + 992(\frac{k^2}{16})^4 + \cdots,$$

with $K' = K(\sqrt{1-k^2})$. Similarly, using the identity $k^2\mathrm{sn}^2(u|k) = 1 - \mathrm{dn}^2(u|k)$, we obtain

$$2\sin^2\frac{\phi}{2} = \sum_{n=-\infty}^{\infty} G_n(J)e^{jn\psi} \approx -\frac{J}{2}\cos 2\psi - \frac{J^2}{32}\cos 4\psi + \cdots, \tag{3.100}$$

$$G_n(J) = \frac{1}{2\pi}\int_0^{2\pi}(1-\cos\phi)e^{-jn\psi}d\psi, \tag{3.101}$$

where $G_{-n} = G_n^*$. Because $1-\cos\phi$ is an even function, $G_n = 0$ for odd n. The expansion of normalized coordinates in action-angle variables is useful for evaluating the effect of perturbation on synchrotron motion, discussed below.

Sum rule theorem

The solutions of many dynamical systems can be obtained by expanding the perturbation potential in action angle variables. For the case of rf phase modulation, the expansion of the normalized off-momentum coordinate is

$$\mathcal{P} = \sum_{n=-\infty}^{\infty} f_n(J)e^{in\psi}, \tag{3.102}$$

where $f_{-n} = f_n^*$ and, from Eq. (3.99), the strength functions f_n are

$$f_{2m+1} = \frac{2\pi\sqrt{k}q^{m+1/2}}{K(k)(1+q^{2m+1})}, \quad f_{2m} = 0.$$

Because $\mathcal{P}$ is an odd function, only odd harmonics exist. Furthermore, the sum of all strength functions is (see Exercise 3.3.2)

$$\sum_{n=-\infty}^{\infty}|f_n|^2 = \frac{\tilde{Q}_s(J)}{\nu_s}J. \tag{3.103}$$

We observe that the strength functions are zero at the center of the rf bucket where $J = 0$ and at the separatrix where $\tilde{Q}_s(J_{sx}) = 0$.

III.2 RF Phase Modulation and Parametric Resonances

If the phase of the rf wave changes by an amount $\varphi(\theta)$, where $\theta = \omega_0 t$ is the orbiting angle serving as time coordinate, the synchrotron mapping equation is

$$\phi_{n+1} = \phi_n + 2\pi h\eta\delta_n + \Delta\varphi(\theta), \tag{3.104}$$

$$\delta_{n+1} = \delta_n + \frac{eV}{\beta^2 E}(\sin\phi_{n+1} - \sin\phi_s), \tag{3.105}$$

where $\Delta\varphi(\theta) = \varphi(\theta_n + 2\pi) - \varphi(\theta_n)$ is the difference in rf phase error between successive turns in the accelerator. In this section, we consider only a sinusoidal rf phase modulation with[14]

$$\varphi = a\sin(\nu_m\theta + \chi_0),$$

where ν_m is the modulation tune, a is the modulation amplitude, and χ_0 is an arbitrary phase factor. The resulting rf phase difference in every revolution is $\Delta\varphi = 2\pi\nu_m a\cos(\nu_m\theta + \chi_0)$.

For simplicity, we consider the case of a stationary bucket with $\phi_s = 0$ for $\eta < 0$. Using the normalized off-momentum coordinate $\mathcal{P} = -(h|\eta|/\nu_s)\delta$, we obtain the perturbed Hamiltonian

$$H = H_0 + H_1 = \frac{1}{2}\nu_s\mathcal{P}^2 + 2\nu_s\sin^2\frac{\phi}{2} + \nu_m a\mathcal{P}\cos(\nu_m\theta + \chi_0), \tag{3.106}$$

where the perturbation potential of rf phase modulation is

$$H_1 = \nu_m a\mathcal{P}\cos(\nu_m\theta + \chi_0). \tag{3.107}$$

[14] M. Ellison *et al.*, *Phys. Rev. Lett.* **70**, 591 (1993); M. Syphers *et al.*, *Phys. Rev. Lett.* **71**, 719 (1993); H. Huang *et al.*, *Phys. Rev.* E **48**, 4678 (1993); Y. Wang *et al.*, *Phys. Rev.* E **49**, 1610 (1994).

Expressing the phase-space coordinate $\mathcal{P}$ in action-angle coordinates with Eq. (3.99), we can expand the perturbation in action-angle variables

$$\begin{aligned} H_1 &= \nu_m a\sqrt{J/2}\,[\cos(\psi+\nu_m\theta+\chi_0)+\cos(\psi-\nu_m\theta-\chi_0)] \\ &\quad +\nu_m a\frac{(2J)^{3/2}}{128}[\cos(3\psi+\nu_m\theta+\chi_0)+\cos(3\psi-\nu_m\theta-\chi_0)]+\ldots, \end{aligned} \tag{3.108}$$

where J and ψ are conjugate action-angle variables. The rf phase error generates only odd order parametric resonances because $\mathcal{P}$ is an odd function. However, two nearby strong parametric resonances can drive secondary and tertiary resonances. For example, the 1:1 and 3:1 parametric resonances driving by a strong phase modulation can produce a secondary 4:2 resonance at $\nu_m \approx 2\nu_s$. In the following, we discuss only the primary parametric resonances, particularly the 1:1 dipole mode.

A. Effective Hamiltonian near a parametric resonance

When the modulation tune is near an odd multiple of synchrotron sideband, i.e. $\nu_m = (2m+1)\nu_s$, stationary phase condition exists for a parametric resonance term. We neglect all non-resonance terms in H_1 to obtain an approximate synchrotron Hamiltonian

$$H \approx \nu_s J - \frac{1}{16}\nu_s J^2 + \nu_m f_{2m+1} J^{m+1/2}\cos\left((2m+1)\psi-\nu_m\theta-\chi_0\right), \tag{3.109}$$

where $f_1 = a/\sqrt{2}$, $f_3 = a/32\sqrt{2}$, etc. The effect of rf phase modulation on phase-space distortion can be solved by using the effective parametric resonance Hamiltonian, that resembles the Hamiltonian for 1-D betatron resonances discussed in Sec. VII, Chap. 2. This primary parametric resonance is called $(2m+1)$:1 resonance. In this section, we consider only the dominant dipole mode below.

B. Dipole mode

If the phase modulation amplitude is small, the dominant contribution arises from the $m=0$ sideband. Near the first-order synchrotron sideband with $\nu_m \approx \nu_s$, the Hamiltonian for the dipole mode is

$$H \approx \nu_s J - \frac{1}{16}\nu_s J^2 + \frac{\nu_s a}{\sqrt{2}}J^{1/2}\cos(\psi-\nu_m\theta-\chi_0). \tag{3.110}$$

The Hamiltonian can be transformed into the resonance rotating frame by using the generating function

$$F_2(\psi, I) = (\psi-\nu_m\theta-\chi_0-\pi)\,I. \tag{3.111}$$

The new phase-space coordinates become

$$\chi = \psi-\nu_m\theta-\chi_0-\pi, \quad I = J; \tag{3.112}$$

and the new Hamiltonian is

$$\tilde{H} = (\nu_s-\nu_m)I - \frac{1}{16}\nu_s I^2 - \nu_s\frac{a}{\sqrt{2}}I^{1/2}\cos\chi. \tag{3.113}$$

Since the new Hamiltonian is time independent in the resonance rotating frame, a torus of particle motion will follow a constant Hamiltonian contour, where Hamilton's equations of motion are

$$\dot{\chi} = \nu_s-\nu_m-\frac{1}{8}\nu_s I - \nu_s\frac{a}{2\sqrt{2I}}\cos\chi, \qquad \dot{I} = -\nu_s\frac{a}{2}\sqrt{2I}\sin\chi. \tag{3.114}$$

The fixed points of the Hamiltonian, which characterize the structure of resonant islands, are given by the solution of $\dot{I}=0$, $\dot{\chi}=0$. Using $g=\sqrt{2J}\cos\chi$, with $\chi=0$ or π, to represent the phase coordinate of a fixed point, we obtain the equation for g as

$$g^3 - 16\left(1-\frac{\nu_m}{\nu_s}\right)g + 8a = 0. \tag{3.115}$$

When the modulation tune is below the *bifurcation tune* ν_{bif} given by[15]

$$\nu_{bif} = \nu_s\left[1-\frac{3}{16}(4a)^{2/3}\right], \tag{3.116}$$

Eq. (3.115) has three solutions:

$$\begin{cases} g_a(x) = -\dfrac{8}{\sqrt{3}}x^{1/2}\cos\dfrac{\xi}{3}, & (\psi=\pi) \\ g_b(x) = \dfrac{8}{\sqrt{3}}x^{1/2}\sin(\dfrac{\pi}{6}-\dfrac{\xi}{3}), & (\psi=0) \\ g_c(x) = \dfrac{8}{\sqrt{3}}x^{1/2}\sin(\dfrac{\pi}{6}+\dfrac{\xi}{3}), & (\psi=0) \end{cases} \tag{3.117}$$

where

$$x = 1-\nu_m/\nu_s, \quad x_{bif} = 1-\nu_{bif}/\nu_s, \quad \xi = \arctan\sqrt{\left(\frac{x}{x_{bif}}\right)^3-1}, \quad x_{bif} = \frac{3}{16}(4a)^{2/3}.$$

Here g_a and g_b are respectively the outer and the inner stable fixed points (SFPs) and g_c is the unstable fixed point (UFP). The reason that g_a and g_b are SFPs and g_c is the UFP will be discussed shortly. Particle motion in the phase space can be described by tori of constant Hamiltonian around SFPs. The lambda-shaped phase amplitudes of the SFPs ($|g_a|$ and $|g_b|$, solid lines) and UFP ($|g_c|$, dashed line) shown in the left plot of Fig. 3.5 vs the modulation frequency is a characteristic property of the dipole mode excitation with nonlinear detuning. In the limit $\nu_m \ll \nu_{bif}$, we have $\xi \to \pi/2$, thus $g_a \to -4x^{1/2}$, $g_c \to 4x^{1/2}$, and $g_b \to 0$.

[15] Find the root of the discriminant of the cubic equation (3.115).

The Hamiltonian tori in phase space coordinates $\mathcal{P} = -\sqrt{2I}\sin\chi$ vs $X = \sqrt{2I}\cos\chi$ are shown in the right plot of Fig. 3.5. The actual Hamiltonian tori rotate about the center of the phase space at the modulation tune $\nu_{\rm m}$, i.e. the phase space ellipses return to this structure in $1/\nu_{\rm m}$ revolutions.

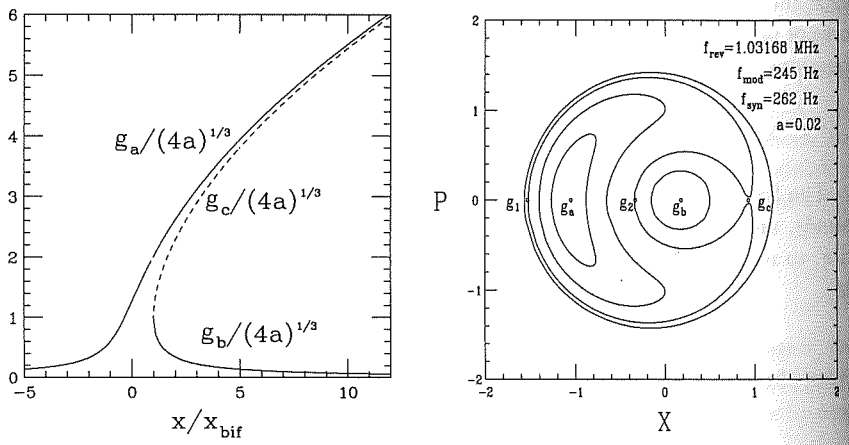

Figure 3.5: Left plot: fixed point amplitudes $|g_a|$, $|g_b|$, and $|g_c|$ (in unit of $(4a)^{1/3}$); and right plot: Poincaré surfaces of section for $f_{\rm m} = 245$ Hz and $f_{\rm s} = 262$ Hz at $a = 0.02$. The stable fixed points are g_a and g_b, and the unstable fixed point is g_c. The torus passing through the UFP is the separatrix, which separates the phase space into two stable islands. The intercept of the the separatrix with the phase axis is denoted by g_1 and g_2.

When the modulation frequency approaches the bifurcation frequency from below, the UFP and the outer SFP move in and the inner SFP moves out. At the bifurcation frequency, where $x = x_{\rm bif}$ and $\xi = 0$, the UFP collides with the inner SFP with $g_b = g_c = (4a)^{1/3}$; and they disappear together. Beyond the bifurcation frequency, $\nu_{\rm m} > \nu_{\rm bif}$ ($x < x_{\rm bif}$), there is only one real solution to Eq. (3.115):

$$g_a(x) = -(4a)^{1/3}\left[\left(\sqrt{1-\left(\frac{x}{x_{\rm bif}}\right)^3}+1\right)^{1/3} - \left(\sqrt{1-\left(\frac{x}{x_{\rm bif}}\right)^3}-1\right)^{1/3}\right]. \tag{3.118}$$

In particular, $g_a = -(8a)^{1/3}$ at $x = 0$ ($\nu_{\rm m} = \nu_{\rm s}$), and $g_a = -2(4a)^{1/3}$ at $x = x_{\rm bif}$. The characteristics of bifurcation appear in all orders of resonances with nonlinear detuning. As the modulation tune approaches the bifurcation tune, resonance islands can be created or annihilated.

C. Island tune

Let y, p_y be the local coordinates about a fixed point of the Hamiltonian, i.e.

$$y = \sqrt{2I}\cos\chi - g, \qquad p_y = -\sqrt{2I}\sin\chi, \tag{3.119}$$

where g is a fixed point of the Hamiltonian. With a local coordinate expansion, the Hamiltonian (3.113) becomes

$$H_{\rm island} = \frac{\nu_{\rm s}a}{4g}\left(1-\frac{g^3}{4a}\right)y^2 + \frac{\nu_{\rm s}a}{4g}p_y^2 + \cdots. \tag{3.120}$$

Therefore the fixed point g is a stable fixed point if $(1 - g^3/4a) \geq 0$. Because $g_a^3/4a \leq 0$ and $0 \leq g_b^3/4a \leq 1$, g_a and g_b are SFPs. Since $g_c^3/4a \geq 1$, g_c is the UFP. The equilibrium beam distribution (see Appendix A, Sec. II.4), which satisfies the Fokker-Planck-Vlasov equation, is generally a function of the local Hamiltonian, Eq. (3.120) can also provide information on the local distortion of the bunch profile.

The island tune for the small-amplitude oscillations is

$$\nu_{\rm island} = \left|\nu_{\rm s}\left(1-\frac{g^2}{16}\right) - \nu_{\rm m}\right|\left(1-\frac{g^3}{4a}\right)^{1/2}. \tag{3.121}$$

The island tune around the inner SFP given by g_b at $\nu_{\rm m} \ll \nu_{\rm bif}$ is approximately given by $\nu_{\rm island} \approx |\nu_{\rm s}(1-\frac{1}{16}g^2)-\nu_{\rm m}|$. This means that the solution of the equations of motion can be approximated by a linear combination of the solution of the homogeneous equation with tune $\nu_{\rm s}(1-\frac{1}{16}g^2)$ and the particular solution with tune $\nu_{\rm m}$.[16] Thus *the island tune is the beat frequency between these two solutions.* When the modulation tune $\nu_{\rm m}$ approaches $\nu_{\rm bif}$, with $(1-g_b^3/4a)^{1/2} \to 0$, the island tune for small-amplitude oscillation about the inner SFP approaches 0 and the small-amplitude island tune for the outer SFP at $\nu_{\rm m} = \nu_{\rm bif}$ is $\nu_{\rm island} = 3|\nu_{\rm s}(1-\frac{1}{16}g^2) - \nu_{\rm m}|$. In this region of the modulation frequency, the linear superposition principle fails. When the modulation frequency becomes larger than the bifurcation frequency so that $[1-(g^3/4a)]^{1/2} \to 1$, we obtain again $\nu_{\rm island} = |\nu_{\rm s}(1-\frac{1}{16}g^2) - \nu_{\rm m}|$, and the linear superposition principle is again applicable. The island tune for large-amplitude motion about a SFP can be obtained by integrating the equation of motion along the corresponding torus of the Hamiltonian in Eq. (3.113).

D. Separatrix of resonant islands

The Hamiltonian torus that passes through the UFP is the separatrix. With the UFP g_c substitutes into the Hamiltonian (3.113), the separatrix torus is

$$H(J,\psi) = \nu_{\rm s}\left[\frac{1}{2}xg_c^2 - \frac{1}{64}g_c^4 - \frac{1}{2}ag_c\right], \tag{3.122}$$

where $x = 1 - \nu_{\rm m}/\nu_{\rm s}$. The separatrix orbit intersects the phase axis at g_1 and g_2. These intercepts, shown in Figs. 3.5 and 3.6, are useful in determining the maximum

[16] M. Ellison *et al.*, *Phys. Rev. Lett.* **70**, 591 (1993).

phase amplitude of synchrotron motion with external phase modulation. With the notation $h_i = g_i/(4a)^{1/3}$, the intercepts of the separatrix are

$$h_1 = -h_c - \frac{2}{\sqrt{h_c}}, \quad h_2 = -h_c + \frac{2}{\sqrt{h_c}}.$$

The intercepts of the separatrix with the phase axis, h_1 and h_2, and the fixed points, h_a, h_b and h_c are shown in 3.6.

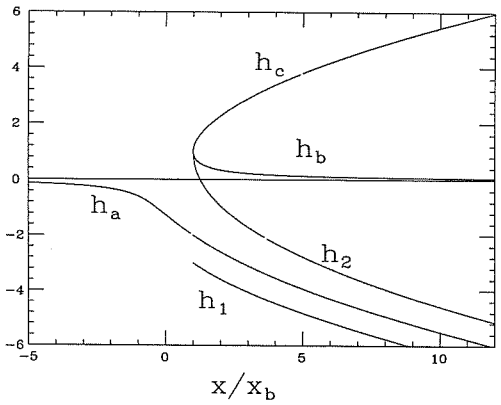

Figure 3.6: The fixed points in units of $(4a)^{1/3}$ are plotted as a function of the modulation frequency in $x/x_{\rm bif}$, where $x = 1 - \nu_{\rm m}/\nu_{\rm s}$ and $x_{\rm bif} = \frac{3}{16}(4a)^{2/3}$ with a as the amplitude of the phase modulation. The SFPs are $h_a = g_a/(4a)^{1/3}$ and $h_b = g_b/(4a)^{1/3}$ and the UFP is $h_c = g_c/(4a)^{1/3}$. The intercepts of the separatrix with the phase axis are shown as $h_1 = g_1/(4a)^{1/3}$ and $h_2 = g_2/(4a)^{1/3}$.

E. The torus passing through the origin

For a beam with small bunch area, all particles can be approximately described as having initial phase-space coordinates at the origin. The Hamiltonian torus passing through the origin, called the torus-O, satisfies the equation $H(J,\psi) = 0$. The intercepts $\phi_{\rm o}$ of the torus-O with the phase axis are then

$$\phi_{\rm o}(\phi_{\rm o}^3 - 32x\phi_{\rm o} + 32a) = 0, \tag{3.123}$$

where $x = 1 - (\nu_{\rm m}/\nu_{\rm s})$. When $x \geq x_{\rm o} = 2^{1/3}x_{\rm bif}$, or $\nu_{\rm m} \leq \nu_{\rm o} = \nu_{\rm s}(1 - 2^{1/3}x_{\rm bif})$, there are three solutions to Eq. (3.123) besides the solution $\phi_{\rm o} = 0$. This means that there are two non-intersecting tori with the same zero Hamiltonian value. One of the tori orbits about the inner SFP, which is the torus-O, and other tori orbit about the outer SFP.

At $x = x_{\rm o}$, two solutions of Eq. (3.123) become degenerate. This means that the torus-O is also the separatrix of islands. When the separatrix passes through the origin, the phase axis intercept of Eq. (3.123) is

$$\hat{\phi}_{\rm o}(x_{\rm o}) = -2^{5/3}(4a)^{1/3}. \tag{3.124}$$

At a higher modulation frequency with $x < x_{\rm o}$, there is only one real root to Eq. (3.123) besides $\phi_{\rm o} = 0$. The torus-O orbits around the outer SFP. The intercept is then

$$\hat{\phi}_{\rm o}(x) = -(16a)^{1/3}\left\{\left[\left(1 - \frac{x^3}{2x_{\rm bif}^3}\right)^{1/2} + 1\right]^{1/3} - \left[\left(1 - \frac{x^3}{2x_{\rm bif}^3}\right)^{1/2} - 1\right]^{1/3}\right\}. \tag{3.125}$$

III.3 Measurements of Synchrotron Phase Modulation

Here we discuss an example of experimental measurements of rf phase modulation at the IUCF Cooler. The experimental procedure started with a single bunch of about 3×10^8 protons with kinetic energy 45 MeV. The corresponding revolution period was 969 ns with an rf frequency of 1.03148 MHz. The cycle time was 10 s. The injected beam was electron-cooled for about 3 s. The full width at half maximum bunch length was about 5.4 m (or 60 ns). The low-frequency rf system of the IUCF Cooler at $h = 1$ was used in this experiment.

For the longitudinal rf phase shift, the beam was kicked longitudinally by a phase shifter and the data acquisition system was started 2000 turns before the phase kick. The principle of the phase shifter used is as follows. The rf signal from an rf source is split into a 90° phase shifted channel and a non-phase shifted channel. A separate function generator produces two modulating voltages, each proportional to the sine and cosine of the intended phase shift $\varphi_{\rm mod}$. As a result of the amplitude modulation, the two rf channels are multiplied by $\sin\varphi_{\rm mod}$ and $\cos\varphi_{\rm mod}$ respectively. These two modulated signals were added, using an rf power combiner, resulting in an rf phase shift $\varphi_{\rm mod}$ in the rf wave. The control voltage versus actual phase shift linearity was experimentally calibrated. Both the phase error due to control nonlinearity and the parasitic amplitude modulation of the IUCF Cooler rf systems were controlled to less than 10%.

The phase lock feedback loop was switched off in our experiment. The response time of the step phase shift was limited primarily by the inertia of the resonant cavity. At 1 MHz, the quality factor Q of the rf cavity was about 40, resulting in a half-power bandwidth of about 25 kHz. The corresponding response time for a step rf phase shift was about 40~50 revolutions. In this experiment, the synchrotron oscillation frequency was chosen to be about 540 Hz, or about 1910 revolutions (turns) in the accelerator. Measurements of subsequent beam-centroid displacements have been discussed in Chap. 3, Sec. II.6.

A. Sinusoidal rf phase modulation

When the bunch, initially at $\phi_i = 0$, $\delta_i = 0$, experiences the rf phase sinusoidal modulation with $\varphi_{\rm mod} = a\sin\nu_{\rm m}\theta$, where $\nu_{\rm m}$ is the modulation tune and a the modulation

amplitude with $a \ll 1$. The synchrotron motion, in terms of a differential equation, is

$$\dot{\phi} = h\eta\delta + \nu_{\rm m} a \cos \nu_{\rm m}\theta, \quad \dot{\delta} = \frac{eV}{2\pi\beta^2 E}\sin\phi - \lambda\delta, \tag{3.126}$$

where ϕ is the particle phase angle relative to the modulated rf phase, the overdot indicates the derivative with respect to the variable θ, and λ is the damping decrement due to electron cooling. Thus the synchrotron equation of motion becomes

$$\ddot{\phi} + \frac{2\alpha}{\omega_0}\dot{\phi} + \nu_{\rm s}^2 \sin\phi = -a\nu_{\rm m}^2 \sin\nu_{\rm m}\theta + \frac{2\alpha}{\omega_0}\nu_{\rm m} a \cos\nu_{\rm m}\theta. \tag{3.127}$$

The measured damping coefficient α at the IUCF Cooler was $\alpha = \omega_0\lambda/4\pi \approx 3 \pm 1$ s^{-1}. Since the measurement time was typically within 150 ms after the phase kick or the start of rf phase modulation, the effect of electron cooling was not important in these measurements.

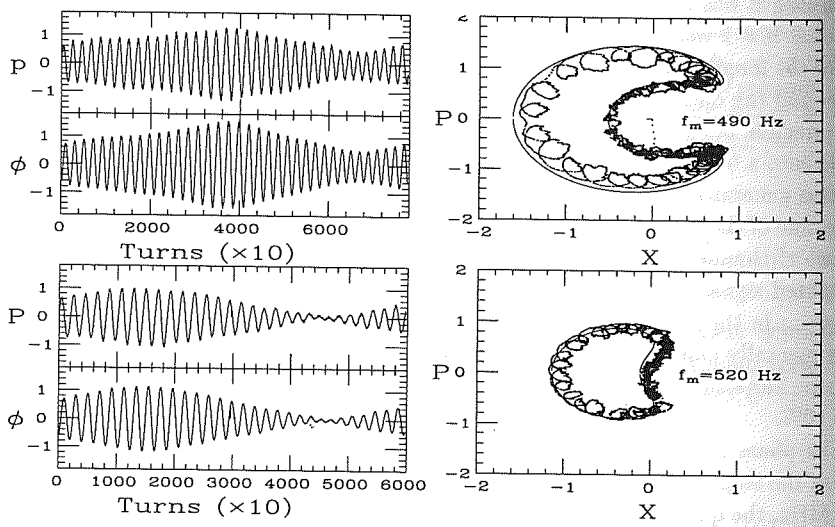

Figure 3.7: The left plots show the normalized off-momentum coordinate $\mathcal{P}$ and the phase ϕ as functions of revolutions at 10-turn intervals. The corresponding Poincaré surfaces of section are shown in the right plots. The upper and lower plots correspond to $f_{\rm m} = 490$ and 520 Hz respectively. The modulation amplitude was $a = 1.45°$, and the initial phase kick amplitude was 45°. The solid line shows the Hamiltonian torus of Eq. (3.110).

The subsequent beam centroid phase-space coordinates are tracked at 10 revolution intervals. The left plots of Fig. 3.7 show examples of measured ϕ and $\mathcal{P} = \frac{h\eta}{\nu_{\rm s}}\frac{\Delta p}{p}$ vs turn number at 10-turn intervals for an rf phase modulation amplitude of 1.45° after an initial phase kick of 42° at modulation frequencies of 490 Hz (upper) and 520

Hz (lower). The resulting response can be characterized by the beating amplitude and period. The beating period is equal to $T_0/\nu_{\rm island}$, where T_0 is the revolution period and $\nu_{\rm island}$ is the island tune, and the beating amplitude is equal to the maximum intercept of Poincaré surface of section with the phase axis.

B. Action angle derived from measurements

For small-amplitude synchrotron motion, Eq. (3.71) can be used to deduce the action and angle variables, i.e.[17]

$$J = \frac{1}{2}(\phi^2 + \mathcal{P}^2), \qquad \tan\psi = -\frac{\mathcal{P}}{\phi} \tag{3.128}$$

in the $(\phi, \mathcal{P})$ phase space.

For large-amplitude synchrotron motion, we need to use the following procedure to deduce the action-angle variables from the measured synchrotron phase-space coordinates. This procedure can improve the accuracy of data analysis.

1. The k value at the phase-space coordinates $(\phi, \mathcal{P})$ is

$$k^2 = \frac{\mathcal{P}^2}{4} + \sin^2\frac{\phi}{2}. \tag{3.129}$$

The action can be obtained from Eq. (3.90) or Eq. (3.91).

2. The synchrotron phase, ψ, can be obtained from the expansion

$$\frac{\mathcal{P}}{2\sin\frac{\phi}{2}} = \frac{\pi}{2K}\tan(\frac{\pi}{2} - \psi) - \frac{2\pi}{K}\sum_{n=1}^{\infty}\frac{q^{2n}}{1+q^{2n}}\sin 2n\psi. \tag{3.130}$$

For synchrotron motion with relatively large k, a better approximation for data analysis can be obtained through the polynomial approximation of Eqs. (17.3.34) and (17.3.36) of Ref. [25] to evaluate $K(k), E(k)$ and q functions in order to obtain the action J and ψ. For each data point $(\phi, \mathcal{P})$, Eq. (3.129) is used to calculate k, and finally, the action J is obtained from Eq. (3.90). The corresponding angle variable ψ is obtained from Eq. (3.130).

C. Poincaré surface of section

The Poincaré map in the resonance frame is then formed by phase-space points in

$$(\sqrt{2J}\cos(\psi - \nu_{\rm m}\theta), -\sqrt{2J}\sin(\psi - \nu_{\rm m}\theta)).$$

[17] Note that the action in the (ϕ, δ) phase space is related to the action in the $(\phi, \mathcal{P})$ space by a constant factor $h|\eta|/(\nu_{\rm s}\sqrt{|\cos\phi_{\rm s}|})$.

The resulting invariant tori are shown in the right plots in Fig. 3.7. It becomes clear that the measured response period corresponds to the period of island motion around a SFP, and the response amplitude is the intercept of the invariant torus with the phase axis. The trajectory of a beam bunch in the presence of external rf phase modulation traces out a torus determined by the initial phase-space coordinates of the bunch. Since the torus, which passes through fixed initial phase-space coordinates, depends on the rf phase modulation frequency, the measured tori depend on the driven frequency. Figure 3.7 shows invariant tori deduced from experimental data. The solid lines are invariant tori of the Hamiltonian in Eq. (3.113), where the synchrotron frequency was fitted to be about 535±3 Hz.

III.4 Effects of Dipole Field Modulation

Ground motion of quadrupoles and power supply ripple in dipoles can cause dipole field modulation. Equation (2.173) in Chap. 2, Sec. III, shows that the path length of a reference orbit is changed by dipole field errors at nonzero dispersion function locations. If the dipole field is modulated, the path length and thus the arrival time at rf cavities of the reference (synchronous) particle are also modulated. This effect is equivalent to rf phase modulation, which gives rise to parametric resonances in synchrotron motion. The effect is a special type of "synchro-betatron coupling" that may limit the performance of high energy colliders.

Here we discuss experimental measurements of dipole field modulation at the IUCF Cooler. For this experiment, the harmonic number was $h = 1$, the phase slip factor was $\eta \approx -0.86$, the stable phase angle was $\phi_0 = 0$, and the revolution frequency was $f_0 = 1.03168$ MHz at 45 MeV proton kinetic energy. The rf voltage was chosen to be 41 V to obtain a synchrotron frequency of $f_s = \omega_s/2\pi = 262$ Hz in order to avoid harmonics of the 60 Hz ripple. The synchrotron tune was $\nu_s = \omega_s/\omega_0 = 2.54 \times 10^{-4}$. We chose $\nu_x = 3.828$, $\nu_z = 4.858$ to avoid nonlinear betatron resonances. The corresponding smallest horizontal and vertical betatron sideband frequencies were 177 and 146 kHz respectively.

With horizontal dipole (vertical field) modulation at location s_0, the horizontal closed-orbit deviation $x_{co}(t)$ becomes (see Chap. 2, Sec. III)

$$x_{co}(t) = \frac{\sqrt{\beta_x(s)\beta_x(s_0)}}{2\sin\pi\nu_x}\theta(t)\cos(\pi\nu_x - |\phi_x(s) - \phi_x(s_0)|),$$

where $\theta(t) = \hat{\theta}\sin(\omega_m t + \chi_0)$; $\hat{\theta} = \hat{B}_m \ell/B\rho$; and $\hat{B}_m$ is the peak modulation dipole field. Furthermore, if the dispersion function at the modulating dipole location is not zero, the path length is also modulated. The change in the circumference is

$$\Delta C = D\theta(t) = D\hat{\theta}\ \sin(\omega_m t + \chi_0), \tag{3.131}$$

where D is the dispersion function at the modulation dipole location. The corresponding rf phase difference becomes $\Delta\phi = 2\pi h(\Delta C/C)$, where $C = 86.82$ m is the circumference of the IUCF Cooler. In our experiment, the maximum rf phase shift per turn $\hat{\Delta\phi}$ was $0.78 \times 10^{-5}\hat{B}_m$ radians, where the magnetic field $\hat{B}_m$ is in Gauss.

The longitudinal phase-space coordinates $(\phi, \Delta p/p_0)$ at the nth and the $(n+1)$th revolutions are transformed according to the mapping equations

$$\phi_{n+1} = \phi_n + 2\pi h\eta\left(\frac{\Delta p}{p}\right)_n + \Delta\phi, \tag{3.132}$$

$$\left(\frac{\Delta p}{p}\right)_{n+1} = \left(\frac{\Delta p}{p}\right)_n + \frac{eV}{\beta^2 E}\sin\phi_{n+1} - \lambda\left(\frac{\Delta p}{p}\right)_n, \tag{3.133}$$

where the fractional momentum deviation of particles $(\Delta p/p_0)$ is the conjugate coordinate to synchrotron phase angle ϕ, and λ is the phase-space damping parameter related to electron cooling. Thus the synchrotron equation of motion, in the presence of transverse dipole field modulation, becomes

$$\frac{d^2\phi}{dt^2} + 2\alpha\frac{d\phi}{dt} + \omega_s^2\sin\phi = \omega_m^2 a\cos\omega_m t + 2\alpha\omega_s a\sin\omega_m t, \tag{3.134}$$

where the damping coefficient is $\alpha = \lambda\omega_0/4\pi$. With an electron current of 0.75 A, the damping time for the 45 MeV protons was measured to be about 0.33 ± 0.1 s or $\alpha = 3 \pm 1\ \mathrm{s}^{-1}$, which was indeed small compared with $\omega_s = 1646\ \mathrm{s}^{-1}$.

Because the synchrotron frequency is much smaller than the revolution frequency in proton storage rings, the phase errors of each turn accumulate. The equivalent phase modulation amplitude is enhanced by a factor $\omega_0/2\pi\omega_m$, i.e. the effective phase modulation amplitude parameter a is

$$a = \frac{h\omega_0 D\hat{\theta}}{\omega_m C} = \frac{\omega_0}{2\pi\omega_m}\hat{\Delta\phi}. \tag{3.135}$$

Although the cooling was weak, the transient solution of Eq. (3.134) was damped out by the time of measurement. We therefore measured the steady state solution, in contrast to the experiment discussed in the previous section, where we measured the transient solutions. Let the steady state solution of the nonlinear parametric dissipative resonant system, Eq. (3.134), be

$$\phi \approx g\sin(\omega_m t - \chi), \tag{3.136}$$

where we used the approximation of a single harmonic. Expanding the term $\sin\phi$ in Eq. (3.134) up to the first harmonic, we obtain the equation for the modulation amplitude g as

$$\left[-\omega_m^2 g + 2\omega_s^2 J_1(g)\right]^2 + [2\alpha\omega_m g]^2 = [\omega_m\omega_s a]^2 + [2\alpha\omega_s a]^2 \tag{3.137}$$

with the phase χ given by

$$\chi = \arctan\left[\frac{g\omega_{\rm m}(\omega_{\rm m}^2 + 4\alpha^2) - 2\omega_{\rm s}^2\omega_{\rm m}J_1(g)}{4\alpha\omega_{\rm s}^2 J_1(g)}\right], \tag{3.138}$$

where J_1 is the Bessel function [25] of order 1. Steady state solutions of Eq. (3.137) are called *attractors* for the dissipative system. The existence of a unique phase factor χ for solutions of the dissipative parametric resonant equation implies that the attractor is a single phase-space point rotating at modulation frequency $\omega_{\rm m}$.

When the modulation frequency is below the bifurcation frequency, $\omega_{\rm bif}$, given by the condition

$$\left.\frac{\partial\omega_{\rm m}}{\partial g}\right|_{\omega_{\rm m}=\omega_{\rm bif}} = 0,$$

Eq. (3.137) has three solutions. A stable solution with a large phase amplitude g_a and phase factor $\chi_a \approx \pi/2$ is the outer attractor. The stable solution at a smaller phase amplitude g_b with $\chi_b \approx -\pi/2$ is the inner attractor. The third solution g_c with $\chi_c \approx -\pi/2$ corresponds to the unstable (hyperbolic) solution, which is associated with the UFP of the effective non-dissipative Hamiltonian. When the damping parameter α is small, these two stable solutions are nearly equal to the SFPs of the effective Hamiltonian, and are almost opposite to each other in the synchrotron phase space, as shown in Fig. 3.5. They rotate about the origin at the modulation frequency [see Eq. (3.136)]. When the damping parameter α is increased, the stable solution (g_a, χ_a) and the unstable solution (g_c, χ_c) approach each other. At a large damping parameter, they collide and disappear, i.e. the outer attractor solution disappears. When the modulation frequency is larger than the bifurcation frequency, only the outer attractor solution exists.

When the modulation frequency is far from the bifurcation frequency, the response amplitude for the inner attractor at $\omega_{\rm m} \ll \omega_{\rm bif}$, or for the outer attractor at $\omega_{\rm m} \gg \omega_{\rm bif}$, can be approximated by solving the linearized equation (3.137), i.e.

$$g = \left(\frac{(\omega_{\rm m}\omega_{\rm s})^2 + (2\alpha\omega_{\rm s})^2}{(\omega_{\rm s}^2 - \omega_{\rm m}^2)^2 + (2\alpha\omega_{\rm m})^2}\right)^{1/2} a. \tag{3.139}$$

A. Chaotic nature of parametric resonances

In the presence of a weak damping force, *fixed points of the time-averaged Hamiltonian become attractors.* A weak damping force does not destroy the resonance island created by external rf phase modulation. Because of phase-space damping, these fixed points of the Hamiltonian become attractors. Particles in the phase space are damped incoherently toward these attractors, while the attractors rotate about the center of the bucket at the modulation frequency. As the damping force becomes larger, the outer SFP and the UFP may collide and disappear.

Numerical simulations based on Eq. (3.133) were done to demonstrate the coherent and incoherent nature of the single particle dynamics of the parametric resonance system. One of the results is shown in Fig. 3.8, where each black dot corresponds to initial phase-space coordinates that converge toward the outer attractor. Complementary phase-space coordinates converge mostly to the inner attractor except for a small patch of phase-space coordinates located on the boundary of the separatrix, which will converge toward two attractors located near the separatrix.

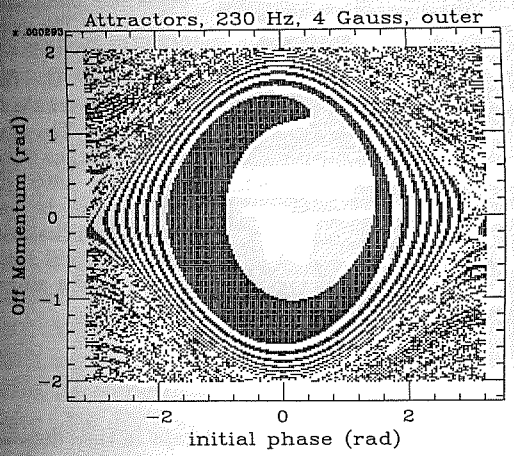

Figure 3.8: Initial normalized phase-space coordinates, obtained from a numerical simulation of Eq. (3.133), which converge to the outer attractor are shown for $\hat{B}_{\rm m} = 4$ Gauss and $f_{\rm m} = 230$ Hz. The synchrotron frequency is 262 Hz. The number of phase-space points that converge to the inner or the outer attractors can be used to determine the beamlet intensity.

The basin of attraction for the inner and the outer attractors forms non-intersecting intervolving spiral rings. To which attractor a particle will converge depends sensitively on the initial phase-space coordinates, especially for particles outside the bucket. The orientation of initial phase-space coordinates converging toward the inner or the outer attractor depends on the initial driving phase χ_0 of the dipole field in Eq. (3.131). Numerical simulations indicate that all particles located initially inside the rf bucket will converge either to the inner or to the outer attractor. However, initial phase-space coordinates in a small patch located at the separatrix of the rf bucket converge toward two attractors moving along the separatrix.

B. Observation of attractors

Since the injected beam from the IUCF K200 AVF cyclotron is uniformly distributed in the synchrotron phase space within a momentum spread of about $(\Delta p/p) \approx \pm 3 \times 10^{-4}$, all attractors can be populated. The phase coordinates of these attractors could be measured by observing the longitudinal beam profile from BPM sum signals on an oscilloscope. Figure 3.9 shows the longitudinal beam profile accumulated through many synchrotron periods with modulation field $\hat{B}_{\rm m} = 4$ G for modulation frequencies of 210, 220, 230, 240, 250, and 260 Hz; it also shows the rf waveform for reference.

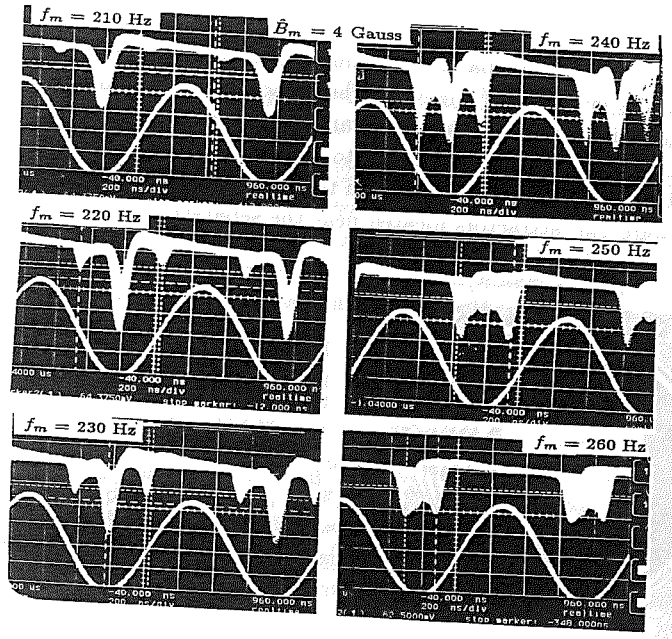

Figure 3.9: Oscilloscope traces of accumulated BPM sum signals showing the splitting of a beam bunch into beamlets below the bifurcation frequency. The modulation amplitude was $\hat{B}_m = 4$ G. The sine waves are the rf waveform. The relative populations of the inner and outer attractors can be understood qualitatively from numerical simulations of the attractor basin.

It was puzzling at first why the longitudinal profile exhibited gaps in time domain, as if there were no synchrotron motion for the beam bunch located at a relatively large phase amplitude. However, using a fast sampling digital oscilloscope (HP54510A) for a single trace, we found that the beam profile was not made of particles distributed in a ring of large synchrotron amplitude, but was composed of two beamlets. Both beamlets rotated in the synchrotron phase space at the modulating frequency, as measured from the fast Fourier transform (FFT) of the phase signal. If the equilibrium distribution of the beamlet was elongated, then the sum signal, which measured the peak current of the beam, would show a large signal at both extremes of its phase coordinate, where the peak current was large. When the beamlet rotated to the central position in the phase coordinate, the beam profile became flat with a smaller peak current. Therefore the profile observed with the oscilloscope offered an opportunity to study the equilibrium distribution of charges in these attractors.

If we assume an equilibrium elliptical beamlet profile with Gaussian distribution, the current density distribution function becomes

$$\rho(\phi, t) = \frac{\rho_1}{\sqrt{2\pi}\sigma_1} e^{-[\phi-\phi_1(t)]^2/2\sigma_1^2} + \frac{\rho_2}{\sqrt{2\pi}\sigma_2} e^{-[\phi-\phi_2(t)]^2/2\sigma_2^2}, \tag{3.140}$$

where ρ_1 and ρ_2 represent the populations of the two beamlets with $\rho_1 + \rho_2 = 1$. Since each particle in the two beamlets rotates in the phase space at modulating frequency

ω_m, the parameters $\phi_{1,2}$ and $\sigma_{1,2}$ are

$$\phi_1(t) = g_a \sin(\omega_m t - \chi_a), \quad \phi_2(t) = g_b \sin(\omega_m t - \chi_b),$$

and

$$\sigma_1^2 = \sigma_{10}^2(1 + r_1 \sin^2 \omega_m t), \quad \sigma_2^2 = \sigma_{20}^2(1 + r_2 \sin^2 \omega_m t).$$

Here $g_{a,b}$ and $\chi_{a,b}$ are the amplitudes and phases of the two beamlets, obtained by solving Eqs. (3.137) and (3.138). Since the profile observed on the oscilloscope was obtained by accumulation through many synchrotron periods, it did not depend on the parameters $\chi_{a,b}$, i.e. these profiles were not sensitive to the relative positions of the two beamlets. The eccentricity parameters r_1 and r_2 signify the aspect ratio of the two beamlets, and σ_{10} and σ_{20} represent the average rms bunch length. For example, the aspect ratio, given by $1 : 1 + r_1$ of the outer beamlet at modulation frequency 220 Hz was found to be about 1:3 from the profile in Fig. 3.9. This means that the peak current for the outer beamlet was reduced by a factor of 3 when this beamlet rotated to the center of the phase coordinate. The relative populations of the two beamlets was about 75% for the inner and 25% for the outer, obtained by fitting the data. As the modulating frequency increased toward the synchrotron frequency, the phase amplitude of the outer beamlet became smaller and its population increased. When the modulating frequency was higher than the bifurcation frequency $\omega_{\rm bif}$, the center peak disappeared (see 260 Hz data of Fig. 3.9).

C. The hysteretic phenomena of attractors

The phase amplitudes of attractors shown in Fig. 3.10 also exhibited hysteresis phenomena. When the modulation frequency, which was initially above the bifurcation frequency, was ramped downward, the phase amplitude of the synchrotron oscillations increased along the outer attractor solution. When it reached a frequency far below the bifurcation frequency, the phase amplitude jumped from the outer attractor to the inner attractor solution. On the other hand, if the modulation frequency, originally far below the bifurcation frequency, was ramped up toward the bifurcation frequency, the amplitude of the phase oscillations followed the inner attractor solution. At a modulation frequency near the bifurcation frequency, the amplitude of the synchrotron oscillations jumped from the inner to the outer attractor solution.

The hysteresis depended on beam current and modulation amplitude a. Since a large damping parameter could destroy the outer attractor, the hysteresis depended also on the dissipative force. The observed phase amplitudes were found to agree well with the solutions of Eq. (3.137). Similar hysteretic phenomena have been observed in electron-positron colliders, related to beam-beam interactions, where the amplitudes of the coherent π-mode oscillations showed hysteretic phenomena.[18] At a large beam-

[18] See T. Ieiri and K. Hirata, *Proc. 1989 Part. Accel. Conf.* p. 926 (IEEE, New York, 1989).

beam tune shift, the vertical beam size exhibited a flip-flop effect with respect to the relative horizontal displacement of two colliding beams.[19]

D. Systematic property of parametric resonances

The formalism discussed so far seems complicated by the transformation of phase-space coordinates into action-angle variables. However, the essential physics is rather simple. In this section, we will show that the global property of parametric resonances can be understood simply from Hamiltonian dynamics.

The circles in Fig. 3.10 show a compilation of beamlet phase amplitude vs modulation frequency for four different experimental phase modulation amplitudes. The solid lines show the synchrotron tune and its third harmonic. We note that the bifurcation of the 1:1 resonance islands follows the tune of the *unperturbed* Hamiltonian system, and the measured third order 3:1 resonance islands fall on the curve of the third harmonic of the synchrotron tune.

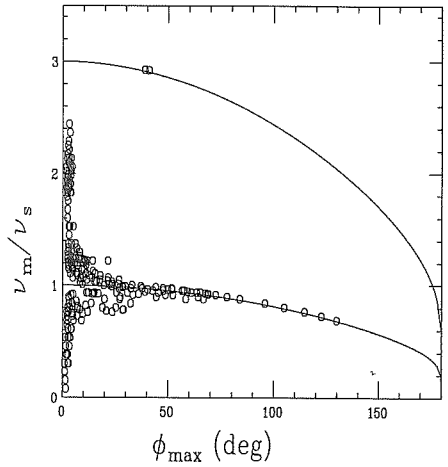

Figure 3.10: The phase amplitudes of beamlets excited by rf phase modulation, measured from the oscilloscope trace, are compared with the theoretical synchrotron tune. The bifurcation of the resonance islands follows the unperturbed tune of the synchrotron Hamiltonian, shown as the lower solid line (see also Fig. 3.5 on the bifurcation of 1:1 parametric resonance). The third order resonance island falls also on the third harmonic of the synchrotron tune. Because the rf phase modulation does not excite 2:1 resonance, we did not find parametric resonances at the second synchrotron harmonic. The sideband around the first order synchrotron tune corresponds to the 60 Hz power supply ripple.

When an external time dependence perturbation is applied to a Hamiltonian system, the perturbed Hamiltonian contains a perturbing term similar to that in Eq. (3.108). On the basis of the KAM theorem, most of the Hamiltonian tori are not perturbed except those encountering a resonance condition. Thus the external perturbation excites only particles locally in the phase space where the amplitude dependent synchrotron tune falls exactly at the modulation tune, where the particle

[19]See M.H.R. Donald and J.M. Paterson, *IEEE Trans. Nucl. Sci.* **NS-26**, 3580 (1979); G.P. Jackson and R.H. Siemann, *Proc. 1987 Part. Accel. Conf.* p. 1011 (IEEE, New York, 1987).

motion can be described by the effective parametric resonance Hamiltonian (3.109).[20] The size of the resonance island depends on the slope of tune vs amplitude, the strength function $g_n(J)$, and the amplitude of perturbation.

In fact, the external perturbation creates a local minimum in the potential energy at the SFP locations. When a weak damping force is applied to the dynamical system, the SFP becomes an attractor, and the local potential well becomes the basin for stable particle motion. Thus a beam inside an rf bucket can split into beamlets.

When the modulation frequency is varied, SFPs (attractors) are formed along the tune of the unperturbed Hamiltonian, i.e.

$$\nu_m = n\tilde{Q}_s(J_{SFP}). \tag{3.141}$$

The measurement of attractor amplitude vs modulation tune is equivalent to the measurement of synchrotron tune vs synchrotron amplitude, as clearly seen in Fig. 3.10. Since the rf phase modulation does not excite even synchrotron harmonics, we do not observe a 2:1 attractor in Fig. 3.10. If, however, a stronger phase modulation is applied to the dynamical system, a 2:1-like (4:2) parametric resonance can be formed by 1:1 and 3:1 resonances through second order perturbation.

An important implication of the above parametric excitation theorem is that chaos at the separatrix orbit is induced by overlapping parametric resonances. This can be understood as follows. Let $Q(J)$ be the tune of a dynamical system, where the tune is zero at the separatrix, i.e. $Q(J_{sx}) = 0$. Now a time dependent perturbation can induce a series of parametric resonances in the perturbed Hamiltonian. These parametric resonances, located at $nQ(J)$ with integer n, can be excited by time dependent perturbation. Since $nQ(J_{sx}) \approx 0$ for all n near the separatrix, a perturbation with low frequency modulation can produce many overlapping parametric resonances near the separatrix and lead to local chaos. This result can be applied to synchrotron motion as well as to betatron motion, where higher order nonlinear resonances serve as the source of time dependent modulation.

Now, we apply this result to evaluate the effect of low frequency modulations on particle motion. If the amplitude of low frequency modulation is not large, it will induce overlapping parametric resonances only near the separatrix. If the beam size is relatively small, the stochasticity at the separatrix will do little harm to the beam motion. However, when the modulation frequency approaches the tune of particles at the center of the bucket, particle orbits near the center of the bucket will be strongly perturbed, forming islands within the bucket.

In reality, the perturbation arising from wakefields, rf phase error, dipole field error, ground vibration, etc., consists of a spectrum of frequency distributions. The

[20]The remaining terms play the role of time dependent perturbations to the effective Hamiltonian of Eq. (3.109). The KAM theorem produces a hierarchy of higher order resonance islands within parametric resonance islands.

mean field of the perturbation gives rise to the effect called potential well distortion, which, solved self-consistently in the Vlasov equation, modifies the unperturbed tune of the system. The remaining time dependent perturbation can generate further bunch deformation, bunch splitting, hysteresis, etc., depending on its frequency spectrum. The complicated collective instability phenomenon is in fact closely related to nonlinear beam dynamics.[21]

III.5 RF Voltage Modulation

The beam lifetime limitation due to rf noise has been observed in many synchrotrons, e.g., the super proton synchrotron (SPS) in CERN.[22] Recently, there has been some interest in employing rf voltage modulation to induce super slow extraction through a bent crystal for very high energy beams,[23] rf voltage modulation to stabilize collective beam instabilities, rf voltage modulation for extracting beam with a short bunch length, etc. Since the rf voltage modulation may be used for enhancing a desired beam quality, we will study the physics of synchrotron motion with rf voltage modulation, that may arise from rf noise, power supply ripple, wakefields, etc. Beam response to externally applied rf voltage modulation has been measured at the IUCF Cooler.[24] The rf voltage modulation has been implemented to stabilize coupled bunch instabilities induced by parasitic rf cavity modes with high brightness beams at the Taiwan Light Source.[25]

A. The equation of motion with rf voltage modulation

In the presence of rf voltage modulation, the synchrotron equations of motion are

$$\phi_{n+1} = \phi_n - 2\pi\nu_s \frac{\eta}{|\eta|}\mathcal{P}_n, \tag{3.142}$$

$$\mathcal{P}_{n+1} = \mathcal{P}_n - 2\pi\nu_s[1 + b\sin(\nu_m\theta_{n+1} + \chi)]\sin\phi_{n+1} - \frac{4\pi\alpha}{\omega_0}\mathcal{P}_n, \tag{3.143}$$

[21] Recently, a series of beam transfer function measurements were made at electron storage rings. Sweeping the rf phase modulation frequency and measuring the response by measuring either the centroid of the beam, or the beam profile from a synchrotron light monitor using a streak camera, the response of the beam to external rf phase modulation can be obtained. For details see M.H. Wang, *et al.*, *Proc. 1997 Part. Accel. Conf.* (1997); J. Byrd, *ibid.* (1997); M.G. Minty *et al.*, *ibid.* (1997); D. Rice, private communications.

[22] D. Boussard, *et al.*, *IEEE Trans. Nucl. Sci.* **NS-26**, 3484 (1979); D. Boussard, *et al.*, *Proc. 11th Int. Conf. on High Energy Accelerators*, p. 620 (Birkhauser, Basel, 1980); G. Dôme, CERN **87-03**, p. 370 (1987); S. Krinsky and J.M. Wang, *Part. Accel.* **12**, 107 (1982).

[23] H.J. Shih and A.M. Taratin, SSCL-389 (1991); W. Gabella, J. Rosenzweig, R. Kick, and S. Peggs, *Part. Accel.* **42**, 235 (1993).

[24] D. Li *et al.*, *Phys. Rev.* E **48**, R1638 (1993); D.D. Caussyn *et al.*, *Proc. Part. Acc. Conf.* p. 29 (IEEE, Piscataway, NJ, 1993); D. Li *et al.*, *Nucl. Instru. Methods* **A 364**, 205 (1995).

[25] M.H. Wang, and S.Y. Lee, *Journal of Applied Physics*, **92**, 555 (2002).

where $\mathcal{P} = -h|\eta|\delta/\nu_s$ is the normalized off-momentum coordinate conjugate to ϕ; $\delta = \Delta p/p_0$ is the fractional momentum deviation from the synchronous particle; η is the phase slip factor; $\nu_s = \sqrt{h|\eta|eV/2\pi\beta^2 E_0}$ is the synchrotron tune at zero amplitude; E_0 is the beam energy; $b = \Delta V/V$ is the fractional rf voltage modulation strength ($b > 0$); ν_m is the rf voltage modulation tune; χ is a phase factor; θ is the orbital angle used as time variable; $\omega_0 = 2\pi f_0$ is the angular revolution frequency; and α is the phase-space damping factor resulting from phase-space cooling.

At the IUCF Cooler, the phase-space damping rate was measured to be about $\alpha \approx 3.0 \pm 1.0\ \mathrm{s}^{-1}$, which is much smaller than $\omega_0\nu_s$, typically about 1500 s^{-1} for the $h = 1$ harmonic system. Without loss of generality, we discuss the case for a particle energy below the transition energy, i.e. $\eta < 0$.

Neglecting the damping term, i.e. $\alpha = 0$, the equation of motion for phase variable ϕ is

$$\ddot{\phi} + \nu_s^2[1 + b\sin(\nu_m\theta + \chi)]\sin\phi = 0, \tag{3.144}$$

where the overdot indicates the time derivative with respect to θ. In linear approximation with $\sin\phi \approx \phi$, Eq. (3.144) reduces to Mathieu's equation. By choosing $\chi = -\pi/2$ and $z = \frac{1}{2}\nu_m\theta$, $p = 4\nu_s^2/\nu_m^2$, and $q = 2b\nu_s^2/\nu_m^2$, we can linearize Eq. (3.144) into Mathieu's equation [25]

$$\frac{d^2\phi}{dz^2} + (p - 2q\cos 2z)\phi = 0. \tag{3.145}$$

In accelerator physics applications, p and q are real with $q \ll 1$. Thus stable solutions of Mathieu's equation are obtained with the condition that the parameter p is bounded by the characteristic roots $a_r(q)$ and $b_{r+1}(q)$, where $r = 0, 1, 2, \cdots$. In other words, unstable solutions are in the region $b_r(q) \le p \le a_r(q)$, where $r = 1, 2, \cdots$. Thus the first unstable region is obtained from $b_1(q) \le p \le a_1(q)$ or, equivalently,

$$2\nu_s(1 - \frac{1}{4}b) \le \nu_m \le 2\nu_s(1 + \frac{1}{4}b). \tag{3.146}$$

Similarly, the second order unstable region is

$$\nu_s(1 - \frac{5}{24}b^2) \le \nu_m \le \nu_s(1 + \frac{1}{24}b^2), \tag{3.147}$$

where the second order Mathieu resonance can be obtained from second order perturbation theory.[26] The width of the instability decreases rapidly with increasing order for small b. In our application, we need to consider only the lowest order Mathieu instability. Since synchrotron motion is nonlinear, the linear Mathieu instability analysis should be extended to nonlinear synchrotron motion as follows.

[26] L.D. Landau and E.M. Lifschitz, *Mechanics*, 3rd. ed. (Pergamon Press, Oxford, 1976).

B. The perturbed Hamiltonian

The synchrotron equation of motion with rf voltage modulation can be derived from the Hamiltonian $H = H_0 + H_1$ with

$$H_0 = \frac{1}{2}\nu_s \mathcal{P}^2 + \nu_s(1-\cos\phi), \tag{3.148}$$

$$H_1 = \nu_s b \sin(\nu_m\theta + \chi)\,[1-\cos\phi], \tag{3.149}$$

where H_0 is the unperturbed Hamiltonian and H_1 the perturbation. For a weakly perturbed Hamiltonian system, we expand H_1 in action-angle coordinates of the unperturbed Hamiltonian

$$H_1 = \nu_s b \sum_{n=-\infty}^{\infty} |G_n(J)| \sin(\nu_m\theta - n\psi - \gamma_n), \tag{3.150}$$

where we choose $\chi = 0$ for simplicity, and $|G_n(J)|$ is the Fourier amplitude of the factor $(1-\cos\phi)$ with γ_n its phase, defined in Eq. (3.101).

Since $(1-\cos\phi)$ is an even function of ψ in $[-\pi,\pi]$, the Fourier integral for G_n from Eq. (3.101) is zero except for n even with $G_{-n} = G_n^*$. Thus rf voltage modulation generates only even-order synchrotron harmonics in H_1. Expanding $G_n(J)$ in power series, we obtain

$$G_0 \approx \tfrac{1}{2}J + \tfrac{1}{2048}J^3 + \cdots, \qquad G_2 \approx -\tfrac{1}{4}J + \tfrac{1}{128}J^2 + \cdots,$$

$$G_4 \approx -\tfrac{1}{64}J^2 + \tfrac{1}{2048}J^3 + \cdots, \quad G_6 \approx \tfrac{3}{4096}J^3 + \cdots.$$

The $G_0(J)$ term in the perturbation can contribute to synchrotron tune modulation with a modulation depth

$$\Delta\tilde{Q}_s \approx \frac{1}{2}\nu_s b \sin\nu_m\theta.$$

C. Parametric resonances

When the modulation frequency is near an even harmonic of the synchrotron frequency, i.e. $\nu_m \approx nQ_s$ ($n =$ even integers), particle motion is coherently perturbed by the rf voltage modulation resulting from a resonance driving term (stationary phase condition). The resonances, induced by the external harmonic modulation of the rf voltage, are called parametric resonances. Using the generating function

$$F_2 = (\psi - \frac{\nu_m}{n}\theta + \frac{\gamma_n}{n} + \frac{\pi}{2n})\tilde{J},$$

we obtain the Hamiltonian in the resonance rotating frame as

$$\tilde{H} = E(\tilde{J}) - \frac{\nu_m}{n}\tilde{J} + \nu_s b|G_n(\tilde{J})|\cos n\tilde{\psi} + \Delta\tilde{H}(\tilde{J},\tilde{\psi},\theta), \tag{3.151}$$

where the remaining small time dependent perturbation term ΔH oscillates at frequencies $\nu_m, 2\nu_m, \cdots$. In the time average, we have $\langle\Delta\tilde{H}\rangle \approx 0$. Thus the time averaged Hamiltonian $\langle\tilde{H}\rangle$ for the nth order parametric resonance becomes

$$\langle\tilde{H}\rangle = E(\tilde{J}) - \frac{\nu_m}{n}\tilde{J} + \nu_s b|G_n(\tilde{J})|\cos n\tilde{\psi}. \tag{3.152}$$

The phase-space contour may be strongly perturbed by the parametric resonance. Note here that $|G_{n+2}/G_n| \sim J$ for $n > 0$. The resonance strength is greatest at the lowest harmonic for particles with small phase amplitude. The system is most sensitive to the rf voltage modulation at the second synchrotron harmonic.

D. Quadrupole mode

When the rf voltage modulation frequency is near the second harmonic of the synchrotron frequency, particle motion is governed by the $n = 2$ parametric resonance Hamiltonian

$$\langle\tilde{H}\rangle = (\nu_s - \frac{\nu_m}{2})\tilde{J} - \frac{\nu_s}{16}\tilde{J}^2 + \frac{\nu_s}{4}b\tilde{J}\cos 2\tilde{\psi} \tag{3.153}$$

in the resonance rotating frame. Since the Hamiltonian (3.153) is autonomous, the Hamiltonian is a constant of motion. For simplicity, we drop the tilde notations. Hamilton's equations are

$$\dot{J} = \frac{\nu_s}{2}bJ\sin 2\psi, \tag{3.154}$$

$$\dot{\psi} = \nu_s - \frac{\nu_m}{2} - \frac{\nu_s}{8}J + \frac{\nu_s}{4}b\cos 2\psi. \tag{3.155}$$

The fixed points that determine the locations of the islands and separatrix of the Hamiltonian are obtained from $\dot{J} = 0$, $\dot{\psi} = 0$. The stable fixed points (SFPs) are

$$J_{\rm SFP} = \begin{cases} 8(1-\frac{\nu_m}{2\nu_s}) + 2b, & \text{if } \nu_m \le 2\nu_s + \frac{1}{2}b\nu_s \\ 0, & \text{if } \nu_m > 2\nu_s + \frac{1}{2}b\nu_s \end{cases} \tag{3.156}$$

with $\psi = 0$ and π. Tori of the Hamiltonian flow around SFPs are shown in Fig. 3.11. The unstable fixed points (UFPs) are located at

$$J_{\rm UFP} = \begin{cases} 8(1-\frac{\nu_m}{2\nu_s}) - 2b, & \text{if } \nu_m \le 2\nu_s - \frac{1}{2}b\nu_s \\ 0, & \text{if } 2\nu_s - \frac{1}{2}b\nu_s \le \nu_m \le 2\nu_s + \frac{1}{2}b\nu_s \end{cases} \tag{3.157}$$

with $\psi = \pi/2$ and $3\pi/2$.

We note that the second harmonic rf voltage modulation can induce an instability at $J_{\rm UFP} = 0$ in the frequency domain $2\nu_s - \frac{1}{2}b\nu_s \le \nu_m \le 2\nu_s + \frac{1}{2}b\nu_s$. This is the first order Mathieu resonance of Eq. (3.146). Nonlinear synchrotron motion extends the instability to lower modulation frequency at larger synchrotron amplitude, according to

$$\nu_m = 2\nu_s(1 - \frac{J_{\rm UFP}}{8}) - \frac{1}{2}\nu_s b, \tag{3.158}$$

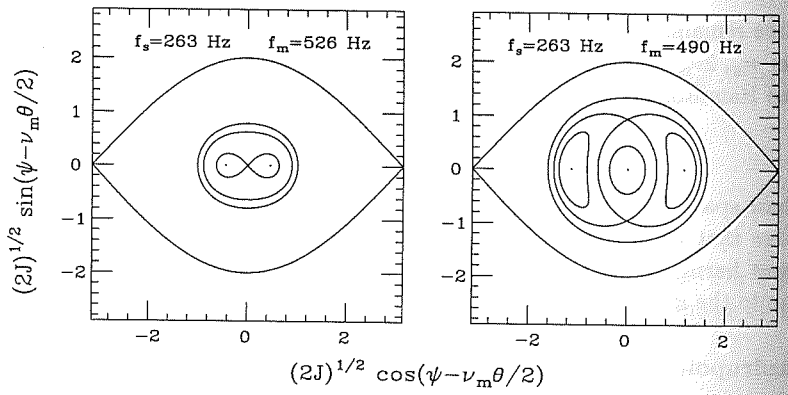

Figure 3.11: The separatrix and tori of the Hamiltonian (3.153) in the resonance rotating frame. The synchrotron frequency is $f_s = 263$ Hz, the voltage modulation amplitude is $b = 0.05$, and the modulation frequencies are $f_m = 526$ Hz (left plot) and $f_m = 490$ Hz (right plot).

which is a nonlinear extension of Mathieu instability.

Modulation of the rf voltage at the second harmonic of the synchrotron tune has been found useful in damping the multi-bunch instabilities for the damping ring of the Stanford linear collider (SLC).[27] By adjusting the amplitude and phase of the rf voltage modulation, the collective instability of high brightness electron beams in the SLC damping ring can be controlled. The damping mechanism may be understood as follows. When the voltage modulation at $\nu_m = 2\nu_s$ is applied, the Mathieu resonance gives rise to an UFP at the origin of the phase space and the SFP is displaced to $J_{SFP} = 2b$. Since electrons are damped incoherently into the SFP by the synchrotron radiation damping, the beam distribution becomes dumbbell-shaped in phase space, rotating about the longitudinal phase space at half the modulation frequency, or equivalently the synchrotron frequency. The size and orientation of the dumbbell can be controlled by parameter b and phase χ.

E. Island tune and equilibrium beamlet profile

The island tune ν_{island}, defined by f_{island}/f_0, is an important property of a resonant system, where f_{island} is the frequency with which a particle rotates around a SFP in the resonant precessing frame. To obtain the island tune, we expand the phase-space coordinates around a fixed point of the Hamiltonian, with

$$y = \sqrt{2J}\cos\psi - \sqrt{2J_0}\cos\psi_0, \quad p_y = -\sqrt{2J}\sin\psi + \sqrt{2J_0}\sin\psi_0,$$

[27] J.D. Fox and P. Corredoura, *Proc. European Part. Accel. Conf.* p. 1079 (Springer-Verlag, Heidelberg, 1992).

where $(\sqrt{2J_0}\cos\psi_0, -\sqrt{2J_0}\sin\psi_0)$ are the phase-space coordinates of a fixed point of the Hamiltonian in the resonance precessing frame. In terms of the local coordinates p_y and y, the Hamiltonian, Eq. (3.153), becomes

$$H = \frac{1}{2}Ap_y^2 + \frac{1}{2}By^2 + \cdots \tag{3.159}$$

with

$$\begin{aligned} A &= \nu_s - \frac{\nu_m}{2} - \frac{1}{4}\nu_s J_0 \sin^2\psi_0 - \frac{1}{4}b\nu_s - \frac{1}{8}\nu_s J_0, \\ B &= \nu_s - \frac{\nu_m}{2} - \frac{1}{4}\nu_s J_0 \cos^2\psi_0 + \frac{1}{4}b\nu_s - \frac{1}{8}\nu_s J_0. \end{aligned}$$

It is clear that the fixed point is stable if the parameters A and B satisfy $AB > 0$. The small amplitude island tune is $\nu_{island} = \sqrt{AB}$.

For $b > 0$, the fixed points associated with $\psi = 0$, π, and $J_0 = J_{SFP} = 8(1 - \nu_m/2\nu_s) + 2b$ are stable because $A = -\frac{1}{2}\nu_s b$ and $B = -\frac{1}{4}\nu_s J_{SFP}$ so that $AB > 0$. The small amplitude island tune at the SFP becomes

$$\nu_{island} = \sqrt{AB} = \nu_s\sqrt{\frac{bJ_{SFP}}{8}}. \tag{3.160}$$

The fixed points associated with $\psi = \pi/2, 3\pi/2$, and $J_0 = J_{UFP}$ are unstable since $A = -\frac{1}{4}\nu_s J_{UFP}$ and $B = \frac{1}{2}b\nu_s$, and so $AB < 0$.

The equilibrium beam profile, which satisfies the Vlasov equation, is a function of the Hamiltonian (3.159). Assuming a Gaussian distribution, we obtain

$$\rho(y, p_y) \approx \frac{\sqrt{AB}}{2\pi\sigma_0^2}\exp\left\{-\frac{1}{2\sigma_0^2}Ap_y^2 - \frac{1}{2\sigma_0^2}By^2\right\} \tag{3.161}$$

in the resonance precessing frame, where $\pi\sigma_0^2/\sqrt{AB}$ is the rms phase-space area of the beamlet. Since the resonance rotating frame rotates in the phase space at half the modulation frequency, the beam profile will retain its shape except for exchange of its local coordinates. The longitudinal profile monitor measures the image current on a wall gap monitor; it is the line density of the bunch or the projection of the density distribution function onto the phase coordinate

$$\rho(y) = \int \rho(y, p_y)dp_y. \tag{3.162}$$

Since the rms widths of the distribution function (3.161) are

$$\sigma_y = \sigma_0/\sqrt{|B|}, \quad \sigma_{p_y} = \sigma_0/\sqrt{|A|}, \tag{3.163}$$

the aspect ratio of the phase-space distribution σ_{p_y}/σ_y is $\sqrt{|B/A|}$ evaluated at the SFP. When the beamlet rotates to the phase coordinate, as shown in Fig. 3.11, the

aspect ratio of the beamlet becomes $\sqrt{J_{\rm SFP}/2b}$, which is normally much larger than 1, and the peak current will be large. On the other hand, when the beamlet rotates to a position 90° from that of Fig. 3.11, the aspect ratio becomes $\sqrt{2b/J_{\rm SFP}}$ and the line density becomes small.

F. The separatrix

The separatrix torus, which passes through the UFPs, is given by

$$H(J,\psi) = H(J_{\rm UFP}, \psi_{\rm UFP}). \tag{3.164}$$

The separatrix intersects the phase axis at the actions J_1 and J_2 given by

$$J_1 = \begin{cases} J_{\rm SFP} + \sqrt{J_{\rm SFP}^2 - J_{\rm UFP}^2} & \text{if } \nu_{\rm m} \le 2\nu_{\rm s} - \frac{1}{2}b\nu_{\rm s} \\ 2J_{\rm SFP} & \text{if } 2\nu_{\rm s} - \frac{1}{2}b\nu_{\rm s} \le \nu_{\rm m} \le 2\nu_{\rm s} + \frac{1}{2}b\nu_{\rm s} \end{cases} \tag{3.165}$$

and

$$J_2 = \begin{cases} J_{\rm SFP} - \sqrt{J_{\rm SFP}^2 - J_{\rm UFP}^2} & \text{if } \nu_{\rm m} \le 2\nu_{\rm s} - \frac{1}{2}b\nu_{\rm s} \\ 0 & \text{if } 2\nu_{\rm s} - \frac{1}{2}b\nu_{\rm s} \le \nu_{\rm m} \le 2\nu_{\rm s} + \frac{1}{2}b\nu_{\rm s}. \end{cases} \tag{3.166}$$

The intercepts can be used to determine the maximum synchrotron phase oscillation due to rf voltage modulation. Figure 3.11 shows also the intercepts of separatrix with phase axis. The island size $\Delta\phi_{\rm island}$ is $\sqrt{2J_1} - \sqrt{2J_2}$.

G. The amplitude dependent island tune of 2:1 parametric resonance

For an autonomous dynamical system governed by the Hamiltonian (3.153), the Hamiltonian is a constant of motion. The Hamiltonian value is $E_{\rm s} = \frac{1}{16}\nu_{\rm s}J_{\rm SFP}^2$ at SFP, and $E_{\rm u} = \frac{1}{16}\nu_{\rm s}J_{\rm UFP}^2$ at UFP. Using Hamilton's equations of motion, we obtain $\dot{J} = f(J,E)$, where

$$f(J,E) = 2\nu_{\rm s}\sqrt{\left[\frac{J^2}{16} + \frac{E}{\nu_{\rm s}} - (1 - \frac{\nu_{\rm m}}{2\nu_{\rm s}} - \frac{b}{4})J\right]\left[(1 - \frac{\nu_{\rm m}}{2\nu_{\rm s}} + \frac{b}{4})J - \frac{E}{\nu_{\rm s}} - \frac{J^2}{16}\right]}. \tag{3.167}$$

For a given Hamiltonian value E, the action J is limited by $J_{\rm min}$ and $J_{\rm max}$ given by

$$J_{\rm min} = (1 - \sqrt{1-x})J_{\rm SFP}, \quad J_{\rm max} = (1 + \sqrt{1-x})J_{\rm SFP},$$

where $x = E/E_{\rm s}$, with $x \in [J_{\rm UFP}^2/J_{\rm SFP}^2, 1]$. Note that $J_{\rm SFP} = \frac{1}{2}(J_{\rm min} + J_{\rm max})$. The island tune becomes

$$Q_{\rm island} = \frac{2\pi}{\oint d\theta} = 2\pi\left[\oint \frac{dJ}{f(J,E)}\right]^{-1} = \frac{\pi\nu_{\rm s}\sqrt{2bJ_{\rm SFP}}}{8K(k)}x^{1/4}, \tag{3.168}$$

where $K(k)$ is the complete elliptical integral of the first kind [25] with

$$k = \frac{1}{\sqrt{2}}\sqrt{1 - \frac{xJ_{\rm SFP} - J_{\rm UFP}}{\sqrt{x}(J_{\rm SFP} - J_{\rm UFP})}}.$$

It is easy to verify that Eq. (3.168) reduces to Eq. (3.160) at $x = 1$. Similarly, the island tune is zero at the separatrix with $x = J_{\rm UFP}^2/J_{\rm SFP}^2$.

H. Physical interpretation

In the longitudinal phase space, particles execute synchrotron motion with an amplitude dependent tune $Q_{\rm s}(J)$, where J is the invariant action of the particle motion. When the rf system is perturbed by a harmonic voltage modulation at $\nu_{\rm m}$, with a non-vanishing perturbation strength function $G_n(J)$, the perturbation creates n resonance islands in the longitudinal phase space around $J = J_{\rm r}$, where $J_{\rm r}$ is obtained from the resonance condition: $\nu_{\rm m} = nQ_{\rm s}(J_{\rm r})$.

Near the resonance island, the action J is no longer invariant and the synchrotron tune is likewise perturbed. These islands precess in the phase space at $1/n$ of the modulation tune, or equivalently the synchrotron tune at the resonance action $J_{\rm r}$. A particle executing synchrotron motion within the nth order resonance island will have a characteristic tune $\nu_{\rm m}/n$ with a regular amplitude oscillation due to the island motion. This oscillation tune is equal to the island tune. For particles located at the "separatrix" of the parametric resonance (not the separatrix of the rf bucket) the period of this amplitude oscillation becomes infinite. In other words, the island tune of the separatrix orbit is zero. The synchrotron tune of a particle on the separatrix is exactly $\nu_{\rm m}/n$. The synchrotron tune for particles at or near SFP is also $\nu_{\rm m}/n$ with an amplitude modulation whose tune is equal to the island tune. Particles located far from resonance islands experience little effect on their synchrotron motion if the voltage modulation amplitude is small.

III.6 Measurement of RF Voltage Modulation

We describe here an rf voltage modulation measurement at the IUCF Cooler. The experiment started with a single bunch of about 5×10^8 protons with kinetic energy 45 MeV. The cycle time was 10 s, with the injected beam electron-cooled for about 3 s, producing a full width at half maximum bunch length of about 9 m (or 100 ns) depending on rf voltage. The low frequency rf system used in the experiment was operating at harmonic number $h = 1$ with frequency 1.03168 MHz.

A. Voltage modulation control loop

The voltage control feedback of the IUCF Cooler rf system works as follows. The cavity rf voltage is picked up and rectified into DC via synchronous detection. The

rectified DC signal is compared to a preset voltage. The error found goes through a nearly ideal integrator that has very high DC gain. The integrated signal is then used to control an attenuator regulating the level of rf signal being fed to rf amplifiers. Because of the relatively low Q of the cavity at the IUCF Cooler, the effect of its inertia can be ignored if the loop gain is rolled off to unity well before $f_0/2Q$, where f_0 is the resonant frequency of the rf cavity and $Q \approx 50$ is the cavity Q value. Thus, no proportional error feedback is needed to stabilize the loop. The overall loop response exhibits the exponential behavior prescribed by a first order differential equation, i.e. $dV/dt = -V/\tau$, where V is the rf voltage and the characteristic relaxation time τ is about $10 - 200\ \mu$ s.

The amplitude modulation is summed with the reference and compared to the cavity sample signal. The modulation causes a change in the error voltage sensed by the control loop and results in modulation of the attenuator around a preset cavity voltage. The maximum modulation rate is limited by the loop response time of about 10 kHz. The modulation rates in our experiments are well within this limit. The modulation amplitude was measured and calibrated.

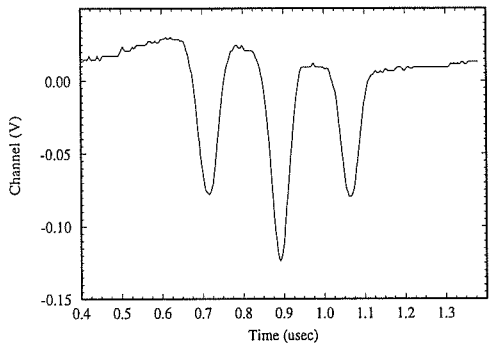

Figure 3.12: The beam bunch was observed to split into three beamlets in a single rf bucket measured from a fast sampling scope. The voltage modulation amplitude is $b = 0.05$ at modulation frequency $f_m = 480$ Hz with synchrotron tune $f_s = 263$ Hz. Note that the outer two beamlets rotated around the center beamlet at a frequency equal to half the modulation frequency.

B. Observations of the island structure

Knowing that the beam bunch will be split into beamlets, as shown in Sec. III.2, we first measured the phase oscillation amplitude of the steady state solution by using the oscilloscope. The beam was injected, the rf voltage was modulated, and the beam was cooled with electron current 0.75 A. Then the steady state bunch distribution was measured. Figure 3.12 shows that the sum signals from a beam position monitor (BPM) on a fast oscilloscope triggered at the rf frequency exhibited two peaks around a central peak. A fast 1×10^9 sample per second oscilloscope was used to measure the profile of the beam in a single pass. The profile shown in Fig. 3.12 indicated that there were three beamlets in the $h = 1$ rf bucket. The beam particles were damped to attractors of the dissipative parametric resonant system. Thus the phase

amplitude of the outer peaks measured from the oscilloscope can be identified as the phase amplitude of the SFP.

Since the attractors (or islands) rotate around the origin of the rf bucket with half the modulation frequency, the observed beam profile in an oscilloscope is a time average of the BPM sum signal. Because the equilibrium beamlet distribution in a resonance island has a large aspect ratio in the local phase-space coordinates, the resulting beam profile will exhibit two peaks at the maximum phase amplitude, resembling that in Fig. 3.12. This implies that when a beamlet rotates to the upright position in the phase coordinate, a larger peak current can be observed. On the other hand, when a beamlet rotates to the flat position, where the SFPs are located on the $\mathcal{P}$ axis, the aspect ratio becomes small and the line density is also small.

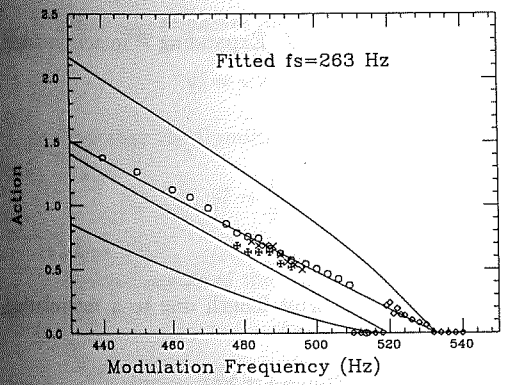

Figure 3.13: The measured action J of outer beamlets as a function of modulation frequency. Here $J \approx \frac{1}{2}\hat{\phi}^2$ with $\hat{\phi}$ as the peak phase amplitude of attractors. Different symbols correspond to measurements at different times for an almost identical rf voltage. The solid line for $J_{\rm SFP}$ obtained from Eq. (3.156) fits data with $f_s = 263$ Hz. The actions of UFP $J_{\rm UFP}$ and intercepts J_1 and J_2 of the separatrix with the phase axis are also shown.

The measured action J of the outer beamlets as a function of modulation frequency is shown in Fig. 3.13, where $J_{\rm SFP}$ of the Hamiltonian (3.153) is also shown for comparison. Experimentally, we found that the action of the outer attractor varied linearly with modulation frequency. Similarly, $J_{\rm SFP}$ is also a linear function of modulation frequency, where the slope depends sensitively on synchrotron frequency. Using this sensitivity, the synchrotron frequency was determined more accurately to be about 263±1 Hz for this run. Our experimental results agreed well with the theoretical prediction except in the region $f_m \in [510, 520]$ Hz, where we did not observe beam splitting. A possible explanation is that the actual beam size was larger than the separation of islands. In this case, the SFPs were about 100 ns from the center of the bucket. Once f_m reached $2f_s - \frac{1}{2}bf_s \approx 520$ Hz, where $J_{\rm UFP} = 0$, the beam was observed to split into only two beamlets. It was also clearly observed that all parametric resonance islands ceased to exist at $f_m = 2f_s + \frac{1}{2}bf_s \approx 532$ Hz.

Exercise 3.3

1. Prove the identity of the action integral in Eq. (3.90).

2. We consider a general Hamiltonian

$$H = \frac{1}{2}\nu_s \mathcal{P}^2 + V(\phi),$$

where $(\phi, \mathcal{P})$ are conjugate phase-space variables with orbiting angle θ as time variable, ν_s is the small amplitude synchrotron tune, and $V(\phi)$ is the potential.[28] The action is $J = (1/2\pi)\oint \mathcal{P} d\phi$. Using the generating function

$$F_2 = \int_0^{\phi} \mathcal{P} d\phi,$$

show that the coordinate transformation between phase variable ψ and coordinate ϕ is

$$d\psi = \frac{Q(J)}{\nu_s} d\phi,$$

where ψ is the conjugate phase variable to the action J. Expanding $\mathcal{P}$ in action-angle variables with

$$\mathcal{P} = \sum_{n=-\infty}^{\infty} f_n e^{in\psi},$$

prove the sum rule theorem

$$\sum_{n=-\infty}^{\infty} |f_n|^2 = \frac{Q(J)}{\nu_s} J.$$

3. From Exercise 2.4.8, we find that the change of orbit length due to a modulating dipole kicker is given by

$$\Delta C = D(s_0)\,\theta(t) = D(s_0)\,\hat{\theta}\,\sin(\omega_m t + \chi_0),$$

where $D(s_0)$ is the dispersion function at the dipole location, $\hat{\theta}$ is the maximum dipole kick angle, ω_m is the modulating angular frequency, and χ_0 is an arbitrary initial phase. The modulating tune is $\nu_m = \omega_m/\omega_0$, where ω_0 is the angular revolution frequency.

(a) Show that the modulating dipole field produces an equivalent rf phase error

$$\Delta\phi = \frac{2\pi h D(s_0)\hat{\theta}}{C}\sin(\omega_m t + \chi_0) = \hat{\Delta\phi}\sin(\omega_m t + \chi_0),$$

where C is the circumference of the synchrotron, and h is the harmonic number.

(b) Show that the amplitude of the equivalent rf wave phase error is

$$a = \hat{\Delta\phi}/2\pi\nu_m.$$

Give a physical argument that the amplitude of the equivalent rf wave phase error a is amplified as the modulation tune ν_m becomes smaller.

[28] In linear approximation, the potential can be expressed as $V(\phi) = \frac{1}{2}\nu_s\phi^2 + \cdots$. However, small amplitude behavior of the potential is not a necessary condition for the sum rule theorem stated in this exercise.

(c) Evaluate the effective rf modulation amplitude a for the accelerators listed in the table below, where C is the circumference, $\Delta B\ell$ is the integrated dipole field error, f_{mod} is the modulation frequency, D is the dispersion function at the dipole, γ is the Lorentz relativistic factor, and h is the harmonic number.

	IUCF Cooler	RHIC	MI	Recycler
C (m)	86.8	3833.8	3319.4	3319.4
$\Delta B\ell$ (Gm)	1	1	1	1
f_{mod} (Hz)	262	60	60	4
D (m)	4	1	1	1
γ	1.04796	24	21.8	9.5
h	1	342	588	1
a				

4. Using the conjugate phase space coordinates

$$Q = \sqrt{2J}\cos(\psi - \frac{1}{2}\nu_m\theta), \qquad P = -\sqrt{2J}\sin(\psi - \frac{1}{2}\nu_m\theta),$$

show that the Hamiltonian (3.153) for the quadrupole mode is

$$H = \frac{1}{2}(\delta + \frac{\nu_s b}{4})Q^2 + \frac{1}{2}(\delta - \frac{\nu_s b}{4})P^2 - \frac{\nu_s}{64}(Q^2 + P^2)^2,$$

where $\delta = \nu_s - (\nu_m/2)$ and, without loss of generality, we assume $b > 0$. Show that the fixed points of the Hamiltonian are located at

$$\begin{aligned}
P_{\text{SFP}} &= 0, \quad Q_{\text{SFP}} = 0 && (\nu_m > 2\nu_s + \nu_s b/2)\\
P_{\text{SFP}} &= 0, \quad Q_{\text{SFP}} = \sqrt{16(1 - \nu_m/2\nu_s) + 4b} && (\nu_m > 2\nu_s + \nu_s b/2)\\
Q_{\text{UFP}} &= 0, \quad P_{\text{UFP}} = 0 && (2\nu_s - \nu_s b/2 \le \nu_m \le 2\nu_s + \nu_s b/2)\\
Q_{\text{UFP}} &= 0, \quad P_{\text{UFP}} = \sqrt{16(1 - \nu_m/2\nu_s) - 4b} && (\nu_m \le 2\nu_s - \frac{1}{2}\nu_s b).
\end{aligned}$$

Compare this result with Eqs. (3.156) and (3.157). Show that the separatrix for $\nu_m \le 2\nu_s - \nu_s b/2$ is given by two circles

$$(Q - Q_c)^2 + P^2 = r^2, \qquad (Q + Q_c)^2 + P^2 = r^2$$

with

$$Q_c = \sqrt{4b}, \qquad r = \sqrt{16\delta/\nu_s}.$$

The separatrix in the betatron phase space for slow beam extraction that employs a half integer stopband is identical to that given in this exercise. Quadrupoles are used to provide resonance driving term b, and octupoles are used to provide nonlinear detuning α_{xx}. The resulting effective Hamiltonian is

$$H_{\text{eff}} = \nu_x J_x + \frac{1}{2}\alpha_{xx} J_x^2 + bJ_x\cos(\psi_x - \frac{\ell}{2}\theta),$$

where $\alpha_{xx} = (1/16\pi B\rho)\oint \beta_x^2 B_3 ds$ is the detuning parameter, B_3 is the octupole strength, and b is the half integer stopband width.

5. Show that the equation of motion for rf dipole on betatron motion in Eq. (2.182) near a betatron sideband can be casted into an effective Hamiltonian

$$H_{\text{eff}} = \nu J + \frac{1}{2}\alpha J^2 + gJ^{1/2}\cos(\psi - \nu_{\text{m}}\theta + \chi),$$

where ν, (J, ϕ), α are the tune, the action-angle coordinates, and the detuning parameter of the betatron motion, g is proportional to the rf dipole field strength, and ν_{m} is the rf dipole modulation tune. Find the fixed points of the Hamiltonian and discuss the dependence of the fixed point on parameters $\nu_{\text{m}} - \nu$, and α.

IV Nonadiabatic and Nonlinear Synchrotron Motion

Transition energy has been both a nuisance in machine operation and a possible blessing for attaining beam bunches with some desired properties, such as enhanced beam separation for filtering ion beams having nearly equal charge to mass ratios, and beam bunches with ultra-small beam width.[29] However, the synchrotron frequency spread vanishes at transition energy, and the circulating beams can suffer microwave instabilities and other collective instabilities for lack of Landau damping, to be discussed in Sec. VII.

Near the transition energy region, the adiabaticity condition (3.43) is not satisfied, i.e. the Hamiltonian is time dependent and is not a constant of motion. This results in non-adiabatic synchrotron motion, where the bucket area increases dramatically, and the phase-space area occupied by the beam bunch is a small fraction of the bucket area. The linearized rf potential is a good approximation. If the phase slip factor is independent of the off-momentum variable, we will obtain analytic solutions for the linearized synchrotron motion near transition energy in Sec. IV.1. The integral of the linearized Hamiltonian is also an ellipse, and the action is a constant of motion. We will discuss the scaling properties of the beam at the transition energy crossing.

However, when the phase slip factor η_0 of Eq. (3.18) becomes small, the nonlinear phase slip factor term η_1 can be important. This again raises another nonlinear problem in synchrotron motion, i.e. parts of a beam bunch can encounter a defocussing force during transition energy crossing. In Sec. IV.2 we study nonlinear synchrotron motion due to nonlinearity in phase slip factor. Although the action of a Hamiltonian flow is invariant, the torus is highly distorted and particles in a beam may be driven out of the rf bucket after crossing the transition energy. In Sec. IV.3 we examine beam manipulation techniques for particle acceleration through transition energy. In Sec. IV.4 we study the effects of nonlinear phase slip factor and examine the properties of the so-called α-bucket, and in Sec. IV.5 we study problems associated with quasi-isochronous (QI) storage rings, which may provide beam bunches with ultra-short bunch length.

[29] Since the bunch width becomes very short and the momentum spread becomes large at transition energy, transition energy may be used to generate short bunches. See e.g., R. Cappi, J.P. Delahye, and K.H. Reich, *IEEE Trans. Nucl. Sci.* **NS-28**, 2389 (1981). Using the sensitivity of the closed orbit to beam momentum at transition energy, one can filter beam momentum from nearly identical Z/A (charge to mass ratio) ion beams. Oxygen and sulfur ions have been filtered at transition energy in the CERN PS.

IV.1 Linear Synchrotron Motion Near Transition Energy

Since the energy gain per revolution in rf cavities is small, we assume $\gamma = \gamma_T + \dot{\gamma}t$, where $\dot{\gamma} = d\gamma/dt$ is the acceleration rate, and t is the time coordinate. The phase slip factor becomes

$$\eta_0 = \alpha_0 - \gamma^{-2} \approx \frac{2\dot{\gamma}t}{\gamma_T^3}. \tag{3.169}$$

Here we have neglected the dependence of the phase slip factor on the off-momentum coordinate δ, and assume that all particles in a bunch pass through transition energy at the same time. Substituting Eq. (3.169) into Eq. (3.27), we obtain

$$\omega_s^2 = \frac{|t|}{\tau_{ad}^3}, \tag{3.170}$$

where τ_{ad} is the *adiabatic time* given by

$$\tau_{ad} = \left(\frac{\pi\beta^2 mc^2\gamma_T^4}{\dot{\gamma}\omega_0^2 heV|\cos\phi_s|}\right)^{1/3}. \tag{3.171}$$

At $|t| \gg \tau_{ad}$, the adiabaticity condition (3.43) is satisfied.[30] Table 3.3 lists the adiabatic time for some proton synchrotrons.[31] Typically τ_{ad} is about 1–10 ms.

Table 3.3: The adiabatic and nonlinear times of some proton synchrotrons.

	FNAL Booster	FNAL MI	AGS	RHIC	KEKPS	CPS
C (m)	474.2	3319.4	807.12	3833.8	339.29	628.32
V (kV)	950	4000	300	300	90	200
h	84	588	12	360	9	6-20
γ_T	5.4	20.4	8.5	22.5	6.76	6.5
$\dot{\gamma}$ (s^{-1})	200	190	70	1.6	40	60
$\mathcal{A}$ (eVs/u)	0.04	0.04	1.	0.3	0.3	0.5
$\hat{\delta}$ ($\times 10^{-3}$)	6.4	2.5	6.7	4.5	5.4	6.6
τ_{ad} (ms)	0.2	2.0	2.5	36	1.8	1.5
τ_{nl} (ms)	0.13	0.19	0.61	63	0.7	0.5

[30] When $|t| \geq 4\tau_{ad}$ the adiabatic condition is approximately fulfilled because $\alpha_{ad} = |d(\omega_s^{-1})/dt| = \frac{1}{2}(\tau_{ad}/|t|)^{3/2} \approx 0.06$.

[31] Note that the beam parameters for RHIC correspond to those of a typical gold beam injected from the AGS with charge number $Z = 79$, and atomic mass number $A = 197$. The injection energy for proton beams in RHIC is above transition energy.

In linear approximation, the synchrotron equations of motion near the transition energy region become

$$\dot{\delta} = \frac{\omega_0 eV}{2\pi\beta^2 E}\cos\phi_s(\Delta\phi), \qquad (\dot{\Delta\phi}) = \frac{2h\omega_0\dot{\gamma}}{\gamma_T^3}t\,\delta, \tag{3.172}$$

where the overdot indicates the derivative with respect to time t, and $\delta = \Delta p/p_0$ and $\Delta\phi = \phi - \phi_s$ are the fractional off-momentum and phase coordinates of a particle. Taking into account the synchronous phase change from ϕ_s to $\pi - \phi_s$ across transition energy, we obtain

$$\frac{d}{dt}\left(\frac{\tau_{ad}^3}{|t|}\frac{d}{dt}\Delta\phi\right) + \Delta\phi = 0. \tag{3.173}$$

Defining a new time variable y as

$$y = \int_0^x x^{1/2}dx = \frac{2}{3}x^{3/2} \qquad \text{with} \qquad x = \frac{|t|}{\tau_{ad}}, \tag{3.174}$$

Eq. (3.173) can be transformed into Bessel's equation of order 2/3,

$$\varphi'' + \frac{1}{y}\varphi' + (1 - \frac{(2/3)^2}{y^2})\varphi = 0, \tag{3.175}$$

where $\varphi = y^{-2/3}\Delta\phi$, and the primes indicate derivatives with respect to time variable y. The solution of Eq. (3.175) can be written readily as[32]

$$\Delta\phi = bx\left[\cos\chi\, J_{2/3}(y) + \sin\chi\, N_{2/3}(y)\right], \tag{3.176}$$

where χ and b are constants to be determined from the initial condition. The off-momentum coordinate δ can be obtained from Eq. (3.172), i.e.

$$\dot{\Delta\phi} = \frac{2h\omega_0\dot{\gamma}t}{\gamma_T^3}\delta = \frac{\Delta\phi}{\tau_{ad}x} + \frac{bx^{2/3}}{\tau_{ad}}\left(\cos\chi\left[\frac{2J_{2/3}}{3y} - J_{5/3}\right] + \sin\chi\left[\frac{2N_{2/3}}{3y} - N_{5/3}\right]\right).$$

Combining this with Eq. (3.176), we obtain the constant of motion

$$\alpha_{\phi\phi}(\Delta\phi)^2 + 2\alpha_{\phi\delta}\Delta\phi\delta + \alpha_{\delta\delta}\delta^2 = 1, \tag{3.177}$$

where

$$\alpha_{\phi\phi} = \frac{\pi^2}{9b^2x^2}\left[\left(\frac{3}{2}yN_{5/3} - 2N_{2/3}\right)^2 + \left(2J_{2/3} - \frac{3}{2}yJ_{5/3}\right)^2\right],$$

$$\alpha_{\phi\delta} = \frac{\pi^2}{9b^2}\left(\frac{2h\dot{\gamma}\omega_0\tau_{ad}^2}{\gamma_T^3}\right)\left[N_{2/3}\left(\frac{3}{2}yN_{5/3} - 2N_{2/3}\right) - J_{2/3}\left(2J_{2/3} - \frac{3}{2}yJ_{5/3}\right)\right],$$

$$\alpha_{\delta\delta} = \frac{\pi^2}{9b^2}x^2\left(\frac{2h\dot{\gamma}\omega_0\tau_{ad}^2}{\gamma_T^3}\right)^2[J_{2/3}^2 + N_{2/3}^2].$$

[32] The Neumann function is defined as $N_\nu(z) = [J_\nu(z)\cos\pi\nu - J_{-\nu}(z)]/\sin\pi\nu$. It is also called the Bessel function of the second kind. The notation used for $N_\nu(z)$ is $Y_\nu(z)$ in Ref. [25].

There is no surprise that the constant of motion for a time dependent *linear* Hamiltonian is an ellipse. In (ϕ, δ) phase-space coordinates, the shape of the ellipse changes with time. The phase-space area enclosed in the ellipse of Eq. (3.177) is a *constant of motion* given by

$$\tilde{\mathcal{A}} = \frac{\pi}{\sqrt{\alpha_{\phi\phi}\alpha_{\delta\delta} - \alpha_{\phi\delta}^2}} = \frac{3b^2\gamma_{\rm T}^3}{2h\dot{\gamma}\omega_0\tau_{\rm ad}^2} = h\mathcal{A}\frac{\omega_0}{\beta^2\gamma_{\rm T}mc^2}, \tag{3.178}$$

where $\mathcal{A}$ is the phase-space area of the bunch in eV-s. Thus the parameter b is

$$b = \left(\frac{2\mathcal{A}h^2\omega_0^2\dot{\gamma}\tau_{\rm ad}^2}{3mc^2\beta^2\gamma_{\rm T}^4}\right)^{1/2}. \tag{3.179}$$

A. The asymptotic properties of the phase space ellipse

The phase-space ellipse is tilted in the transition energy region. Using a Taylor series expansion around $y = 0$, we obtain

$$\alpha_{\phi\phi} = \frac{\pi^2}{9b^2}\frac{4}{3^{1/3}[\Gamma(\frac{2}{3})]^2}, \tag{3.180}$$

$$\alpha_{\phi\delta} = -\frac{\pi^2}{9b^2}\left(\frac{2h\dot{\gamma}\omega_0\tau_{\rm ad}^2}{\gamma_{\rm T}^3}\right)\frac{\sqrt{3}}{\pi}, \tag{3.181}$$

$$\alpha_{\delta\delta} = \frac{\pi^2}{9b^2}\left(\frac{2h\dot{\gamma}\omega_0\tau_{\rm ad}^2}{\gamma_{\rm T}^3}\right)^2\frac{3^{4/3}[\Gamma(\frac{2}{3})]^2}{\pi^2}. \tag{3.182}$$

The tilt angle, the maximum momentum spread, and the maximum bunch width of the ellipse are

$$\psi = \frac{1}{2}\tan^{-1}\frac{2\alpha_{\phi\delta}}{\alpha_{\phi\phi} - \alpha_{\delta\delta}}, \tag{3.183}$$

$$\hat{\delta}\Big|_{\gamma=\gamma_{\rm T}} = \frac{\gamma_{\rm T}}{3^{1/6}\beta\tau_{\rm ad}\Gamma(\frac{2}{3})}\left(\frac{2\mathcal{A}}{3mc^2\dot{\gamma}}\right)^{1/2} \approx 0.502\frac{\gamma_{\rm T}}{\beta\tau_{\rm ad}}\left(\frac{\mathcal{A}}{mc^2\dot{\gamma}}\right)^{1/2}, \tag{3.184}$$

$$\hat{\phi}\Big|_{\gamma=\gamma_{\rm T}} = \sqrt{\frac{\alpha_{\delta\delta}}{\alpha_{\phi\phi}\alpha_{\delta\delta} - \alpha_{\phi\delta}^2}} = \frac{3^{2/3}\Gamma(\frac{2}{3})}{\pi}\left(\frac{2\mathcal{A}h^2\omega_0^2\dot{\gamma}\tau_{\rm ad}^2}{3mc^2\beta^2\gamma_{\rm T}^4}\right)^{1/2}. \tag{3.185}$$

Note that $\hat{\delta}$ is finite at $\gamma = \gamma_{\rm T}$ for a nonzero acceleration rate. At a higher acceleration rate, the maximum momentum width of the beam will be smaller. Substituting the adiabatic time $\tau_{\rm ad}$ of Eq. (3.171) into Eq. (3.184), we obtain the following scaling property:

$$\hat{\delta}\Big|_{\gamma=\gamma_{\rm T}} \sim h^{1/3}V^{1/3}\mathcal{A}^{1/2}\dot{\gamma}^{-1/6}\gamma_{\rm T}^{-1/3}. \tag{3.186}$$

The scaling property is important in the choice of operational conditions.

In the adiabatic region where $x \gg 1$, we can use asymptotic expansion of Bessel functions to obtain

$$\alpha_{\phi\phi} \to \frac{\pi^2}{3b^2}x^{-1/2}, \quad \alpha_{\phi\delta} \to 0, \quad \alpha_{\delta\delta} \to \frac{\pi^2}{3b^2}\left(\frac{2h\dot{\gamma}\omega_0\tau_{\rm ad}^2}{\gamma_{\rm T}^3}\right)^2 x^{1/2}.$$

The phase-space ellipse is restored to the upright position.

B. The equilibrium Gaussian distribution function at transition energy

The distribution function that satisfies the Vlasov equation is a function of the invariant ellipse (3.177). Using the Gaussian distribution function model, we obtain

$$\begin{aligned}\Psi_0(\Delta\phi, \delta) &= \frac{3N_{\rm B}(\alpha_{\phi\phi}\alpha_{\delta\delta} - \alpha_{\phi\delta}^2)^{1/2}}{\pi}\, e^{-3[\alpha_{\phi\phi}(\Delta\phi)^2 + 2\alpha_{\phi\delta}\delta(\Delta\phi) + \alpha_{\delta\delta}\delta^2]} \\ &= N_{\rm B}G_1(\Delta\phi)G_2(\delta),\end{aligned} \tag{3.187}$$

where $N_{\rm B}$ is the number of particles in the bunch, the factor 3 is chosen to ensure that the phase-space area $\mathcal{A}$ of Eq. (3.178) corresponds to 95% of the beam particles, and the normalized distribution functions $G_1(\Delta\phi)$ and $G_2(\delta)$ are

$$G_1(\Delta\phi) = \sqrt{\frac{3(\alpha_{\phi\phi}\alpha_{\delta\delta} - \alpha_{\phi\delta}^2)}{\pi\alpha_{\delta\delta}}}\, \exp\{-\frac{3(\alpha_{\phi\phi}\alpha_{\delta\delta} - \alpha_{\phi\delta}^2)}{\alpha_{\delta\delta}}(\Delta\phi)^2\}$$

$$G_2(\delta) = \sqrt{\frac{3\alpha_{\delta\delta}}{\pi}}\, \exp\{-3\alpha_{\delta\delta}(\delta + \frac{\alpha_{\phi\delta}}{\alpha_{\delta\delta}}\Delta\phi)^2\}.$$

Note here that $G_1(\Delta\phi)$ is the line charge density, and the peak current is still located at $\Delta\phi = 0$. Using the ellipse of Eq. (3.177), we can evaluate the evolution of the peak current at the transition energy crossing.

IV.2 Nonlinear Synchrotron Motion at $\gamma \approx \gamma_{\rm T}$

In Sec. IV.1, all particles were assumed to cross transition energy at the same time. This is not true, because the phase slip factor depends on the off-momentum coordinate δ. Near the transition energy region, the nonlinear phase slip factor of Eq. (3.17) becomes quite important. Expanding the phase slip factor up to first order in δ, the synchrotron equations of motion become

$$\dot{\Delta\phi} = h\omega_0\left(\frac{2\dot{\gamma}t}{\gamma_{\rm T}^3} + \eta_1\delta\right)\delta, \qquad \dot{\delta} = \frac{\omega_0 eV\cos\phi_{\rm s}}{2\pi\beta^2 E}(\Delta\phi), \tag{3.188}$$

where the synchronous particle crosses transition energy at time $t = 0$, and, to a good approximation, the phase slip factor has been truncated to second order in δ. At time

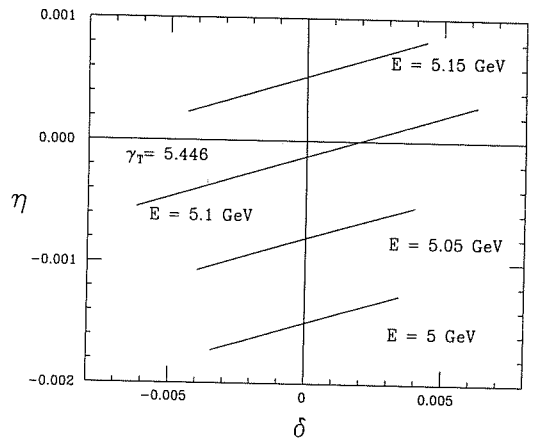

Figure 3.14: Schematic plot of η vs δ near the transition energy region for the Fermilab Booster, where $\gamma_T = 5.446$, $\gamma_T^2\alpha_1 = 0.5$, and a phase-space area of 0.05 eV-s are used to calculate $\eta(\delta)$ for the beam. A beam bunch is represented by a line of $\eta(\delta)$ vs δ. The synchrotron motion corresponds to particle motion along this line. At the beam synchronous energy of $E = 5.1$ GeV, which is below the transition energy of 5.11 GeV, particles at $\delta > 0.0018$ will experience unstable synchrotron motion due to the nonlinear phase slip factor.

$t = 0$, the synchronous phase is also shifted from ϕ_s to $\pi - \phi_s$ in order to achieve stable synchrotron motion.

Figure 3.14 shows the phase slip factor η vs the fractional off-momentum coordinate δ near transition energy for a beam in the Fermilab Booster. A beam bunch with momentum width $\pm\hat{\delta}$ is represented by a short tilted line. At a given time (or beam energy), particles are projected onto the off-momentum axis represented by this line. Since the phase slip factor is nonlinear, the line is tilted. When the beam is accelerated (or decelerated) toward transition energy, a portion of the beam particles can cross transition energy and this leads to unstable synchrotron motion, as shown in the example at 5.1 GeV beam energy in Fig. 3.14. Since the synchrotron motion is slow, we hope that the unstable motion does not give rise to too much bunch distortion before particles are recaptured into a stable bucket.

To characterize nonlinear synchrotron motion, we define the *nonlinear time* τ_{nl} as the time when the phase slip factor changes sign for the particle at the maximum momentum width $\hat{\delta}$ of the beam, i.e. $\eta_0 + \eta_1\hat{\delta} = -(2\dot{\gamma}\tau_{nl}/\gamma_T^3) + \eta_1\hat{\delta} = 0$, or

$$\tau_{nl} = \gamma_T^3 \frac{\eta_1}{2\dot{\gamma}}\hat{\delta} = \gamma_T \frac{\frac{3}{2}\beta_0^2 + \gamma_T^2\alpha_1}{2\dot{\gamma}}\hat{\delta}, \tag{3.189}$$

where $\hat{\delta}$ is the maximum fractional momentum spread of the beam, η_1 is obtained from Eq. (3.17), and the α_1 term can be adjusted by sextupoles. For a lattice without sextupole correction, we typically have $\gamma_T^2\alpha_1 \approx 1$ (see footnote 3). Within the nonlinear time $\pm\tau_{nl}$, some portions of the beam could experience unstable synchrotron motion. Note that the nonlinear time depends on the off-momentum width of the beam. Table 3.3 lists the nonlinear time of some accelerators, where $\alpha_1 = 0$ is assumed. Note that the nonlinear time for RHIC is particularly long because superconducting magnets can tolerate only a slow acceleration rate.

When the beam is accelerated toward transition energy to within the range

$$\gamma_T - \dot{\gamma}\tau_{nl} \le \gamma \le \gamma_T + \dot{\gamma}\tau_{nl},$$

the phase equation begins to change sign for particles at higher momenta while the phase angle ϕ_s has not yet been shifted. Therefore these particles experience defocussing synchrotron motion. After the synchronous energy of the bunch reaches transition energy and the synchronous phase has also been shifted from ϕ_s to $\pi - \phi_s$, lower momentum portions of the bunch will experience defocussing synchrotron motion. The problem is most severe for accelerators with a slow acceleration rate.

The relative importance of non-adiabatic and nonlinear synchrotron motions depends on the adiabatic time of Eq. (3.171) that governs the adiabaticity of the synchrotron motion, and the nonlinear time τ_{nl}, within which some portion of the beam particles experiences unstable synchrotron motion. Using Eq. (3.188), we obtain

$$\delta'' = -x\delta + \frac{\tau_{nl}}{\tau_{ad}}\frac{\delta^2}{\hat{\delta}}, \tag{3.190}$$

where the primes indicate derivatives with respect to $x = |t|/\tau_{ad}$. Note that when the nonlinear time τ_{nl} vanishes, the solution of Eq. (3.190) is an Airy function, discussed in Sec. IV.1. Since the solution of the nonlinear equation is not available, we estimate the growth of momentum width by integrating the unstable exponent. The growth factor is

$$G = \exp\left\{\int_0^{\tau_{nl}/\tau_{ad}} \left(-x + \frac{\tau_{nl}}{\tau_{ad}}\right)^{1/2} dx\right\} = \exp\left\{\frac{2}{3}\left(\frac{\tau_{nl}}{\tau_{ad}}\right)^{3/2}\right\} \tag{3.191}$$

for a particle with $\delta = \hat{\delta}$. The maximum momentum height is increased by the growth factor G, which depends exponentially on τ_{nl}/τ_{ad}. Depending on the adiabatic and nonlinear times, the effects of nonlinear synchrotron motion and of microwave instability can be analyzed.[33]

We have seen that the momentum width will increase due to the nonlinear phase slip factor. However, we should bear in mind that the synchrotron motion can be derived from a Hamiltonian

$$H = \frac{1}{2}h\omega_0\left[\eta_0 + \frac{2}{3}\eta_1\delta\right]\delta^2 - \frac{\omega_0 eV}{4\pi^2\beta^2 E}\cos\phi_s(\Delta\phi)^2, \tag{3.192}$$

where $\eta_0 = 2\dot{\gamma}t/\gamma_T^3$. Expressing Hamilton's equation as a difference mapping equation, we can easily prove that the Jacobian is 1. Therefore the area of the phase-space ellipse of each particle is conserved, and the 1D dynamical system is integrable. The action integral is a distorted curve in phase-space coordinates. When the bunch is

[33] The microwave instability will be discussed in Sec. VII.

accelerated through transition energy, some portions of the phase-space torus may lie outside the stable ellipse of the synchrotron Hamiltonian. They may be captured by other empty buckets of the rf system, or may be lost because of the aperture limitation. For a modern high intensity hadron facility, the loss would cause radiation problems; therefore efforts to eliminate transition energy loss are important.

IV.3 Beam Manipulation Near Transition Energy

Near the transition energy, the revolution frequencies of all particles are nearly identical, i.e. the beam is isochronous or quasi-isochronous. Since there is no frequency spread for Landau damping, the beam can suffer microwave instability. The tolerance of microwave instability near transition energy will be discussed in Sec. VII.

The nonlinear phase slip factor can cause defocussing synchrotron motion for a portion of the bunch. The growth of the bunch area is approximately $G^2 = \exp\{\frac{4}{3}(\tau_{\rm nl}/\tau_{\rm ad})^{3/2}\}$ shown in Eq. (3.191). The 5% beam loss at transition energy found for proton synchrotrons built in the 60's and 70's may arise mainly from this nonlinear effect. Bunched beam manipulation are usually needed to minimize beam loss and uncontrollable emittance growth. Minimizing both $\tau_{\rm ad}$ and $\tau_{\rm nl}$ provides cleaner beam acceleration through the transition energy.

A. Transition energy jump

By applying a set of quadrupoles, transition energy can be changed suddenly in order to attain fast transition energy crossing (see Chap. 2, Sec. IV.8). The effective $\gamma_{\rm T}$ crossing rate is $\dot{\gamma}_{\rm eff} = \dot{\gamma} - \dot{\gamma}_{\rm T}$. For example, if $\gamma_{\rm T}$ is changed by one unit in 1 ms,[34] the effective transition energy crossing rate is 1000 s^{-1}, which is much larger than the beam acceleration rates listed in Table 3.3.

Transition $\gamma_{\rm T}$ jump has been employed routinely in the CERN PS. The scheme has also been studied in the Fermilab Booster and Main Injector, the KEK PS, and the AGS. The minimum $\gamma_{\rm T}$ jump width is

$$\Delta\gamma_{\rm T} = 2\dot{\gamma} \times {\rm Max}(\tau_{\rm ad}, \tau_{\rm nl}). \tag{3.193}$$

B. Use of momentum aperture for attaining faster beam acceleration

The synchronization of dipole field with synchronous energy is usually accomplished by a "radial loop," which provides a feedback loop for rf voltage and synchronous phase angle. In most accelerators, the maximum $\dot{B}$ is usually limited, but the rf voltage and synchronous phase angle can be adjusted to move the beam across the

[34] The $\gamma_{\rm T}$ jump time scale is non-adiabatic with respect to synchrotron motion. However, the time scale can be considered as adiabatic in betatron motion so that particles adiabatically follow the new betatron orbit.

momentum aperture. The radial loop can be programmed to keep the beam closed orbit inside the nominal closed orbit below transition energy, and to attain faster acceleration across transition energy so that the beam closed orbit is outside the nominal closed orbit above transition energy. For an experienced machine operator to minimize the beam loss with a radial loop, the essential trick is to attain a faster transition energy crossing rate.

C. Flatten the rf wave near transition energy

Near transition energy, partial loss of focusing force in synchrotron motion can be alleviated by flattening the rf wave. This can be done by choosing $\phi_{\rm s} = \pi/2$ or employing a second or third harmonic cavity.[35] In the flattened rf wave, all particles gain an equal amount of energy each turn, and thus δ of each particle is approximately constant in a small energy range.

The solution of Eq. (3.188) with $\dot{\delta} = 0$ is

$$\Delta\phi = \Delta\phi_1 + \frac{h\omega_0\dot{\gamma}\delta}{\gamma_{\rm T}^3}(t^2 - t_1^2) + \eta_1 h\omega_0\delta^2\ (t - t_1), \tag{3.194}$$

where t_1 is the rf flattening period, $(\Delta\phi_1, \delta_1)$ are the initial phase-space coordinates of the particle, and $\delta = \delta_1$. Figure 3.15 shows the evolution of the phase-space torus when the rf wave is flattened across the transition energy region; the parameters used in this calculations are $\gamma_{\rm T} = 22.5$, $\omega_0 = 4.917 \times 10^5$ rad/s, $\dot{\gamma} = 1.6$ s^{-1}, $h = 360$, $t_1 = -63$ ms, and $\gamma_{\rm T}^2\eta_1 \approx 2$. Note that the ellipse evolves into a boomerang shaped distribution function with an equal phase-space area. The rf flattening scheme is commonly employed in isochronous cyclotrons.

IV.4 Synchrotron Motion with Nonlinear Phase Slip Factor

In the production of secondary beams, very short proton bunches are needed for attaining small emittance. Very short electron bunches, e.g. sub-millimeter in bunch length, have many applications such as time resolved experiments with synchrotron light sources, coherent synchrotron radiation, and damping rings for the next linear colliders. Since the ratio of bunch length to bunch height is proportional to $\sqrt{|\eta|}$, a possible method of producing short bunches is to operate the accelerator in an isochronous condition for proton synchrotrons, or to reduce the momentum compaction factor for electron storage rings. Because of its potential benefit of the low η condition, we carefully study the physics of the QI dynamical system.[36]

[35] see e.g., C.M. Bhat *et al.*, *Phys. Rev.* E **55**, 1028 (1997). The AVF cyclotron has routinely employed this method for beam acceleration. This concept was patented by G.B. Rossi, U.S. Patent 2778937 (1954).

[36] A. Riabko *et al.*, *Phys. Rev.* E**54**, 815 (1996); D. Jeon *et al.*, *Phys. Rev.* E**54**, 4192 (1996); M. Bai *et al.*, *Phys. Rev.* E**55**, 3493 (1997); C. Pellegrini and D. Robin, *Nucl. Inst. Methods*, A **301**,

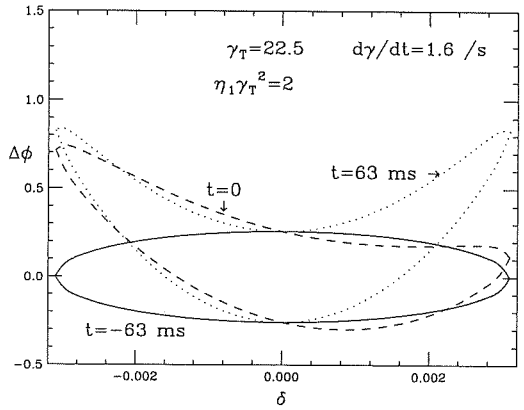

Figure 3.15: The evolution of a phase-space ellipse in the flattened rf wave near the transition energy region. Note that the off-momentum coordinates of each particle are unchanged, while the bunch length elongates along the ϕ axis.

Table 3.2 and Eq. (3.60) show that the synchrotron bucket height and momentum spread become very large when $|\eta|$ is small. This requires careful examination because when the phase slip factor η is small, its dependence on the fractional momentum deviation δ becomes important. The synchrotron Hamiltonian needs to take into account the effects of nonlinear phase slip factor.

Expanding the phase slip factor as $\eta = \eta_0 + \eta_1\delta + \cdots$ and using the orbiting angle θ as the independent variable, we obtain the Hamiltonian for synchrotron motion as

$$H = \frac{1}{2}h\left(\eta_0 + \frac{2}{3}\eta_1\delta\right)\delta^2 + \frac{eV}{2\pi\beta^2 E}[\cos\phi - \cos\phi_s + (\phi - \phi_s)\sin\phi_s], \tag{3.195}$$

where we have truncated the phase slip factor to the second order in δ. The fixed points of the nonlinear synchrotron Hamiltonian are

$$(\phi, \delta)_{\rm SFP} = (\phi_s,\ 0), \qquad (\pi - \phi_s,\ -\eta_0/\eta_1), \tag{3.196}$$

$$(\phi, \delta)_{\rm UFP} = (\pi - \phi_s,\ 0), \qquad (\phi_s,\ -\eta_0/\eta_1). \tag{3.197}$$

Note that the nonlinear phase slip factor introduces another set of fixed points in the phase space. The fixed points with $\delta_{\rm FP} = 0$ are the nominal fixed points. The fixed points with $\delta_{\rm FP} = -\eta_0/\eta_1$ arising from the nonlinear-phase-slip factor are called nonlinear-phase-slip-factor (NPSF) fixed points. These fixed points play important role in determining the dynamics of synchrotron motion.

We define $\nu_s = \sqrt{h|\eta_0|eV/2\pi\beta^2 E}$ for small amplitude synchrotron tune, and use the normalized phase space coordinates ϕ and $\mathcal{P} = (h\eta_0/\nu_s)\delta$. The Hamiltonian of

27 (1991); D. Robin, *et. al.*, *Phys. Rev.* **E48**, 2149 (1993); H. Bruck *et al.*, *IEEE Trans. Nucl. Sci.* **NS20**, 822 (1973); L. Liu *et al.*, *Nucl. Instru. Methods*, **A329**, 9 (1993); H. Hama, S. Takano and B. Isoyama, *Nucl. Instru. Methods*, **A329**, 29 (1993); S. Takano, H. Hama and G. Isoyama, *Japan J. Appl. Phys.* **32**, 1285 (1993); A. Nadji *et al.*, *Proc. EPAC94* p. 128 (1994); D. Robin, H. Hama, and A. Nadji, LBL-37758 (1995).

synchrotron motion becomes

$$H = \frac{1}{2}\nu_s\mathcal{P}^2 + \frac{1}{2y}\nu_s\mathcal{P}^3 + \nu_s[\cos\phi - \cos\phi_s + (\phi - \phi_s)\sin\phi_s]. \tag{3.198}$$

The parameter

$$y = 3h\eta_0^2/2\eta_1\nu_s \tag{3.199}$$

signifies the relative importance of the linear and nonlinear parts of the phase slip factor. If $|y| \gg 1$, the nonlinear phase slip factor is not important, and if $|y|$ is small, the phase space tori will be deformed.

Figure 3.16 shows the separatrix of the nonlinear Hamiltonian in normalized phase space coordinates for $\phi_s = 150°$ and $180°$ respectively, where, without loss of generality, we have assumed $\eta_0 > 0$ and $\eta_1 > 0$. The separatrix that passes through the nominal fixed points are nominal separatrix. When the nominal separatrix crosses the unstable NPSF fixed point, the separatrix of two branches will become one (see the middle plots of Fig. 3.16 and Exercise 3.4.6). This condition occurs at $y = y_{\rm cr}$, given by

$$y_{\rm cr} = \sqrt{27[(\pi/2 - \phi_s)\sin\phi_s - \cos\phi_s]}. \tag{3.200}$$

For $y \gg y_{\rm cr}$, the stable buckets of the upper and lower branches are separated by a distance of $\Delta\mathcal{P} = 2y/3$. Particle motion can be well described by neglecting the $\mathcal{P}^3$ term in the Hamiltonian.

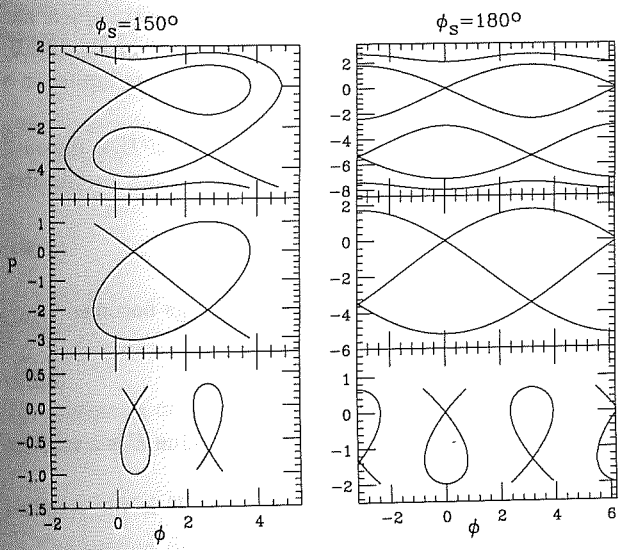

Figure 3.16: Left: Separatrix in the normalized phase space (ϕ, $P = \mathcal{P}$) for the synchrotron Hamiltonian with parameters $\phi_s = 150°$ and $y = 5$ (top), $y = y_{\rm cr} = 3.0406$ (middle) and 1 (bottom); Right: Separatrix with parameters $\phi_s = 180°$ and $y = 8$ (top), $y = y_{\rm cr} = 5.1962$ (middle), and 3 (bottom). In this example, we assume $\eta_0 > 0$ and $\eta_1 > 0$. Note the dependence of the Hamiltonian tori on the parameter y.

For $y < y_{\rm cr}$, the separatrix ("fish") is deformed into up-down shape (see lower plots). They are called "α-bucket." Since the α-bucket is limited in a small region

of the phase coordinate ϕ, small angle expansion is valid. The particle motion inside such a quasi-isochronous (QI) dynamical system can be analytically solved as follows.

IV.5 The QI Dynamical Systems

The synchrotron equation of motion for the rf phase coordinate ϕ of a particle is

$$\dot{\phi} = h\eta\delta, \tag{3.201}$$

where h is the harmonic number, $\delta = \Delta p/p_0$ is the fractional momentum deviation from a synchronous particle, the overdot indicates the derivative with respect to the orbiting angle $\theta = s/R_0$, and η is the phase slip factor given by

$$\eta = \eta_0 + \eta_1\delta + \cdots, \tag{3.202}$$

where η_0 and η_1 are the first order and second order phase slip factors. In many storage rings, truncation of the phase slip factor at the η_1 term is a good approximation. Similarly, the equation of motion for the fractional off-momentum deviation is

$$\dot{\delta} = \frac{eV_0}{2\pi\beta^2 E_0}[\sin(\phi+\phi_s) - \sin\phi_s] \approx \frac{eV_0\cos\phi_s}{2\pi\beta^2 E}\,\phi, \tag{3.203}$$

where V_0 and ϕ_s are the rf voltage and synchronous phase angle, βc is the speed, and E_0 is the energy of the beam. Here, the linearized phase coordinate in Eq. (3.203) is a good approximation because the (up-down) synchrotron bucket is limited in a small range of the phase coordinate (see Fig. 3.16).

With $t = \nu_s\theta$ as the time variable, where $\nu_s = \sqrt{heV_0|\eta_0\cos\phi_s|/2\pi\beta^2 E_0}$ is the small amplitude synchrotron tune, and with (x, p) as conjugate phase-space coordinates, where

$$x \doteq -\frac{\eta_1}{\eta_0}\frac{\Delta p}{p_0}, \quad p = \frac{\nu_s\eta_1}{h\eta_0^2}\phi, \tag{3.204}$$

the synchrotron Hamiltonian for particle motion in QI storage rings becomes

$$H_0 = \frac{1}{2}p^2 + \frac{1}{2}x^2 - \frac{1}{3}x^3. \tag{3.205}$$

This universal Hamiltonian is autonomous and the Hamiltonian value E is a constant of motion with $E \in [0, \frac{1}{6}]$ for particles inside the bucket.

The equation of motion for the QI Hamiltonian with $H_0 = E$ is the standard Weierstrass equation,

$$\left(\frac{d\wp(u)}{du}\right)^2 = 4(\wp - e_1)(\wp - e_2)(\wp - e_3), \tag{3.206}$$

where $u = t/\sqrt{6}$, $\wp = x$, and the turning points are

$$e_1 = \frac{1}{2} + \cos(\xi), \quad e_2 = \frac{1}{2} + \cos(\xi - 120°), \quad e_3 = \frac{1}{2} + \cos(\xi + 120°)$$

with $\xi = \frac{1}{3}\arccos(1 - 12E)$. The ξ parameter for particles inside the bucket varies from 0 to $\pi/3$. Figure 3.17 shows the separatrix of the QI bucket QI potential, and the turning points, where e_2 and e_3 are turning points for stable particle motion.

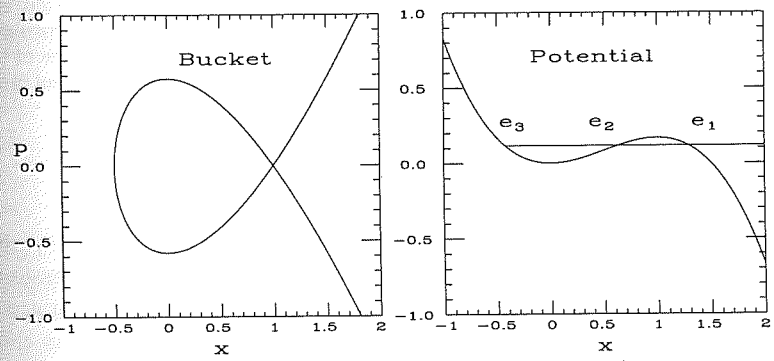

Figure 3.17: Schematic plots of the QI bucket (left) and the QI potential (right). The turning points e_1, e_2, and e_3 are also shown. The separatrix of the QI bucket is one of the separatrix, plotted sideway, shown in Fig. 3.16.

The Weierstrass elliptic $\wp$-function is a single valued doubly periodic function of a single complex variable. For particle motion inside the separatrix, the discriminant $\Delta = 648E(1 - 6E)$ is positive, and the Weierstrass $\wp$ function can be expressed in terms of the Jacobian elliptic function [25]

$$x(t) = e_3 + (e_2 - e_3)\,\mathrm{sn}^2\left(\sqrt{\frac{e_1 - e_3}{6}}\,t|m\right), \tag{3.207}$$

$$m = \frac{e_2 - e_3}{e_1 - e_3} = \frac{\sin\xi}{\sin(\xi + 60°)}. \tag{3.208}$$

The separatrix orbit, which corresponds to $m = 1$, is

$$x_{sx}(t) = 1 - \frac{3}{\cosh t + 1}, \quad p_{sx}(t) = \frac{3\sinh t}{(\cosh t + 1)^2}. \tag{3.209}$$

The tune of the QI Hamiltonian is

$$Q(E) = \frac{\pi[\sqrt{3}\sin(\xi + 60°)]^{1/2}}{\sqrt{6}K(m)}. \tag{3.210}$$

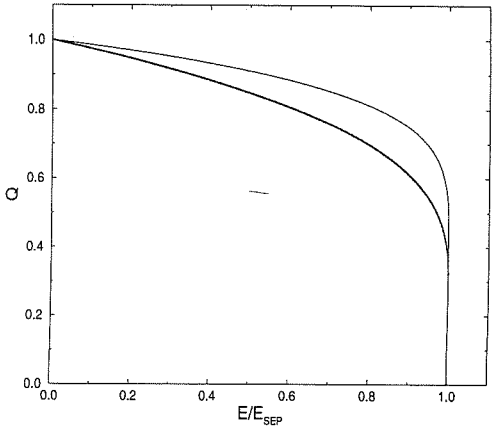

Figure 3.18: The synchrotron tune of the QI dynamical system (upper curve) is compared with that of a single rf potential (lower curve). Note that the sharp drop of the QI synchrotron tune at the separatrix can cause chaotic motion for particles with large synchrotron amplitudes under the influence of the low-frequency time-dependent perturbation.

The tune of the QI Hamiltonian is compared with that of the normal synchrotron Hamiltonian in Fig. 3.18. Here, we note that the synchrotron tune decreases to zero very sharply near the separatrix. Because of the sharp decrease in synchrotron tune, time dependent perturbation will cause overlapping parametric resonances and chaos near the separatrix.[37]

The action of a torus is

$$J = \frac{1}{2\pi}\oint p dx = \frac{1}{8}\sqrt{\frac{2}{3}}\,(e_2 - e_3)^2(e_1 - e_3)^{1/2} F\left(\frac{3}{2}, -\frac{1}{2}; 3; m\right), \tag{3.211}$$

where F is the hypergeometric function [25]. The action of the separatrix orbit is $J_{sx} = 3/5\pi$, or equivalently the bucket area id 6/5. Using the generating function

$$F_2(x, J) = \int_{e_3}^{x} p\, dx, \tag{3.212}$$

the angle variable is $\psi = \partial F_2/\partial J = Qt$. The resulting Hamiltonian is

$$H_0(J) \approx J - \frac{5}{12}J^2 + \cdots.$$

Because of the synchrotron radiation damping, the equation of motion for QI electron storage rings is

$$x'' + Ax' + x - x^2 = 0, \tag{3.213}$$

[37] H. Huang, *et al.*, *Phys. Rev.* **E48**, 4678 (1993); M. Ellison, *et al.*, *Phys. Rev. Lett.* **70**, 591 (1993); M. Syphers, *et al.*, *Phys. Rev. Lett.* **71**, 719 (1993); Y. Wang, *et al.*, *Phys. Rev.* **E49**, 1610 (1994). D. Li, *et al.*, *Phys. Rev.* **E48**, R1638 (1993); D. Li, *et al.*, *Nucl. Inst. Methods*, **A364**, 205 (1995).

where the effective damping coefficient is

$$A = \frac{\lambda}{\nu_s} = \frac{U_0 J_E}{2\pi E_0 \nu_s}. \tag{3.214}$$

Here λ is the damping decrement, U_0 is the energy loss per revolution, and J_E is the damping partition number. In QI storage rings, the effective damping coefficient is enhanced by a corresponding decrease in synchrotron tune, i.e. $A \sim |\eta_0|^{-1/2}$, where the value of A can vary from 0 to 0.5.

Including the rf phase noise, the Hamiltonian in normalized phase-space coordinates is

$$H = \frac{p^2}{2} + \frac{1}{2}x^2 - \frac{1}{3}x^3 + \omega_m B x \cos\omega_m t, \tag{3.215}$$

where

$$B = \frac{\eta_1 a}{\eta_0 \nu_s} \tag{3.216}$$

is the effective modulation amplitude, a is the rf phase modulation amplitude, $\omega_m = \nu_m/\nu_s$ is the normalized modulation tune, and ν_m is the modulation tune of the original accelerator coordinate system. Note that the effective modulation amplitude B is greatly enhanced for QI storage rings by the smallness of η_0, i.e. $B \sim |\eta_1|/|\eta_0|^{3/2}$. Including the damping force, the equation of motion becomes

$$x'' + A\,x' + x - x^2 = -\omega_m\, B \cos\omega_m t. \tag{3.217}$$

The stochasticity of such a dynamical system has been extensively studied.[38] Experimental verification of the QI dynamical system has not been fully explored. Detailed discussions of this topic is beyond this introductory textbook.

Exercises 3.4

1. Verify the adiabatic time, the nonlinear time, and the momentum spread of the beam $\hat{\delta}$ at $\gamma = \gamma_T$ for the accelerators listed in Table 3.3.

2. Show that Eq. (3.172) can be reduced to

$$\delta'' + x\delta = 0$$

where the primes indicate derivatives with respect to the variable $x = |t|/\tau_{ad}$, where τ_{ad} is the adiabatic time of Eq. (3.171).

(a) Express the solution in terms of Airy functions and find the equation for the invariant torus.

[38] A. Riabko *et al.*, *Phys. Rev.* **E54**, 815 (1996); D. Jeon *et al.*, *Phys. Rev.* **E54**, 4192 (1996); M. Bai *et al.*, *Phys. Rev.* **E55**, 3493 (1997).

(b) Verify Eq. (3.177).

3. Show that $\tau_{\rm nl}/\tau_{\rm ad} \propto \dot{\gamma}^{-5/6}\gamma_{\rm T}^{-2/3}$. Discuss the effects of high vs low $\gamma_{\rm T}$ lattices on the dynamics of synchrotron motion near the transition energy.

4. The Fermilab Main Injector accelerates protons from 8.9 GeV to 120 GeV in 1 s. Assuming $\gamma_T = 20.4$, calculate the characteristic time and the maximum momentum spread for a phase space area of 0.04 eV-s.

5. Show that the phase space area enclosed by $(\Delta\phi, \delta)$ of Eq. (3.194) is equal to the phase space area enclosed by $(\Delta\phi_1, \delta_1)$ of the initial ellipse.

6. Using the normalized phase space coordinates ϕ and $\mathcal{P}$, show that the Hamiltonian (3.195) with nonlinear phase slip factor depends only on a single parameter $y = 3h\eta_0^2/2\nu_s\eta_1$. Show that the separatrices of the Hamiltonian are

$$\nu_s\mathcal{P}^3 + y\mathcal{P}^2 + 2y[\cos\phi + \cos\phi_{\rm s} + (\phi + \phi_{\rm s} - \pi)\sin\phi_{\rm s}] = 0,$$
$$\nu_s\mathcal{P}^3 + y\mathcal{P}^2 + 2y[\cos\phi - \cos\phi_{\rm s} + (\phi - \phi_{\rm s})\sin\phi_{\rm s}] - \frac{4}{27}y^3 = 0.$$

Show that when $y = y_{\rm cr}$ of Eq. (3.200) the separatrix of the upper branch passes through the UFP of the lower branch.

7. Show that the QI Hamiltonian can be reduced to Eq. (3.205) and that the solution is given by the Weierstrass elliptical function.

V Beam Manipulation in Synchrotron Phase Space

A charged particle beam is usually produced by an intense ion source, pre-accelerated by an electrostatic Cockcroft-Walton or an RFQ, prebunched and injected into a linac to reach an injection energy for low energy synchrotrons, called booster synchrotrons or boosters. The beam is accumulated, phase-space painted, stacked in a low energy booster, and accelerated toward higher energies by a chain of synchrotrons of various sizes. The reasons for this complicated scheme are economics and beam dynamics issues. Since dipole and quadrupole magnets have low and high field operational limits, the range of beam energy for a synchrotron is limited. The mean-field Coulomb force can also have a large effect on the stability of low energy beams in boosters, where the space-charge tune shift, proportional to circumference of the synchrotron, is limited to about 0.3–0.4.

For acceleration of ion beams, the fractional change of beam velocity in low energy boosters can be large; accordingly, rf frequency for a low energy booster has to be tuned in a wide range. The rf voltage requirement is determined by technical issues such as rf cavity design, rf power source, etc., and the beam dynamics issues of minimum momentum aperture and phase-space area. During beam acceleration, phase-space area is normally conserved. The beam distribution function can thus be manipulated to attain desirable properties for experiments. Careful consideration is thus needed to optimize the operation and construction costs of accelerators.

On the other hand, electrons are almost relativistic at energies above 10 MeV, and the required range of rf frequency change is small. However, electrons emit synchrotron radiation, which must be compensated by the longitudinal rf electric field in a storage ring. Since synchrotron radiation power depends on particle energy, and the mean energy loss of a beam is compensated by the rf field, particle motion in synchrotron phase-space is damped. The synchrotron radiation emitted by a relativistic electron is essentially concentrated in a cone with an angular divergence of $1/\gamma$ along its path, and the energy compensation of the rf field is along the longitudinal direction; the betatron motion is also damped. Equilibrium is reached when the quantum fluctuation due to the emission of photons and the synchrotron radiation damping are balanced. The resulting momentum spread is independent of the rf voltage, and the transverse emittance depends essentially on the lattice arrangement. The effects of synchrotron radiation must be taken into account in beam manipulation.

In this section we examine applications of the rf systems in the bunched beam manipulations, including phase displacement acceleration, phase-space stacking, adiabatic capture, bucket to bucket transfer, bunch rotation, and debunching. We carefully study the double rf systems, that have often been applied in the space charge dominated beams and high brilliance electron storage rings for providing a larger tune spread for Landau damping. We also study the barrier rf systems that have been proposed for low energy proton synchrotrons. In general, innovative bunched

beam manipulation schemes can enhance beam quality for experiments.

V.1 RF Frequency Requirements

Particle acceleration in synchrotrons requires synchronism between rf frequency and particle revolution frequency. Thus the rf frequency is an integer multiple of the revolution frequency $\omega_{\rm rf} = h\omega_0(B, R_0)$, where h is the harmonic number, and the angular revolution frequency ω_0 is a function of the magnetic field B and the average radius of the synchrotron R_0. The momentum p_0 of a particle is related to the magnetic field by $p_0 = e\rho B$, where ρ is the bending radius, and e is the particle's charge. Thus the rf frequency is

$$\omega_{\rm rf} = h\frac{\beta c}{R_0} = \frac{he\rho B}{R_0\gamma m} = \frac{hc}{R_0}\left[\frac{B^2(t)}{B^2(t) + (mc^2/ec\rho)^2}\right]^{1/2}, \tag{3.218}$$

where m is the particle's mass. The rf frequency is a function of the dipole magnetic field. Since

$$\frac{mc^2}{ec\rho} = \begin{cases} 3.1273/\rho\,[\text{m}]\ \text{Tesla} & \text{for protons,} \\ 0.001703/\rho\,[\text{m}]\ \text{Tesla} & \text{for electrons,} \end{cases} \tag{3.219}$$

rf frequency ramping is particularly important for low energy proton or ion accelerators. In low to medium energy synchrotrons, the rf system is usually limited by the range of required frequency swing. Table V.1 lists parameters of some proton synchrotrons.

Table 3.4: RF parameters of some proton synchrotrons

	AGS BST	AGS	RHIC	FNALBST	FNALMI
Inj. K.E. [GeV/u]	0.001/0.2	0.2(1.5)	12	0.2(0.4)	8.0
Acc. Rate [GeV/s]	100	60	3.7	200	100
Max. K.E. [GeV]	1.5	30	250	8	500
$f_{\rm rf}$ [MHz]	0.18–4.1	2.4–4.6	26.68–26.74	30.0–52.8	52.8–53.1
Av. Radius [m]	$(1/4)R_{\rm ags}$	128.457	$(19/4)R_{\rm ags}$	75.47	528.30
h	1–3 (2)	12 (8)	6×60	84	7×84
$V_{\rm rf}$ [kV]	90	300	300	950	4000

In some applications, the magnetic field can be ramped linearly as $B = a + bt$, or resonantly as $B = (\hat{B}/2)(1 - \cos\omega t) = \hat{B}\sin^2(\omega t/2)$, with ramping frequency $\omega/2\pi$ varying from 1 Hz to 50 Hz; the rf frequency should follow the magnetic field ramp according to Eq. (3.218), for which cavities with ferrite tuners are usually used. On the other hand, electrons are nearly relativistic at all energies, and the rf frequency swing is small. High frequency pill-box-like cavities are usually used. Normally the

frequency range can be in the 200, 350, 500, and 700 MHz regions, where rf power sources are readily available. In recent years, wideband solid state rf power sources and narrowband klystron power sources have been steadily improved. New methods of beam manipulation can be employed.

Requirements of rf systems depend on their applications. To achieve high beam power in meson factories and proton drivers for spallation neutron sources, a fast acceleration rate is important.[39] On the other hand, acceleration rate is less important in storage rings used for internal target experiments.

A. The choice of harmonic number

The harmonic number determines the bunch spacing and the maximum number of particles per bunch obtainable from a given source, which can be important for colliding beam facilities. The harmonic numbers are related by the mean radii of the chain of accelerators needed to reach an efficient box-car injection scheme.[40] For example, the average radius of the AGS Booster is 1/4 that of the AGS, and the ratio of harmonic numbers is 4. Similar reasoning applies to the chain of accelerators.

Since the damping time of electron beams in electron storage rings (see Table I.4, Chap. 4, Sec. I.4) is short, the injection scheme of damping accumulation at full energy is usually employed in high performance electron storage rings. The choice of harmonic number for high energy electron storage rings is determined mainly by the availability of the rf power source, efficient high quality cavity design, and the size of the machine. Since rf power sources are available at 200, 350, 500, 700 MHz regions, most of the rf cavities of electron storage rings are operating at these frequencies. The harmonic number is then determined by the rf frequency and circumference of the storage ring.

B. The choice of rf voltage

High intensity beams usually require a larger bunch area to control beam instabilities. Since the rf bucket area and height are proportional to $\sqrt{V_{\rm rf}}$, a minimum voltage is needed to capture and accelerate charged particles efficiently.

In electron storage rings, the choice of rf voltage is important in determining the beam lifetime because of quantum fluctuation and Touschek scattering, a large angle Coulomb scattering process converting the horizontal momenta of two electrons into longitudinal momenta.

In general, the rf voltage is limited by the rf power source and the Kilpatrick limit of sparking at the rf gap. The total rf voltage of synchrotrons and storage rings is

[39] The ISIS at the Rutherford Appleton Laboratory has a 50 Hz ramp rate, whereas the rf systems in the Spallation Neutron Source (SNS) provide only beam capture.

[40] A box-car injection scheme is equivalent to bucket to bucket transfer from one accelerator to another accelerator.

usually limited by the available space for the installation of rf cavities.

V.2 Capture and Acceleration of Proton and Ion Beams

At low energy, the intensity and brightness of an injected beam are usually limited by space-charge forces, intrabeam scattering, microwave instability, etc.; phase-space painting for beam distribution manipulation can be used to alleviate some of these problems (see Chap. 2, Sec. III.8, for transverse phase-space painting).

Since the injected beam from a linac normally has a large energy spread, the rf voltage requirement in booster synchrotrons needs enough bucket height for beam injection.[41] The resulting captured beam brightness depends on the rf voltage manipulation. The following example illustrates the difference between adiabatic capture and non-adiabatic capture processes.

A. Adiabatic capture

During multi-turn injection (transverse or longitudinal phase-space painting or charge exchange strip injection), very little beam loss in the synchrotron phase-space can theoretically be achieved by adiabatically ramping the rf voltage with $\phi_s = 0$. The right plots, (e) to (h), of Fig. 3.19 show an example of adiabatic capture in the IUCF cooler injector synchrotron (CIS). The proton beam was accelerated from 7 to 200 MeV at 1 Hz repetition rate, and the rf voltage $V_{rf}(t)$ was increased from a small value to 240 V adiabatically, plots (e) and (f), while the synchronous phase was kept at zero. The adiabaticity coefficient of Eq. (3.43) becomes

$$\alpha_{ad} = \frac{T_s}{4\pi V_{rf}}\frac{dV_{rf}}{dt} = \frac{T_s}{2\pi \mathcal{A}_B}\frac{d\mathcal{A}_B}{dt}, \tag{3.220}$$

where T_s is the synchrotron period and $\mathcal{A}_B$ is the bucket area. In order to satisfy the adiabatic condition, the initial rf voltage should have a small finite initial voltage V_0, and the rf voltage is ramped to a final voltage smoothly (see also Exercise 3.5.1).

After beam capture, the synchronous phase was ramped adiabatically to attain a desired acceleration rate. Good acceleration efficiency requires adiabatic ramping of V and ϕ_s while providing enough bucket area during beam acceleration. In this numerical example, we find that the capture efficiency is about 99.6%. In reality, the momentum spread of the injected beam is about 0.5% instead of 0.1% shown in this example. The maximum voltage is only barely able to hold the momentum spread of the injected beam from linac. The actual capture efficiency is much lower. A possible solution is to install a debuncher in the injection transfer line for lowering the momentum spread of the injected beam.

[41] The peak voltage is usually limited by the power supply and electric field breakdown at the rf cavity gap. A debuncher or a bunch rotator in the transfer line can be used to lower the momentum width of injected beams.

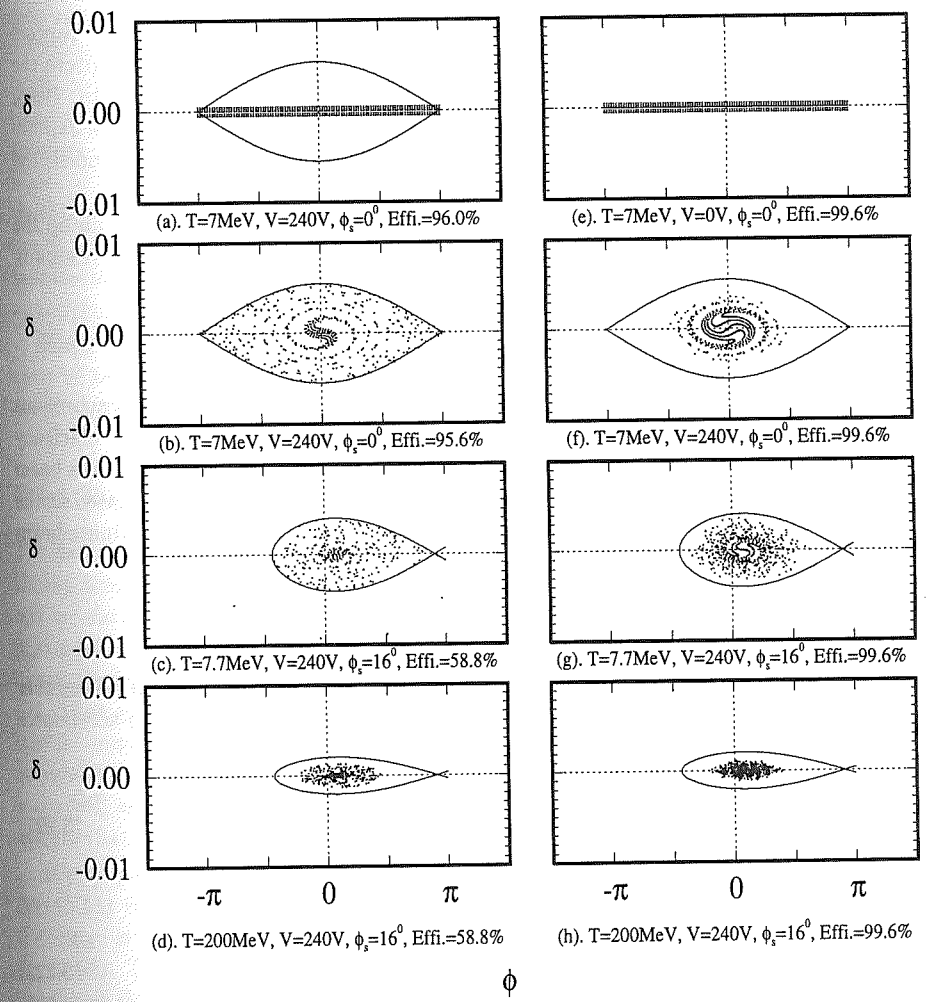

Figure 3.19: The left plots, (a) to (d), show non-adiabatic beam capture during injection and acceleration. The right plots, (e) to (h), show adiabatic capture of the injected beam: the rf voltage is ramped from 0 to 240 V adiabatically to capture the injected beam with a momentum spread of 0.1%. The rf synchronous phase is then ramped adiabatically to achieve the required acceleration rate. The actual momentum spread of the injected beam is about ±0.5%, and thus the actual adiabatic capture efficiency is substantially lower. Space-charge force and microwave instability are not included in the calculation. This calculation was done by X. Kang (Ph.D. Thesis, Indiana University, 1998).

B. Non-adiabatic capture

The left plots, (a) to (d), of Fig. 3.19 show an example of non-adiabatic capture with nonzero initial rf voltage. When the rf voltage is set to 240 V to capture the injected beam, the beam fills up the entire phase-space, as shown in plot (b). Beam loss occurs during acceleration, the final phase-space area is larger, and the capture efficiency is low. With microwave instability and space-charge effects included, the capture efficiency may be even lower.

As seen in plots (b) and (f), the injected beam particles decohere and fill up the entire bucket area because of synchrotron tune spread. The decoherence results in emittance growth.

C. Chopped beam at the source

Many fast cycling synchrotrons require nonzero rf voltage and nonzero rf synchronous phase $\phi_s > 0$ to achieve the desired acceleration rate. In this case, capture efficiency is reduced by the nonadiabatic capture process. To circumvent low efficiency, a beam chopper consisting of mechanical or electromagnetic deflecting devices, located at the source, can be used to paint the phase-space of the injected beam and eliminate beam loss at high energy.

V.3 Bunch Compression and Rotation

When a bunch is accelerated to its final energy, it may be transferred to another accelerator or used for research. When the beam is transferred from one accelerator to another, the beam profile matching condition is

$$\left[\frac{\hat{\delta}}{R\hat{\theta}}\right]_{\text{acc.1}} = \left[\frac{\hat{\delta}}{R\hat{\theta}}\right]_{\text{acc.2}}, \tag{3.221}$$

or equivalently, the rf parameter matching condition is

$$\left[\frac{1}{R}\sqrt{\frac{hV}{|\eta|}}\right]_{\text{acc.1}} = \left[\frac{1}{R}\sqrt{\frac{hV}{|\eta|}}\right]_{\text{acc.2}}. \tag{3.222}$$

This matching condition may be higher than the limit of a low frequency rf system. Similarly, the bunch length of a beam may need to be shortened in many applications. A simple approach is to raise the voltage of the accelerator rf system. However, the peak voltage of an rf system is limited by the breakdown of electric field at the acceleration gap. According to the empirical Kilpatrick criterion, the rf frequency f [MHz] is related to the peak electric field gradient E_K [MV/m] by

$$f = 1.64\, E_K^2\, e^{-8.5/E_K}. \tag{3.223}$$

Because of this limitation, we have to use different beam manipulation techniques such as bunch compression by rf gymnastics, etc.

Bunched beam gymnastics are particularly important for shortening the proton bunch before the protons hit their target in antiproton or secondary beam production. Generally, the emittance of secondary beams is equal to the product of the momentum aperture of the secondary-beam capture channel and the bunch length of the primary beam. When the bunch length of a primary proton beam is shortened, the longitudinal emittance of the secondary antiproton beam becomes smaller. The antiproton beam can be further debunched through phase-space rotation in a debuncher by converting momentum spread to phase spread, and the final antiproton beam is transported to an accumulator for cooling accumulation (see Exercise 3.5.3).

Beam bunch compression is also important in shortening the electron bunch in order to minimize the beam breakup head-tail instabilities in a linac (see Sec. VIII). A few techniques of bunch compression are described below.

V.3.A Bunch compression by rf voltage manipulation

The first step it to lower the rf voltage adiabatically, e.g. $V_0 \to V_1$, so that the bucket area is about the same as the bunch area. Then the rf voltage is increased non-adiabatically from V_1 to V_2. The unmatched beam bunch rotates in synchrotron phase-space. At 1/4 or 3/4 of the synchrotron period, a second rf system at a higher harmonic number is excited to capture the bunch, or a kicker is fired to extract beams out of the synchrotron. Figure 3.20 shows schematic phase-space ellipses during the bunch compression process. The lower-left plot shows the final phase-space ellipse in an idealized linear synchrotron motion. In reality, the maximum attainable rf voltage is limited, and the final phase-space ellipse is distorted by the nonlinear synchrotron motion that causes emittance dilution.

For a given bunch area, the rms bunch width and height are obtained from Eq. (3.58) during the adiabatic rf voltage compression from V_0 to V_1. After the rf voltage is jumped to V_2, the bunch height will become bunch width according to Eq. (3.59). The maximum bunch compression ratio, defined as the ratio of the bunch lengths at $(V_0 = V_2) \to V_1 \to V_2$, becomes

$$r_c = \frac{\sigma_{\phi,\text{i}}}{\sigma_{\phi,\text{f}}} = \left(\frac{V_2}{V_1}\right)^{1/4} = \left(\frac{\mathcal{A}_{\text{bucket,max}}}{\mathcal{A}_{\text{bunch}}}\right)^{1/2} = \frac{2\sqrt{2}}{\sqrt{3\pi}\sigma_\phi}, \tag{3.224}$$

where we have used the properties that the bunch area supposedly fills up the bucket area at $V_{\text{rf}} = V_1$, and the fact that the bucket area is 16 (see Table 3.2), and the bunch area containing 95% of the beam is $6\pi\sigma_\phi^2$ in the normalized synchrotron phase space coordinates.

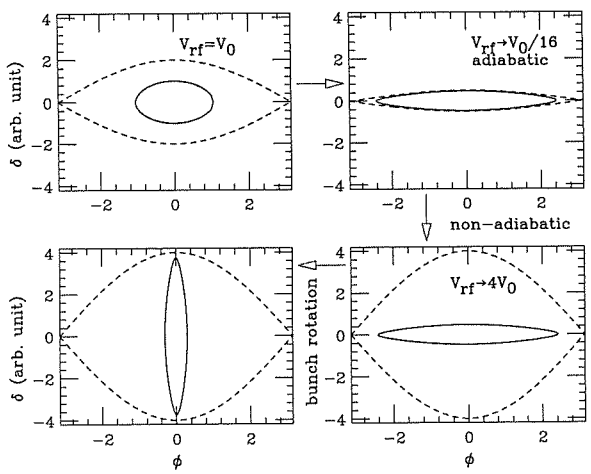

Figure 3.20: Schematic drawings (clockwise) of bunch compression scheme using rf voltage manipulation. The bunch area is initially assumed to be about 1/5 of the bucket area (top-left). The voltage is adiabatically reduced by 16 times so that the bunch is almost fill the bucket area (top-right). As the voltage is non-adiabatically raised to four times the original rf voltage, the mismatched bunch begins to rotate. When the bunch length is shortened (lower-left) at 1/4 of the synchrotron period, a kicker can be fired to extract the beam.

V.3.B Bunch compression using unstable fixed point

If the rf phase is shifted so that the unstable fixed point (UFP) is located at the center of the bunch, the bunch will begin compressing in one direction and stretching in the other direction along the separatrix orbit (see Sec. II.4 and Exercise 3.2.5). In linear approximation, the bunch length and bunch height change according to $\exp\{\pm\omega_s t_{\rm ufp}\} = \exp\{\pm 2\pi t_{\rm ufp}/T_s\}$, where ω_s is the small amplitude synchrotron angular frequency, T_s is the synchrotron period, and $t_{\rm ufp}$ is the time-duration that the bunch stays at the UFP. The length of stay at the UFP can be adjusted to attain a required aspect ratio of the beam ellipse.

When the SFP of the rf potential is shifted back to the center of the bunch. The mis-matched bunch profile will begin to execute synchrotron motion. At 3/8 of the synchrotron period, the bunch can be captured by a matched high frequency rf system or kicked out of the accelerator by fast extraction.

We now derive the ultimate bunch compression ratio for the rf phase shift method as follows. In the normalized phase-space coordinates, ϕ and $\mathcal{P} = -(h|\eta|/\nu_s)(\Delta p/p)$, the Hamiltonian for stationary synchrotron motion is given by Eq. (3.88).

Near the UFP, the separatrix of the Hamiltonian in Eq. (3.88) can be approximated by two straight lines crossing at 45° angles with the horizontal axis ϕ. When the rf phase is shifted so that the beam sits on the UFP, the bunch width and height will stretch and compress along the separatrix. The rate of growth is equal to $\exp(\omega_s t_{\rm ufp})$. The maximum rf phase coordinate $\phi_{\rm max}$ that a bunch width can increase and still stay

within the bucket after the rf phase is shifted back to SFP is given approximately by

$$\frac{1}{2}\phi_{\rm max}^2 + 2\sin^2\left(\frac{\phi_{\rm max}}{2}\right) \approx 2, \tag{3.225}$$

where we assume linear approximation for particle motion near SFP. Thus we obtain $\phi_{\rm max} \approx \sqrt{2}$. Using Liouville's theorem, conservation of phase-space area, we find

$$\pi\sigma_{\phi,\rm i}^2 = \pi\sigma_{\mathcal{P},\rm f}\sigma_{\phi,\rm f}. \tag{3.226}$$

Assuming that 95% of the beam particles reach $\phi_{\rm max} = \sqrt{2}$ so that $\sigma_{\mathcal{P},\rm f} = \frac{\sqrt{2}}{\sqrt{6}}\phi_{\rm max} = \sqrt{2/3}$, we find the compression ratio as

$$r_{\rm c,max}^{\rm p} = \frac{\sigma_{\phi,\rm i}}{\sigma_{\phi,\rm f}} = \frac{\sigma_{\mathcal{P},\rm f}}{\sigma_{\phi,\rm i}} \approx \frac{\sqrt{2}}{\sqrt{3}\sigma_{\phi,\rm i}}, \tag{3.227}$$

The time needed to reach this maximum compression ratio is

$$\omega_s \hat{t}_{\rm ufp} = \ln\frac{1}{\sigma_{\phi,\rm i}} - 0.203. \tag{3.228}$$

A difficulty associated with bunch compression using rf phase-shift is that the rf voltage may remain at a relatively low value during the bunch rotation stage. The effect of non-linear synchrotron motion will be more important because the ratio of bucket-area to the bunch-area is small.

The difficulty of nonlinear synchrotron motion in the final stage of bunch rotation can be solved by using the buncher in the transport line. After proper bunch compression, the beam is kicked out of the synchrotron and the R_{56} transport matrix element will compress bunch, i.e. lower energy particles travel shorter path, and the higher energy particle travel a longer path. However, the resulting compression ratio is reduced by a factor of $1/\sqrt{2}$. Since there is no constraint that the final bunch size should fit into the bucket, one can regain the factor of $\sqrt{2}$ in staying longer at the UFP.

V.3.C Bunch rotation using buncher/debuncher cavity

The principle of bunch rotation by using a buncher/debuncher cavity is based on the correlation of the time and off-momentum coordinates (the transport element R_{56}). By employing a cavity to accelerate and decelerate parts of the beam bunch, the bunch length and the momentum spread can be adjusted. This method is commonly used in the beam transfer line. For example, a simple debuncher used to decrease the energy spread of a non-relativistic beam out of a linac can function as follows. First, let the beam drift a distance L so that higher energy particles are ahead of lower

energy particles. A cavity that decelerates leading particles and accelerates trailing particles can effectively decrease the energy spread of the beam.

For relativistic particles, a drift space can not provide the correlation for the transport element R_{56} because all particles travel at almost the same speed. It requires bending magnets for generating local dispersion functions so that the path length is correlated with the off-momentum coordinate.[42] A buncher/debuncher cavity can then be used to shorten or lengthen the bunch.

V.4 Debunching

When rf systems are non-adiabatically turned off, particles drift and fill up the entire ring because the rotation frequency depends on the off-momentum variable. The debunching rate is $\dot{\phi} = h\omega_0\eta\delta$. Neglecting synchrotron radiation loss, the momentum spread will not change. The bunch shape will be distorted because particles of higher and lower momenta drift in different directions. The debunching time can be expressed as

$$T_{\rm db} = 2\pi/h\omega_0\eta\hat{\delta}, \tag{3.229}$$

where $\hat{\delta}$ is the maximum momentum spread of a beam. Note that the momentum spread of the entire beam remains the same in this non-adiabatic debunching process.

To reduce the momentum spread in the debunching process, we can adiabatically lower the rf voltage. In this case, the resulting debunched beam has a smaller momentum spread. The phase-space area remains the same if we can avoid collective beam instability.

V.5 Beam Stacking and Phase Displacement Acceleration

The concept of beam stacking is that groups of particles are accelerated to a desired energy and left to circulate in a fixed magnetic field; and subsequent groups are accelerated and deposited adjacent to each other. The accumulated beam will overlap in physical space at special locations, e.g. small β and zero $D(s)$ locations, which increases the density and the collision rate. In a successful example of beam stacking in the ISR pp collider, a single beam current of 57.5 A was attained. To accomplish phase-space stacking, phase displacement acceleration is usually employed.[43]

In a Hamiltonian system, particles can not cross the separatrix, therefore particles outside the bucket can not be captured during acceleration. Since the magnetic field

[42] See e.g., T. Raubenheimer, P. Emma, and S. Kheifets, *Proc. 1993 Part. Accel. Conf.*, p. 635 (1993).

[43] K.R. Symon and A.M. Sessler, *Methods of radio-frequency acceleration in fixed field accelerators with applications to high current and intersecting beam accelerators*, p. 44, CERN Symp. 1956; L.W. Jones, C.H. Pruett, K.R. Symon and K.M. Terwilliger, in *Proc. of Int. Conf. on High-Energy Accelerators and Instrumentation*, p. 58 (CERN, 1959).

depends on rf frequency, only particles inside the stable rf bucket are accelerated toward high energy. Particles outside the rf bucket are lost in the vacuum chamber because of the finite magnet aperture.

What happens to the unbunched coasting beam outside the separatrix when an empty moving bucket is accelerated through the beam? Since the beam is outside the separatrix, it may not be captured into the bucket if the rf bucket acceleration is adiabatic. Particles flow along lines of constant action, and their energies are lowered. The change in energy is $\Delta E = \omega_0 A/2\pi$. Similarly, when a bucket is decelerated toward lower energy, the beam energy will be displaced upward in phase-space, i.e. accelerated. Phase displacement acceleration has been used to accelerate coasting beams in the Intersecting Storage Ring (ISR) at CERN[44] and to compensate synchrotron radiation loss in electron storage rings.

In a storage rings with electron cooling or stochastic cooling, a newly injected beam accelerated by phase displacement can be moved toward the cooling stack to achieve a high cooling rate. This method has been successfully used to accumulate polarized protons at low energy cooling storage rings, and to accumulate antiprotons at antiproton accumulators. For example, the cooling stacking method can enhance polarized proton intensity by a factor of 1000 in the IUCF Cooler.[45] Similarly, with phase displacement acceleration, antiprotons can be moved to the cooling stack for cooling accumulation.

V.6 Double rf Systems

Space charge has been an important limitation to beam intensity in many low energy proton synchrotrons. Space charge induces potential well distortion and generates coherent and incoherent betatron tune shifts, which may lower the thresholds for transverse and longitudinal collective instabilities. Fast beam loss may occur during accumulation and storage when the peak beam current exceeds a threshold value.

To increase the threshold beam intensity, a double rf system has often been used to increase the synchrotron frequency spread, which enhances Landau damping in collective beam instabilities. As early as 1971, an attempt was made to increase Landau damping by installing a cavity operating at the third harmonic of the accelerating frequency in the Cambridge Electron Accelerator (CEA).[46] This technique was also successfully applied to cure coupled bunch mode instabilities at ISR, where

[44] A high current stack at the ISR has a momentum spread of about 3%, that can be handled by a low power rf system in the ISR. By employing the phase displacement acceleration, the circulating beams in ISR were accelerated from 26 GeV to 31.4 GeV without loss of luminosity. The installation of low-β superconducting quadrupoles in 1981 brought a record luminosity of 1.4×10^{32} cm^{2}s^{-1}. The machine stopped operation in December 1983, giving its way to a fully operational SP$\bar{\rm P}$S, that observed its first $p\bar{p}$ collision at the center of mass energy of 540 GeV on July 10, 1981.

[45] A. Pei, Ph.D. Thesis, Indiana University (1993).

[46] R. Averill *et al.*, *Proc. 8th Int. Conf. on High Energy Accelerators*, p. 301 (CERN 1971).

an additional cavity was operated at the sixth harmonic of the primary rf frequency.[47]

Adding a higher harmonic rf voltage to the main rf voltage can flatten the potential well. Since the equilibrium beam profile follows the shape of the potential well, a double rf system can provide a larger *bunching factor*, defined as the fraction of the circumference occupied by a beam or the ratio of average current to peak current, than that of a single rf system. Therefore, for a given DC beam current in a synchrotron, the peak current and consequently the incoherent space-charge tune shift are reduced. For example, a double rf system with harmonics 5 and 10 was successfully used in the Proton Synchrotron Booster (PSB) at CERN to increase the beam intensity by 25 – 30% when the coherent longitudinal sextupole and decapole mode instabilities were suppressed by beam feedback systems.[48] At the Indiana University Cyclotron Facility (IUCF), a recent beam dynamics experiment showed that with optimized electron cooling the beam intensity in the cooler ring was quadrupled when two rf cavities were used.[49]

A. Synchrotron equation of motion in a double rf system

For a given particle at angular position θ relative to the synchronous angle θ_s, the phase angle of the primary rf system can be expressed as

$$\phi = \phi_{1s} - h_1(\theta - \theta_s), \tag{3.230}$$

where ϕ is the phase coordinate relative to the primary rf cavity, ϕ_{1s} is the phase angle for the synchronous particle, and h_1 is the harmonic number for the primary rf system. Similarly, the rf phase angle for the second rf system is

$$\phi_2 = \phi_{2s} - h_2(\theta - \theta_s) = \phi_{2s} + \frac{h_2}{h_1}(\phi - \phi_{1s}), \tag{3.231}$$

where h_2 is the harmonic number for the second rf system and ϕ_{2s} is the corresponding synchronous phase angle. The equation of motion becomes

$$\dot{\delta} = \frac{\omega_0 e V_1}{2\pi\beta^2 E}\left\{\sin\phi - \sin\phi_{1s} + \frac{V_2}{V_1}\left(\sin\left[\phi_{2s} + \frac{h_2}{h_1}(\phi - \phi_{1s})\right] - \sin\phi_{2s}\right)\right\}, \tag{3.232}$$

where the overdot is the derivative with respect to orbiting angle θ, and V_1 and V_2 are the voltages of the rf cavities. Equations (3.21) and (3.232) are Hamilton's equations of motion for a double rf system.

[47] P. Bramham *et al.*, *Proc. 9th Int. Conf. on High Energy Accel.* (CERN, 1974); P. Bramham *et al.*, *IEEE Trans. Nucl. Sci.* **NS-24**, 1490 (1977).

[48] see J.M. Baillod *et al.*, *IEEE Trans. Nucl. Sci.* **NS-30**, 3499 (1983); G. Galato *et al*, *Proc. PAC*, p. 1298 (1987).

[49] See S.Y. Lee *et al.*, *Phys. Rev.* **E49**, 5717 (1994); J.Y. Liu *et al.*, *Phys. Rev.* **E50**, R3349 (1994); J.Y. Liu *et al.*, *Part. Accel.* **49**, 221-251 (1995).

Using the normalized momentum coordinate $\mathcal{P} = -(h_1|\eta|/\nu_s)(\Delta p/p_0)$, the Hamiltonian is

$$H = \frac{1}{2}\nu_s\mathcal{P}^2 + V(\phi), \tag{3.233}$$

where the potential $V(\phi)$ is

$$\begin{aligned} V(\phi) &= \nu_s\{(\cos\phi_{1s} - \cos\phi) + (\phi_{1s} - \phi)\sin\phi_{1s} \\ &\quad - \frac{r}{h}\left[\cos\phi_{2s} - \cos\left(\phi_{2s} + h(\phi - \phi_{1s})\right) - h(\phi - \phi_{1s})\sin\phi_{2s}\right]\}. \end{aligned} \tag{3.234}$$

Here $\nu_s = \sqrt{h_1 e V_1|\eta|/2\pi\beta^2 E_0}$ is the synchrotron tune at zero amplitude for the primary rf system, $h = h_2/h_1$, $r = -V_2/V_1$, and ϕ_{1s} and ϕ_{2s} are the corresponding rf phase angles of a synchronous particle. Here, the conditions $r = 1/h$ and $h\sin\phi_{2s} = \sin\phi_{1s}$ are needed to obtain a flattened potential well. For $r > 1/h$, there are two inner buckets on the ϕ axis. The effective acceleration rate for the beam is $\Delta E = eV_1(\sin\phi_{1s} - r\sin\phi_{2s})$ per revolution.

Because the rf bucket is largest at the lowest harmonic ratio, we study the double rf system with $h = 2$. To simplify our discussion, we study a stationary bucket with $\phi_{1s} = \phi_{2s} = 0°$. However, the method presented in this section can be extended to more general cases with $\phi_{1s} \neq 0$ and $\phi_{2s} \neq 0$.

B. Action and synchrotron tune

When the synchrotron is operating at $\phi_{1s} = \phi_{2s} = 0$, the net acceleration is zero and the Hamiltonian becomes

$$H = \frac{\nu_s}{2}\mathcal{P}^2 + \nu_s\left[(1 - \cos\phi) - \frac{r}{2}(1 - \cos 2\phi)\right]. \tag{3.235}$$

The fixed points $(\phi_{FP}, \mathcal{P}_{FP})$ are listed in Table V.6.

Table 3.5: SFP and UFP of a double rf system.

	SFP	UFP
$0 \le r \le \frac{1}{2}$	(0,0)	$(\pi, 0)$
$\frac{1}{2} < r$	$(\pm\arccos(\frac{1}{2}), 0)$	$(0,0)$, $(\pm\pi, 0)$

Since the Hamiltonian is autonomous, the Hamiltonian value E is a constant of motion with $E/\nu_s \in [0, 2]$. The action is

$$J(E) = \frac{1}{\pi}\int_{-\hat{\phi}}^{\hat{\phi}} \mathcal{P}\, d\phi, \tag{3.236}$$

where $\hat{\phi}$ is the maximum phase angle for a given Hamiltonian torus. The value E is related to $\hat{\phi}$ by $E = 2\nu_s(1 - 2r\cos^2(\hat{\phi}/2))\sin^2(\hat{\phi}/2)$; the phase-space area is $2\pi J$; and the synchrotron tune is $Q_s = (\partial J/\partial E)^{-1}$. The bucket area $\mathcal{A}_b$ is

$$\mathcal{A}_b = 2\pi\hat{J} = 8\left[\sqrt{1+2r} + \frac{1}{\sqrt{2r}}\ln(\sqrt{1+2r}+\sqrt{2r})\right], \tag{3.237}$$

which is a monotonic increasing function of the ratio r. The corresponding bucket area for the single rf system is $\mathcal{A}_b(r \to 0) = 16$ (see Table 3.2).

C. The $r \le 0.5$ case

Changing the variables with

$$t = \tan\frac{\phi}{2}, \quad d\phi = \frac{2}{1+t^2}dt, \quad t_0 = \tan\frac{\hat{\phi}}{2}, \quad \tau = \frac{t}{t_0},$$

we obtain

$$\frac{\partial J}{\partial E} = \frac{2(1+t_0^2)}{\pi\nu_s t_0[1+(1+2r)t_0^2]^{1/2}}\int_0^1\left[(1-\tau^2)\left(\frac{1-2r+t_0^2}{t_0^2[1+(1+2r)t_0^2]}+\tau^2\right)\right]^{-1/2}d\tau. \tag{3.238}$$

Thus the synchrotron tune becomes [26]

$$\frac{Q_s}{\nu_s} = \frac{\pi\sqrt{(1-2r)+2t_0^2+(1+2r)t_0^4}}{2(1+t_0^2)K(k_1)}, \tag{3.239}$$

where $K(k_1)$ is the complete elliptic integral of the first kind with modulus

$$k_1 = \frac{t_0\sqrt{1+(1+2r)t_0^2}}{\sqrt{(1-2r)+2t_0^2+(1+2r)t_0^4}}. \tag{3.240}$$

In fact, this formula is also valid for $r > 0.5$ and $\hat{\phi} > \phi_b$, where ϕ_b is the intercept of the inner separatrix with the phase axis.

D. The $r > 0.5$ case

For $r > 0.5$, the origin of phase-space $\mathcal{P} = \phi = 0$ becomes a UFP of the unperturbed Hamiltonian. Two SFPs are located at $\mathcal{P} = 0$ and $\phi = \pm\phi_f$, where $\cos(\phi_f/2) = 1/2r$. The inner separatrix, which passes through the origin, intersects the phase axis at $\pm\phi_b$ with $\cos(\phi_b/2) = 1/\sqrt{2r}$.

A given torus inside the inner bucket corresponds to a Hamiltonian flow of constant Hamiltonian value. Let ϕ_l and ϕ_u be the lower and upper intercepts of a torus with the

phase axis, where $\phi_u = \hat{\phi}$ and $\sin(\phi_l/2) = \sqrt{\sin^2(\phi_b/2) - \sin^2(\phi_u/2)}$. The derivative of the action with respect to the energy for the torus becomes

$$\frac{\partial J}{\partial E} = \frac{\sqrt{(1+t_u^2)(1+t_l^2)}}{\pi\nu_s\sqrt{2r}}\int_{t_l}^{t_u}\frac{dt}{\sqrt{(t_u^2-t^2)(t^2-t_l^2)}}, \tag{3.241}$$

where $t_u = \tan(\phi_u/2)$, $t_l = \tan(\phi_l/2)$, $t = \tan(\phi/2)$, and $d\phi = 2dt/(1+t^2)$. Thus the synchrotron tune is

$$\frac{Q_s}{\nu_s} = \frac{\sqrt{2r}\pi t_u}{\sqrt{(1+t_u^2)(1+t_l^2)}}\frac{1}{K(k_2)}, \tag{3.242}$$

where modulus $k_2 = \sqrt{t_u^2 - t_l^2}/t_u$.

Figure 3.21 shows the synchrotron tune as a function of the amplitude of synchrotron oscillation for various voltage ratios. At $r = 0$, the system reduces to a single primary rf cavity, where the synchrotron tune is $Q_s/\nu_s = 1$ at zero amplitude. As r increases, the derivative of synchrotron tune vs action becomes large near the origin. Since large tune spread of the beam is essential for Landau damping of collective beam instabilities, an optimal rf voltage ratio is $r = 0.5$, where the synchrotron tune spread of the beam is maximized for a given bunch area.

At $r = 0.5$, the synchrotron tune becomes

$$\frac{Q_s}{\nu_s} = \frac{\pi t_0}{\sqrt{2(1+t_0^2)}K(k)} = \frac{\pi(E/2\nu_s)^{1/4}}{\sqrt{2}K(k)} \tag{3.243}$$

with modulus

$$k = \sqrt{\frac{1}{2}\left(1+\frac{t_0^2}{1+t_0^2}\right)} = \sqrt{\frac{1}{2}\left(1+\sqrt{\frac{E}{2\nu_s}}\right)},$$

where $t_0 = \tan(\hat{\phi}/2)$. For small amplitude synchrotron motion, $t_0 = 0$ and $k_0 = 1/\sqrt{2}$. In this case, the maximum synchrotron tune is $\hat{Q}_s = 0.7786\nu_s$, located at $\hat{\phi} = 117°$ (or $E = 1.057\nu_s$). Near this region, $\partial Q_s/\partial\hat{\phi}$ is very small or zero. When the voltage ratio is $r > 0.5$, a dip in $Q_s(J)$ appears at the inner separatrix of inner buckets, and two small potential wells are formed inside the inner separatrix.

E. Action-angle coordinates

Although analytic solutions for action-angle variables, presented in this section, are valid only for the case with $r = 0.5$, the method can be extended to obtain similar solutions for other voltage ratios. Using the generating function

$$F_2(\phi, J) = \int_{\hat{\phi}}^{\phi}\mathcal{P}(\phi')d\phi', \tag{3.244}$$

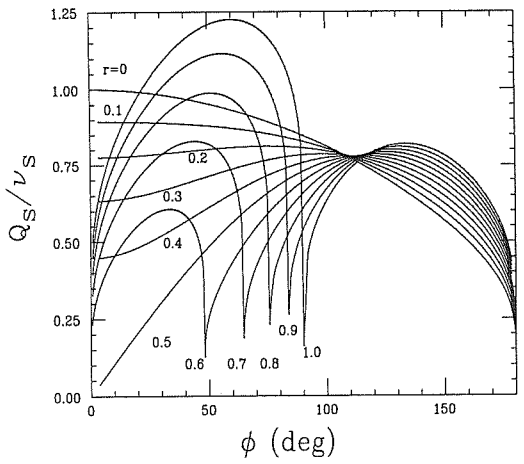

Figure 3.21: The normalized synchrotron tune as a function of the peak phase $\phi = \hat{\phi}$ for various values of voltage ratio r. Note that when $r > 0.5$, the center of the bucket becomes an UFP, and two SFPs are produced.

we obtain the angle coordinate as

$$\psi = \frac{\partial F_2}{\partial J} = \frac{\partial E}{\partial J}\int_{\hat{\phi}}^{\phi}\frac{\partial \mathcal{P}}{\partial E}d\phi' = \frac{Q_s}{\nu_s}\int_{\hat{\phi}}^{\phi}\frac{d\phi'}{\mathcal{P}}, \tag{3.245}$$

where the action variable is given in Eq. (3.236).

Using the generating function

$$F_2(\phi, J) = \int_{\hat{\phi}}^{\phi}\mathcal{P}(\phi')d\phi', \tag{3.246}$$

the angle coordinate becomes

$$\begin{aligned}\psi &= \frac{\partial F_2}{\partial J} = \frac{\partial E}{\partial J}\int_{\hat{\phi}}^{\phi}\frac{\partial \mathcal{P}}{\partial E}d\phi' = \frac{Q_s}{\nu_s}\int_{\hat{\phi}}^{\phi}\frac{d\phi}{\mathcal{P}} \\ &= \frac{Q_s}{\nu_s}\frac{(1+t_0^2)}{t_0\sqrt{1+2t_0^2}}\int_1^{\tau}\left((1-\tau^2)(\frac{1}{1+2t_0^2}+\tau^2)\right)^{-1/2}d\tau = \frac{Q_s}{\sqrt{2}\nu_s}\frac{\sqrt{1+t_0^2}}{t_0}u,\end{aligned}$$

where

$$u = \int_1^{\mathrm{cn}u}\frac{dx}{\sqrt{(1-x^2)(k'^2+k^2x^2)}}, \quad k = \sqrt{(1+2t_0^2)/[2(1+t_0^2)]}, \quad k' = \sqrt{1-k^2},$$

and the Jacobian elliptical function cn$u$ is

$$\mathrm{cn}u = \frac{\tan(\phi/2)}{\tan(\hat{\phi}/2)} = \frac{2\pi}{kK(k)}\sum_{n=0}^{\infty}\frac{q^{n+1/2}}{1+q^{2n+1}}\cos[(2n+1)\psi], \tag{3.247}$$

with $q = e^{-\pi K'/K}$, $K' = K(\sqrt{1-k^2})$, and

$$\psi = \frac{Q_s}{\nu_s}\frac{\sqrt{1+t_0^2}}{\sqrt{2}t_0}u = \frac{\pi u}{2K(k)}, \tag{3.248}$$

From Eq. (3.247), we obtain

$$\phi = 2\arctan\left(\tan\frac{\hat{\phi}}{2}\,\mathrm{cn}u\right), \quad \text{or} \quad \tan\frac{\phi}{2} = \tan\frac{\hat{\phi}}{2}\mathrm{cn}u, \tag{3.249}$$

and from Hamilton's equation of motion, we get

$$\mathcal{P} = -2\sqrt{2}\sin\left(\frac{\hat{\phi}}{2}\right)\tan\left(\frac{\hat{\phi}}{2}\right)\frac{\mathrm{sn}u\ \mathrm{dn}u}{1+[\tan(\hat{\phi}/2)\,\mathrm{cn}u]^2}. \tag{3.250}$$

When the voltage ratio is not 0.5, Eqs. (3.248) to (3.250) remain valid provided that the modulus is replaced by k_1 of Eq. (3.240) or k_2 of Eq. (3.242).

Thus the transformation of the phase-space coordinates $(\phi, \mathcal{P})$ to the action-angle variables (J, ψ) can be accomplished by using Eqs. (3.249) and (3.250) or equivalently

$$\sin\frac{\phi}{2} = \frac{\xi^{1/4}\,\mathrm{cn}u}{\sqrt{1-\xi^{1/2}\,\mathrm{sn}^2u}}, \qquad \frac{\mathcal{P}}{2} = \pm\xi^{1/2}\sqrt{1-\frac{\mathrm{cn}^4u}{(1-\xi^{1/2}\,\mathrm{sn}^2u)^2}}, \tag{3.251}$$

where $\xi = E/2\nu_s$.

F. Small amplitude approximation

A tightly bunched beam occupies a small phase-space area. The formulas for small amplitude approximation are summarized as follows:

$$\begin{aligned}J &\approx \frac{8\sqrt{2}K}{3\pi}\left(\frac{E}{2\nu_s}\right)^{3/4} = \frac{8\sqrt{2}K}{3\pi}\sin^3\frac{\hat{\phi}}{2}, \\ \frac{Q_s}{\nu_s} &\approx \frac{\pi}{\sqrt{2}K}\sin\frac{\hat{\phi}}{2}, \\ \phi &\approx \hat{\phi}\frac{2\pi}{kK}\sum_{n=0}^{\infty}\frac{q^{n+1/2}}{1+q^{2n+1}}\cos(2n+1)\psi, \\ \mathcal{P} &= -\hat{\phi}^2\frac{\pi^2}{\sqrt{2}kK^2}\sum_{n=0}^{\infty}\frac{(2n+1)q^{n+1/2}}{1+q^{2n+1}}\sin(2n+1)\psi,\end{aligned} \tag{3.252, 3.253}$$

where $k \approx 1/\sqrt{2}$, $K = K(k) \approx 1.8541$, and $q \approx e^{-\pi}$.

Let $\mathcal{A}$ be the rms phase-space area of the bunch, and $\sigma_{\mathcal{P}}$ and σ_ϕ the rms conjugate phase-space coordinates. We then obtain

$$\sigma_\phi = \left(\frac{3\mathcal{A}}{2\sqrt{2}K}\right)^{1/3}, \quad \sigma_{\mathcal{P}} = \left(\frac{3\mathcal{A}}{8K}\right)^{2/3}. \tag{3.254}$$

The rms tune spread of the beam is then

$$\Delta Q = \frac{\pi}{\sqrt{2}K}\left(\frac{3\mathcal{A}}{16\sqrt{2}K}\right)^{1/3}\nu_s. \tag{3.255}$$

G. Sum rule theorem and collective instabilities

The perturbing potential due to rf phase modulation is linearly proportional to $\mathcal{P}$ of Eq. (3.250). Expanding $\mathcal{P}$ in action-angle coordinates as $\mathcal{P} = \sum_n f_n(J)e^{jn\psi}$, we find that the strength functions $f_n(J)$ satisfy the sum rule shown in Eq. (3.103). The sum rule can be used to identify the region of phase-space that is sensitive to rf phase modulation (see Exercise 3.3.1).

Since $dQ/dJ = 0$ occurs inside the bucket, it may be of concern that large amplitude particles can become unstable against collective instabilities. When an rf phase or voltage noise is applied to beams in a double rf system, particle motion near the center of the bucket may become chaotic because of overlapping resonances. However, the chaotic region is bounded by invariant tori, and the effect on beam dilution may not be important. A most critical situation arises when the synchrotron amplitude of the beam reaches the region where Q_s is maximum or near the rf bucket boundary, where the tune spread is small. The beam may be susceptible to collective instabilities, and feedback systems may be needed for a high intensity beam that occupies a sizable phase-space area.

V.7 The Barrier RF Bucket

Bunch beam gymnastics have been important in antiproton production, beam coalescence for attaining high bunch intensity, multi-turn injection, accumulation, phase-space painting, etc. The demand for higher beam brightness in storage rings and higher luminosity in high energy colliders requires intricate beam manipulations at various stages of beam acceleration. In particular, a flattened rf wave form can be employed to shape the bunch distribution in order to alleviate space-charge problems in low energy proton synchrotrons and to increase the tune spread in electron storage rings. The extreme of the flattened rf wave form is the barrier bucket.[50]

For achieving high luminosity in the Fermilab TeV collider Tevatron, a Recycler has been built, which would recycle unused antiprotons from the Tevatron. The recycled antiprotons can be cooled by stochastic cooling or electron cooling to attain high phase-space density. At the same time, the Recycler would also accumulate newly produced, cooled antiprotons from the antiproton Accumulator. To maintain the antiproton bunch structure, a barrier rf wave form can be used to confine the

[50]See J. Griffin, C. Ankenbrandt, J.A. MacLachlan, and A. Moretti, *IEEE Trans. Nucl Sci.* **NS-30**, 3502 (1983); V.K. Bharadwaj, J.E. Griffin, D.J. Harding, and J.A. MacLachlan, *IEEE Trans. Nucl. Sci.* **NS-34**, 1025 (1987); S.Y. Lee and K.Y. Ng, *Phys. Rev.* **E55**, 5992 (1997).

beam bunch and shape the bunch distribution waiting for the next collider refill. The required bunch length and the momentum spread of the beam can be adjusted more easily by gymnastics with barrier rf waves than with the usual rf cavities.

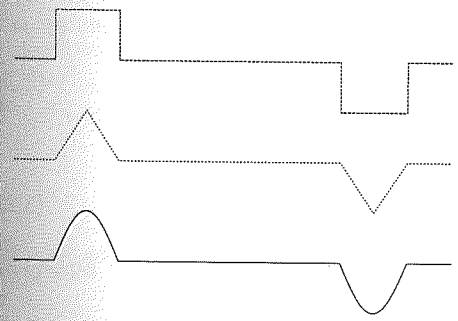

Figure 3.22: Possible wave forms for the barrier bucket. The barrier rf wave is characterized by a voltage height V_0, a pulse width T_0, and a pulse gap T_1.

The barrier rf wave is normally generated by a solid state power amplifier, which has intrinsic wide bandwidth characteristics. An arbitrary voltage wave form can be generated across a wideband cavity gap. Figure 3.22 shows some possible barrier rf waves with half sine, triangular, and square function forms. These wave forms are characterized by voltage amplitude $V(\tau)$, pulse duration T_1, pulse gap T_2 between positive and negative voltage pulses, and integrated pulse strength $\int V(\tau)d\tau$. For example, the integrated pulse strength for a square wave form is V_0T_1. The rf wave form is applied to a wideband cavity with frequency hf_0, where h is an integer, and f_0 is the revolution frequency of synchronous particles. The effect on the beam depends mainly on the integrated voltage of the rf pulse. Acceleration or deceleration of the beam can be achieved by employing a biased voltage wave in addition to the bunch-confining positive and negative voltage pulses.

Most of the time, orbiting particles see no cavity field in passing through the cavity gap. When a particle travels in the time range where the rf voltage is not zero, its energy can increase or decrease depending on the sign of the voltage it encounters. In this way, the accelerator is divided into stable and unstable regions. Thus the wide bandwidth rf wave can create a barrier bucket to confine orbiting particles.

A. Equation of motion in a barrier bucket

For a particle with energy deviation ΔE, the fractional change of the orbiting time $\Delta T/T_0$ is

$$\frac{\Delta T}{T_0} = \eta\frac{\Delta E}{\beta^2 E_0}, \tag{3.256}$$

where η is the phase slip factor, βc and E_0 are the speed and the energy of a synchronous particle, and T_0 is its revolution period. Without loss of generality, we

consider here synchrotron motion with $\eta < 0$. For $\eta > 0$, the wave form of the barrier bucket is reversed.

The time coordinate for an off-momentum particle $-\tau$ is given by the difference between the arrival time of this particle and that of a synchronous particle at the center of the bucket. The equation of motion for the phase-space coordinate τ is

$$\frac{d\tau}{dt} = -\eta \frac{\Delta E}{\beta^2 E_0} . \tag{3.257}$$

Passing through a barrier wave, the particle gains energy at a rate of

$$\frac{d(\Delta E)}{dt} = \frac{eV(\tau)}{T_0} . \tag{3.258}$$

The equations of particle motion in a barrier rf wave are governed by Eqs. (3.257) and (3.258).

B. Synchrotron Hamiltonian for general rf wave form

From the equations of motion (3.257) and (3.258), we obtain the general synchrotron Hamiltonian for an arbitrary barrier rf wave form:

$$H = -\frac{\eta}{2\beta^2 E_0}(\Delta E)^2 - \frac{1}{T_0}\int_0^{\tau} eV(\tau)d\tau. \tag{3.259}$$

Thus the maximum off-energy bucket height can be easily derived:

$$\Delta E_b = \left(\frac{2\beta^2 E_0}{|\eta| T_0}\left|\int_{T_2/2}^{T_2/2+T_1} eV(\tau)d\tau\right|\right)^{1/2} , \tag{3.260}$$

where T_1 is the width of the barrier rf wave form. Since the barrier rf Hamiltonian is time independent, an invariant torus has a constant Hamiltonian value. We define the W parameter for a torus from the equation below:

$$\frac{|\eta|}{2\beta^2 E_0}(\hat{\Delta E})^2 = \frac{1}{T_0}\left|\int_{T_2/2}^{T_2/2+W} eV(\tau)d\tau\right|. \tag{3.261}$$

The synchrotron period of a Hamiltonian torus becomes

$$T_s = 2\frac{T_2}{|\eta|}\left(\frac{\beta^2 E_0}{|\hat{\Delta E}|}\right) + 4T_c , \tag{3.262}$$

where T_c is

$$T_c = \frac{\beta^2 E_0}{|\eta|}\int_0^W \left[(\hat{\Delta E})^2 - \frac{2\beta^2 E_0}{|\eta| T_0}\int_{T_2/2}^{T_2/2+\tau} eV(\tau')d\tau'\right]^{-1/2} d\tau. \tag{3.263}$$

Clearly, all physical quantities depend essentially on the integral $\int V(\tau)d\tau$. Thus, the essential physics is independent of the exact shape of the barrier rf wave.

C. Square wave barrier bucket

Since the effect of the barrier rf wave on particle motion depends essentially on the integrated rf voltage wave, we consider only the square wave forms with voltage heights $\pm V_0$ and pulse width T_1 in time, separated by a gap of T_2. When the particle passes through the cavity gap at voltage $\pm V_0$, it gains (loses) an equal amount of energy eV_0, i.e. $d(\Delta E)/dt = \pm eV_0/T_0$ every turn. The number of cavity passages before the particle loses all its off-energy value $\hat{\Delta E}$ is

$$N = \frac{|\hat{\Delta E}|}{eV_0}. \tag{3.264}$$

Thus the phase-space trajectory for a particle with maximum off-energy $\hat{\Delta E}$ is

$$(\Delta E)^2 = \begin{cases} (\hat{\Delta E})^2 & \text{if } |\tau| \le T_2/2 \\ (\hat{\Delta E})^2 - \left(|\tau| - \frac{T_2}{2}\right)\frac{\omega_0 \beta^2 E_0 e V_0}{\pi|\eta|} & \text{if } T_2/2 \le |\tau| \le (T_2/2) + T_1, \end{cases} \tag{3.265}$$

where $\omega_0 = 2\pi f_0$ is the angular revolution frequency of the beam. The phase-space ellipse is composed of a straight line in the rf gap region and a parabola in the square rf wave region. The phase-space area of the invariant phase-space ellipse is

$$\mathcal{A} = 2T_2\hat{\Delta E} + \frac{8\pi|\eta|}{3\omega_0\beta^2 E_0 e V_0}(\hat{\Delta E})^3. \tag{3.266}$$

The maximum energy deviation or the barrier height that a barrier rf wave can provide is

$$\Delta E_b = \left(\frac{eV_0 T_1}{T_0}\frac{2\beta^2 E_0}{|\eta|}\right)^{1/2} , \tag{3.267}$$

where T_1 is the pulse width of the rf voltage wave, and T_0 is the revolution period of the beam. The bucket height depends on $V_0 T_1$, which is the integrated rf voltage strength $\int V(\tau)d\tau$. The synchrotron period is

$$T_s = 2\frac{T_2}{|\eta|}\left(\frac{\beta^2 E_0}{|\hat{\Delta E}|}\right) + 4\frac{|\hat{\Delta E}|}{eV_0}T_0 \tag{3.268}$$

for particles inside the bucket. The mathematical minimum synchrotron period of Eq. (3.268) is

$$T_{s,\min} = \left(\frac{32 T_0 T_2 \beta^2 E_0}{|\eta| e V_0}\right)^{1/2} , \tag{3.269}$$

and the corresponding maximum synchrotron tune is

$$\nu_{s,\max} = \left(\frac{T_0}{T_2}\frac{|\eta| e V_0}{32\beta^2 E_0}\right)^{1/2} . \tag{3.270}$$

Note here that $\pi T_0/(16T_2)$ plays the role of harmonic number h of a regular rf system. The synchrotron tune is a function of the off-energy parameter $\Delta\hat{E}$ given by

$$\nu_s = 4\nu_{s,\max}\sqrt{\frac{T_1}{T_2}\frac{\Delta\hat{E}}{\Delta E_b}}\left(1+4\left[\frac{\Delta\hat{E}}{\Delta E_b}\right]^2\frac{T_1}{T_2}\right)^{-1}. \tag{3.271}$$

Note that when the rf pulse gap width decreases to $T_2/T_1 < 4$, the synchrotron tune becomes peaked at an amplitude within the bucket height. This feature is similar to that of a double rf system.[51] Figure 3.23 shows ν_s vs ΔE with Fermilab Recycler parameters $E_0 = 8.9$ GeV, $\gamma_T = 20.7$, $f_0 = 89.8$ kHz, $T_1 = 0.5$ μs, $V_0 = 2$ kV, and $T_2/T_1 = 1, 2, 4$, and 8. For example, $\nu_{s,\max} = 3.7\times10^{-5}$ for $T_2 = T_1$, i.e. the synchrotron frequency is 3.3 Hz.

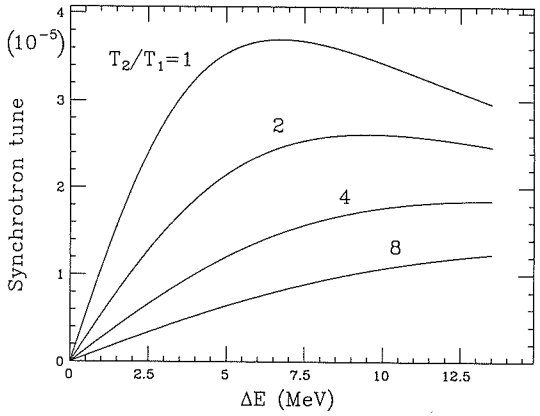

Figure 3.23: Synchrotron tune vs off-energy parameter ΔE. Parameters used are $E_0 = 8.9$ GeV, $f_0 = 89.8$ kHz, $V_0 = 2$ kV, $\gamma_T = 20.7$, and $T_1 = 0.5$ μs. Note that if $T_2 > 4T_1$, the synchrotron tune is a monotonic function of ΔE. On the other hand, if $T_2 < 4T_1$, the synchrotron tune is peaked at an off-energy ΔE smaller than the bucket height ΔE_b.

D. Hamiltonian formalism

The Hamiltonian for the phase-space coordinates $(\tau, \Delta E)$ is

$$H_0 = \frac{\eta}{2\beta^2 E_0}(\Delta E)^2 + \frac{\omega_0 e V_0 T_1}{2\pi} f_0(\tau, T_1, T_2), \tag{3.272}$$

where

$$\begin{aligned} f_0(\tau,T_1,T_2) &= -1+\frac{1}{T_1}\Big[(\tau+T_1+\frac{T_2}{2})\theta(\tau+T_1+\frac{T_2}{2})-(\tau+\frac{T_2}{2})\theta(\tau+\frac{T_2}{2}) \\ &\quad -(\tau-\frac{T_2}{2})\theta(\tau-\frac{T_2}{2})+(\tau-T_1-\frac{T_2}{2})\theta(\tau-T_1-\frac{T_2}{2})\Big]. \end{aligned} \tag{3.273}$$

[51] S.Y. Lee *et al.*, *Phys. Rev.* **E49**, 5717 (1994); J.Y. Liu *et al.*, *Phys. Rev.* **E50**, R3349 (1994).

Here $\theta(x)$ is the standard step function with $\theta(x) = 1$ for $x > 0$ and $\theta(x) = 0$ for $x < 0$.

For a constant T_1, T_2 and V_0, the Hamiltonian H_0 is a constant of motion. The action of a Hamiltonian torus is

$$J = \frac{1}{2\pi}\oint \Delta E d\tau = \frac{1}{2\pi}\sqrt{\frac{\omega_0\beta^2 E_0 e V_0}{\pi|\eta|}}\oint\sqrt{W+f_0(\tau,T_1,T_2)}d\tau. \tag{3.274}$$

The parameter W with a dimension of time is related to the Hamiltonian value by

$$H_0 = -\frac{\omega_0 e V_0}{2\pi}W = \frac{\eta}{2\beta^2 E_0}\left(\Delta\hat{E}\right)^2. \tag{3.275}$$

For a given Hamiltonian torus, W has the physical meaning that it is equal to the maximum phase excursion $|\tau|$ in the rf wave region. Therefore $W = 0$ corresponds to an on-momentum particle, and $W = T_1$ is associated with particles on the bucket boundary.

The action for a particle torus inside the bucket is

$$J = \frac{1}{2\pi}\sqrt{\frac{\omega_0\beta^2 E_0 e V_0}{\pi|\eta|}}\left[2T_2\sqrt{W}+\frac{8}{3}W^{3/2}\right] = \frac{1}{2\pi}\left[2T_2+\frac{8}{3}W\right]\Delta\hat{E}. \tag{3.276}$$

The bucket area is related to the maximum action with $W = T_1$, i.e.

$$\mathcal{B} = 2\pi\hat{J} = \left(2T_2+\frac{8}{3}T_1\right)\Delta E_b. \tag{3.277}$$

Again, the bucket area depends only on the integrated rf voltage strength $\int V(\tau)d\tau = V_0T_1$.

E. Action-angle coordinates

Canonical transformation from the phase-space coordinates $(\tau, \Delta E)$ to the action-angle variable can be achieved by using the generating function

$$F_2(J,\tau) = \int_{-\hat{\tau}}^{\tau}\Delta E d\tau, \tag{3.278}$$

where $\hat{\tau} = W + (T_2/2)$. The angle variable ψ is

$$\psi = \frac{\partial F_2}{\partial J} = \frac{\pi\sqrt{W}}{T_2+4W}\int_{-\hat{\tau}}^{\tau}\frac{d\tau}{\sqrt{W+f_0}}. \tag{3.279}$$

The integral can be evaluated easily to obtain

$$\psi = \begin{cases} \dfrac{2\pi\sqrt{W}}{T_2+4W}\sqrt{W+\dfrac{1}{2}T_2+\tau} & \text{if } -W-\frac{1}{2}T_2 \le \tau \le -\frac{1}{2}T_2,\ \Delta E>0 \\ \psi_c + \dfrac{\pi}{T_2+4W}\left(\tau+\dfrac{1}{2}T_2\right) & \text{if } -\frac{1}{2}T_2 \le \tau \le \frac{1}{2}T_2,\ \Delta E>0 \\ 2\psi_c+\psi_s - \dfrac{2\pi\sqrt{W}}{T_2+4W}\sqrt{W+\dfrac{1}{2}T_2-\tau} & \text{if } \frac{1}{2}T_2 \le \tau \le W+\frac{1}{2}T_2,\ \Delta E>0 \\ 2\psi_c+\psi_s + \dfrac{2\pi\sqrt{W}}{T_2+4W}\sqrt{W+\dfrac{1}{2}T_2-\tau} & \text{if } \frac{1}{2}T_2 \le \tau \le W+\frac{1}{2}T_2,\ \Delta E<0 \\ 3\psi_c+\psi_s + \dfrac{\pi}{T_2+4W}\left(\dfrac{1}{2}T_2-\tau\right) & \text{if } -\frac{1}{2}T_2 \le \tau \le \frac{1}{2}T_2,\ \Delta E<0 \\ 4\psi_c+2\psi_s - \dfrac{2\pi\sqrt{W}}{T_2+4W}\sqrt{W+\dfrac{1}{2}T_2+\tau} & \text{if } -W-\frac{1}{2}T_2 \le \tau \le -\frac{1}{2}T_2,\ \Delta E<0, \end{cases}$$

where

$$\psi_c = \frac{2\pi W}{T_2+4W}, \quad \psi_s = \frac{\pi T_2}{T_2+4W} \tag{3.280}$$

are respectively the synchrotron phase advances for a half orbit in the rf wave region and in the region between two rf pulses. Note that $2\psi_c + \psi_s = \pi$ for one half of the synchrotron orbit, and that the motion of a stable particle orbit in the barrier bucket with $\eta < 0$ is clockwise. We choose the convention of $\dot{\psi} > 0$ corresponding to a clockwise motion in synchrotron phase-space.

When a perturbation, such as rf noise, is applied to the barrier rf system, stable bucket area may be reduced. The resonance strength functions and their associated sum rules can be derived analytically. The resonance strength function decreases slowly with mode number. The rf phase and voltage modulation can severely dilute bunch area if the modulation frequency is near the top of the synchrotron tune and its harmonics. The rf phase modulation due to orbit length modulation resulting from ground vibration can be important. Because the solid state amplifier is a low power device, it is important to avoid a large reduction of stable phase-space area. Active compensation may be used to compensate the effect of rf phase modulation.[52]

Exercise 3.5

1. The Cooler Injector Synchrotron (CIS) accelerates protons from 7 MeV to 200 MeV in 1.0 Hz. The circumference is 17.364 m. The rf system operates at $h = 1$ with a maximum voltage 240 V. The momentum compaction factor is $\alpha_c = 0.6191$. The momentum spread of the injection linac is about $\pm 5.0 \times 10^{-3}$.

   (a) Assuming that the rf voltage is ramped according to

$$V_{rf}(t) = V_0 + (V_1 - V_0)\left(3\frac{t^2}{T_1^2} - 2\frac{t^3}{T_1^3}\right), \quad t \in [0, T_1],$$

[52] See S.Y. Lee and K.Y. Ng, *Phys. Rev.* **E55**, 5992 (1997).

where V_0 and $V_1 = 240$ V are the initial and the maximum final rf voltages, T_1 is the voltage ramp time. Calculate the adiabaticity coefficient of Eq. (3.43), and the rf bucket height during the rf voltage ramping as functions of time t with $V_0 = 10$ V and $T_1 = 10$ ms. Change these parameters to see the variation of the adiabaticity coefficient.

   (b) If the magnetic field of a proton synchrotron is ramped according to

$$B(t) = B_0 + \left(3\frac{t^2}{t_1^2} - 2\frac{t^3}{t_1^3}\right)(B_1 - B_0), \quad t \in [0, t_1]$$

   where B_0 and B_1 are magnetic field at the injection and at the flat top, and $t = 0$ and $t = t_1$ are the time at the beginning of ramp and at the flat top, find the frequency ramping relation of the rf cavity, and find the maximum $\dot{B}$.

2. In proton accelerators, the rf gymnastics for bunch rotation is performed by adiabatically lowering the voltage from V_1 to V_2 and suddenly raising the voltage from V_2 to V_1 (see also Exercise 3.2.5). Using Eq. (3.58) and conservation of phase-space area, show that the bunch length in the final step is

$$\hat{\theta}_{\text{final}} = \left(\frac{\nu_{s2}}{\nu_{s1}}\right)^{1/2} \hat{\theta}_{\text{initial}},$$

   where $\hat{\theta}_{\text{initial}}$ is the initial bunch length in orbital angle variable, and ν_{s1} and ν_{s2} are the synchrotron tune at voltages V_1 and V_2. Apply the bunch rotation scheme to proton beams at $E = 120$ GeV in the Fermilab Main Injector, where the circumference is 3319.4 m, the harmonic number is $h = 588$, the transition energy is $\gamma_T = 21.8$, and the phase-space area is $\mathcal{A} = 0.05$ eV-s for 6×10^{10} protons. Find the voltage V_2 such that the final bunch length is 0.15 ns with an initial voltage $V_1 = 4$ MV. The energy of the secondary antiprotons is 8.9 GeV. If the acceptance of the antiproton beam is $\pm 3\%$, what is the phase-space area of the antiproton beams? If the antiproton production efficiency is 10^{-5}, what is the phase-space density of the antiproton beams?

3. Neglecting wakefield and other diffusion mechanisms, the momentum spread of an electron beam in a storage ring is determined mainly by the equilibrium between the quantum fluctuation of photon emission and the radiation damping. For an isomagnetic ring, it is given by

$$\left(\frac{\sigma_E}{E}\right)^2 = C_q \frac{\gamma^2}{\mathcal{J}_s \rho},$$

   where $\mathcal{J}_s$ is the damping partition number with $\mathcal{J}_s \approx 2$ for separate function machines, and

$$C_q = \frac{3C_u\hbar}{4mc} = \frac{55}{32\sqrt{3}}\frac{\hbar}{mc} = 3.83 \times 10^{-13} \text{ m}.$$

   Using the electron storage ring parameters listed in Exercise 3.1.4, calculate the phase-space area in eV-s.

4. Verify Eq. (3.232) and derive the Hamiltonian for the double rf system. For a flattened potential well in the double rf system with $\phi_{1s} = \phi_{2s} = 0$, show that the Hamiltonian for small amplitude synchrotron motion is

$$H \approx \frac{1}{2}\mathcal{P}^2 + \nu_s b \phi^4,$$

where $b = (h^2 - 1)/24$, h is the ratio of the harmonic numbers, and the independent "time" variable is the orbital angle θ. We solve the synchrotron motion for the quartic potential below.

(a) Since the Hamiltonian is time independent, the Hamiltonian value E is a constant of motion. Show that the action variable is related to the Hamiltonian value by

$$J = \frac{4K}{3\pi b^{1/4}}\left(\frac{E}{\nu_s}\right)^{3/4} = \frac{4K}{3\pi} b^{1/2}\hat{\phi}^3,$$

where $K = K(\sqrt{\frac{1}{2}}) = 1.85407468$ is the complete elliptical integral with modulus $k = 1/\sqrt{2}$, $\hat{\phi}$ is the amplitude of the phase oscillation.

(b) Show that the synchrotron tune is

$$\frac{Q_s(J)}{\nu_s} = \frac{\pi}{K} b^{1/4}\left(\frac{E}{\nu_s}\right)^{1/4} = \frac{3^{1/3}\pi^{4/3}b^{1/3}}{4^{1/3}K^{4/3}} J^{1/3} = \frac{\pi}{K} b^{1/2}\hat{\phi}.$$

(c) Define the generating function

$$F_2(\phi, J) = \int_0^{\phi} \mathcal{P}\, d\phi,$$

and show that the solution of the synchrotron motion is given by

$$\phi = \hat{\phi}\ \mathrm{cn}\left(\frac{2K}{\pi}\psi|\frac{1}{2}\right),$$
$$\mathcal{P} = -\sqrt{2}\hat{\mathcal{P}}\ \mathrm{sn}\left(\frac{2K}{\pi}\psi|\frac{1}{2}\right)\ \mathrm{dn}\left(\frac{2K}{\pi}\psi|\frac{1}{2}\right),$$

where cn, sn, and dn are elliptical functions with modulus $k = 1/\sqrt{2}$. Compare your results with that of Eq. (3.253) for the $h = 2$ case.

VI Fundamentals of RF Systems

The basic function of rf cavities is to provide a source of electric field for beam acceleration. The longitudinal electric field must be synchronized with the particle arrival time. Resonance cavities, where only electromagnetic fields at resonance frequencies can propagate, are a natural choice in rf cavity design.

Cavities are classified according to their operational frequencies. For cavities operating at a few hundred MHz or higher, pillbox cavities with nose-cone or disk loaded geometry can be used. At lower frequencies, coaxial geometry is commonly employed. Some fundamental parameters of cavities are transit time factor, shunt impedance, and quality factor.

The transit time factor of Eq. (3.3) reflects the finite passage time for a particle to traverse the rf cavity, while the accelerating field varies with time. The transit time factor reduces the effective voltage seen by passing particles. We may reduce the accelerating voltage gap to increase the transit time factor, but a smaller gap can cause electric field breakdown due to the Kilpatrick limit (see Sec. V.3).

The quality factor (Q-factor) depends on the resistance of the cavity wall and the characteristic impedance of the rf cavity structure. It is defined as the ratio of the rf power stored in the cavity to the power dissipated on the cavity wall. The shunt impedance, defined as the ratio of the square of the rf voltage seen by the beam to the dissipated power, is an important figure of merit in cavity design. Generally, the ratio of shunt impedance to Q-factor depends only on the geometry of the cavity and the characteristic impedance. Thus a cavity with a higher Q-factor has a higher shunt impedance.

In this section we examine some basic principles in cavity design. Properties of pillbox and coaxial-geometry cavities will be discussed. Some fundamental characteristic parameters, the shunt impedance, the Q-factor, and the filling time, of a resonance cavity will be defined and discussed. At a given resonance frequency, we will show that a resonance cavity can be well approximated by an equivalent RLC circuit. Beam loading and Robinson dipole-mode instability will be addressed. Further properties of high frequency cavities used in linacs will be discussed in Sec. VIII.

VI.1 Pillbox Cavity

We first consider a cylindrically symmetric pillbox cavity [18] of radius b and length ℓ (left plot of Fig. 3.24). Maxwell's equations (see Appendix B Sec. V) for electromagnetic fields inside the cavity are

$$\nabla\cdot\vec{B} = 0, \quad \nabla\times\vec{B} = \mu\epsilon\frac{\partial\vec{E}}{\partial t}, \quad \nabla\cdot\vec{E} = 0, \quad \nabla\times\vec{E} = -\frac{\partial\vec{B}}{\partial t}, \tag{3.281}$$

where ϵ and μ are dielectric permittivity and permeability of the medium. The EM waves in the cavity can conveniently be classified into transverse magnetic (TM)

mode, for which the longitudinal magnetic field is zero, and transverse electric (TE) mode, for which the longitudinal electric field is zero. The TM modes are of interest for beam acceleration in the rf cavity.

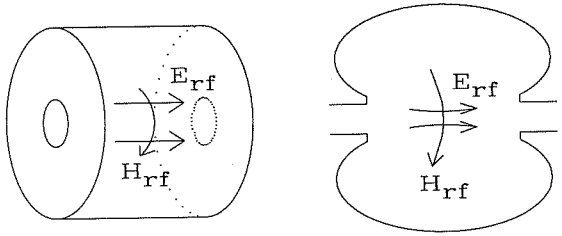

Figure 3.24: Schematic drawings of high frequency cavities. Left: pill-box cavity with disk load; right: nose-cone cavity. Although their names and shapes are different, these high frequency cavities have similar basic features.

In an ideal acceleration cavity, the electromagnetic fields satisfy the boundary condition: $\hat{n} \times \vec{E} = 0$, $\hat{n} \cdot \vec{H} = 0$, where $\hat{n}$ is the vector normal to the conducting surface. There is *no tangential component of electric field*, and *no normal component of magnetic field.*

Assuming a time dependence factor $e^{j\omega t}$ for electric and magnetic fields, the TM standing wave modes in cylindrical coordinates (r, ϕ, s) are (see the Appendix B Sec. V)[53]

$$\begin{cases} E_s = A\, k_r^2\ J_m(k_r r) \cos m\phi \cos ks \\ E_r = -A\, k k_r\ J_m'(k_r r) \cos m\phi \sin ks \\ E_\phi = A\,(mk/r) J_m(k_r r) \sin m\phi \sin ks \\ B_s = 0 \\ B_r = -jA\,(m\omega/c^2 r)\ J_m(k_r r) \sin m\phi \cos ks \\ B_\phi = -jA\,(\omega k_r/c^2)\ J_m'(k_r r) \cos m\phi \cos ks \end{cases} \tag{3.282}$$

where A is a constant, $s = 0$ and ℓ correspond to the beginning and end of the pillbox cavity, m is the azimuthal mode number, k, k_r are wave numbers in the longitudinal and radial modes, and $\omega/c = \sqrt{k^2 + k_r^2}$.

The longitudinal wave number k is determined by the boundary condition that $E_r = 0$ and $E_\phi = 0$ at $s = 0$ and ℓ, i.e.

$$k_{s,p} = \frac{p\pi}{\ell}, \quad p = 0, 1, 2, \cdots. \tag{3.283}$$

Similarly the radial wave number is determined by the boundary condition with $E_s = 0$ and $E_\phi = 0$ at $r = b$, i.e.

$$k_{r,mn} = \frac{j_{mn}}{b}, \tag{3.284}$$

where j_{mn}, listed in Table V.2, are zeros of Bessel functions $J_m(j_{mn}) = 0$.

[53] A standing wave can be decomposed into traveling waves in the $+\hat{s}$ and $-\hat{s}$ directions.

The resonance wave number k for mode number (m, n, p) is

$$k_{mnp} = \sqrt{k_{r,mn}^2 + k_{s,p}^2} = \sqrt{\frac{j_{mn}^2}{b^2} + \frac{p^2\pi^2}{\ell^2}} = \frac{\omega_{mnp}}{c} = \frac{2\pi}{\lambda_{mnp}}. \tag{3.285}$$

The lowest frequency mode is usually called the fundamental mode. Other resonance frequencies are called high order modes (HOM). The art (science) of cavity design is to damp HOMs without affecting the fundamental mode. The EM field of the lowest mode TM_{010} $(k_{s,p} = 0)$ is

$$E_s = E_0 J_0(kr), \quad B_\phi = j\frac{E_0}{c} J_1(kr), \quad k_{010} = \frac{2.405}{b}, \quad \lambda = \frac{2\pi b}{2.405}. \tag{3.286}$$

For example, a 3 GHz structure corresponds to $\lambda = 10$ cm and $b = 3.8$ cm. Such a structure is usually used for high frequency cavities.

The phase velocity, $\omega/k_{s,p}$, for the traveling wave component of the TM_{010} mode with $k_{s,p} = 0$ is infinite. Thus beam particles traveling at speed $v \le c$ do not synchronize with the electromagnetic wave. To slow down the phase velocity, the cavity is loaded with one beam hole with an array of cavity geometries and shapes. Figure 3.24 shows high frequency cavities with disk and nose-cone loaded geometries. Many different geometric shapes are used in the design of high frequency cavities, but their function and analysis are quite similar. All cavities convert TEM wave energy into TM mode to attain a longitudinal electric field. We will return to this subject in Sec. VIII.

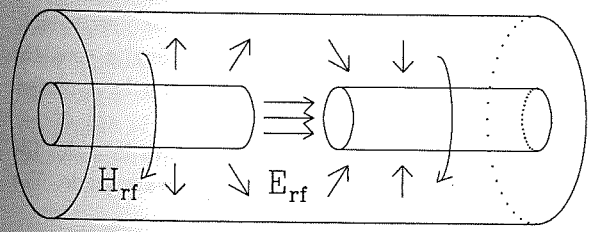

Figure 3.25: Schematic drawing of a low frequency coaxial cavity. Note that the TEM wave is matched to a TM wave at the capacitive loaded gap for the acceleration electric field.

VI.2 Low Frequency Coaxial Cavities

Lower frequency rf systems usually resemble coaxial wave guides, where the length is much larger than the width. Figure 3.25 shows an example of a coaxial cavity. The TEM wave in the coaxial wave guide section is converted to the TM mode at the cavity gap through the capacitive load. When the cavity is operating in 50 to 200 MHz range, it requires a very small amount of ferrite for tuning.[54] When the cavity

[54] Ferrite is magnetic ceramic material that combines the property of high magnetic permeability and high electric resistivity. The material is made of double oxide spinel Fe_2O_3MO, where M can

is operating at a few MHz range, the TEM wave guide is usually ferrite loaded with magnetic dipole or quadrupole fields for bias frequency tuning. At lower rf frequency, ferrite rings in the cavity are needed to slow down EM waves.[55] Using the wave guide transmission line theory, characteristic properties of rf systems can be analyzed.

Let r_1 and r_2 be the inner and outer radii of a wave guide. The inductance and the capacitance of the concentric coaxial wave guides are

$$L = \frac{\mu\ell}{2\pi}\ln\frac{r_2}{r_1} + \frac{\mu_c\delta_{\rm skin}\ell}{4\pi}\left(\frac{1}{r_1}+\frac{1}{r_2}\right), \quad C = \frac{2\pi\epsilon\ell}{\ln(r_2/r_1)}, \tag{3.287}$$

where μ_c is the permeability of the conductor, $\delta_{\rm skin} = \sqrt{2/\omega\mu_c\sigma}$ is the skin depth of flux penetration, and ℓ is the length of the structure. Neglecting the flux penetration in the conductor, the resonating frequency is

$$\omega = \frac{1}{\sqrt{LC}} = \frac{1}{\ell\sqrt{\mu\epsilon}} \approx \frac{c}{\ell\sqrt{\mu/\mu_0}}, \tag{3.288}$$

where $\epsilon = \epsilon_0$ is assumed for the dielectric permittivity. Thus the required cavity length for the fundamental mode is

$$\ell = \frac{c}{\omega\sqrt{\mu/\mu_0}} = \frac{47.7\text{m}}{f[\text{MHz}]\sqrt{\mu/\mu_0}}. \tag{3.289}$$

For a cavity operating beyond 20 MHz, ferrite can be used only for tuning purposes. At frequencies below tens of MHz, the rf cavities must be ferrite loaded in order to fit into the available free space in an accelerator. Typically the magnetic permeability of ferrite is about $1500\mu_0$. When a biased field is applied to the ferrite core, the magnetic permeability can be tuned to match the change of the particle revolution frequency.

To understand the capacitive loading that converts the TEM wave into the TM wave at the cavity gap, we study the rf electromagnetic wave in the wave guide. The characteristic impedance of a wave guide is

$$Z_c = R_c = \sqrt{L/C} = \omega L \approx \frac{1}{2\pi}\sqrt{\frac{\mu}{\epsilon}}\ \ln\frac{r_2}{r_1}. \tag{3.290}$$

Now, we consider an ideal lossless transmission line, where the electromagnetic field has no longitudinal component. Assuming a time dependent factor $e^{j\omega t}$, the current and voltage across the rf structure are (see Exercise 3.6.3)

$$I(s,t) = I_0\cos ks + j(V_0/R_c)\sin ks, \quad V(s,t) = V_0\cos ks + jI_0R_c\sin ks, \tag{3.291}$$

be Mn, Zn, Cr, Ni, etc. Ferrites are commonly used in frequency synthesis devices, Touch-Tone telephone, low loss microwave devices, etc. Application in accelerator can be found in induction linac, frequency tuning for rf cavities, kickers, etc.

[55] W.R. Smythe, *IEEE Trans. Nucl. Sci.*, **NS-30**, 2173 (1983).

where s is the distance from one end of the transmission line, V_0 and I_0 are the voltage and current at the end of the line where $s = 0$, and the wave number of the line is

$$k = \frac{2\pi}{\lambda} = \frac{\omega}{c}.$$

For a standing wave, where the end of the transmission line is shorted, the boundary condition at the shorted side is $V = 0$ at $s = 0$, i.e.

$$I(s,t) = I_0(t)\cos ks, \quad V(s,t) = +jI_0(t)R_c\sin ks. \tag{3.292}$$

The line input impedance becomes

$$Z_{\rm in} = \frac{V(\ell,t)}{I(\ell,t)} = +jR_c\tan k\ell. \tag{3.293}$$

The line impedance is inductive if $k\ell < \pi/2$. The length of the line is chosen to match the gap capacitance at a required resonance frequency:

$$Z_{\rm in} + Z_{\rm gap} = 0, \quad \text{or} \quad \tan k\ell_r = \frac{1}{\omega R_c C_{\rm gap}} \equiv \frac{1}{g}, \tag{3.294}$$

where g is the geometry factor of the cavity, $Z_{\rm gap} = -j/(\omega C_{\rm gap})$ is the gap impedance, and $C_{\rm gap}$ is the capacitance of a half gap. For example, a total capacitance of 10 pF implies that $C_{\rm gap} = 20$ pF. The length ℓ_r of one-half cavity, the gap capacitance, the biased current, and the external loading capacitance can be designed to attain a resonance condition for a given frequency range.

In principle, for a given ℓ_r, R_c, and $C_{\rm gap}$, there are many resonance frequencies that satisfy Eq. (3.294). The lowest frequency is called the fundamental TEM mode. If the loading capacitance is small, the resonance condition of Eq. (3.294) becomes $k\ell_r = \pi/2$, i.e. $\ell_r = \lambda/4$: the length of the coaxial cavity is equal to 1/4 of the wavelength of the TEM wave in the coaxial wave guide. Thus such a structure is also called a quarter-wave cavity. The gap voltage of the coaxial cavity is

$$V_{\rm rf} = +jI(0)R_c\sin k\ell_r = +j\frac{I(0)R_c}{\sqrt{1+g^2}}. \tag{3.295}$$

A. Shunt impedance and Q-factor

The surface resistivity R_s of the conductor and the resistance R of a transmission line are

$$R_s = \sqrt{\frac{\mu_c\omega}{2\sigma}}, \quad R = \frac{R_s\ell}{2\pi}\left(\frac{1}{r_1}+\frac{1}{r_2}\right), \tag{3.296}$$

where σ is the conductivity of the material, ω is the rf frequency, r_1 and r_2 are the inner and outer radii of the transmission line, and ℓ is the length. Thus the quality factor becomes

$$Q = \frac{R_c}{R} = \frac{\omega L}{R} \approx \frac{2r_1r_2}{(r_1+r_2)\delta_{\rm skin}}\frac{\mu}{\mu_c}\ln\frac{r_2}{r_1}. \tag{3.297}$$

Table VI.2 lists typical Q-factors for a copper cavity as a function of cavity frequency, where we have used $\ln(r_2/r_1) \approx 1$ and $r_1 \approx 0.05$ m, and $\sigma_{\rm Cu} \approx 5.8 \times 10^7$ $[\Omega\text{m}]^{-1}$ at room temperature. The total power of dissipation $P_{\rm d}$ is

$$P_{\rm d} = \frac{I^2(0)R}{2}\int_0^{k\ell_{\rm r}} \cos^2 x\, dx = \frac{I^2(0)R}{4(1+g^2)}[(1+g^2)\cot^{-1} g + g]. \tag{3.298}$$

Table 3.6: Some characteristic properties of copper RF cavities

f [MHz]	1	10	100
$\delta_{\rm skin}$ [μm]	66.	21.	6.6
r_1	0.05	0.05	0.05
Q	1100	3500	11000

An important quantity in the design and operation of rf cavities is the shunt impedance. This is the resistance presented by the structure to the beam current at the resonance condition, i.e.

$$R_{\rm sh} = \frac{|V_{\rm rf}|^2}{2P_{\rm d}}. \tag{3.299}$$

For a transmission line cavity, the shunt impedance becomes

$$R_{\rm sh} = \frac{4}{\pi}\left[\frac{\pi/2}{(1+g^2)\cot^{-1} g + g}\right] R_{\rm c}{\rm Q}, \tag{3.300}$$

where the expression in brackets is a shunt impedance reduction factor due to the gap capacitance loading. If $C_{\rm gap} = 0$, i.e. $g = 0$, the capacitance loading factor is 1. As the gap capacitance increases, the shunt impedance decreases.

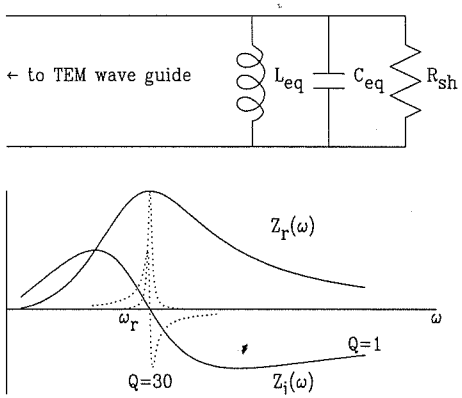

Figure 3.26: Top: Schematic drawing of an equivalent circuit of a cavity. The input impedance of the wave guide is represented by an equivalent inductance. The wave guide is loaded with capacitive cavity-gap and real shunt impedance. The resonance frequency and the Q-factor of the equivalent RLC-circuit are $\omega_{\rm r} = 1/\sqrt{L_{\rm eq}C_{\rm eq}}$ and ${\rm Q} = R_{\rm sh}\sqrt{C_{\rm eq}/L_{\rm eq}}$. Bottom: Plot of the impedance of Eq. (3.301). The solid lines are the real and the imaginary impedances for Q=1, and the dashed lines are the corresponding impedances for Q=30.

From the transmission-line point of view, the cavity gap presents a capacitance and resistive load shown in Fig. 3.26, where $Z_{\rm in} = j\omega L_{\rm eq}$, and $C_{\rm eq} = C_{\rm gap}$. The matching condition of Eq. (3.294) implies that the reactance of the cavity is zero on resonance, and the effective impedance is $R_{\rm sh}$. The impedance of the rf system, represented by a parallel RLC circuit, becomes

$$Z = \left(\frac{1}{R_{\rm sh}} + j\omega C_{\rm eq} + \frac{1}{j\omega L_{\rm eq}}\right)^{-1} = \frac{R_{\rm sh}}{1 + j{\rm Q}(\omega/\omega_{\rm r} - \omega_{\rm r}/\omega)} \approx R_{\rm sh}\cos\psi e^{-j\psi}, \tag{3.301}$$

where $L_{\rm eq}$ and $C_{\rm eq}$ are the equivalent inductance and capacitance, $\omega_{\rm r} = (L_{\rm eq}C_{\rm eq})^{-1/2}$, ${\rm Q} = R_{\rm sh}\sqrt{C_{\rm eq}/L_{\rm eq}}$, and

$$\psi = \tan^{-1}\frac{2{\rm Q}(\omega - \omega_{\rm r})}{\omega_{\rm r}}. \tag{3.302}$$

Here ψ is the cavity detuning angle. At the resonance frequency $\omega_{\rm r}$ particles see a pure resistive load with an effective resistance $R_{\rm sh}$. The rf system becomes capacitive at $\omega > \omega_{\rm r}$, and inductive at $\omega < \omega_{\rm r}$. The right plot of Fig. 3.26 shows the real and imaginary parts of the impedance of Eq. (3.301) for Q=1 and Q=30.

Accelerator cavities usually contain also many parasitic HOMs. Each HOM has its shunt impedance and Q-value. If the frequency of one of the HOMs is equal to that of a synchrotron or betatron sideband, the beam can be strongly affected by the parasitic rf driven resonance. Correction, detuning, and lowering the Q-factor of these sidebands are very important in rf cavity design and operation.

B. Filling time

The quality factor defined in Eq. (3.297) is equal to the ratio of the stored power $P_{\rm st}$ to the dissipated power $P_{\rm d}$, i.e.

$${\rm Q} = \frac{P_{\rm st}}{P_{\rm d}} = \frac{\omega W_{\rm s}}{P_{\rm d}}, \tag{3.303}$$

where $W_{\rm s}$ is the stored energy. Using energy conservation, we obtain

$$\frac{dW_{\rm s}}{dt} = -P_{\rm d} = -\frac{\omega}{{\rm Q}}W_{\rm s}, \quad W_{\rm s} = W_{\rm s0}e^{-\omega t/{\rm Q}}. \tag{3.304}$$

The time for the electric field or voltage to decay to $1/e$ of its original value is equal to the unloaded *filling time*

$$T_{\rm f0} = \frac{2{\rm Q}}{\omega}. \tag{3.305}$$

C. Qualitative feature of rf cavities

Qualitatively, the rf voltage is the time derivative of the total magnetic flux linking orbit (Faraday's law of induction). Assuming that the magnetic flux density varies as $1/r$ in a coaxial structure and assuming a sinusoidal time dependent magnetic flux density, we obtain

$$V_{\rm rf} = \omega_{\rm rf}\ell \int_{r_1}^{r_2} B(r)dr = \omega_{\rm rf}\ell B_1 r_1 \ln\frac{r_2}{r_1} \approx \omega_{\rm rf} B_1 A, \tag{3.306}$$

where $A = \ell r_1 \ln(r_2/r_1) \approx \ell(r_2 - r_1)$ is the effective area of the ferrite core and B_1 is the peak magnetic flux at $r = r_1$. Note that increasing the outer radius of the ferrite core is an inefficient way of increasing the rf voltage. The peak magnetic flux in Eq. (3.306) depends on the ferrite material.

The shunt impedance of an rf structure is the resistance presented to the beam current at the resonance condition, i.e.

$$R_{\rm sh} = \frac{|V_{\rm rf}|^2}{2P_{\rm d}} = \frac{R_{\rm c}P_{\rm st}}{P_{\rm d}} \approx R_{\rm c}{\rm Q}, \tag{3.307}$$

where $P_{\rm st}$ is the power stored in the cavity and $P_{\rm d}$ is the dissipated power.

The quality factor Q of the ferrite loaded accelerating cavity is dominated by the Q value of the ferrite material itself, i.e.

$${\rm Q}_{\rm ferrite} \approx 50 - 300, \tag{3.308}$$

which alone is not adequate for the required frequency tuning range. Frequency tuning can be achieved by inducing a DC magnetic field in the ferrite core, using an external magnet or bias current to encircle the ferrite without contributing a net rf flux. By adjusting the bias current and the bias field direction, the effective permeability for rf field can be changed.

Since the Q-value of ferrite is relatively low, power dissipation in ferrite is an important consideration. The dissipation power

$$P_{\rm d} = \frac{\omega_{\rm rf}\hat{B}^2 A}{4\pi\mu{\rm Q}} \approx \frac{V_{\rm rf}^2}{4\pi\mu\omega_{\rm rf}A{\rm Q}} \tag{3.309}$$

in a cavity should be efficiently removed by cooling methods, where A is the effective area of the ferrite core. To obtain high rf voltage at low frequencies, we need a large volume of ferrite to decrease the flux density in order to minimize energy loss.

At an rf frequency above tens of MHz, the cavity size (normally 1/2 or 1/4 wavelength) becomes small enough that a resonant structure containing little or no ferrite may be built with significantly lower power loss at Q $\approx 10^4$ with a narrower bandwidth.

At frequencies of a few hundred MHz, where adequate and efficient rf power sources are commercially available, the main portion of the rf cavity can be made of copper or aluminum with a small amount of ferrite used for tuning. The cavity can still be considered as a coaxial wave guide, and Eqs. (3.287) to (3.306) remain valid. The characteristic impedance $R_{\rm c}$ of Eq. (3.290) is about 60 Ω. The stored power is $I^2R_{\rm c}$ and the power dissipation is I^2R, where I is the surface current and R of Eq. (3.296) is the surface resistance of the structure. At frequencies above a few hundred MHz, resonance frequency can be tuned only by a slotted tuner or by physically changing the size of the cavity.

D. Example: The rf cavity of the IUCF cooler injector synchrotron

The IUCF cooler injector synchrotron (CIS) is a low energy booster for the IUCF cooler ring. It accelerates protons (or light ions) from 7 MeV to 225 MeV. The cavity is a quarter-wave coaxial cavity with heavy capacitance loading.[56] To make the cavity length reasonably short and to achieve rapid tuning, required for synchrotron acceleration, ten Phillips 4C12 type ferrite rings are used. The μ of the ferrite material is changed by a superimposed DC magnetic field provided by an external quadrupole magnet. The ferrite rings return the magnet flux between the two adjacent quadrupole tips (Fig. 3.27).

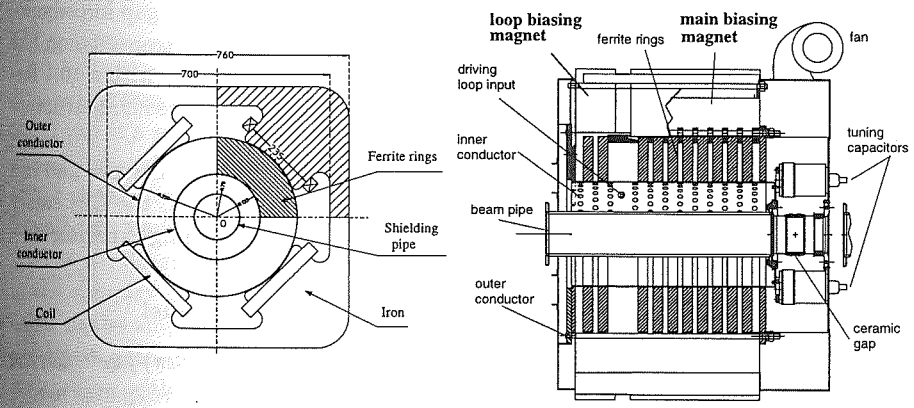

Figure 3.27: The cross section (left) and the longitudinal view of the CIS rf cavity. The external quadrupole magnet provides biased field in ferrite rings to change the effective permeability.

Analysis of such a field shows that the field direction is mostly parallel to the rf field, i.e. along the azimuthal direction, except near the tips of the quadrupole, where the biased fields in the ferrite rings are perpendicular to the rf field. In the working

[56] A. Pei, private communications.

region of the ferrite biasing strength, the effect of the perpendicular component on ferrite rf-μ is small. The effective rf-μ, to first order in wave propagation, is determined by dB/dH, as in parallel biasing analysis, rather than B/H, as in perpendicular analysis. The phenomenon of gyromagnetic resonance associated with perpendicular biasing, however, needs to be considered and avoided in the design of the cavity.

The advantages of using an external biasing magnet include making it possible to separate the rf field from the biasing elements, and the rf field in the cavity will not be affected by the biasing structure. As many windings of the bias coils as practical can be used — resulting in a smaller amperage requirement for the bias supply. In CIS and the IUCF cooler ring, the bias supplies for these external quadrupole biasing magnet type cavities are rated at only 20 A. If the biasing field is to be produced only by a bias winding threaded through the rf cavity, the number of windings is usually limited to no more than a few turns because of possible resonance and arcing. It usually takes 1000 A or more to bias such a cavity.

As the frequency changes, the power loss in ferrite material varies (usually increasing as frequency increases). As a result, it has been difficult to feed the rf generator power to the cavity efficiently because of the high voltage standing wave ratio (VSWR) caused by impedance mismatch (see Appendix B.V.3). In the CIS cavity this problem was solved by dividing the ferrite rings into two sections; the strength of the biasing magnet in each section can be adjusted by the coupling loop. The coupling coefficient can be used to compensate the change in the gap impedance, and the input impedance can be maintained constant to match the transmission line impedance of the rf amplifier. The CIS cavity is thus able to operate with a 10:1 frequency ratio with high efficiency, due to the higher impedance of a resonant structure and optimized amplifier coupling.

The loading capacitor reduces the length requirement of coaxial cavities and can also be used conveniently to switch frequency bands. For example, the CIS cavity can be operated at 0.5 – 5 MHz or 1 – 10 MHz by varying its loading capacitor.

E. Wake-function and impedance of an RLC resonator model

If we represent a charged particle of charge q by $I(t) = q\delta(t) = (1/2\pi)\int qe^{j\omega t}d\omega$, the energy loss due to the passage of an rf gap, represented by an RLC resonator model, is

$$\Delta U = \int |I(\omega)|^2 Z(\omega)d\omega = 2k_r q^2, \tag{3.310}$$

where

$$k_r = \frac{\omega_r R_{sh}}{4\pi Q}$$

is the *loss factor* of the impedance at frequency ω_r. This means that the passing particle loses energy and induces a wakefield in the cavity.

Since the longitudinal impedance is defined as the Fourier transform of the wake function,

$$Z(\omega) = \int_0^\infty W(t)e^{-j\omega t}dt = \int_{-\infty}^\infty W(t)e^{-j\omega t}dt, \tag{3.311}$$

the wake function, given by the inverse Fourier transform of the impedance, for the RLC resonator model becomes

$$W(t) = \frac{1}{2\pi}\int Z(\omega)e^{j\omega t}d\omega = 2k_r\left[\cos\tilde{\omega}_r t - \frac{1}{\tilde{\omega}_r T_{f0}}\sin\tilde{\omega}_r t\right]e^{-t/T_{f0}}\,\Theta(t), \tag{3.312}$$

where $\Theta(t) = 1$ if $t > 0$, and 0 if $t < 0$; $T_{f0} = 2Q/\omega_r$ is unloaded filling time defined in Eq. (3.305); and $\tilde{\omega}_r = \omega_r\ (1 - (1/4Q^2))^{1/2}$. If the filling time is long, then the wake potential is a sinusoidal function with angular frequency $\tilde{\omega}_r$, i.e.

$$W(t) \approx 2k_r e^{-t/T_{f0}}\cos\omega_r t.$$

Thus the filling time corresponds also to the wakefield decay time. When beams pass repetitively through the cavity, the effective voltage is the sum of the voltage supplied by the generator current and the wakefields of all beams. Beam loading is important in the design and operation of rf cavities.

VI.3 Beam Loading

A passing beam charge can induce wakefields in an rf cavity. The effective voltage at the rf gap is a superposition of voltage due to generator current and induced voltage due to induced rf current. Without proper compensation, the resulting rf voltage acting on the passing beam may cause beam deceleration in an uncontrollable manner. Thus beam loading needs to be considered in the operation of rf cavities.

The rf voltage, oscillating at frequency ω_{rf}, can be considered as a vector rotating in the complex plane at an angular frequency ω_{rf}. The magnitude of the vector is equal to the amplitude of the rf voltage, and the rf voltage seen by the beam is the projection of the rotating vector on the real axis. Now, we choose a coordinate system that rotates with the rf frequency, and thus the rf voltage is stationary in this rotating coordinate system. Let V_0 and θ be respectively the amplitude and the angle with respect to the real axis of the rf voltage vector. By definition, we have

$$V_0\cos\theta = V_0\sin\phi_s,$$

where ϕ_s is the synchronous phase angle. The representation of sinusoidal waves in a rotating frame is called a phasor diagram and is particularly useful in analyzing beam loading compensation problems.

A. Phasor

The electromagnetic fields and voltages in a standing wave rf structure are normally expressed as complex quantities, $\tilde{V} = Ve^{j(\omega t+\theta)}$, where ω is the frequency and θ is a phase angle. In the rotating coordinate system, the voltage is expressed as a phasor

$$\tilde{V} = Ve^{j\theta}. \tag{3.313}$$

Phasors are manipulated by using usual rules of complex vector algebra. The properties of rf fields can be studied by using graphic reconstruction in phasor diagrams.

B. Fundamental theorem of beam loading

The cavity provides a longitudinal electric field for particle acceleration. However, when a charged particle passes through the cavity, the image current on the cavity wall creates an electric field that opposes the particle motion. The question arises: what fraction of the electric field or voltage created by the beam affects the beam motion? The question can be addressed by the fundamental theorem of beam loading due to Wilson.[57]

Theorem: *A charged particle sees exactly $\frac{1}{2}$ of its own induced voltage.*

To prove this fundamental theorem, we assume that the stored energy in a cavity in any given mode is

$$W = \alpha V^2. \tag{3.314}$$

We assume that a fraction f of the induced voltage is seen by the inducing particle, and the effective voltage is $V_e = fV_b$, where V_b is the induced voltage in each passage. We assume further that the induced voltage lies at phase angle χ with respect to the inducing current or charge.

Now, we consider two identical charged particles of charge q, separated by phase angle θ, passing through the cavity. The total energy deposited in the cavity is

$$W_c = \alpha|\tilde{V}_b(1) + \tilde{V}_b(2)|^2 = \alpha\left(2V_b\cos\frac{\theta}{2}\right)^2 = 2\alpha V_b^2(1+\cos\theta). \tag{3.315}$$

The energy loss by these two particles is

$$\Delta U = [qV_e] + [qV_e + qV_b\cos(\chi+\theta)], \tag{3.316}$$

where the first and second brackets are the energy losses due to the first and second particles respectively. From the conservation of energy, $\Delta U = W_c$, we obtain

$$\chi = 0, \quad V_b = \frac{q}{2\alpha}, \quad V_e = \frac{1}{2}V_b, \quad f = \frac{1}{2}. \tag{3.317}$$

The result can be summarized as follows:

[57] P. B. Wilson, *AIP Conf. Proc.* **87**, 452 (1981).

1. The induced voltage of a beam must have a phase maximally opposite the motion of the charge, i.e. the phase angle $\chi = 0$.
2. $V_e = V_b/2$. The particle sees exactly 1/2 of its own induced voltage.
3. $W_c = \alpha V_b^2 = q^2/4\alpha = kq^2$, where k is the loss factor, $k = V_b^2/(4W_c)$.
4. $V_b = 2kq$ or $V_e = kq$.

C. Steady state solution of multiple bunch passage

Consider an infinite train of bunches, separated by time T_b, passing through an rf cavity gap. When the cavity is on resonance, the induced voltage seen by the particle is

$$V_b = \frac{1}{2}V_{b0} + V_{b0}(e^{-(\lambda+j\phi)} + e^{-2(\lambda+\phi)} + \cdots) = V_{b0}(-\frac{1}{2} + \frac{1}{1-e^{-(\lambda+j\phi)}}), \tag{3.318}$$

where $\phi = -(\omega-\omega_r)T_b$ [Mod 2π] is the relative bunch arrival phase with respect to the cavity phase at the rf gap; ω_r is the resonance frequency of the rf cavity; and $\lambda = T_b/T_f$ is the decay factor of the induced voltage between successive bunch passages, and $T_f = 2Q_L/\omega_r$ is the cavity time constant or the cavity filling time. Here Q_L is the loaded cavity quality factor, taking into account the generator resistance R_g in parallel with the RLC circuit of the cavity, i.e.

$$Q_L = \frac{R_{sh}R_g}{(R_{sh}+R_g)R_c} = \frac{Q_0}{1+d}, \quad d = \frac{R_{sh}}{R_g}. \tag{3.319}$$

The filling time of the loaded cavity is reduced by a factor $1/(1+d)$.

When the cavity is detuned by a detuning angle ψ,

$$\psi = \tan^{-1}\left[\frac{2Q_L(\omega-\omega_r)}{\omega_r}\right] = \tan^{-1}[(\omega-\omega_r)T_f], \tag{3.320}$$

where ω is the cavity operation frequency, the rf phase shift is

$$\phi = (\omega-\omega_r)T_b = +(T_b/T_f)\tan\psi = +\lambda\tan\psi. \tag{3.321}$$

For rf cavities used in accelerators, we have $\lambda = T_b/T_f = \omega_r T_b/2Q_L \ll 1$, and the induced voltage seen by the beam is

$$V_b = I_i R_{sh}\lambda(-\frac{1}{2} + \frac{1}{1-e^{-(\lambda+j\phi)}}) \approx I_i\frac{R_{sh}}{(1+d)}\cos\psi e^{-j\psi} \quad (\lambda\to 0), \tag{3.322}$$

where I_i is the rf image current, $V_{b0} = I_i R_{sh}T_b/T_f$, and the term $-1/2$ is neglected. The beam induced voltage across the rf gap at the steady state is exactly the rf image current times the impedance of the rf system.

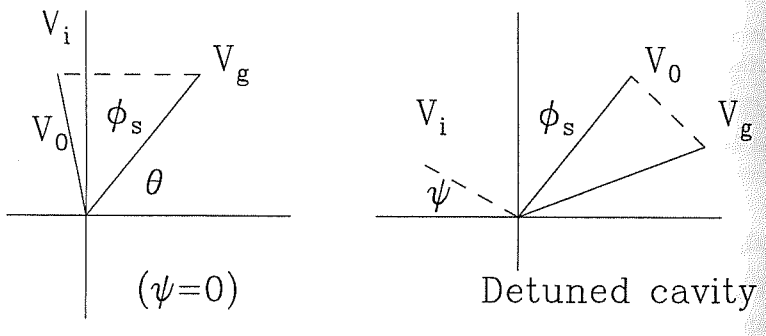

Figure 3.28: Phasor diagrams for beam loading compensation. Left: The beam loading voltage for a cavity tuned on resonance. The combination of generator voltage V_g and induced voltage V_i gives rise to a decelerating field V_0. Right: When the cavity is detuned to a detuning angle ψ, the superposition of the generator voltage V_g and the beam loading voltage V_i gives a proper cavity voltage V_0 for beam acceleration.

VI.4 Beam Loading Compensation and Robinson Instability

To provide particle acceleration in a cavity, we need a generator rf current $\tilde{I}_0 = I_0 e^{j\theta}$ with phase angle θ so that the voltage acting on the beam is $V_{acc} = V_g \cos\theta = V_g \sin\phi_s$, where ϕ_s is the synchronous phase angle. It appears that the rf system would be optimally tuned if it were tuned to on-resonance so that it had a resistive load with $V_g = I_0 R_{sh}$. However, we will find shortly that the effect of beam loading would render such a scheme unusable.

When a *short* beam bunch passes through the rf system, the image rf current I_i generated by the beam is twice the DC current, as shown in Eq. (2.211). The beam will induce $I_i R_{sh}$ across the voltage gap (see dashed line in Fig. 3.28). The voltage seen by the beam is the sum of the voltage produced by the generator current and the beam induced current. Thus the stable phase angle ϕ_s of the synchrotron motion will be changed by the induced voltage. This is shown schematically in Fig. 3.28 (left), where the required gap voltage $I_0 R_{sh}$ and the synchronous phase angle ϕ_s are altered by the voltage induced by the image current. The projection of the resultant vector V_0 on the real axis is negative, and results in deceleration of the beam.

One way to compensate the image current is to superimpose, on the generator current, current directly opposite to the image current. Such a large rf generator current at a phase angle other than that of the rf acceleration voltage is costly and unnecessary.

An alternative solution is to detune the accelerating structure.[58] The detuning angle and the generator current are adjusted so that the resultant voltage has a correct

[58] J.E. Griffin, *AIP Conf. Proc.* **87**, 564 (1981); F. Pedersen, *IEEE Tran. Nucl. Sci.* **NS-32**, 2138 (1985); D. Boussard, CERN 91-04, p. 294 (1991).

magnitude and phase for beam acceleration. This scheme will minimize the generator current. We define the following phasor currents and voltages for the analysis of this problem.

$$\begin{cases} \tilde{I}_0 = I_0 e^{j\theta} & \text{generator current necessary for accelerating voltage in the absence of beam} \\ \tilde{I}_g = I_g e^{j(\theta+\theta_g)} & \text{required generator current with beam} \\ \tilde{I}_i = -I_i = -I_b & \text{rf beam image current, } I_i \text{ is a positive quantity} \\ \tilde{V}_g = V_g e^{j\theta} & \text{required rf accelerating voltage} \\ \psi = \tan^{-1} \frac{2Q(\omega-\omega_r)}{\omega_r} & \text{detuning angle} \\ Y = I_i/I_0 & \text{ratio of image current to unloaded generator current} \end{cases}$$

The equation for a proper accelerating voltage is

$$\tilde{V}_g = I_0 R_{sh} e^{j\theta} = [I_g e^{j(\theta+\theta_g)} - I_i] R_{sh} \cos\psi e^{-j\psi}. \tag{3.323}$$

Here the induced voltage is derived from the steady state beam loading. By equating the real and imaginary parts, we obtain

$$\tan\theta_g = \frac{\tan\psi - Y\sin\theta}{1 + Y\cos\theta}, \quad I_g = I_0 \frac{1 + Y\cos\theta}{\cos\theta_g}, \tag{3.324}$$

where θ_g is the phase angle of the generator current relative to the ideal $\tilde{I}_0$. The optimal operating condition normally corresponds to $\theta_g = 0$, which minimizes I_g, i.e. the generator current is optimally chosen to be parallel to $\tilde{I}_0$, and Eq. (3.324) reduces to

$$I_g = I_0(1 + Y\sin\phi_s), \quad \tan\psi = Y\cos\phi_s. \tag{3.325}$$

Figure 3.28 (right) shows the beam loading phasor diagram with a detuned cavity angle ψ. The resultant vector of the generator voltage and the image current voltage is the effective accelerating voltage for the beam.

A. Robinson dipole mode instability

In accelerators, beams experience many sources of perturbation such as power supply ripple, mis-injection, mismatched beam profile, rf noise, voltage error, etc. Beam stability may sometimes need sophisticated active feedback systems. The topic of control and feedback is beyond the scope of this textbook. Here, we discuss only the dipole mode stability condition related to beam loading, studied by Robinson in 1964.[59]

We consider a small perturbation by shifting the arrival time of all bunches by a phase factor ξ. The accelerating rf voltage will be perturbed by the same phase factor,

$$V_{acc} = V_0 \cos(\theta - \xi) = V_0 \cos\theta + \xi V_0 \sin\theta = V_0 \sin\phi_s + \xi V_0 \cos\phi_s. \tag{3.326}$$

[59] K.W. Robinson, CEA report CEAL-1010 (1964).

where the first term is the intended accelerating voltage and the second term is the effect of phase perturbation due to an error in arrival time.

The wrong arrival time shifts the image beam current by a phase angle ξ. The perturbation to the image rf current is

$$\Delta\tilde{I}_{\rm i} = j\xi\tilde{I}_{\rm i} = -j\xi I_{\rm i}, \tag{3.327}$$

and its induced rf voltage is

$$\Delta\tilde{V}_{\rm g} = -j\xi I_{\rm i} R_{\rm sh}\cos\psi e^{-j\psi}. \tag{3.328}$$

The induced accelerating voltage is equal to the projection of the phasor voltage onto the real axis:

$$\Delta V_0 = -\xi Y V_0 \cos\psi\sin\psi. \tag{3.329}$$

The net change in accelerating voltage seen by the *bunch* becomes

$$\Delta V_{\rm acc} = \xi V_0\cos\phi_{\rm s}\left[1 - Y\frac{\sin\psi\cos\psi}{\cos\phi_{\rm s}}\right]. \tag{3.330}$$

A small perturbation in arrival time causes a perturbation in acceleration voltage proportional to the phase shift. If the voltage induced by the image charge is not significant, the bunches in the accelerator will execute synchrotron motion. Thus the equation of motion for the phasor error ξ is (see Exercise 3.6.7)

$$\ddot{\xi} = -\nu_{\rm s}^2\left(1 - Y\frac{\sin\psi\cos\psi}{\cos\phi_{\rm s}}\right)\xi. \tag{3.331}$$

Using Eq. (3.325), we find that the Robinson stability condition becomes

$$1 - Y\frac{\sin\psi\cos\psi}{\cos\phi_{\rm s}} \geq 0 \quad \text{or} \quad 1 - \frac{\sin^2\psi}{\cos^2\phi_{\rm s}} \geq 0. \tag{3.332}$$

This means that Robinson stability requires $\psi < \theta = |\frac{1}{2}\pi - \phi_{\rm s}|$. In general, Eq. (3.332) is applicable to all higher order modes. For those modes, Robinson stability can be described as follows.

Below transition energy, with $\cos\phi_{\rm s} > 0$, Robinson stability can be attained by choosing $\sin\psi < 0$, i.e. the cavity frequency is detuned with $\omega < \omega_{\rm r}$. Above transition energy, with $\cos\phi_{\rm s} < 0$, the cavity should be detuned so that $\sin\psi > 0$ or $\omega > \omega_{\rm r}$ in order to gain Robinson stability. Since the stability condition is a function of bunch intensity, instability is a self-adjusting process. Beam loss will appear until the Robinson stability condition can be achieved. Active feedback systems are used to enhance the stability of bunched beam acceleration.[60]

[60] See D. Boussard, CERN 87-03, p. 626 (1987); CERN 91-04, p. 294 (1991).

B. Qualitative feature of Robinson instability

Robinson instability can be qualitatively understood as follows. The wakefield produced in a cavity by a circulating bunch is represented qualitatively in Fig. 3.29, where the impedance of the cavity is assumed to be real.

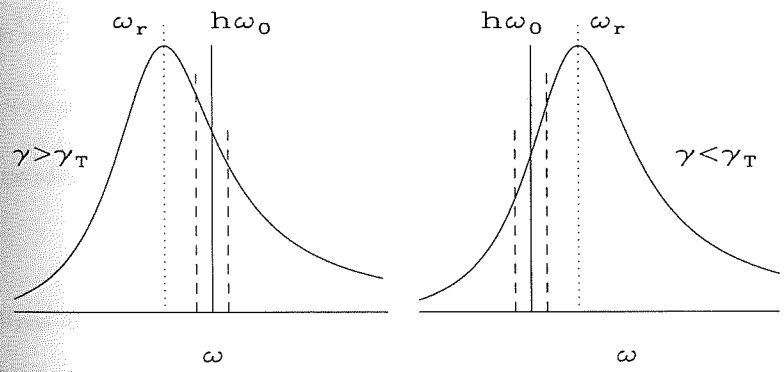

Figure 3.29: A schematic drawing of the real part of impedance arising from a wakefield induced by the circulating beam. To avoid Robinson instability, the cavity should be detuned to $h\omega_0 > \omega_{\rm r}$ above transition energy and $h\omega_0 < \omega_{\rm r}$ below transition energy. Above transition energy, higher energy particles have a smaller revolution frequency and thus lose more energy if the cavity detuning is $h\omega_0 > \omega_{\rm r}$. A similar argument applies to rf cavities operating below transition energy.

Since the revolution frequency is related to the fractional momentum spread by

$$\frac{\Delta\omega}{\omega_0} = -\eta\frac{\Delta E}{\beta^2 E_0},$$

a higher beam energy has a smaller revolution frequency above the transition energy. If the cavity is detuned so that $h\omega_0 > \omega_{\rm r}$, where $\omega_{\rm r}$ is the resonance frequency of the cavity (Fig. 3.29, left), the beam bunch at higher energy sees a higher shunt impedance and loses more energy, and the beam bunch at lower beam energy sees a lower shunt impedance and loses less energy. Thus the centroid of the beam bunch will damp in the presence of beam loading, and the dipole mode of beam motion is Robinson damped. Similarly, if the cavity is detuned such that $h\omega_0 < \omega_{\rm r}$, Robinson stability will be attained below transition energy.

Exercise 3.6

1. The skin depth $\delta_{\rm skin}$ of an AC current with angular frequency ω traveling on a conductor of bulk conductivity σ is $\delta_{\rm skin} = \sqrt{2/\mu\sigma\omega}$, where μ is the permeability.

   (a) Show that the surface resistivity defined as $R_{\rm s} = 1/\sigma\delta_{\rm skin}$ [in Ohm] is given by

$$R_{\rm s} = \sqrt{\frac{\mu\omega}{2\sigma}}.$$

Note that the surface resistivity does not depend on the geometry of the conductor.

(b) Show that the resistance of a coaxial structure is given by Eq. (3.296) with

$$R = \frac{R_s \ell}{2\pi}\left(\frac{1}{r_1} + \frac{1}{r_2}\right),$$

where ℓ is the length of the structure and r_1, r_2 are the inner and outer radii of the coaxial wave guide.

2. Show that the solution of Maxwell's equation in the cylindrical coordinate is given by Eq. (3.282).

3. In a lossless transverse electromagnetic (TEM) wave transmission line, the equation for the current and voltage is

$$\frac{\partial V}{\partial s} = -L\frac{\partial I}{\partial t}, \quad \frac{\partial I}{\partial s} = -C\frac{\partial V}{\partial t},$$

where L and C are respectively the inductance and capacitance per unit length.

(a) Show that the general solution of the right/left traveling TEM wave is given by

$$V = f(t \mp s\sqrt{LC}), \quad I = \pm\frac{1}{R_c} f(t \mp s\sqrt{LC}),$$

where $R_c = \sqrt{L/C}$ is the characteristic impedance of the line, i.e. the characteristic impedance is the impedance seen by traveling waves with $V = IR_c$.

(b) Show that the current and voltage of Eq. (3.291)

$$\begin{cases} I(s,t) = [I_0 \cos ks + j(V_0/R_c)\sin ks]e^{j\omega t} \\ V(s,t) = [V_0 \cos ks + jI_0 R_c \sin ks]e^{j\omega t} \end{cases}$$

satisfies the TEM wave equation.

4. Verify Eqs.(3.301) and plot Z vs ω for $\omega_r = 200$ MHz, $Q = 10^4$, and $R_{sh} = 25$ MΩ.

5. Evaluate the integral of Eq. (3.310) and show that the loss factor of a parallel RLC resonator is given by[61]

$$k_r = \frac{\omega_r R_{sh}}{4\pi \mathrm{Q}},$$

where R_{sh} is the shunt resistance, Q is the Q-factor, and ω_r is the resonance frequency. Verify the Fourier integral of Eq. (3.312).

6. Verify Eq. (3.322)

7. Use the following steps to derive Eq. (3.331).

[61] Use the identity $\left[1 + \mathrm{Q}^2(x - 1/x)^2\right]^{-1} = x^2\left[\mathrm{Q}^2(x^2 - r_{1+}^2)(x^2 - r_{1-}^2)\right]^{-1}$, where $r_{1\pm} = \sqrt{1 - (1/4\mathrm{Q}^2)} \pm j(1/2\mathrm{Q})$.

(a) Let ξ be the rf phase associated with the error in beam arrival time. Show that

$$\dot{\xi} = h\eta\delta_b,$$

where the overdot indicates the derivative with respect to orbiting angle θ, and δ_b is the momentum error of the beam centroid.

(b) Show that

$$\dot{\delta}_b = \frac{eV_0 \cos\phi_s}{2\pi\beta^2 E}\left[1 - Y\frac{\sin 2\psi}{2\cos\phi_s}\right]\xi.$$

Thus you have arrived at Eq. (3.331).

(c) Draw the Robinson stability region, i.e. $1 \geq (\sin 2\psi/2\cos\phi_s)Y$, in (Y, ψ) for $\phi_s = 0°, 30°, 60°, 120°, 150°, 180°$.

VII Longitudinal Collective Instabilities

As the demand for beam brightness increases, the physics of collective instabilities becomes more important. Indeed, almost all accelerators and storage rings have suffered some type of collective instability that limits beam intensity. This section provides an introduction to the collective instability in synchrotron motion induced by the wakefield, similar to the transverse collective dipole mode instability discussed in Chap. 2, Sec. VIII. The wakefield generated by the beam bunch can further induce collective motion of beam particles. In the frequency domain, the collective motion is governed by the impedance, which is the Fourier transform of the wakefield. The impedance responsible for collective instabilities can be experimentally derived from beam transfer function measurements,[62] or from passive measurements of beam loss, coherent and incoherent tune shift, and equilibrium momentum spread and emittance. The results of collective instabilities are bunch lengthening, beam brightness dilution, luminosity degradation, beam loss, and problems in machine operation.[63]

Longitudinal collective instabilities have many modes. The collective synchrotron motion can be classified according to synchrotron modes, as discussed in Sec. III, where the phase space are split into resonance islands. On the other hand, since the growth rate of the microwave instability is very large, it can be classified according to the longitudinal mode with density fluctuation. This causes a beam bunch to form microbunches, and decoherence due to nonlinear synchrotron motion generates emittance dilution.

In this introduction to the collective beam instability, we discuss only single bunch effects without mode coupling. In Sec. VII.1, we discuss the coherent frequency spectra of beams in a synchrotron. Knowledge of coherent synchrotron modes provides useful information about possible sources, and about the signature at onset, of collective instabilities. An experimental measurement of coherent synchrotron mode will be discussed. Detecting the onset of instabilities and measuring coherent synchrotron modes can help us understand the mechanism of collective instabilities. In Sec. VII.2, we study the linearized Vlasov equation with a coasting beam, and derive a dispersion relation for the collective frequency in single mode approximation. In Sec. VII.3, we list possible sources of longitudinal impedances. In Sec. VII.4, we examine the microwave instability for a beam with zero momentum spread and for a beam with Gaussian momentum spread, and discuss the Keil-Schnell criterion and the turbulent bunch lengthening. Mode coupling and coupled bunch collective instabilities and other advanced topics can be found in a specialized advanced textbooks [3].

[62] A. Hofmann, *Proc. 1st EPAC*, p. 181 (World Scientific, Singapore, 1988).

[63] See Ref. [3], and T. Suzuki, Y. Chin and K. Satoh, *Part. Accel.* **13**, 179 (1983); B. Zotter, *Proc. 3rd EPAC*, p. 273 (Edition Frontiere, Gif-sur-Yvette Cedex, 1992).

VII.1 Longitudinal Spectra

The current observed at a wall gap monitor or a BPM from a circulating charged particle is represented by a periodic δ-function in Eq. (2.211); and the corresponding frequency spectra occur at all harmonics of the revolution frequency f_0. Similarly, the current of N equally spaced circulating particles is described by Eq. (2.221), where the Fourier spectra are separated by Nf_0. Since $N \sim 10^8 - 10^{13}$, Nf_0 is well above the bandwidths of BPMs and detection instruments, the coherent rf signal is invisible. Such a beam is called a coasting or DC beam because only the DC signal is visible. This analysis is applicable to a single short bunch or equally spaced short bunches; for the effect of a finite bunch length, see Eq. (2.215). The frequency spectra of a single short bunch occur at all harmonics of the revolution frequency f_0. For B equally spaced short bunches, the coherent frequency spectra are located at harmonics of Bf_0.[64]

A. Coherent synchrotron modes

The synchrotron motion of beam particles introduces a modulation in the periodic arrival time. We expand the current Eq. (3.87) of an orbiting particle with a linear synchrotron motion in Fourier series,

$$\begin{aligned} I_e(t) &= e \sum_{\ell=-\infty}^{\infty} \delta(t - \hat{\tau}\cos(\omega_s t + \psi) - \ell T_0) \\ &= \frac{e}{T_0} \sum_{n=-\infty}^{\infty} \sum_{m=-\infty}^{\infty} j^{-m} J_m(n\omega_0 \hat{\tau}) e^{j[(n\omega_0 + m\omega_s)t + m\psi]}, \end{aligned} \tag{3.333}$$

where e is the charge, $\hat{\tau}$ and ψ are the synchrotron amplitude and phase of the particle, $\omega_s = \omega_0\sqrt{heV|\eta\cos\phi_s|/2\pi\beta^2 E}$ is the synchrotron angular frequency with ϕ_s as the rf phase of the synchronous particle, T_0 is the revolution period, and J_m is the Bessel function of order m. The resulting spectra of the particle motion are classified into synchrotron modes, i.e. there are synchrotron sidebands around each orbital harmonic n. The amplitude of the mth synchrotron sideband is proportional to the Bessel function J_m.

A bunch is made of particles with different synchrotron amplitudes and phases, the coherent synchrotron modes of the bunch can be obtained by averaging the synchrotron mode over the bunch distribution. For a ψ-independent particle distribution function $\rho(\hat{\tau}, \psi) = \rho_0(\hat{\tau})$, the beam current becomes

$$I_0(t) = \int I_e(t)\rho_0(\hat{\tau})\hat{\tau}\, d\hat{\tau}\, d\psi = I_{\rm av} \sum_{n=-\infty}^{\infty} A_{n,0} e^{jn\omega_0 t}, \tag{3.334}$$

[64] The power of a coherent signal is proportional to $N_{\rm B}^2$, where $N_{\rm B}$ is the number of particles in a bunch.

where $I_{\rm av} = N_{\rm B} e f_0$ is the average current, and $A_{n,0}$ is the Hankel transformation of ρ_0,

$$A_{n,0} = 2\pi \int_0^\infty J_0(n\omega_0\hat{\tau})\rho_0(\hat{\tau})\hat{\tau}d\hat{\tau}. \tag{3.335}$$

Note that Eq. (3.334) contains only orbital harmonics $n\omega_0$, i.e. all synchrotron sidebands of individual particles are averaged to zero. Note also that ρ_0 can be obtained from the inverse Hankel transformation, although one can detect incoherent synchrotron sidebands from the Schottky signal, whose power is about $1/N$ of the coherent ones.

Now, if there is a coherent synchrotron mode in the bunch distribution, e.g. $\rho(\hat{\tau},\psi) = \rho_0(\hat{\tau}) + \Delta\rho(\hat{\tau},\psi)$ with

$$\Delta\rho(\hat{\tau},\psi) = \rho_m(\hat{\tau})e^{j(\Omega_c t - m\psi)}, \tag{3.336}$$

where Ω_c is the coherent frequency, the coherent current signal becomes

$$I(t) = I_0(t) + \int I_e(t)\Delta\rho(\hat{\tau},\psi)\hat{\tau}d\hat{\tau}d\psi = I_0(t) + I_{\rm av}\sum_{n=-\infty}^{\infty} A_{n,m}e^{j(n\omega_0+m\omega_s+\Omega_c)t}, \tag{3.337}$$

where $A_{n,m}$ is the mth order Hankel transformation,

$$A_{n,m} = 2\pi \int_0^\infty J_m(n\omega_0\hat{\tau})\rho_m(\hat{\tau})\hat{\tau}d\hat{\tau}. \tag{3.338}$$

The mth order synchrotron sideband appears around all coherent revolution harmonics. It is a coherent synchrotron mode. Using the inverse Hankel transformation, we can deduce the beam distribution function from the amplitudes of coherent modes $A_{n,m}$. These coherent mode integrals form the kernel for the Sacherer integral equation in determining the longitudinal collective instability.[65]

The coherent synchrotron sidebands can be measured by taking the fast Fourier transform (FFT) spectrum of the longitudinal beam profile digitized at fixed times during the onset of coherent mode instability.[66] This requires a digital oscilloscope with a sizable memory. However, a spectrum analyzer (SA), tuned to a synchrotron sideband, can also measure beam power arising from the coherent synchrotron mode excitation, i.e. $|A_{n,m}|^2$. With the power spectrum of the the mth synchrotron mode known, the inverse Hankel transformation can be used to reconstruct the coherent longitudinal distribution ρ_m, which is important in identifying the source of coherent excitations. As an illustrative example, we measure the power of a synchrotron mode of a longitudinally kicked beam.

[65] F. Sacherer, *IEEE Trans. Nucl. Sci.* **NS-20**, (1973), ibid **NS-24**, (1977); see also J.L. Laclare, CERN 87-03, p. 264 (1987).

[66] X. Lu and G. Jackson, *Proc. IEEE PAC*, p. 3366 (IEEE, Piscataway, NJ, 1993).

B. Coherent synchrotron modes of a kicked beam

For simplicity, we assume an initial Gaussian equilibrium beam distribution (see Eq. (3.40) for the phase space coordinates):

$$\rho_0\left(\tau, \frac{\dot{\tau}}{\omega_s}\right) = \frac{1}{2\pi\sigma_\tau^2}\exp\left(-\frac{\tau^2 + (\dot{\tau}/\omega_s)^2}{2\sigma_\tau^2}\right). \tag{3.339}$$

When the beam is phase kicked by $\tau_{\rm k}$, the initial beam distribution becomes

$$\begin{aligned}\rho(\tau, \frac{\dot{\tau}}{\omega_s}) &= \frac{1}{2\pi\sigma_\tau^2}\exp(-\frac{\tau_{\rm k}^2}{2\sigma_\tau^2} - \frac{\hat{\tau}^2}{2\sigma_\tau^2} - \frac{\hat{\tau}\tau_{\rm k}}{\sigma_\tau^2}\cos\psi), \\ &= \frac{1}{2\pi\sigma_\tau^2}\exp(-\frac{\tau_{\rm k}^2}{2\sigma_\tau^2} - \frac{\hat{\tau}^2}{2\sigma_\tau^2})\sum_{m=-\infty}^{\infty}(-1)^m I_m(\frac{\hat{\tau}\tau_{\rm k}}{\sigma_\tau^2})e^{jm\psi},\end{aligned} \tag{3.340}$$

where $I_{-m} = I_m$. Thus the coherent distribution is

$$\rho_m(\hat{\tau}) = \frac{(-1)^m}{2\pi\sigma_\tau^2}\exp(-\frac{\tau_{\rm k}^2}{2\sigma_\tau^2} - \frac{\hat{\tau}^2}{2\sigma_\tau^2})I_m(\frac{\hat{\tau}\tau_{\rm k}}{\sigma_\tau^2}), \tag{3.341}$$

and the coherent mode integral of Eq. (3.338) becomes[67]

$$A_{n,m} = e^{-\frac{1}{2}(n\omega_0\tau_{\rm k})^2(\frac{\sigma_\tau}{\tau_{\rm k}})^2}J_m(n\omega_0\tau_{\rm k}). \tag{3.342}$$

The power of the mth sideband of a kicked beam is proportional to the square of the mth order Bessel function. For non-Gaussian beams, the power spectrum is a weighted average of Bessel functions in Eq. (3.338). We describe below an experiment measuring the coherent mode power at the IUCF Cooler.

C. Measurements of coherent synchrotron modes

The experiment started with a single bunched beam of about 5×10^8 protons at a kinetic energy of 45 MeV and harmonic number $h = 1$. The revolution frequency was $f_0 = 1.03168$ MHz and the phase slip factor was $\eta = -0.86$. The cycle time was 5 s, while the injected beam was electron-cooled for about 3 s. The typical bunch length, which could be adjusted by varying the rf voltage, was about 4.5 m (50 ns) FWHM, i.e. the rms bunch length σ_τ was about 20 ns.

The bunched beam was kicked longitudinally by phase-shifting the rf cavity wave form (see Sec. III). A function generator was used to generate a 0 to 10 V square wave to control the phase kick. The rf phase lock feedback loop, which normally locks the rf cavity to the beam, was switched off. The resulting phase oscillations of the bunch relative to the rf wave form were measured by a phase detector, which was used to

[67] See e.g. 6.633.4 of Ref. [26]

calibrate the control voltage for the phase shifters versus the actual phase shift. Both the phase error due to control nonlinearity and the parasitic amplitude modulation of the IUCF Cooler rf systems were kept to less than 10%. The response time of the step phase shifts was limited primarily by the inertia of the rf cavities, which had a quality factor Q of about 40. The magnitude of the phase shift was varied by the size of the applied step voltage.

To measure the FFT spectrum of the coherent signal, the spectrum analyzer (SA) was triggered about 5 ms before the phase shift. The power observed at a synchrotron sideband from the SA is shown in Fig. 3.30, where the top and bottom traces show the SA responses at the sidebands of the first harmonic $f_0 - f_s$ and the sixth harmonic $6f_0 - f_s$ vs time. The kicked amplitude was 90 ns, or equivalently $\omega_0\tau_k = 0.58$ rad. The resolution bandwidth of SA was 100 Hz, thus the measurement of the sideband power was taken at 10 ms after the phase kick. The sideband power shown in Fig. 3.30 was proportional to $|A_{1,1}|^2$ for the upper trace and $|A_{6,1}|^2$ for the lower trace.

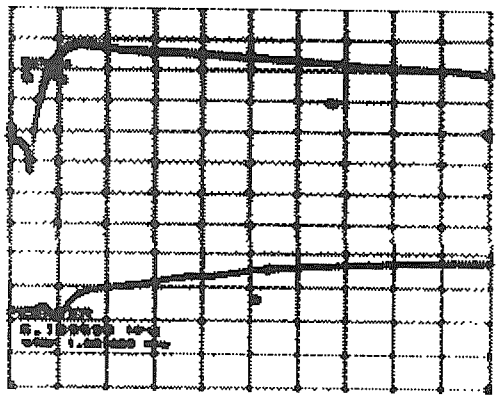

Figure 3.30: The synchrotron sideband power of a kicked beam observed from a spectrum analyzer tuned to the first revolution sideband (upper trace) and the 6th revolution sideband (lower trace) as a function of time. The revolution frequency was 1.03168 MHz. The setting of the SA was resolution bandwidth 100 Hz, video bandwidth 100 Hz, and frequency span 0 Hz. Note that the sideband power decreased with time for the first harmonic and increased for the 6th harmonic, probably because of electron cooling in the IUCF Cooler. The vertical axis is coherent synchrotron power in dB, and the horizontal axis is time at 10 ms per division.

Since $\omega_0\tau_k \approx 0.58$ and $\sigma_\tau = 20$ ns for the case shown in Fig. 3.30, we obtain

$$A_{1,1} \sim e^{-0.0083} J_1(0.58), \quad A_{6,1} \sim e^{-0.299} J_1(3.48).$$

Thus the initial power at the fundamental harmonic sideband, which is proportional to $|A_{1,1}|^2$, after the phase kick will be a factor of 6 larger than that of the 6th orbital harmonic. As the synchrotron phase amplitude decreases because of electron cooling, the power $A_{1,1}$ decreases because $J_1(\omega_0\tau_a)$ decreases with decreasing $\omega_0\tau_a$, where τ_a is the synchrotron amplitude. On the other hand, as $6\omega_0\tau_a$ decreases, $J_1(6\omega_0\tau_a)$ increases. Therefore the power spectrum shown in the lower plot of Fig. 3.30 increases with time.

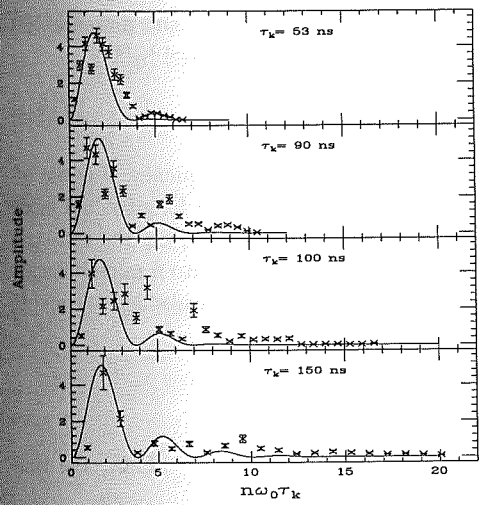

Figure 3.31: Measured $m = 1$ synchrotron sideband power vs frequency for different phase kicked amplitudes is compared with theory based on a Gaussian beam distribution. Plots from top to bottom correspond to a kicking amplitude (time) of 53, 90, 100 and 150 ns. These data were normalized to the peak. The curves were theoretical predictions with no adjustable parameter except the normalization constant.

Figure 3.31 shows the power of the $m = 1$ sideband, for various kicking times, as a function of $\omega\tau = n\omega_0\tau_k$, where n is the revolution harmonic. For a kicked Gaussian beam, the power $P_{n,1}$ is proportional to $|A_{n,1}|^2$:

$$P_{n,1} \sim |A_{n,1}|^2 = e^{-(n\omega_0\tau_k)^2(\sigma_\tau/\tau_k)^2} |J_1(n\omega_0\tau_k)|^2. \tag{3.343}$$

Because the actual power depends on the beam intensity, all data are normalized at the first peak around $n\omega_0\tau_k \approx 1.8$. Solid curves are obtained from Eq. (3.343) normalized to the peak. The effect of finite bunch length is visible in Fig. 3.31.

When a bunched beam encounters collective instability, the observed sideband power $|A_{n1}|^2$ is proportional to the weighted average of the coherent mode density $\rho(\hat{\tau})$ shown in Eq. (3.342). Measurement of $A_{n,1}$ for all orbital harmonics can be used to obtain the coherent mode distribution function. Similarly, setting up the central frequency at the second synchrotron harmonic, we can measure the $m = 2$ synchrotron modes for the kicked beam.

VII.2 Collective Microwave Instability in Coasting Beams

For coasting beams, there is no rf cavity and the unperturbed distribution function is a function only of the off-momentum coordinate $\delta = \Delta p/p_0$. Let $\Psi_0(\delta)$ be the normalized distribution function with $\int \Psi_0 d\delta = 1$. Because of the impedance of the ring, the beam generates wakefields, which in turn perturb particle motion.

A self-consistent distribution function obeys the Vlasov equation

$$\frac{d\Psi}{dt} = \frac{\partial\Psi}{\partial t} + \dot{\theta}\frac{\partial\Psi}{\partial\theta} + \dot{\delta}\frac{\partial\Psi}{\partial\delta} = 0, \tag{3.344}$$

where the overdot is the derivative with respect to time t. In the presence of a wakefield, we assume that the distribution function is approximated by[68]

$$\Psi = \Psi_0(\delta) + \Delta\Psi_n e^{j(\Omega t - n\theta)}, \tag{3.345}$$

where Ψ_0 is the unperturbed distribution, Ω is the coherent frequency, θ is the orbiting angle, and $\Delta\Psi_n(\delta)$ is the perturbation amplitude for the longitudinal mode n. The perturbation causes density fluctuation along the machine, i.e. the collective instability of mode number n can cause a coasting beam to split into n microbunches.

By definition, the energy gain/loss per revolution due to the wakefield is equal to the current times the longitudinal impedance:

$$\Delta E\Big|_{\text{per turn}} = Z_{\|}\left(eI_0 \int \Delta\Psi_n d\delta\right) e^{j(\Omega t - n\theta)},$$

where the impedance is evaluated at the collective frequency Ω. Thus, the time derivative of the δ coordinate in a coasting beam becomes

$$\dot{\delta} = \frac{\omega_0}{2\pi\beta^2 E}\left(eI_0 Z_{\|} \int \Delta\Psi_n d\delta\right) e^{j(\Omega t - n\theta)}. \tag{3.346}$$

Since $|\Delta\Psi_n| \ll \Psi_0$ at the onset threshold of collective instability, we linearize the Vlasov equation to obtain

$$j(\Omega - n\dot{\theta})\Delta\Psi_n = -\frac{\omega_0 e I_0 Z_{\|}}{2\pi\beta^2 E}\frac{\partial\Psi_0}{\partial\delta}\left(\int \Delta\Psi_n d\delta\right). \tag{3.347}$$

Using $\dot{\theta} = \omega$ and integrating Eq. (3.347), we obtain the dispersion relation

$$1 = j\frac{eI_0 n\omega_0 (Z_{\|}/n)}{2\pi\beta^2 E}\int \frac{\partial\Psi_0/\partial\delta}{\Omega - n\omega}d\delta = j\frac{eI_0 n^2\omega_0 (Z_{\|}/n)}{2\pi\beta^2 E}\int \frac{\Psi_0}{(\Omega - n\omega)^2}\frac{\partial\omega}{\partial\delta}d\delta, \tag{3.348}$$

where partial integration has been carried out in the second equality.

The eigenfrequency Ω of the collective motion is given by the solution of the dispersion relation. If the imaginary part of the coherent mode frequency is negative, i.e. $\operatorname{Im}\Omega < 0$, the perturbation amplitude grows exponentially, and the beam encounters the collective microwave instability. The terminology is derived from the fact that the coherent frequency observed is in the microwave frequency range. With the relation $\omega = \omega_0 - \omega_0\eta\delta$, the dispersion integral can be analytically obtained for some distribution functions of the beam. First we examine possible sources of longitudinal impedance.

[68] Here we assume a single longitudinal mode. In general, the perturbing distribution function should be written as a linear superposition of all possible modes. The frequencies of the collective motion are eigenfrequencies of the coupled system.

VII.3 Longitudinal Impedance

The impedance of an accelerator is related to the wake function by

$$Z_{\|}(\omega) = \int_{-\infty}^{\infty} W_{\|}(t)e^{-j\omega t}d\omega, \tag{3.349}$$

and similarly, the wake function is related to the impedance by

$$W_{\|}(t) = \frac{1}{2\pi}\int_{-\infty}^{\infty} Z_{\|}(\omega)e^{j\omega t}d\omega. \tag{3.350}$$

Since the wakefield obeys the causality principle, the impedance must not have singularities in the lower complex plane,[69] and the real and imaginary parts of the impedance are related by the Hilbert transform

$$\operatorname{Re} Z_{\|}(\omega) = -\frac{1}{\pi}\int_{\text{P.V.}} d\omega' \frac{\operatorname{Im} Z_{\|}(\omega')}{\omega' - \omega}, \tag{3.351}$$

$$\operatorname{Im} Z_{\|}(\omega) = +\frac{1}{\pi}\int_{\text{P.V.}} d\omega' \frac{\operatorname{Re} Z_{\|}(\omega')}{\omega' - \omega}, \tag{3.352}$$

where P.V. stands for the principal value integral.

Because the wake function is real, the impedance has the symmetry property

$$Z_{\|}(-\omega) = Z_{\|}^*(\omega). \tag{3.353}$$

Thus the real part of the longitudinal impedance is positive and is a symmetric function of the frequency. In fact, the property of $Z_{\|}(\omega)/\omega$ is similar to that of $Z_{\perp}(\omega)$. Without making the effort to derive them, we list below some sources of commonly used impedance models.

A. Space-charge impedance

Let a be the radius of a uniformly distributed coasting beam, and let b be the radius of a beam pipe (Fig. 3.32). The electromagnetic fields of the coasting beam are

$$E_r = \begin{cases} \dfrac{e\lambda r}{2\pi\epsilon a^2} \\ \dfrac{e\lambda}{2\pi\epsilon r} \end{cases} \qquad B_\phi = \begin{cases} \dfrac{\mu_0 e\lambda\beta c r}{2\pi a^2} & r \le a \\ \dfrac{\mu_0 e\lambda\beta c}{2\pi r} & r > a \end{cases} \tag{3.354}$$

where λ is the particle's line density, e is the charge, βc is the speed, and ϵ_0 and μ_0 are the permittivity and permeability of the vacuum.

Now we consider a small fluctuation in the line density and current with

$$\lambda = \lambda_0 + \lambda_1 e^{j(\Omega t - n\theta)}, \quad I = I_0 + I_1 e^{j(\Omega t - n\theta)},$$

[69] See K.Y. Ng, p. 472 in Ref. [12]; see also Appendix 2.

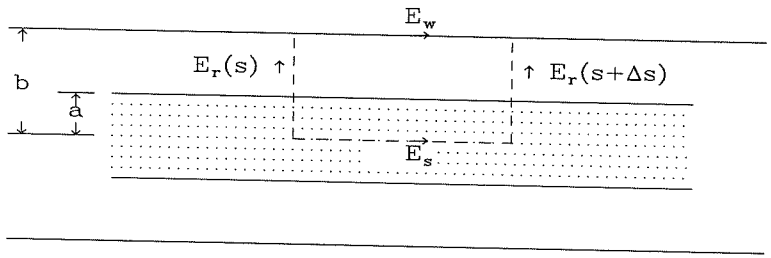

Figure 3.32: The geometry of a uniformly distributed beam with radius a in a beam pipe of radius b. The induced electric fields that arise from impedance are shown schematically. The rectangular loop is used for the path integral of Faraday's law.

where $I_0 = e\beta c\lambda_0$ and $I_1 = e\beta c\lambda_1$. The perturbation generates an electric field on the beam. Using Faraday's law

$$\oint \vec{E}d\vec{l} = -\frac{\partial}{\partial t}\int \vec{B}\cdot d\vec{\sigma}$$

along the loop shown in Fig. 3.32, where $d\vec{\sigma}$ is the surface integral, we obtain

$$(E_s - E_w)\Delta s + \frac{eg_0}{4\pi\epsilon_0}[\lambda(s+\Delta s) - \lambda(s)] = -\Delta s\frac{\mu_0 e\beta c g_0}{4\pi}\frac{\partial\lambda}{\partial t},$$

where E_s and E_w are the electric fields at the center of the beam pipe and at the vacuum chamber wall, and the geometry factor $g_0 = 1+2\ln(b/a)$ is obtained from the integral along the radial paths from the beam center to the vacuum chamber wall.[70] Assuming that the disturbance is propagating at the same speed as the orbiting beam particles, i.e. $\partial\lambda/\partial t = -\beta c(\partial\lambda/\partial s)$, the electric field acting on the circulating beam becomes

$$E_s = E_w - \frac{eg_0}{4\pi\epsilon_0\gamma^2}\frac{\partial\lambda}{\partial s}, \tag{3.355}$$

where the factor $1/\gamma^2$ arises from cancellation between the electric and magnetic fields.

For most accelerators, the vacuum chamber wall is inductive at low and medium frequency range. Let $L/2\pi R$ be the inductance per unit length, then the induced wall electric field is

$$E_w = \frac{L}{2\pi R}\frac{dI_w}{dt} = \frac{e\beta^2c^2L}{2\pi R}\frac{\partial\lambda}{\partial s}. \tag{3.356}$$

Thus we have

$$E_s = -e\left[\frac{g_0}{4\pi\epsilon_0\gamma^2} - \frac{\beta^2c^2L}{2\pi R}\right]\frac{\partial\lambda}{\partial s}.$$

[70] If the impedance is averaged over the beam cross section, the geometric factor becomes $g_0 = \frac{1}{2} + 2\ln(b/a)$. On the other hand, if the perturbation is on the surface of the beam, the geometry factor becomes $g_0 = 2\ln(b/a)$.

The total voltage drop in one revolution on the beam is

$$\Delta U = -e\beta cR\frac{\partial\lambda}{\partial s}\left[\frac{g_0Z_0}{2\beta\gamma^2} - \omega_0 L\right], \tag{3.357}$$

where $\beta c = \omega_0 R$ is the speed of the orbiting particles, and $Z_0 = 1/\epsilon_0 c = 377$ ohms is the vacuum impedance. Using $R(\partial\lambda/\partial s) = (\partial\lambda/\partial\theta)$, and $e\beta c\lambda_1 = I_1$, we obtain the impedance, defined as the voltage drop per unit current, as

$$\frac{Z_\parallel}{n} = -\frac{\Delta U}{nI_1} = -j\left[\frac{g_0Z_0}{2\beta\gamma^2} - \omega_0 L\right]. \tag{3.358}$$

The first term in Eq. (3.358) is the space-charge impedance and the second term is the inductance of the vacuum chamber wall. Typical values of the space-charge impedance at transition energy are listed in Table VII.3.

Table 3.7: Typical space-charge impedance at $\gamma = \gamma_T$.

	AGS	RHIC	Fermilab BST	Fermilab MI	KEKPS
γ_T	8.7	22.5	5.4	20.4	6.8
$\lvert Z_{\parallel,sc}\rvert/n$ [Ω]	13	1.5	30	2.3	20

In fact, the vacuum chamber wall is not perfectly conducting, and E_w has a resistive contribution that depends on the conductivity, microwave frequency, and skin depth.

B. Resistive wall impedance

Because the resistivity of the vacuum chamber wall is finite, part of the wakefield can penetrate the vacuum chamber and cause energy loss to the beam. Penetration of electromagnetic wave into the vacuum chamber can be described by Maxwell's equations

$$\nabla\times\vec{E} = -\mu\frac{\partial\vec{H}}{\partial t}, \qquad \nabla\times\vec{H} = \vec{J} = \sigma_c\vec{E}, \tag{3.359}$$

where σ_c is the conductivity and μ is the permeability. Here we have used Ohm's law, and neglected the contribution of the displacement current for electromagnetic wave with not so high frequencies.[71] From Eq. (3.359), we find

$$\nabla^2\vec{E} = \mu\sigma_c\frac{\partial\vec{E}}{\partial t}. \tag{3.360}$$

[71] For frequencies $\omega \ll \sigma_c/\epsilon \approx \sigma_c Z_0 c \approx 10^{19}$ Hz, where ϵ is the permittivity, the displacement current contribution to Maxwell's equation is small.

Substituting the ansatz of the electric field

$$\vec{E} = \hat{s}\, E_0 \exp\{j(\omega t - kx)\}$$

into Eq. (3.360), where x is the distance in the vacuum chamber wall, we obtain the wave number

$$k = (1-j)\sqrt{|\omega|\sigma_c\mu/2}.$$

The imaginary part of the wave number is the inverse of the penetration depth, or equivalently, the skin depth is $\delta_{\rm skin} = \sqrt{2/\mu\sigma_c\omega}$. The electromagnetic fields penetrate a skin depth inside the vacuum chamber wall. The resistance due to the electric field becomes

$$Z_{\|}^{\rm real} \approx \frac{2\pi R}{2\pi b\sigma_c\delta_{\rm skin}} = \frac{Z_0\beta}{2b}\left(\frac{|\omega|}{\omega_0}\right)^{1/2}\delta_{\rm skin,0}, \tag{3.361}$$

where Z_0 is the vacuum impedance, β is Lorentz's relativistic velocity factor, b is the vacuum chamber radius, $\delta_{\rm skin,0} = \sqrt{2/\mu\sigma_c\omega_0}$ is the skin depth at frequency ω_0, μ is the permeability, and σ_c is the conductivity of the vacuum chamber. Since the magnetic energy is equal to the electric energy, the magnitude of the reactance is equal to the resistance. The resistive wall impedance becomes

$$Z_{\|}(\omega) = (1 + j\,{\rm sgn}(\omega))\,\frac{Z_0\beta}{2b}\left(\frac{|\omega|}{\omega_0}\right)^{1/2}\delta_{\rm skin,0}, \tag{3.362}$$

where the sign function, ${\rm sgn}(\omega) = +1$ if $\omega > 0$ and -1 if $\omega < 0$, is added so that the impedance satisfies the symmetry property.

C. Narrowband and broadband impedances

Narrowband impedances arise from parasitic modes in rf cavities and cavity-like structures in accelerators. Broadband impedances arise from vacuum chamber breaks, bellows, and other discontinuities in accelerator components. The longitudinal narrowband and broadband impedances can conveniently be represented by an equivalent RLC circuit

$$Z(\omega) = \frac{R_{\rm sh}}{1 + j{\rm Q}(\omega/\omega_{\rm r} - \omega_{\rm r}/\omega)}, \tag{3.363}$$

where $\omega_{\rm r}$ is the resonance frequency, $R_{\rm sh}$ is the shunt impedance, and Q is the quality factor. The high order mode (HOM) of rf cavities is a major source of narrowband impedances. Parameters for narrowband impedances depend on the geometry and material of cavity-like structures.

For a broadband impedance, the Q-factor is usually taken to be 1, and the resonance frequency to be the cut-off frequency

$$\omega_{\rm r,bb} = \omega_0 R/b = \beta c/b, \tag{3.364}$$

where ω_0 is the revolution frequency, R is the average radius of the accelerator, and b is the vacuum chamber size. The magnitude of the broadband shunt impedance can range from 50 ohms for machines constructed in the 60's and 70's to less than 1 ohm for recently constructed machines, where the vacuum chamber is carefully smoothed.

To summarize, the longitudinal impedances $Z_{\|}(\omega)/\omega$ or $Z_{\|}/n$ are schematically shown in Fig. 3.33, where the solid and dashed lines correspond to the real and imaginary parts respectively. The symmetry of the impedance as a function of ω is also shown.

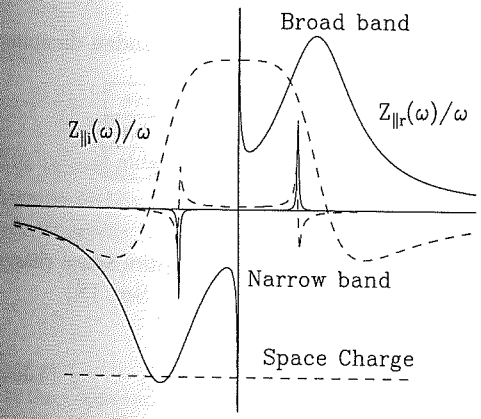

Figure 3.33: Schematic of a longitudinal impedance that includes broadband, narrowband, and space-charge impedances. Including the resistive wall impedance in the longitudinal impedances, we find that $|{\rm Re}(Z_{\|}/\omega)|$ becomes large at $\omega \approx 0$.

VII.4 Microwave Single Bunch Instability

The negative mass instability was predicted in 1960's. Experimental observations were obtained in the intersecting storage rings (ISR), where microwave signal was detected in the beam debunching process. Subsequently, it was observed in almost all existing high intensity accelerators. In this section, we discuss the single bunch microwave instability.

A. Negative mass instability without momentum spread

First, we consider negative mass instability. In the absence of momentum spread with $\Psi_0(\delta) = \delta_{\rm d}(\delta)$, where $\delta = \Delta p/p_0$ and $\delta_{\rm d}(x)$ is the Dirac δ-function, the solution of Eq. (3.348) is

$$\left(\frac{\Omega}{n\omega_0}\right)^2 = -j\frac{eI_0\, Z_{\|}/n}{2\pi\beta^2 E}\,\eta\,. \tag{3.365}$$

The condition for having a real Ω is $-j(Z_{\|}/n)\eta > 0$. This condition is only satisfied for a space-charge (capacitive) impedance below the transition energy, or an induc-

tive impedance above the transition energy. If $Z_{\|}/n$ is capacitive, e.g. space-charge impedance, the collective frequency is a real number below the transition energy with $\eta < 0$. This results in a collective frequency shift without producing collective instabilities. On the other hand, if the impedance is inductive, the collective frequency becomes a complex number below the transition energy, and the solution with a negative imaginary part gives rise to collective instability. For resistive impedance, the beam with a zero momentum spread is unstable. Table VII.4 shows the characteristic behavior of microwave collective instability.

Table 3.8: Characteristic behavior of collective instability without Landau damping.

	$Z_{\|}/n$	capacitive	inductive	resistive
Below transition	$\eta < 0$	stable	unstable	unstable
Above transition	$\eta > 0$	unstable	stable	unstable

The terminology of negative mass instability is derived from a pure space charge effect. The *mass*, $-\eta$, in the longitudinal Hamiltonian (see Chap. 2, Sec. IX)

$$H = -\frac{1}{2}\eta\left(\frac{\Delta p}{p_0}\right)^2 - \frac{eV}{2\pi h\beta^2 E_0}[\cos\phi - \cos\phi_s + (\phi - \phi_s)\sin\phi_s], \tag{3.366}$$

is negative above the transition energy with $\eta > 0$. A higher energy particle takes longer to complete one revolution, or it appears to have a negative mass. Since the "microwave instability" resulting from the space-charge impedance occurs when $\eta > 0$, it is also called *negative mass instability*. However, a beam with a small frequency spread can also encounter microwave instability at $\gamma < \gamma_T$ if the impedance is inductive, or resistive.

B. Landau damping with finite frequency spread

For a beam with a finite momentum spread with $\eta \neq 0$, the coherent mode frequency can be obtained by solving the dispersion relation. In this case, there is a finite region of impedance value where the growth rate of collective instability is zero, and collective motion is Landau damped.

If the distribution function is a symmetric function of momentum deviation δ, the threshold impedance for microwave instability is reflectively symmetric with respect to the real part of the impedance. Depending on the actual distribution function, the threshold of collective instability can be estimated from the dispersion relation.[72]

[72] A.G. Ruggiero and V.G. Vaccaro, CERN ISR TH/68-33 (1968); see also Ref. [3].

For example, we consider a Gaussian beam model of a coasting beam given by

$$\Psi_0 = \frac{1}{\sqrt{2\pi}\sigma_\delta}\exp\left\{-\frac{\delta^2}{2\sigma_\delta^2}\right\},$$

where $\delta = \Delta p/p_0$ and σ_δ is the rms momentum spread. In the limit of small frequency spread, the distribution becomes the Dirac δ-function. The rms frequency spread of the beam becomes $\sigma_\omega = \omega_0\eta\sigma_\delta$. The dispersion relation can be integrated to obtain

$$\frac{Z_{\|}}{n} = j\frac{4\pi\beta^2 E\sigma_\delta^2\eta}{eI_0}J_G^{-1}, \tag{3.367}$$

where

$$J_G = \sqrt{\frac{2}{\pi}}\int_{-\infty}^{\infty}\frac{xe^{-x^2/2}}{x + \tilde{\Omega}/(n\omega_0\eta\sigma_\delta)}dx = 2[1 + j\sqrt{\pi}yw(y)], \tag{3.368}$$

$\tilde{\Omega} = \Omega - n\omega_0$, and $w(y)$ is the complex error function with $y = -\tilde{\Omega}/(\sqrt{2}n\omega_0\eta\sigma_\delta)$. Asymptotically, we have $J_G \to y^{-2}$ as $y \to \infty$. Thus in the limit of zero detuning (or zero frequency spread), Eq. (3.367) reduces to Eq. (3.365).

We usually define the effective U and V parameters, or U' and V' parameters as

$$U + jV = \frac{eI_0\,(Z_{\|}/n)}{2\pi\beta^2 E\sigma_\delta^2\eta}, \qquad U' + jV' = \frac{eI_0\,(Z_{\|}/n)}{\beta^2 E\delta_{\text{FWHM}}^2\eta}. \tag{3.369}$$

For the Gaussian beam, we find $\delta_{\text{FWHM}} = \sqrt{8\ln 2}\,\sigma_\delta$. In terms of U and V parameters, Eq. (3.367) becomes $-j(U + jV)J_G/2 = 1$.

The solid line in the left plot of Fig. 3.34 shows the threshold V' vs U' parameters of collective microwave instability with $\text{Im}(\Omega) = 0$. Dashed lines inside the threshold curve correspond to stable motion, and the dashed lines outside the threshold curve are unstable with growth rates $-(\text{Im}\,\Omega)/\sqrt{2\ln 2}\,\omega_0\eta\sigma_\delta = 0.1, 0.2, 0.3, 0.4$, and 0.5 respectively. The right plot of Fig. 3.34 shows the threshold V' vs U' parameters, from inside outward, for the normalized distribution functions $\Psi_0(x) = 3(1-x^2)/4$, $8(1-x^2)^{3/2}/3\pi$, $15(1-x^2)^2/16$, $315(1-x^2)^4/32$, and $(1/\sqrt{2\pi})\exp(-x^2/2)$. All distribution functions, except the Gaussian distribution, are limited to $x \leq 1$. Note that a distribution function with a softer tail, i.e. a less sudden cutoff, gives a larger stability region in the parametric space.

C. Keil-Schnell criterion

Figure 3.34 show that the stability region depends on beam distribution. Based on experimental observations and numerical calculations of the dispersion relation, a simplified estimation of the stability condition is to draw a circle around the origin in the impedance plane

$$\left|\frac{Z_{\|}}{n}\right| \leq \frac{2\pi\beta^2 E\sigma_\delta^2|\eta|F}{eI_0}, \tag{3.370}$$

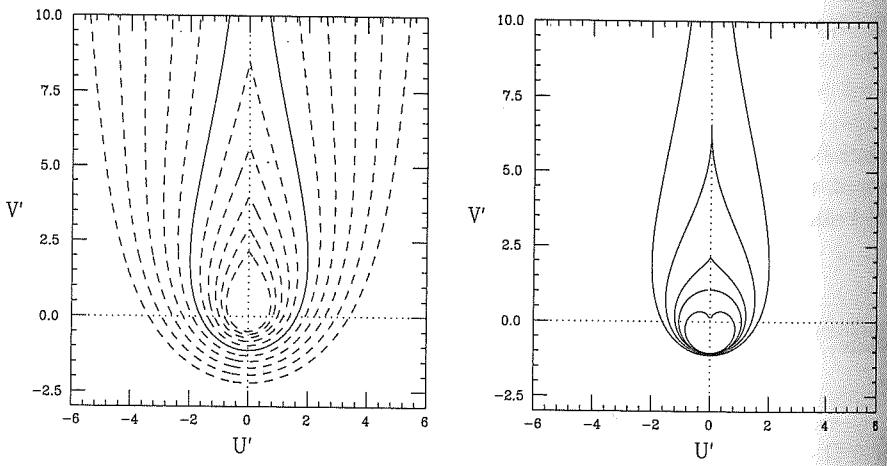

Figure 3.34: Left: The solid line shows the parameters V' vs U' for a Gaussian beam distribution at a zero growth rate. Dashed lines inside the threshold curve are stable. They correspond to $-\mathrm{Im}\,\Omega/(\sqrt{2\ln 2}\,\omega_0\eta\sigma_\delta) = -0.1, -0.2, -0.3, -0.4$, and -0.5. Dashed lines outside the threshold curve have growth rates $-\mathrm{Im}\,\Omega/(\sqrt{2\ln 2}\,\omega_0\eta\sigma_\delta) = 0.1, 0.2, 0.3, 0.4$, and 0.5 respectively. Right: The threshold V' vs U' parameters for various beam distributions.

where F is a form factor that depends on the distribution function. For a Gaussian beam, $F = 1$; and for a tri-elliptical distribution with $\Psi_0(x) = 8(1-x^2)^{3/2}/3\pi$, $F \approx 0.94$ [3]. This is the Keil-Schnell criterion.[73]

The Keil-Schnell criterion states that if the beam is stable, the total longitudinal energy drop from impedance, $eI_0|Z_\parallel|$, per unit frequency spread $n|\eta|\sqrt{2\pi}\sigma_\delta$ for mode number n should be less than the total energy spread $\sqrt{2\pi}\beta^2 E\sigma_\delta$ of the beam.

Since the microwave growth rate is usually fast, and the the wavelength of the coherent wave is usually small compared with the bunch length, the Keil-Schnell criterion can be applied to the bunched beam by replacing the average current I_0 by the peak current $\hat{I}$, i.e.

$$\left|\frac{Z_\parallel}{n}\right| \le \frac{2\pi\beta^2 E\sigma_\delta^2|\eta|F}{e\hat{I}}, \tag{3.371}$$

where $\hat{I} = F_\mathrm{B} I_0$, and $F_\mathrm{B} = 2\pi/\sqrt{2\pi}\sigma_\phi$ is the bunching factor. This Boussard conjecture has been well tested in the Intersecting Storage Ring (ISR).[74]

[73] E. Keil and W. Schnell, CERN-ISR-TH-RF/69-48 (July 1969); A.G. Ruggiero and V.G. Vaccaro, CERN ISR TH/68-33 (1968).

[74] Since the growth rate of the microwave instability is normally very fast, the threshold condition can be obtained from the local peak current of the beam. See e.g. J.M. Wang and C. Pellegrini, *Proc. 11th HEACC*, p. 554 (1980).

D. Microwave instability near transition energy

Near the transition energy, Landau damping for microwave single bunch instability vanishes because of a small synchrotron frequency spread. The Keil-Schnell criterion is not applicable in this region. For a pure capacitive impedance, e.g. space-charge impedance, instability occurs when $\gamma \ge \gamma_\mathrm{T}$. For a pure inductance impedance, instability exists only below transition. Since the beam distribution function is non-adiabatic in the transition energy region, determination of microwave instability needs careful evaluation of the dispersion integral.

We assume a model of collective microwave instability such that the longitudinal modes are nearly decoupled and thus the coherent growth rate can be obtained by solving the dispersion relation Eq. (3.348). Furthermore, we assume a Gaussian beam model with the threshold impedance determined by the peak current. The peak current is located at the center of the bunch $\Delta\phi = 0$, and the distribution function is therefore given by (see Sec. IV.1)

$$\Psi_0(\delta) = \sqrt{\frac{3\alpha_{\delta\delta}}{\pi}}\,e^{-3\alpha_{\delta\delta}\delta^2}, \tag{3.372}$$

where $\alpha_{\delta\delta}$ is given by Eq. (3.177). The peak current is

$$\hat{I} = I_0\sqrt{\frac{3(\alpha_{\phi\phi}\alpha_{\delta\delta} - \alpha_{\phi\delta}^2)}{\pi\alpha_{\delta\delta}}} = I_0\frac{\sqrt{3\pi}}{\tilde{A}\sqrt{\alpha_{\delta\delta}}}, \tag{3.373}$$

where I_0 is the average current and $\tilde{A}$ is the rms phase-space area of the beam. The dispersion integral can be integrated to obtain the coherent mode frequency given by

$$1 = j\frac{3eI_0\,(Z_\parallel/n)}{2\pi^{3/2}\beta^2 E\eta}\frac{\pi\sqrt{3\alpha_{\delta\delta}}}{\tilde{A}}\,J_\mathrm{G}^{-1}, \tag{3.374}$$

where

$$J_\mathrm{G} = 2[1 + j\sqrt{\pi}yw(y)], \quad y = -\frac{\Omega}{n\omega_0\eta}\sqrt{6\alpha_{\delta\delta}}.$$

For a given broadband impedance model with constant $Z_\parallel/n$, we can find the eigenvalue of the growth rate Im $(\Omega(\mathrm{t}))$ by solving Eq. (3.374).[75] Landau damping plays an important role in damping collective instability. The region of collective instability can be estimated by using the Keil-Schnell criterion.

The solution of Eq. (3.374) shows that the growth rate near the transition energy is nearly equal to the growth rate without Landau damping. This is easy to understand:

[75] see e.g. S.Y. Lee and J.M. Wang, *IEEE Trans. Nucl. Sci.* **NS-32**, 2323 (1985). The impedance model $Z_\parallel/n = 5 - j(Z_{\parallel,\mathrm{sc}}/n)$ ohms was used to study the growth rate around the transition energy for RHIC. Microwave instability below transition may arise from the real impedance. Because of a large space-charge impedance, the growth rate appears to be larger above the transition energy.

at $\gamma = \gamma_T$, the frequency spread of the beam becomes zero, and Landau damping vanishes. Fortunately, the growth rate is also small at $\gamma \approx \gamma_T$.

The total growth factor across the transition energy region can be estimated by

$$G = \exp\left\{\int (-\mathrm{Im}\Omega)_{\mathrm{unstable}} dt\right\}. \tag{3.375}$$

The total growth factor is a function of the scaling variable $|Z_{\|}/n|N_b/\tilde{A}$. Note that the growth factor is much smaller if the initial phase-space area is increased. Phase-space dilution below transition energy has become a useful strategy in accelerating high intensity proton beams through transition energy. The CERN PS and the AGS employ this method for high intensity beam acceleration. Bunched beam dilution can be achieved either by using a high frequency cavity as noise source or by mismatched injection at the beginning of the cycle.

The distribution function model Eq. (3.372) does not take into account nonlinear synchrotron motion near the transition energy. For a complete account of microwave instability, numerical simulation is an important tool near transition energy.[76] A possible cure for microwave instability is to pass through transition energy fast with a transition energy jump. Furthermore, blow-up of phase-space area before transition energy crossing can also alleviate the microwave growth rate.

We have discussed microwave instabilities induced by a broadband impedance. In fact, it can also be generated by a narrowband impedance. Longitudinal bunch shapes in the KEK proton synchrotron (PS) were measured by a fast bunch-monitor system, which showed the rapid growth of the microwave instability at the frequency of 1 GHz and significant beam loss just after transition energy (see Fig. 3.35).[77] Temporal evolution of the microwave instability is explained with a proton-klystron model. The narrowband impedance of the BPM system causes micro-bunching in the beam that further induces wakefield. The beam-cavity interaction produces the rapid growth of the microwave instability. This effect is particularly important near the transition energy, where the frequency spread of the beam vanishes, and the Landau damping mechanism disappears.

E. Microwave instability and bunch lengthening

When the current is above the microwave instability threshold, the instability can cause micro-bunching. The energy spread of the beam will increase until the stability condition is satisfied. For proton or hadron accelerators, the final momentum spread of the beam may be larger than that threshold value caused by decoherence of the synchrotron motion.

[76] W.W. Lee and L.C. Teng, *Proc. 8th Int. Conf. on High Energy Accelerators*, CERN, p. 327 (1971); J. Wei and S.Y. Lee, *Part. Accel.* **28**, 77-82 (1990); S.Y. Lee and J. Wei, *Proc. EPAC*, p. 764 (1989); J. McLachlan, private communications on ESME Program.

[77] K. Takayama *et al.*, *Phys. Rev. Lett.*, **78**, 871 (1997).

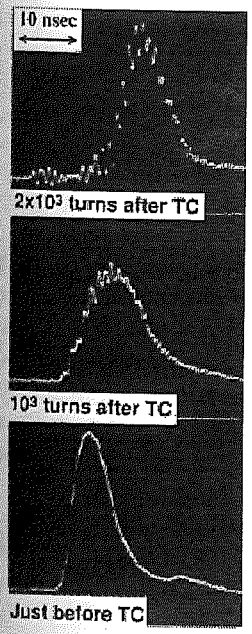

Figure 3.35: The longitudinal beam profiles observed at KEK PS revealing microwave bunching in the tail of the bunch. The bottom figure shows the longitudinal bunch profile before the transition energy, the middle figure at 1 ms after the transition energy, and the top figure at 2 ms after the transition energy. The microwave instability occurs near the transition energy for lack of Landau damping. The instability was found to be driven by a narrowband impedance caused by the BPM system. [Courtesy of K. Takayama, KEK]

For electron storage rings, the final momentum spread is equal to the microwave instability threshold due to synchrotron radiation damping. Using the Keil-Schnell-Boussard condition of Eq. (3.371), we find

$$\sigma_\theta = \omega_0 \sigma_t = \left(\frac{eI_0|\eta Z_{\|}/n|}{(2\pi)^{3/2} F \nu_s^2 \beta^2 E}\right)^{1/3}, \tag{3.376}$$

where ν_s is the synchrotron tune. Note that the bunch length depends only on the parameter $\xi = (I_0|\eta|/\nu_s^2\beta^2 E)$ provided that the impedance does not depend on the bunch length. Chao and Gareyte showed that the bunch lengths of many electron storage rings scaled as

$$\sigma_\theta \sim \xi^{1/(2+a)}. \tag{3.377}$$

This is called Chao-Gareyte scaling law. For a broadband impedance, we have $a = 1$. The scaling law is not applicable if the impedance depends on the beam current and bunch length.

F. Microwave instability induced by narrowband resonances

At low energy, the longitudinal space charge potential, shown as the first term in Eq. (3.357), can be large for high intensity beam bunch. It requires a costly large rf cavity potential to keep beam particles bunched inside the rf bucket. In particular,

if it requires a beam gap for a clean extraction, and for minimizing the effect of the electron-cloud instability.

The longitudinal space charge potential can be compensated by the inductive impedance shown in the second term of Eq. (3.357). We consider a cavity with ferrite ring filling a pillbox. The inductance is

$$L = \frac{2\mu'\mu_0\ell}{4\pi}\ln\frac{R_2}{R_1}, \tag{3.378}$$

where μ' is the real part of the ferrite permittivity, R_1 and R_2 are the inner and outer radii of the ferrite rings, and ℓ is the length of the pillbox cavity. The inductive inserts carried out at PSR experiment employs coaxial pillbox cavity with 30 ferrite rings each with width 2.54 cm, 12.7 cm inner diameter (id), and 20.3 cm outer diameter (od). The Proton Storage Ring (PSR) at Los Alamos National Laboratory compresses high intensity proton beam from the 800 MeV linac into a bunch of the order of 250 ns. The parameters for PSR are $C = 90.2$ m, $\gamma_T = 3.1$, $\nu_x = 3.2$, $\nu_z = 2.2$, $\nu_s = 0.00042$, and $f_0 = 2.8$ MHz.

To cancel the space charge impedance at 800 MeV for PSR at the harmonic $h = 1$, one requires about 3 pillbox cavities. The experimental test for this experiment was indeed successful.[78] Unfortunately, the beam also encounters collective microwave beam instability at high intensity. The left plot of Fig. 3.36 shows the initial bunched coasting beam, and the right plot shows the microbunching of the beam under the action of three ferrite inserts.

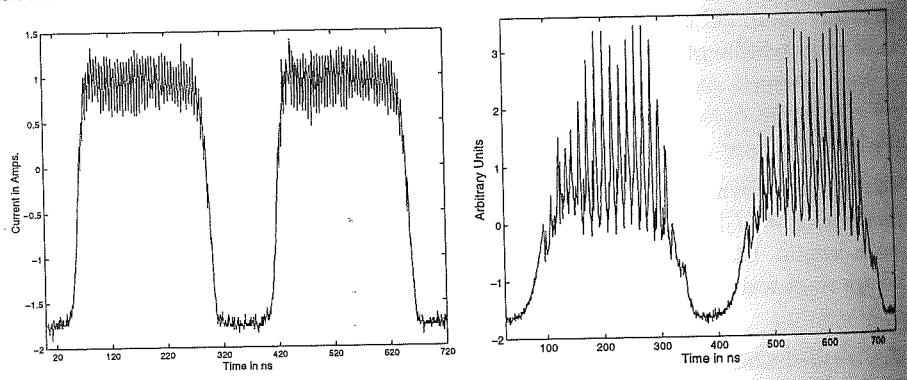

Figure 3.36: The longitudinal beam profiles observed at PSR the bunched coasting beam in the presence of inductive inserts, where three 1-m long ferrite ring cavities were installed in the PSR ring. [Courtesy of R. Macek, LANL]

The microwave instability is induced by a narrowband impedance with $Q \approx 1$ at the center frequency of $f_{\rm res} \approx 27 f_0$.[79] Although the inductive inserts can be used

[78] M.A. Plum, *et al.*, Phys. Rev. Special Topics, Accelerators and Beams, **2**, 064201 (1999).
[79] see C. Beltran, Ph.D. thesis, Indiana University (2003).

to cancel the space charge impedance, the pillbox cavity can generate a narrowband impedance to cause microwave instability of the beam at higher harmonics. In order to alleviate this problem, it is necessary to broaden the narrowband impedance by either choosing different design geometries for different ferrite inserts, or by heating the ferrite so that the imaginary part (μ'') of the permittivity is larger at the cavity resonance frequency. At PSR, the cavities was heated to 125-150° C, so that the beam is below the microwave instability threshold.

Exercise 3.7

1. In synchrotrons, beam bunches are filled with a gap for ion-clearing, abort, extraction kicker rise time, etc. Show that the frequency spectra observed from a BPM for short bunches filled with a gap have a diffraction-pattern-like structure. Specifically, find the frequency spectra for 10 buckets filled with 9 equal intensity short bunches. The revolution frequency is assumed to be 1 MHz.

2. Show that the impedance of Eq. (3.363) has two poles in the upper half of the ω plane, and find their loci. Use the inverse Fourier transformation to show that the wake function of the RLC resonator circuit is

$$W_{\|} = \frac{R_{\rm sh}\omega_{\rm r}}{Q}e^{-\omega_{\rm r}t/2Q}\left[\cos\tilde{\omega}_{\rm r}t - \frac{1}{\sqrt{4Q^2-1}}\sin\tilde{\omega}_{\rm r}t\right],$$

where $\tilde{\omega}_{\rm r} = \omega_{\rm r}\sqrt{1-1/4Q^2}$.

3. The parameters of the SLC damping ring are $E = 1.15$ GeV, $\nu_x = 8.2$, $\nu_z = 3.2$, $\alpha_c = 0.0147$, $\gamma\epsilon_{x,z} = 15\ \pi$ mm-mrad, $\sigma_{\Delta p/p} = 7.1\times10^{-4}$, $V_{\rm rf} = 800$ kV, $C = 35.270$ m, $h = 84$, $f_{\rm rf} = 714$ MHz, $\rho = 2.0372$ m, and the energy loss per revolution is $U_0 = 93.1$ keV. If the threshold of bunch lengthening is $N_{\rm B} = 1.5\times10^{10}$, use the Keil-Schnell formula to estimate the impedance of the SLC damping ring.[80]

4. We assume that the growth rate of microwave instability in a quasi-isochronous electron storage ring can be obtained from Eq. (3.365). For electron beams, synchrotron motion is also damped because of the energy dependence of synchrotron radiation energy loss. The damping rate is given by $\tau_s = 2ET_0/\mathcal{J}_sU_0$, where E is the energy of the particle, T_0 is the revolution period, the damping partition $\mathcal{J}_s \approx 2$, $U_0 = C_\gamma E^4/\rho$, $C_\gamma = 8.85\times10^{-5}$ m/(GeV^3), and ρ is the bending radius. Assuming that the growth rate is equal to the damping rate at equilibrium, find the tolerable impedance as a function of the machine parameters. Discuss an example of an electron storage ring at $E = 2$ GeV.

5. Consider a pillbox-like cavity with length ℓ (see Sec. VII.4). The cavity is filled with ferrite rings with inner and outer radii a and b respectively. Show that the longitudinal

[80] G.E. Fisher *et al.*, *Proc. 12th HEACC*, p. 37 (1983); L. Rivkin, *et al.*, *Proc. 1988 EPAC*, p. 634 (1988); see also P. Krejcik, *et al.*, *Proc. 1993 PAC*, p. 3240 (1993). The authors of the last paper observed sawtooth instability at the threshold current $N_{\rm B} = 3\times10^{10}$.

impedance for TM_{010} mode is[81]

$$\frac{Z_{\|}}{\ell} = j\frac{Z_0}{2\pi a}\sqrt{\frac{\mu' - j\mu''}{\epsilon_r}}\,\frac{H_0^{(1)}(k_c a)H_0^{(2)}(k_c b) - H_0^{(1)}(k_c b)H_0^{(2)}(k_c a)}{H_1^{(1)}(k_c a)H_0^{(2)}(k_c b) - H_0^{(1)}(k_c b)H_1^{(2)}(k_c a)}.$$

where $H_m^{(n)}$ are Hankel functions which represent incoming and outgoing waves, $Z_0 = 377\Omega$ is the impedance of free space. $k_c = \omega\sqrt{\mu\epsilon} = k\sqrt{\epsilon_r(\mu' - j\mu'')}$, $k = \frac{\omega}{c} = \omega\sqrt{\mu_0\epsilon_0}$ in vacuum, ϵ_r is the relative permittivity and μ' and μ'' are the real and complex parts of the relative complex permeability.

[81] The general formula to calculate the shunt impedance is $\Delta V = -IZ_{\|} = -E_s\ell$, where E_s is the longitudinal electric field, ℓ is the total length, and I is obtained by Ampere's law: $I = \oint H dl = 2\pi a H_\phi$.

VIII Introduction to Linear Accelerators

By definition, any accelerator that accelerates charged particles in a straight line is a linear accelerator (linac).[82] Linacs includes induction linacs; electrostatic accelerators such as the Cockcroft-Walton, Van de Graaff and Tandem; radio-frequency quadrupole (RFQ) linacs; drift-tube linacs (DTL); coupled cavity linacs (CCL); coupled cavity drift-tube linacs (CCDTL); high-energy electron linacs, etc. Modern linacs, almost exclusively, use rf cavities for particle acceleration in a straight line. For linacs, important research topics include the design of high gradient acceleration cavities, control of wakefields, rf power sources, rf superconductivity, and the beam dynamics of high brightness beams.

Linacs evolved through the development of high power rf sources, rf engineering, superconductivity, ingenious designs for various accelerating structures, high brightness electron sources, and a better understanding of high intensity beam dynamics. Since electrons emit synchrotron radiation in synchrotron storage rings, high energy e^+e^- colliders with energies larger than 200 GeV per beam can be attained only by high energy linacs. Current work on high energy linear colliders is divided into two camps, one using superconducting cavities and the other using conventional copper cavities. In conventional cavity design, the choice of rf frequency varies from S band to millimeter wavelength at 30 GHz in the two beam acceleration scheme. Research activity in this line is lively, as indicated by bi-annual linac, and annual linear collider conferences.

Since the beam in a linac is adiabatically damped, an intense electron beam bunch from a high brightness source will provide a small emittance at high energy. The linac has also been considered as a candidate for generating coherent synchrotron light. Many interesting applications will be available if high brilliance photon beam experiments, such as LCLS, SASE, etc., are successful.

This section provides an introduction to a highly technical and evolving branch of accelerator physics. In Sec. VIII.1 we review some historical milestones. In Sec. VIII.2 we discuss fundamental properties of rf cavities. In Sec. VIII.3 we present the general properties of electromagnetic fields in accelerating cavity structures. In Sec. VIII.4 we address longitudinal particle dynamics and in Sec. VIII.5, transverse particle dynamics. Since the field is evolving, many advanced school lectures are available.

VIII.1 Historical Milestones

In 1924 G. Ising published a first theoretical paper on the acceleration of ions by applying a time varying electric field to an array of drift tubes via transmission lines; subsequently, in 1928 R. Wideröe used a 1 MHz, 25 kV rf source to accelerate potas-

[82] See G.A. Loew and R. Talman, *AIP Conf. Proc.* **105**, 1 (1982); J. Le Duff, CERN 85-19, p. 144 (1985).